University *of the* Western Cape

FABRICATION OF NANOMATERIALS FROM BIOMASS FOR ADSORPTION AND ANTIMICROBIAL APPLICATIONS

By

COSMAS CHINEDU UCHE

BTech Pollution Control (*Federal University of Technology, Owerri*)
MSc Pollution Control (*Federal University of Technology, Owerri*)

A thesis submitted in fulfilment of the requirements for the degree of

Doctor of Philosophy in Chemistry

In the

Department of Chemistry
Faculty of Natural Sciences
University of the Western Cape

Supervisor: Prof. Leslie Petrik

Co-Supervisor: Dr Chionyedua Theresa Onwordi

SEPTEMBER 2020

DECLARATION OF AUTHORSHIP

I herein, declare that "*Fabrication of nanomaterials from biomass for adsorption and antimicrobial applications*" is my original work and that it has not been submitted for any degree or examination in any other university. Furthermore, all the resources used or quoted have been indicated and acknowledged by appropriate references.

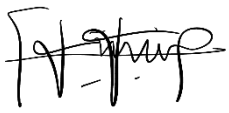

COSMAS C. UCHE **SEPTEMBER 2020**

ABSTRACT

The Black soldier fly (BSF) is an environmentally friendly and sustainable insect utilised in the decomposition of organic waste. This is due to its voracious consumption capability, disruptive functions and economic importance. The sustained global increase in commercial BSF farming has resulted in an expanded waste generation from its carcases to which beneficial uses ought to be developed. This study focused on the beneficial use of the generated waste by extracting chitosan from waste pupae and commercially reared BSF adult carcases. The study also considered the conversion of the extracted chitosan to nanofibres and nanoparticles for application in adsorption of inorganic Pb^{2+} or Cd^{2+} and antimicrobial studies, respectively. To achieve the aim of this study, the optimal extraction conditions of chitin and chitosan from both pupal exuviae and adult BSF waste materials were attained after a series of experiments. The extraction process involved three stages which were demineralisation, deproteination and deacetylation. The extracted adult and pupal chitin and chitosan were characterised using Fourier transform infrared spectroscopy (FTIR), thermogravimetric analysis (TGA), X-ray diffraction studies (XRD), high resolution scanning electron microscopy (HRSEM) and solid-state carbon nuclear magnetic resonance spectroscopy (^{13}C NMR). Additionally, the adult (ACH20_9) and pupal (PCH21_9) chitosan samples, due to their solubility, were further characterised to determine their molecular weight, fat and water binding capacities, solubility and ash contents. The pupal chitosan was transformed to nanofibres and nanoparticles using electrospinning and electrospraying techniques, respectively. The nanofibres were used for adsorption of Pb^{2+} or Cd^{2+} from aqueous solutions in a batch process after crosslinking with tannic acid while the nanoparticles were applied in antimicrobial and cytotoxic studies. The results obtained showed that the optimal demineralisation conditions for both samples were 1.0 M NaOH, 100 min, 50 °C; optimal conditions for deproteination were 1.0 M NaOH, 14 h, 95 °C for pupae samples and 1.0 M NaOH, 12 h, 95 °C for adult samples while deacetylation was 70% NaOH, 100 °C, 5 h for both samples. The two chitin samples were of the α-form with the scissoring of the Amide 1 band at 1621 and 1650 cm^{-1}. Both chitosan samples were of lower molecular weight (179 and 198 kDa) with excellent solubility in 1.0% acetic acid (93.4±2.4 and 92.7±3.1%), fat (420.70±5.4 and 392.30±3.6%) and water (530.26±4.2 and 462.65±5.1%) binding capacities and very low ash content (0.73±0.01 and 0.86±0.02%) for pupae and adult chitosan, respectively. The chitin yields (dry weight basis) of the pupal and adult BSF waste materials were 14.1 and 5.3% while the chitosan yields were 11.3 and 2.5%, respectively. It was observed that the pupal BSF waste had 3 times more chitin yield and 4.5 times more

chitosan yield than the adult BSF waste material. Due to the better yield, the pupal BSF chitosan (PCH21_9) was selected for further investigations.

Chitosan nanofibre (ES-D3) was successfully fabricated from the PCH21_9 without blending with a synthetic polymer, using electrospinning technique. The optimal electrospinning conditions were; flow rate of 0.3 mL/h, solution concentration of 5 wt%, applied voltage of 25 kV and tip-to-collector distance of 100 mm. The obtained ES-D3 at the optimum conditions had an average fibre diameter of 128 nm. The characterisation of the nanofibres using FTIR showed that the fibres maintained their chemical integrity and had the characteristic Amide 1, 11 and 111 signals of chitosan at 1674, 1533 and 1315 cm^{-1}, respectively. However, the electrospinning process influenced the thermal properties of the chitosan nanofibres (ES-D3) by imparting reduced thermal stability (258 ^{o}C) compared to the pupal BSF chitosan (306 ^{o}C).

Chitosan nanoparticles (BSF_NPs) were further synthesised from the PCH21_9. The chitosan nanoparticles showed similar spectral features as the ES-D3 but with different morphological features from both PCH21_9 and ES-D3 under HRSEM examination. The average size of 289±98 nm was determined for the BSF_NPs using the dynamic light scattering technique. A high positive zeta potential value of 54.7±2.96 mV was also obtained for the BSF_NPs in solution with a polydispersity index of 0.16.

Tannic acid was used to crosslink the ES-D3 to achieve stability in aqueous solutions. The optimal concentration of the crosslinker was 5 wt%. The crosslinked mats (TA_CHS_2) had an increased fibre diameter of 72% more than the ES-D3 nanofibres (142±65 nm). The TA_CHS_2 adsorbents were not soluble in 1.0 M acetic acid, deionised water and 1.0 M NaOH solutions and the fibrous morphologies were maintained after 72 h of contact time. Therefore, the TA_CHS_2 showed stability in aqueous solution needed for adsorption studies while maintaining the characteristic Amide 1, 11 and 111 functional groups of chitosan. The presence of the peak at 1661 cm^{-1} at a lower frequency with an increased signal compared to the ES-D3 is an indication of a successful crosslinking. Other peaks observed on the TA_CHS_2 adsorbents were 1322 cm^{-1} (CH_2 bend and CH_3 symmetric distortion of the amide III), 1200 cm^{-1} (C-O stretching mode of the ester moiety) and 2878 - 2958 cm^{-1} (symmetric and asymmetric stretching of the C-H from the carboxylic group).

The crosslinked nanofibres were used for adsorption of inorganic Pb^{2+} or Cd^{2+} from aqueous solution in a batch process. The result showed that the equilibrium adsorption was attained after 60 min of contact with an adsorption capacity of 90.41 and 87.56 mg/g for Pb^{2+} or Cd^{2+}, respectively. The study further revealed that the Langmuir and the Pseudo-second order kinetic models have correlation coefficients (R^2) greater than 0.99 for both Pb^{2+} or Cd^{2+}. These two

models appropriately fitted the obtained adsorption data and precisely explained the adsorption processes. The thermodynamic studies showed that the adsorption process was endothermic, spontaneous with increased randomness at the solid-liquid boundary, as shown by the values of standard enthalpy change (ΔH°) (17.57 or 9.74 kJ/mol), standard entropy change (ΔS°) (68.25 or 43.02 J/mol.K) and standard Gibbs free energy change (ΔG°) (at various temperatures) for Pb^{2+} or Cd^{2+}, respectively. The regeneration of the TA_CHS_2 adsorbent was achieved using 0.01 M NaOH solution, 89 and 86% desorption were attained for Pb^{2+} or Cd^{2+}, respectively after three consecutive regeneration cycles.

Further investigation conducted included the antimicrobial studies focusing on the effectiveness of the PCH21_9 and BSF_NPs in eradicating microbial cells of *E. faecalis*, *S. mutans* or *C. albicans* using the Time-kill analysis and Kaplan-Meier survival function test. The result showed that PCH21_9 and BSF_NPs were effective in eradicating the *E. faecalis* or the *S. mutans.* The BSF_NPs was more effective as it killed the organisms within 30 min of contact while the PCH21_9 eradicated all the microbes within 2 and 8 h for *S. mutans* or *E. faecalis*, respectively. Both PCH21_9 and BSF_NPs showed fungistatic action against *C. albicans* as the organisms' mass was reduced significantly but the organisms re-emerged after 2 h of contact time. Finally, the study demonstrated that the PCH21_9 and BSF_NPs were not toxic on KMST-6 human skin fibroblast cell lines. The result of the investigation showed that both the PCH21_9 and BSF_NPs did not inhibit the growth of skin cells, rather the cells proliferated up to 9% or 5% for PCH21_9 and BSF_NPs, respectively compared to the control samples.

In all, this study has demonstrated that useful biopolymers, such as chitin and chitosan could be obtained from waste materials of commercial BSF rearing. This study is, therefore, reporting the synthesis of nanofibres and nanoparticles from BSF chitosan and their subsequent applications in adsorption and antimicrobial studies, respectively.

KEYWORDS

Adsorption

Nanofibres

Nanoparticles

Electrospinning

Electrospraying

Waste materials

Biomass

Black soldier fly

Chitosan

Chitin

Antimicrobial

Lead

Cadmium

Streptococcus mutans

Enterococcus faecalis

Candida albicans

ACADEMIC OUTPUTS

1 Publication related to this study

Chionyedua T. Onwordi, Cosmas C. Uche, Alechine E. Ameh and Leslie F. Petrik (2019). Comparative study of the adsorption capacity of lead (II) ions onto bean husk and fish scale from aqueous solution. *Journal of Water Reuse and Desalination,* **9**(3): 249-262. *doi:* 10.2166/wrd.2019.061.

Uche, C.C., Zimri, M.N., Onwordi, C.T., Fatoba, O.O., Massima Mouele E.S., Missengue, R, M., Omoniyi, E.O. and Petrik, L.F. Properties of chitin and chitosan biomaterials isolated from commercially reared Black soldier fly waste. Submitted to Biomaterials.

2 Presentations at scientific conferences

Cosmas Uche; Monushia Zimri; Chionyedua Onwordi; Olarenwaju Fatoba, Missengue Roland and Leslie Petrik (2018). Physicochemical characterisations of structural polymers from *Hermetia illucens.* Proceedings of the 7th European association for chemical and molecular sciences (EuCheMS) Chemistry Congress, Liverpool, United Kingdom 26 - 30 August 2018. (https://www.euchems2018.org/programme/browse-posters/?session_id=6531). Abstract No: PE95.

Cosmas Uche, Chionyedua Onwordi, Alexander Naechev, Yuri Kochnev and Leslie Petrik (2018). Electrospinning of chitosan/polyvinylpyrrolidone blend on titanium-coated track-etched membrane. Proceedings of 5th South Africa – JINR Symposium with the theme "Advances and challenges in Physics within JINR and South Africa", Erinvale, Somerset West, South Africa, 4-9 Nov; 2018.

Franschke Soudens, Chionyedua T. Onwordi, Cosmas C. Uche, Leslie F. Petrik (2019). Adsorption studies of Cu^{2+} ions from aqueous solution using acid-treated fish scale as efficient low-cost adsorbent. Proceedings of 4th Annual Symposium of American Chemical Society (*Nigeria Chapter*), University of Lagos, Lagos, Nigeria 4 - 6 March 2019.

Chionyedua Onwordi, Cosmas Uche and Leslie Petrik (2018). Isolation and characterisation of collagen from scales of white Craoker fish (*Micropogonica furnieri*) using modified acid and alkali processes. Proceedings of the 7th European association for chemical and molecular sciences (EuCheMS) Chemistry Congress, Liverpool, United Kingdom 26 - 30 August 2018. (https://www.euchems2018.org/programme/browse-posters/?session_id=6531). Abstract No: PL43.

Onwordi, C.T., Uche, C.C., Badmus, K.O., Zimri, M.N, and Petrik, L.F (2018). Determination of agricultural waste point of zero charge: Usefulness in the adsorption of Cu (II) ion from aqueous solutions. Proceedings of 57 Conference of Society of Toxicology, Atalanta, USA 11 - 15 March 2018.

C.T. Onwordi, C.C. Uche, A.E. Ameh and L.F. Petrik (2018). Comparative study of the adsorption capacity of lead (II) ions onto bean husk and fish scale from aqueous solution. Proceedings of 5th Royal Society of Chemistry early career Symposium, Liverpool, United Kingdom 30 - 31 August 2018. http://www.rsc.org/events/detail/30662/ecs2018-5th-rsc-early-career-symposium.

DEDICATION

This work is dedicated to:

the memory of my beloved parents, Pa Nathan Nduaṅusionwu Uche and Ezinne Cecilia Nwanyisunday Uche.

AND

my darling wife and better half Cosmas-Uche, Christiana Ogemdi and to my lovely children Chimbusomma and Munachimso.

ACKNOWLEDGEMENTS

My appreciation goes to God Almighty, the author and finisher of my faith, the unseen hand in all my successes and the silent listener to all my thoughts. He is always beside me providing the wisdom and the strength to navigate through life challenges.

My deepest gratitude goes to my ebullient and amiable supervisor, the academic "IROKO" and the silent force in the success of many in the ENS team, **Professor Leslie Felicia Petrik**. You are indeed a true definition of motherhood. God bless the day and the source of my meeting you. You have demystified Professorship and demonstrated that people could achieve their dreams irrespective of their background. As Goethe said, "Treat people as if they were what they ought to be and you help them to become what they are capable of being". You indeed treated me awesomely as though I could reach the heavens. Here I am today because of you Prof. God bless you! My appreciation also goes to the most wonderful co-supervisor, **Dr Chionyedua Theresa Onwordi**. What a personality! One of the most charitable beings I have met. She has a heart of gold. Thank you for all those kind words and positive mind-set; they were instrumental to my attaining this enviable height. I sincerely appreciate both of you for your support, inspiration and excellent supervision.

My heartfelt gratitude goes to my beloved wife and help-meet **Christiana Ogemdi** for her support, perseverance and guiding our kids in my absence. Your support and undying love have been my pillar of strength. Indeed, you are a blessing to me.

My gratitude also extends to my siblings and family members: Samuel, Evarestus, Precious, Chinasa, Onyinyechi, Amarachi and Chinwe. I say thank you for the enduring support. To my uncles Dee Jonathan Nwachukwu, "Duruekwueme aku 1 of Ihiagwa" Ozo Stanley Onyewuotu and Supol Nichodemus Omeje, you are true uncles, friends, father figures and a saving grace at a point in my life. To Samson Oselusi, thank you for everything. To "*ndi enyi ka nwanne*" Engr Uchenna Nnaokoro, Engr Eberendu Ikechukwu and Ekwa Temerity, thank you, I appreciate you. To my colleagues and mentors at FUTO, especially Professor Emeka Oguzie, Professor John D. Njoku and others too numerous to mention. I say *"unu emela, chi m gozie unu"*.

To the wonderful team at Environmental and Nanosciences Research Group (ENS): Dr Emmanuel Ameh, Dr Emile Massima, the Abegundes, Jean-Luc Mukaba, Dr Kassim Badmus, Dr Omoniyi Pereao, Dr Chris Bode-Aluko, Dr Olanrewaju Fatoba, Dr Paul Chuks Eze, Dr Mero-Lee Cornelius, Dr Roland Missengue, George Ndilowe, Monushia Zimri, Raissa Andong Omores, Sheyi Emmanuel, and those I could not mention because of limited space, I gratefully acknowledge you all.

How can I forget Vanessa Kellerman (Mama V), Denzel and Ilse. You were exceptional and always willing to assist. Thank you for those orders and the orderliness you brought to ENS.

My well deserved appreciation extends to **Mrs Annette Olivier** of the Oral and Dental Research Institute, Faculty of Dentistry and **Dr Dorcas Wusu** and **Oladapupo** "**Dipo" David** for assisting with the *in vitro* cytotoxicity testing, I say thank you. To Dr Amir Omer I say thank you for your assistance with the antimicrobial investigations. I am also grateful to Mr Adrian Jacobs of Physics Dept, UWC (SEM analysis), Mr Yunus Kippie of Pharmacy Department, UWC (FTIR and TGA), Remmy Bucher of iThemba Labs (XRD) and Professor Edith Beukes (NMR, UWC).

"The financial assistance of the National Research Foundation (NRF) of South Africa and The World Academy of Sciences (TWAS) towards this study is hereby acknowledged". Similarly, the financial support of AgriProtein Technologies and the provision of the Black soldier fly waste materials is highly appreciated. The Federal University of Technology Owerri and the entire staff of Environmental Technology Department is not left out and hereby higly appreciated for their support.

TABLE OF CONTENTS

LIST OF FIGURES

LIST OF TABLES

ABBREVIATIONS

^{13}C NMR	carbon nuclear magnetic resonance
AFD	average fibres diameter
APD	average pore diameter
ATCC	American type culture collection
ATR-FTIR	attenuated total reflection Fourier-transform infrared spectroscopy
BHI	brain heart infusion
C. albicans	*Candida albicans*
CA	cellulose acetate
CFU	colony forming unit
CHS	chitosan
C/N	the ratio of carbon to nitrogen
CP/MAS	cross polarization/magic angle spinning
DA	degree of acetylation
DD	degree of deacetylation
DMEM	Dulbecco's modified Eagle's medium
DMSO	dimethyl sulfoxide
DTG	derivative of thermal gravimetry profile
E. coli	*Escherichia coli*
EDTA	ethylenediaminetetraacetic acid
HMW	high molecular weight
HRSEM	high-resolution scanning electron microscope
ICP-OES	inductively coupled plasma-optical emission spectroscopy
kDa	kilo dalton
LMW	low molecular weight
MBC	minimum bactericidal concentration
Mcf	McFarland standard
MIC	minimum inhibitory concentration
mRNA	messenger ribonucleic acid
MTT	3-(4,5-dimethylthiazol-2-yl)-2,5-diphenyltetrazolium bromide
NPs	nanoparticles
PBS	phosphate buffered saline
PdI	polydispersity index

pKa	acid dissociation constant
rpm	revolutions per minute
S. mutans	*Streptococcus mutans*
TFA	trifluoroacetic acid
TLTC	too low to count
TNTC	too numerous to count
UV-Vis	ultraviolet-visible spectrometry
UWC	University of the Western Cape
w/v	weight/volume
wt%	weight percentage
XRD	x-ray diffraction

CHAPTER 1

INTRODUCTION

1.0 Synopsis

This chapter highlights the introduction to this study. It briefly discusses the background to this study, the statement of the research problem, the rationale/motivation for this research, the aim and objectives of the research, questions raised in the course of the study and the research approach adopted in the study. The background to the study examined the Black soldier fly (BSF) and its economic importance including chitin and chitosan. In addition, the research approach highlighted the systematic measures followed to actualise the aim of this work. Finally, the outline or organisation of the entire work is laid out discussing the various processes undertaken on each chapter of the work.

1.1 Background to the study

Biological polymers, otherwise called biopolymers are polymeric materials derived from natural sources. They are abundant, biodegradable, renewable and are categorised into various groups according to their biological makeup. These groups include proteins, polyphenols, polysaccharides, lipids, among others (Mohanty *et al*., 2005). Among these groups are the polysaccharides such as starch, cellulose, glycogen, chitin and chitosan with their individual defining properties and the various roles each play in the life of an organism. These roles, such as storage of molecules or supporting function, depend on the individual polysaccharide structures and the nature of their repeating units (Dumitriu, 2004).

Chitosan is a linear polysaccharide consisting of several units of D-glucosamine and *N*-acetyl-D-glucosamine residues distributed randomly along its structure (Younes and Rinaudo, 2015). The D-glucosamine unit of chitosan is made up of the free amino groups, which are positively charged in solution and confers essential properties such as solubility and antimicrobial property on the chitosan. The free amino and hydroxyl groups of chitosan also ensure it functions as an excellent chelating agent due to its polycationic properties, binding varieties of metal ions by electrostatic attraction (Ngah *et al*., 2011; de Queiroz Antonino *et al*., 2017). The chelation property of chitosan ensures its application in water and wastewater treatment for the removal of potential metal ions

in solution. Ma *et al*. (2017) reported that the chelation ability of chitosan in solution could be responsible for the antimicrobial activities of chitosan, as microbial cell membranes contain trace levels of metal ions. Additionally, Ma *et al*. (2017) asserted that the presence of these metal ions could result in the initiation of chelation by chitosan thus disrupting the cell balance leading to cell lysis. Furthermore, chitosan has been reported to possess wound healing properties, hemostatic features, biocompatibility, biodegradability and mucoadhesivity properties (Szymańska and Winnicka, 2015; Tchobanian *et al*., 2019). Moreso, the molecular weight (MW) and the degree of deacetylation (DD) play a critical role in determining the effectiveness, solubility, absorbability and biodegradability of chitosan. The synthesis of chitosan necessitates the partial removal of the acetamide group of chitin (Muxika *et al*., 2017).

Chitin is natural occurring, renewable and biodegradable linear nitrogenous polysaccharide. It consists of two units of 2-acetamido-2-deoxy-β-D-glucopyranose linked by β-(1 → 4) glycosidic bonds (Jolanta *et al*., 2010; Kaya *et al*., 2016a). Researchers have asserted that the characteristics of chitin can vary based on the source of the chitin, stage of metamorphosis, sex of the organism and the processing conditions (Kaya *et al*., 2014a; Vilar Junior *et al*., 2016). Chitin is found in the exoskeleton of crustaceans such as shrimps, prawns, crabs, and in some fungi and cuticle of insects (Skołucka-Szary *et al*., 2016). Insect chitin has attracted increased attention recently due to their uniqueness in exhibiting slightly different properties with respect to their source (Kaya *et al*., 2016a; Was´ko *et al.*, 2016; Ma *et al*., 2015). For instance, Kaya *et al*. (2016a) reported that the insect, *Vespra Crabro,* had about 3-fold increase in chitin content as it metamorphosed from the larvae to the pupal stage. However, Was´ko *et al.* (2016) did not observe any significant difference in the physicochemical properties of the BSF chitin. In lieu of these contrasting reports, insect chitin ought to be accorded attention considering the critical role chitin play in insect physiology.

The BSF is a non-pest insect. The adult fly does not transmit any known disease to man. Additionally, the BSF do not have functional mouthparts for feeding. They depend on accumulated fats stored during the larval stage of metamorphosis for overall development (Newton *et al*., 2005). The larvae of BSF can decrease waste dry matter significantly as they are voracious consumers with powerful mouthparts and excellent digestive enzymes (Newton *et al*., 2005). The BSF have great economic importance as they degrade organic waste effectively and have high feed

conversion efficiency thus generating high protein contents for animal feed formulation (Sripontan *et al*., 2017). Furthermore, the usefulness and viability of BSF larvae as a potential feedstock for biodiesel production has been investigated (Li *et al*., 2011) and reports suggested a great biodiesel potential. Additionally, the exuviae of adult and imago of BSF have been reported to contain chitin (Waśko *et al*., 2016). These studies suggested the usefulness of BSF and especially the larvae as an effective waste management tool, excellent feedstock for animal feed formulation and the possibility of exploring the chitin content for advanced biomaterial synthesis.

1.2 Problem statement

The sudden global interest in BSF has led to the expansion in industrial processes for BSF farming with the aim of contributing to sustainable technologies for managing organic waste (Law and Wein, 2018). This is achieved by nurturing BSF on organic waste that would have been disposed off in landfills. Many companies have up-scaled the rearing of BSF to commercial-scale specifically as a protein source for animal feed formulation and nutrient-rich soil for crop production. These companies include AgriProtein Technologies (South Africa), Enterrra Feed Corporation (Canada) and Hermetia Baruth GmbH (Germany), among others. Despite these concerted efforts in the use of BSF for waste management, green production processes and environmental sustainability, the consequence of this innovation is the generation of bio-waste from dead flies and pupae shells. With their 250 tonnes per day food waste processing plant in Cape Town, South Africa, AgriProtein Technologies generate a combined 17 metric tonnes of dead flies and pupae casings per annum (Missengue R, personal communication, May 15, 2018). These wastes, presently, have no market value and can create ecological challenges such as environmental pollution if mismanaged. To deal with this problem efficiently and sustainably, the beneficial use of these generated industrial waste materials is essential. This necessitated the extraction of high value-added materials (chitin and chitosan) from the waste products of BSF farming in South Africa. The conversion of these BSF wastes into useful products such as chitin, chitosan and further synthesis of advanced biomaterials such as nanofibres and nanoparticles would assist in reducing environmental waste problems and add economic value to BSF farming. Additionally, it could provide industries and research institutions utilising chitin, chitosan and other advanced products of chitosan with this versatile product.

1.3 The rationale of the research

Man-made polymeric materials have been a constant factor in our daily lives for a long time. They are involved in several applications from household items, dietary products, food packaging to medical devices (Namazi, 2017). With all these advantages, they have, however, created disposal problems as they are non-biodegradable. Synthetic polymers take a considerable amount of time to degrade; they could take millions of years to finally disintegrate in the environment. They, therefore, accumulate in the environment constituting aesthetic problems, vitiating air quality and generally causing environmental pollution. Biodegradable polymers are gaining attention in alleviating the present environmental challenges posed by synthetic polymers. Chitosan, as a biopolymer has excellent characteristics including biodegradability, biocompatibility, non-toxic and antimicrobial properties. This has necessitated an increase in demand for chitosan globally. These demands then create the need for an alternative source of chitosan which is non-allergenic unlike the traditional sea-food by-product sources presently dominating the chitosan market in which inflammatory reactions have been reported in some cases (Trutnau *et al*., 2011). Therefore, understanding the efficiency of chitin and chitosan extraction from BSF waste materials and its subsequent conversion to advanced materials such as nanofibres and nanoparticles via electrospinning and electrospraying techniques, respectively will create a large market for this source of chitosan, improve the quality of products and provide additional benefits to BSF farming in South Africa such as job creation opportunities.

1.4 Aim and objectives of the study

The study is aimed at extracting chitosan from waste pupae and adult of commercially reared BSF materials and its conversion to nanofibres and nanoparticles for application in adsorption and antimicrobial studies. To achieve this aim, the following objectives will suffice.

- To extract chitin and chitosan from both pupae and adult BSF.
- To synthesise chitosan nanofibres from the extracted BSF chitosan by electrospinning technique.
- To synthesise chitosan nanoparticles from the extracted BSF chitosan by electrospraying technique
- To crosslink the fabricated chitosan nanofibres using tannic acid (TA) and determine its stability in aqueous solutions.

- To undertake adsorption studies of Pb^{2+} or Cd^{2+} using the crosslinked chitosan nanofibres.
- To determine the efficiency of the desorption and regeneration of the adsorbents.
- To investigate and compare the effects of the extracted BSF chitosan on the survival time of three different microorganisms of *E. faecalis, S. mutans* and *C. albicans* using the Time-Kill test technique.
- To investigate and compare the effects of the synthesised chitosan nanoparticles on the survival time of three different microorganisms of *E. faecalis, S. mutans* and *C. albicans* using the Time-Kill test technique.
- To evaluate the cytotoxic effect of the extracted BSF chitosan and the chitosan nanoparticles against KMST-6 human skin fibroblasts cell lines using the MTT assay.

1.5 Research questions

a. What are the optimal conditions for the extraction of chitin and chitosan from both pupal exuviae or adult BSF carcass?
b. Between adult and pupae BSF samples which has a better chitin and chitosan yield?
c. Can the extracted chitosan from BSF be electrospun to nanofibres and nanoparticles without blending with synthetic polymers?
d. What are the optimum conditions for the electrospinning of BSF chitosan biopolymer to nanofibres?
e. Can TA effectively crosslink chitosan nanofibres?
f. What is the effect of pH, concentration, time and temperature variations on the adsorption capacity of Pb^{2+} or Cd^{2+} by the TA crosslinked chitosan nanofibres?
g. Can the crosslinked BSF nanofibre adsorbents be regenerated after adsorption of Pb^{2+} or Cd^{2+}?
h. How effective are the chitosan nanoparticles in eradicating microbial cells of *E. faecalis, S. mutans* or *C. albicans*?
i. Are the extracted chitosan and the nanoparticles toxic to human skin cells?

1.6 Scope and delimitations of the study

This study centres on the extraction of chitin and chitosan from waste products of agricultural processes. Chitin and chitosan were extracted from both pupal shells and dead adult BSF. Characterisation of these materials to determine their conformity to commercially available shrimp chitin and chitosan were also undertaken. Chitosan nanofibres was fabricated via electrospinning technique while nanoparticles were through electrospraying method. The nanofibres was crosslinked with TA and applied for the adsorption of inorganic pollutants (Pb^{2+} or Cd^{2+}). Furthermore, the nanoparticles were applied for antimicrobial studies specifically on *C. albicans, S. mutans* and *E. faecalis*. Moreso, cytotoxic effects of the nanoparticles were studied and were examined only on KMST-6 human skin cell lines. However, this study did not use the extracted chitosan for direct adsorption of contaminants due to its solubility in aqueous solution. Furthermore, this study did not conduct Brunauer-Emmett-Teller (BET) analysis to determine the surface area and porosity of the TA crosslinked nanofibres due to time constraints occasioned by the unavailability of the equipment.

1.7 Research approach

The research approach to this study is identified as shown in Figure 1.1.

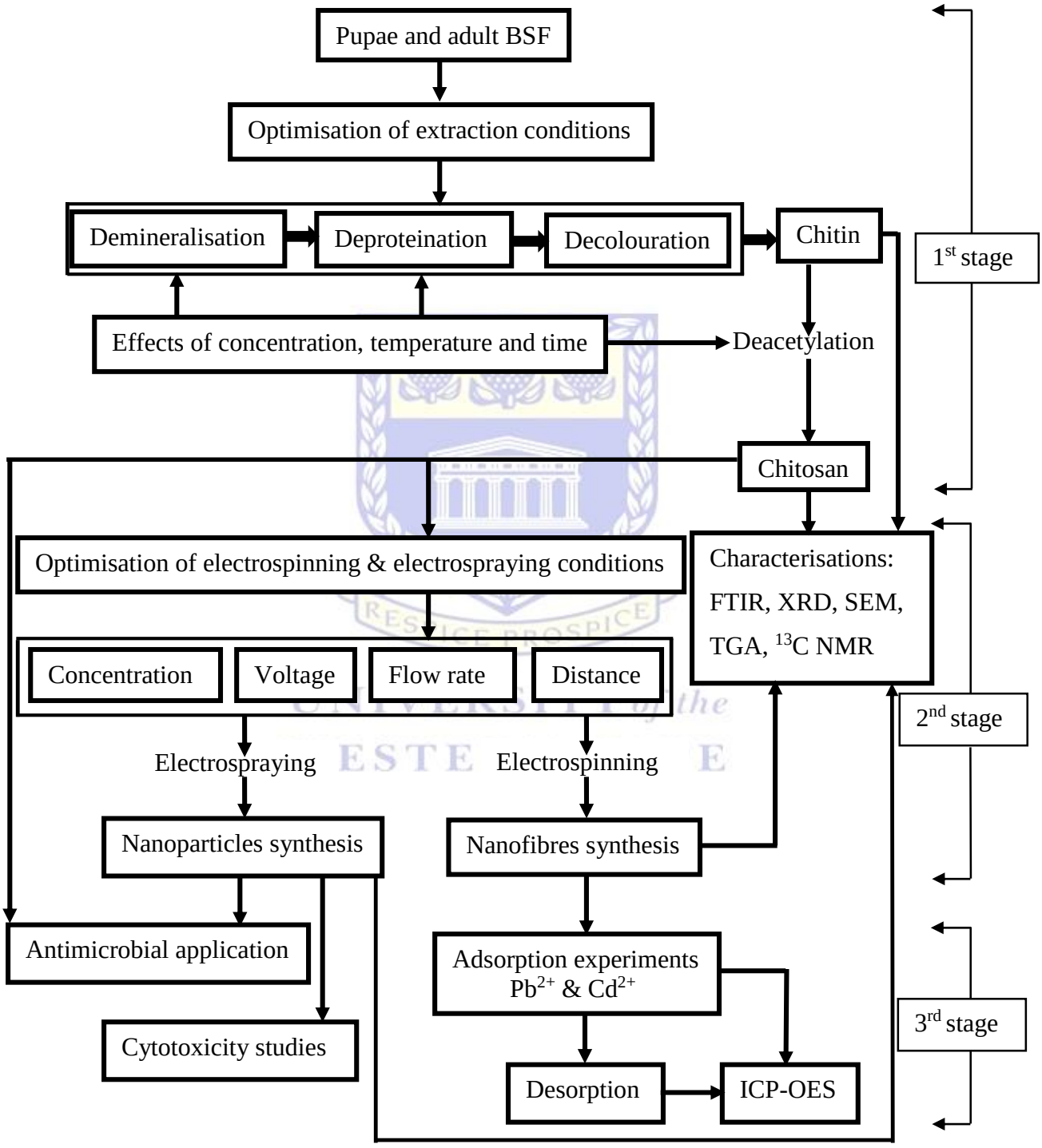

Figure 1. 1: Flow chart of the research approach to this study.

Figure 1.1 presents the flow chart of the approach to this study. The experimental approach encompasses 3 different stages. The first stage involves the extraction of chitin from both pupae casings and the adult BSF waste, and the synthesis of chitosan from the resulting chitin through deacetylation process. The second stage involves the fabrication of chitosan nanofibres and nanoparticles through the electrospinning and electrospraying techniques, accordingly. Finally, the third stage involves the applications of the synthesised biomaterials (chitosan nanofibres and nanoparticles) in antimicrobials and inorganic pollutants (Pb^{2+} or Cd^{2+}) adsorption studies. Furthermore, the risk involved in the handling of the biomaterials were assessed using human skin cell lines to determine if the biomaterials were toxic to skin cells.

1.8 Thesis outline

The thesis has nine chapters. The brief description of each chapter is presented as follows:

Chapter 1: This chapter focuses on a brief introduction of the various aspects of this study. Areas covered include Black Soldier fly, chitin extraction from BSF waste, synthesis of chitosan from extracted chitin. Also covered in this chapter are the problem statements, rationale and motivation for the study, the research questions and aim and objectives of the study likewise research scope and delimitations. The research outline and the chapters of this thesis were also included in this chapter.

Chapter 2: This chapter centres on the review of relevant literature on the concepts involved in this study. These concepts, among others, includes Black soldier fly in generality, sources of chitin, methods of chitin and chitosan extraction; which includes chemical and biological methods, physicochemical properties of chitin and chitosan, chitin deacetylation conditions. Other aspects reviewed include electrospinning process and the working principles and parameters involved *vis-à-vis* solvents involved in electrospinning, needle to collector distance, flow rate, etc. Also included in this chapter are the characterisation techniques for the fabricated nanofibres. The chapter ended with a summary of various areas reviewed and the gap in the literature which necessitated this work.

Chapter 3: This chapter outlines the detailed experimental protocols, chemicals and reagents, materials and instruments that ensured the successful extraction, characterisation and application

of the biomaterials in adsorption and antimicrobial studies. Chapter 3 has three sections. The first section focuses on the description and the sources of materials, chemicals, and equipment used in this study. The second section presents and describes the experimental procedures adopted while the third section briefly describes the analytical techniques involved in the characterisation of the extracted materials, nanofibres, nanoparticles and other samples used in this study.

Chapter 4: This chapter focuses on the results from chitin and chitosan extraction processes and the characterisation methods applied to corroborate the successful extraction of chitin and chitosan. The biomaterials were characterised to study their various properties, which include surface morphologies, physical, chemical and thermal properties.

Chapter 5: This chapter presents the results of the optimisation of process conditions for the electrospinning of the extracted pupal Black Soldier fly chitosan to nanofibres and nanoparticles. This chapter discusses the effects of these conditions on the morphology and fibre diameter of the electrospun chitosan nanofibres. The chapter specifically investigated the parameters affecting electrospinning, which include the biopolymer concentration, the applied voltage, the needle tip-to-collector distance and the flow rate to determine the optimum condition for each parameter in the electrospinning of the extracted pupal chitosan to nanofibres.

Chapter 6: This chapter presented the results of the crosslinking experiments of the chitosan nanofibres using TA. Moreover, the solubility and stability results of the TA crosslinked nanofibres in aqueous, neutral or basic solutions were also assessed at the convenient conditions. Furthermore, the obtained crosslinked nanofibres were also characterised by high resolution scanning electron microscopy (HRSEM), Fourier transform infrared spectroscopy (FTIR) and thermogravimetric analysis (TGA).

Chapter 7: This chapter presents the findings from the adsorption experiments performed using the TA crosslinked chitosan nanofibres. It has three sections. The first section dealt with the optimisation of adsorption parameters including solution pH, metal ion concentration, contact time and reaction temperature and their effect on the adsorption of Pb^{2+} or Cd^{2+} by the synthesised nanofibres. The second section focuses on the application of various models to analyse the

obtained data from the first section. The last section of this chapter discusses the desorption, regeneration and reusability of the adsorbent.

Chapter 8: This chapter presents the results of the antimicrobial studies of using the extracted pupal chitosan and the synthesised nanoparticles on *Enterococcus faecalis, Streptococcus mutans* or *Candida albicans*. In this chapter, further comparative studies on the antimicrobial effects of the pupal chitosan nanoparticles and the pupal chitosan were conducted to determine the differences in their antimicrobial actions. This chapter also evaluated the cytotoxicity of the pupal chitosan and the nanoparticles on the growth rate of KMST-6 human skin fibroblast cells *in vitro*.

Chapter 9: This chapter summarises the findings of the study with conclusions drawn, recommendations reached and suggestions on the future research possibilities in line with this study. The list of all the references cited in this study is presented after this chapter.

CHAPTER 2

LITERATURE REVIEW

2.0 Introduction

In this chapter, the overview of previous studies on Black Soldier fly, chitin, chitosan and their physicochemical properties are presented. In addition, the preparation of nanofibres and nanoparticles using electrospinning and electrospraying techniques, respectively and the various parameters affecting the success of obtaining smooth materials of desirable quality were presented. Furthermore, the crosslinking and stability studies on chitosan-based materials are examined. Besides these areas, the application of the extracted chitosan, the nanoparticles and the nanofibres as an antimicrobial agent and for adsorption studies were reviewed. Finally, this chapter ended with the various techniques for characterising the biomaterials identified in the literature. In all, the literature review provided the links among these outlined areas towards the extraction and fabrication of pure biomaterials from Black Soldier fly waste materials.

2.1 Black Soldier fly

Hermetia illucens, commonly known as Black Soldier fly (BSF) is an insect of the Stratiomyidae family. It is native to tropical, subtropical and warm temperate regions of the Western hemisphere. However, it is now widespread in warmer regions across the globe between latitudes 45° N and 40° S (Diener *et al*., 2011) mostly due to the development of international transportation. The matured BSF is a non-pest insect. It does not transmit any known disease and does not have functional mouthparts or digestive organs to consume waste. The fly relies on the fats accumulated during the larval stage for its physiological functions (Makkar *et al*., 2014).

The larvae of BSF are voracious consumers with powerful mouthparts and excellent digestive enzymes (Newton *et al*., 2005). They feed on a wide range of organic remains including animal manures, leftover foods, human excreta, decaying plants and animals resulting in waste reduction and conversion of organic materials into their body mass and mineral-rich frass. BSF can decrease waste dry matter by up to 56% (van Huis *et al*., 2013). They have a feed conversion ratio higher than those of crickets and mealworms (Wang and Shelomi, 2017). They are creamy in colouration and mature in about two (2) months when conditions are ideal, but can extend up to four (4) months

in an unfavourable environment deficient of feedstock. At the end of the larval stage, the BSF larvae excrete all the contents of their digestive tract, stop feeding and migrate in search of a dry and secured area for pupation. This pupation period can last up to 14 days if conditions are favourable or to five (5) months in an unfavourable environment (Diener *et al*., 2011). The overall survival rate and development of the BSF larvae have been reported at temperatures ranging from 27-36 ˚C, with the optimal performance occurring at 30 ˚C (Tomberlin *et al*., 2009). BSF larvae which are high in protein, are good feed for fish and chicken in both backyard and commercial purposes (Sheppard *et al*., 1994; Erickson *et al*., 2004). Sheppard *et al*. (1994) in their study on value-added manure management system using the BSF larvae revealed that BSF can convert poultry manure into larval biomass which could be used as an animal feedstock containing 42% protein, 35% fat and 8% dry matter. The above underscores the importance of BSF as an effective waste management tool likewise effective replacement for protein-based feed sources.

2.1.1 *The life cycle of BSF*

The BSF is a holometabolic insect with four stages of metamorphosis; egg, larvae, pupae and adult (Figure 2.1). The BSF life cycle lacks the nymphal stage. The BSF, from egg to adult stage, has an estimated life cycle of 40-44 days. However, this duration depends on the environmental conditions present and the composition of their diet (Müller *et al*., 2017). The adults mate and the females lay eggs in cracks near larval habitats (Sheppard *et al*., 1994; Diener *et al*., 2011). The eggs required about 102–105 h to hatch at 24 ˚C. The larvae weigh up to 220 mg and can reach up to 27 mm in length and 6 mm in width at their final larval stage. Larvae feed on decomposing organic material such as fruit and vegetable waste, as well as human and animal manure (Diener *et al*., 2011). Under ideal conditions (food supply, temperature and humidity) BSF larvae can develop into pre-pupae within two weeks, amassing sufficient resources to attain critical mass. The critical mass is associated with the minimal body mass needed to undergo pupation at a normal time interval of 8 to 14 days. The attainment of critical weight ends the growth process of the larval BSF. At the end of the larval stage, the pre-pupae empties their digestive tract, stop feeding and migrate out of the food source to find a dry and suitable site for pupation (Tomberlin *et al*., 2009). The life cycle of BSF is presented in Figure 2.1.

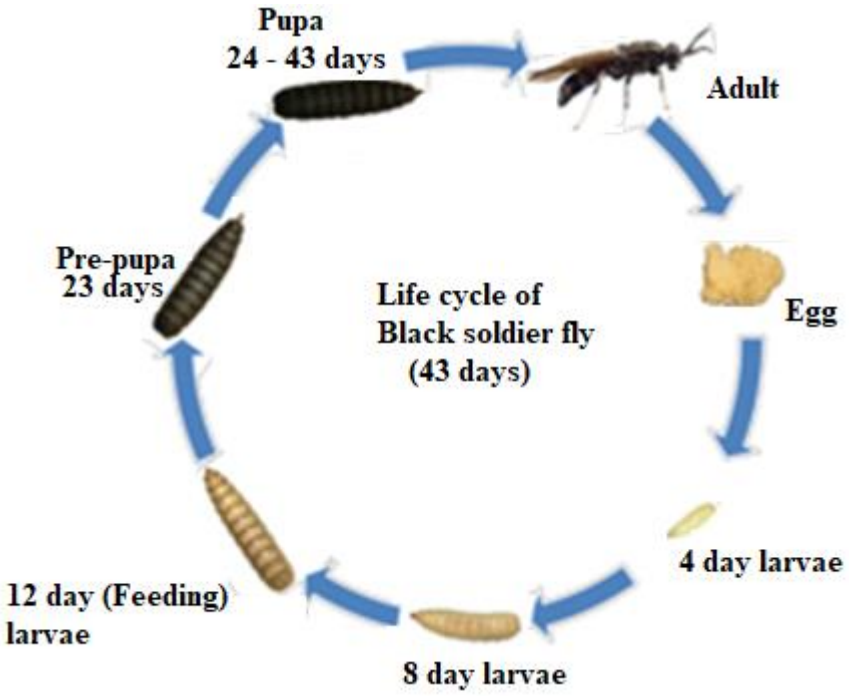

Figure 2. 1: The graphical presentation of the life cycle of *Hermetia illucens* (Black soldier fly) (Zhu *et al*., 2019).

2.1.2 *Economic importance of Hermetia illucens*

The increasing attention on large scale farming of BSF has emanated from economic importance derived from BSF. Some of these reasons are discussed in the subsequent subsection.

2.1.2.1 *Sustainable protein and lipid source*

Globally, there is a sustained increase in the demand for protein and lipid sources. This increased demand has led to the depletion of protein and lipid sources and the destruction of valuable ecosystems worldwide due to competition (Müller *et al*., 2017). The production of these valuable resources could be achieved without slash and burn of vast agricultural lands or wide fishing in the oceans which disrupts the ecosystem. The use of insects has become a global focus as a veritable source of protein and lipids due to several reasons. They have high feed conversion efficiency (van Huis *et al*., 2013), take less space to rear and could be reared on organic waste (Rumpold and Schlüter, 2013), are highly nutritious and have low greenhouse gases and ammonia generation than pigs and cattle (Oonincx *et al*., 2010), and requires lower water requirement per kilogram of protein than livestock (Müller *et al*., 2017). A typical insect which can achieve the above-mentioned advantages efficiently and effectively and serve as animal feedstock is BSF

(Wang and Shelomi, 2017). Several studies have reported the usefulness of BSF as a potential protein source which could replace the conventional protein-based sources, such as fishmeal, used extensively in aquaculture (Katya *et al*., 2017; Fawole *et al*., 2020). Katya and co-workers experimented with Barramundi (*Lates calcarifer*) and reported that 28.4% ≤ BSF larva meal ≤ 50% could be an excellent replacement for fishmeal in the diet of freshwater juvenile barramundi for optimum growth without detrimental effects on the fish's bioactive components and the body proximate compositions (Katya *et al*., 2017). Fawole *et al*. (2020) investigated the substitution of fishmeal with BSF larval meal and its effect on growth, nutrient utilisation, oxidative stress marker and the haemato-physiological response of the African catfish (*Clarias garienpinus).* Their study showed that replacing fishmeal with 50% BSF larval meal-induced the maximum bodyweight, better nutrient utilisation indices and improved haemato-physiological data of the *C. garienpinus* compared to the control groups fed with fishmeal. This implies that BSF larval meal can effectively substitute fishmeal without impairing the physiological parameters and the growth of the African catfish. Furthermore, the BSF larva has been reported by Wang and Shelomi (2017) to partially replace maize and soybean-based feedstock due to their ability to breakdown poultry droppings. Schiavone *et al*. (2017) reported that using defatted BSF larva as a supplement for broiler chicken diet reduced the impact of the feedstock on the broilers' fatty acid profile and carcass quality. The researchers concluded that BSF larva is a promising source of high-quality protein feed formulation in poultry farming as the supplementation ensured an increased carcass and meat quality of the broilers. Kawasaki *et al*. (2019) substituted soya bean meal of layers (egg-laying hens) with household waste reared BSF larva meal. They observed an increased thickness in the eggshells of the hens supplemented with BSF larval meal compared to the hens fed with the soybean meal. Kawasaki and co-workers believed that the presence of chitin in the BSF larval meal could have been responsible for the increased thickness of the eggshells. It has, therefore, been practically established that BSF larvae could serve as a sustainable alternative to animal feed and fishmeal without impairing the growth, proximate and bioactive compositions of the animals.

2.1.2.2 *Environmental sustainability tool*

Adult BSF are not attracted to human habitats or foods and are not considered a nuisance (van Huis *et al*., 2013). The larvae rapidly degrade organic waste by aerating and drying the organic matter preventing the growth of bacteria. Erickson *et al*. (2004) reported that the BSF larvae modify the microflora of manure, potentially reducing harmful bacteria such as *Escherichia coli* 0157:H7 and *Salmonella enterica*. As an excellent waste management tool, the BSF larvae liquefy manure by their secretions and thus inhibiting other vector-prone insects such as housefly larvae habitation and laying of eggs. Newton *et al*. (2005) in their study of the BSF as a value-added tool for the management of swine manure, observed that BSF larvae reduced the housefly population of pig and poultry manure by 94–100%. This finding suggests that they could control housefly populations in livestock farms and in households with poor sanitation. This, thus could contribute to improving the health status of animals and people around a farm since housefly is a major vector of diseases (Newton *et al.,* 2005).

The BSF larvae could also degrade organic matter content and total nitrogen concentration in a waste stream by about 50 - 60% with the composted residue being a potential source of organic fertilizer for plant growth (Sheppard *et al.,* 2002). Furthermore, the process of feeding on organic waste by the BSF larva ensures the complete reduction or absence of leachates which arises from decayed materials thereby preventing certain environmental problems such as odour generation and surface water pollution (Popa and Green, 2012). Therefore, the BSF has been established as an excellent waste management tool and has been utilised as an efficient tool in the sustainability of the environment.

2.1.2.3 *Forensic entomology*

The BSF has been observed on decomposing corpses at various stages after death of humans and animals. Forensic entomologists use BSF present at a human remains to establish the duration of the insect activity on the remains and decipher the period of colonisation (Benecke, 2001). The colonisation time is a part of the post colonisation duration equivalent to the minimum post-mortem interval (Tomberlin *et al*., 2005). The knowledge of the minimum post-mortem interval could guide the forensic analysts to determine unknown victims, narrow the list of potential suspects, and corroborate a suspect's alibi. The minimum post-mortem interval could be

ascertained by the determination of the ages of the insects with the longest period of development on the carcass. It is based on the time the BSF attained the developmental stage retrieved at the crime scene. For reliability of the evidence, BSF is reared in conditions mimicking those of the crime scene and the data generated are compared (Pujol-Luz *et al*., 2008). BSF larva has served as supporting evidence from crime scenes in numerous solved cases in Italy, Brazil and the United States (Pujol-Luz *et al*., 2008).

2.1.2.4 *Biodiesel production*

Biodiesels are types of diesel obtained from biomass. They have been utilised to reduce the consumption of petroleum-based diesel due to their environmental advantages, renewability and excellent combustion properties (Esteves *et al*., 2017). They have been produced from cooking oils such as palm oil, sunflower oil, rapeseed oil and soybean oil (Su *et al*., 2019). Due to the high cost of biodiesel production from these edible oils, the price has become exorbitant, about one half the price of petroleum-based diesel. This limits the economic competitiveness of biodiesels. Additionally, the production of biodiesel from edible oil could negatively impact on food security (Mardhiah *et al*., 2017). An alternative source of biodiesel production is, therefore, necessary to maximise the advantages of using biodiesel in production and combustion processes. BSF larvae have been investigated for biodiesel potentials as a result of their fast reproduction rate, high fat composition and short life cycle which could lead to sustainable and cost-effective energy production. Li *et al*. (2011) studied the impact of growing BSF larvae on different organic wastes of chicken, cattle and pig manure. Chicken manure-grown BSF larvae had the highest crude fat yield of 98.5 g from a larval population of 1000 BSFs. The crude fat resulted in a 93% biodiesel yield which had similar properties with rapeseed oil-derived biodiesel and met the European biodiesel standard, EN14214 (Li *et al*., 2011). Nguyen *et al*. (2019) studied the transesterification of insect biomass for biodiesel production and reported the synthesised BSF larval biodiesel contained 71 and 43.4% saturated fatty acids and medium-chain fatty acids, respectively which were substantially higher than those of the rapeseed-derived biodiesel. This is an indication that the BSF derived biodiesel has more stability against oxidation than rapeseed-derived biodiesel (Nguyen *et al*., 2019). This demonstrates the usefulness and viability of BSF as a potential alternative feedstock for biodiesel production since the BSF larvae could be reared on waste materials to enhance their fatty acid composition.

2.1.2.5 *Chitin generation*

Evolution has endowed insects with extracellular components such as peritrophic matrices and cuticles. These two structures protect the insects from harsh environmental conditions while ensuring it performs its fundamental physiological functions such as respiration, growth and movement. A major component of these structural matrices of insects' exoskeleton is chitin. The insect chitin in conjunction with associated proteins, the cuticle and peritrophic matrix forms a composite with varying properties (Zhu *et al*., 2016). The cuticle of an insect is composed of the exocuticle, endocuticle, procuticle and the epicuticle. Chitin is found within three of these layers excluding the epicuticle with higher amount occurring in the procuticle which consists of layers of strands of fibres linked by glycoproteins (Muthukrishnan *et al.*, 2012). The chitin composition of insects is modified at every stage of their development and thus fluctuates as the metamorphic stages occur. This dynamic modification of the chitin-containing matrices is influenced by a series of enzymes which digest it to acetylglucosamine including the synthases, chitinases and the β-N-acetylglucosaminidases (Filho *et al*., 2002). This fluctuation is as a result of the moulting, a process of breaking down the less stabilised portions of the exoskeleton while shedding the sclerotised portions as exuviae.

Having reviewed this all-important insect, BSF, and its economic benefits, there arises the question of a detailed and in-depth study of its chitin content and possible conversion to more useful materials for varied applications.

2.2 Chitin structure and properties

The word chitin derived from "Chiton", a Greek word meaning coat of nail, was first reported by Bradconnot in 1881 (Shahidi *et al.*, 1999). Chitin is a natural occurring, renewable and biodegradable linear nitrogenous polysaccharide. It consists of β-(1 → 4) bonds linked 2-acetamido-2-deoxy-D-glucose units (Jolanta *et al*., 2010). It is a natural organic compound with the largest amount of nitrogen on Earth, except for protein (Teng, 2012). They form the main support component existing in the exoskeleton of crustaceans, insects, as well as the internal structure of invertebrates (Ahing and Wid, 2016; Kaya *et al*., 2016a). Chitin $(C_8H_{13}O_5N)_n$ has a structural resemblance to cellulose $(C_6H_{10}O_5)_n$, often termed a derivative of cellulose. The difference being the presence of an acetamide group (-NH-CO-CH_3) replacing the hydroxyl group

(O-H) at C2 position of the monomer unit (Figure 2.2). Chitins are always associated with proteins, forming a chitin-protein complex (Shillito *et al*., 1995). Also associated with chitins are pigments, lipids and minerals. These compositions can be separated through chemical or enzymatic processes.

Chitin has hydrophobic characteristics and thus exhibit insolubility in most solvents. This is due to the high content of intramolecular and intermolecular hydrogen-bond networks. These hydrogen bonds control solubility, swelling and reactivity of chitin (Ahyat and Azmi, 2016). In addition, low chemical reactivity of chitin limits its applications in virtually all fields.

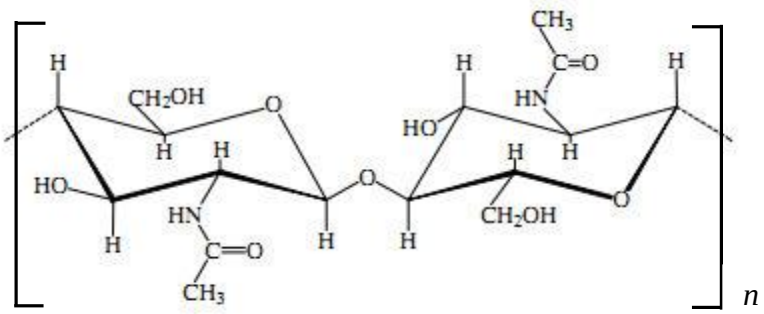

Figure 2. 2: Chemical structure of chitin (Younes and Rinaudo, 2015).

2.2.1 *Sources of Chitin*

Most of the commercial sources of chitin are waste from agro-based processes, especially seafood industries (Al Sagheer *et al*., 2009). In the native state, chitin occurs as an ordered microfibrils which form structural frameworks in arthropod exoskeletons (Kaya *et al*., 2015), crustaceans (Vilar Junior *et al*., 2016), cell walls and structural membranes of fungi, yeast and green algae (Minke and Blackwell, 1978; Younes and Rinaudo, 2015), wings of cockroaches, grasshoppers and spider species (Kaya *et al*., 2016a), potato beetle (Kaya *et al*., 2014a), aquatic invertebrates (Kaya *et al.*, 2013) and cuticles of insects (Kaya *et al*., 2014a, Was´ko *et al*., 2016). Till date, the main commercial sources of chitin and its derivatives are crabs, krills and shrimps (Tajik *et al*., 2008). However, alternative chitin sources such as insects, fungi, squid pens, cuttlebone, mushrooms and corals are currently being exploited.

2.2.2 *Composition of Chitin*

Shells of selected crustaceans so far studied shows that chitin contains 30 - 50% minerals, 0 - 14% lipids, 20 - 40% protein, 10 - 30% chitin and contain pigments of a lipidic nature such as carotenoids (astaxanthin, astathin, canthaxanthin, lutein and β-carotene) and their proportions vary with species and seasons. (Abdulwadud *et al*., 2013). Among these compositions of crustacean shells, minerals (carbonate and phosphate of calcium), protein and chitin constitute about 90% (Minke and Blackwell, 1978). Theoretically, chitin ($C_8H_{13}O_5N$) is elementally composed of 47.29% carbon, 6.45% hydrogen, 6.89% nitrogen and 39.37% oxygen (Daraghmeh *et al.*, 2011).

2.2.3 *Forms of chitin*

Based on its natural source and biological functions, chitin is presented in three different structural forms; the alpha (α), the beta (β) and the gamma (ɣ) (Jang *et al*., 2004). They can be distinguished by various characterisation techniques including infrared, NMR spectroscopy, X-ray diffraction and thermal gravimetric analysis. These forms are differentiated based on the alignment of the carbohydrate chains within its structure (Jang *et al*., 2004).

The α-chitin is the most abundant structure. It is the more stable and widely spread allomorph and occurs where rigidity and mechanical resistance are required. It occurs in fungal and yeast cell walls, in krills, lobsters and crab tendons and shrimp shells. It also occurs in insect cuticles (Philibert *et al*., 2016). The α form consists of tightly packed orthorhombic cells aligned in parallel and antiparallel chains (Minke and Blackwell, 1978; Stawski *et al*., 2008; Ogawa *et al*., 2010). The unit cell of α-chitin has dimensions of a = 4.74 Å, b = 18.86 Å and c = 10.32 Å, where the c axis represents the molecular chain axis. The interplanar distances, $d_{hkl,}$ for α-chitin lattice planes is calculated using Equation (2.1):

$$d_{hkl} = \left[\left(\frac{h}{a}\right)^2 + \left(\frac{k}{b}\right)^2 + \left(\frac{l}{c}\right)^2\right]^{-1/2} \qquad 2.1$$

They are strongly stabilised by intra- and inter-sheet bonds, thus ensuring that all the hydroxyl groups were involved in hydrogen bonding (Kurita, 2001). Additionally, the inter-sheet hydrogen bonds prevent movement of small molecules into the crystalline phase. This hydrogen bonding exists along the b unit cell parameter (Figure 2.3) which forms an association with the

hydroxymethyl groups of adjacent chains. Such a feature is non-existent in the structure of β-chitin, making it (β-chitin) more prone to swelling than the α-chitin (Rinaudo *et al*., 2006).

These alignments make α-chitin the most stable of the three forms of chitin. This is corroborated by α-chitin having the maximum thermal degradation temperature among the three chitin polymorphs (Jang *et al*., 2004). The presence of intra and inter-sheet hydrogen bonding are further made manifest in the ^{13}C NMR spectra of α-chitin (Figure 2.4). Here, the signals for C3 and C5 carbon atoms appear as a doublet, are clearly resolved in α-chitin and appear around 73 and 75 ppm, respectively (Jang *et al.*, 2004). Similarly, the FTIR spectra of α-chitin are characterised by three main peaks at 1650 cm^{-1}, 1621 cm^{-1} (Amide 1) and 1552 cm^{-1} (Amide 11) bands. With the intra and inter sheet hydrogen bonding responsible for the scissoring effect on the Amide 1 band (Sayari *et al*., 2016).

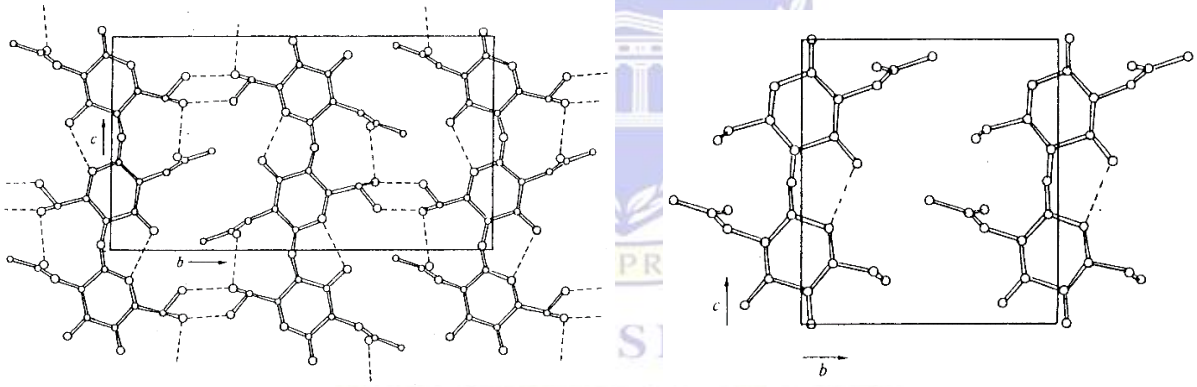

(a) **(b)**

Figure 2. 3: Arrangement of chitin molecules in (a) α-chitin (b) β-chitin (Kurita, 2001).

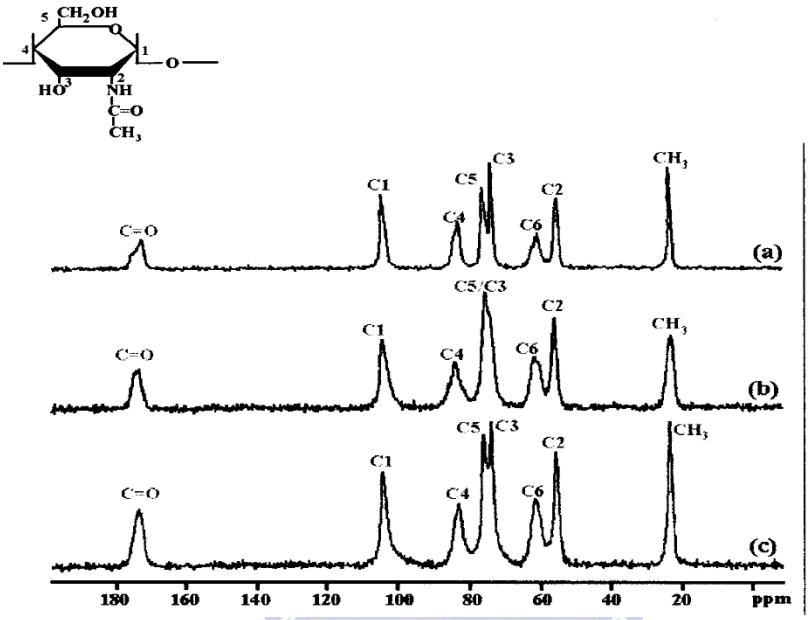

Figure 2.4: ^{13}C NMR spectra of (a) α-chitin (b) β-chitin, and (c) γ-chitin (Jang *et al*., 2004).

The β-chitin are less abundant in nature. They are found in association with proteins in squid pens and cuttlefish bones (Hajji *et al*., 2014), in the materials synthesised by pogonophoran and vestimetiferan worms (Blackwell *et al*., 1965; Younes and Rinaudo, 2015). They are made up of monoclinic unit cells arranged in parallel formation and forms only intrasheet hydrogen bonding (Gardner and Blackwell, 1975). This bonding form weak intermolecular forces between the β-chitin unit cells. The unit cell of β-chitin has dimensions of a = 4.85 Å, b = 9.26 Å, c = 10.38 Å (fibre axis), and γ = 97.5° (Stawski *et al*., 2008; Ianiro *et al*., 2014). Since they have monoclinic unit cell arrangement, the interplanar distances, d_{hkl}, are different from the α-chitin and are computed using Equation (2.2):

$$d_{hkl} = \left[\frac{\left(\frac{h}{a}\right)^2 + \left(\frac{k}{b}\right)^2 - \left(\frac{2hk}{ab}\right)cos\gamma}{sin^2\gamma} + \left(\frac{l}{c}\right)^2 \right]^{-1/2} \qquad 2.2$$

where a, b and c are the unit cell dimensions whereas hkl are the individual planes.

Studies by Gardner and Blackwell (1975) show that β-chitin adopts a molecular sheet in *a c* plane (Figure 2.5) formed by the combination of the hydrophobic forces of glucoside rings and the

intermolecular hydrogen bonds (C=O···H–N and C=O···H–O6) of the acetamide group. This prevents hydrogen bonding formation between the molecular sheets in the 010 direction (Gardner and Blackwell, 1975; Ianiro *et al*., 2014). This explains the behaviour of β-Chitin in the presence of polar guest molecules as they could penetrate the crystal lattice of β-Chitin molecules without disturbing the sheet's organisation and the crystallinity of the sample. β-chitin, therefore, has higher solubility, reactivity, swelling and affinity with solvents compared to α-chitin (Shushizadeh *et al*., 2015). In addition, the ^{13}C NMR spectra of β-chitin (Figure 2.4) appears as singlet for C3 and C5 peaks at 74 ppm (Jang *et al.*, 2004; Abdou *et al*., 2008) thus distinguishing it further from α-chitin (which has double peaks as reported earlier). Under favourable conditions, β-chitin can transform into α-chitin in an irreversible reaction. Noishiki, *et al*. (2003) and Teng (2012) have reported that β-chitin can be converted to α-chitin by treating the sample with ≥ 30% NaOH solution or with ≥ 8 N aqueous hydrochloric acid in a non-reversible reaction (Equation 2.3). This shows that β-chitin is an unstable entity with a different mechanism of formation from α-chitin.

$$\beta\text{-chitin} \xrightarrow[\geq 8\ N\ HCl]{\geq 30\%\ NaOH} \text{Alkali chitin} \underset{H_2O}{\overset{\geq 30\%\ NaOH}{\rightleftharpoons}} \alpha\text{-chitin} \qquad 2.3$$

The γ-chitin is assumed as an intermediate or composed of the α- and the β- forms of chitin, rather than a third polymorph. They contain two parallel polysaccharide chains while the third layer appears in a reverse direction (Figure 2.6) to the two preceding chains (Roberts, 1992). The γ-chitin form intersheet hydrogen bonding and shows a double peak for C3 and C5 carbon atoms (Figure 2.4) in ^{13}C NMR spectra (Jang *et al.*, 2004). The γ-chitin are extracted from fungi, yeast, and cocoons of insects (Campana-Fillho *et al*., 2007).

Therefore, the various forms of chitin vary in reactivity and solubility because of their structural differences and also the type of hydrogen bonding they exhibit. Both are insoluble in all common solvents which is a major problem in developing applications of chitin.

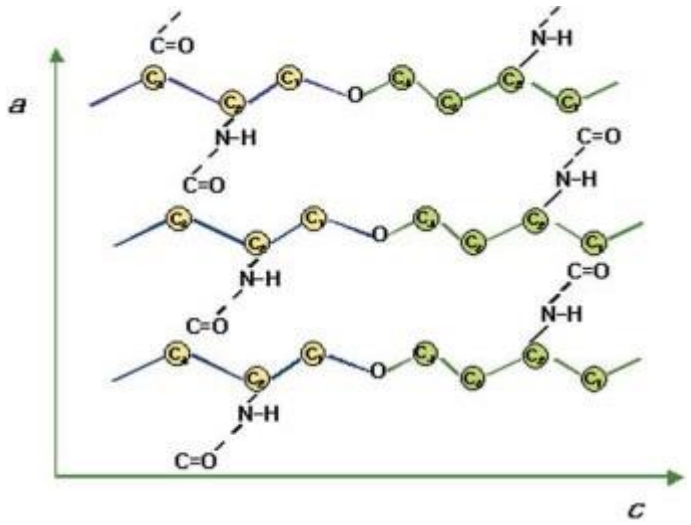

Figure 2. 5: The β-chitin chains in parallel arrangement linked by hydrogen bonding (Jang *et al*., 2004).

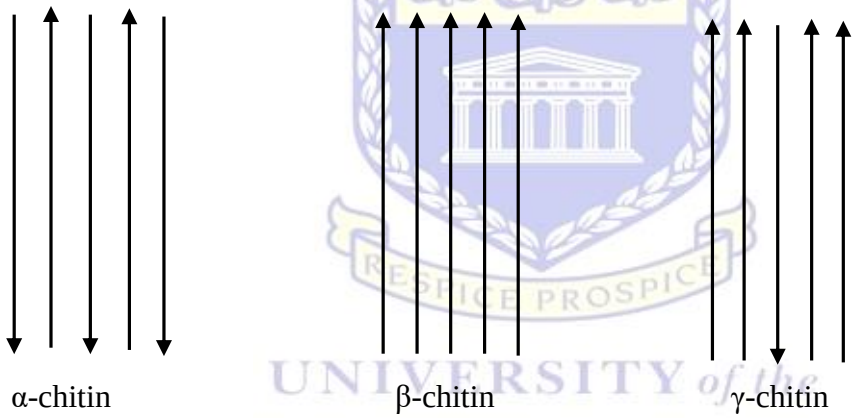

Figure 2.6: Description of polymorphs of chitin showing the alignments of the carbohydrate chains within its structure.

2.3 Chitin extraction and Economic feasibility

The chitin extraction process is economically feasible. This is because the raw material, mostly waste products of agro-processing industries constitute a nuisance in the environment and has zero cost. Moreover, the processing of chitin can include the recovery of astaxanthin and other carotenoid compounds which serves as pigmentation. Astaxanthin is powerful, naturally occurring carotene pigment and antioxidant found in some species of plants, algae, animals, bacteria and fungi (Zhang *et al.*, 2015; Su *et al.*, 2018).

Chitin is more stable against acid and bases compared with other natural polymers such as cellulose, protein, pectin, among others and it is insoluble in most solvents (Kurita *et al*., 2001). As a result of its insolubility, it is extracted as the residue left after the degradation of other component units of the material using acids and alkali (Kurita *et al*., 2001). Several protocols have been developed for the extraction of chitin from various sources. These protocols could either be chemical, biological or fermentation protocols. Chitin extraction by fermentation technique is very expensive (Cauchie, 2002). Similarly, the biological method (discussed in details in 2.3.2) does not depolymerise the chitin, it is cost-effective and eco-friendly. However, the biological method is not feasible on industrial scale because of the cost of enzymes (deacetylates) and low productivity of the process (Vilar Junior *et al*., 2016). The chemical method is described in detail in Section 2.3.1.

2.3.1 *Chemical extraction*

The chemical method involves processes such as demineralisation of inorganic matter using dilute acid, deproteination using an alkaline solution and decolouration using an oxidising agent. All these treatments must be adapted to the chitin source, owing to differences in the ultrastructure of the initial material, to produce first high-quality chitin and then chitosan. The chemical extraction method is preferred industrially due to the short extraction time involved compared to the biological method.

Demineralisation is the removal of mineral contents of an organic matter, basically carbonates or phosphates of calcium with the release of CO_2 (Equation 2.4). The extent of CO_2 release is determined by the mineral content of the sample (Ahyat and Azmi, 2016). The salts are filtered off and the residue washed severally using deionised water to neutral pH. Demineralisation is undertaken to achieve a very low ash content chitin needed for low impurity tolerance applications (Zuber *et al*., 2013).

$$CaCO_3\,(s) + 2HCl\,(aq) \longrightarrow CaCl_2\,(s) + H_2O\,(l) + CO_2\,(g) \qquad 2.4$$

Deproteination is the process of removal of the protein content of chitin sample. Chitins are associated with proteins forming a chitin-protein complex (Shillito *et al*., 1995). The protein is

converted to water-soluble amino acids during deproteination process. Deproteination does not only remove proteins but also pigments such as carotenoids and lipids. The reaction is done in a low base concentration to prevent loses of acetyl group and to maintain the polymerisation of chitin chain.

Several researchers have undertaken chitin extraction from different sources by adopting different reaction conditions. In most of the processes, demineralisation had preceded deproteination process. Islam *et al*. (2011) performed demineralisation of shrimp shell waste using 4% HCl solution (1:14 w/v) for 36 h at room temperature. The resultant slurry was filtered and the residue dried in an oven for deproteination process.

Sayari *et al*. (2016) demineralised Norway lobster by-products using 1.5 M HCl solution (1:10 w/v) at room temperature with constant stirring. Sayari and his colleagues achieved the demineralisation process by varying the reaction time from 2 – 6 h. Kumari *et al*. (2017) describe the extraction of chitin and chitosan from fish scales, *Labeo rohita*, using 1% HCl solution for 36 h and 0.5 N of NaOH solutions for 18 h for demineralisation and deproteination steps respectively. Marei *et al*. (2016) isolated chitin from different insects in Egypt. Demineralisation was done using 1.0 M HCl solution (1:15 w/v) at room temperature while deproteination was carried out using an alkaline solution of 1.0 M NaOH at 100 °C for 8 h. The entire process was repeated severally to obtain high purity chitin as reported by Marei and his co-workers. Wang *et al*. (2013) reported the demineralisation of Antarctic krill (*Euphausia superba*) shells using 1.7 M solution of HCl at room temperature for 6 h after which the samples were filtered, rinsed severally to neutral pH using deionised water and dried in an oven. The deproteination process was carried out by reacting the demineralised samples with 2.5 M NaOH solution for 1 h at 75 °C to obtain pure chitin after decolourising with 1.0% potassium permanganate solution. Few reports had reported a certain amount of treatments on the samples before the extraction process. Teli and Sheikh (2012) firstly soaked the shrimp shells in 1.0 M NaOH solution for 24 h, washed it to neutral pH and dried the samples before undertaking the demineralisation process using 1.0 M HCl solution. The researchers could not specify the time of reaction and the temperature of the demineralisation reaction. Teli and Sheikh performed deproteination using 1.0 M NaOH solution and decolouration with oxalic acid and $KMnO_4$.

Despite the importance of demineralisation in chitin extraction, some researchers have extracted chitin without undergoing this process. Cuong *et al*. (2016) succeeded in isolating pure chitin from squid pens by using 4% NaOH solution at a temperature of 80 °C for 10 h. They concluded that the demineralisation process was not essential as the one-step deproteination process could yield chitin of high quality.

Hydrochloric acid (HCl) appears to be the most preferred solution for the demineralisation process judging from the review outcome. This, according to Benhabiles *et al*. (2013), is to prevent the chitin from being hydrolysed. Furthermore, dilute HCI produces water-soluble calcium chloride ($CaCI_2$) (Equation 2.3) which is easily filtered off after the reaction (Zuber *et al.,* 2013).

Furthermore, the use of stirred reactor to improve chemical contact and penetration into the sample matrix was also reported by Bajaj *et al*. (2011) and Arbia *et al*. (2013) to enhance the quality of the isolated chitin by improving the reaction efficiency and reducing the time of reaction. In addition, it was reported by Marquis-Duval (2008) that the penetration of solvent into the chitin matrix strongly depends on the particle size of the sample and the contact between the sample matrix and the solvent. For smaller particles, an increase in surface area will increase the reaction rate thereby actualising demineralisation at a shorter time interval.

2.3.2 *Biological extraction*

The biological method of chitin extraction has gained increased interest in recent years. This could have resulted from the challenges posed by the chemical method, including environmental challenges and energy consumption (Hembach *et al*., 2017; Casadidio *et al*., 2019). The biological extraction method is considered more advantageous because it is eco-friendly, reproducible, consumes fewer solvents and eliminates the irregular deacetylation and MW reduction associated with chemical extraction method (Arbia *et al*., 2013). Additionally, the liquid fraction left could be used as a protein-mineral rich supplement for animal feed formulation (Rao *et al*., 2000; Ghorbel-Bellaaj *et al*., 2012). Organic acid-producing bacteria in the fermentation process and proteolytic enzymes are used in the biological method of chitin extraction. The proteolytic enzymes act exclusively on protein contents of the chitin while the fermentation process uses microorganisms to ferments both the protein and the mineral contents of the sample.

The fermentation method is categorised into two: the use of lactic acid and the use of non-lactic acid fermentation methods. The lactic acid bacteria produce calcium lactate in contact with calcium carbonate of the waste material which could easily be removed by filtration and washing (Philibert *et al*., 2016). The effectiveness of lactic acid fermentation process is dependent on the carbon source of the waste material, the species of the fermenting microorganism, initial pH of the culture and the extent of variation of the pH during the fermentation process, likewise the temperature and the duration of the fermentation (Younes and Rinaudo, 2015).

Several studies have been conducted by adopting the lactic acid fermentation technique. Castro *et al.* (2018) isolated chitin from the crab, *Allopetrolisthes punctatus* waste using the *Lactobacillus plantarum* sp for the fermentation process. Demineralisation and deproteination were carried out simultaneously with a 99.6 and 95.3% effectiveness respectively after 60 h of fermentation. Dun *et al.* (2019) reported a novel chitin extraction method by utilising both the enzymatic hydrolysis and fermentation technique simultaneously. Dun and his co-workers carried out demineralisation and deproteination by using *Bacillus coagulans* LA204 and proteinase K to eliminate the mineral and protein contents of crayfish shell waste. After 48 h of fermentation, the efficiency of the demineralisation, deproteination and the chitin yield were 91%, 93% and 94% respectively. Further studies have also been carried out on chitin extraction using the lactic acid fermenting bacteria *Lactobacillus pentosus* 4023 on crayfish, *procambarus clarkia* exoskeleton (Arbia *et al*., 2013), *Pseudomonas aeruginosa* on the shrimp, *Penaeus merguiensis* shells (Sedaghat *et al*., 2017), among others.

The proteolytic enzymes are obtained from plants, animals and microorganisms. They include pepsin, chymotrypsin, papain, bromelain, Alcalase, *et cetera* (Jardine *et al*., 2016). Many studies have applied these enzymes in chitin extraction especially during the deproteination process, and in some instances, in combination with chemical or fermentation methods. Arancibia *et al*. (2014) isolated chitin from the shrimp, *Litopenaeus vannamei* waste materials. Demineralisation was achieved using lactic acid (1:3 w/v) at 21 ℃ for 36 h while enzymatic deproteination was performed by using Viscozyme at 50 °C and pH 4.5 followed by Alcalase hydrolysis at 50 °C and pH 8.5. The experiment was heat-inactivated at 90 °C for 10 mins, centrifuged and lyophilised to obtain the chitin residue. Abdelmalek *et al*. (2017) reported the extraction of β-chitin from squid

gladius using 1.5 M HCl solution at 50 °C and time ranging from 2 to 8 h during the demineralisation process. The deproteination process was carried out using the enzyme Alcalase to digest the protein content of the squid at 50 °C for 3 h. Busto and Michael (1994) reported the use of protease isolated from *Pseudomonas maltophilia* for deproteination process. After 6 days of incubation, they recorded a 64% deproteination of crustacean shell wastes. Hongkulsup and his co-workers recorded a protein removal of 91.10% after 3 h of deproteination by using protease isolated from *Streptomyces griseus* (Hongkulsup *et al*., 2016). Younes *et al*. (2016) extracted chitin through the enzymatic process. They investigated several proteases from different microbial and fish sources and reported an appreciable level of protein removal and the isolation of high purity chitin (Younes *et al.,* 2016).

The advantages of biological method of chitin extraction have been highlighted, however, this method is still limited to laboratory-scale studies. Furthermore, the enzymes involved in the process are costly, time-consuming, have low efficiency and could result in high residual proteins levels (Younes and Rinaudo, 2015; Philibert *et al*., 2016).

2.3.3 *Chitin yield*

The economic viability and the commercialisation of chitin and chitosan as a product depend on the yield obtainable from the sample. Several studies have reported the chitin content of various species of organisms studied from crustaceans, fungi to insects. Kaya *et al*. (2013) and Ivashchenko *et al*. (2002) in separate studies on *Gammarus argaeus* a crustacean of the aquatic ecosystem established a dry weight of 11-12 and 8.7% respectively. Chitin yield from other studies are shrimp shells, *Parapenaeopsis stylfera*, crab shells and cuttlefish bones 20 ± 2%; 10 ± 2% and 5 ± 2% respectively (Hajji *et al*., 2014); squid pen, *Illex argentinus*, 31% (Cortizo *et al*., 2008). Table 2.1 presents the chitin yields associated with various organisms on dry weight basis obtained from other studies.

Table 2. 1: Chitin yields from different organisms.

Organisms	% chitin yield (dry wt basis)	Source
Insects		
Vespa crabro (larva, pupa and adult)	2.1, 6.2 & 10.3	Kaya *et al*. (2016a)
Schistocerca gregaria (desert locust)	12.2	Marei *et al*. (2016)
Apis mellifera (honey bee)	2.5	Marei *et al*. (2016)
Calosoma rugose (beetles)	5.0	Marei *et al*. (2016)
Musca domestica (housefly)	7.71	Kim *et al*. (2016)
Silkworm chrysalides	20	Paulino *et al*. (2006)
Cicada sloughs	36	Sajomsang and Gonil (2010)
Anthropods		
Artemia urmiana	29.33–34.5	Tajik *et al*. (2008)
Holotrichia parallela	15	Liu *et al*. (2012)
Crustaceans		
Krill	27.8	Wang *et al*. (2013)
Shrimp shell	20	Al Sagheer *et al*. (2009)
Squid pen	31	Cortizo *et al*. (2008)
Fungi		
Basidiomycetes	8.5–19.6	Di Mario *et al*. (2008)
Lactarius vellereus	19	Arbia *et al*., 2013
Saccharomyces cerevisiae	2.9	Arbia *et al*., 2013
Others		
Rhinolophus hipposideros (Horseshoe bat)	28	Kaya *et al*. (2014b)
Palomena prasina (Green shield bug)	10.8	Kaya *et al*. (2015)

Table 2.1 shows that the percentage yield of chitin (on dry weight) ranged from 2.1 to 36%. Among these organisms studied and the reported yield from insects, the chitin content of Black soldier fly has not been reported.

2.4 Chitosan synthesis

Like the chitin, chitosan is a natural occurring, renewable and biodegradable linear nitrogenous polysaccharide. A fully deacetylated chitosan is made up of β-(1-4) bonds linked 2-amino-2-deoxy-D-glucosamine strands. Chitosan is synthesised by the partial removal of the acetyl functional groups of chitin to yield amine ($-NH_2$) at the C2 position of the glucosamine unit, a process termed deacetylation. The deacetylation of chitin to produce chitosan could be achieved through chemical method or enzymatic technique. Chitosan can also be found naturally in the cell

walls of some fungi, especially Zygomycetes (Trutnau *et al*., 2011). However, chemical methods are used extensively for commercial purpose of chitosan preparation due to their low cost and suitability for mass production (Younus and Rinaudo, 2015).

2.4.1 *Chemical deacetylation*

The chemical deacetylation involves high-temperature hydrolysis of chitin due to the resistance resulting from the trans arrangement of the C2 and C3 units of the chitin sample (Focher *et al*., 1990; Zuber *et al*., 2013). This process involves the removal of the acetamide functional group (-$NHCOCH_3$) to yield an amine group (-NH_2) from chitin backbone by hydrolysis (Fiamingo *et al*., 2016). Both acids or alkalis could be used to deacetylate chitin. However, the β-(1-4) bonds of chitin are more susceptible to acid attack leading to hydrolysis of the polymer backbone. Therefore, the use of an alkaline solution in deacetylation is more frequent to prevent hydrolysis (Younes and Rinaudo, 2015). This process can be performed using traditional protocol or physical assisted techniques. The traditional protocol of chitin deacetylation is carried out by refluxing the chitin in aqueous NaOH solution (concentration 40-70%) at high temperature for several hours (Knidri *et al*., 2018). Moreover, steeping the chitin in strong NaOH solution at room temperature for several hours before refluxing at an elevated temperature may increase the DD of chitosan (Kumari *et al*., 2015). Another alternative approach for chitosan synthesis, which requires shorter reaction time is the microwave-assisted alkaline hydrolysis (Shushizadeh *et al*., 2015). In addition, variations in chitosan preparation may also result in changes to the DD, the distribution of acetyl functional groups within the polymer, the MW and the viscosity of the solution. Several critical factors have been identified that affect the extent of deacetylation including temperature, time of deacetylation, alkali concentration, prior treatment applied to the chitin, the ratio of chitin to alkali solution, the density of the chitin and particle size of the samples (Younes and Rinaudo, 2015). Figure 2.7 shows the reaction mechanism of the deacetylation process in alkaline medium.

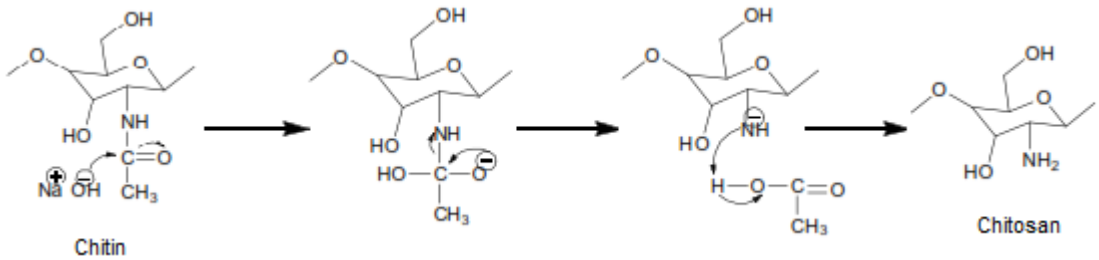

Figure 2. 7: The mechanism of the deacetylation reaction (Ahyat and Azmi, 2016).

2.4.2 *Enzymatic deacetylation*

The chemical deacetylation method presents some disadvantages such as high energy input, waste of concentrated alkaline solution, an increase of environmental pollution, broad and heterogeneous range of soluble and insoluble products (Shirvan *et al*., 2019). The enzyme assisted method is an alternative procedure to overcome these drawbacks and obtain chitosan with higher MW and tailored DD. This alternative explores the use of chitin deacetylase (EC 3.5.1.41) or chitinases (EC 3.2.1.14). These enzymes catalyse the hydrolysis of the β-(1 → 4) glycosidic bonds in chitin to yield chitosan (Jaworska, 2012). The conversion of chitin to chitosan through the use of chitin deacetylase or chitinases offers a well-controlled process leading to a non-depolymerised chitosan sample in contrast to the chemical deacetylation method (Hamer *et al*., 2015; Kaczmarek *et al*., 2019). Some studies have adopted the enzymatic deacetylation method in chitosan extraction. Rass-Hansen *et al*. (2007) undertook deacetylation of pre-treated chitin sample extracted by the biological method using a mixed culture of *Lactobacillus salvarius, Enteroccus facium* and *Pedoicoccus acidilactici* microbial strains. Chitin deacetylase isolated from *Colletotrichum lindemuthianum* was used in the deacetylation process. Harmsen *et al*. (2019) investigated the possibility of using chitin deacetylase isolated from *Vibrio cholerae* to synthesise chitosan from both α- and β-chitin samples. The result showed that the enzyme was able to reduce the degree of acetylation (DA) of both chitin samples (α- and β-chitin) by introducing NH_2 functional groups on the chitin surface which could serve as a starting point for further modifications. Martinou *et al*. (1998) demonstrated that chitin deacetylase, *M. rouxii,* isolated from fungus could reasonably deacetylate chitin samples. However, the DD of the sample was very low. Martinou *et al*. suggested the pre-treatment of the chitin sample before introducing the enzymes to improve the accessibility of the acetyl groups of the chitin by the enzymes thereby enhancing the deacetylation process.

It is, therefore, pertinent that enzymatic processes could be used in the conversion of chitin to chitosan as an environmental-friendly approach. Its major drawback is the inability to efficiently deacetylate chitin substrate, as demonstrated by Arnold *et al*. (2020) who showed that the enzymatic deacetylation process strictly depends on the pre-treatment conducted on the native chitin substrate. Furthermore, the enzymatic method is expensive due to the high cost of enzymes and the multiple steps associated with the method. These factors contribute to rendering the

enzymatic deacetylation process unfavourable in commercial and scale-up applications (Kim and Rajapakse, 2005).

2.4.3 *Characteristics of chitosan*

2.4.3.1 *Molecular* weight

Molecular weight (MW) is among the most important features that describes a polymer. Polymers are made up of covalently linked repeating units with differing chain lengths (Oberlerchner *et al*., 2015). This results in most polymers not having a specific MW as is obtainable with most compounds. MW of a polymer is obtained by multiplying that of the monomer unit by the degree of polymerisation (DP). The DP represents the number of monomer units in a polymer chain (Oberlerchner *et al*., 2015). Chitosan, therefore, is polydisperse with respect to MW. This implies that they contain non-uniform lengths of polymer chains, thereby giving rise to variable MW. The MW varies with the source, method of preparation and the DD (Hajji *et al*., 2014; Oberlerchner *et al*., 2015). Generally, high temperature can cause degradation of chitosan structure thereby lowering the MW. For example, at 280 °C and above, chitosan tends to thermally degrade by breaking down of the polymer chains which lowers the MW (Rout, 2001). Furthermore, processing conditions such as the use of high temperature or concentrated solutions results in depolymerisation of the molecules, with minimal structural degradation, causing MW changes (Rout, 2001).

Chitosan of different MW could be obtained by the depolymerisation of chitosan solution in a controlled environment. This could be done through hydrolysis using mild acids such as HCl, HNO_2, free radicals including H_2O_2 and $K_2S_2O_8$, enzymatic processes using pectinase, chitosanase, the use of radiations (UV, γ rays), heat treatments, microwave and ultrasound (Prashanth and Tharanathan, 2007). According to Chattopadhyay and Inamdar (2010), when chitosan solution is reacted with nitrous acid (Equation 2.5), it attacks the amino group of the D-unit leading to deamination reaction and subsequent cleavage of the adjacent β-glycosidic linkage. They further reported that the depolymerisation did not affect the chemical structure of the chitosan. It did rather induce a MW reduction of the resulted chitosan solution which is evidenced by the reduction in viscosity of the solution. In addition, Zamani and Taberzadeh reported that the MW of chitosan can be reduced by treatment with a low concentration of aqueous sulphuric acid. In their study,

they reacted high molecular weight chitosan with 72, 216 and 360 mM H_2SO_4 from 5 to 240 minutes at 120 °C to obtain a progressive reduction of 98% from the starting MW (Zamani and Taberzadeh, 2010). High MW chitosan has decreased solubility in contrast to low MW chitosan. This, as suggested by Franca *et al.* (2011), resulted from the increased hydrogen bonds and Van der Waal's forces interacting in the chitosan structure. Thus, the lower the MW, the lesser the intermolecular forces acting on the unit and the higher the solubility of chitosan in water.

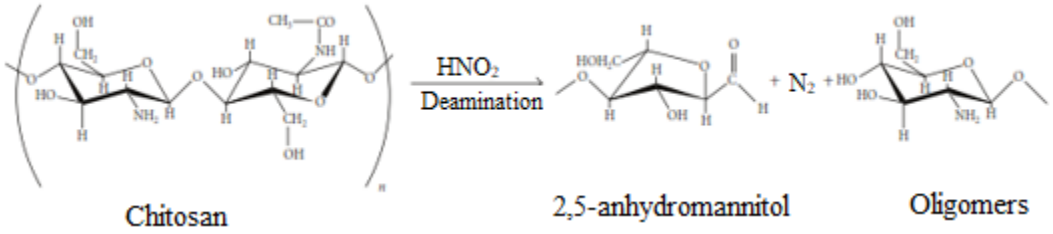

2.5

2.4.3.2 *Degree of deacetylation*

The degree of deacetylation (DD) is the fraction of the deacetylated units in a chitosan chain. It is achieved by the partial elimination of the acetyl functional groups from the chitin structure. The deacetylation process determines the number of free amino groups present in the chitosan molecule. The free amino groups, in turn, determine the overall functionality and suitability for various applications. It affects the physicochemical properties of chitosan such as solubility, viscosity, polarity, flocculation, chelating ability and selective acylation (Chattopadhyay and Inamdar, 2010). Furthermore, the DD also affects the biodegradability and immunological activities of chitosan. The DD is thus an important property in chitosan synthesis.

2.4.3.3 *Viscosity*

The viscosity of polymer solution measures the hydrodynamic amount of the polymer molecules in the solution. It is influenced by the chain length of the molecule, which signifies the MW of the polymer (Chattopadhyay and Inamdar, 2010). Viscosity is a vital factor in chitosan studies and plays a significant role in determining its commercial applications. High MW chitosan results in highly viscous solutions as the concentration increases. This ideally may not be desirable for some industrial applications. Many factors affect the viscosity of a chitosan solution. They include DD,

MW, solution concentration, pH, temperature, extraction time and ionic strength of the acidic solution (Chattopadhyay and Inamdar, 2010). Among these outlined factors, the ionic strength of the solution is unique and influences the type of viscosity adopted in chitosan viscometric studies. Rinaudo *et al*. (1999) investigated the viscosity of chitosan in HCl and acetic acid solutions and reported an increase in the relative viscosity of chitosan as HCl concentration increases while a fairly constant viscosity was observed with acetic acid even at high concentrations. Rinaudo and his colleagues were of the opinion that the observed behaviour was due to the complete protonation of chitosan in acetic acid solution. They further stated that it could have also resulted from the low ionic concentration of acetic acid as a result of its low pKa (4.74) value. This, therefore, necessitates the use of intrinsic viscosity in chitosan viscometric studies (Yeul and Rayalu, 2013).

The effect of storage on the stability of chitosan as regards changes in solution viscosity is important in chitosan studies. Researchers have observed that the viscosity of a chitosan solution is impacted negatively by the length of storage. This is as a result of degradation of the polymer chains to lower particle sizes leading to reduction in the hydrodynamic volume of the polymer molecules. This volume reduction then leads to increased mobility of the molecules thus impacting the viscosity of the solution (Chattopadhyay and Inamdar, 2010). Dongre (2019) reported that storing chitosan solution at 5 °C in a refrigerator did not affect the viscosity of the solution and therefore prevents chitosan solution degradation and viscosity reduction.

2.4.3.4 *Solubility*

Chitosan is readily soluble in dilute acidic solutions below its pKa value of pH 6.5. Organic acids including acetic, lactic and formic acids are used in the dissolution of chitosan. Chitosan is also soluble in 1.0 % HCl and acetic acids but insoluble in polyprotic acids such as sulphuric acid at room temperature. The insolubility of chitosan in H_2SO_4 might be due to over protonation and crosslinking by too-strong acid as H_2SO_4 forms a crystalline chitosan sulphate when it reacts with chitosan (Zamani *et al*., 2007). When the pH of chitosan solution increases above 6.5, the amine groups become deprotonated, causing an increase in the size of the aggregates, phase separation and coagulation, and can be recovered as insoluble amorphous solid through filtration (El-hefian *et al*., 2011). The pKa value of chitosan is highly dependent on the degree of acetylation of the sample while the solubility is influenced by the DD, which has to be at least 85% for the desired

solubility to be achieved (Soon *et al*., 2018). Figure 2.8 describes the state of ionisation and the equilibrium reaction of chitosan at various pH.

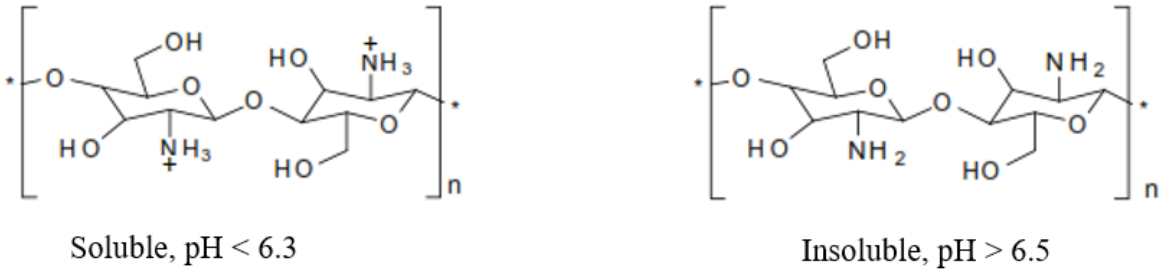

Soluble, pH < 6.3 Insoluble, pH > 6.5

Figure 2. 8: Schematics depicting the solubility and insolubility conditions of chitosan in aqueous solution (Ahyat and Azmi, 2016).

2.5 Nanofibre production

Nanofibres have attracted the attention of researchers for several years in various fields due to their remarkable nano-structural characteristics. These characteristics are high surface area, small pore size and the ease of generating three-dimensional structures for the development of advanced materials. Several fabrication methods have been developed for nanofibres production such as phase separation (Venugopal and Ramakrishna, 2005), template synthesis (Chen *et al*., 2017), self-assembly (Tiwari *et al.*, 2010), three dimensional (3D) printing (Song *et al*., 2017) and electrospinning (Li *et al*., 2018). Among these methods, the electrospinning process has become the most attractive because it is cost-effective, simple to assemble, highly productive and applicable to a variety of polysaccharides. Additionally, electrospinning has the advantage of controlling the morphology, diameter, alignment and porosity of the nanofibres produced.

2.5.1 *Electrospinning and the principle involved*

Electrospinning relies on the application of electrostatic force in breaking down molecules of a viscoelastic fluid to form atomized and charged jets (Wang *et al*., 2019). It involves energising the droplets of a solution held by its surface tension at the tip of a spinneret by the presence of a high voltage. Basically, an electrospinning system consists of three major components as shown in Figure 2.9A:

- a high voltage generator to induce a high electric field (100 – 500 kV/m).
- a spinneret

- grounded collector (Bhardwaj and Kundu, 2010; Wang and Hsiao, 2016).

Under a sufficiently high field, electric charge is induced on the emerging droplets. As the voltage increases, the droplet is deformed due to the repulsion and contraction of their surface charges. At the critical voltage, the ensuing jet enlarges into a cone-shape at the tip of the spinneret otherwise called Taylor cone (Taylor, 1969). When the electrostatic force exceeds the surface tension of the solution, a thin jet emerges and it is emitted through the spinneret. Ejection of the jets results in three different processes (Figure 2.9B) which are responsible for nano-sized polymer fibre formation. The processes are jet initiation and stretching or elongation (due to influence of electric force), bending and whipping instabilities (because of solvent evaporation and charge repulsion) and jet aggregation and deposition on the collector and fibre solidification as the solvent evaporates (Hohman *et al*., 2001; Wang and Hsiao, 2016). The rapid solidification of the fibre could lead to nucleation and growth of the phase separation between the chitosan fibres and the solvent. This could result in different morphologies of the resulting fibre such as beaded, porous, branched, tubular and zonal structures (Xue *et al*., 2019).

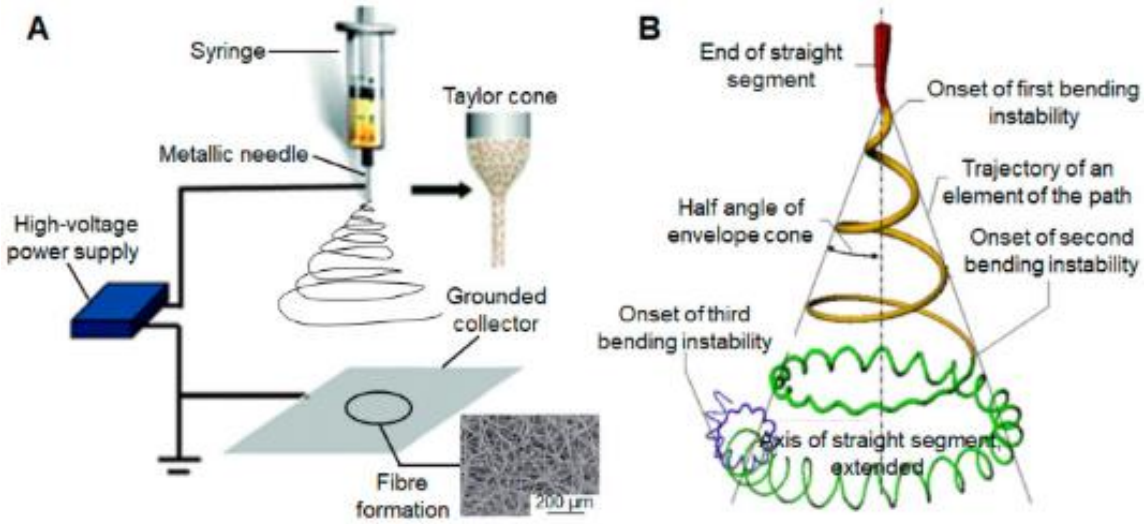

Figure 2. 9: Standard vertical electrospinning setup (A) showing the major components of the process (B) schematics depicting the occurrences of bending instabilities during the electrospinning process (Wang *et al*., 2019).

Electrospun fibres can be produced in wide-ranging diameters from the nanoscale to micron sizes that could compare favourably with the sizes of biological systems such as microbes (viruses and

bacteria) and proteins (Greiner and Wendorff, 2007). Figure 2.10 shows a comparative analysis of the size range of electrospun nanofibres and typical microbial species and some engineered materials.

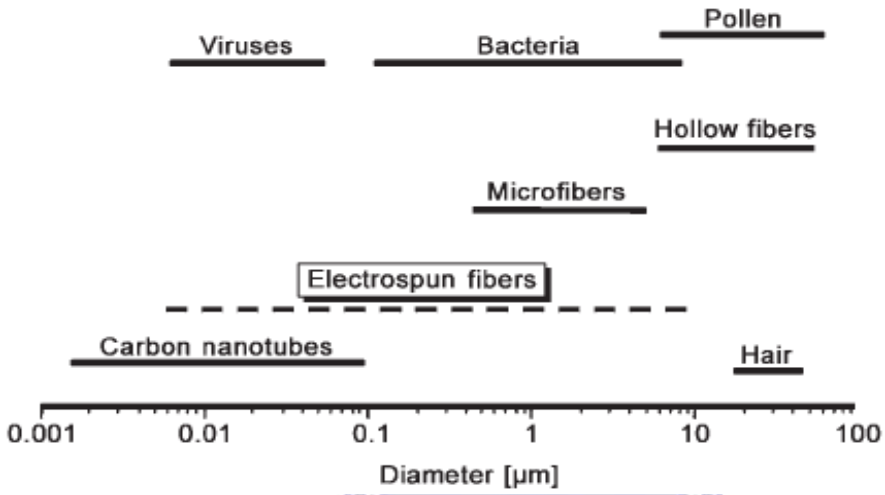

Figure 2. 10: Comparison of electrospun fibres with biological and technological objects of nanoscale sizes (Greiner and Wendorff, 2007).

2.5.2 *Polymers used in electrospinning*

Presently, more than 100 polymers have been electrospun to fibres in the nano to micron range of sizes for various applications (Xue *et al*., 2019). Electrospun nanofibres have been reported from various natural polymers such as chitin, chitosan (CHS), collagen, cellulose, protein; synthetic polymers such as polyethylene oxide (PEO), polyethylene terephthalate (PET), polyacrylonitrile (PAN), polyvinyl acetate (PVA); a blend of natural and synthetic polymers such as CHS/PEO (Aliabadi *et al*., 2013), CHS/PET (Jurak *et al*., 2017), CHS/PAN (Chaúque *et al*., 2016), CHS/PVA (Abraham *et al*., 2016) or a blend of proteins and nucleic acids (Bhardwaj and Kundu, 2010; Wang and Hsiao, 2016).

In the medical and biomedical applications, the natural polymers are preferred over the synthetic polymers because they exhibit better biocompatibility, low immunogenicity and they possess cell-binding abilities due to their detailed protein sequence such as arginine-glycine-aspartic acid (RGD) (Bhardwaj and Kundu, 2010). Our emphasis among the natural polymers enumerated in this section is on chitosan.

2.5.3 *Electrospinning of pure chitosan*

The electrospinning of pure chitosan solution has remained a challenging task due to chitosan's strong hydrogen bonding and polycationic nature in solution, its rigid chemical structure and unusual high viscosity (Geng *et al*., 2005). The strong inter and intra-molecular interactions of chitosan units restrict the free movement of the individual chains in contact with electric field causing jet breakage during electrospinning. In addition, adequate chain entanglement which could have ensured a continuous fibre formation during stretching, bending and whipping instabilities of the jet is hampered by the strong repulsive forces between the ionic groups on the chitosan backbone. The strong repulsive force results in the formation of beads in lieu of fibres when spinning chitosan (Min *et al*., 2004). To overcome this challenge, acids that could lower the surface tension of the solution and form stable salts with chitosan were investigated for electrospinning of pure chitosan. Trifluoroacetic acid (TFA) and acetic acid (AA) form stable salts with chitosan and effectively restricts the hydrogen bonding between individual units of chitosan thereby favouring electrospinning (Ohkawa *et al*., 2004). Geng *et al*. (2005) and Homayoni *et al*. (2009) reported the successful electrospinning of chitosan using a strong acetic acid solution. These reported electrospinning of pure chitosan have been from those extracted from shrimp source. However, a recent report by Kaya *et al.* (2016b) investigated the electrospinning of pure chitosan from the insect, *Drosophila melanogaster* using acetic acid solution. An ultrathin fibre diameter of 40.0073 ± 12.347 nm was reportedly produced.

2.5.4 *Effects of various parameters on electrospinning*

The electrospinning process is influenced by many parameters classified broadly into three: process, solution and ambient parameters. Each of these parameter significantly affects the fibre morphology and diameter and the appropriate combination of these parameters could result in nanofibers of desired properties (Chong *et al*., 2007).

2.5.5 *Process parameters*

The process parameters that determine the diameters of electrospun fibres and influence fibre formation and their overall characteristics include the applied voltage, the flow rate and the tip-to-collector distance.

2.5.5.1 *Applied voltage*

The applied voltage in an electrospinning process affects the amount of charge on the emerging jets, the magnitude of the repulsive force among the charges and the strength of the interaction between the external electric field and the jets. Increase in voltage was suggested by Charernsriwilaiwat *et al*. (2010) and Hu *et al*. (2011) to favour the production of fibre with reduced diameter. However, Demir *et al*. (2002) had argued that an increase in applied voltage led to the increased ejection of the polymer solution from the spinneret resulting in fibres with larger diameters. In many instances, increased voltage results in increased stretching of the emerging jets as a result of higher coulombic forces and a strong electric field. These effects combine to induce the rapid evaporation of the electrospinning solvent and the deposition of fibres devoid of beads with reduced diameters on the grounded collector (Haider *et al*., 2012). It has also been pointed out that the various instability modes which influence fibre formation take place during the interaction of the electric field and the electrospinning solution. These modes influence the morphology of the electrospun fibres and depend mostly on the shape of the jet surface and the degree of the instability (Deitzel *et al*., 2001). There exists a relationship between the applied voltage and the variation in the instability mode of the electrospinning process. Geng *et al.* investigated the impact of applied voltage on the electrospinning of chitosan and concluded that uniform and continuous bead-free fibres could only be obtained at an electric field strength of 3 kV/cm and above. Lower electric fields (1 kV/cm) tends to produce spindle-like fibres with beads, while higher electric fields (4.5 kV and above) leads to the formation of fibres with many beads and defects (Geng *et al*., 2005). According to the researchers, this might be due to the increase in elongation force and instability of the charged polymer solution by the strong electric field. Varying the voltage and the distance to the collector while keeping the electric field constant does not affect the fibre morphology (Geng *et al*., 2005). Figure 2.11 showcases the impact of applied voltage on the solution jet during electrospinning.

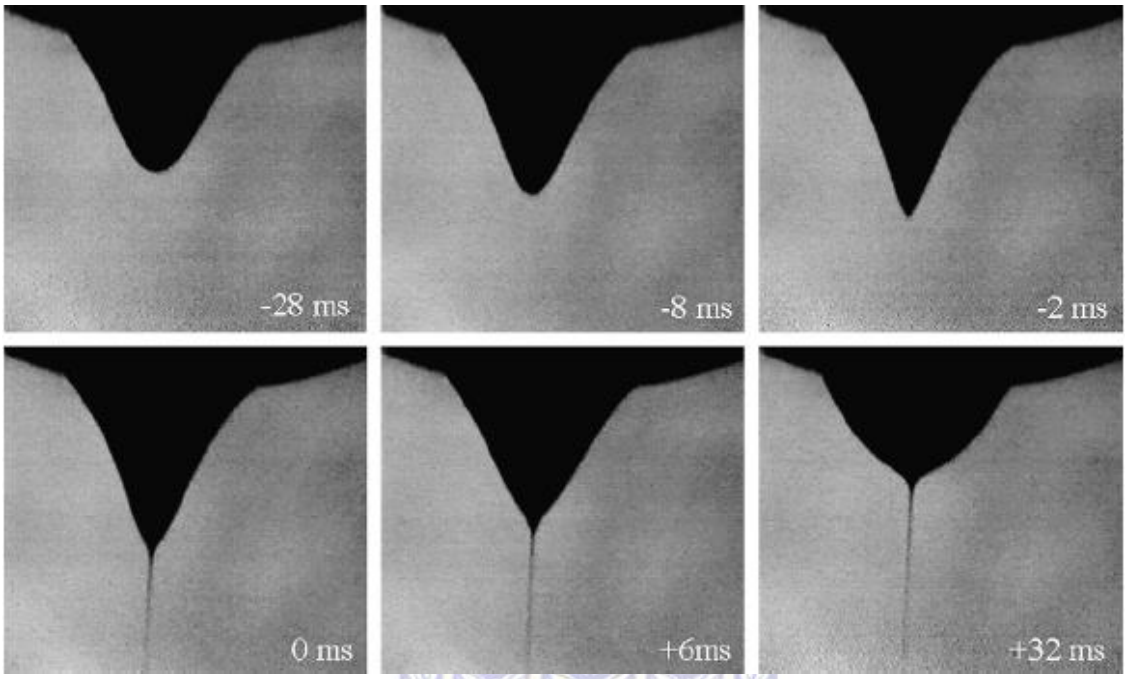

Figure 2. 11: The impact of applied voltage on Taylor cone formation, jet elongation, thinning and persistent flow towards the collector (Reneker and Yarin, 2008).

2.5.5.2 *Flow rate*

The flow rate of an electrospinning setup affects polymer solution transfer rate from the syringe and the velocity of the ensuing jet. Additionally, it affects the drying rate of the deposited fibres. Increase in flow rate induces the formation of fibres with increased diameter and beads due to reduced drying time of the jets before deposition at the collector (Yuan *et al*., 2004). Megelski *et al*. (2002) reported that increase in solution flow rate increased the pore diameter of electrospun fibres. Studies by Hartman *et al*. (2000) revealed that the jet diameter (d) is related to the flow rate (q) of the polymer solution by the relation $d \sim q^{0.48}$ and they attributed this to the bending instabilities of the ensuing jet. A reduced solution flow rate is preferable as the polymer jet gets ample time within the field environment to evaporate the solvent and deposit dry mats on the collector (Yuan *et al*., 2004). It is essential to note that homogenous nanofibres occur at a critical flow rate which varies based on the polymer solution. Increase or decrease in flow rate beyond this critical value results in the formation of beaded fibres. Therefore, a minimum flow rate is needed to sustain the equilibrium between the exiting polymer jet and the replacement solution for the sustenance of continuous flow (Megelski *et al*. 2002). Shamim *et al*. showed that steady flow rate influences the formation of stable Taylor cone and prevent the presence of receding jets which

could lead to the formation of fibres with heterogeneous diameters and sometimes, the ejection of unspun polymer droplets (Shamim *et al*., 2012).

2.5.5.3 *Needle tip to collector distance*

The spinneret-tip-to collector distance plays a vital role in defining the diameter and the morphology of electrospun nanofibres. This distance varies with polymer type. The rate of solvent evaporation, the solution flight time and the instability regime of the jet within the field environment is influenced by the spinneret tip to the collector distance and therefore affects the morphology and the quality of the nanofibres (Matabola and Moutloali, 2013). To electrospun neat and uniform nanofibres, a critical distance ought to be maintained as any variation will affect the quality and the morphology of the nanofibres (Bhardwaj and Kundu, 2010). The effect of collector distances on electrospun fibre diameters has been studied by many researchers. Matabola and Moutloali (2013) and Bhattarai *et al*. (2019) in separate studies showed that reduced collector distance increased the field strength of the process leading to increased instability of the jets and the formation of defective and large diameter nanofibres. However, Sedghi and Shaabani (2016) observed decreased fibre diameters with increased needle-tip-to collector distance and concluded that the observation may have resulted from the elongated flight time and the increased stretching of the jets within the electric field. It is, therefore, pertinent to maintain an optimum needle tip-to-collector distance during electrospinning process to ensure timely evaporation of the solvents, adequate drying of the deposited mats and the formation of defect-free nanofibres with improved morphology.

2.5.6 *Solution parameters*

The successful electrospinning of a polymer solution depends strongly on the solution parameters. They influence the spinnability or otherwise of the solution, the morphology and the structure of the produced fibres. The following subsection describes in detail these solution parameters.

2.5.6.1 *Concentration*

The concentration of a polymer solution plays a vital role in nanofibre production. This is because of the variation of the solution viscosity and its surface tension on the polymer concentration. At low polymer concentrations, the solution does not contain enough materials to cause entanglement

of the polymer chains for stable and continuous fibres formation (Rajak *et al*., 2019). In lieu of this, droplets are produced because of the effect of low surface tension. These droplets on microscope form microspheres. Too low solution concentration results in low surface tension, low viscosity and reduced chain entanglement and leads to the formation of beads, microspheres and droplets on the collector (Rajak *et al*., 2019). On the contrary, high polymer concentration increases the solution viscosity by increasing the strong hydrogen bond interaction between the -OH and -NH_2 groups of chitosan (Bhattarai *et al*., 2005). As the interchain association of the chitosan molecule increases, it leads to the formation of a highly viscous gel. This renders the solution unspinnable since it could not flow and elongate through the spinneret irrespective of the applied voltage. The viscous solution tends to build up and clog the spinneret, eventually dropping vertically due to gravity influence (Si *et al.*, 2014). Continuous and stable electrospinning with the formation of bead-free uniform nanofibres are achieved when the concentration of the polymer solution exceeds its entanglement concentration by about 2.5 times. The entanglement concentration is the concentration at which polymer chains in solution transforms from a free-floating state to twisting or entangling with one another (Tiwari and Venkatraman, 2012). The relationship between the concentration of a solution and the diameter of electrospun nanofibres was studied by Demir *et al*. (2002). They found a power-law relationship that the increase in concentration causes a corresponding increase in the fibre diameter.

2.5.6.2 *Viscosity*

The viscosity of a polymer solution is vital in determining its electrospinnability, the morphology and the diameter of the resulting electrospun nanofibres. Studies have shown that too low solution viscosity results in the disruption of a continuous flow of polymer leading to the formation of droplets and beaded fibres while a high viscous solution is difficult to eject from the spinneret due to longer stress relaxation time impeding the movement of the jets (Tiwari and Venkatraman, 2012). Different polymer solutions have different viscosity ranges depending on the solvent used and the MW of the polymer and range from 1 to 215 poise (Deitzel *et al*., 2002). The viscosity of a polymer is related to the concentration of the polymer which is in turn influenced by the MW of the polymer and the type of solvent used (Panthi *et al*., 2015). Therefore, polymer concentration is a vital parameter in controlling the viscosity of a polymer solution and in turn the quality of the nanofibre formed.

2.5.6.3 *Surface tension*

Surface tension, as a property of a liquid, shows how strong the cohesiveness of liquid molecules and thus the distinction in the phases at the interface of the liquid. It is strongly influenced by the solvent type and thus the selection of the right solvent is crucial not only to obtain a homogenous polymer solution but also the right surface tension (Hohman *et al*., 2001). High solution surface tension obstructs electrospinning process by inducing instability on the emerging jets thereby generating sprayed droplets (Hohman *et al*., 2001). The formation of polymer jets results from the action of electric charges which overcomes the surface tension of the polymer solution inducing instabilities on the jets and magnifying the breaking tendency of the extruding filaments forming droplets on the collector (Afshari, 2017). Surface tension can be adjusted by the addition of a surfactant or the alteration of the polymer/solvent ratio to achieve uniformity and homogenous fibre formation (Amariei *et al*., 2017). Surface tension also creates additional radial pressure in the electrospun nanofibres leading to the contraction of the polymer matrix thereby decreasing the free volume of the nanofibre, at the same time increasing its specific volume (Arinstein, 2018). Surface tension is therefore crucial as it determines the limits of an electrospinning process provided other variables are kept constant.

2.5.6.4 *Effect of solution conductivity*

The process of electrospinning requires the transfer of electrical charges from the positive electrode to the polymer jets at the needle tip. A minimum electrical conductivity of the solution is paramount for an electrospinning process. The conductivity of a polymer solution is an indication of the number of charges inherent on the surface of a polymer solution and it influences the formation of nanofibres or droplets (Pereao *et al*., 2016). The dissolution of a polymer in a solvent increases the solution's conductivity due to the presence of ionic species in the polymer structure (Bhardwaj and Kundu, 2010). However, Amariei *et al*. (2017) reported that an increase in the concentration of polymer in a solution could lead to the decrease in the electrical conductivity of the solution. Exception to this is if the polymer is a polyelectrolyte. In this case, the conductivity of the solution would be much higher. To improve the conductivity of a polymer solution, some researchers have introduced electrolytes to the polymer solution to (a) increase the electrical charge density of the solution and the force generated by the applied voltage and (b) increase the conductivity of the solution. This, in turn, would lead to increase in the stretching

capacity of the solution by reducing the field acting tangentially to the surface of the fluid. These favours the formation of homogenous fibres with reduced diameters (Huang *et al*., 2003). However, the extensive reduction of the tangential field could cause a reduction in the electrostatic force on the surface of the fluid thus affecting the formation of Taylor cone (Haider *et al.*, 2018).

Haghi and Akbari (2007) investigated the electrospinning of natural polymers and concluded that the reduction in the fibre diameter observed was due to the increased electrical conductivity of the solution and that the jet radius was inversely proportional to the cube root of the solution's electrical conductivity. The effect of 1% (w/v) of three ionic salts (KH_2PO_4, NaH_2PO_4, and NaCl) on the morphology of poly (D, L-lactic acid) was investigated by Zong *et al*. (2002). The nanofibres produced were smooth, bead free and of smaller diameter when compared to the control samples without salt addition. Therefore, the conductivity of a solution affects the elongation and thinning of the emerging jets and invariably influences the quality of the fibre produced.

2.5.7 *Ambient parameters*

Besides the process and solution parameters, ambient conditions such as temperature, relative humidity, airflow velocity or gas and vacuum environment (for molten solutions) have been reported to influence the morphology of electrospun nanofibres (Huan *et al*., 2015). Humidity impact changes to the fibres by influencing the drying and solidification of the polymer jets. Sharma *et al*. (2013) reported that polymers electrospun at a relative humidity of 60% and above do not dry properly and are difficult to detach as they entangle on the collector. Contrary to the observation of Sharma and his colleagues, Pelipenko *et al*. (2013) investigated the effect of change in humidity on the diameter of pristine PEO and a chitosan/PEO blend nanofibres. Their investigation showed that the diameter of the electrospun fibres decreased from 252 nm to 75 nm (for pristine PEO) with increase in humidity from 4 to 60% while the chitosan/PEO blend nanofibres also had a decreased diameter from 231 to 46 nm as the humidity was lowered from 4 to 50% (Pelipenko *et al*., 2013). Park and Lee (2010) and Hardick *et al*. (2011) reported similar observation of better quality and decreased nanofibre diameter with an increase in humidity of the spinning environment. However, Nezarati *et al*. (2013) reported breakage and loss of nanofibre morphology at relative humidity of 50% and below for electrospun polyethylene glycol, polycaprolactone and polycarbonate urethane polymers. Nezarati *et al*. (2013) believed that the

volatility of the solvent, the hydrophobicity of the polymer used and the miscibility of the electrospinning solvents with water influenced the observed effects on the nanofibre morphology. Some studies have reported that the use of mixed solvents in electrospinning of polymers contributes to the formation of porous nanofibres with humidity playing a key role. Bae *et al*. (2013) produced a highly porous polymethyl methacrylate (PMMA) nanofibre by using a mixed solvent of dichloromethane (DCM) and dimethylformamide (DMF) in a ratio of 8:2. The researchers attributed the formation of porous nanofibres to the different evaporation rates of the two solvents which caused cooling effects on the jets resulting in the condensation of water vapour to droplets on the fibres. With water being miscible with DMF, both solvents combine on the surface and the inner parts of the fibres with their complete evaporation resulting in the formation of porous nanofibres.

Temperature affects the diameter of electrospun nanofibres by influencing the rate of evaporation of electrospinning solvent and a decrease in the viscosity of the solution. The two processes work simultaneously and result in a decrease of the fibre diameter. Demir *et al*. (2002) observed that an increase in temperature (70 °C) produced more uniform nanofibres than the polyurethane nanofibres electrospun at room temperature. They further observed that 12.8% of the polymer concentration could be electrospun at room temperature whereas a concentration of 21.2% (65% increase) was electrospun when the temperature increased to 70 °C. The electrospinning of polyamide-6 was investigated at a temperature range of 25 to 60 °C by Mit-Uppatham *et al*. (2004). They observed that the increase in temperature produced fibres with decreased diameter. This, they suggested, resulted from the decrease in viscosity of the solution as the temperature increased. It is pertinent that a successful electrospinning exercise involves the optimisation of all the parameters including the solution, ambient and process parameters which ensure that fibres with desirable qualities such as morphologies and diameters are produced.

2.5.8 *The role of solvents in electrospinning*

The solvent used in an electrospinning process is of critical importance in ascertaining the quality of the electrospun nanofibres. A solvent performs several functions during an electrospinning process but two are paramount. The first is the dissolution of the polymer and the second is to transport the dissolved polymer in solution to the collector (Ohkawa *et al*., 2004). To actualise

these two roles, a solvent must possess excellent vapour pressure, good volatility, boiling point and should maintain the integrity of the dissolved polymer solution (Bhardwaj and Kundu, 2010). Rapid solvent evaporation occurs due to jet thinning and therefore solvent volatility plays a vital role in nanofibre formation and morphology as it influences the process of phase separation and the drying time of the fibres. A successful electrospinning process necessitates the selection of an appropriate solvent system. Bhardwaj and Kundu (2010) enumerated various solvents used in the electrospinning of both synthetic and natural polymers with their various properties. Some of the solvents are presented in Table 2.2.

Table 2. 2: Different solvents used in solution electrospinning and their properties.

Solvents	Surface tension (mN/m)	Dielectric constant	Boiling point (°C)	Density (g/cm^3)
Acetic acid	26.9	6.2	118.1	1.049
Acetone	25.2	21.0	56.1	0.786
Chloroform	26.5	4.8	61.6	1.498
Dichloro methane	27.2	9.1	40.0	1.326
Dimethyl formamide	37.1	38.3	153.0	0.994
Ethanol	21.9	24.0	78.3	0.789
Formic acid	37.0	58.0	100.0	1.210
Hexafluoro isopropanol	16.1	16.7	58.2	1.596
Methanol	22.3	33.0	64.5	0.791
Tetrahydrofuran	26.4	7.5	66.0	0.886
Trifluoro acetic acid	13.5	8.4	72.4	1.525

Source: (Bhardwaj and Kundu, 2010)

There are basically two solvents described in previous studies that have been used in the electrospinning of pure chitosan. The first is trifluoroacetic acid (TFA), which can destroy the rigid interaction between the chitosan molecules by forming salt ($-NH_3^+CF_3COO^-$) with the amino-functional groups (Sangsanoh and Supaphol, 2006). The advantages of TFA as an excellent solvent for electrospinning chitosan are low surface tension (13.5 mN/m), high dielectric constant (42.1) and low boiling point (72.4 °C) which favours the breakdown of the rigid structure of chitosan forming smaller diameter fibres (Wang *et al*., 2012). Its volatility and low surface tension are advantageous for the rapid solidification and subsequent drying of the electrified jet of the chitosan-TFA solution (Ohkawa *et al*., 2004). Ohkawa *et al*. (2004) further reported that the

addition of dichloromethane (DCM) to the TFA solvent eased the chitosan electrospinning process and produced homogenous fibres with an average diameter of 330 nm. The second solvent often reported in the electrospinning of chitosan is aqueous acetic acid, a monobasic organic acid. However, aqueous acetic acid solutions can only dissolve a small amount of chitosan. This soluble amount would be insufficient to provide the required chain entanglement and the minimum solution viscosity for effectice electrospinning process (Jayakumar *et al*., 2010).

Despite the many difficulties of spinning chitosan linked to the high viscosity in solution, some studies have reported the electrospinning of chitosan solution. Geng *et al*. (2005) investigated the effect of varying concentrations of acetic acid as a solvent for chitosan electrospinning. They reported that by increasing the concentration of the solvent, there was a gradual decrease in surface tension of the solution which favoured the formation of thinner fibres. Nevertheless, a major drawback of electrospun chitosan nanofibres is their solubility in neutral and acidic solutions below pH 6. To overcome this solubility problem, chitosan nanofibre requires crosslinking.

2.6 Crosslinking and stability of chitosan nanofibres in aqueous solution

Electrospun chitosan nanofibre is soluble in neutral and weak acidic solutions due to the high presence and solubility of ammonium acetate ($-NH_3^+CF_3COO^-$) salt residue formed by the amino group of chitosan acting as a proton acceptor in the presence of TFA (Figure 2.12) (Sangsanoh and Supaphol, 2006; Schiffman and Schauer, 2007; Cremar *et al*., 2018). To improve the chemical and mechanical stability of chitosan, crosslinking is undertaken. This can be achieved by physical or chemical crosslinking. In the chemical crosslinking, the crosslinker bonds to two different ends of a polymer functional group within the chain in a repeating arrangement thereby preventing dissolution in aqueous solutions. In the physical crosslinking, the various functional groups on the chain interact with one another without necessarily forming a chemical linkage. The interaction could be hydrogen bonding, hydrophobic interactions or coordination complexes (Croisier and Jerome, 2013). Figure 2.12 presents the reactions between TFA and chitosan in solution while Figure 2.13 shows the interactions occurring between the functional groups of chitosan and a crosslinking agent.

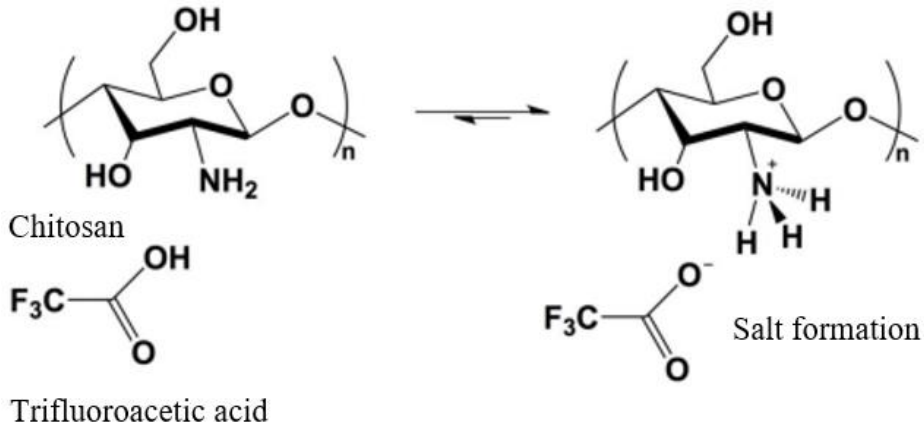

Figure 2. 12: The formation of ammonium acetate salt leading to the solubility of chitosan in TFA (Cremar *et al*., 2018).

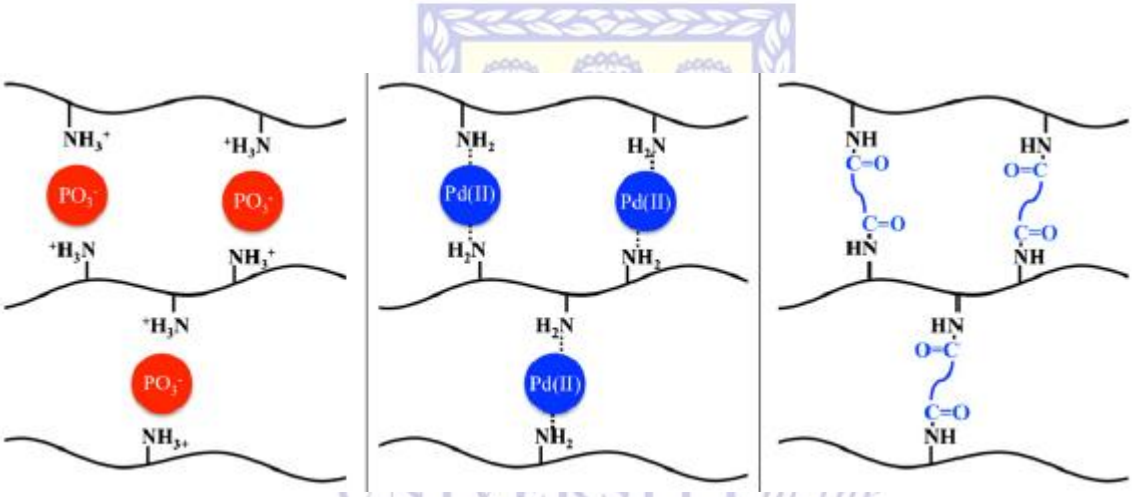

A B C

Figure 2.13: The crosslinking types obtainable with chitosan nanofibres and a possible crosslinker (A) electrostatic interactions (B) coordination complex and (C) covalent crosslinking (Croisier and Jerome, 2013).

Several crosslinking agents have been studied in a bid to stabilise chitosan nanofibres in aqueous solution. Some of these crosslinkers are glutaraldehyde (Schiffman and Schauer, 2007), epichlorohydrin (Austero *et al*., 2012), epoxides (Fu *et al*., 2011), isocyanates (Furuzono *et al*., 2000; Qasim *et al*., 2018) and genipin (Austero *et al*., 2012). The most widely used crosslinker as reported in the literature is glutaraldehyde (GA). The GA has two highly reactive aldehyde groups that can easily interact with functional groups such as hydroxyls, phenols, thiols and amines forming a covalent bond. The advantage of using glutaraldehyde include cost-effectiveness, ease

of availability and being highly effective in the stabilisation of biomaterials (Pal *et al*., 2013). However, GA is relatively toxic to biological systems if not effectively neutralised (Sung *et al*., 2001). Some studies have reported fibrosis and calcification of implants in some instances (Pettenazzo *et al*., 2001). These limitations necessitated the research for biocompatible, stable and non-cytotoxic crosslinking agents.

Biocompatible non-cytotoxic crosslinkers

The need for crosslinkers with biocompatibility and non-cytotoxic properties led to the use of genipin and tannic acid (TA) as crosslinking agents. The genipin and TA are natural occurring molecules having been used in the crosslinking of chitosan films and hydrogels with stability in aqueous solutions (Kiechel *et al*., 2013; Norowski *et al*., 2015). Despite the biocompatibility of genipin with biological systems, its major drawback is cost-effectiveness, as genipin is expensive (Mekhail *et al*., 2014; Zhao and Sun, 2017).

TA is a cost-effective, available and a hydrolysable polyphenol compound consisting of a mixture of polygalloyl glucose molecules with each having different degrees of esterification. The dominating gallate moiety in the TA structure is the decagalloyl glucose unit (Mori *et al*., 2012; Allais *et al*., 2018). The exact mechanisms of TA crosslinking with compounds having amine functionality is not yet known. However, Barry *et al*. (1984) suggested that it was through hydrogen bonding interaction. Figure 2.14 shows the proposed interaction between TA and chitosan.

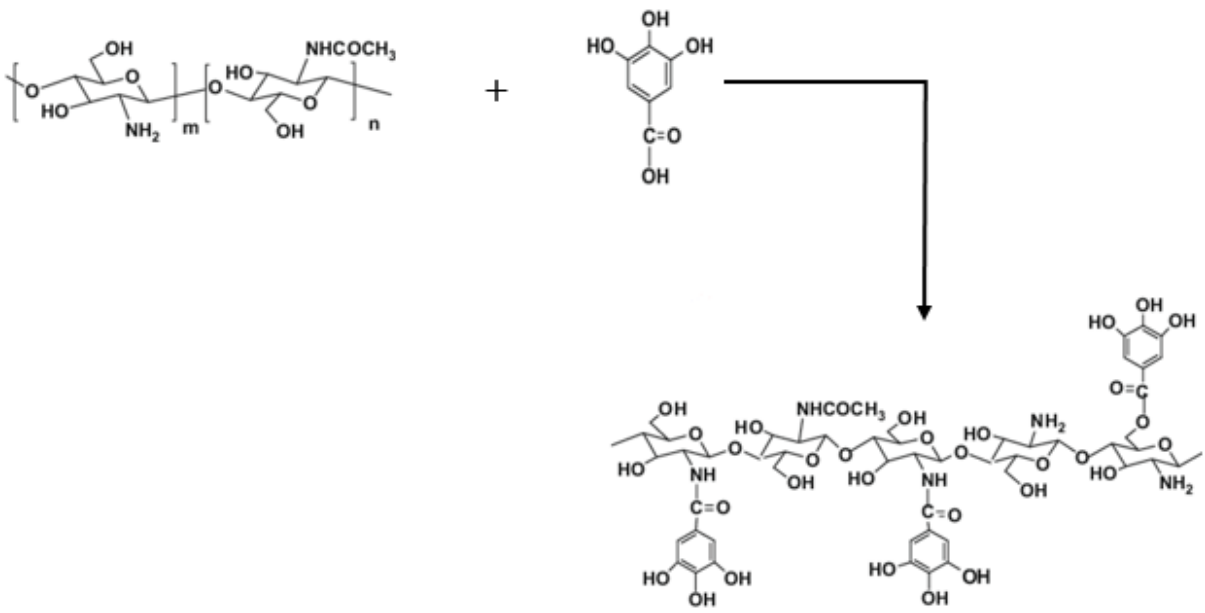

Figure 2.14: Schematics of the proposed pathway for the crosslinking of chitosan fibres by TA (Kang *et al*., 2017).

TA has been investigated as a crosslinking agent. Whittaker *et al*. (2016) fabricated insoluble homogenous poly(N-vinylcaprolactam) (PVCL) nanofibres by one-step electrospinning technique with TA as the crosslinking agent. The established optimal ratio for smooth and uniform nanofibres with a hydrophobic property was 0.15:1 and 0.29:1 (TA:PVCL). Vihola *et al*. (2008) stabilised a PVCL hydrogel using TA. The crosslinked hydrogel exhibited hydrophobic properties in aqueous solution from the initial super-hydrophilic properties of both PVCL and TA. In addition to the crosslinking capability of TA, they have been found to possess antimicrobial and antioxidant properties. Cremar *et al*. (2018) fabricated chitosan/cinnamaldehyde composite nanofibrous scaffold with antimicrobial properties for the attachment of cells using forced electrospinning technology. The stability of the spun composite scaffold was improved by the addition of TA as a crosslinking agent and treatment with a strong alkaline solution. The electrospun composite membrane showed no cytotoxic effects on NIH 3T3 mouse fibroblast cells as the cells grew close to the membranes. Kiechel *et al*. (2013) investigated TA as a non-covalent crosslinking agent for chitosan nanofibrous membranes in a two-step process. Smooth and uniform nanofibres with average fibre diameter 284 nm, 114% larger than the as-spun fibres were obtained. The fibres survived up to 72 h of immersion in aqueous solutions of 1.0 M acetic acid (AA), NaOH and distilled water.

2.7 Nanoparticles

Nanoparticles are materials with particle sizes between 1 – 100 nm. However, the definition of nanoparticles for medical and biomedical applications seems more liberal as a result of distinct characteristics of some particles above the 100 nm size distribution such as cell permeability (Maeda, 2001). Because of this, the traditional definition of nanoparticles is a subject of debate as many researchers are of the opinion that polymeric nanoparticles range from 10 – 1000 nm (Bhatia, 2016; Jahangiri and Barghi, 2018). Various materials have been used in the preparation of nanoparticles. These materials are grouped under inorganic and organic-based nanoparticles. Inorganic-based nanoparticles have been studied extensively because of their unique properties including magnetic, biological, electrochemical and photocatalytic properties. These properties have ensured their wide applications in light catalysed degradations, in magnetic resonance imaging, as antimicrobial agents and many more (Dizaj *et al.*, 2014; Manikandan, *et al*., 2017; Rashmi *et al*., 2019). Organic-based nanoparticles otherwise called polymeric nanoparticles, on the contrary, have attracted increased attention recently resulting from their distinctive structural, metallic, electronic features, ease of modification, stability properties and antimicrobial activities (Hatton *et al*., 2008). Biopolymers such as chitin, chitosan, cellulose and pectin-derived nanoparticles have added advantages of biocompatibility, biodegradability and non-toxicity (Ghormade *et al*., 2011) which has fuelled the increasing interest by researchers.

Polymeric nanoparticles have been prepared using two principal techniques classified as bottom-up and top-down approaches. The top-down processes involve the reduction of the bulk material size using methods such as fragmentation, milling, sonication, sputtering, thermal deposition, etc. These techniques mainly use physical processes, and results in nanoparticles with heterogeneous size distribution and poor morphological features. In the bottom-up approach, nanoparticles are formed by the gradual interaction of atoms, ions or molecules to form a nucleus which acts as a precursor to the building up of further atoms (Aimé and Coradin, 2017).

2.7.1 *Chitosan nanoparticles preparation*

Chitosan nanoparticles (CHS NPs) can be obtained through various bottom-up and top-down techniques. The selection of any of these techniques is dependent on several factors including the thermochemical stability of the particles, residual toxicity, process requirement and the particle

size of the synthesised products (Mitra and Dey, 2011). Figure 2.15 presents a schematic illustration of the various methods for the synthesis of CHS NPs.

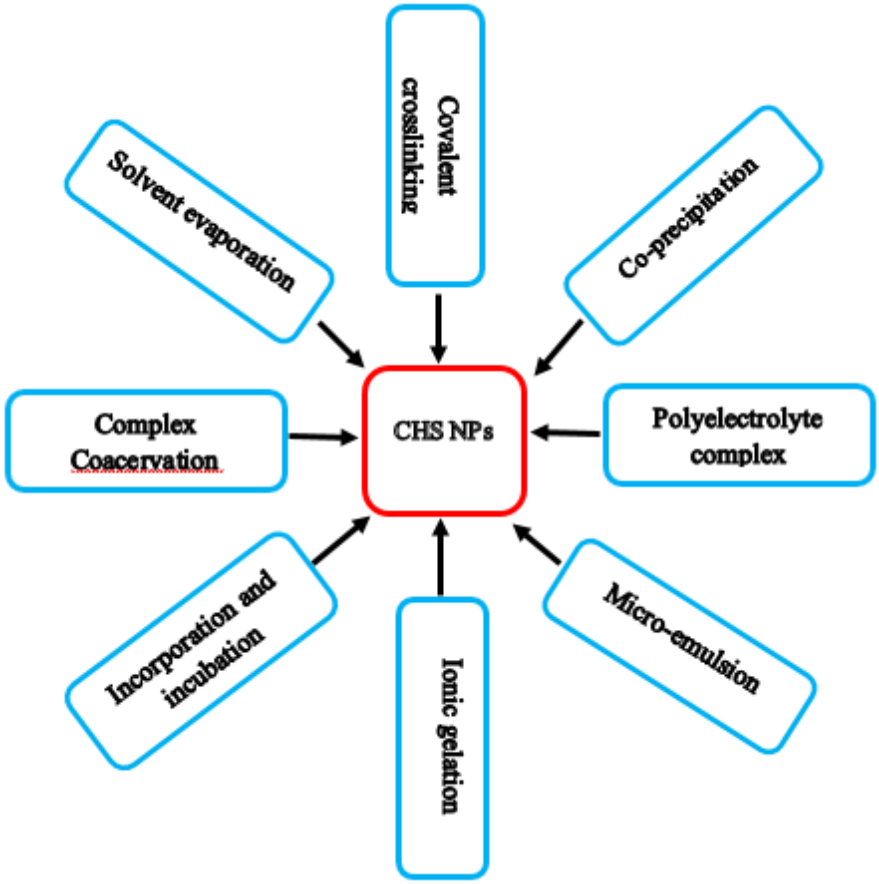

Figure 2.15: Methods of chitosan nanoparticle synthesis.

Among these methods, the ionic gelation and the polyelectrolyte complex techniques are widely used. The ionic gelation technique has been widely utilised in the synthesis of CHS NPs because of its flexibility, simplicity and the production of particles devoid of residual toxicity (Fan *et al.*, 2012). The technique explores the electrostatic interaction between the negatively charged polyanions such as tripolyphosphate (TPP) and the cationic amino ($-NH_3^+$) groups of chitosan. The electrostatic interactions modify the structure and the surface charge of the chitosan sample forming nanoparticles in the process (Divya *et al.*, 2017). The nanoparticle formation is spontaneous and results through intra and intermolecular crosslinking under constant stirring at ambient temperature. The interactions occurring is schematically illustrated in Figure 2.16.

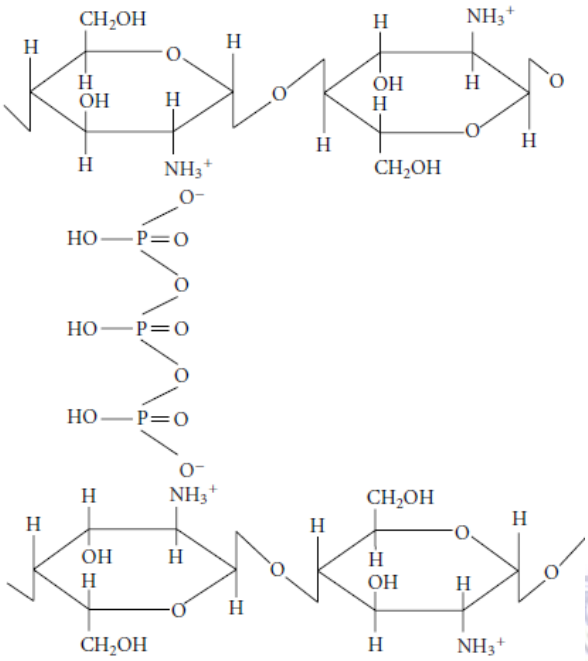

Figure 2. 16: Ionotropic crosslinking of chitosan and TPP (Chattopadhyay and Inamdar, 2010).

The ionic gelation interaction is pH sensitive. A better result is achieved by dissolving the chitosan in an acidic media. This promotes higher positive charge density in the chitosan molecules thereby facilitating the electrostatic interaction of the oppositely charged ions (Gan *et al.*, 2005). The CHS NPs synthesised by the ionic gelation approach exhibits varying hydrodynamic sizes, shapes and morphologies, influenced by several factors such as the concentration of the reactants, the ratio of the chitosan to the polyanions (TPP) and the MW of the chitosan used (Sreekumar *et al*., 2018; Rizeq *et al*., 2019).

Calvo *et al*. (1997) reported that the concentration of the chitosan and the TPP contributed strongly to the size of the synthesised nanoparticles. They opined that lower concentration of both reactants produced nanoparticles of smaller diameters while higher concentration leads to the synthesis of larger sized nanoparticles. The report of Fan *et al*. (2012) corroborated the study by Calvo *et al*. (1997) and showed that lower concentration of both chitosan and TPP produced nanoparticles with a mean diameter of 138 nm. They asserted that increase in the concentration of chitosan in the solution caused the reduction in the molecular distances of chitosan particles limiting their intermolecular crosslinking hence the increase in nanoparticle sizes formed (Fan *et al*., 2012). Fan *et al*. (2012) therefore suggested that the maximum concentration of chitosan and TPP needed to synthesise CHS NPs with an average diameter of 138 nm is 1.5 and 1.0 mg/mL, respectively.

The ratio of chitosan to the TPP affects the size and the surface charge of synthesised nanoparticles. Jonassen *et al*. (2012) and Fan *et al*. (2012) observed that the increase in the ratio of chitosan to the TPP did increase the size of the synthesised nanoparticles.
The MW of the chitosan used contributes significantly to the hydrodynamic diameter, size and charge density of the nanoparticles synthesised. Garrido-Maestu *et al*. (2018) reported that low MW chitosan produced particles with a smaller diameter than higher MW chitosan.

The ionic gelation approach of synthesising CHS NPs has proven to be more versatile than other techniques due to the number of researchers that have utilised it. However, there are the inherent limitations of aggregation of the particles resulting in difficulty controlling the final hydrodynamic size of the synthesised nanoparticles (Fan *et al.*, 2012). Furthermore, the solubility of the nanoparticles in water is, in some instances, in doubt (Qi *et al*., 2004). Additionally, the separation and re-dispersion processes of ionic gelation synthesised nanoparticles are very challenging (Pereira *et al*., 2011). An alternative approach to synthesising nanoparticles outside the traditional techniques is important. A major consideration as an alternative to nanoparticle synthesis is the electrospraying technique.

Electrospraying, otherwise called electrohydrodynamic spraying is the application of an electric field to break down bulk molecules of a conducting solution into smaller charged droplets of micro and nanoscale sizes (Nguyen *et al.*, 2016). The emitted droplets from the spinneret dry up before reaching the collector and are deposited as solid particles. Electrospraying shares the same operating principle with electrospinning. However, studies on nanoparticles synthesis using electrospraying are rare and hence lags behind electrospinning in terms of application. The use of electrospraying in nanoparticle synthesis has several advantages (Jaworek, 2007; Bock *et al.*, 2012; Nguyen *et al.*, 2016), including:

- ease of reproducibility,
- could be applied to varieties of polymers,
- the simplicity of the operation and experimental setup,
- minimal agglomeration tendency of resultant nanoparticles,
- produce highly charged particles due to the use of electrical current,

- a low-cost technique of nanoparticle fabrication,
- involves a one-step process of nanoparticle synthesis,
- easy to manipulate the size, distribution and morphology of the nanoparticles,
- synthesised nanoparticles do not require further purification.

The morphology and size of nanoparticles synthesised via electrospraying are influenced by the elongation ability of the polymer chain, the rate of solvent evaporation and the solution conductivity (Guarino *et al.*, 2015). Zhang and Kawakami (2010) observed that increased solution conductivity resulted in a decrease in the particle diameter as a result of increased repulsive force on the surface of the droplets. It, therefore, implies that for each solution and particle size range desired, a threshold conductivity is required which, if exceeded, could result in stronger repulsion on the droplets causing instability and limiting successful electrospraying/nanoparticle formation.

The solvent system used plays a vital role in the electrospraying process. A solvent determines the viscosity, conductivity, surface tension and to an extent, the charge density of the polymer solution, as well as the solubility and drying rate of the droplets (Jaworek, 2007; Ardila *et al*., 2018). Solvent to be adopted should have the volatility to completely evaporate from the droplets during the jet flight time. Solvents with low volatility, thus, slow evaporation rate could result in the deposition of wet particles on the collector with irregular morphology. Similarly, highly volatile solvents would result in rapid evaporation and drying of the droplets before getting to the collector leading to the formation of particles with porous morphology. In both instances, nanoparticles with undesired qualities would result (Nguyen *et al.*, 2016; Ardila *et al*., 2018). Therefore, proper consideration is required before the choice of solvent is made. In general, the solidification and complete drying of deposited nanoparticles are functions of polymer chain entanglement, the rate of solvent evaporation and the polymer diffusion rate. These factors simultaneously play vital roles in the quality of produced nanoparticles.

CHS NPs synthesis via electrospraying has been investigated by a handful of researchers. Ardila *et al*. (2018) investigated various parameters that affect process stability and particle formation. The solvent system investigated independently were acetic acid (AA), lactic acid (LA), citric acid (CA) and hydrochloric acid (HCl). The result showed that no electrospraying and jet deposition

was observed for the chitosan dissolved in LA, CA and HCl due to surface tension (44, 67 and 74 mN/m, respectively) which were high for the jets and particle formation. However, AA with a lower surface tension of 36.2 mN/m formed jets and deposited nanoparticles with an average diameter of 128 nm on the collector. They suggested that solutions with low surface tension and higher vapour pressure would produce nanoparticles with desired qualities if other conditions were kept constant. Pancholi *et al*. (2009) investigated the influence of surface tension and viscosity on the morphology and particle size of electrosprayed CHS NPs. They used acetic acid as solvent and high MW chitosan. They showed that low surface tension resulted in smaller particle-sized materials while high viscosity yielded materials with larger particle sizes. At the optimum surface tension and viscosity, the average size of the formed particles significantly decreased from 2500 to 500 nm, a 400 per cent reduction.

Zhang and Kawakami (2010) investigated the influence of various solution parameters on the formation of nanoparticles using the one-step electrospraying technique. The study was conducted using acetic acid as a solvent. Their preliminary result showed that low conductivity and high viscosity were the critical factors that affected the electrospraying process. The addition of ethanol to the chitosan solution stabilised the process by reducing the conductivity and increasing the viscosity of the solution. The optimisation and stabilisation of these solution parameters resulted in the deposition of particles with a mean diameter of 124 nm. Zhang and Kawakami concluded that CHS NPs synthesis by electrospraying is dependent on the concentration of the chitosan and the solvent, the flow rate and the viscosity of the solution.

Studies that investigated and addressed the synthesised CHS NPs using electrospraying technique are relatively few in the literature. The few that investigated this technique using acetic acid as a solvent while others used ethanol as a co-solvent and surfactants in very few instances (Geng *et al*., 2005). Additionally, the source of chitosan affects its physicochemical properties. Therefore, the use of insect chitosan extracted from BSF for the synthesis of CHS NPs will contribute towards the knowledge base of the electrospraying technique.

2.8 Application of chitosan against microbial species

Several research groups have investigated the efficacy of chitosan on Gram-positive, Gram-negative (Helander *et al.*, 2001) and fungal species (Palmeira-de-Oliveira *et al.*, 2010; Tayel *et al.*, 2010). The mode of action of chitosan against these organisms, as suggested by Kong *et al*. (2010), could result from many factors. Among these factors are environmental factors (e.g. pH), type of the microorganisms (bacteria, fungi, *et cetera*), and state of the chitosan sample during application.

The activities of chitosan are dependent on the type of microorganism and on the structure of the cell membrane of the organism (Chung *et al.,* 2004). There are no generally accepted mechanisms of chitosan action against microorganisms. However, Anush *et al.* (2018) suggested that the chitosan mechanism of action is based on its ability to bind cell membranes of microbes disrupting the equilibrium metabolic dynamics of the cells. This ultimately results in cell lysis and eventual death. The action of chitosan results from the positively charged amino groups interacting with negatively charged surface components of most bacteria cells (Anush *et al.,* 2018).

2.8.1 *Structure of the bacterial cell*

Bacteria cells consist of cell walls, cell membrane and a cytoplasmic membrane that collectively acts as barriers to diffusing materials into the cells. Peschel *et al.* (2001) had reported that some of the surface components of the cytoplasmic membranes are mureins, peptidoglycans and teichoic acids that exist only in Gram-positive bacteria. The teichoic acids are polyanions and they play a significant role in the negative charge exhibited by the cell walls of *S. aureus,* a Gram-positive bacterium (Figure 2.17). The lipopolysaccharides, on the other hand, are similar to the teichoic acids, however, they exist only in Gram-negative bacteria. These two components, the teichoic acids and lipopolysaccharides, are critical in binding to chitosan molecules disrupting the fundamental cell functions (Raafat *et al*., 2008). Ma *et al*. (2017) were of the opinion that the chitosan particles could penetrate the cell membranes of the microorganisms inhibiting most enzyme functions such as DNA transcription, protein and mRNA synthesis. Despite this suggested mechanism of actions, some researchers have expressed a contrary view. Bowman and Leong (2006) reported that hydrated chitosan particles were too large to penetrate the cell wall barrier of microorganisms and therefore could not reach the target within the cytoplasm.

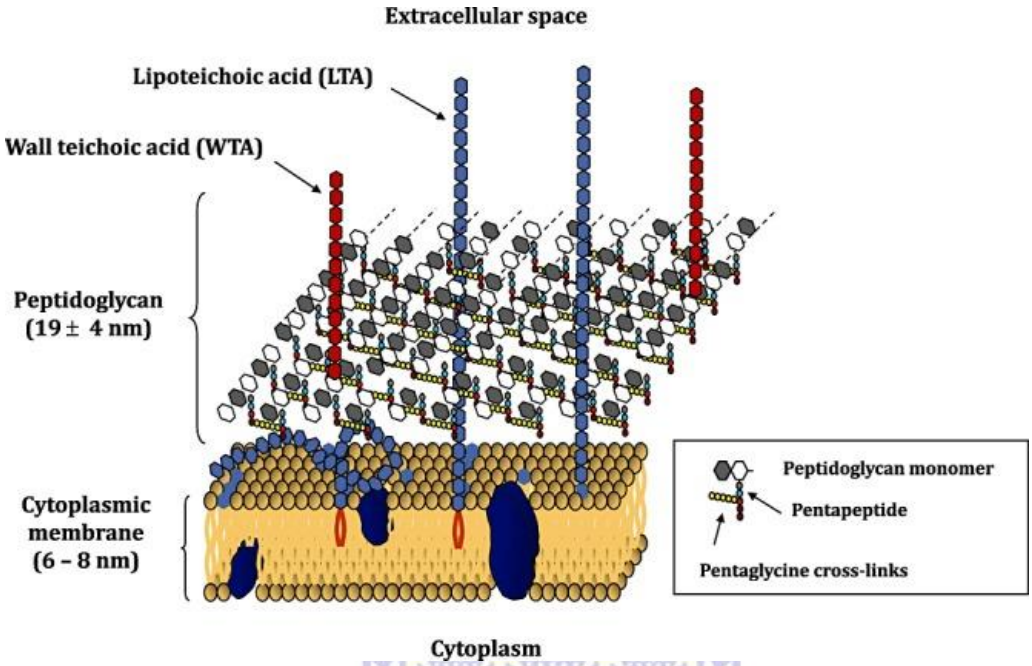

Figure 2.17: The cell walls of *Staphylococcus aureus* showing the multilayers of glycan strands and the teichoic acids polymers passing through the peptidoglycan layer contributing to the negative charge on the cell wall (Raafat and Sahl, 2009).

Several factors are associated with the antimicrobial activities of chitosan including the DD, MW and the capacity of chitosan to chelate metallic ions from the microbial cell walls.

One of the major reported modes of chitosan action against microbes is the binding of the charged amino groups of chitosan to the negatively charged bacteria cells (Anush *et al.*, 2018). The extent of the positive charge on the chitosan surface determines its charge density. The DD of chitosan is, therefore, crucial as it determines the solubility and the charge density ($-NH_3^+$) of chitosan in solution. High DD positively correlates high charge density on the chitosan backbone that influences its (chitosan) antimicrobial efficacy by interacting with the negatively charged cell wall of the microbes causing lysis. As the DD increases, the charged species increases which in turn increases the charge density favouring a higher electrostatic reaction and ultimately an increased antimicrobial activity results (Kong *et al.*, 2010; Ma *et al*., 2017).

Molecular weight is very fundamental in the antimicrobial activities of chitosan. Low molecular weight (LMW) chitosan has been reported to possess better antimicrobial functions than the higher molecular weight (HMW) chitosan samples. This assertion was corroborated by Kumar *et al*. (2005) who hypothesised that the increased antimicrobial activity of LMW CHS was due to its

decreased chain length which could easily attach to the microbial cell wall disrupting the cells vital functions. Despite the antimicrobial potentials of LMW CHS, there seems to be a threshold of polymerisation below which the antimicrobial activities diminishes. Jeon *et al*. (2001) suggested that MW above 10 kDa is essential for the inhibition of microbial species below which chitosan antimicrobial potentials diminishes. This assertion was re-echoed by Raafat *et al.* (2008) in their study of the chitosan mode of action as antimicrobial agent. Apart from the degree of polymerisation, the type of microorganisms investigated can influence the antimicrobial efficacy of chitosan. Zheng and Zhu (2003) reported that LMW was more potent against Gram-negative *E. coli* while HMW CHS showed effectiveness against Gram-positive *S. aureus*. They suggested that the observed difference in activity could have resulted from the ability of the LMW CHS to penetrate the semi-permeable cell membrane of the Gram-negative *E. coli* and altering the metabolic functions. Furthermore, the HMW CHS could not penetrate the cell walls due to increased size of the particles that rather stack on the cell wall, enveloping it and eventual starving the cells of essential nutrients exchange from its surrounding (Zheng and Zhu, 2003).

The antimicrobial properties of chitosan could also be attributed to its chelating potentials to various metal ions. In the microbial cell wall, chitosan has been hypothesised to bind to trace elements that are essential for the functions of the cell inhibiting microbial proliferation and in some instances limiting toxin production (Kravanja *et al*., 2019). Kumar *et al.* (2005) have suggested that the antimicrobial activities of chitosan emanate by inhibiting microbial growth through the blockade of nutrient flow to the cells. They opined that chitosan achieves this by continuously being deposited on the bacteria surface due to difference in potentials across the cells hence preventing material exchange through the semi-permeable membrane of the cells. This thereby distorts the fundamental metabolic processes of the cells causing lysis and eventual deaths (Kumar *et al.*, 2005).

The state of the chitosan sample used for the antimicrobial studies could also affect its antimicrobial activities. Chitosan could be applied in the solid or liquid state. Chitosan in the liquid state is more potent due to its ability to dissociate in solution and could penetrate the cell cavity leading to increased antimicrobial activity, unlike the solid-state chitosan which affects its environment by surface contact (Kong *et al.*, 2010).

The pH of the solution is fundamental in determining the effectiveness of chitosan against microbes. Li *et al*. (2016) investigated the potency of chitosan against microbial species of *Escherichia coli* and *Staphylococcus aureus* and concluded that the chitosan displayed higher bactericidal activity at acidic pH more than at neutral or basic conditions. They asserted that the protonation of the amine functional group (from $-NH_2$ to $-NH_3^+$) of the chitosan in acidic medium was instrumental to its increased bactericidal activity. Furthermore, Li and colleagues stated that the cationic property of chitosan in acidic medium influences their interaction with the negatively charged cell walls of bacteria, smothering its fundamental metabolic activities.

2.9 Antimicrobial effects of chitosan nanoparticles against microorganisms

CHS NPs have gained increasing interest among researchers since its discovery by Ohya and co-workers in 1994. This may not be unconnected with its distinctive properties including environmentally friendly, biocompatibility, GRAS (generally recorgnised as safe) bioactive material, non-toxic, biodegradable, antimicrobial properties, and excellent surface-to-volume ratio (Malmiri *et al*., 2012; Divya and Jisha, 2017). The antimicrobial activities of CHS NPs emanate from chitosan's ability to electrostatically attach to the negatively charged cell walls of microbes due to their polycationic nature and disrupt the microbes fundamental cell functions (Pelgrift and Friedman, 2013). The functions could be nutrient exchange, respiration and/or material balance within the cells. After binding to the cell wall of the microbes, the nanoparticles could also penetrate their cytoplasm thus binding to the DNA and leading to the modifications in the synthesis process of protein and mRNA by the cells (Chávez de Paz *et al*., 2011). These combined modes of actions could lead to cell lysis and eventual death of the microorganism.

The potential of CHS NPs against microbial species have been evaluated in several studies. Aliasghari *et al*. (2016) synthesised CHS NPs through ionic gelation method and compared its efficacy with bulk chitosan sample in the treatment of *S. mutans*. The results show that CHS NPs were 50% more potent than the bulk chitosan samples from the minimum inhibitory concencentration (MIC) and minimum bactericidal concentration (MBC) studies. Chávez de Paz *et al*. (2011) in their study of the antimicrobial efficacy of CHS NPs against *S. mutans* reported that the nanoparticles reduced the planktonic state of the organism by 95% and the biofilm state

by 93.4%. The nanoparticles, according to Chávez de Paz *et al*. (2011) were synthesised from LMW chitosan using the ionic gelation approach.

Ikono *et al*. (2019) successfully synthesised CHS NPs with a mean particle size of 25 nm using the ionotropic gelation method. They investigated the inhibition capacity of the nanoparticles against the biofilms of *S. mutans* and *C. albicans in vitro.* The result showed that the biofilm mass was reduced significantly as the concentration of the nanoparticles increased with maximum inhibition occurring at 18 h of contact.

CHS NPs have also been studied and found to possess antifungal properties. Yien *et al*. (2012) comparatively studied the effect of CHS NPs and bulk chitosan against *C. albicans*. The result showed that the nanoparticles were more potent than the bulk chitosan. Though the observed effects were obtained at an increased concentration of the nanoparticles.

2.10 Adsorption

Adsorption is adjudged as a simple, flexible, cost-effective and efficient method of removal and recovery of metal ions from water and wastewater streams. It has gained wide acceptance in water treatment processes because of its ease of operation, absence of sludge and secondary contaminants formation and neutrality from the effects of toxic pollutants (Akpomie and Dawodu, 2016). These advantages made the United States Environmental Protection Agency (USEPA) to classify adsorption among the best available contaminant control measures (Albadarin *et al.*, 2017). In the adsorption process, solubilised metal ions are transferred to the active sites or functional groups on the surface of an adsorbent by diffusion or convection and are held by physical, chemical or a combination of both forces on the adsorbent's active sites (Guo and Wang, 2019).

The adsorption experimental process is influenced by several factors such as pH of the solution, the contact time, the dosage, concentration of the pollutants (metal ions), temperature, adsorbate volume, and many more. The variation in any of these conditions in an experimental process automatically varies the outcome of the investigation and shows that no two adsorption investigations are the same (Kyzas and Bikiaris, 2015). The success of an adsorption investigation

is dependent on the adsorption capacity, the kinetic parameters and the regeneration ability of the sorbents. Adsorption capacity determines the extent of removal of the metal ions and hence the process cost while the regeneration potential is important, especially if the sorbent is expensive. The kinetic parameters are pointers to the adsorption rate of the sorbents and hence the spontaneity or otherwise of the process.

Different types of adsorbents have been studied for metal ion removal from aqueous solutions. Among those studied are activated carbons (Hu *et al*., 2003), natural zeolites (Inglezakis *et al*., 2003), magnetic nanoparticles (El-Dib *et al*., 2019), biosorbents (Onwordi *et al*., 2019), silica-based sorbents (Omotunde *et al*., 2018) and nanofibres (Martín *et al*., 2017).
Among these aforementioned adsorbents, nanofibres are a subject of intense investigation in the removal and, sometimes, the recovery of contaminants such as metal ions from wastewater. This is due to their flexible surface functionalities, large surface-to-volume ratio, ability to be processed into different shapes, forms and sizes, and could be produced from wide-ranging materials of organic and inorganic origin (Angammana and Jayaram, 2015).

2.10.1 *Chitosan nanofibre for adsorption of studies*

Chitosan nanofibres possess ideal functionalities such as large surface area, excellent pore volume, biodegradability, excellent adsorption capacity, and many others. However, the use of chitosan nanofibre as an adsorbent has some drawbacks including low stability in aqueous solutions and low mechanical strength. This necessitated some researchers to prepare chitosan composite nanofibres by blending with synthetic polymers and chemically modifying the composites to achieve stability in an aqueous environment (Aliabadi *et al*., 2013; Abdolmaleki *et al*., 2017; Wu *et al*., 2018). Studies have been undertaken that involved the use of electrospun chitosan nanofibres for adsorption.

Min *et al*. (2015) investigated As(v) adsorption onto an electrospun chitosan nanofibrous membrane in a batch process. The process parameters studied were pH, As(v) concentration, time of reaction and ionic strength of the solution. The solution pH was vital in the studies as a substantial adsorption capacity of 30.8 mg/g was recorded at lower pH time. Min *et al*. (2015)

further reported that the adsorption data obeyed the pseudo-second-order model with $R^2 > 0.99$, and the Langmuir model perfectly explained the obtained data.

Li *et al*. (2016) obtained chitosan nanofibres by one-step electrospinning technique for the adsorption of Pb^{2+} from aqueous solution. Li *et al*. (2016) investigated the effects of time, pH and concentration on the adsorption of Pb^{2+}. An equilibrium adsorption capacity of 110 mg/g was attained at a pH of 7.0. The adsorbent was thus stable and could be reused for more than three cycles. A Pure chitosan nanofibrous membrane was also fabricated by Li *et al*. (2018) for treating acid blue-113 dye contaminated solutions. A batch adsorption method was adopted by the researchers. They achieved an acid blue-113 dye removal efficiency of 1377 mg/g with the adsorption process following the pseudo-second-order kinetic model.

Haider *et al*. (2009) investigated the adsorption potential of electrospun chitosan nanofibre adsorbents for Pb^{2+} and Cu^{2+} in aqueous solutions. The adsorption results indicate equilibrium adsorption capacities of 485.44mg/g and 263.15mg/g were recorded for Pb^{2+} and Cu^{2+}, respectively. The experiment followed the monolayer adsorption with the Langmuir model was a better fit and therefore could explain the obtained data.

Nthunya *et al*. (2018) fabricated pure chitosan nanofibres crosslinked with glutaraldehyde for the removal of phenol from water. The nanofibres showed a 90% reduction efficiency for 3-methyl-4-nitrophenol from the aqueous solution. The adsorption followed the Freundlich isotherm, implying that the adsorption took place at different layers present at the surface of the nanofibrous mats.

The forgoing is a strong indication that pure chitosan nanofibrous membranes could be used for adsorption purposes without blending with a synthetic polymer.

2.11 Analytical techniques for characterising the synthesised materials.

Several analytical techniques used in characterising chitin, chitosan and chitosan nanomaterials to better understand their structural, physical, chemical and crystalline properties do exist in the literature. This section provides an overview of some of these techniques.

2.11.1 *Fourier transform infrared spectroscopy (FTIR)*

The Fourier Transform-Infrared spectroscopy (FTIR) is a simple but essential analytical technique for the identification of functional groups of most materials. The FTIR measures the absorbance or transmittance of infrared radiation by a material with respect to wavelength (Ngo *et al*., 2016). Molecular components, structures and compounds can be identified using infrared absorption bands as similar functional groups would display similar spectral bands. Identification is possible because by radiating a material, the molecules are excited to a higher vibrational state. This leads to the absorption of IR at various wavelengths. The signals produced by the absorbed radiation are indication of the properties of the sample's molecular structure (Adato and Altug, 2013). Infrared spectroscopy offers several advantages. It is fast since no monochromator is used, the instrument is available, it requires less sample preparation and the analysis is independent of sample solubility (Petit and Puskar, 2018). They are used to distinguish the two chitin isomorphs (α- and β-), determination of the DA and invariably the DD, hydrogen bonding of the molecules and for the control of extraction and purification conditions. The instrument operates in various modes; the transmittance and the attenuated total reflectance (ATR) modes (Steiner and Koch, 2009). In the transmittance mode, light is captured as it passes through a thin and transparent sample while in the ATR mode, light is projected at an angle to the sample surface which is incidentally reflected and captured for signal processing to spectra (Steiner and Koch, 2009). Several peaks of interest obtainable in chitin, chitosan and the synthesised nanomaterial studies and their merits and demerits are summarised in Table 2.3. From these peaks, the DA for chitin, and DD for chitosan could be computed using Equation 2.6 (Kaya *et al*., 2015).

$$\text{DA (\%)} = \left(\frac{A_{1655}}{A_{3450}}\right) x100 \qquad 2.6$$

Where A_{1655} and A_{3450} are the absorbance at wavelengths of 1655 cm^{-1} and 3450 cm^{-1}, respectively.

Table 2. 3: Reference peaks and wavenumbers of chitin and chitosan IR spectra.

Absorption band	Wavenumber (cm^{-1})	Merits	Demerits
O-H stretching	3451	O-H has a high peak height	(1) O-H of the water molecule is found in this region. (2) Always has a broad peak due to O-H groups involvement in hydrogen bonding (3) The peak intensity varies with the DA due to interference from N-H stretching peak found around 3300 cm^{-1}
C-H stretching	2870	i) Has well-defined peak intensity The band is not affected by: ii) hydrogen bonding iii) water	The C-H stretching of the N- acetyl groups varies with the DA
CH_2 bending	1421		Realignment of the hydrogen bonds influences the crystallinity of the sample which in turn affects the shape and size of the absorption band (Prashanth *et al.*, 2002)
C-O stretching	1031, 1070		i) most of the absorption bands in a chitin/chitosan spectra are found in this region ii) the C-O stretching band (1070 cm^{-1}) is not well resolved from this peak iii) has a weak intensity

Source: (Kasaai, 2008)

2.11.2 *X-ray Diffraction (XRD)*

XRD is a multipurpose, non-destructive analytical technique. It gives detailed information about the crystallographic and chemical compositions of materials. It uses the arrays of diffractions emanating as a result of bombardment of structures with x-rays to determine its crystal structure and crystallite sizes (Zuber *et al*., 2013). The pattern of diffraction is obtained and analysed to determine the crystal nature.

The XRD analysis has been adopted by several researchers to characterise extracted chitin and chitosan (Kaya *et al*., 2015; Adeosun *et al*., 2017). Adeosun *et al.* (2017) reported on the crystallinity of chitins from snail shell. In their study, they discovered one weak peak around 9° and several sharp peaks typical of the α-crystal structure of chitin were detected around 19°, 20.55°, 23.65° and 29.32°. This was consistent with previous studies on the α-crystal structure extracted from insects and shrimps (Kaya *et al*., 2015; Gbenebor *et al*., 2017). In the case of chitosan, two sharp peaks appeared at around 10.26° and 19.82° that correspond to the (020) and (110) crystallographic planes that are characteristic of chitosan (Sayari *et al*., 2016; Ahing and Wid, 2016).

An important factor deduced from the XRD studies of chitin and chitosan is the degree of orderliness or disorderliness of the samples. This factor indicates the fraction of a chitin/chitosan biopolymer material with an ordered or amorphous structural arrangement. The degree of orderliness (Crl) is calculated using Equation 2.7.

$$\text{Crl (\%)} = \left(\frac{I_{110} - I_{am}}{I_{110}}\right) x100 \qquad 2.7$$

Where I_{110} = diffraction intensity at 2θ ≈ 20° and

Iam = intensity of the amorphous diffraction at 2θ ≈ 16°.

2.11.3 *High resolution scanning electron microscopy (HRSEM)*

The HRSEM determines the surface morphology of a material by bombarding it with electrons. The interaction of the incident electrons and the sample surface provides vital information on the sample (Akhtar *et al*., 2018). The HRSEM has been carried out by researchers to image chitin and chitosan samples. Erdogen and Kaya (2016) observed the morphologies of chitins extracted from adult and nymph grasshoppers (*Dociostaurus macroccanus*) and reported that they consisted of long nanofibres with many having nanopores. Kaya *et al*. (2014a) conducted experiments on potato beetles (*Leptinotarsa decemlineata*) and concluded that chitin extracted from adults and larvae of those insects did not differ in nanofibre structure but in the number of pores. In characterising the surface morphologies of chitin and chitosan, the HRSEM remains a rapid technique for examining the morphologies of fabricated nanofibres.

2.11.4 *CP/MAS ^{13}C NMR*

The ^{l3}C NMR, with cross-polarisation and magic-angle spinning capabilities, is a powerful tool in the study of the structure and packing of molecules in the solid-state. It is very sensitive to changes in the arrangement of structures and measures only the carbon skeleton of a structure or compound and does not measure the proton attached to the structure (Tanner *et al*., 1990). Kasaai (2010) evaluated various spectroscopic techniques in the determination of DA and reported that ^{13}C NMR had better chemical shift dispersions than ^{1}H NMR and, therefore, could be used in the investigation of structures of chitosan. The solid-state NMR experiments combine three phenomena; cross-polarisation, dipolar decoupling and magic-angle spinning. The cross-polarisation enhances the sensitivity of the signal-to-noise ratio, dipolar decoupling ensures the elimination of dipolar interactions of protons while the magic-angle spinning enables the achievement of high-resolution chemical shifts (Gonil and Sajomsang, 2012). An impurity-free ^{13}C NMR chitin spectra have eight resonances, the C1 – C6, CH_3 and the C=O all occurring at chemical shifts between 20 and 180 ppm. The chitin spectra have both CH_3 and C=O peaks visible and with higher intensity. As the samples are subjected to deacetylation, the intensity of the CH_3 and C=O peaks starts to decrease. Thus, chitosan with low-intensity CH_3 signal is adjudged to have higher DD. The DA and the DD values of chitin and chitosan are determined from the ^{13}C NMR spectra by dividing the integral of the methyl carbon resonances by the average integral of the glucosyl ring carbon resonances according to Equation 2.8 (Gonil and Sajomsang, 2012; Hajji *et al*., 2014).

$$DA = 100\left\{\frac{I_{CH3}}{\frac{1}{6}(I_{C1}+I_{C2}+I_{C3}+I_{C4}+I_{C5}+I_{C6})}\right\} \quad 2.8$$

Where, I_{CH3} is the integral of methyl carbon resonance and I/6(I_{C1} + I_{C2} + I_{C3} + I_{C4} + I_{C5} + I_{C6}) is the summation of the average integrals of the glucosyl ring carbon atoms.

2.11.5 *Thermogravimetric analysis (TGA)*

The TGA is a valuable technique that measures the amount of weight change of a material, either as a function of increasing temperature or isothermally as a function of time. The weight loss observed on the thermogram is evidence of degradation phases. The investigation is usually conducted in an atmosphere of nitrogen, helium, air or vacuum (Kumari *et al*., 2017). The TGA is a complementary analytical technique which can detect the presence of impurities in a sample/composite material. The thermal profiles of chitin and chitosan have been studied extensively. Erdogan and Kaya (2016) studied the thermal behaviour of chitin and chitosan extracted from adults and nymphs of the grasshopper, *D. maroccanus*. They observed two profiles of mass loss. The first resulted from the evaporation of water embedded in the materials while the second stage was due to the degradation of the structure of both chitin and chitosan. They reported a maximum thermal degradation temperature of 386 and 383 °C for the adult and the nymph chitin while the chitosan had 302 and 308 °C for adult and nymph, respectively. Various researchers have reported similar degradation profiles in the literature (Younes and Rinaudo, 2015; Kaya *et al.*, 2015; Gámiz-González *et al.*, 2017). The thermal behaviour of chitosan nanofibres has been studied by numerous researchers (Haider *et al*., 2012; Su *et al*., 2011). In all the studies, two stages of mass loss with varying maximum temperatures of degradation were reported.

2.11.6 *Viscosity and molecular weight*

The capillary viscometric method is the easiest method to determine the viscosity of a dilute chitosan solution. In this method, the flow time of the chitosan solution, t_i, and the solvent, t_o, are recorded. The ratio of the flow time of a polymer solution to that of pure solvent (t/t_o) is equal to the ratio of their viscosities (η/η_0) if their densities are equal. The equality of densities is only feasible at extremely dilute concentrations where the density differences cancel out (Oberlerchner *et al.*, 2015). Because unity is the lower limit of the relative viscosity (η_r), the specific viscosity (η_{sp}) is more useful, as it represents the relative viscosity

increase resulting from the dissolved polymer in solution (Kapadnis *et al*., 2019). The various viscosities of a chitosan solution are expressed mathematically as:

Relative viscosity, $\eta_{rel} = t_i/t_o = \eta/\eta_o$

Specific viscosity, $\eta_{sp} = (t_i/t_o) - 1 = \eta_{rel} - 1$

Reduced viscosity, $\eta_{red} = \eta_{sp}/c$

Inherent viscosity, $\eta_{inh} = \ln \eta_{red} /C$ also expressed as $\lim_{c\to 0} \eta_{sp}/c$

The plotting of the η_{red} and/or the η_{inh} against the concentration of the solution and extrapolating the graph to the Y-axis yields the intrinsic viscosity. Intrinsic viscosity is, therefore, the limit of the reduced viscosity as concentration approaches zero.

The intrinsic viscosity of a chitosan solution has a direct relationship with the MW of the chitosan in the solution. This relationship has been explored to compute the MW of chitosan at a specific temperature by applying the Kuhn–Mark–Houwink–Sakurada equation (Costa *et al*., 2015).

$$[\eta] = KM^a \qquad 2.9$$

Where $[\eta]$ is the intrinsic viscosity (mL/g)

M is viscosity average MW (g/mol or Da)

K is a constant which is dependent on a given polymer type (mL/g)

a is a constant which depends on the chosen solvent.

The various solvents and their corresponding values of the constants *K* and *a* for MW determination are given in Table 2.4.

Table 2. 4: The values of the constants *K* and *a* at 25 °C for various solvents.

Acetic acid (M)	Buffer used (M)	*K* (mL/g)	*a*	Reference
0.5	0.2 (Na acetate)	3.5×10^{-4}	0.76	Laka and Chernyavskaya, 2006
0.3	0.2 (Na acetate)	7.6×10^{-2}	0.76	Rinaudo *et al*., 1999; Costa *et al*., 2015
0.1	0.2 (NaCl)	1.8×10^{-3}	0.93	Homayoni *et al*., 2009; Jung and Zhao, 2013
0.3	0.1 (Na acetate)	7.95×10^{-2}	0.79	Hajji *et al*., 2014

2.11.7 *Inductively coupled plasma-optical emission spectroscopy (ICP-OES).*

The ICP-OES is an essential, powerful, modern analytical technique for the determination of a broad range of metal ions in a variety of solubilised samples (Ndayambaje *et al.*, 2016; Yang *et al*., 2018). It is a highly sensitive analytical tool and uses the emission spectra of a sample to detect and quantify the elemental compositions of the sample (Hou *et al*., 2000; Ndayambaje *et al*., 2016; Yang *et al*., 2018). The mechanism of operation of this analytical technique starts by feeding a liquid sample into the system using a nebuliser. On getting to the plasma, the sample is vapourised, ionised and excited at a high temperature. A photodetector converts the wavelengths of the excited atoms to electrical signals which are amplified, processed, displayed and stored in the computer library (Hou *et al*., 2000). The introduction of the ICP as an analytical tool has relegated hitherto powerful methods such as atomic absorption spectrometry (AAS) and flame and graphite furnace atomic absorption spectrometry (GFAAS) to a second choice technique. The ICP-OES has the capability to detect and quantify up to 70 elements from a sample simultaneously. The ICP-OES has been adopted by several researchers in adsorption and desorption studies using chitosan and chitosan blend nanofibres (Baran and Mentes, 2015; Zhang *et al*., 2019).

2.12 Chapter summary

The reviewed literature showcased the extraction of chitin and chitosan from different sources including fungi, crustaceans and insects. The various processes of extraction of these materials including chemical and biological methods and the properties of chitosan were evaluated in this review. Electrospinning technique as a multipurpose, viable and cost-effective method of fabricating fibres in nanoscale sizes was examined. The principle involved, the parameters affecting the successful formation of fibres with the desired qualities, the electrospinning of polymer blends and finally the electrospinning of pure chitosan were critically examined in this review. Chitosan nanofibres were found to be soluble in aqueous solutions. To this end, the crosslinking of electrospun fibres were investigated and the various crosslinking agents including the biocompatible and non-toxic crosslinkers used in chitosan studies were examined to understand their merit and demerits. After the literature review, it was found that chitosan has been isolated from many sources including insects. However, no report in the literature highlighted on the deacetylation processes, optimisation of process conditions and the physicochemical properties of chitosan extracted from Black soldier fly waste materials. Another gap identified is that no

study has reported the fabrication of chitosan nanofibre and nanoparticles from commercially reared BSF waste materials by electrospinning and related techniques.

This study seeks to fill these identified gaps with a major focus on the optimisation of the conditions for the extraction of chitosan from both the pupal and adult of commercially reared Black soldier fly waste materials. Additionally, the production of nanofibres and nanoparticles from the extracted BSF chitosan through electrospinning and electrospraying techniques, respectively would be investigated. Finally, the application of the extracted chitosan, the nanofibres and the nanoparticles in antimicrobial and adsorption studies will be explored.

The next chapter discusses the detailed experimental procedures adopted in the optimisation of the extraction conditions, the synthesis of nanomaterials and the analytical techniques involved in the characterisation of the obtained samples.

CHAPTER 3

EXPERIMENTAL AND ANALYTICAL TECHNIQUES

3.0 Introduction

The previous chapter discussed the literature on BSF, chitin, chitosan and also the electrospinning techniques involved in chitosan nanofibre fabrication. This chapter is divided into three sections. The first section focuses on the description and the sources of the waste materials, chemicals, and equipment used in this study. The second section presents and describes the experimental procedures adopted while the third section briefly describes the analytical techniques involved in the characterisation of the extracted materials, nanofibres, nanoparticles and other samples used in this study.

3.1 Sources of materials, chemicals and equipment

3.1.1 *Sources, sample handling and storage*

The Black soldier fly was sourced from AgriProtein Technologies Ltd, a fly farm located at Phillipi, Western Cape Province, South Africa. The pupal shells/casings and dead adult BSF collected were delivered to the laboratory in sealed plastic bags to avoid external contamination. They were dried, pulverised using a Waring commercial laboratory blender Model HGBTWTS3 (Timer Blender MX – 8010S) and sieved (using 1 mm mesh size Universal Test Sieve ISO 3310-1). Finally, the samples were stored in a dark cool cupboard devoid of heat source, sunlight and fluctuating temperatures.

3.1.2 *List of equipment*

All the experiments and the solutions prepared were done using deionised water of conductivity 1.12 µS/cm and Milli-Q water (18.2 MΩ cm) purified by a Milli-TQM system. The chemicals used in this study, their sources and percentage purities are presented in Table 3.1.

Table 3. 1: List of reagents used in the study

Reagents	% Purity	Sources
Lead nitrate $Pb(NO_3)_2$	98	Sigma Aldrich
Cadmium nitrate $Cd(NO_3)_2$	99	Sigma Aldrich
Sodium hydroxide (NaOH)	99	Sigma Aldrich
Hydrochloric acid (HCl)	36	Sigma Aldrich
Ethanol (CH_3CH_2OH)	96	Sigma Aldrich
Sodium hypochlorite (NaOCl)	12	KIMIX
Acetic acid (CH_3COOH)	99.7	Sigma Aldrich
Tannic acid ($C_{76}H_{52}O_{46}$)		Sigma Aldrich
Trifluoroacetic acid (TFA)	99.9	Sigma Aldrich
Sodium acetate ($C_2H_3NaO_2$)	99	KIMIX
Dimethyl sulfoxide (DMSO)	99.7	Sigma Aldrich
Dulbecco's Modified Eagle's medium (DMEM)		Sigma Aldrich
3-(4,5-dimethylethylthiazol-2-yl)-2,5-diphenyl tetrazolium bromide (MTT).		Sigma Aldrich
Phosphate-buffered saline (PBS)	pH 7.4	Sigma Aldrich
Commercial chitin (P.Code: C9213)	85	Sigma Aldrich
Low Molecular Weight Chitosan (50 – 190,000 Da) P.code: 101816167	85	Sigma Aldrich

3.1.3 *List of equipment*

Table 3.2 presents the list of equipment used in this study and their various applications.

Table 3. 2: List of equipment used in this study

Equipment	Application
pH meter (SCS 200-K, Metler Toledo, Switzerland)	To determine the pH of the solutions
Fourier Transform Infrared Spectroscopy (PerkinElmer spectrum 400 FTIR/FT-NIR spectrophotometer)	To determine the functional groups and spectral differences/specifics between the synthesised materials.
Field Emission High-resolution scanning electron microscope (HRSEM) (Zeiss Gemini Auriga, Germany)	To determine the surface morphologies and fibre diameters of the synthesised materials.
Quorum Q150T ES Sputter coater	For coating the chitin, chitosan and nanofibres with Au for morphological examination.
Nuclear Magnetic Resonance (Bruker Avance III HD 400 MHz)	To identify the carbon skeletal structure of the materials and also calculate their degree of (de)acetylation.

Continuation of list of equipment used in this study

Equipment	**Application**
Waring commercial Laboratory Blender Model HGBTWTS3 (Timer Blender MX – 8010S).	For the granulation of the BSF.
Universal test sieve 1 mm mesh size (ISO 3310-1).	To sieve the pulverised BSF.
Syringe.	To hold and discharge the chitosan solution during the electrospinning process.
Programmable syringe pump, (Pump 33 Harvard Apparatus, Holliston MA, USA.	To provide a steady flow rate for the chitosan solution during electrospinning.
Inductively Coupled Plasma-Optical emission spectrometer (Varian Radial).	To determine the metal content during and after adsorption/desorption experiments.
Thermogravimetric analyser (TGA 4000) PerkinElmer Pyris Series.	To determine the thermal properties and weight loss regime of the materials.
X-Ray Diffraction (XRD) D8 Advance Diffractometer Bruker AXS, Germany.	To examine the degree of orderliness of the extracted chitin, chitosan and the chitosan nanofibres.
CHN PerkinElmer 2400 Elemental Analyser.	To determine the elemental (CHN) composition of the extracted samples.
Hot plate with a magnetic stirrer (LAB-smart MS-H-Pro^{+}).	To heat and stir solutions.
Zeta sizer, Malvern Zetasizer, Nano-ZS90, Worcestershire, UK.	To study the hydrodynamic size and zeta potential of the nanoparticles in solution.
Ubbelohde viscometer, Paragon Scientific size 1C, diameter 0.78 mm.	To determine the viscosity and the molecular weight of the extracted chitosan.
Digital balance (New Classic MF Model ML204/01, Mettler Toledo, Switzerland).	To accurately weigh the desired amount of samples.
Furnace Labofurn (Kiln contracts, Pty, Cape Town).	To investigate the ash content of the extracted chitin and chitosan.
Laboport vacuum filter, KNF Lab, Germany.	To provide desired pressure for filtration.
Oven, EcoTherm, Model 221, Labotech, South Africa.	For drying the samples.
Freeze dryer, HT 40 Telstar Ly Quest, Beijer electronics.	To obtain pure chitosan sample through freezing and sublimation via low temperature and pressure drying.
Centrifuge, MRC centrifuge, model MDCEN-301-SD, Essex, UK.	To separate precipitated chitosan samples from its solvent.
Microplate reader (Rayto RT–2100C, Germany.	For measuring the optical density of the living cells in cytotoxic studies.
Helios Epsilon Spectrometer, Thermo Fisher Scientific, Inc., MA, USA	To measure the absorbance or transmittance of chitosan solutions.

3.2 Experimental procedures of the study

This study comprises of five major aspects including extraction of chitin, synthesis of chitosan, electrospinning of chitosan, antimicrobial properties of the materials and adsorption studies using the fabricated nanofibres.

3.2.1 *Extraction of chitin*

The Black soldier fly (BSF) contain both organic and inorganic components. Chitin present in BSF are associated with proteins, pigments, lipids and minerals, (of which calcium carbonate is abundant) forming a chitin-protein complex (Shillito *et al*., 1995). These compositions can be separated through demineralisation, deproteination and decolouration processes. Each process is discussed in the subsequent sections.

3.2.1.1 *Demineralisation*

Demineralisation was done according to the method of Abdel-Rahman *et al.* (2015) with modifications. Briefly, the pulverised samples were demineralised using 1.0 M HCl solution (1:20 w/v) at a temperature of 50 $^{\circ}$C for 1.67 h (100 minutes). This was done under reflux and constant stirring using a magnetic stirrer (LAB-smart MS-H-Pro^{+}). The mixtures were filtered using a vacuum filter (Laboport Vacuum Filter, KNF Lab, Germany) and rinsed with distilled water to pH 6.5. The samples were oven-dried (EcoTherm, Model 221, Labotech, South Africa) at 70 $^{\circ}$C for 5 h and weighed using a digital balance (New Classic MF Model ML204/01, Mettler Toledo, Switzerland). The dried samples were kept in a desiccator before the deproteination process. The concentration, temperature and time optimisations for the demineralisation of both pupae (PCH) and adult (ACH) chitin are presented in Table 3.3, 3.4 and 3.5, respectively.

Table 3. 3: Demineralisation concentration optimisation for the chitin production

Sample	Temperature ($^{\circ}$C)	Time (h)	Concentration (M)
PCH1	50	1.0	0.5
PCH2	50	1.0	1.0
PCH3	50	1.0	2.0
ACH1	50	1.0	0.5
ACH2	50	1.0	1.0
ACH3	50	1.0	2.0

Table 3. 4: Demineralisation temperature optimisation for the chitin extraction

Sample	Temperature (˚C)	Time (h)	Concentration (M)
PCH4	30	1.0	1.0
PCH5	50	1.0	1.0
PCH6	70	1.0	1.0
PCH7	90	1.0	1.0
ACH4	30	1.0	1.0
ACH5	50	1.0	1.0
ACH6	70	1.0	1.0
ACH7	90	1.0	1.0

Table 3. 5: Demineralisation time optimisation for the chitin extraction

Sample	Temperature (˚C)	Time (h)	Concentration (M)
PCH8	50	1.0	1.0
PCH9	50	1.33	1.0
PCH10	50	1.67	1.0
PCH11	50	2.0	1.0
ACH8	50	1.0	1.0
ACH9	50	1.33	1.0
ACH10	50	1.67	1.0
ACH11	50	2.0	1.0

3.2.1.2 *Deproteination*

Deproteination followed the method of Abdel-Rahman *et al*. (2015) with slight modification. Demineralised samples were treated with varying concentrations of NaOH (0.5, 1.0 and 2.0 M) solutions (1:20 w/v) under reflux and constant stirring at various temperatures (85, 95, 105 and 120 ˚C) and time (10, 12, 14, 16 and 18 h) to obtain the optimal condition for the process. Afterwards, the samples were filtered using a Whatman No. 1 filter paper and rinsed multiple times with distilled water to pH 6.5. The extracts were dried at 70 ˚C for 5 h and weighed using a digital balance. Characterisations were done to ascertain the optimal deproteination conditions. The samples with the optimum conditions were subjected to the deacetylation process. The concentration, temperature and time optimisations for the deproteination of both

demineralised pupae and adult chitin are presented in Tables 3.6. 3.7 and 3.8, respectively.

Table 3. 6: Deproteination concentration optimisation for the chitin extraction

Sample	Temperature (˚C)	Time (h)	Concentration (M)
PCH12	85	12	0.5
PCH13	85	12	1.0
PCH14	85	12	2.0
ACH12	85	12	0.5
ACH13	85	12	1.0
ACH14	85	12	2.0

Table 3. 7: Deproteination temperature optimisation for chitin production

Sample	Temperature (˚C)	Time (h)	Concentration (M)
PCH15	85	12	1.0
PCH16	95	12	1.0
PCH17	105	12	1.0
PCH18	120	12	1.0
ACH15	85	12	1.0
ACH16	95	12	1.0
ACH17	105	12	1.0
ACH18	120	12	1.0

Table 3. 8: Deproteination time optimisation for chitin production

Sample	Temperature (˚C)	Time (h)	Concentration (M)
PCH19	95	10	1.0
PCH20	95	12	1.0
PCH21	95	14	1.0
PCH22	95	16	1.0
PCH23	95	18	1.0
ACH19	95	10	1.0
ACH20	95	12	1.0
ACH21	95	14	1.0
ACH22	95	16	1.0
ACH23	95	18	1.0

3.2.1.3 *Decolouration*

The decolouration step aimed at removing the leftover pigments associated with the BSF. These dried deproteinised samples were decoloured by stirring in a 2% sodium hypochlorite solution at a ratio of 1:20 (w:v) for 2 h at room temperature. The sample was rinsed to neutral pH and finally dried at 70 ˚C for 24 h in an oven. With this, the chitin extraction process was completed. The chitin content was determined using the dry weight of the extracted material compared to the starting material. The extracted chitin was stored in a desiccator awaiting the deacetylation process.

3.2.2 *Chitosan extraction (Deacetylation process)*

Deacetylation is the process of removal of the acetyl group of the chitin structure which helps to unleash the enormous potential of this material. Deacetylation was done using the modified method of Erdogan and Kaya (2016). The chitins extracted as described under Section 3.2.1.1 to 3.2.1.3 were refluxed in a 70% NaOH solution (1:20 w:v) under constant stirring for 5 h at 100 ˚C. These optimised conditions were obtained by varying the extraction conditions as shown in Table 3.5. The products were filtered using Whatman No. 1 filter paper under vacuum and washed to pH 6.5. The wet samples were dried at 60 ˚C for 12 h, weighed and the chitosan percentage yield estimated. Table 3.9, 3.10 and 3.11 show the concentration, temperature and time optimisations experiments, respectively for the extraction of chitosan from chitin.

Table 3. 9: Optimisation of deacetylation concentration for chitosan extraction

Sample	Temperature (˚C)	Time (h)	Concentration (%)
PCH21_1	80	5	30
PCH21_2	80	5	50
PCH21_3	80	5	70
ACH20_1	80	5	30
ACH20_2	80	5	50
ACH20_3	80	5	70

Table 3. 10: Optimisation of deacetylation temperature for chitosan extraction

Sample	Temperature (˚C)	Time (h)	Concentration (%)
PCH21_4	60	5	70
PCH21_5	80	5	70
PCH21_6	100	5	70
PCH21_7	120	5	70
ACH20_4	60	5	70
ACH20_5	80	5	70
ACH20_6	100	5	70
ACH20_7	120	5	70

Table 3. 11: Optimisation of deacetylation time for chitosan extraction

Sample	Temperature (˚C)	Time (h)	Concentration (%)
PCH21_8	100	3	70
PCH21_9	100	5	70
PCH21_10	100	7	70
ACH20_8	100	3	70
ACH20_9	100	5	70
ACH20_10	100	7	70

3.2.3 Chitin and chitosan yield determination

The yield (dry weight basis) of the extracts was estimated based on the starting waste materials and the extracted chitin. The optimised conditions of demineralisation, deproteination and deacetylation were applied for the extraction. The samples (chitin and chitosan) were weighed and the yield determined using Equations 3.1 and 3.2 for chitin and chitosan, respectively.

$$\text{Chitin yield (\%)} = \frac{\text{Dry weight of extracted chitin (g)}}{\text{Dry weight of pupae shells/adult BSF (g)}} \times 100 \quad (3.1)$$

$$\text{Chitosan yield (\%)} = \frac{\text{Dry weight of extracted chitosan (g)}}{\text{Dry weight of chitin used (g)}} \times 100 \quad (3.2)$$

3.3 Electrospinning of Chitosan

Figure 3.1 presents a schematic diagram of the dissolution and electrospinning process while Figure 3.2 shows an electrospinning set-up used for the production of the pupae chitosan nanofibres and nanoparticles in this study.

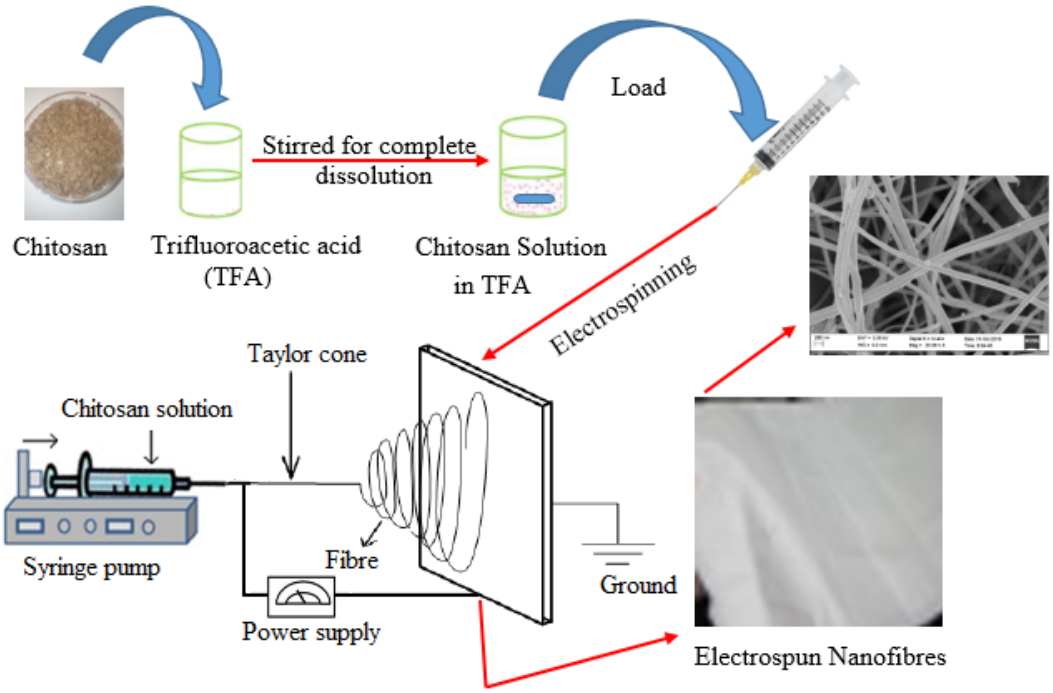

Figure 3. 1: Schematic of the electrospinning process used in this study.

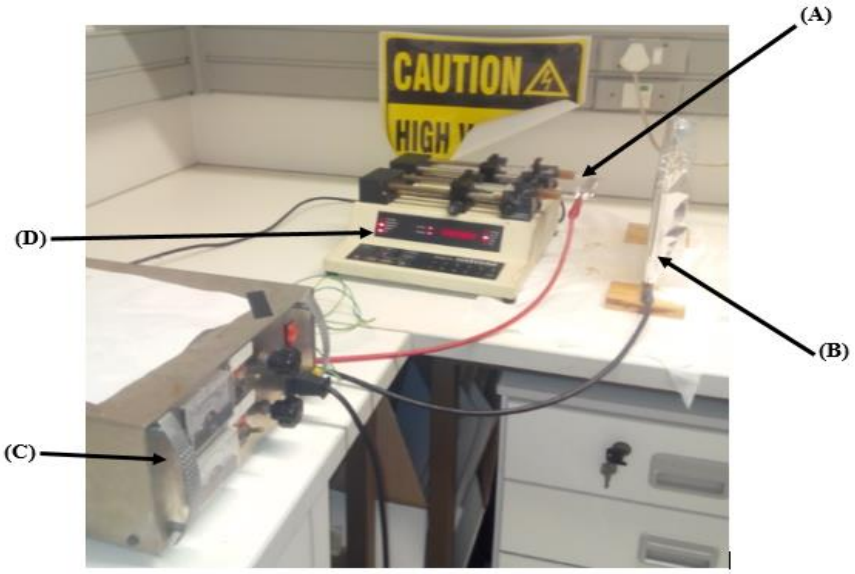

Figure 3. 2: Pictorial view of the electrospinning experimental setup (A) 20 mL syringe with a 19-gauge needle containing the chitosan solution connected to a high voltage machine (red cable), (B) grounded aluminium foil collector, (C) high voltage generator and (D) pump 33 dual-drive (DDS) programmable syringe pump.

Five different concentrations 3 %, 4 %, 5 %, 6 % and 7 % (w/v) of pupal CHS (PCH21_9) in a 99% trifluoroacetic acid (TFA) solution were stirred vigorous for 24 h to completely dissolve the samples. (For nanoparticles synthesis, 6 wt% of PCH21_9 was electrosprayed using aqueous TFA in a ratio of 9:1 TFA: deionised water). The electrospinning process was carried out at 25 °C. The completely dissolved chitosan solutions were introduced into a plastic syringe mounted with a 19-gauge stainless steel needle of 0.686 mm internal diameter. To remove the trapped air, each syringe was manually depressed until the polymer solution emerged at the needle tip. The syringes were then fastened to the syringe pump (33 DDS dual drive system, Harvard Apparatus, USA) horizontally. The positive terminal of the voltage supply was connected to the spinneret using an alligator clip while the negative terminal was connected to a 90 x 90 mm grounded collecting plate wrapped with aluminium foil to complete the circuit and create the needed electric field for the process. The high voltage supply and the syringe pump were then powered on. As droplets of the polymer solution start to appear at the tip of the needle, a Taylor cone becomes visible and a liquid jet of the polymer is seen extending towards the collector. The optimal conditions that were applied for the electrospinning were applied voltage of 25 kV, a collector distance of 100 mm, a flow rate of 0.3 mL/h while electrospraying were at applied voltage of 25 kV, a collector distance of 100 mm and a flow rate of 0.6 mL/h. The electrospinning process was then allowed to continue till a definite collection area was established. The nanofibre/nanoparticles were removed manually from the collector, left in ambient conditions to evaporate excess TFA and later dried in an oven (EcoTherm, Model 221, Labotech, South Africa) at 60 °C for 24 h, labelled and stored in a desiccator for further characterisation. The nanofibres/nanoparticles were characterised using HRSEM. The diameter of nanofibres from respective concentrations were measured from the HRSEM image using Image J software and the average value determined. The optimal nanofibre and nanoparticles (at concentrations of 5 and 6 wt%, respectively) were further characterised using ATR-FTIR, TGA and XRD techniques. The flow rate, applied voltage, needle tip-to-collector distance and concentration of the pupae chitosan solutions for nanofibre production were optimised in this study.

3.3.1 *Effects of solution concentration on electrospinning of chitosan*

This experiment was conducted to determine the effect of the pupae chitosan concentration in TFA on the spinnability of the biopolymer solution. To achieve this, the concentration of the solution was varied while keeping other process parameters of voltage, flow rate and tip-to-collector distance constant. Initially, the optimisation of this condition was done using acetic

acid but it could not achieve the objective, hence the use of TFA as a solvent. The experimental conditions are shown in Table 3.12.

Table 3. 12: Optimisation of concentration for electrospinning of chitosan in TFA solvent.

	Variable	Fixed parameters		
Sample code	Concentration (wt %)	Voltage (kV)	Distance (mm)	Flow rate (mL/h)
ES-C1	3	17	100	0.4
ES-C2	4	17	100	0.4
ES-C3	5	17	100	0.4
ES-C4	6	17	100	0.4
ES-C5	(*)	17	100	0.4

Table 3.12 shows the variable and fixed parameters in the chitosan concentration optimisation for the electrospinning of bead free nanofibres. The concentrations of 3, 4, 5 and 6 wt % were obtained by dissolving 0.4804, 0.6204, 0.7836, and 0.9504 g, respectively of the PCH21_9 sample in 10 mL of trifluoroacetic acid. The chitosan solution was stirred for 24 h using a magnetic stirrer until the complete dissolution of the sample was achieved. The viscous solution was introduced into a 10 mL syringe and fastened on a syringe pump. The 7 wt% chitosan concentration could not spin and therefore is denoted as (*). The electrospinning was carried out as described in Section 3.3.

3.3.2 *Effects of voltage on the electrospinning of chitosan*

These experiments were carried out to study the effect of voltage on the electrospinning of extracted BSF chitosan solution. The applied voltage was varied while other parameters, including the optimised concentration, were kept constant. The parameters studied in this experiment are presented in Table 3.13.

Table 3. 13: Optimisation of voltage for electrospinning of chitosan.

	Variable	Fixed parameters		
Sample code	Voltage (kV)	Concentration (wt %)	Distance (mm)	Flow rate (mL/h)
ES-V1	18	5	100	0.4
ES-V2	20	5	100	0.4
ES-V3	22	5	100	0.4
ES-V4	25	5	100	0.4

3.3.3 *Effects of flow rate on the electrospinning of chitosan*

This experiment was conducted to determine the effect of flow rate on the electrospinning of chitosan biopolymer. To achieve this, the flow rate of the solution was varied through the programmable pump while other parameters were kept constant. Sections 3.3.2 and 3.3.3 had earlier described the optimisation of concentration and voltage for nanofibre formation using the PCH21_9 sample. The experimental conditions are shown in Table 3.14.

Table 3. 14: Optimisation of flow rate for electrospinning of BSF chitosan

	Variable	Fixed parameters		
Sample code	Flow rate (mL/h)	Voltage (kV)	Distance (mm)	Concentration (wt %)
ES-F1	0.5	25	100	5
ES-F2	0.4	25	100	5
ES-F3	0.3	25	100	5
ES-F4	0.1	25	100	5

3.3.4 *Effects of needle tip-to-collector distance on the electrospinning of chitosan*

This experiment was performed to investigate the effect of needle tip-to-collector distance on the electrospinning process. In this experiment, the collector distance was varied while all other parameters remained constant. The optimised conditions of concentration, voltage and flow rate for nanofibre formation are described in Sections 3.3.1, 3.3.2 and 3.3.3. The experimental conditions for needle tip-to-collector distance are shown in Table 3.15.

Table 3. 15: Optimisation of collector distance for the electrospinning of BSF chitosan.

	Variable	Fixed parameters		
Sample code	Distance (mm)	Voltage (kV)	Concentration (wt %)	Flow rate (mL/h)
ES-D1	50	25	5	0.3
ES-D2	80	25	5	0.3
ES-D3	100	25	5	0.3
ES-D4	120	25	5	0.3

Table 3.15 shows the process conditions applied in the determination of the optimum needle tip-to-collector distance in this study. Optimised conditions of concentration (5 wt%), flow rate (0.3 mL/h) and voltage (25 kV) were previously discussed in Sections 3.3.1, 3.3.2 and 3.3.3.

3.3.5 *Crosslinking of chitosan nanofibre*

The two-step crosslinking method adopted by Kiechel *et al*. (2013) with modifications was employed in this study. The two-step method was performed on the electrospun nanofibres. The nanofibre mats were immersed in varying concentrations of 3, 5 and 7 wt% TA solutions in deionised water and stirred for 2 h using a magnetic stirrer at room temperature. Afterwards, the mats were rinsed with distilled water to pH 6.5, dried at 60 ˚C for 24 h in an oven and stored in a desiccator for further investigation. Before the immersion in the crosslinker solution, the fibres were neutralised with freshly prepared 5% NaOH solution for a period of 1 h, washed with distilled water to pH 6.5 and dried at 60 ˚C in an oven. The fibres corresponding to TA concentrations of 3, 5 and 7 wt% have the following codes: TA_CHS_1, TA_CHS_2 and TA_CHS_3, respectively.

3.3.6 *Solubility/stability tests of crosslinked adsorbents*

The solubility and stability of the crosslinked mats were carried out under acidic, neutral and basic solutions. This was done according to the method of Austero *et al*. (2012) with slight modifications. Samples were cut to square shape (10 × 10 mm) from the crosslinked mat, weighed and placed in a 50 mL beaker containing 10 mL each of 1.0 M acetic acid (AA) (pH 3), deionised water (pH 6.5) and 1.0 M NaOH (pH 13) solutions. The solubility of the mats was ascertained after 10 min and 72 h of immersion in the various solutions at room temperature. This was determined by measuring the transmittance of each solution at 600 nm

(T_{600}) using a spectrometer (Helios Epsilon Spectrometer, Thermo Fisher Scientific, Inc., MA, USA). Additionally, the mats were visually examined (VE) while in the three solutions. Mats with $T_{600} \geq 90$ and VE = 100 indicate "insoluble", $T_{600} < 70$ and VE = 0 indicates "soluble"; while those with $70 \leq T_{600} < 90$ and VE = 100 indicate "partially soluble". The measurements were done in triplicate.

3.3.7 *Degree of swelling of the crosslinked adsorbent*

The swelling behaviour of the dry adsorbent was investigated using the procedure described by Yao *et al*. (2018) with modifications. The crosslinked adsorbents of approximately 5 mg were carefully weighed (M_d) and recorded. The adsorbents were immersed in 10 mL of phosphate-buffered saline (PBS) solution with a pH of 7.4 at room temperature. The adsorbents were allowed to stand at different time intervals of 0.5, 1, 2, 4, 6, 8 and 24 h in the PBS solutions. Afterwards, the adsorbents were retrieved and were carefully wiped off of excess PBS by placing them between absorbent papers, applying slight pressure, and reweighed (M_w). The swelling behaviour of the adsorbents was computed using Equation 3.3. All the experiments were done in triplicate.

$$\text{Degree of swelling (\%)} = \left(\frac{M_w - M_d}{M_d}\right) \times 100 \qquad 3.3$$

where M_w and M_d are the weights of the wet and dried crosslinked membranes, respectively.

3.4 Adsorption studies

Batch adsorption studies were undertaken to investigate the performance of the electrospun BSF chitosan adsorbents in removing inorganic metal species from aqueous solutions.

The experiments were conducted at room temperature. 1000 mg/L of the stock solutions of the Pb^{2+} or Cd^{2+} were prepared by dissolving reagent-grade $Pb(NO_3)_2$ and $Cd(NO_3)_2$ in ultrapure water (Milli-Q UV Plus, Millipore). The adsorption experiments were conducted by diluting from the stock solutions to target concentrations with milli-Q water. The pH of the solutions was adjusted by introducing drops of 0.1 M HCl or NaOH. The solutions were filtered using 20 - 25 µm Whatman® Grade 4 filter paper before analysis. The ICP-OES was used to determine the concentration of the stock and the experimental solutions.

3.4.1 *Effect of pH*

These experiments were conducted to determine the effects of pH on the adsorption process of Pb (II) ions onto chitosan nanofibres. Experiments were conducted in the pH range of 1.0, 2.0, 3.0, 4.0 and 5.0 for Pb (II) ions. Pb precipitated as $Pb(OH)_2$ forming a cloudy solution at pH 6.0 and beyond and, therefore, the experiment could not go beyond pH 5.0. Cd (II) ions were studied at pH range of 2.0, 3.0, 4.0, 5.0, 6.0, 7.0 and 8.0. The amount of 0.005 g of the adsorbent was introduced into Erlenmeyer flasks containing 20 mL of 50 mg/L Pb^{2+} or Cd^{2+} solutions adjusted to the desired pH ranges. The solutions were agitated using an orbital shaker for 2 h and afterwards, ICP-OES analysis of the filtrates was conducted.

3.4.2 *Effect of the equilibrium concentration*

The effect of the equilibrium concentrations of the metal ions was studied for a range of standard solution concentrations to determine the adsorption isotherms. The experimental procedure was as follows: the electrospun chitosan adsorbent (TA_CHS_2, 5 mg, dry basis) was added to 20 mL of the metal ion (Pb^{2+} or Cd^{2+}) solutions (10, 20, 40, 60, 80, 100, 150 and 200 mg/L) and the mixture was vigorously agitated using an orbital shaker for 2 h. The solutions were filtered and the concentration of the metal ions remaining in the filtrate determined using ICP-OES. The adsorbed metal ions were obtained by subtracting the final from the initial concentrations of the solutions. The experiments were performed in triplicate and the mean value computed to minimise error. The adsorption capacities of the adsorbent were determined using Equation 3.4.

$$q_e = \left(\frac{C_o - C_e}{M}\right) V \qquad 3.4$$

where q_e is the adsorption capacity (mg/g), C_o and C_e (mg/L) are the initial and equilibrium metal ions concentrations in the solutions, respectively. M (g) is the mass of the adsorbent while V (L) is the volume of the adsorbate used.

Adsorption isotherms

Adsorption isotherms describe the interaction of the adsorbates and the adsorbents in solutions. From these interactions, the optimum sorption capacity can be determined. Several isotherm models exist for investigating equilibrium parameters of adsorption processes. Langmuir and Freundlich models are the most common and are applied in this study.

Langmuir Isotherm: The Langmuir isotherm explains the adsorption of materials from solutions and is based on four assumptions, namely that monolayer adsorption occurs on the adsorbent surface, the adsorbent surface is homogeneous, adsorption occurs at identical sites and there are no lateral interactions between molecules of the adsorbate (Meroufel *et al*., 2013). The Langmuir is one of the most useful and widely used isotherms for sorption studies.
The Langmuir isotherm is mathematically expressed as Equation 3.5 and the linear form of the model is given in Equation 3.6.

$$q_e = \frac{q_m b c_e}{1 + b c_e} \qquad 3.5$$

$$\frac{1}{q_e} = \frac{1}{q_m} + \frac{1}{b q_m}\frac{1}{c_e} \qquad 3.6$$

where q_e (mg/g) is the equilibrium adsorption capacity of the adsorbent, C_e (mg/L) is the equilibrium concentration of the adsorbate in the solution. q_m (mg/g) and b (L/mg) are constants representing the maximum monolayer adsorption capacity and the Langmuir constant which relates the affinity of the metal ions to the adsorbent, respectively. The values of q_m and b are obtained from the intercept and slope, respectively of the plot of Equation 3.6.

The dimensionless separation factor (R_L) is an important parameter obtained from the Langmuir isotherm. The value of the factor relates to the extent of the adsorption process taking place and is classified into various groups between 0 and 1. When $R_L = 0$ (irreversible), $0 < R_L < 1$ (favourable), $R_L = 1$ (linear) and $R_L > 1$ (unfavourable) (Garba *et al*., 2016). The R_L value is determined using Equation 3.7.

$$R_L = \frac{1}{1 + b C_o} \qquad 3.7$$

Freundlich Isotherm: The Freundlich isotherm explains the relationship existing between the concentration of the adsorbate and the adsorbent's surface in contact with it. The isotherm is built on the assumption that the adsorption is purely empirical and is based on sorption on heterogeneous surfaces of the adsorbent and is expressed as Equation 3.8. The linearised form of the Freundlich model is given as Equation 3.9.

$$q_e = K_f C_e^{1/n} \quad 3.8$$

$$\ln q_e = \ln K_f + {}^{1}/_{n} \ln C_e \quad 3.9$$

where q_e is the adsorption capacity at equilibrium concentration and C_e is the equilibrium concentration of the metal ions in solution. *n* (g/L) is the adsorption intensity of the adsorbent which measures surface heterogeneity or deviation from the linearity of the adsorption process while K_f {(mg/g) (L/mg)$^{1/n}$} is the adsorption coefficient and indicates the amount of adsorbate adsorbed onto the adsorbent at each equilibrium concentration. The value of *n* below unity is an indication of unfavourable adsorption while values above unity signify favourable adsorption that occurred by a physical process (Meroufel *et al*., 2013).

3.4.3 *Effect of contact time*

The effect of contact time on the uptake of Pb^{2+} or Cd^{2+} ions onto the chitosan adsorbent was done at contact times ranging from 10, 30, 45, 60, 90, 120 to 180 min at the optimised pH value determined in Section 3.4.1. Other experimental parameters were kept constant. ICP-OES was used to determine the adsorbate concentration after filtration using Whatman filter paper.

Adsorption kinetics

The experimental data obtained in this study were tested using kinetic models. This was done to determine the adsorption mechanisms and the rate-controlling steps of the process.

The kinetic models used were the pseudo-first-order and pseudo-second-order models. These models are reaction-based kinetic models that describe the behaviour of batch adsorption processes.

The pseudo-first-order model integrates adsorption and both internal and external diffusions which, in combination, make up the phases of the adsorption process. This model also postulates that the driving force for every adsorption process is the constant variation in the occupied adsorption sites at any given moment, which is directly proportional to the number of available sites. The pseudo-first-order equation, also known as the Lagergren rate equation (Lagergren, 1898) is expressed in linear form as Equation 3.10:

$$ln(q_e - q_t) = lnq_e - k_1.t \quad 3.10$$

Where q_e and q_t are the amounts of the adsorbate removed (mg/g) at equilibrium and at time *t* (min), respectively. k_1 is the rate constant of pseudo-first-order adsorption (min^{-1}).

By plotting $ln(q_e - q_t)$ against *t* for the adsorbate removal, k_1 and q_e are obtained from the intercept and slope of the plot, respectively.

The pseudo-second-order kinetic model is based on similar assumptions as to the pseudo-first-order model. They differ because, in the pseudo-second-order model, the rate of occupation of adsorption sites is directly proportional to the square of the number of available sites. Moreover, the overall adsorption process is influenced by chemisorption. The knowledge of the kinetics of adsorption processes is important in selecting and designing optimum sorption systems for batch processes (Krishnani *et al.*, 2008).

The pseudo-second-order kinetic equation is mathematically expressed as:

$$q_t = \frac{k_2 q_e^2 t}{1 + k_2 q_e t} \quad 3.11$$

The linear form of Equation 3.11 is obtained by integration using the boundary conditions *t* = 0 to *t* = *t* and *q* = 0 to *q* = *qt* to yield Equation 3.12.

$$\frac{t}{q_t} = \frac{1}{k_2 q_e^2} + \frac{1}{q_e}.t \quad 3.12$$

where k_2 is the pseudo-second-order sorption rate constant ($gmg^{-1}min^{-1}$).

The initial adsorption rate, *h* (mg/g/min) is given by Equation 3.13.

$$h = k_2 q_e^2 \quad 3.13$$

A plot of *t*/*qt* against *t* (Equation 3.12) gives a linear relationship with *q*e and *h* as the slope and the intercept, respectively. The pseudo-second-order rate constant, k_2, can be determined from Equation 3.13.

3.4.4 *Effect of temperature*

The effect of temperature on the sorption of Pb^{2+} or Cd^{2+} was studied to determine the optimal adsorption temperature and the thermodynamic parameters. Temperature is a very important

parameter which is often avoided by most adsorption studies. Temperature affects adsorption processes by influencing the molecular actions, mobility and solubility of adsorbates and adsorbents (Maleki *et al*., 2016). It affects the chemical reactions between the functional groups of the adsorbents and the adsorbates. The experimental procedure was as follows: the adsorbent (5 mg, dry basis) was added to 20 mL of the metal ion (Pb^{2+} or Cd^{2+}) solutions at a concentration of 50 mg/L and the mixture placed on a temperature-controlled oil bath at varying temperatures of 25, 35, 45, 55 and 65 $^{\circ}$C for 1 h. The solution was filtered whilst hot and the concentration of the metal ion remaining in the filtrate determined using ICP-OES. The adsorbed metal ions were obtained by subtracting the final from the initial concentrations of the solutions. Each experiment was performed in triplicate and the average value computed to minimise error. The adsorption capacities of the adsorbent for the Pb^{2+} or Cd^{2+} were determined using Equation 3.4.

Thermodynamic parameters

Thermodynamic parameters such as standard Gibbs free energy change (ΔG°), standard enthalpy change (ΔH°) and standard entropy change (ΔS°) provides additional detailed information about various adsorption processes such as the viability and spontaneity of the sorption process. The ΔG° is important in that it gives information about the availability of useful energy required to actualise and also determines the level of the adsorption process (Uzoije and Uche, 2014). Increase in the values of ΔG° with an increase in temperature implies a spontaneous reaction at a lower temperature while a decrease with increasing temperature signifies that the adsorption process is spontaneous at a higher temperature.

The heat associated with the adsorption process is described by the ΔH°. The magnitude of the enthalpy of adsorption process gives insight to the extent of adsorbates binding to the adsorbent's surface and determines the heat of the reaction *vis-à-vis* endothermic and exothermic reactions. A negative value of the enthalpy of reaction ($-\Delta H^{\circ}$) is an indication that an increase in temperature does not favour the adsorption process (Uzoije and Uche, 2014).

The thermodynamic equilibrium constant (K_d, L/g) for the adsorption of Pb^{2+} or Cd^{2+} onto TA_CHS_2 adsorbent was calculated for all temperatures of measurement using Equation 3.14.

$$K_d = \lim_{Ce \to 0} \frac{q_e}{C_e} \qquad 3.14$$

Where q_e (mg/g) is the equilibrium adsorption capacity of the adsorbent (solid phase) and C_e (mg/L) is the equilibrium concentration of the metal ions in solution after adsorption (liquid phase) at each temperature.

The Gibbs energy change is determined by Equation 3.15.

$$\Delta G° = \Delta H° - T\Delta S° \quad 3.15$$

While the standard Gibbs free energy of adsorption is given as Equation 3.16 (Talebi *et al*., 2017; Mudzielwana *et al*., 2019).

$$\Delta G° = -RTlnK_d \quad 3.16$$

The equilibrium constant, otherwise called distribution coefficient (K_d), is related to the temperature of adsorption by the combination of Equations 3.15 and 3.16 to give the Van't Hoff Equation (Equation 3.17) (Onwordi *et al*., 2019; Talebi *et al*., 2017).

$$lnK_d = \frac{\Delta S°}{R} - \frac{\Delta H°}{R}.\frac{1}{T} \quad 3.17$$

Where R (8.314 J/mol K) is the gas constant. From the plot of lnK_d against 1/T, enthalpy change (ΔH°, J/mol) and entropy change (ΔS°, J/mol.K) were computed from the slope and intercept of the linear relation, respectively.

3.5 Desorption and reusability studies

This investigation was performed to desorb and regenerate the TA_CHS_2 adsorbent for further use and for the recovery of the metal ions in solution. 5 mg of the TA_CHS_2 adsorbent was introduced into 20 mL of 50 mg/L solution of Pb^{2+} or Cd^{2+} and adjusted to the optimal pH of 4.0 or 6.0, respectively obtained from the protocol described in Section 3.4.1. The solution was shaken using an orbital shaker for 60 minutes at room temperature to adsorb the Pb^{2+} or Cd^{2+} by the adsorbent. The solution was filtered and the metal ions remaining in the solution determined using ICP-OES. The adsorbent was carefully rinsed afterwards without agitation using deionised water to remove any unadsorbed metal ion on its surface and dried in an oven at 50 $^{\circ}$C overnight. The completely dried, metal ion-loaded TA_CHS_2 adsorbent was introduced into a 20 mL of 0.1, 0.01 and 0.001 M NaOH solutions and agitated for 60 minutes using an orbital shaker at room temperature to desorb the Pb^{2+} or Cd^{2+}. The resulting solutions

were filtered and analysed using ICP-OES to determine the optimal desorption concentration. The experiment was continued using the optimal NaOH concentration established for Pb^{2+} or Cd^{2+} desorption. Three regeneration cycles were performed, each in triplicate. The desorption performance (DP) was computed using Equation 3.18.

.

$$D\text{p} = \left(\frac{VC_d}{qM}\right) x100 \qquad 3.18$$

where C_d (mg/L) is the concentration of adsorbates in the desorption solution, V is the volume of the solution used for desorption, q (mg/g) is the amount of adsorbates adsorbed on the TA_CHS_2 adsorbent before desorption studies, and M (mg) is the amount of the adsorbent (5 mg) used in the desorption experiments (Laus *et al*., 2010).

3.6 Antimicrobial analysis of extracted chitosan

The chitosan samples from pupae BSF (PCH21_9) obtained using techniques described in Sections 3.2.1.1 to 3.23 were evaluated for their antimicrobial potency against Gram-positive and negative microbes. Three microbial species, two bacteria and one fungus, were studied. The two bacteria species, *Streptococcus mutans* (ATCC 25175) and *Enterococcus faecalis* (ATCC 29212) and one fungus species, *Candida albicans* (ATCC 90028) were of the American type culture collections (ATCC) and generously provided by the Oral and Dental Research Laboratory, Faculty of Dentistry, UWC, Tygerberg Hospital, Cape Town. The microbial species were incubated in brain heart infusion (BHI) broth at 37 ˚C for 24 h. After 24 h of incubation, the organisms (*S. mutans*, *E. faecalis* or *C. albicans)* were sub-cultured in BHI agar plates and incubated at 37 ˚C for 24 h. The microbial cells were removed and later suspended in phosphate-buffered saline (PBS) solution and the concentration adjusted to 0.5 McFarland standard (Mcf).

3.7 Determination of the antimicrobial effect of chitosan nanoparticles

The time-kill test technique was adopted in this study to ascertain the survival time of the three pathogenic microorganisms after exposure to BSF_NPs solution. 3% BSF_NPs were prepared by dissolving 0.3 g of BSF_NPs in 10 mL of distilled water and agitated vigorously for complete solubilisation. 100 µL of the BSF_NPs solution was introduced into aseptic wells of a 12-well culture plate containing 200 µL of 0.5 Mcf of microbial suspensions and 1700 µL of BHI and labelled. The experimental groups were A (*E. faecalis)*, group B (*S. mutans*) and group

C (*C. albicans*). Similar conditions were adopted for the positive control group (D), however, BSF_NPs were not added to the culture plates. 100 µL of the microbial culture suspensions from each experimental group was transferred into an aseptic 96-well microtitre plate containing 50 µL of PBS solution. The suspension was diluted two-fold by withdrawing 50 µL from the first well into the second well and continued to the sixth well with its final volume of 100 µL. 2 µL from the sixth well of each group was withdrawn and streaked on BHI agar plates and incubated at 37 $^{\circ}$C for 24 h in aerobic condition. The serial dilution procedure was repeated every 30 minutes, 1, 2, 4, 6, 8 and 24 h. The experiment was conducted in triplicate. After 24 h of incubation, the number of the colony-forming units (CFU) in each test plate were counted and recorded. The sample with numbers exceeding 300 were considered too numerous to count (TNTC) and were recorded as 300 (CFU), while those less than 30 were designated as too low to count (TLTC) and recorded as zero.

3.8 Cytotoxicity testing of PCH21_9 or BSF_NPs

Cytotoxicity of the PCH21_9 or BSF_NPs samples was performed by measuring the viability of the cells in contact with the samples. Skin fibroblast cell lines (KMST-6) were used in this study. The cells were incubated at 37 ^{o}C under 5% carbon dioxide and 95% humidity in Dulbecco's Modified Eagle's medium (DMEM). The medium was supplemented with 10% fetal bovine serum and 1% Penicillin/Streptomycin mix. The resultant solution was filtered to maintain sterility with a 0.45 µm filter paper, and its pH adjusted to 8.

The fibroblast cells were grown to about 80% confluency (strong growth), trypsinised with trypsin and plated out into a 96-well plate at a relatively low count of about $3.5x10^5$ cells/mL. The 96-well cells were plated in 4 rows with 100 µL of the skin cell lines and allowed to grow and attach to the surface for 24 h. Afterwards, DMEM in two rows of the 96-well cells were replaced with 100 µL PCH21_9 or BSF_NPs sample medium and the other 2 rows replaced with normal DMEM to act as control for the cells with sample medium for each repetition giving 16 sample values and 16 control values. After 24 h of incubation, the standard cell viability assay (Mosmann, 1983) was performed using 3-(4,5-dimethylethylthiazol-2-yl)-2,5-diphenyl tetrazolium bromide (MTT) (Sigma Aldrich, South Africa) to evaluate the survival rate of the cell lines.

MTT assay

5.0 mg of 3-(4,5-dimethylethylthiazol-2-yl)-2,5-diphenyl tetrazolium bromide (MTT) (Sigma Aldrich, South Africa) was dissolved in 1.0 mL of PBS and sterilised. 10 µL of the solution was introduced to each well of the two groups and incubated at 37 ˚C. After 3 h, the medium containing MTT was discarded in all the groups. 100 µL of dimethylsulfoxide (DMSO) was added to each well to solubilise the resultant Formazan crystal before measuring the colour change. The change in colour, measured by the optical density of the living cells using a microplate reader (Rayto RT–2100C, Germany) at a wavelength of 540 nm, was determined. The readings obtained were compared with the control value, which is assumed to be 100%. The analyses were performed in triplicate. Figure 3.3 presents the technique for MTT assay and the variations in the colour of the experimental and the control groups.

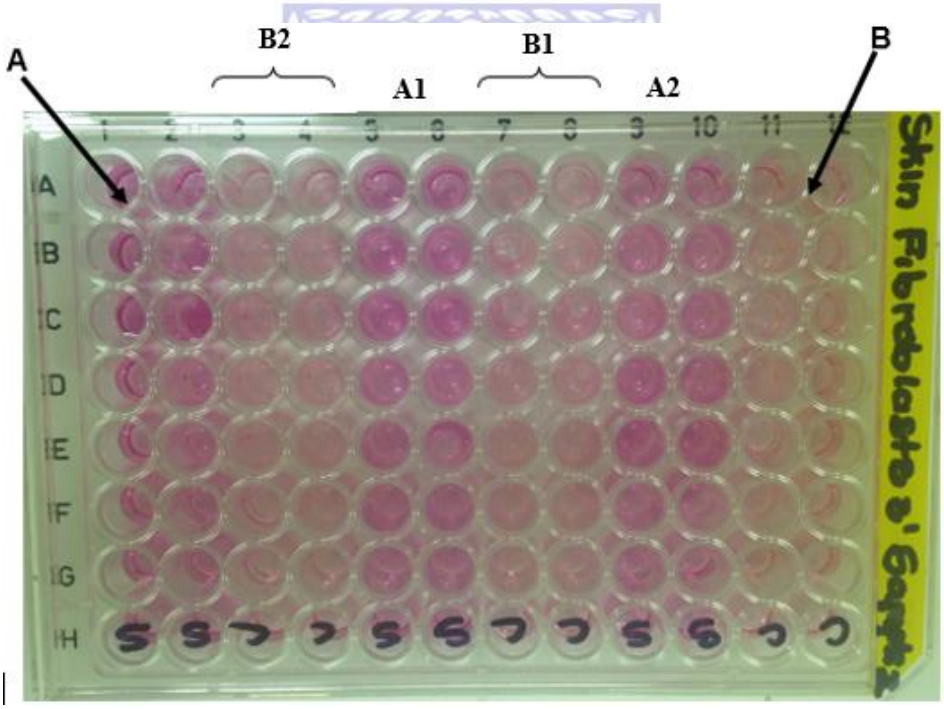

Figure 3. 3: Test plate showing variation in colour between the experimental groups (A, A1 and A2) and the control groups (B, B1 and B2) in triplicate.

The data obtained from each group in Sections 3.6, 3.7 and 3.8 were expressed as the mean of the log CFU/mL for the antimicrobial studies and the mean of the optical density values for the cytotoxicity studies. The data were tabulated and transferred to an Excel sheet (Microsoft Excel version 2016) for time-kill plots. Furthermore, the survival function analysis was performed using SPSS® statistics software (version 25, IBM, USA).

3.9 Characterisation techniques used in this study

The following sections describe in detail the instrumental principles and methods applied in characterising the extracted samples at each stage. Characterisation provides information and reveals the intrinsic properties of a material. Some of the instrumental analysis used are, but not limited to, pH determination, FTIR, HRSEM, TGA, elemental analysis, XRD, ^{13}C NMR and viscometric analysis.

3.9.1 *pH measurement*

The pH measurement compares the hydrogen ion (H^+) of an unknown solution to that of known reference potential. The pH measurements of all solutions in this study were done using SCS 220-K pH/Ion meter, Mettler-Toledo, Switzerland. The pH meter was calibrated using pH 4.00 and 7.00 buffer solutions. The probe was rinsed with deionised water before and after each pH measurement.

3.9.2 *Elemental analysis (CHN) of the sample*

An elemental analyser was used to determine the carbon (C) and nitrogen (N) contents in the extracted pupal and adult chitin and chitosan samples. The degree of acetylation (DA) and deacetylation (DD) of the chitin and chitosan samples were calculated according to Equations 3.19 and 3.20 (Abdel-Rahman *et al.*, 2015).

$$DA = \left(\frac{\frac{C}{N} - 5.14}{1.72}\right) * 100 \qquad 3.19$$

$$DD = \left(\frac{6.86 - \frac{C}{N}}{1.72}\right) * 100 \qquad 3.20$$

Where C/N is the ratio of carbon to nitrogen (w/w).

The value of 5.14 represents the theoretical ratio of C/N in a fully deacetylated chitosan.

6.86 represents the theoretical ratio of C/N in fully N-acetylated chitin.

1.72 is the theoretical difference between the C/N ratio of N-acetylated chitin and fully deacetylated chitosan.

3.9.3 *Fourier transform infrared (FTIR) spectroscopy*

Chitin and chitosan samples were subjected to FTIR analysis using a spectrum 400 FTIR/FT-NIR spectrophotometer equipped with universal ATR sampling accessory by PerkinElmer. The FTIR technique was used to determine functional groups on the surface of the chitin and chitosan samples. The FTIR spectra also provided information about the change in the molecular structure of the starting and the final product of chitin, chitosan, nanofibres and nanoparticles. In this study, samples were placed on a diamond crystal sample holder and screwed down in place for proper contact with the crystal. This technique is particularly useful because little or no sample preparation is required for the analysis. Furthermore, very small sample amount is needed. Automatic signals were collected in 32 scans at a resolution of 4 cm^{-1} over a range of 4000−650 cm^{-1} (mid-IR region) and were ratioed against a background spectrum recorded from ethanol-cleaned and empty sample holder at the same operating conditions. Spectra were then analysed using OriginPro 8.5 Software (OriginLab Corporation, Massachusetts, USA).

3.9.4 *X-ray diffraction studies*

In this study, XRD measurements on powdered samples were carried out using a D8 Advance X-ray machine by Bruker AXS, Germany. The X-ray source was Cu-K α-radiation equipped with a position-sensitive LynxEye detector operated at 40 kV and 40 mA. The powdered CHS samples were scanned at a 2θ range from 5˚ – 90˚ with a measurement time of 0.5 sec per step at 25 ˚C (Liu *et al.*, 2012). The intensities of the peaks at 110 lattices (I_{110}, at 2θ ≈ 20˚ corresponding to maximum intensity) and at 2θ ≈ 16˚ (disordered diffraction) were used to calculate the degree of orderliness using Equation 3.21 while the interplanar distances of the unit cells were computed using Equation 3.22.

$$\text{Degree of orderliness (\%)} = \left(\frac{I_{110} - I_{am}}{I_{110}}\right) x100 \qquad 3.21$$

I_{110} is the intensity of the peak at the ordered region at 2θ ≈ 20˚

I_{am} is the diffraction intensity in the structurally disordered region at 2θ ≈ 16˚

$$\text{Interplanar distance (h,k,l) } d_{hkl} = \left[\left(\frac{h}{a}\right)^2 + \left(\frac{k}{b}\right)^2 + \left(\frac{l}{c}\right)^2\right]^{-1/2} \qquad 3.22$$

Where d is the interplanar distance; h, k and l are the various planes while a, b and c are the unit cell dimensions.

3.9.5 *Thermal gravimetric analysis (TGA)*

The TGA of the chitin, chitosan and the chitosan nanofibres were conducted to determine the thermal behaviour of the extracted biomaterials. The analysis was carried out using a PerkinElmer Pyriss Simultaneous TGA/DTA Analyzer (TG-4000) fitted with an Accupik autosampler under an inert atmosphere of nitrogen at a pressure of 300 MPa. Chitin samples (3.60 mg - 6.50 mg) were introduced into the platinum crucible using a spatula and gently lowered into the sample holder. Accurate weights of the samples were determined using Pyris system software. The thermal degradation profiles of the samples were conducted over a temperature range of 20 $^{\circ}$C to 600 $^{\circ}$C at a heating rate of 10 $^{\circ}$C/min and nitrogen gas flow rate of 20 mL/min. The crucible was cleaned and the TGA instrument calibrated before each analysis to stabilise the instrument baseline.

3.9.6 *High-resolution scanning electron microscopy (HRSEM)*

HRSEM was used to examine the surface morphologies of the chitin and chitosan samples. The micrographs were taken at a voltage of 25.0 kV from low to high magnifications using a Zeiss Gemini Auriga HRSEM and a Nova NanoSEM 230 microanalyser.

SEM was done on samples prepared by placing a small amount on stubs whereafter the samples were coated with a thin film of gold to ensure the conductivity of the surface, and to improve the resolution of the micrographs. The coating process was done using Quorum Q150T ES sputter coater machine. SEM images were taken at different positions with variation in image magnifications. Particle sizes and fibre diameters of the electrospun materials were determined using ImageJ software© with the image scale used for the appropriate unit conversion from the micrographs obtained. The results were plotted as a histogram after randomly measuring 20 or more sample sizes distributed uniformly within the micrograph. The average particle and fibre size distribution were determined for each condition. Table 3.16 presents the operating parameters of the HRSEM.

Table 3. 16: List of HRSEM operating parameters

Instrument parameters	Instrument settings for the analysis
Voltage	25 kV
Current	10 mA
Aperture	0.4 mm
Magnification	Varies (500 – 100,000x)
Emitter	Thermal field emission type
Resolution	1 nm but sometimes varies
Working distance	4−10.4 mm
Signal A	Inlens

3.9.7 *Nuclear magnetic resonance (^{13}C-NMR) analysis*

The structural analysis of chitin and chitosan were carried out using a solid-state ^{13}C-NMR Bruker High-Performance Digital FT-NMR 400 Avance III HD Spectrometer equipped with CP/MAS (cross-polarisation, magic-angle-spinning) accessories. The aim of these analyses was to examine the samples to understand if there are the presence of impurities (such as residual protein or other functional groups) in the extracted samples. Also to identify all the carbons atoms present in the structure of the materials. This information would be used to compute the DA and the DD of the chitin and chitosan samples, respectively.

3.0 mg of the samples were used for the analysis. NMR spectra were obtained at a frequency of 125.737 MHz, a temperature of 296 K and a 50 ms acquisition time. CP/MAS sequence used was spin-lattice contact time of 8 min and a repetition time of 5 s. Data were acquired after 1000 scans, processed and the integral values obtained using TopSpin$^{(R)}$ NMR software. The DA of the samples were determined by dividing the value of the integral area of the methyl group carbon resonance by the average integral of the resonances C1 – C6 carbon atoms. The DA was computed using Equation 3.23 (Song *et al*., 2013, Hajji *et al*., 2014):

$$DA = 100 * \left\{ \frac{I_{CH3}}{\frac{1}{6}(I_{C1}+I_{C2}+I_{C3}+I_{C4}+I_{C5}+I_{C6})} \right\} \quad 3.23$$

Where I_{CH3} is the integral of methyl carbon resonance and

$\frac{1}{6}(I_{C1} + I_{C2} + I_{C3} + I_{C4} + I_{C5} + I_{C6})$ is the summation of the average integrals of the glucosyl ring carbon atoms.

3.9.8 *Water binding capacity (WBC)*

Water binding capacity was determined by adopting the method of Marei *et al*. (2016) with slight modification. A centrifuge tube (50 mL) containing 0.5 g of the pupae CHS was weighed and recorded. Water (10 mL) was added to the samples and homogenised by vortex at maximum speed for 1 min. The contents of the tube were left for 50 mins at ambient temperature with intermittent shaking every 5 min. The samples were then centrifuged at 3600 rpm for 20 min. The supernatant was decanted and the tube was weighed again. The water-binding capacity was calculated using Equation 3.24. The experiment was conducted in triplicate.

$$\text{WBC (\%)} = \left(\frac{Water\ bound\ (g)}{Sample\ weight\ (g)}\right) x100 \qquad 3.24$$

Where WBC is water binding capacity.

3.9.9 *Fat-binding capacity*

The same technique for water-binding capacity was used but the water was replaced with Soybean oil.

The fat-binding capacity was calculated from the following Equation 3.25.

$$\text{FBC (\%)} = \left(\frac{Fat\ bound\ (g)}{Sample\ weight\ (g)}\right) x100 \qquad 3.25$$

Where FBC is fat binding capacity.

3.9.10 *Determination of ash content*

Ash content of chitosan is an important parameter which shows the mineral content of the sample. High-quality chitosan should have an ash content of less than 1%. Chitin and chitosan ash contents were determined by combustion using a constant weight crucible.

The porcelain crucible was weighed (W_0) and 2 g of the samples were placed in the crucible and reweighed (W_1) and heated in a temperature-controlled muffle furnace to 600 ± 20 ˚C and held constant at this temperature for 2 h. After heating, the furnace was allowed to cool and the crucible was transferred to a desiccator and allowed to equilibrate for 30 min and weighed

(AOAC, 2000). The weighing and cooling process was repeated every 30 min until a constant weight was established (W_2). The ash percentage was calculated using Equation 3.26.

$$\% \text{ Ash} = \left(\frac{W_2 - W_0}{W_1 - W_0}\right) x100 \quad 3.26$$

Where W_0 = weight of the crucible (g), W_1 = weight of the sample and the crucible (g), and W_2 = weight of the ash and the crucible (g).

3.9.11 *Chitosan solubility test*

The solubility of chitosan in aqueous acetic acid is very important in determining its quality. The solubility of PCH21_9 was determined by the addition of 0.1 g of the sample in 10 mL of 1.0% acetic acid solution and stirred using a magnetic stirrer (LAB-smart MS-H-Pro$^+$) to obtain a homogeneous solution. The chitosan solution was filtered using a 0.45 µm filter paper (previously dried at 105 °C for 1 h and the weight determined) and a vacuum pump (Laboport Vacuum Filter, KNF Lab, Germany). The procedure was repeated three times where each was dried at 105 °C for 1 h in an oven. The percentage insolubility of the sample was computed using Equation 3.27 (Kumari *et al*., 2017). The percentage solubility of the sample was computed by subtracting the insolubility value from 100.

$$\text{Insoluble (\%)} = \left(\frac{W_2 - W_1}{W_0}\right) x100 \quad 3.27$$

Where W_2 is the weight of filter paper + extract (g), W_1 is the weight of filter paper only (g), and W_o is the weight of the sample used (0.1 g).

3.9.12 *Chitosan viscosity determination*

Six concentrations of the chitosan solution were prepared. Firstly, 0.001 mL/g was prepared by dissolving 0.1 g of the PCH21_9 in 100 mL of acetic acid and sodium acetate mixed solvents (0.3 M CH_3COOH/0.2 M CH_3COONa (1:1 v/v)). The mixed solvent was gently stirred with a magnetic stirrer (LAB-smart MS-H-Pro+) for 18 h at 25 °C. This was to ensure complete dissolution of the chitosan in the solvent mixture. The solution was serially diluted to five different concentrations (0.002, 0.003, 0.004, 0.005 and 0.006 g/mL). Acetic acid was used as a solvent because it has been adopted as the standard solvent for the determination of the solubility of chitosan in solution (Roberts, 2007) while sodium acetate acts as a buffer to

prevent pH variation. Viscosities of the polymer solutions were investigated using an Ubbelohde viscometer for transparent liquids (Paragon Scientific size 1C, diameter 0.78 mm). Readings were taken at 25 ± 0.1 ˚C. Five consecutive measurements of the solutions (t_i) and solvent (t_o) flow times were recorded using a stopwatch. The values of the reduced (η_{red}) and inherent (η_{inh}) viscosities were computed and plotted against chitosan concentrations. Intrinsic viscosity (η), which is the limiting viscosity as concentration tends to zero, was determined by extrapolating the linear graph of reduced viscosity to zero concentration (y-axis) (Costa *et al*., 2015). Reduced, inherent and intrinsic viscosities were obtained using Equations 3.28, 3.29 and 3.30, respectively.

$$\eta_{red} = \frac{1}{C}\left(\frac{t_i}{t_o} - 1\right) \qquad 3.28$$

$$\eta = \frac{1}{C}\left(\frac{ti}{to} - 1\right)_{C=0} \qquad 3.29$$

Viscosity-average molecular weight determination

For a given polymer-solvent system, the intrinsic viscosity is a unique function of molecular mass and a measure of the volume of a single polymer molecule in an ideal condition (Costa *et al.*, 2015). The Kuhn-Mark-Houwink-Sakurada equation relates the MW of a polymer and its solvent at a specified temperature to the intrinsic viscosity (Laka and Chernyavskaya, 2006) thus:

$$[\eta] = KM^a \qquad 3.30$$

Where $[\eta]$ is the intrinsic viscosity (mL/g)

M is the molecular weight (Dalton or g/mol)

K is a constant which is dependent on a given polymer type (mL/g)

a is a constant which depends on the chosen solvent.

For chitosan and 0.3 M CH_3COOH/0.2 M CH_3COONa as a solvent, these constants, *K* and *a* have values of 0.076 mL/g and 0.76 respectively, at 25 ˚C (Rinaudo *et al.*, 1999).

3.9.13 *Inductively coupled plasma-optical emission spectroscopy (ICP-OES)*

ICP-OES is an analytical technique used in determining metal ion concentrations in solutions. It operates on the principle of excitation-emission of the elemental composition of a sample under the influence of heat. The Varian Radial ICP-OES using a High Matrix Introduction accessory and helium as collision gas was used in this study. The instrument determines the metal concentration of interest by measuring the intensity of emitted light waves at a specific wavelength. The instrument was calibrated daily before analysis. The analysis was performed in triplicate to reduce the error margin and to achieve reproducibility. The operating parameters of the ICP-OES equipment are presented in Table 3.17.

Table 3. 17: Operating parameters of the ICP OES**.**

Parameters	**Instrument settings**
Sampling depth	8.5 mm
Sample flow rate (peristaltic pump)	50 rpm
Argon gas flow rate	5 L/min
Auxiliary gas flow rate	0.5 L/min
Applied radio frequency power (RF)	1150 W
Nebulizer argon gas	1.5 L/min
Sample flash time	300 s
Total integration time	30 s/metal analyte
Time scan acquisition	50 ms/point
Optics temperature	36 ˚C
Generator temperature	24 ˚C
Cooled spraying chamber temperature	4 ˚C
Sample replication	Triplicate

3.9.14 *The determination of the hydrodynamic parameters*

The zeta potential (ζ-potential) is the potential difference across solid and liquid interphase. The process measures the electrical charge of particles in suspension and also the magnitude of the attractive/repulsive forces between these particles. These forces, in turn, determine the stability of colloidal dispersions in an aqueous environment. 0.5 mg/mL of both PCH21_9 and BSF_NPs samples were dissolved in 1.0% acetic acid solution and distilled water, respectively. The solution was homogenised under a vortex mixer and later stirred using a magnetic stirrer

(LAB-smart MS-H-Pro^{+}) at 25 °C for 6 h, sonicated for 10 mins and filtered using cellulose acetate filter paper. The zeta (ζ-) potential of each solution was determined using a dip cell (DTS1070, Malvern Instruments) with a pair of parallel palladium electrodes and placed in the zeta potential analyser (Malvern Zetasizer, Nano-ZS90, Worcestershire, UK). The particle sizes were measured using disposable cuvettes. The signals were collected at 12.8° and the data analysed using Zetasizer Software. The Smoluchowski model was used to convert the dispersed particle motions to zeta potential values (Malvern Zetasizer, 2017). The analysis was performed in triplicate.

3.9.15 *Chapter summary*

This chapter summarises all the experimental procedures and characterisation techniques used in this study. The materials, reagents and their suppliers were appropriately listed. The experimental processes adopted in optimising the extraction of the chitin and chitosan samples from BSF were highlighted in this chapter. Furthermore, parameters such as the effect of concentration of the reagents, temperature and the reaction time on the extraction of the materials were discussed. Additionally, the optimisation of nanofibre production from the extracted pupal chitosan was enumerated. Moreover, the experimental procedures for the application of the extracted chitosan, nanofibres and the nanoparticles in antimicrobial, cytotoxic and adsorption studies were also discussed. The various methods of characterisation of the extracted biopolymers were also discussed in this chapter.

CHAPTER 4

CHITIN AND CHITOSAN EXTRACTION AND CHARACTERISATIONS

4.0 Introduction

It is pertinent to understand the processes of isolation and synthesis of the BSF chitin and chitosan in this study. Furthermore, the materials extracted were characterised to study their various properties, which include surface morphologies, physical, chemical and thermal properties. This chapter, therefore, presents the extraction protocols and the characterisation results of both isolated chitin and chitosan samples outlined in Chapter three of this study.

4.1 Chitin extraction

The chitin and chitosan samples were extracted from BSF (pupae shells and dead adult). This chapter, therefore, discusses the results of the extraction and characterisation of the extracted materials. For chitin extraction, three processes were involved. They are demineralisation, deproteination, and decolouration. A total of forty-six (46) trials were conducted on both the pupae and adult BSF wastes to obtain the optimum conditions for chitin extraction as detailed in Tables 3.3 – 3.8 of Section 3.2.1.1. These biomaterials were extracted by varying the process parameters of temperature, time and concentration. Optimised conditions at each extraction process were utilised for the overall isolation of the chitin samples and in the determination of the percentage yield of each sample (Table 4.2). The samples obtained using the optimised conditions were characterised to understand the physicochemical features and the purity of the obtained products.

4.1.1 *Demineralisation*

One-step at a time optimisation was applied in this study. A detailed description of the experimental procedure is found in Section 3.2.1.1 of Chapter 3. The preliminary characterisation employed at this stage is FTIR described in Section 3.9.3. The various processes and their corresponding parameters are discussed in the subsequent sub-sections.

4.1.1.1 *Concentration optimisation*

The HCl concentration of the demineralisation reactions was varied at this stage while maintaining a constant temperature and time of 50 ˚C and 80 min, respectively. The various conditions were coded as PCH1, PCH2 and PCH3 for pupae BSF samples and ACH1, ACH2

and ACH3 for adult BSF samples, each representing concentrations of 0.5, 1.0 and 2.0 M HCl solutions. Figure 4.1 shows the spectra obtained as the concentration was varied for both pupae and adult BSF waste at constant temperature and time of reaction.

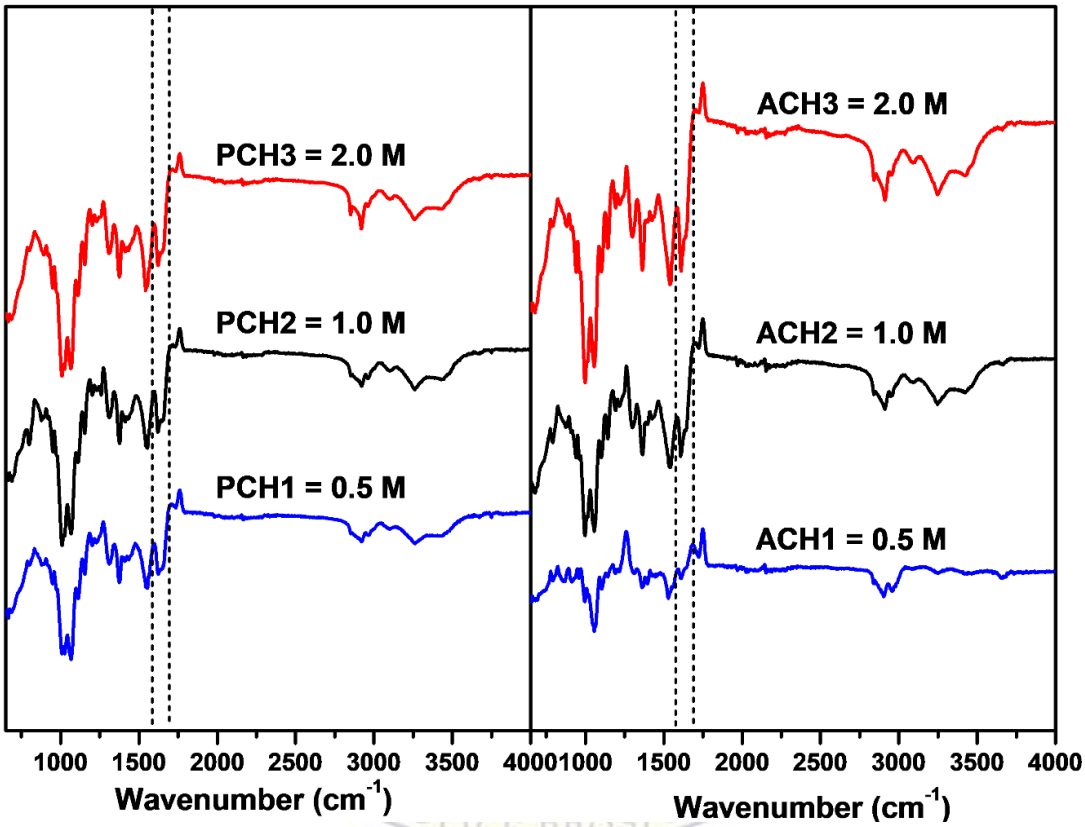

Figure 4. 1: FTIR spectra obtained as the HCl concentrations for demineralisation were varied from 0.5 M – 2.0 M for both pupae and adult BSF waste. Temperature and time were kept constant at 50 ˚C and 80 minutes.

In Figure 4.1, the characteristic peak of interest is the Amide 1 band (highlighted with double vertical lines). The aim was to determine the HCl concentration that will induce the splitting of the Amide 1 band in the samples analysed. Amide 1 band is the characteristic chitin peak of the alpha form of which insect chitin belongs. It is clear that in Figure 4.1, the peaks displayed by the samples treated with 0.5 M HCl (PCH1 and ACH1) showed a broad peak in this region compared to the 1.0 M HCl (PCH2 and ACH2) and 2.0 M HCl (PCH3 and ACH3) treated samples. The observed spectra of the PCH1 and ACH1 samples are not consistent with the spectra of chitin obtainable in literature (Erdogan and Kaya, 2016). The PCH2, ACH2, PCH3 and ACH3 samples showed a promising result as the split in the peak of interest, showing the amide band became visible and showed splitting on both samples. The PCH3 and ACH3 samples had a better peak intensity on both spectra than the PCH2 and ACH2 samples.

However, the differences were insignificant considering a 100% increase in HCl concentration from 1.0 to 2.0 M. Therefore, the 1.0 M HCl condition used for PCH2 and ACH2 samples were chosen as the optimum concentration for demineralisation of both adult and pupae BSF waste. The next stage of the demineralisation process was the temperature optimisation presented in the next sub-section.

4.1.1.2 *Temperature optimisation*

Temperature helps to weaken the bonds linking the minerals and the chitin ensuring the effective removal of the inorganic constituents through the reagents. To actualise temperature optimisation, concentration (1.0 M HCl solution obtained in Section 4.1.1.1) and time (80 minutes) were kept constant. The varied temperatures were 30 ˚C (PCH4 and ACH4), 50 ˚C PCH5 and ACH5), 70 ˚C (PCH6 and ACH6) and 90 ˚C (PCH7 and ACH7). Figure 4.2 shows the FTIR spectra obtained as the temperature were varied for both pupae and adult BSF waste at constant concentration and time.

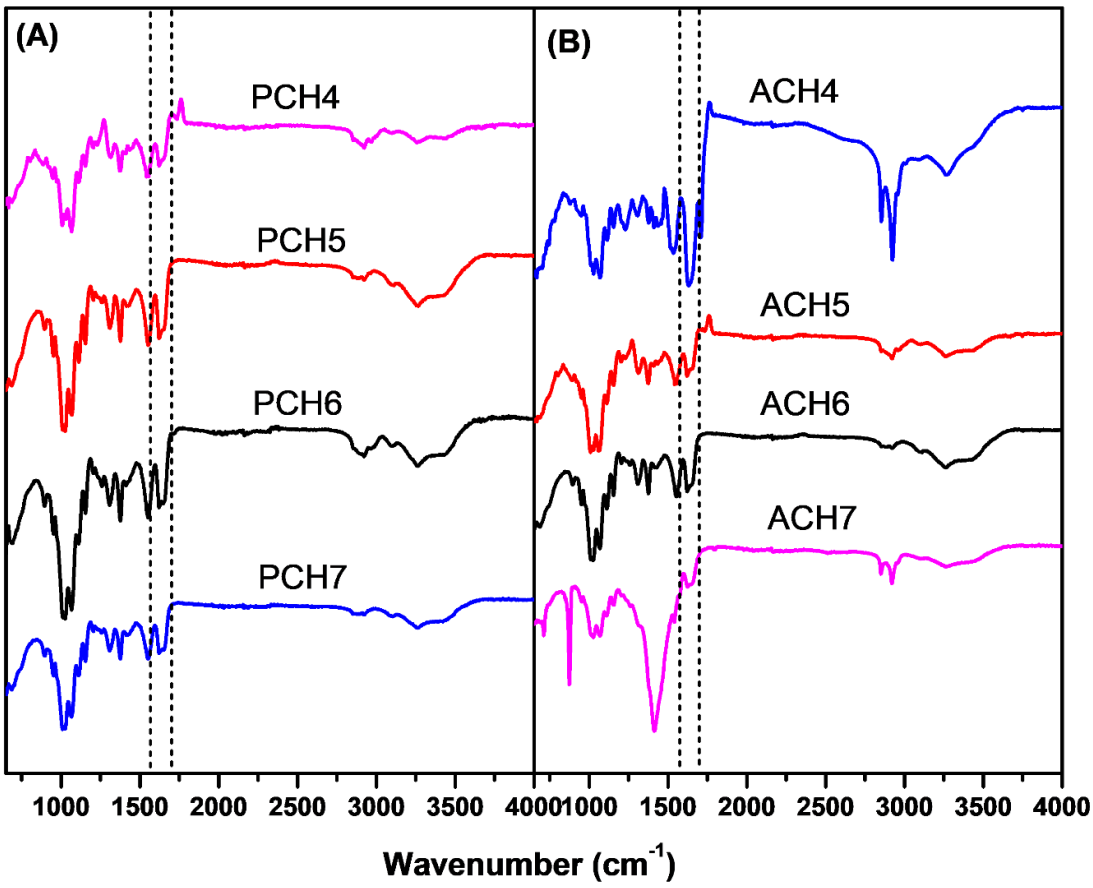

Figure 4. 2: FTIR spectra obtained as the temperature for demineralisation was varied between 30 – 90 ˚C for both pupae (A) and adult (B) BSF waste (concentration and time were kept constant at 1.0 M HCl and 80 minutes).

Figure 4.2 shows that the spectra obtained at 30 ˚C for both pupal and adult chitin (PCH4 and ACH4) were different from other spectra. A peak appeared at 1725 cm^{-1}. This peak, according to Bogdanova *et al.* (2016), is associated with inorganic minerals found in combination with chitin. This implies that a temperature of 30 ˚C was not effective for the demineralisation process for both the pupal and adult chitin. The chitin spectra at 50, 70 and 90 ˚C appear similar, with the absence of the peak at 1725 cm^{-1} observed in PCH4 and ACH4 spectra. Additionally, PCH5, PCH6, PCH7, ACH5 ACH6 and ACH7 all showed signs of the splitting of the Amide 1 band, the major spectral feature of chitin at 1560 cm^{-1} (marked peak in Figure 4.2). 90 ˚C (ACH7) seemed too high for the demineralisation of the adult BSF, as the intensities of the peak were affected. Since there were few noticeable differences in these spectra between 50 – 70 ˚C on the pupal and adult BSF samples, the temperature, 50 ˚C (condition for sample coded PCH5 and ACH5), was selected as the optimal temperature for demineralisation studies. The time of the demineralisation reaction was further investigated to determine the optimal time for demineralisation of both pupal and adult chitin.

4.1.1.3 *Time optimisation*

The aim was to investigate the time required to achieve complete elimination of the minerals associated with chitin. The times investigated were 60, 80, 100 and 120 minutes with sample codes PCH8, ACH8; PCH9, ACH9; PCH10, ACH10; and PCH11, ACH11, respectively while the concentration of the HCl solution and the temperature of the reaction were kept constant. The detailed description of the protocol is found in Section 3.2.1.1 of Chapter 3. Figure 4.3 presents the spectra of the pupal and adult BSF at varying times of demineralisation.

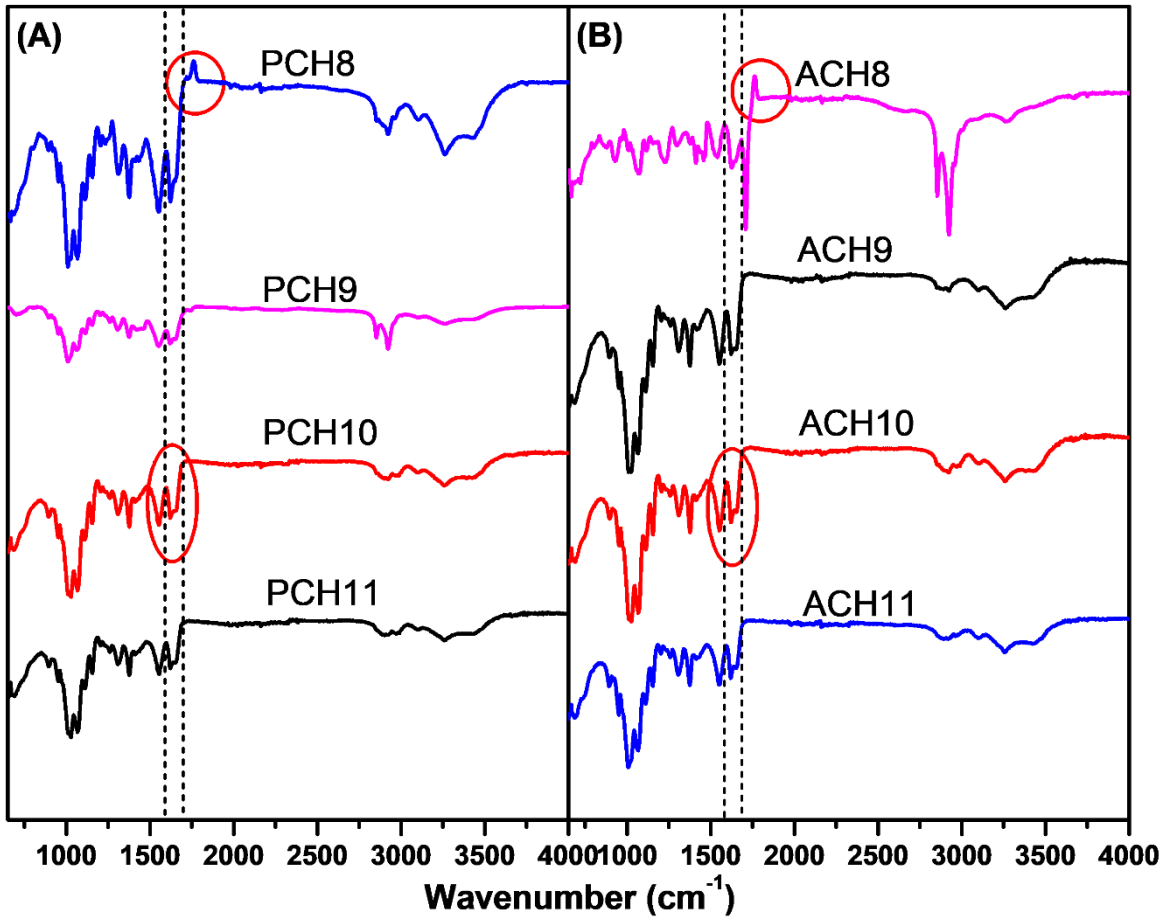

Figure 4. 3: FTIR spectra obtained as the time for demineralisation was varied between 60 – 120 mins for both pupae (A) and adult (B) BSF waste (concentration and temperature were kept constant at 1.0 M HCl and 50 ˚C).

Four different reactions times, 60, 80, 100 and 120 minutes were investigated with concentration and temperature kept constant at 1.0 M HCl and 50 ˚C. From the Figure 4.3, dimineralising both the pupal and adult BSF samples for 60 minutes (PCH8 and ACH8) still showed mineral bands around 1726 cm^{-1} wavelength on the FTIR spectra, an indication of the existence of minerals in both samples. This signifies that 60 minutes' reaction time was not enough to completely eliminate the inorganic constituents in PCH8 and ACH8 samples. The spectra of PCH9, ACH9, PCH10 and ACH10 samples (conducted at 80 and 100 minutes) looked similar. However, PCH10 and ACH10 (the pupal and adult BSF samples demineralised for 100 minutes) showed a better splitting of the Amide 1 band (highlighted), an indication of a better quality extract. Furthermore, PCH11 and ACH11 (the samples from both pupal and adult BSF demineralised for 120 minutes) did not differ significantly from PCH10 and ACH10 and, therefore, adjudged the same. This clear splitting of the Amide 1 peak (Figure 4.3), reduced time of reaction and the absence of the mineral peak on PCH10 and ACH10 were the

justifications for choosing its condition (100 minutes) as the optimal time adopted for the demineralisation process in this study.

Having established the optimised demineralisation conditions (HCl concentration of 1.0 M, temperature of 50 ^{o}C and reaction time of 100 minutes), the next stage of the study was the deproteination process. This process is discussed in the next sub-section.

4.1.2 *Deproteination process*

Chitin are always associated with proteins and form a chitin-protein complex. Therefore, deproteination is the process of removal of the protein associated with chitin forming a water-soluble amino acid. This process is very important for the medical and biomedical applications of chitin and its derivative, chitosan. Like the demineralisation process, a one-step at a time optimisation process was also adopted in the deproteination process. The process parameters varied were concentration, time and temperature. The process is described in detail in Section 3.2.1.2 of Chapter 3. The preliminary characterisation employed at this stage, like in the demineralisation process, was FTIR to study the peak of interest. The various processes and their corresponding parameters are discussed in the next subsections.

4.1.2.1 *Concentration optimisation*

The various conditions were presented in Table 3.6 of Section 3.2.1.2 in Chapter 3. Concentration (0.5, 1.0 and 2.0 M NaOH solution) was the variable parameter while temperature (95 $^{\circ}$C) and time (12 h) were kept constant in this investigation. The samples have the various codes of PCH12 and ACH12 for 0.5 M, PCH13 and ACH13 for 1.0 M and PCH14 and ACH14 for 2.0 M NaOH solutions. Figure 4.4 shows the FTIR spectra of the various samples investigated.

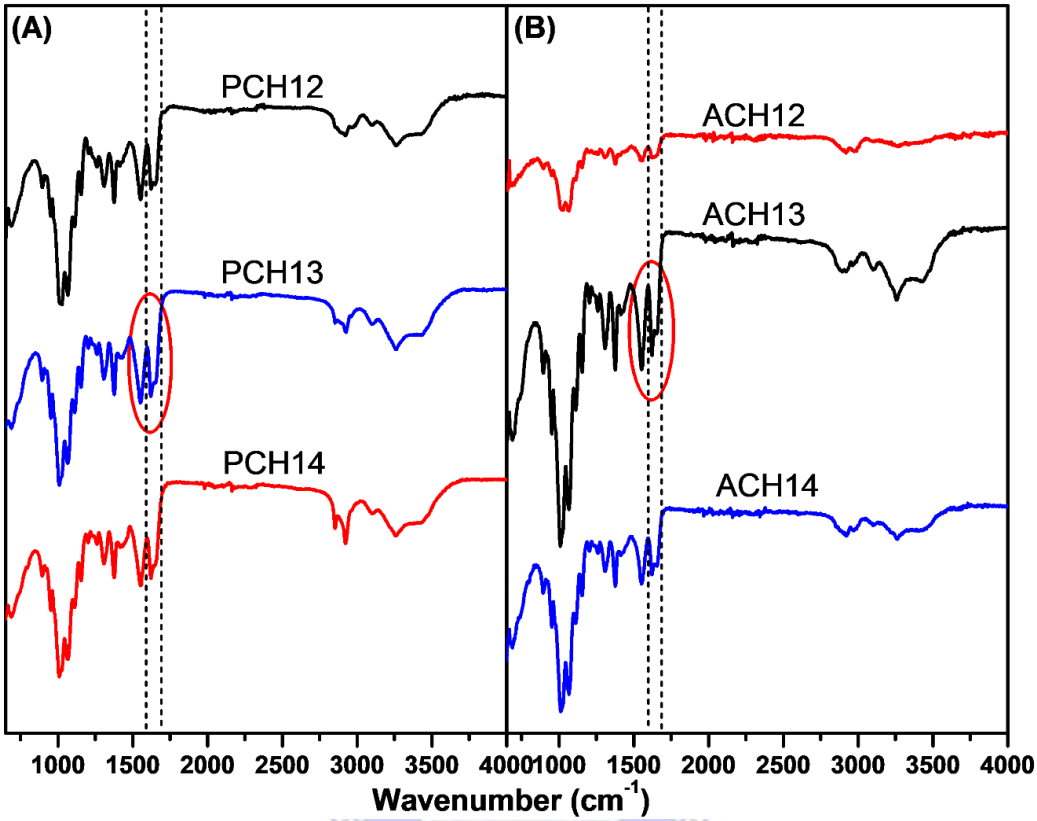

Figure 4. 4: FTIR spectra obtained as the NaOH concentration for deproteination was varied (0.5, 1.0 and 2.0 M NaOH solutions) while temperature (95 ˚C) and time (12 h) were kept constant for both pupae (A) and adult (B) BSF waste.

From Figure 4.4, it appears that none of the spectra displayed the characteristic protein peak (1540 cm^{-1}). However, the solution concentration affected the samples differently. This manifested on FTIR spectra of all the samples by the display of varying degree of splitting of the peak of interest, the Amide 1 band. This splitting was more prominent on PCH13, ACH13 and PCH14, ACH14 samples (the BSF samples treated with 1.0 and 2.0 M NaOH solutions) than on PCH12 and ACH12 samples (those treated with 0.5 M NaOH solution). In view of this, 1.0 M NaOH solution was selected as the optimal NaOH concentration for the deproteination process.

4.1.2.2 *Temperature optimisation*

Temperature is an important parameter in the deproteination process. As temperature increases, the heat generated contributes in denaturing the associated protein in chitin ensuring the penetration of reagents into the sample (Bernardi *et al.*, 2018). Temperature is therefore vital in the overall removal of protein in chitin extraction. Investigation of the deproteination temperature was conducted as described in Table 3.6 of Section 3.2.1.2. The optimised

concentration (1.0 M NaOH) determined in Section 4.1.2.1 was adopted at a constant time of 12 h in this investigation while varying the deproteination temperature (85, 95, 105 and 120 °C) for both BSF samples. The samples are coded as PCH15 and ACH15 (85 °C), PCH16 and ACH16 (95 °C), PCH17 and ACH17 (105 °C) and PCH18 and ACH18 (120 °C). Figure 4.5 shows the spectra of the samples studied to determine the optimal temperature for the deproteination process.

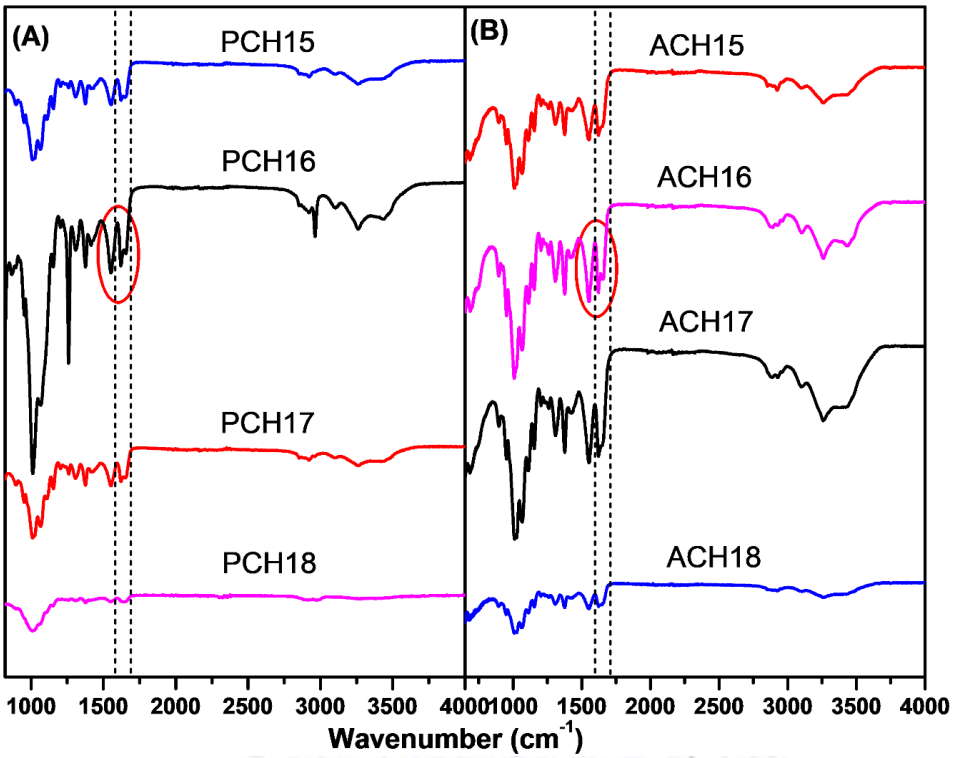

Figure 4. 5: FTIR spectra obtained as the temperature of deproteination was varied (85, 95, 105 and 120 °C) while concentration (1.0 M NaOH solution) and time (12 h) were kept constant for both pupae (A) and adult (B) BSF waste.

Figure 4.5 A and B presents the FTIR spectra of the pupal and adult samples studied, respectively. For both BSF samples, deproteination at 85 °C (PCH15 and ACH15) did not induce a clear splitting of the peak of interest, the Amide 1 band. Although the temperature had a greater effect on ACH15 (the adult sample) than PCH15 (the pupal sample), it was not considered to be the optimal temperature. A clear splitting was observed on PCH16 and ACH16 (95 °C) on both samples. For the adult BSF sample, the spectra of the ACH16 and ACH17 (deproteinated at 95 and 105 °C) were similar, an indication that the temperature impacted both uniformly. As the temperature increased to 120 °C, the peaks of the samples (PCH18 and ACH18) started to fade away due to the effect of high temperature. 95 °C (on PCH16 and

ACH16) was, therefore, adopted as the optimal temperature for the deproteination of both pupal and adult BSF samples in this study. Deproteination time was investigated in the next sub-section.

4.1.2.3 *Time optimisation*

The optimised concentration (1.0 M NaOH) and temperature (95 ˚C) determined in Section 4.1.2.1 and 4.1.2.2, respectively were adopted while varying the time of the reaction (10, 12, 14, 16 and 18 h) for both BSF samples. The samples investigated in this study were coded as PCH19 and ACH19 (10 h), PCH20 and ACH20 (12 h), PCH21 and ACH21 (14 h), PCH22 and ACH22 (16 h) and PCH23 and ACH23 (18 h). Figure 4.6 shows the FTIR spectra of the samples investigated to determine the optimal time for the deproteination process.

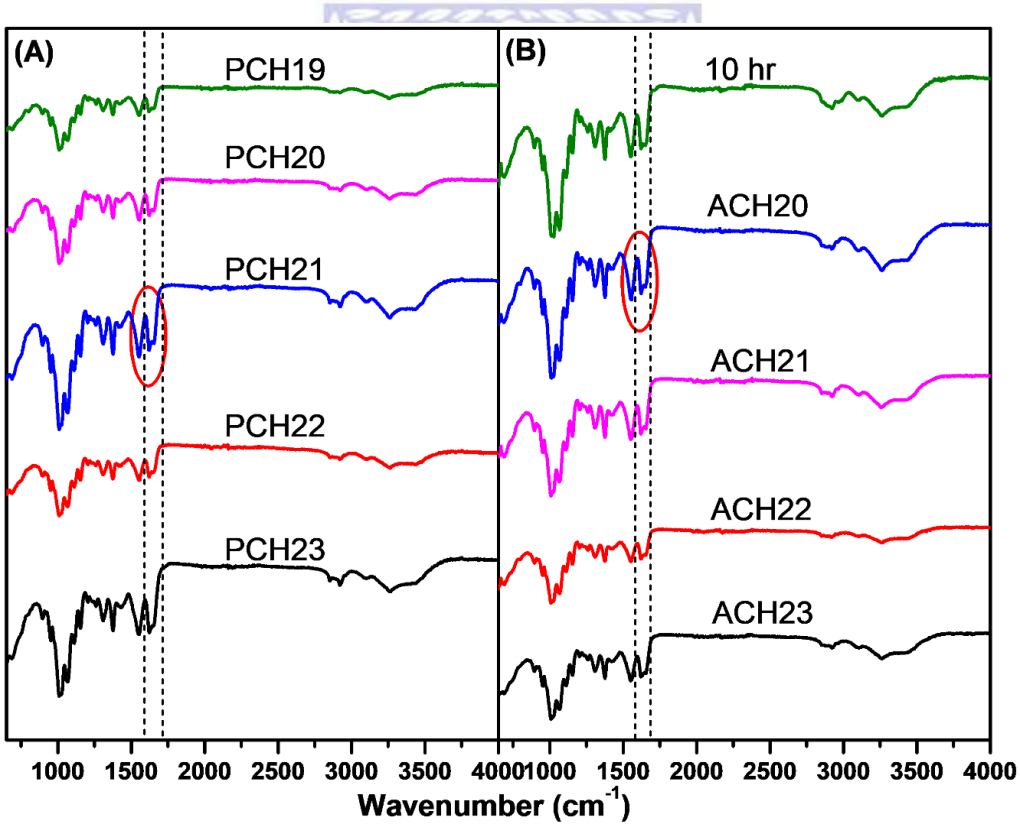

Figure 4. 6: FTIR spectra obtained as the time of deproteination was varied (10, 12, 14, 16 and 18 h) while concentration (1.0 M NaOH solution) and temperature (95 ˚C) were kept constant for both pupae (A) and adult (B) BSF waste.

Figure 4.6 shows the various FTIR spectra acquired after the deproteination of the pupal and adult BSF samples at various time intervals. The spectra of the samples investigated for 10 h (PCH19 and ACH19) displayed a low peak intensity (though only for the pupal sample) and

also a weak splitting of the Amide 1 peak (for both samples). Increased peak height and a better splitting of the amide band were observed on samples PCH21 and ACH20 (times of 14 and 12 h respectively). Further increase in time did not improve the peak separation of the Amide 1 on the samples. Consequently, a time of 12 or 14 h was adopted as the optimal deproteination temperature for adult or pupal BSF samples, accordingly.

The time, temperature and concentration of the extraction for the demineralisation process were varied to obtain the optimum conditions as described in Chapter 3 Section 3.2.1. The optimised demineralisation conditions were 1.0 M HCl (PCH2 and ACH2), 50 °C (PCH5 and ACH5) and 1.67 h (100 minutes) (PCH11 and ACH11) for both BSF samples. Therefore, the demineralisation extraction conditions were mild compared to crustacean shells of *Leptinotarsa decemlineata* which were treated using 2.0 M HCl, at 75 °C for 2 h (Kaya *et al.*, 2014a). This is due to lower inorganic composition of insect cuticles (about 10%) relative to crustacean exoskeletons having values ranging from 20 – 40% (Jardine and Sayed, 2016). This makes the demineralisation process easier and, therefore, was achieved under mild conditions.

For the deproteination process, the parameters of time, temperature and concentration were varied to also determine the optimum conditions for chitin extraction. The deproteination process is described in Section 3.2.1.2 of Chapter 3. The optimum deproteination conditions determined in this study were 1.0 M NaOH solution (PCH13), 95 °C (PCH16 and ACH16) and 14 h (PCH21) for pupal chitin isolation and 1.0 M NaOH solution (ACH13), 95 °C (ACH16) and 12 h (ACH20) for adult chitin extraction. The deproteination conditions in this study is mild compared to the 2.0 M NaOH, 85 °C and 24 h conditions adopted by Erdogan *et al.* (2017).

4.1.3 *Chitin content of pupae and adult BSF*

The series of optimisation experiments conducted revealed that chitin extraction and yield depend on the process parameters of time, temperature and concentration. In addition, the sequence of the extraction process (deproteination or demineralisation occurring first) has been reported to influence the yield of chitin. Chitin is a major component of the insect cuticle, which is always covalently bound to catechol compounds and sclerotin-like proteins thereby providing mechanical support to the insect (Shillito *et al.*, 1995; Nessa *et al.*, 2011). The removal of the protective protein matrix if deproteination is conducted first exposes the chitin to acid attack during the demineralisation process, leading to hydrolysis of the biopolymer (Lertsutthiwong *et al.*, 2002). Deproteination before demineralisation, therefore, leads to low

yield of chitin. To avoid this, demineralisation was conducted prior to deproteination in this study and the results obtained are shown in Section 4.1.1 and 4.1.2.

4.1.3.1 *Chitin yield determination*

To determine the yield of each BSF sample, the established optimal demineralisation (Section 4.1.1) and deproteination (Section 4.1.2) conditions were utilised as shown in Table 4.1 to compute the yield of each sample.

Table 4. 1: The yield (%) of the BSF samples after demineralisation with HCl

Samples	Concentration of HCl (M)	Temperature (°C)	Time (h)	Yield (%)
Pupae shells	1	50	1.67	78.3±3.6
Adult	1	50	1.67	67.5±2.1

Table 4. 2: The yield (%) of the BSF samples after deproteination using NaOH solution

Samples	Concentration of NaOH (M)	Temperature (°C)	Time (h)	Yield (%)
Pupae shells	1	95	14	14.1±1.4
Adult	1	95	12	5.3±1.1

The dry weight chitin contents of the adult BSF and pupae casings were computed to be 5.3 and 14.1%, respectively using Equation 3.1. The chitin yield of the pupae casings was approximately 3-fold higher than that of the adult BSF at the optimised conditions (Table 4.2). This could have been caused by the presence of fully formed peritrophic membrane in the pupae BSF. The peritrophic membrane (PM) is an acellular chitin-containing enclosure, which functions to protect the insect against pathogens and abrasion (Hegedus *et al*., 2016). In the pupae stage, chitin fibrils and associated chitin-binding peritrophin membranes are produced in the PM. The thickness of the structures varies based on the stage of metamorphosis or species of the insect (Merzendorfer *et al*., 2016). Moreso, the depth and structure of the PM is affected by the developmental stage of the insect, as it significantly diminishes during moulting (Hegedus *et al*., 2016). The moulting process and the inability of the adult BSF to feed due to the absence of functional mouthparts, which affects the formation of PM, could be responsible for the low chitin yield obtained from the adult BSF (Table 4.2).

Several researchers have studied other sources of chitin and concluded that the yield varies. Al Sagheer *et al.* (2009) and Wang *et al.* (2013) in separate reports found the chitin content of

shrimp, crayfish, krill and crab to be between 20 and 31%. Contrary to these crustacean sources, Sajomsang and Gonil (2010) reported that cicada sloughs, an insect, contain 36% chitin. However, Santos *et al.* (2011) in their study on the shrimp, *Macrobrachium jelskii* reported a chitin content of only 5.9%. Furthermore, Ibitoye *et al*. (2018) reported 3 - 7% in Daphnia, a microcrustacean, while Kaya *et al*. (2015) and Marei *et al.* (2016) reported values of 5.3 - 8.9% in grasshoppers and 5% for beetles, respectively.

For insects, their chitin content depends on their developmental stages and species, with values ranging from 2.2 to 10.3% (Kaya *et al*., 2016a). This study shows that the pupal BSF had more chitin yield than most insect species reported in the literature but lower when compared to the crustacean sources such as crabs, krills and some insects such as cicada sloughs. This study, for the first time, has successfully determined the chitin content of pupal exuviae and adult BSF.

4.1.3.2 *Elemental analysis*

The nitrogen (N) and carbon (C) content of chitin are important in that they signify the extent of deproteination and, most importantly, the quality of the obtained biopolymer. An N value above 6.89%, the theoretical amount of nitrogen in fully acetylated chitin, is indicative of an incomplete extraction process with the presence of impurities while lower values of N is an indication of hydrolytic deamination of the extracted samples (Soon *et al*., 2018). The ratio of carbon to nitrogen (C/N) for the extracts were also determined. C/N is important in chitin studies as it is applied in the computation of the DA of the chitin. The DA is an important parameter in chitin studies and it, among other properties, determines the application of chitin in various areas. The percentage N and C content obtained in this study, as well as the DA and C/N ratio, are presented in Table 4.3.

Table 4. 3: Composition of the extracted BSF chitin compared with commercial shrimp chitin

Chitin	TC (%)	TN (%)	C/N	DA
Commercial	42.8	6.3	6.80	96.50
Adult	43.6	6.5	6.71	91.30
Pupal	44.1	6.2	7.12	115.10

TC = Total carbon, TN = total nitrogen, C/N = carbon/nitrogen ratio.

There was a difference in N contents of pupae (7.12) and adult (6.71) chitin in this study. The N content of adult chitin was slightly lower than the N value of fully acetylated chitin (6.89%).

These obtained N values were in agreement with those reported in previous studies for insects. Liu *et al.* (2012) reported a value of 6.3% for *H. parallela*, while Kaya *et al*. (2014a) obtained a value of 6.41% for *L. decemlineata.* In a separate study, Kaya *et al.* (2016a) obtained values of 6.5, 6.3 and 6.49% for different developmental stages of larva, pupa and adult *Vespa crabro,* respectively.

DA values of 115.12, 91.3 and 96.5% were computed (using Equation 3.19 in section 3.9.2 of Chapter 3) for pupae, adult and commercial chitin, accordingly. Theoretically, the DA values should be 100%. Sajomsang and Gonil (2010) reported that a DA value greater than 100% is an indication of the presence of organic compounds in the sample. Nevertheless, these results are better when compared with results from similar studies in the literature. Waśko *et al.* (2016) obtained values of 250 and 179% for larva and Imago of *H. illucens,* while Erdogan and Kaya (2016) had DA values of 187 and 232% for nymph and adult grasshopper (*D. maroccanus*), respectively. The DA values obtained by elemental analysis in this study were far less than those reported by previous research as enumerated above and points to the high degree of acetylation of the obtained biopolymers. Further characterisations conducted on the extracted pupal and adult BSF chitin are discussed in detail in the subsequent sections.

4.1.4 *Characterisations of the extracted chitin*

Characterisation provides information and reveals the intrinsic properties of a material. Subsequent sections will describe in detail the results of the characterisation conducted on both the extracted chitin (PCH21 and ACH20) in this study. PCH21 and ACH20 were chosen for further characterisation because their FTIR spectra revealed the peaks of interest, the Amide 1 band and displayed the most improved scissoring effect of this peak among the samples extracted using other conditions.

4.1.4.1 *ATR-FTIR spectra of the extracted BSF chitin*

The ATR-FTIR analysis was employed to study the functional groups on the extracted chitin structures (PCH21 and ACH20). It determines and compares the chemical compositions using the spectral peaks on the PCH21 and ACH20 BSF chitin and commercially available shrimp chitin (Sigma Aldrich). The ATR-FTIR analysis was carried out at a wavelength ranging from 650 - 4000 cm^{-1}. The details of the procedure are described in Section 3.9.3 of Chapter 3. Figure 4.7 shows the ATR-FTIR spectra of the PCH21 and ACH20 and the commercial chitin used as a reference in this study.

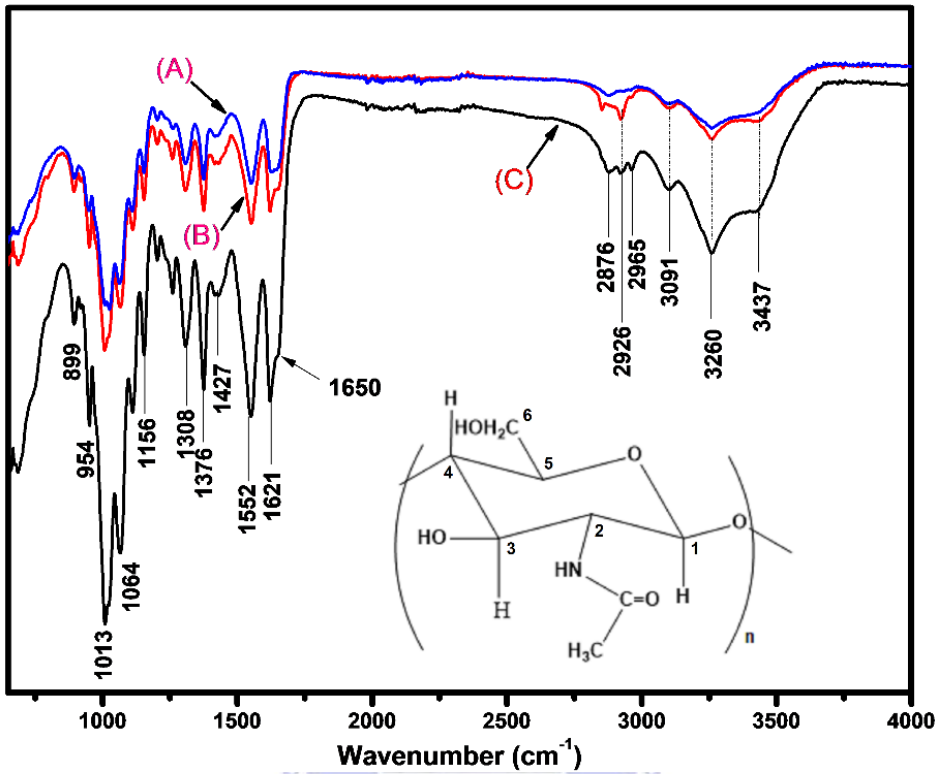

Figure 4. 7: FTIR of the spectral features of BSF chitin with the commercial showing similarity (A = commercial, B = PCH21 and C = ACH20. The inset shows the structure of chitin.

The spectrum of both PCH21 and ACH20 had the following characteristic peaks of chitin. The peaks at 3260 and 3437 cm^{-1} correspond to the stretching and vibration of the hydroxyl (O–H) group. The reduced peak at 2920 cm^{-1} indicates the symmetric and asymmetric vibration of C–H from the $–CH_3$ group. According to Gbenebor *et al*. (2017), the most important signals in the spectrum of chitin are the peaks at 1661, 1559 and 1312 cm^{-1} with characteristic stretching vibrations of Amides I, II and III bands, respectively. Interestingly, the Amide 1 band in all the spectra did split into two peaks that were observed at 1650 and 1621 cm^{-1}. This is a clear indication that both PCH21 and ACH20 were chitin and of the α-form (Sayari *et al*., 2016). The Amide 1 band has a weak signal at 1650 cm^{-1}, corresponding to the intermolecular hydrogen bond CO· · ·HN due to the acetamide ($–NHCOCH_3$) group, and a strong and well-defined peak at 1621 cm^{-1} due to intramolecular hydrogen bonding CO· · ·$HOCH_2$ (Sayari *et al*., 2016). The characteristic absorptions peak at 1552 cm^{-1} indicates the –NH bending vibration of the Amide 11 band from the acetamide group while the peak at 1427 cm^{-1} shows the stretching vibration of the CN group (also from the acetamide group). The absorption band at 1013 cm^{-1} is the symmetric stretch corresponding to –C–O–C– of the glucosamine ring, while the peak at 899 cm^{-1} results from the CH ring stretching, a characteristic band for β-(1-

4) bond (Wysokowski, *et al.*, 2013). The scissoring of the Amide 1 peak (1650 and 1621 cm^{-1}) is the distinguishing feature between α-chitin and β-chitin. This is as a result of the parallel and anti-parallel arrangements of the α-chitin structures necessitated by intermolecular (CO···HN) and intramolecular ($CO\cdots HOCH_2$) hydrogen bonding (Kaya *et al*., 2013; Sayari *et al*., 2016). These confer chitin with its characteristic high insolubility.

The effectiveness of the demineralisation and deproteination processes were ascertained by the absence of the characteristic mineral bands (1720 - 1798, 1420 - 1430 and 876 cm^{-1}) and protein peak (1540 cm^{-1}) on the spectra of both PCH21 and ACH20 (Mohammed *et al*., 2013; Was´ko *et al*., 2016; Bogdanova *et al.*, 2016). Table 4.2 shows the absorption bands identified from the spectra of both PCH21 and ACH20 and the commercial reference chitin samples.

Table 4. 4: Identified absorption bands on the spectra of the extracted BSF chitins (PCH21 and ACH20) and the commercial chitin samples.

	Wavenumber (cm^{-1})			
Functional group and Vibration mode	Adult Chitin	Pupae Chitin	*Com Chitin	Classifications
O-H stretching vibration	3437	3437	3437	Aliphatic compound
N-H stretching	3259	3260	3259	-
Symmetric and asymmetric vibration of C-H from -CH_3	2925	2926	2925	Aliphatic compounds
CH_3 symmetric stretch (Methylene group stretching	2876	2875	2876	Aliphatic compounds
Carbonyl group (C=O) vibration & stretching secondary Amide	1650	1651	1651	Amide 1
C=O secondary Amide stretch	1621	1620	1623	Amide 1
N-H bend, C-N stretch	1552	1553	1553	Amide 11
CH_2 bending and CH_3 vibration band symmetric distortion	1427	1426	1426	-
CH bend, CH_3 symmetric distortion	1376	1376	1375	-
CH_2 wagging (C-N vibration from Amides)	1308	1309	1309	Amide 111
C-N Stretch	1259	1259	1259	-
Asymmetric bridge oxygen (C-O-C) stretching	1156	1153	1153	-
Asymmetries in-phase ring stretch mode.	1109	1114	1112	-
C-O-C asymmetric stretch in phase ring.	1064	1065	1065	Saccharide ring
C-O-C symmetric stretch in-phase (glucosamine) ring.	1013	1010	1012	Saccharide ring
CH3 wagging.	954	954	954	Along chain
CH ring stretch (deformation).	899	892	893	Saccharide ring
OH, out-of-plane bending.	687	687	687	-

*Com = commercial

4.1.4.2 *X-ray diffraction studies (XRD)*

The XRD investigation was conducted to study the degree of orderliness of the chitin extracted from pupae shells and adult BSF (PCH21 and ACH20) at optimised conditions which were compared to commercial shrimp chitin. The X-ray diffraction patterns were obtained on a Bruker AXS D8 Advance diffractometer and were recorded at 40 kV, 30 mA and 2θ (experimental details in Section 3.9.4 of Chapter 3). The XRD patterns of PCH21 and ACH20

and the commercial shrimp chitin are presented in Figure 4.8 while the parameters deduced from the figure are presented in Table 4.5.

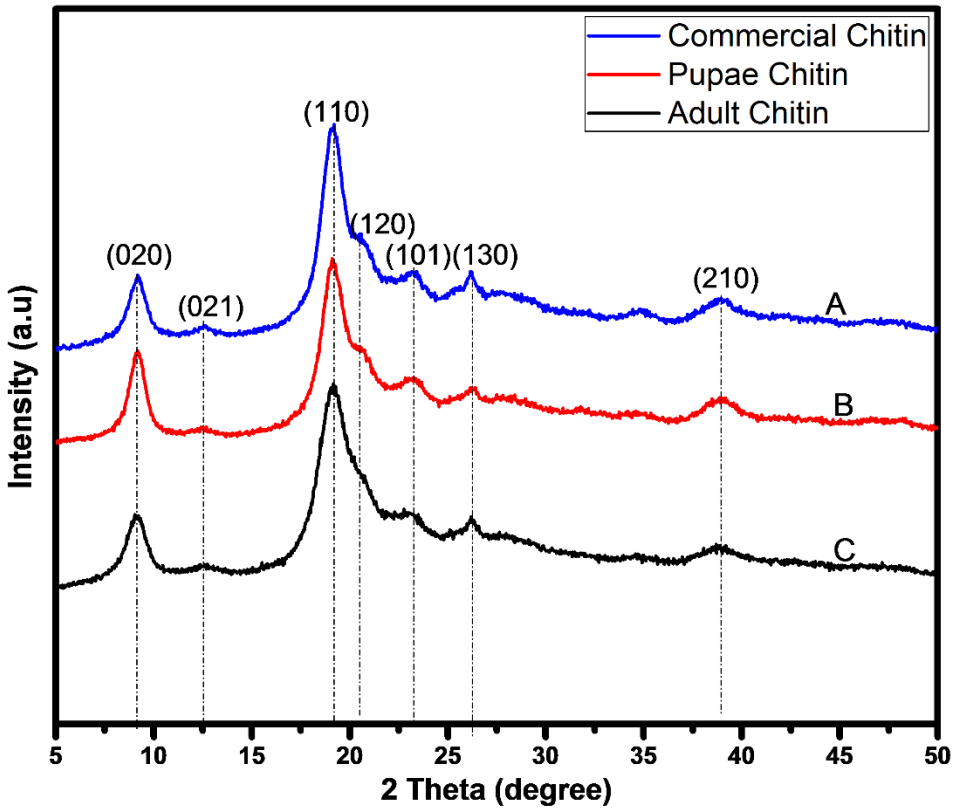

Figure 4. 8: XRD patterns of the extracted chitins showing the various crystallographic planes. A = commercial chitin, B = pupae chitin and C = adult chitin.

Seven crystalline reflections (020, 021, 110, 120, 101, 130 and 210 at 2θ with values as tabulated in Table 4.5) were observed for all the chitin samples. Measurements were taken at 2θ from 5° to 50° (Figure 4.8). Two strong peaks located approximately at 9.13° and 19.18° 2θ values though with slight variations were observed for all the chitin samples while broad and less intense peaks were observed at 12.60°, 23.05°, 26.27° and 38.80°. The strong reflection at 9.13° resulted from the presence of bound water molecules in the crystal lattice of the chitin (Abdou *et al*., 2008). Similar findings were reported by Sajomsang and Gonil (2010) and Liu *et al*. (2012). The degree of orderliness (Crl) is presented in Table 4.5.

Table 4. 5: Structural parameters of chitins obtained from X-ray diffraction studies

Chitin Sample	Plane	2θ	d (Å)	Crl (%)
Pupae (PCH21)	(020)	9.13	9.68	
	(021)	12.6	7.02	
	(110)	19.18	4.62	77
	(120)	23.05	3.85	
	(101)	26.32	3.38	
	(130)	38.80	2.32	
Adult (ACH20)	(020)	9.13	9.68	
	(021)	12.65	6.99	
	(110)	19.16	4.63	79
	(120)	23.06	3.85	
	(101)	26.27	3.39	
	(130)	38.80	2.32	
Commercial	(020)	9.14	9.67	
	(021)	12.6	7.02	
	(110)	19.18	4.62	82
	(120)	23.05	3.85	
	(101)	26.27	3.39	
	(130)	38.70	2.32	

The interplanar distances of the unit cells of the BSF chitin structures were computed using Equation 3.22 (Section 3.9.4 of Chapter 3) and are presented in Table 4.5. These distances were computed considering that α-chitin has an orthorhombic structure with unit dimensions of a = 4.74 Å, b = 18.86 Å and c = 10.32 Å (Minke and Blackwell, 1978; Stawski *et al*., 2008). For pupal chitin, the longest distance of 9.68 Å was determined at (020) plane while the lowest value of 2.32 Å was recorded at (130) plane. Similar observations were made for adult and commercial chitins. Cárdenas *et al.* (2004) investigated chitin from different sources and obtained the longest interplanar distance of 9.65 Å at (020) plane for shrimp, lobster, crab and king crab chitins while their lowest value was at (013) plane with a value of 3.39 Å.

The degree of orderliness (Crl (%)) were also computed using Equation 3.21 (Section 3.9.4 of Chapter 3) from the absorption band with the highest intensity (110 planes, Figure 4.8). The values obtained were 77, 79 and 82% for pupae, adult and commercial chitin, respectively.

Kaya *et al*. (2014a) had reported that the Crl values of chitins vary between 47 and 91% according to insect species and the isolation method. Therefore, the Crl values found in this study were within these reported values.

4.1.4.3 *Thermal gravimetric analysis (TGA/DTGA) of chitin*

Thermal gravimetric analysis was carried out on the extracted BSF chitins to determine, quantify and compare the thermal profiles of the chitin (pupal (PCH21), adult (ACH20) and commercial) samples. The experimental detail is described in Section 3.9.5. of Chapter 3. Figure 4.9 and 4.10 present the TGA and DTG (derivative thermal analysis) profiles of pupal and adult chitins.

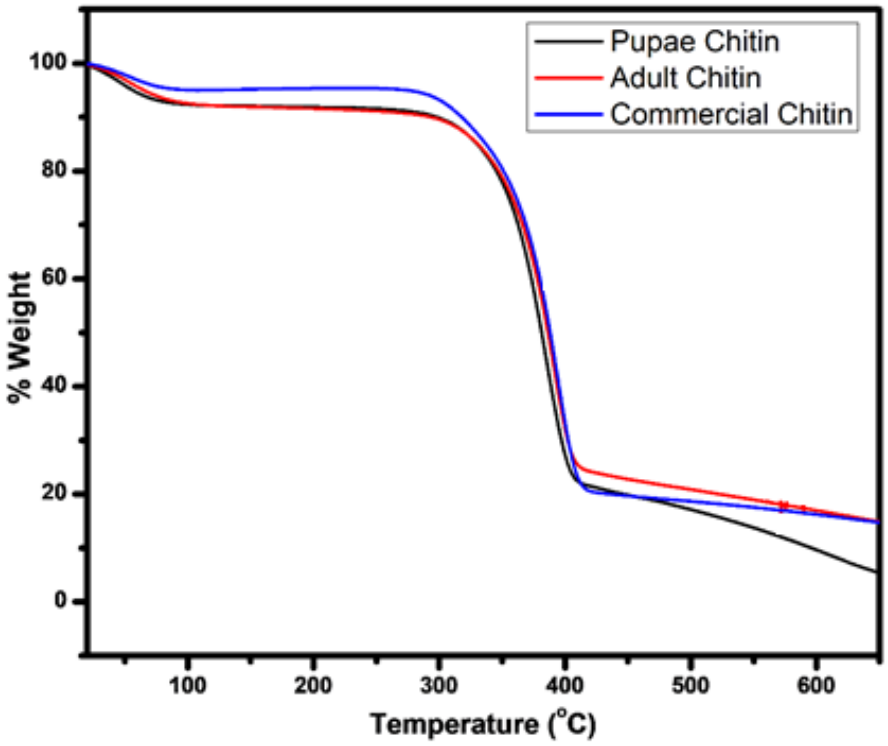

Figure 4. 9: Thermograms (TGA) of adult and pupae chitins compared with commercial chitin.

The profiles in Figure 4.9 indicate that all the three chitin have two stages of weight losses. The first stage of decomposition corresponds to the loss of bound or lattice water contained in the chitin structure. In the pupal chitin (PCH21), the temperature at which the maximum water loss occurred was at 46 ˚C (starting from 22 ˚C to 106 ˚C) with a sample weight loss (which equally corresponds to water loss) of 5.5%. The adult chitin (ACH20) had a weight loss of 5.2%, starting from 20 ˚C and ending at 106 ˚C. The maximum weight loss was observed at a

temperature of 54 ˚C (Figure 4.9). The commercial chitin exhibited the same trend with a sample weight loss of 3.2% and the temperature of maximum weight/water loss being 53 ˚C (from 21 ˚C to 106 ˚C).

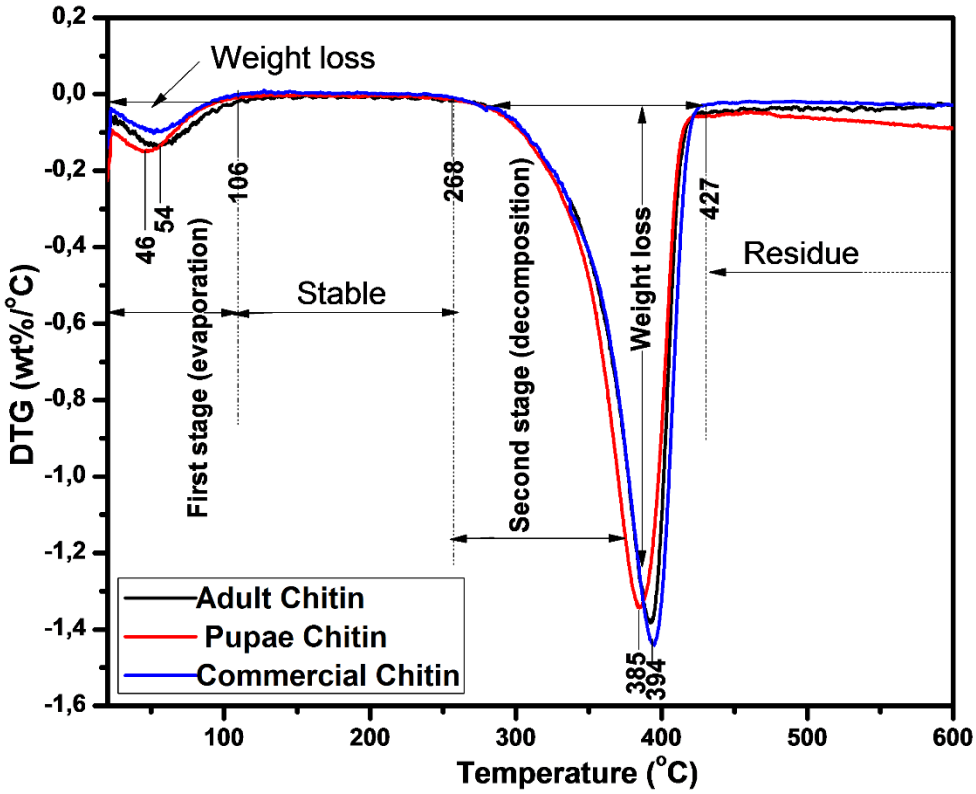

Figure 4. 10: The derivative thermograms (DTG) of the adult, pupae and commercial chitins.

The second decomposition stage involves the determination of the thermal stability of the chitin samples. It was observed that all the chitin samples were stable up to 268 ˚C (Figure 4.10). The sharp decrease in the thermal profile (Figure 4.9) of the samples is attributed to the depolymerisation and decomposition of the acetylated group of the chitin molecule; likewise, the dehydration and subsequent degradation of the saccharide backbone (Paulino *et al.*, 2006; Gonil and Sajomsang, 2012). Weight losses (the area under the degradation profile of the derivatograms) resulting from the second phase of decomposition were estimated to be 65%, 61% and 73% for pupal, adult and commercial chitin, respectively. The commercial chitin lost 11% and 16% more weight than the pupal and adult chitins, respectively. The maximum degradation temperature (DTG_{max}) of the samples, the temperature at which the maximum components in the materials decomposed, varied from 385 ˚C in the pupal chitin, 392 ˚C in the adult chitin to 394 ˚C in the commercial chitin. This is depicted by the gradual peak shift of the

derivative thermograms (Figure 4.10) to the right. These results corroborate the findings of Jang *et al.* (2004) who reported a 396 ˚C DTG_{max} for alpha chitin extracted from crab. Table 4.6 summarises the findings from the thermal profiles of the chitins and presents the temperatures at which various mass losses occurred.

Table 4. 6: Parameters deduced from the derivative thermograms of the extracted BSF chitins (PCH21 and ACH20) compared to the commercial shrimp chitin used as a reference

Processes	Parameters	Commercial	Pupae	Adult
Evaporation (first stage)	Temperature (˚C)	21 – 106	22 – 106	27 – 106
	T_{me} (˚C)	53	46	54
	Mass loss (%)	3.2	5.5	5.2
Degradation (second stage)	Temperature (˚C)	268– 427	268 – 427	268 – 427
	T_{md} (˚C)	394	385	392
	Mass loss (%)	73	65	61

T_{me} = temperature of maximum evaporation; T_{md} = temperature of maximum degradation.

4.1.4.4 *Scanning electron microscopy analysis*

Scanning electron microscopy (SEM) analysis was carried out to examine the surface morphologies of the extracted BSF chitin. The morphology of the extracts was examined by using Zeiss Gemini Auriga HRSEM as described in the experimental details in Section 3.9.6 of Chapter 3. The SEM micrographs of chitin extracted from pupae shells (PCH21) and adult BSF (ACH20), along with the commercial shrimp chitin studied at different magnifications are presented in Figure 4.11.

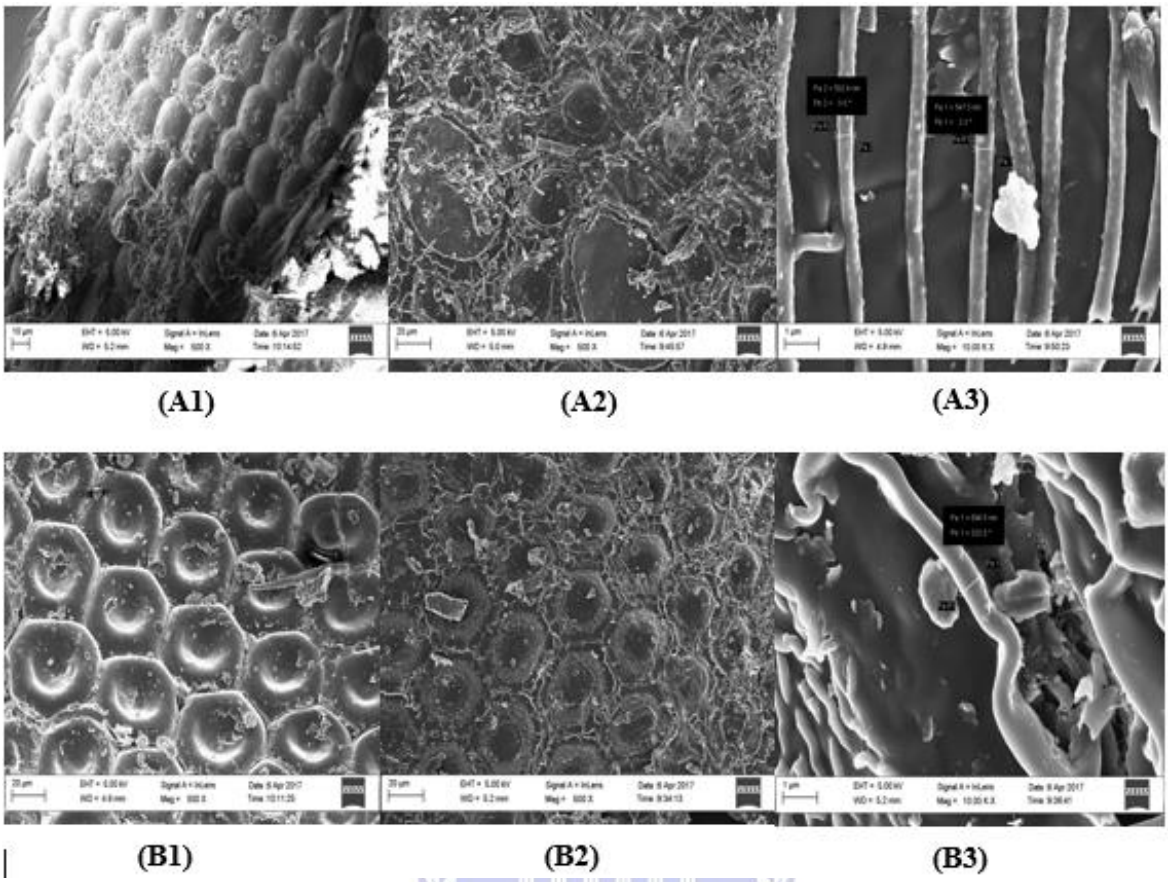

Figure 4. 11: Scanning electron micrographs of the BSF chitins (A1) raw adult (A2) adult chitin (A3) higher magnification showing presence of fibre; (B1) raw pupae (B2) pupae chitin (B3) higher magnification showing the presence of fibre and its arrangement.

The micrographs revealed tightly packed structures with reoccurring hexagonal shapes arranged in honeycomb-like positions for pupal chitin; PCH21 (Figures 4.11, B 1-3). Adult chitin, ACH20 showed repeating oval arrangements (Figure 4.11, A1-3) as processing progresses from demineralisation to deproteination. Further increase in magnification revealed that the structure of both chitin was fibrous in appearance (Figure 4.11 A3 and B3) with the pupae (PCH21) (Figure 4.11 B3) having some irregularly arranged thick fibres and others in a diagonal orientation, while the adult chitins (ACH20) showed parallel fibre arrangement. The size of the fibrils (Figures 4.11 A3 and B3) for both pupal and adult chitins (Figure 4.11 A3) were determined to be 694 nm and 506 nm, respectively. Both chitin structures did not exhibit porosity. According to Kaya *et al*. (2014a), the surface morphology of chitin could be grouped into three main types; surfaces without pores and nanofibres, those with nanofibres but no pores and those consisting of nanofibres and pores. The surface morphology of chitin from pupae and adult BSF, in this study, falls among the surfaces without pores. This corroborates the findings of Kaya *et al*. (2014a). Some researchers had reported chitin consisting of only fibrils,

while others reported a combination of both fibrils and pores. Kaya and co-workers had also reported in various studies that chitin extracted from certain organisms consisted only of fibrils while others consisted of both fibrils and pores (Kaya *et al.*, 2013; Kaya *et al.*, 2015; Kaya *et al.*, 2016a). Thus, the surface morphology of chitin varies depending on the species of the insect. This variation also extends to different stages of metamorphosis as can be seen in the micrographs of the ACH20 and PCH21. Marei *et al*. (2016) reported that chitins with pore structures were characterised with a high metal sorption ability and thus were useful in the removal of metal ions from solutions, while fibril-structured chitin could be used in textiles.

Additional characterisation is needed to further understand the chemical properties of the extracted materials. Therefore, NMR spectroscopy was performed on both PCH21 and ACH20 (the extracted chitin biomaterials) and is discussed in the next section.

4.1.4.5 *^{13}C CP/MAS-NMR spectroscopic analysis*

The NMR technique is the most preferred approach for determining the degree of acetylation/deacetylation (DA/DD) of a chitin/chitosan sample. This is because it is simple to operate and does not require tedious sample preparation. Furthermore, the analysis utilises a sufficient amount of sample to solve the problem of low ^{13}C isotope sensitivity. Moreso, calibration curves are not required for data generation/acquisition and it gives result irrespective of the presence of minute impurities in the sample (Khor, 2014).

Solid-state ^{13}C CP/MAS NMR spectroscopy was carried out as detailed in Section 3.9.7 of Chapter 3. The acquisition parameters were a frequency of 125.735 MHz, 50 ms acquisition time, 8 ms contact time and 5 s repetition time. Figure 4.12 present the ^{13}C NMR spectra of the pupal and the adult BSF chitin samples.

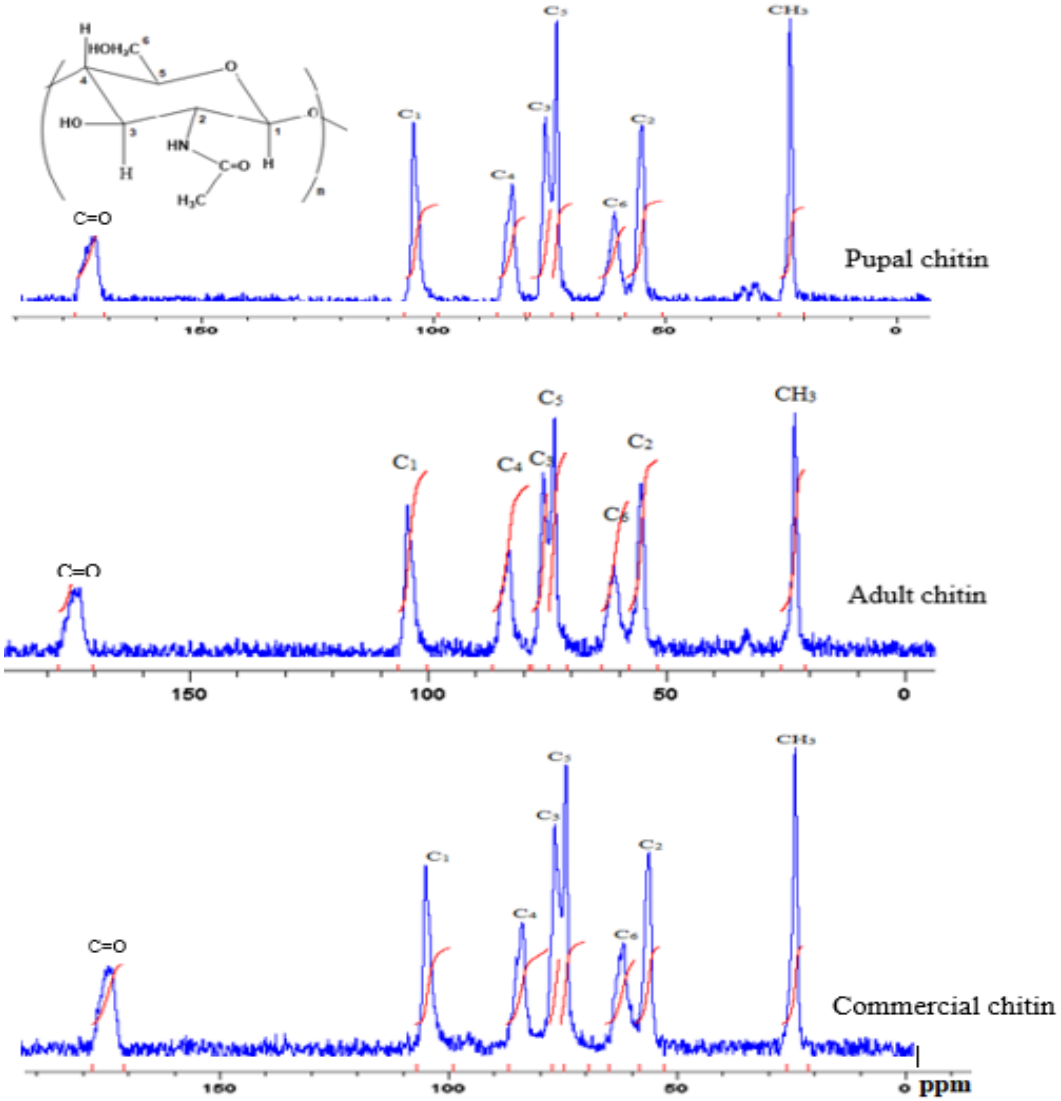

Figure 4. 12: ^{13}C NMR spectra of the extracted pupae and adult chitins as compared to the commercial shrimp chitin. Inset is the structure of chitin.

Figure 4.12 shows that the spectra of pupal (PCH21) and adult (ACH20) chitin presented similar features to the commercial chitin and conform to α-chitin structure. All the three chitin spectra consisted of eight resonances. These carbon atoms corresponding to the N-acetylglucosamine repetitive units in both PCH21 and ACH20 appear at the following chemical shifts as shown in Table 4.7. Hajji *et al*. (2014) had reported that in β-chitin, the C3 and C5 resonances merge into a single signal at 75.0 ppm. In this study, the C3 and C5 resonances on all the chitin profiles were clearly separated and appeared at 73.55 and 76.10 ppm, 73.55 and 76.74 ppm, and 73.55 and 76.10 ppm for PCH21, ACH20 and commercial reference chitin, respectively (Figure 4.12, Table 4.7). This splitting is linked to the various alignments of C3 and C5 atoms in the structure of chitin due to the formation of inter and intramolecular hydrogen bonds (Cárdenas *et al*., 2004). This is an indication of a high structural resemblance

to the α-form and corroborates the findings of Abdou *et al*. (2008) and Song *et al*. (2013) whose study also reported the splitting of the C3 and C5 into well-defined resonances. The C=O signals were observed at a fairly uniform position (173.57, 173.10 and 173.44 for PCH21, ACH20 and commercial chitin, respectively) on all the chitin profiles and, therefore, show a distinct conformational state only exhibited by the α-chitin (Kumirska *et al*., 2010).

The effectiveness of the deproteination process was justified by the absence of additional peaks on all the spectra, especially catechol, a protein associated with insect cuticles (Schaefer *et al*., 1987; Paulino *et al*., 2006). Different peaks associated with protein residuals appear at approximately 181.5, 128.7, 32.9, 30.0 and 14.2 ppm (Abdel-Rahman, *et al.,* 2015). These peaks were completely absent on all the ^{13}C-NMR spectra of chitin in this study. This is an indication of the absence of residual proteins in the extracted chitin samples. The resonances of the various carbon atoms in the chitin spectra and their integral values are presented in Table 4.7.

Table 4. 7: ^{13}C NMR spectral data of PCH21, ACH20 and commercial chitins.

C Signal	Pupal		Adult		Commercial	
	***δ (ppm)**	**Integral**	***δ (ppm)**	**Integral**	***δ (ppm)**	**Integral**
C=O	173.57	9.6952	173.10	9.5500	173.44	9.9898
C1	104.44	13.3144	104.44	12.7362	104.44	12.8412
C4	83.11	11.000	83.42	11.4898	83.42	12.9482
C5	76.10	13.6380	76.74	12.4512	76.10	12.4238
C3	73.55	13.5162	73.55	14.5447	73.55	13.8972
C6	60.82	9.4518	61.45	10.1281	61.45	10.9082
C2	55.09	13.9556	55.72	13.7836	55.40	12.9813
—CH_3	**23.24**	**12.7927**	**22.93**	**12.9025**	**23.56**	**13.1507**

*δ = resonance

With the uniformity in the structural and chemical properties of the extracted samples, as validated by the various characterisations carried out, it was therefore established that the samples were chitin. The subsequent sections are dedicated to chitosan production from the extracted chitin and further characterisations.

4.2 Synthesis of chitosan

One of the most important distinguishing features between chitin and chitosan is the DD. The DD of both chitin and chitosan determines their properties of which solubility is one. The European Chitin Society has proposed that chitin and chitosan be distinguished based on their solubility and insolubility in 1.0% acetic acid solution. Accordingly, the biomaterial that solubilises should be termed chitosan, while the insoluble material is called chitin (Roberts, 2007). Deacetylation involves the partial removal of the intractable acetyl ($-CH_3$) component of the acetamide group ($NHCOCH_3$) on the chitin structure using strong alkaline solutions to give an amine (NH_2) moiety. This process renders the material soluble in a mild, acidic solution. Section 4.2.1. focuses on the investigation of the optimum conditions for the deacetylation of both pupal (PCH21) and adult (ACH20) BSF chitin (isolated in Section 4.1) to chitosan. The process involves the optimisation of concentration, temperature and time of reaction. To actualise the synthesis of chitosan, termed deacetylation, twenty (20) trials were conducted and the optimum chitosan synthesis conditions, as detailed in Tables 3.9 – 3.11 of Section 3.2.1.2 were obtained after characterisations. Like in the chitin extraction, the preliminary characterisation technique applied was FTIR analysis as described in Section 3.9.3.

4.2.1 *Concentration optimisation*

The temperature and time of the deacetylation reaction were kept constant at 80 ^oC and 5 h, respectively while the concentration was varied (30, 50 and 70% NaOH solution). The various pupal and adult samples investigated have the following codes PCH21_1 and ACH20_1 for 30%, PCH21_2 and ACH20_2 for 50% and PCH21_3 and ACH20_3 for 70%. Table 3.9 of Section 3.2.2 described in detail the experimental protocol. Figure 4.13 shows the spectra obtained as the NaOH concentration was varied for both pupae and adult BSF chitin at constant temperature and time.

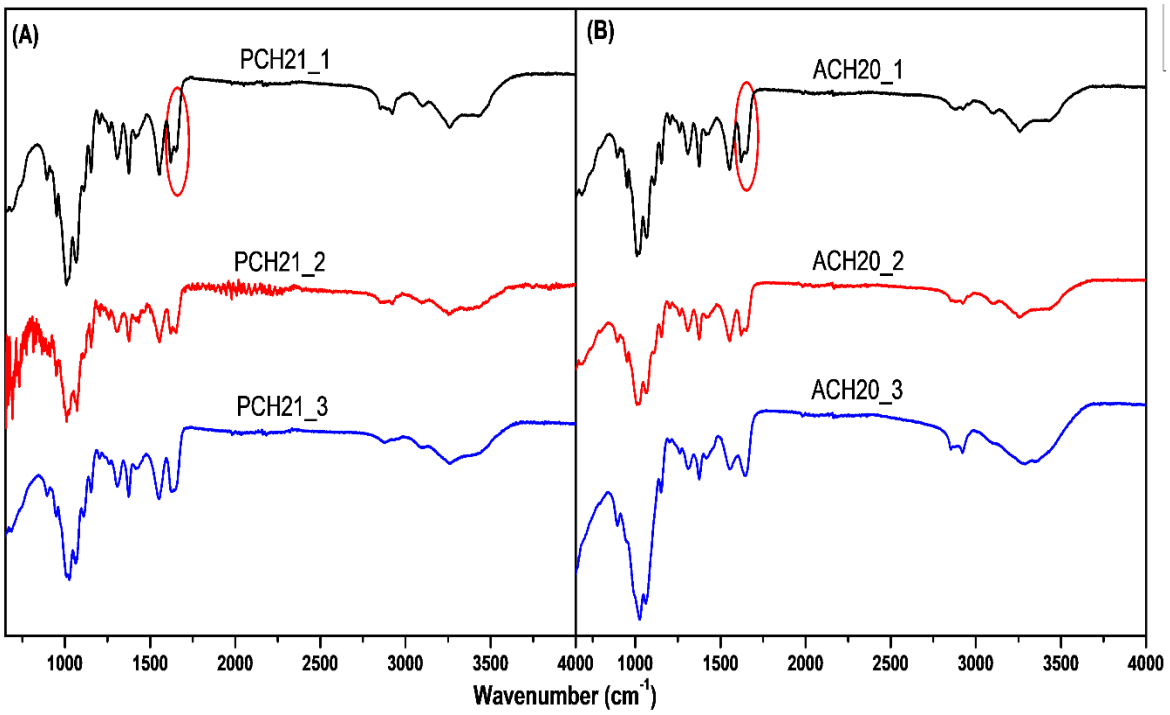

Figure 4. 13: FTIR spectra obtained as the deacetylation concentration was varied (30, 50 and 70% NaOH solution) at constant temperature (80 ^{o}C) and time (5 h) for both pupae (A) and adult (B) BSF chitin.

From Figure 4.13, the pupal and adult BSF samples that were deacetylated using 30% NaOH (PCH21_1 and ACH20_1) maintained the characteristic chitin spectra. This is shown by the definite splitting of the Amide 1 band into two different peaks at 1625 and 1655 cm^{-1} for PCH21_1 and 1621 and 1659 cm^{-1} for ACH20_1 as they appeared in chitin. This implies that the 30% NaOH solution was not effective in the deacetylation of the chitin samples. Similarly, the samples treated with 50% NaOH solution (PCH21_2 and ACH20_2) showed a slight change in their spectra. The Amide 1 signal on both spectra of BSF chitin samples decreased significantly. Furthermore, the clear scissoring of the Amide 1 band at 1625 and 1655 cm^{-1} observed in the 30% treated samples (PCH21_1 and ACH20_1) gradually decreased in the 50% (PCH21_2 and ACH20_2) treated pupal and adult chitin samples. This is an indication that 50% NaOH solution had more effect in deacetylating both chitin samples than the 30% NaOH solution. At 70%, the chitin samples (PCH21_3 and ACH20_2) did not display the two peaks associated with the Amide 1 band. Rather both fused together as one peak and appeared at 1638 cm^{-1} and 1646 cm^{-1} for PCH21_3 and ACH20_3, accordingly. With these observations made on the samples treated with 30, 50 and 70% NaOH solution, 70% NaOH was adopted as the optimum concentration for the deacetylation of BSF chitin samples in this study. Further

trials were conducted to determine the optimum temperature required to effectively deacetylate the BSF chitin samples and they are discussed in the next sub-section.

4.2.2 *Temperature optimisation*

Temperature optimisation was performed by keeping the deacetylation concentration (70% NaOH solution obtained in Section 4.2.1) and time (5 h) constant. The temperatures varied in this study were 60 °C, 80 °C, 100 °C and 120 °C for both pupal and adult chitin samples. The samples had the following codes: PCH21_4 and ACH20_4 for 60 °C, PCH21_5 and ACH20_5 for 80 °C, PCH21_6 and ACH20_6 for 100 °C, and PCH21_7 and ACH20_7 for 120 °C. The experimental details are presented in Section 3.2.2 of Chapter 3. Figure 4.14 shows the spectra obtained as the temperature was varied for both pupae and adult BSF chitin at constant concentration and time.

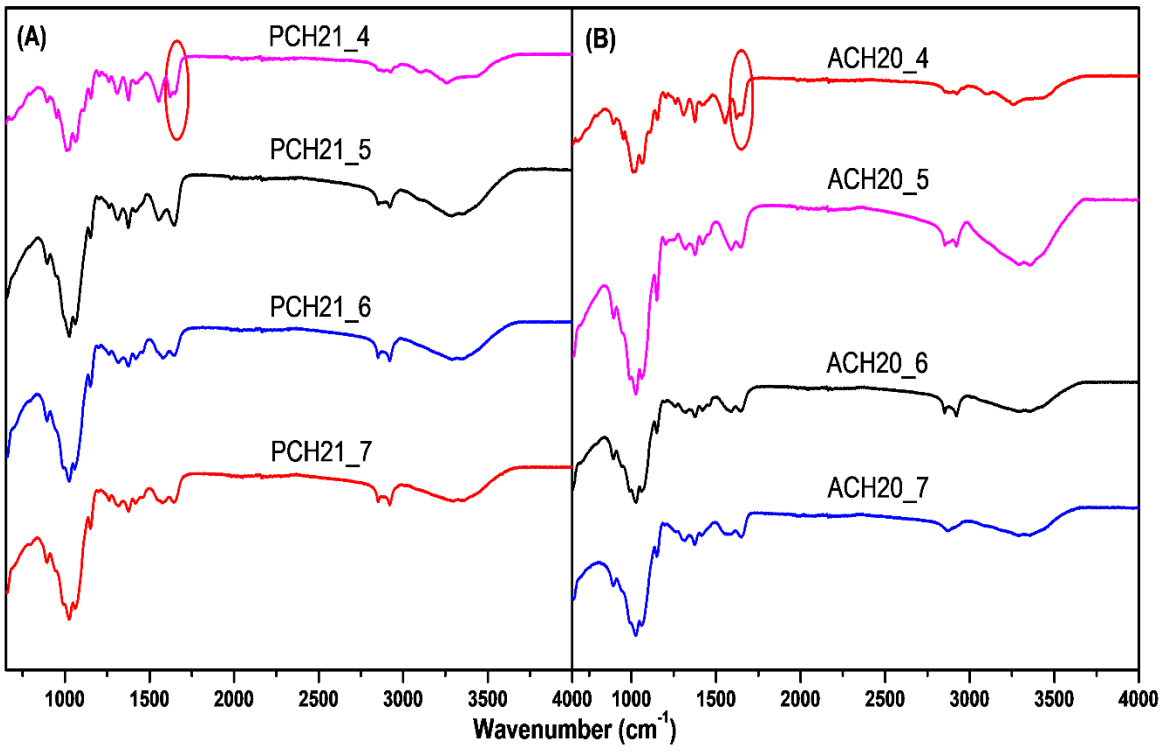

Figure 4. 14: FTIR spectra obtained as the deacetylation temperature is varied (60, 80, 100 and 120 °C) at a constant concentration (70% NaOH solution) and time (5 h) for both pupae (A) and adult (B) BSF chitin.

From Figure 4.14, varying temperatures of 60, 80, 100 and 120 °C were investigated to determine the optimal condition for the deacetylation of the extracted pupal and adult chitin to obtain chitosan. At 60 °C, the spectra of the samples (PCH21_4 and ACH20_4) did not show

any noticeable difference to the chitin spectra observed in Section 4.4. The Amide 1 band maintained the splitting at wavelengths of 1625 and 1655 cm^{-1} for PCH21_4 (Figure 4.14 A) and 1621 and 1659 cm^{-1} for ACH20_4 (Figure 4.14 B). This is an indication that the samples were not deacetylated to chitosan at a temperature of 60 $^{\circ}$C. As the temperature was increased to 80 $^{\circ}$C, the peak of interest, the two Amide 1 peaks observed on the previous spectra fused into one peak at 1648 cm^{-1} (Figure 4.14A) and 1651 cm^{-1} (Figure 4.14B) for PCH21_5 and ACH20_5, respectively. This shows that the 80 $^{\circ}$C temperature impacted the samples and increased the DD. Further increasing the temperature to 100 $^{\circ}$C reduced the intensity of most of the signature peaks occurring between 1250 cm^{-1} to 1750 cm^{-1}, especially the Amide 1 bands on both PCH21_6 and ACH20_6. This indicated a greater impact of the increased temperature on the samples and a likely increase in their DD. To buttress this assertion, the DD computed for both pupal and adult chitin samples (using Equation 3.23 of Section 3.9.7) were 79%. There was a slight change in the spectra of the samples deacetylated at 120 $^{\circ}$C compared to those deacetylated at 100 $^{\circ}$C. Therefore, with no significant difference between the samples deacetylated at 100 and 120 $^{\circ}$C, 100 $^{\circ}$C was adopted as the optimum temperature for the deacetylation of both pupal and adult chitin to obtain chitosan.

4.2.3 *Time optimisation*

Time was the last parameter optimised in the series of experiments aimed at obtaining the optimum conditions for the deacetylation of extracted pupal and adult BSF chitin to chitosan. Time optimisation was conducted by keeping the concentration and temperature (previously obtained in Section 4.2.1 and 4.2.2) of deacetylation constant. The time of the reaction considered in this study were 3, 5 and 7 h. The experiments were coded as PCH21_8 and ACH20_8 for 3 h, PCH21_9 and ACH20_9 for 5 h, and PCH21_10 and ACH20_10 for 7 h. The experimental protocol is found in Section 3.2.2 of Chapter 3. Figure 4.15 presents the FTIR spectra of the deacetylated pupae and adult BSF samples at constant concentration and temperature.

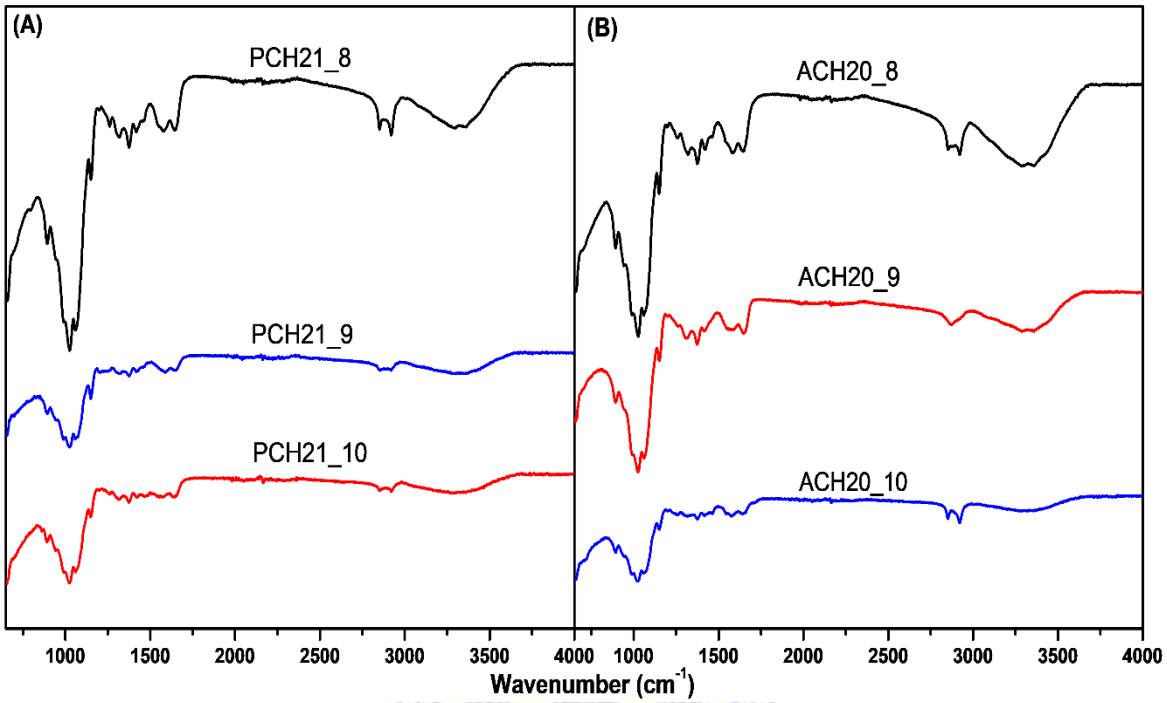

Figure 4. 15: FTIR spectra obtained as the time of deacetylation was varied (3, 5 and 7 h) at a constant concentration (70% NaOH solution) and temperature (100 ˚C) for both pupae (A) and adult (B) BSF chitin.

The spectra in Figure 4.15 show that 3 h was not enough to reasonably remove the amide group of PCH21_8 and ACH20_8 samples. Hence the increased height of the Amide 1 peak at 1641 and 1643 cm^{-1} on both samples (A and B) which is an indication of insufficient deacetylation. Deacetylation for 5 h (PCH21_9 and ACH20_9) impacted on the samples by reducing the peak intensity, an indication of a reduction in the number of amide ($NHCOCH_3$) functional groups on both chitin samples. Deacetylating for 7 h drastically affected the signature profiles of the FTIR spectra. The peaks of interest, the Amide 1 band at approximately 1642 cm^{-1} was practically non-existent on the spectra of both samples (PCH21_10 and ACH20_10). Although, this signifies a higher DD, however, the sample mass remaining after the experiment was negligible which may have arisen from the degradation of the sample at an elongated time of reaction.

After the optimisation of time of reaction, the samples were subjected to a solubility test, a standard test for chitosan. The samples were introduced into a 1.0% acetic acid solution. The procedure is described in Section 3.9.13 of Chapter 3. Using Equation 3.30, the solubility of samples deacetylated at 3 h (62 and 59%), 5 h (93.4 and 92.7%) and 7 h (96 and 95%) for pupal and adult BSF chitin, respectively were computed. Samples deacetylated for 5 and 7 h had

solubilities greater than 90%. Considering the additional time of 2 h it took to achieve only 3% solubility for the 7 h deacetylated samples, 5 h was adopted as the optimum time of deacetylation in this study. The yield of the samples at the optimum deacetylation conditions is discussed in Section 4.2.4. Figure 4.16 shows the reaction occurring in the deacetylation process of chitosan synthesis, while Figure 4.17 shows the overall mechanism involved in the deacetylation process.

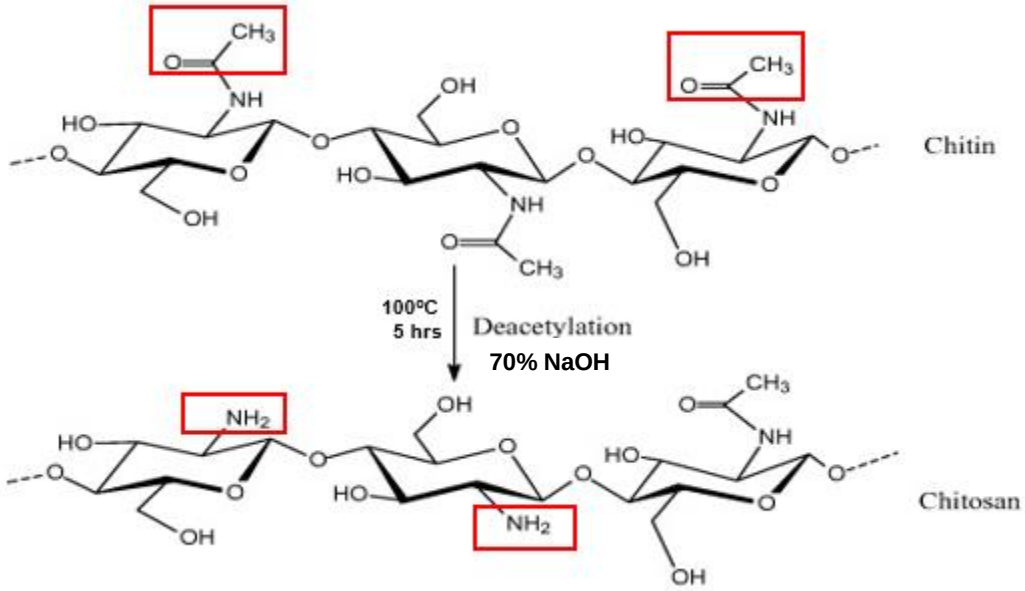

Figure 4. 16: Deacetylation process for pupal chitosan extraction. Extraction conditions are 70% NaOH solution @ 100 ˚C for 5 h for both samples.

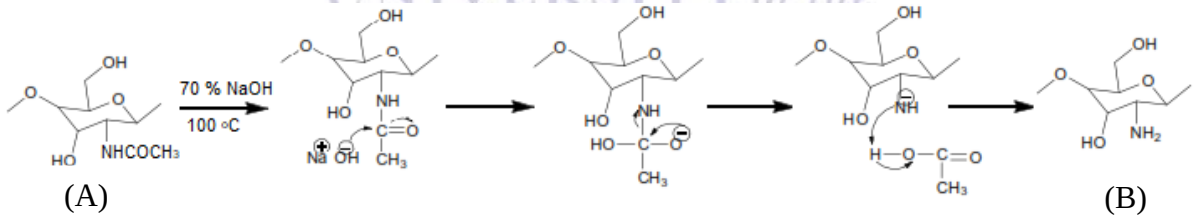

Figure 4. 17: The mechanism of deacetylation reaction A = chitin, B = chitosan (adapted from Ahyat and Azmi, 2016).

4.2.4 *Chitosan yield determination*

The optimum deacetylation conditions obtained from Section 4.2.1 – 4.2.3 were adopted in the determination of the yield of both pupal (PCH21_9) and adult (ACH20_9) chitosan. Equation 3.2 of Section 3.2.3 was used to compute the yield on a dry weight basis while Table 4.8 presents the yield of each sample.

Table 4. 8: The yield (%) of the extracted chitosan in NaOH solution.

Samples	Concentration (%)	Temperature (°C)	Time (h)	Yield (%)
Pupae chitosan	70	100	5	11.3±0.6
Adult chitosan	70	100	5	2.5±.1

Table 4.8 shows the yield obtained for the optimised conditions of the deacetylation process used for chitosan extraction for both pupal (PCH21_9) and adult (ACH20_9) chitosan samples. The PCH21_9 had a higher yield, more than 4.5 times the yield of ACH20_9. The difference in yield between the chitosan samples from pupae or adults implies that the deacetylation process affected the adult chitosan the more. Different metamorphosis stage of the organism used in the synthesis of the chitosan may have influenced the observed yield and the differences in the two samples. More so, the low yield for the adult chitosan sample may have also resulted from depolymerisation of the samples during the extraction process. Furthermore, the excessive washing and rinsing of the sample to achieve neutral pH may have also affected the yield of the samples. The samples were washed severally using distilled water to ensure they attained neutral pH.

Several studies have reported the yield of chitosan from various insect species. The yield of PCH21_9 and ACH20_9 obtained in this study were higher than the 0.24% yield reported by Wanule *et al.* (2014) in their study of the American cockroach, *Periplaneta americananwere*. The value of 5.9% obtained by Kim *et al.* (2016) from house fly, *Musca domestica* was higher than the yield of adult chitosan in this study but less than that of pupal chitosan. However, in comparison to the crustacean sources such as shrimps, krills and prawns, the obtained yield in this study was lower. Hossain and Iqbal (2014) reported a chitosan yield of 15.4% and 14% from shrimps and krills, respectively.

The yield obtained in this study shows that the pupal and adult chitosan were higher than most reported insect species in the literature, however, they are lower than those reported from crustacean sources.

4.2.5 *Characterisation of the isolated pupal and adult BSF chitosan*

To ascertain if the extracted materials from pupal (PCH21_9) and adult (ACH20_9) BSF chitin are indeed chitosan, their (PCH21_9 and ACH20_9) physicochemical characteristics were compared to a reference commercial chitosan sample. Therefore, a commercial chitosan sample

from shrimp was used as a reference in this study and characterised alongside the synthesised, PCH21_9 and ACH20_9, samples. The FTIR result is presented in the next section.

4.2.5.1 *ATR-FTIR spectroscopy*

The FTIR spectroscopy was conducted to identify the presence of functional groups specific to chitosan on the synthesised PCH21_9 and ACH20_9 samples. This was done by comparing the spectra of the extracted samples to the spectra of commercial shrimp chitosan obtained from Sigma Aldrich. The FTIR experimental detail is described in Section 3.9.3 of Chapter 3. Figure 4.9 shows the recorded FTIR spectra of both PCH21_9 and ACH20_9.

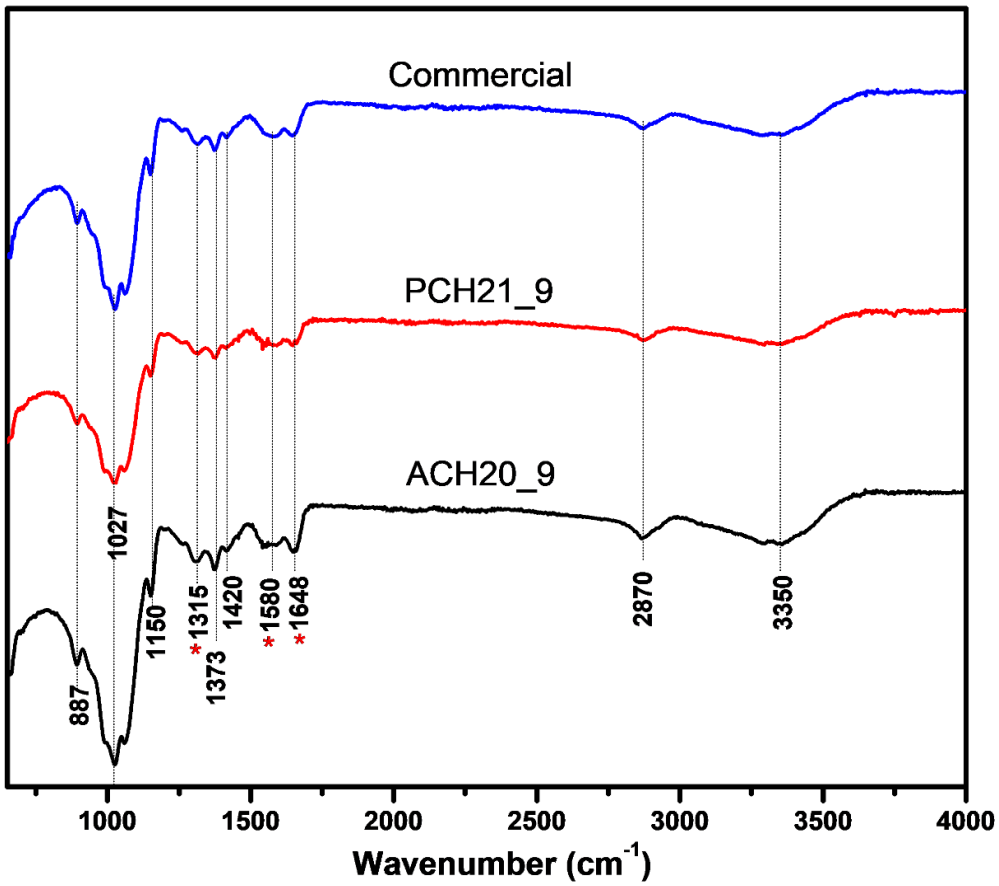

Figure 4. 18: FTIR spectra of the commercial, pupae (PCH21_9) and adult (ACH20_9) chitosan samples showing the various functional groups on the extracts.

The FTIR spectra of the PCH21_9 and ACH20_9 in Figure 4.18 showed similar bands to those of the commercial chitosan sample without noticeable differences in wavelength and adsorption intensity. The principal spectral features of chitosan are as follows: 3326 cm^{-1} (O–H stretch overlapped with N–H extension vibration and inter-hydrogen bonds of the polysaccharide), 2870 cm^{-1} correspond to asymmetric and symmetric C–H stretching

vibrations 1648 and 1580 cm^{-1} (Amide I and 11 bands, respectively corresponding to -NH bending vibrations and C=O stretch for primary amines). Furthermore, the assignment of bands at 1373 cm^{-1} (CH bend), 1420 cm^{-1} (C–H bending), and 1315 cm^{-1} (Amide III band, C–N stretching vibration), 1150 cm^{-1} (asymmetric bridge C–O–C stretch), 1027 cm^{-1} (C–O asymmetric stretch of the glycoside ring) were noted and 887 cm^{-1} was assigned to C-H out-of-plane vibration (Song *et al*., 2013). The free N-H and O-H stretching vibrations are found in the range of 3400-3440 cm^{-1} and 3500 cm^{-1} and above, respectively. When these functional groups (N-H and O-H groups) are involved in intermolecular hydrogen bonding, their position tends to shift to lower frequencies (Muyonga *et al*., 2004). In this study, the absence of absorption peak around 3400 and 3500 cm^{-1} in the spectra of chitosan shows there are no free O-H and N-H groups available. This absence is attributed to the involvement of these groups (-OH in C3, CH_2OH in C6 and C-N in C2 positions) in inter and intramolecular hydrogen bonding (Focher, 1990).

Table 4. 9: The functional groups identified in the extracted pupal (PCH21_9) and adult (ACH20_9) chitosan samples as compared to the commercial reference chitosan sample

	Wavenumbers (cm^{-1})			
Functional group and Vibration mode	Pupae CHS	Adult CHS	*Com CHS	Classifications
O-H stretching vibration	3350	3351	3350	Aliphatic compound
CH_2 symmetric stretch of CH_2OH group	2870	2872	2872	Aliphatic compounds
C=O vibration & stretching of $NHCOCH_3$ group	1650	1652	1651	Amide 1
N-H bend, C-N stretch of $NHCOCH_3$ group	1580	1581	1576	Amide 11
CH_2 bending of CH_2OH group	1417	1420	1417	-
CH_3 symmetric distortion of $NHCOCH_3$ group	1375	1373	1376	-
CH_2 wagging, N-H bending and C-N stretching from amide linkages	1312	1315	1313	Amide 111
C-O-C asymmetric stretch of glycoside ring.	1153	1150	1153	Saccharide ring
C-O-C symmetric stretch in-phase (glucosamine) ring.	1063	1063	1062	-
C-O wagging in secondary OH group.	1027	1025	1028	Along chain
CH pyranose ring stretch vibration.	896	897	896	Saccharide rings

*Com = commercial

4.2.5.2 *X-ray diffraction studies (XRD)*

XRD analysis was once again applied in this study to investigate the degree of orderliness of the extracted BSF chitosan, PCH21_9 and ACH20_9, at optimised conditions of 70% NaOH solution, 100 °C and 5 h and compared to commercial shrimp chitosan used as a reference. The XRD profiles of the extracted chitosan and commercial shrimp chitosan and their structural parameters are presented in Figure 4.19 and Table 4.10, respectively.

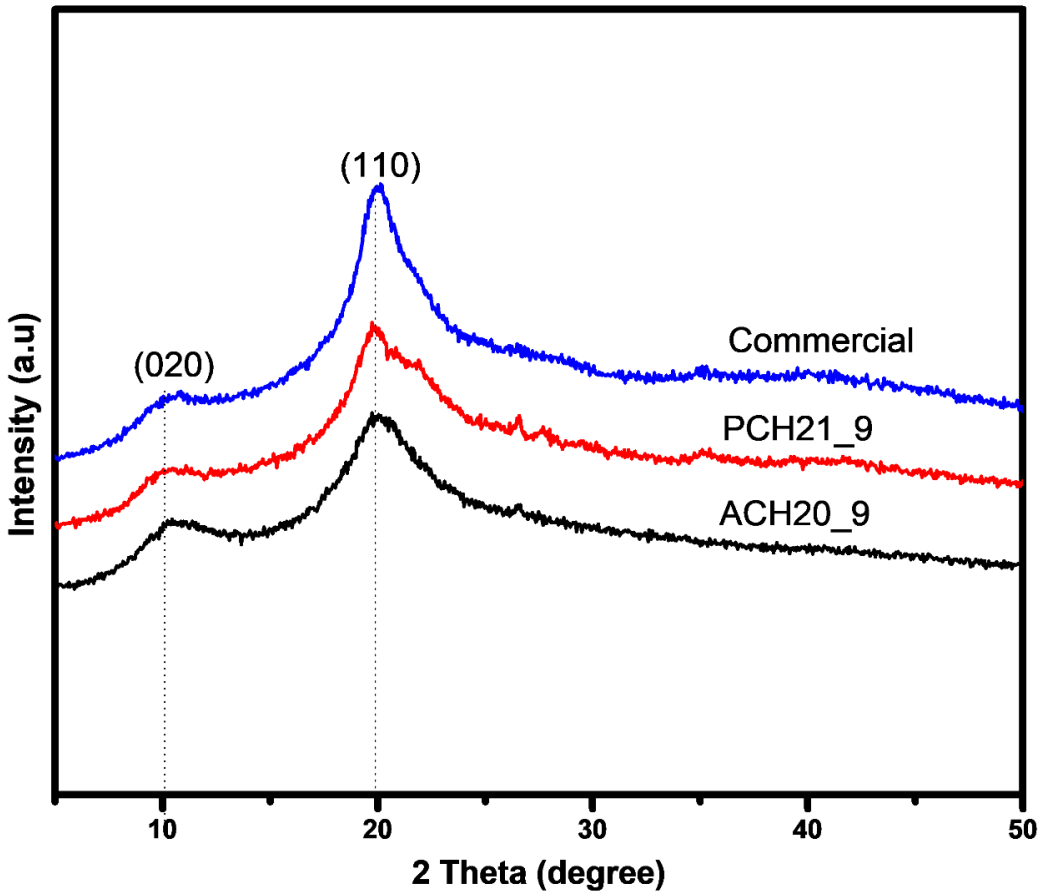

Figure 4. 19: X-ray diffractograms of the commercial, pupae (PCH21_9) and adult (ACH20_9) chitosan samples showing the crystallographic planes of the samples.

Deacetylation brought about the excision of most of the chitin reflections (compare Figures 4.8 and 4.19). The chitin spectra, as observed from the peaks at 9.2° and 19.2° (Figure 4.8 of Section 4.1.4.2) shows a significant reduction in peak intensity and subsequent shifting to a higher angle after deacetylation (Figure 4.19) (Focher *et al.*, 1990).

Deacetylation resulted in the considerable broadening of the peak widths and reduction in peak height at both the 020 and 110 reflections on the chitosan spectra (Figure 4.19). This led to a reduction in the intensities of these peaks due to the removal of the protein matrix. The d-

spacing of the unit cells had a marked reduction in length from 9.68 Å (Table 4.5 of Section 4.1.4.2) in all the chitin samples to 8.71 Å (pupae) and 8.60 Å (adult and commercial) chitosan samples along the 020 plane. Similarly, the same observations were made on the 110 interplanar distance, which had a 4% reduction in all the chitosan spectra (Table 4.10) compared to the chitin (Table 4.5) samples. These observed differences may have resulted from the disorientation of the chitin crystallites due to the removal of the protein matrix and the penetration of reagents into the structure of the chitin during the deacetylation process (Bogdanova *et al*., 2016). The penetration of reagents leads to cleavage of the strong hydrogen bonds present in the chitin structure (Gbenebor *et al*., 2017) causing a shift in the intensity of the XRD spectra to a higher wavenumber in chitosan (Figure 4.19). As reported by Muyonga *et al*. (2004) this shift in intensity is related to a change in molecular order in the structure of the samples.

Table 4. 10: Structural parameters of chitosans obtained from XRD studies.

Chitosan Sample	Plane	2θ	d (Å)	Crl (%)
Pupae (PCH21_9)				
	(020)	10.15	8.71	
	(110)	19.78	4.48	51
Adult (ACH20_9)				
	(020)	10.28	8.60	
	(110)	20.05	4.42	54
Commercial				
	(020)	10.28	8.60	
	(110)	20.05	4.42	57

The degree of orderliness (Crl) was also determined for the extracted samples. The Crl was computed using Equation 3.21 in Chapter 3 were 51, 54 and 57% for pupae, adult and commercial chitosan, respectively.

Knidri *et al*. (2016) has reported Crl values of 50.54 and 56.42% for chitosan extracted from shrimp waste using conventional heating and microwave irradiation methods, respectively. The Crl values from this study were within the range of values reported in the literature for insect species (Knidri *et al*., 2016). This result alludes to the fact that, compared to the commercial shrimp chitosan, no difference exists between the degree of orderliness of chitosan extracted from pupae (PCH21_9) and adult (ACH20_9) BSF. Therefore, the developmental stage of the

BSF did not influence/induce any noticeable change in the structural properties of the insect chitosan.

4.2.5.3 *Thermal gravimetric analysis (TGA)*

The procedure for the thermal analysis of the chitosan samples, PCH21_9 and ACH20_9 from pupae and adult BSF, respectively have been described in Section 3.9.5 of Chapter 3.

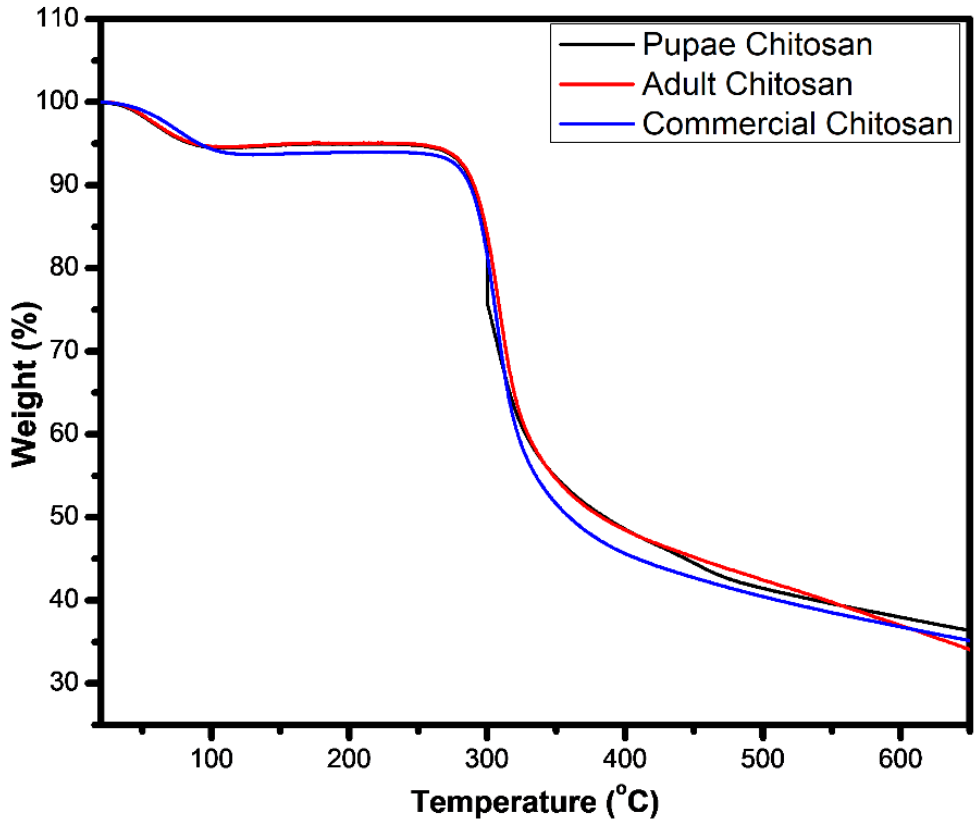

Figure 4. 20: The thermal profiles of the extracted and the commercial chitosan.

The thermal profiles (Figure 4.20) show that all the chitosan samples, like the chitin, have two decomposition stages. The first stage, as stated earlier, corresponds to the loss of bound water from the chitosan structure. In all the chitosan samples, the weight losses started at 20 ^{o}C to about 128 ^{o}C with corresponding values of 6.7, 7.2 and 7.2% for adult, pupal and commercial chitosan, respectively. The temperature at which the maximum water losses occurred were 67, 57 and 76 ^{o}C for pupal, adult and commercial chitosan accordingly. From Figure 4.21, it is evident that the pupal chitosan contains slightly more water within its structure hence the slightly higher weight loss observed in the thermal profile. Chitosan being a hygroscopic compound, absorbs moisture from the atmosphere when exposed, thus the need for proper storage.

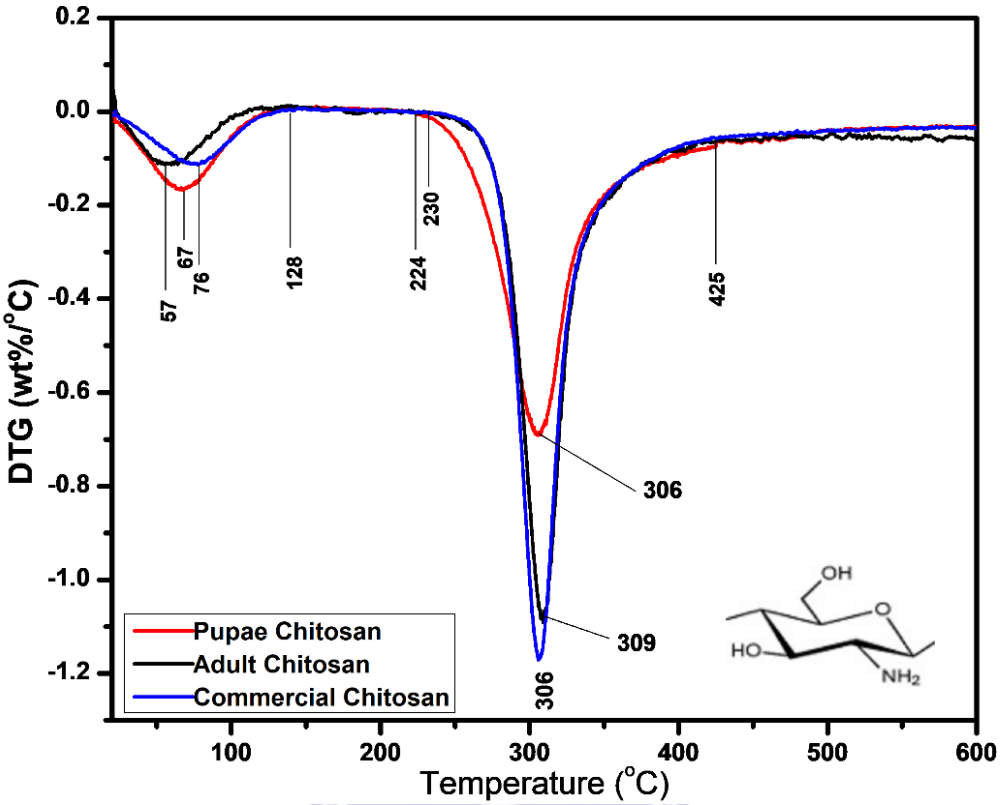

Figure 4. 21: The derivative thermal profiles of the extracted and the commercial chitosan.

The second decomposition stage involves the degradation of the acetylated units of the chitosan sample. This stage of decomposition determines the thermal stability of the chitosan samples. From the profiles (Figure 4.21), it was observed that pupal chitosan has thermal stability up to 224 ^{o}C while adult and commercial chitosans were stable up to 230 ^{o}C. The pupal chitosan, therefore, showed a slight (6 ^{o}C) decrease in its thermal stability. This result conformed with the structural property of the pupal chitosan as it had the lowest value of ordered units among the three chitosan samples studied. The decrease in gradient and accompanied weight loss resulted from the loss of volatile materials/compounds during the thermal degradation of the chitosan structure (Mohammed *et al.*, 2013). The maximum degradation temperatures (DTG_{max}) of the samples varied from 306 ^{o}C in the pupal and commercial reference chitosan to 309 ^{o}C in the adult chitosan. This is depicted by the gradual shifting of the derivative thermograms (Figure 4.21) to the right. Table 4.11 presents the parameters deduced from the DTG plots of the extracted samples.

Weight loss as a result of the degradation (the area under the degradation profiles of the derivatograms) were determined to be 46% in the pupal chitosan, 45% in the adult chitosan and 51% in the commercial chitosan.

Table 4. 11: Parameters deduced from the derivative thermograms of the extracted BSF chitosans compared to the commercial shrimp chitosan.

Processes	Parameters	**Commercial**	**Pupae**	**Adult**
Evaporation (first stage)	Temperature (°C)	20 – 128	20– 128	20 – 128
	T_{me} (°C)	76	67	57
	Mass loss (%)	7.2	7.2	6.7
Degradation (second stage)	Temperature (°C)	230– 425	224 – 425	230 – 425
	T_{md} (°C)	306	306	309
	Mass loss (%)	51	46	45

T_{me} = temperature of maximum evaporation; T_{md} = temperature of maximum degradation

Erdogan and Kaya (2016) has reported weight losses of 59% and 62%, likewise, DTG_{max} values of 308 °C and 302 °C for chitosan extracted from nymph and adult *Dociostaurus maroccanus*, respectively. Other studies have reported varying DTG_{max} values for their samples. Paulino *et al.* (2006) reported a value of 300 °C for silkworm chrysalides while Kaya *et al*. (2014a) reported a value of 290 °C for potato beetle. Therefore, the DTG_{max} values of chitosan obtained in this study were in agreement with those reported in the literature.

The results of this thermal study have shown that chitosan samples have lower thermal stability than those of the chitin, degrading at about 90 °C lower (Figure 4.21 Table 4.11) than the chitin samples (Figure 4.10. Table 4.6). This could have resulted from the disorientation and the eventual reduction of the chitosan crystallites due to the penetration of reagents into the structure of the chitin during the deacetylation process (Bogdanova *et al*., 2016). This, therefore, eliminates the amide functional group, leaving the amine group on the chitosan structure. The outcome of this is chitosan sample with a more structural disorder, higher water retention and lower repeating long-range order compared to the chitin, thus having high solubility.

4.2.5.4 *High-resolution scanning electron microscopy (HRSEM)*

HRSEM analysis was carried out to examine the surface morphologies of the extracted chitosans. Before the HRSEM analysis, the chitosan samples were coated with gold and palladium to improve the conductivity of the samples. The experimental detail is in Chapter 3

Section 3.9.6. The micrographs of the extracted chitosan and the commercial shrimp chitosan are presented in Figure 4.22.

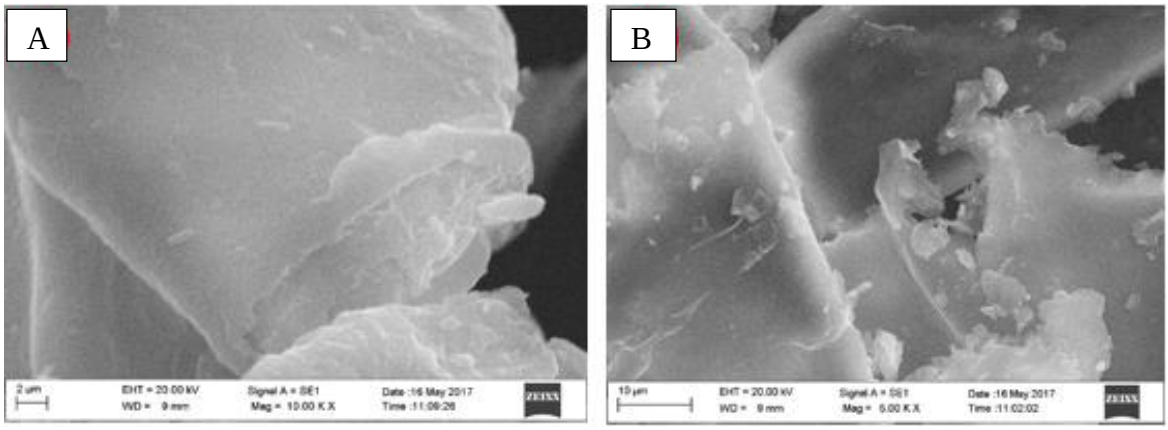

Figure 4. 22: Surface morphologies of (A) pupal (PCH21_9) and (B) adult (ACH20_9) chitosan samples.

Micrographs of pupae (PCH21_9) and adult (ACH20_9) chitosan show that both exhibited neither fibres nor pores (Figure 4.22). The pupae chitosan had a smooth surface (Figure 4.22A) while the adult appeared to have greater surface roughness with occasional flake-like deposits on its surface (Figure 4.22B). This observation corroborates the findings of Yen and Mau (2007) who stated that the surface morphology of Shiitake supes (*L. edodes*) had neither pores nor fibrils on its surface. A similar finding was reported by Erdogan *et al.* (2017) in their study on two species of mushrooms; *Lactarius vellereus* and *Phyllophora ribis*. They concluded that both mushroom species had neither fibrils nor pores. It can, therefore, be said that the two chitosan samples in this study differ only slightly in their surface morphologies. This difference could be due to different parts of the insects from which the chitosan was extracted. This difference could also be the different developmental stages (pupae and adult) of BSF the chitosans were extracted from since moulting and feeding habit affects the peritrophic matrix (Hegedus *et al*., 2016) thereby influencing the properties of chitin and chitosan. Kaya *et al.* (2016a) observed that chitin and chitosan extracted from different parts of an insect, their developmental stages and different sexes exhibit varying surface morphologies. Surface morphology is one of the most important property that determines the efficient use of chitin and its derivatives, especially chitosan (Marei *et al*., 2016). Synowiecki and Al-Khateeb (2003) and Younes and Rinaudo (2015) in separate reviews reported that chitosan surfaces with pores enhance metal ion sorption and also find application in tissue engineering while those with fibrous surfaces can find application in textile industries.

4.2.5.5 *^{13}C CP/MAS-NMR spectroscopic analysis*

The NMR technique is the most reliable method of determining the DD of chitosan. The analysis was carried out to investigate the carbon spectral features of the biopolymers, and hence compute the DD of the samples. The NMR spectra of PCH21_9 and ACH20_9 were obtained as detailed in Section 3.9.7 of Chapter 3. Figure 4.23 shows the spectra of the PCH21_9 and ACH20_9 obtained in this study as compared to the commercial shrimp chitosan samples used as reference.

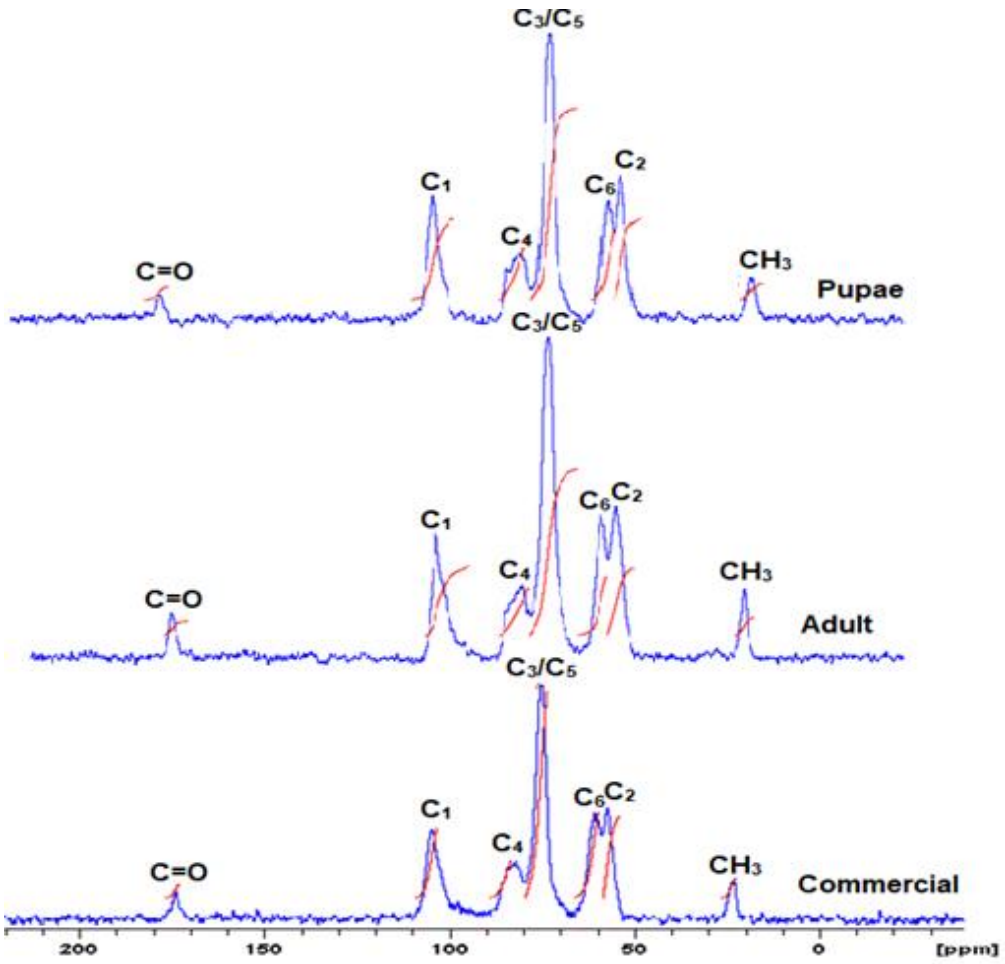

Figure 4. 23: ^{13}C NMR spectra of the extracted chitosan from pupae (PCH21_9) or adult (ACH20_9) compared to commercial chitosan.

Figure 4.23 shows that the spectra of both chitosan samples were similar to the commercial reference chitosan, thus conforming to the typical chitosan structure. The spectra provide evidence for the successful production of chitosan from BSF chitin as noticed from the characteristic peaks corresponding to the carbon atoms of the glucosamine backbone. This

confirms the retention of the structural identity of chitosan in the extracted adult and pupae samples.

All the spectra in Figure 4.23 consist of seven well-defined resonances compared to eight in the chitin spectra (Figure 4. 24 of Section 4.1.4.5) . These carbon atom resonances corresponding to glucosamine repetitive units appear at the following chemical shifts as shown in Table 4.12.

Table 4. 12: Solid-State CP–MAS ^{13}C NMR spectral data of adult, pupal, and commercial chitosans.

C Signal	Pupal		Adult		Commercial	
	δ (ppm)	Integral	δ (ppm)	Integral	δ (ppm)	Integral
C=O	174.38	2.4013	173.92	3.3136	173.98	2.3336
C1	105.10	15.1292	104.68	15.5923	104.71	17.4970
C4	82.41	12.2520	81.05	10.8179	82.41	12.3242
C5/ C3	74.85	35.2813	74.94	37.4226	75.24	36.0042
C6	60.51	13.6204	60.69	13.6586	60.91	16.3235
C2	56.93	15.1238	56.62	15.2127	57.33	12.0480
—CH_3	23.10	3.1716	23.22	3.9827	23.49	3.4695
DD	**85%**		**83%**		**85%**	

δ = resonance

The spectra also show the incomplete conversion of chitin to chitosan during the deacetylation process. The signal of the CH_3 group could still be found at 23 ppm (Figure 4.23) for all the samples, which is an indication of incomplete deacetylation of the extracted chitosan samples as well as in the case of the commercial chitosan used as a reference. The carbonyl (C=O) resonance was also observed at ~174 ppm on all the chitosan spectra. An apparent distinguishing feature between the spectra of chitin and chitosan is the fusion of the C3 and C5 signals in the chitin spectra (Figure 4.12) forming only one signal at ~75 ppm on all the chitosan spectra (Figure 4.23).

The C2 and C6 signals were not clearly separated in all the chitosan spectra. This results from differing molecular order. This diversity confers varying crystallographic positions on the planes because of the presence of independent chain lengths in the atomic unit of the chitosan structures (Prashanth *et al*., 2002). The chemical shifts arising from C1 and C4 carbon in 1,4-

linked polysaccharides are highly sensitive to changes at the glycosidic linkage as reported by Tanner *et al*. (1990). Pupae and adult chitosan showed a weak cleavage of C4 signal (Figure 4.23). This may have resulted from extraction/processing factors such as temperature and concentration of the extracting solution. Also, the methyl and the carbonyl group intensities varied in the three samples studied. The adult chitosan (ACH20_9) had a higher peak height for both the CH_3 and C=O signals while both pupae (PCH21_9) and commercial chitosan had smaller peak heights. This is an indication of varying DD of the samples. Samples with lower peaks will result in lower DD since DD is calculated from the ratio of the methyl group to the glycosyl carbons (C1-C6) (Song *et al.*, 2013).

The effectiveness of the extraction processes was further ascertained by the absence of other absorption peaks on the chitosan spectra (Paulino *et al*., 2006). The absence of absorption bands at 30, 117, 146 and 174 ppm, which are resonances associated with proteins and catechol compounds was also noted as reported by the studies of Zhang *et al.* (2000). The work of Song *et al.* (2013) effectively confirmed the quality of the extracted materials. The ^{13}C-NMR results confirmed the FTIR spectral outcomes where the peaks associated with protein and inorganic compounds were not detected.

The computed DD for the three samples using Equation 3.23 in Section 3.9.7 for pupae (PCH21_9), adult (ACH20_9) and commercial chitosan were 85%, 83% and 85%, respectively. This result is in alignment with both XRD and TGA studies and shows that pupal chitosan exhibited a slightly higher degree of orderliness and temperature of maximum degradations (DTG_{max}) when compared with the adult chitosan.

Proposed molecular weight based on NMR analysis

Based on the NMR analysis of the DD of the chitosan from both pupal and adult BSF, MW is proposed for the extracted samples. Chitosan consists of repetitive units of N-acetylglucosamine and glucosamine running into hundreds of thousands of units within its structure. For a single unit of the chitosan with hygroscopic properties and less than 100% DD, its MW is given by:

$$MW = ((GlcNHAc)_{1-DD}(GlcNH_2)_{DD}(H_2O))_n$$

Where

GlcNHAc is the N-acetylglucosamine unit, $GlcNH_2$ is the glucosamine unit, n is the number of units in the chitosan structure and DD is the degree of deacetylation.

DD computed for pupal chitosan was 85%. This implies that the degree of acetylation of the sample is 1-DD (1-0.85 = 0.15).

Therefore, MW = $((GlcNHAc)_{0.15}(GlcNH_2)_{0.85}(H_2O))_n$, equivalent to $((C_8H_{13}NO_5)_{0.15}(C_6H_{11}NO_4)_{0.85}(H_2O))_n$.

$C_8H_{13}NO_5$ = 203 g/mol, $C_6H_{11}NO_4$ = 161 g/mol while H_2O = 18 g/mol.

Therefore, the MW of a single unit of the extracted pupal chitosan sample is given as:

$203*0.15 + 161*0.85 + 18 = 43.645 + 126.385 + 18 = (188.03)_n$ g/mol.

A similar procedure was adopted and MW of the adult chitosan was computed to be $(186.16)_n$ g/mol. Commercial chitosan has the same MW as the pupal chitosan. The unit, g/mol, used in this computation is equivalent to Dalton (Da), which is mostly adopted when dealing with polymers with high MW. Table 4.13 presents the computed molecular weights of a repeating chitosan unit.

Table 4. 13: Computed molecular weight of a repeating unit of the chitosan samples.

Chitosan sample	Molecular weight $(g/mol)_n$
Pupal (PCH21_9)	188.03
Adult (ACH20_9)	186.16
Commercial	188.03

n = number of repeating units (chain length) in each chitosan sample

Further characterisations, different from the conventional techniques discussed above, were performed on the extracted chitosan samples. Some of these studies are presented in the next sections.

4.2.6 *Water binding capacity*

Water binding capacity (WBC) of the chitosan is the ability of the chitosan molecules to trap and hold water within its structure. The WBC of chitosan is affected by the method of extraction of the biomaterial. Nessa *et al.* (2011) and Kumari *et al*. (2017) stated that variation of the step sequence during the extraction of chitin results in an increase in WBC of chitosan when demineralisation was conducted before deproteination. Therefore, in this study,

demineralisation of chitin was conducted before the deproteination process as detailed in Section 3.9.8 of Chapter 3.

The WBC results obtained were 530.26±4.2% and 462.65±5.1% for pupae and adult chitosan, respectively while commercial chitosan is 524.18±4.6% (Table 4.14). It is not surprising that the pupal chitosan had a higher WBC value than the adult chitosan. This could be attributed to both the TGA and the Crl values of the samples. Pupal chitosan has a lower DTG_{max} value (Table 4.11) likewise a degree of orderliness (Table 4.10) and also higher DD (Table 4.12) which is an indication of having slightly more amine functional groups than the adult chitosan. The increase in thermal stability and degree of orderliness in the adult chitosan sample is due to the presence of CH_3 functional groups in the chitosan structure. This confers it with its higher DTG_{max} value and low WBC compared to the pupal chitosan.

Various researchers have reported WBC of chitosan in the recent past. Kumari *et al*. (2017) obtained WBC values of 492%, 138% and 358% from different chitosan sources (fish, crab, and shrimp), respectively. Nesaa *et al.* (2010) obtained WBC values ranging from 335.5 to 589%. Cho *et al.* (1998) reported WBC values ranging from 458 to 805% for five chitosan samples obtained from crab shells, while Hossain and Iqbal (2014) in their study of chitosan from shrimp shells obtained a value of 537.29%. However, Sarbon *et al*. (2014) in their study of mud crab chitosan obtained a low WBC value of 180±0.00%. They concluded that the low WBC value was because of undertaking the deproteination step before the demineralisation process during chitin extraction.

The WBC values obtained in this study corroborates the reports of previous studies. The effectiveness of chitosan samples binding to fats in the tissues, otherwise called fat-binding capacity is discussed in the next section.

4.2.7 *Fat binding capacity (FBC)*

Like the WBC, the fat binding capacity of the chitosan determines the effectiveness of the chitosan molecules to trap and hold fats and cholesterol within its structure when in contact with these compounds. This property of chitosan is essential in weight loss, obesity and cholesterol management (Moraru *et al*., 2018). The experimental procedure is given in Section 3.9.9 of Chapter 3. Extracted pupae and adult chitosan have 420.70±5.4% and 392.30±3.6% FBC values, respectively while the commercial chitosan sample has 408.36±6.4% (Table 4.14). Studies previously have reported on FBC of chitosan from various sources. Cho *et al*. (1998)

reported FBC values ranging from 314 to 535% with an average of 417%. Hossain and Iqbal (2014) also reported a value of 427.98% while Nessa *et al*. (2011) had FBC ranging from 348.7 to 568.1%. FBC signifies the ability of chitosan to bind and therefore remove fats, oils or lipids from a system. Low FBC implies low deacetylation degree of the chitosan, which invariably signifies that high DD undoubtedly enhances high-fat binding by chitosan. The variation in the extraction process of chitosan where demineralisation was conducted before deproteination of chitin resulted in increased FBC compared to when deproteination was conducted before demineralisation (Suneeta *et al.*, 2016).

These results indicate that FBC of chitosan from BSF is within the range previously reported in the literature (Cho *et al*., 1998; Nessa *et al*., 2011; Hossain and Iqbal, 2014) and further confirms the purity of the extracted chitosan samples. The summary of the characterisation results is presented in Table 4.14 while the ash content of the extracted pupal and adult chitosan is discussed in the next section.

Table 4. 14. Parameters obtained from the physicochemical characterisation of BSF and commercial shrimp chitosan

Sample	WBC± S.D (%)	FBC±S.D (%)	Ash (%)	Solubility (%)	Intrinsic viscosity (dL/g)	MW (kDa)	DD (NMR) (%)	Crl (%)	Thermal stability (°C)
Pupae (PCH21_9)	530.26±4.2	420.70±5.4	0.73±0.01	93.4±2.4	746.33	179	85	51	224
Adult (ACH20_9)	462.65±5.1	392.30±3.6	0.86±0.02	92.7±3.1	806.70	198	83	54	230
Commercial	524.18±4.6	408.36±6.4	0.68±0.01	95.0±5.2	697.73	164	85	57	230

MW = molecular weight, S.D = standard deviation, kDa = kilo Dalton, NMR = nuclear magnetic resonance, DD = degree of deacetylation, Crl = degree of orderliness.

4.2.8 *Ash content*

Ash content of chitosan is an important parameter in chitosan studies and it shows the level of the inorganic constituents present in the samples. The ash content of the chitosan samples was determined according to the procedure in Section 3.9.10 of Chapter 3.

The ash content of pupal and adult BSF chitosan are presented in Table 4.14 as 0.73±0.01% for pupal chitosan (PCH21_9) and 0.86±0.02% for adult chitosan (ACH20_9). The ash content of the pupal chitosan is slightly lower than that of the adult chitosan. Since ash content affects the properties of chitosan, No and Meyer (1995) have asserted that for chitosan to be adjudged high in quality, its ash content should be less than 1.0%. The ash contents of pupal and adult BSF chitosan in this study were less than 1.0%. This, therefore, shows that they are of high quality because the inorganic constituents of the extracted biopolymers were reasonably well removed. Although the ash contents of the samples (Table 4.14) were very low, showing their purity, they can affect the physicochemical properties of the chitosan. The properties that could be affected are solubility, viscosity and MW. Mohanasrinivasan *et al*. (2014) in their study of isolated shrimp and commercial chitosan had reported that high ash content affected the viscosity and the MW of the chitosan solution.

The ash content values obtained in this study corroborate the findings of previous studies. Hossain and Iqbal (2014) reported an ash content of 0.48 and 0.36% for shrimp chitosan demineralised with increasing concentration of HCl, while Marei *et al*. (2016) reported values ranging from 1.6 to 9.2%. The solubility PCH21_9 and ACH20_9 compared to the commercial reference shrimp chitosan sample is discussed next.

4.2.9 *Chitosan solubility test*

The solubility of chitosan in aqueous acetic acid is very important in determining its quality and subsequent application. The solubility was investigated according to the procedure outlined in Section 3.9.11 of Chapter 3. The values of the extracted pupal, adult and commercial shrimp chitosan are presented in Table 4.14 as 93.4±2.4% for PCH21_9, 92.7±3.1% for ACH20_9 and 95.0±5.2% for commercial chitosan samples. The adult chitosan was least soluble among the three chitosan samples investigated. The solubility of chitosan, like its MW, is a vital parameter that determines the properties and the application of chitosan. Chitosan of high quality is characterised by greater solubility in a given solvent. Solubility, in turn, depends on the DD of the chitosan (Kapadnis *et al.,* 2019). In this study, the DD of the pupal, adult and commercial

chitosan were 85, 83 and 85%, respectively. The slightly low DD of the adult chitosan may have resulted in its lowest solubility among the three samples.

Hossain and Iqbal (2014) reported that several factors, including temperature, time of deacetylation, enzyme and/or solution concentration, solid-to-solution ratio and particle size affected the solubility of chitosan. Kapadnis *et al.* (2019) observed a proportional increment in the solubility of chitosan solution as the DD and inter-particulate spaces of the chitosan sample increased and concluded that it was due to the progressive removal of the acetamide group of the chitin during deacetylation process that resulted in variation in the solubility of the samples. This implies that a low insolubility value of a chitosan sample denotes partial deacetylation, and could, therefore, affect the solubility results. The chitosan samples extracted in this study showed a high solubility. The values of 93.4±2.4% for PCH21_9, 92.7±3.1% for ACH20_9 and 95.0±5.2% for commercial chitosan samples were higher than the 73 and 65% obtained by Kapadnis *et al.* (2019), while slightly lower than the 97% obtained by Hossain and Iqbal (2014).

4.2.10 *Viscosity-average molecular weight determination*

The intrinsic viscosity of the extracted chitosan, in this study, are presented in Table 4.14. The values were used in computing the MW of the chitosan solutions, according to Equation 3.30 in Section 3.9.12 of Chapter 3. Molecular weight (MW) is a vital parameter that affects the properties and applications of chitosan. To determine the MW, the intrinsic viscosity of the chitosan solutions would have to be computed first. The viscosity-average MW of the chitosan from the BSF was determined using an Ubbelohde viscometer for transparent liquids. The extrapolation to the y-axis of the plot of reduced viscosity against concentration gave the intrinsic viscosity. Intrinsic viscosity is the limiting viscosity as the concentration of the solution tends to zero. It is a function of the solution's ionic strength and its degree of ionisation (Hossain and Iqbal, 2014). Hwang and Shin (2000) had reported that the intrinsic viscosity of a chitosan solution is generally greater than that of other natural polymers of similar MW. This, the researchers stated, is due to the rigid arrangement of the β-(1→4) glycosidic linkage inherent in the structure of chitosan.

The MW of the chitosan from adult and pupae BSF as well as that of the commercial chitosan (P. code 101816167) are presented in Table 4.14 as 179, 198 and 164 kDa for PCH21_9, ACH20_9 and commercial chitosan, respectively. The MW obtained in this study was higher

than the 5201, 6273 and 6267 Da obtained from fish, shrimp and crab, respectively by Kumari *et al.* (2017) but in agreement with the study of Nemtsev *et al*. (2004) who obtained values between 200 - 250 kDa from honeybee chitosan. However, the values were lower than MW of 450 - 570 and 483 - 570 kDa obtained by Tajik *et al*. (2008) and Yen *et al*. (2009) from crustaceans, brine shrimp and crab shells, respectively.

Several factors, including temperature, solution concentration, reaction time, particle size and source of material can influence the MW of chitosan (Yen *et al*., 2009). Chitosan could be of low, medium or high MW according to the chain length of the polymer structure. Mishra (2016) reported that MW between 50 - 190, 190 - 700 and 700 - 1000 kDa represents low, medium and high MW, respectively. Therefore, chitosan obtained in this study falls within the low MW range.

The MW plays a key role in determining the physicochemical and functional characteristics of chitosan and, therefore, influences its application in various areas. Erdogan and Kaya (2016) have reported that for medical and agricultural applications, chitosan of low MW was more effective than higher MW chitosan. In a similar vein, Aranaz *et al.* (2009) in an earlier review of chitosan applications determined that low MW chitosan was more efficient in gene transfer, food preservation and wound healing properties while high MW chitosan can effectively serve in diets as it binds cholesterol and fats effectively.

The plots of reduced viscosity against concentrations for the chitosan samples are shown in Figure 4.24. Extrapolation of the graphs to the Y-axis gives the intrinsic viscosity applied in calculating the MW of the chitosan samples.

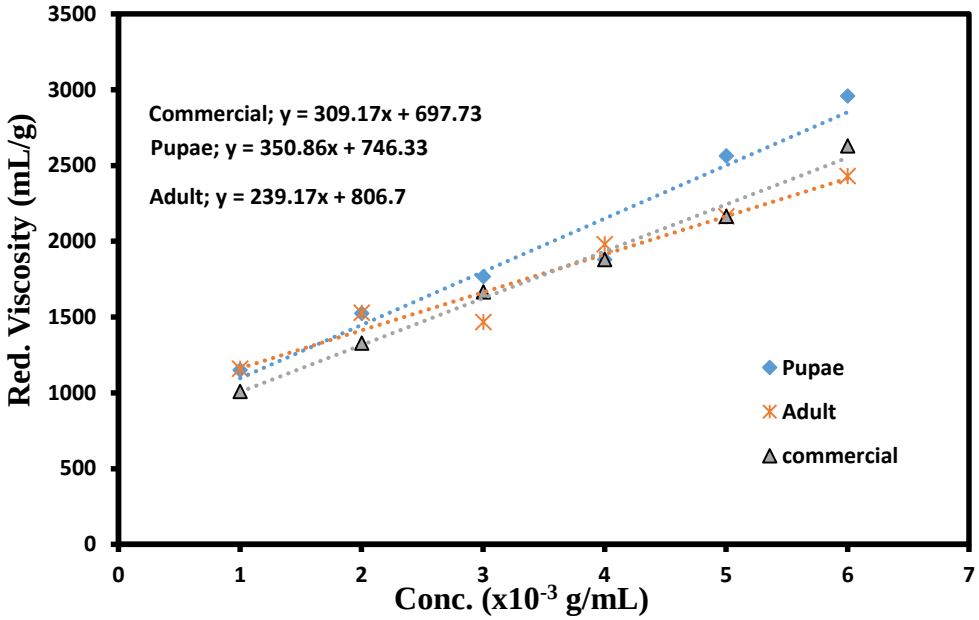

Figure 4. 254: Viscosity versus concentrations for the chitosan samples.

The MW of each repeating unit (Figure 4.25) of the chitosan, PCH21_9, ACH20_9 and commercial reference samples as determined in Section 4.4.6.6 were 188.03, 186.16 and 188.03 Da (g/mol), accordingly. Moreover, the MW of the chitosan samples, PCH21_9, ACH20_9 and commercial reference sample had been determined to be 179, 198 and 164 kDa.

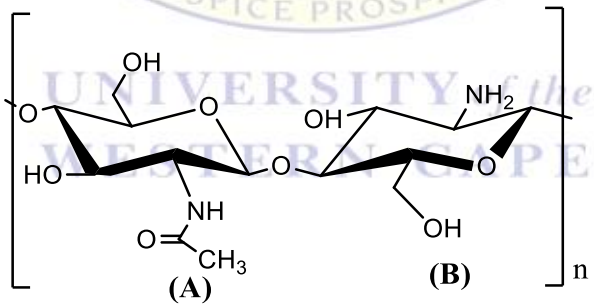

Figure 4.25: The repeating arrangement of a chitosan molecule (A) *N*-acetylglucosamine unit and (B) glucosamine unit.

Therefore, the chain length otherwise called the total number of repeating units in the extracted chitosan samples (PCH21_9, ACH20_9) and the commercial reference shrimp chitosan could be computed as follows:

The MW of the chitosan biopolymer = MW of each repeating unit * number of repeating units in the chitosan structure.

For pupal chitosan, PCH21_9,

$$179{,}000 = 188.03 * n$$

$$n = \frac{179{,}000}{188.03} = 952.$$

A similar procedure was adopted for the adult chitosan, ACH21_9 and n was computed to be 1,064 while the commercial reference chitosan was determined to be 872.

This result shows that there are 952, 1,064 and 872 repeating units in the structure of pupal (PCH21_9), adult (ACH21_9) and commercial reference chitosan samples, respectively. This justifies the classification of BSF chitosan as a polymer of biological origin (biopolymer) with the possession of hundreds of repeating *N*-acetylglucosamine and glucosamine units within its structure.

4.3 Chapter summary

This study focused on the extraction of chitin from waste pupae and commercially reared adult BSF and further conversion to chitosan. The optimum conditions obtained for the demineralisation process were 1.0 M NaOH, 1.67 h (100 minutes), 50 ˚C for both pupal and adult chitin samples. The optimised deproteination conditions were 1.0 M NaOH, 14 h, 95 ˚C for pupal chitin and 1.0 M NaOH, 12 h, 95 ˚C for adult chitin. The yield of both extracted chitin was computed to be 14.1% and 5.3% for pupae and adult BSF, respectively. The pupae BSF had approximately a 3-fold increase in yield more the adult chitin. The series of optimisations conducted showed that the process parameters of time, temperature and concentration affected the yield of the samples. Furthermore, it was ascertained that deproteination before demineralisation leads to hydrolysis of the sample hence affecting its yield. Therefore, this study conducted demineralisation before deproteination and obtained chitin yield exceeding most results of insect origin reported in the literature. The extracted chitin, from pupal and adult BSF were deacetylated with optimised conditions of 70% NaOH, 100 ˚C and 5 h.

The SEM analysis revealed that pupae chitin composed of tightly packed structures with reoccurring hexagonal shapes arranged in honeycomb-like positions while the adult chitin showed repeating oval arrangements. Both chitins consisted of fibrous morphology at higher magnifications while the chitosan samples possess neither fibres nor pores. Elemental characterisation of the extracts showed the nitrogen content of pupae (6.20%) and adult

(6.50%) chitin was slightly lower than the theoretical nitrogen content of fully acetylated chitin (6.89%), suggesting slight deamination of the samples.

The FTIR analysis confirmed the successful extraction of α-chitin from pupae shells and adult BSF waste materials with the scissoring of the Amide I band at 1650 and 1621 cm^{-1}. The adult chitin showed a higher thermal degradation value (392 ˚C) than the pupal chitin (384 ˚C) while the chitosan samples have 21 and 20% lower thermal degradation temperatures for adult and pupal BSF samples, respectively. The viscosity average MW of the samples were determined to be 179 kDa for pupae and 198 kDa for adult BSF chitosan, accordingly. Meanwhile, the estimated chain lengths of the extracted pupal and adult chitosan samples were determined to be 952 and 872 repeating N-acetylglucosamine and glucosamine units, respectively.

It can, therefore, be said that chitin and chitosan with similar physicochemical properties as the commercially available shrimp samples could be obtained from the pupae casings and adult BSF waste materials.

CHAPTER 5

SYNTHESIS OF NANOMATERIALS FROM EXTRACTED BSF CHITOSAN

5.0 Introduction

This chapter is divided into two sections. The first deals with the optimisation of the process parameters for the electrospinning of BSF chitosan to nanofibres and its subsequent characterisation, while the second section details the physicochemical properties of synthesised BSF CHS NPs. The first section of this chapter specifically investigated the parameters affecting electrospinning, which include the process parameters and solution properties to determine the optimum conditions for the electrospinning of extracted BSF chitosan (PCH21_9). Electrospun nanofibres are different from the normal polymer material with the possession of a larger surface area and other intrinsic properties, and therefore effectively applied in various areas (Yuan *et al*., 2004).

The characteristics of the nanofibres, such as diameter, influences its use in specific applications. For instance, filtration membranes of nanoscale size require more uniformly distributed fibre diameters to achieve increased diffusion interception, and passive compaction efficiencies (Lin *et al*., 2007). This section describes the processes for the electrospinning of chitosan into nanofibres using trifluoroacetic acid (TFA). This was to obtain fibres of smaller diameters with smooth morphologies and was achieved through the control of process parameters such as the biopolymer concentration, applied voltage, the needle tip-to-collector distance and the flow rate. The relevance of TFA as a choice solvent in the electrospinning of extracted PCH21_9 is discussed next.

5.1 The use of TFA as electrospinning solvent

Trifluoroacetic acid (TFA) was used for the electrospinning process in this study. TFA is an analogue of acetic acid. The difference is that fluorine atoms in the structure of TFA have replaced the hydrogen atoms of the acetic acid. The electrospinning of chitosan is reported by Bhardwaj and Kundu (2010) to be most successful using TFA, more than any other solvent. The reasons for this success could be that TFA forms salts with the amino-functional groups of chitosan (Sangsanoh and Supaphol, 2006). This salt ($-NH_3^+CF_3COO^-$) formation eliminates the strong interaction existing between the chitosan molecules, making them amenable to electrospinning. Secondly, TFA has a high vapour pressure and has the lowest surface tension

(13.5 nM/m) among the electrospinning solvents (Bhardwaj and Kundu, 2010). This volatility and low surface tension are advantageous for the rapid solidification and subsequent drying of the electrified jet of the chitosan-TFA solution (Ohkawa *et al*., 2004). Subsequent sections focused on the optimisation of electrospinning conditions for the fabrication of nanofibres from the BSF chitosan biopolymer.

5.2 Electrospinning of extracted BSF chitosan (PCH21_9)

The application of an electric field in the production of fibres of various sizes is termed electrospinning. The extracted pupal chitosan (PCH21_9) was investigated for electrospinnability into fibres. The following parameters were investigated in this study; concentration of 3, 4, 5, 6 and 7 wt% in 99% TFA solution. The applied voltage was varied between 18, 20, 22 and 25 kV. The flow rates studied were 0.1, 0.3, 0.4 and 0.5 mL/h while the needle tip-to-collector distances were 50, 80, 100 and 120 mm. The experimental details were as presented in Section 3.3 of Chapter 3. Subsequent subsections describe these parameters in details.

5.2.1 *Optimisation of solution concentration for the electrospinning of BSF chitosan*

The effect of concentration was studied to determine the optimum value for the nanofibre formation. The experiment was conducted at different chitosan concentrations of (a) 3, (b) 4, (c) 5, (d) 6 and (e) 7 wt % in TFA. Each experiment was code-named as ES-C1 for 3 wt%, ES-C2 for 4 wt%, ES-C3 for 5 wt%, ES-C4 for 6 wt% and ES-C5 for 7 wt% chitosan in TFA. The higher the concentration, the longer it took the sample to dissolve in 99% TFA. 6 wt % chitosan (ES-C4) took a longer period to dissolve in the presence of low heat (50 ^{o}C) while 7 wt% (ES-C5) formed too viscous and gel-like samples. The fibres were, therefore, electrospun from chitosan solutions of 3 – 6% (w/v) using TFA at an applied voltage of 17 kV, collection distance of 100 mm and flow rate of 0.4 mL/h. The experimental procedure is described in Section 3.3 of Chapter 3 while the micrographs of the electrospun nanofibres illustrating the effect of different polymer concentrations are presented in Figure 5.1 (a-d).

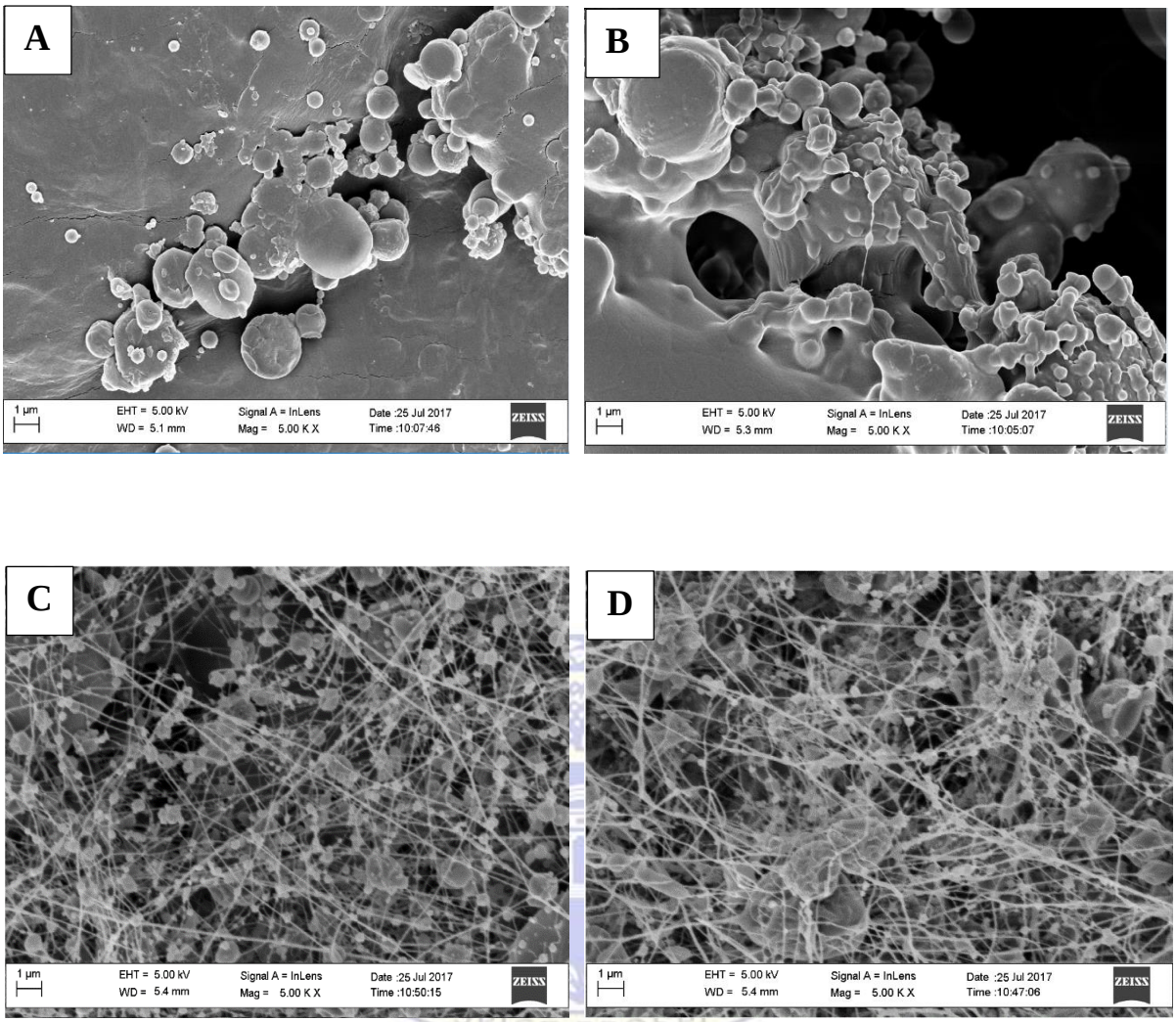

Figure 5. 1: Micrographs of fibres formed at different chitosan concentrations in TFA (a) 3 (ES-C1), (b) 4 (ES-C2), (c) 5 (ES-C3), and (d) 6 (ES-C4) wt % (fixed values were flow rate – 0.4 mL/h; voltage - 17 kV and distance - 100 mm).

Figure 5.1 (a) represents the surface morphology of ES-C1. Physical examination shows that the deposit, after detaching it from the collector, was creamy in colour and transparent, film-like material. ES-C1 and ES-C2 could not be successfully electrospun into fibres but formed films. The micrographs show the formation of beads with various sized particles (Figure 5.1a) which were not uniformly distributed throughout the collecting space (Figure 5.1b). The formation of beads and microspheres could have resulted from a low concentration of chitosan in the electrospinning solution. This resulted in the spraying process under the influence of the electric field, due to low surface tension, low viscosity and insufficient chain entanglement (Rajak *et al.*, 2019). Chain entanglement is very important in fibre formation during electrospinning and it is aided by an increase in charge density resulting from solvent evaporation. It was also observed from the micrographs (Figure 5.1b) that an increase in CHS

concentration to 4% in TFA led to an increased number and a decreased size of the beads formed under the applied conditions. Fibres were observed when the concentration of the solution increased to 5% and 6% (w/v) (ES-C3 and ES-C4, Figure 5.1c&d). The increase in chitosan concentration caused an increase in the solution's viscosity, which affected elongation and stretching of the ensuing polymer jet. The bead sizes became smaller with the coexistence of thin fibres among the beads and microspheres. The micrographs and morphologies of both ES-C3 and ES-C4 appear similar, although ES-C4 appears to have a higher concentration of larger beads and microspheres. This is an indication that beaded fibres could be obtained at both (5 and 6 wt%) concentrations.

Electrospinning did not occur at 7 wt% (ES-C5) chitosan concentration. This could be because the solution was too viscous and could not flow past the spinneret. As the solution emerged at the needle tip, it clogged and the build-up at the spinneret eventually dropped vertically on to the base. Apparently, the applied voltage was not able to overcome the viscous force of the solution under the conditions used.

The formation of beads in the electrospinning of chitosan solution could be due to low polymer concentration, higher surface tension and reduced viscosity of the polymer solution (Lemma *et al*., 2016). These findings were in agreement with the work of Geng *et al.* (2005) and Ohkawa *et al.* (2004) who reported that beads and microspheres were obtained during electrospinning process of shrimp chitosan at lower polymer concentrations. Low chitosan concentration affects the extent of the entanglement of polymer chains resulting in breaking up of the viscous solution before the formation of the Taylor cone on the needle tip (Haider *et al*., 2013). This causes fragmentation of the polymer chain and subsequent formation of droplets rather than fibres on the collector (Figure 5.3). The effect of applied voltage on the electrospinning of the BSF CHS is discussed in the next section.

5.2.2 *Effect of applied voltage on electrospinning of BSF chitosan*

This study was undertaken to determine the effect of applied voltage on the electrospinning of the extracted chitosan from BSF and the subsequent properties of the electrospun fibre using a Nova NanoSEM 230 microanalyser. The results obtained and the mean fibre diameters are presented in Figure 5.2 (a-d). The fibres were obtained from a chitosan solution of 5% (w/v) in 99% TFA, using an applied voltage range of 18 to 25 kV. A fixed collection distance of 100 mm from the needle tip and a solution flowing at the rate of 0.6 mL/h were used in this

optimisation experiment. The experiments have the following codes: ES-V1 for 18 kV, ES-V2 for 20 kV, ES-V3 for 22 kV and ES-V4 for 25 kV. The experimental procedure is described in Chapter 3 Section 3.2.3. The effect of applied voltages (18 to 25 kV) on the morphology, average diameter and distribution of electrospun fibres are presented in Figures 5.2 (a-c).

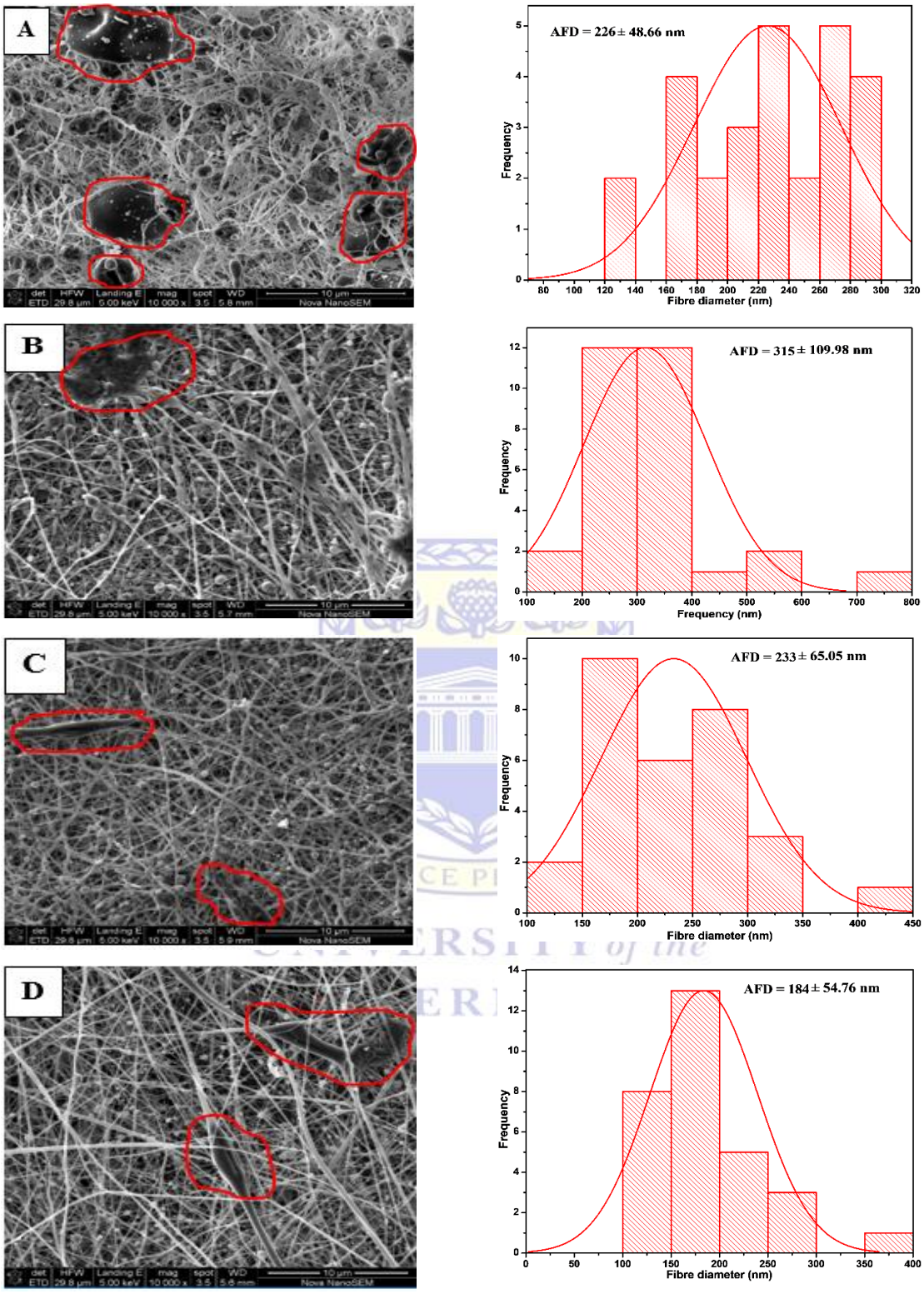

Figure 5. 2: Micrographs of electrospun CHS nanofibres in TFA and the corresponding distributions of fibre diameter at various applied voltages {A = 18 kV (ES-V1), B = 20 kV (ES-V2), C = 22 kV (ES-V3) and D = 25 kV (ES-V4)} and fixed conditions (distance to collector of 100 mm, solution flow rate of 0.6 mL/h and concentration of 5 wt%).

Figure 5.2a indicates that at low voltage (ES-V1), a thick mass of the chitosan was formed with poor morphology, irregularly shaped fibres and occasional deposits of large microspheres. The beads and microsphere morphologies varied from round/spherical shape (Figure 5.2a) at low voltage to partly stretched droplets or ellipsoidal fibres with the majority having smooth shapes (Figure 5.2d) with increasing voltage. This may have occurred due to an insufficient electric field, which is a prelude to the formation of fibres. It could also be observed that as the applied voltage increased, the microspheres and beads decreased, with the emergence of more fibres of irregular sizes. Furthermore, the majority of the fibres formed at 20 and 22 kV had many joints along their cylindrical surface, signifying poor uniformity of the fibres at these voltages. The poor uniformity of the fibres may have resulted from the electric field strength, which affected the instabilities of the emanating jet solution as seen on the micrographs. There also existed in the micrographs what appeared to be incompletely dried chitosan solution deposited and trapped in the ensuing jet (highlighted). Moreover, the average diameter of the fibres decreased in ES-V4 (Figure 5.2d) and the morphology of the as-spun fibres was improved. Geng *et al.* (2005) had opined that formation of more fibres with an increment in the applied voltage might be due to the increase in elongation force and instability of the charged polymer solution by the strong electric field. The average distribution of fibre diameters for ES-V1, ES-V2, ES-V3 and ES-V4 were 226±49, 315±110, 233±65 and 184.54±55 nm, respectively as seen in Figure 5.3.

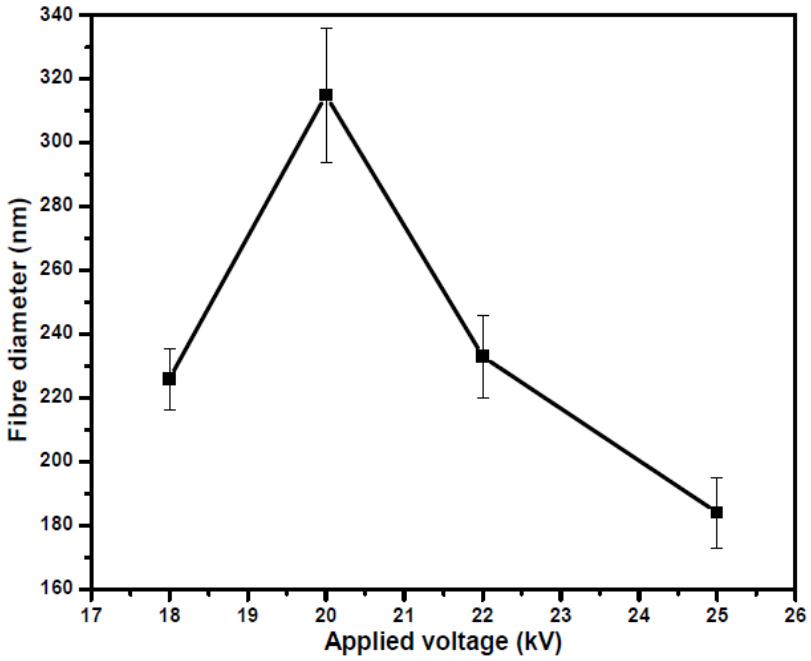

Figure 5. 3: Trend of fibre diameter as a function of voltage for 5% PCH21_9 in TFA at applied voltages of (a) 18, (b) 20 (c) 22 (d) 25 kV (flow rate - 0.6 mL/h and distance - 100 mm).

The results of these experiments are consistent with the findings of previous researchers. Unal *et al*. (2019) reported that increasing the field strength leads to an increase in the repulsive force acting on the charged polymer jet thereby favouring the formation of decreased fibre diameter. It is worthy to note that chitosan is a polyelectrolyte and, therefore, exhibits polycationic behaviour in an acidic medium due to the numerous amino groups within its backbone (Mazoochi and Jabbari, 2011). The presence of ionic species in its structure increases the charge on the jets during electrospinning. This leads to increased elongation forces on the charged jet causing stretching and instability of the particles, induced by the electric field. Therefore, the increase in charge density leads to a decrease in the final fibre diameter (Charernsriwilaiwat *et al*., 2010). However, Haider *et al*. (2015) and Al-Enizi *et al*. (2018) have also argued that too high an applied voltage could also cause the acceleration of charges on the spinning solution and, therefore, cause an increase in the jet length, which ultimately could lead to an increase in the fibre diameters. Generally, increased voltages could lead to more charge generation at the Taylor cone, likewise greater electrostatic forces, both contributing to stretching the jets maximally and overcoming the solutions' surface tension. These effects favour the formation of fibres with smaller diameters and decreased number and size of beads and microsphere (Theron *et al*., 2004; Haider *et al*., 2012). The next section will discuss the effect of solution flow rate on electrospinning of extracted pupal chitosan (PCH21_9).

5.2.3 *Effect of flow rate on the electrospinning of PCH21_9*

This experiment was conducted to investigate the influence of flow rate on the electrospinning of BSF chitosan and determine the optimum flow rate for fibres of uniform diameter formation. Figure 5.4 (a-d) shows the scanning electron micrographs and fibre distributions of electrospun BSF chitosan at varying flow rates (a) 0.5, (b) 0.4, (c) 0.3 and (d) 0.1 mL/h (polymer concentration 5%; applied voltage of 25 kV; distance of 100 mm). The various investigations were code-named ES-F1 for 0.5 mL/h, ES-F2 for 0.4 mL/h, ES-F3 for 0.3 mL/h and ES-F4 for 0.1 mL/h. The electrospinning process is described in Section 3.3.3 of Chapter 3.

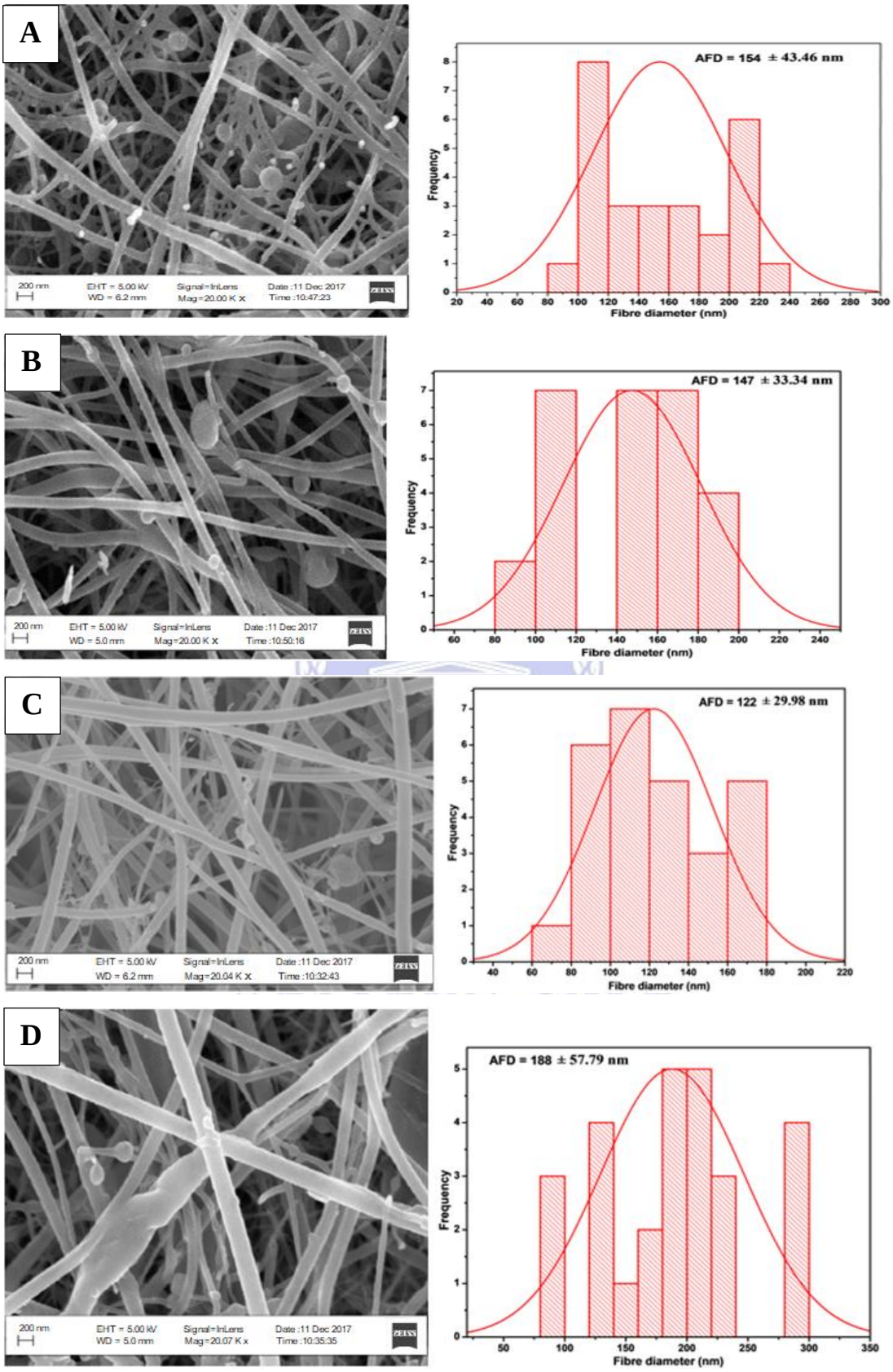

Figure 5. 4: Trend of BSF nanofibre diameter as a function of solution flow rate (a) 0.5 (ES-F1), (b) 0.4 (ES-F2), (c) 0.3 (ES-F3) (d) 0.1 (ES-F4) mL/h (voltage 25 kV; polymer concentration in TFA - 5 wt % and collector distance - 100 mm).

Figure 5.4 shows the micrographs and their corresponding fibre diameter distributions for the electrospun chitosan (CHS) nanofibres in TFA at flow rates of 0.5 - 0.1 mL/h. The process conditions are a chitosan concentration of 5 wt%, a voltage of 25 kV and a 100 mm collection distance. At 0.5 mL/h flow rate (ES-F1), the chitosan solution was being ejected at a faster rate thus the field force could not completely overcome the viscous force. This gave rise to the occasional ejection and deposition of solution droplets on the collector which resulted in the appearance of beads-on-strings and microspheres along with the fibre (Figure 5.4a). As the flow rate decreased while keeping other process conditions constant, the deposited fibres had a non-uniform but reduced diameter. With a flow rate of 0.3 mL/h (ES-F3), the obtained fibres showed a much-improved fibre distribution devoid of beads and microspheres. It implies 0.3 mL/h (Figure 5.4c) is the ideal flow rate as it aligned with the field strength to form the Taylor cone, overcoming the viscous force of the solution while ensuring the solvent evaporated before reaching the collector. It was interesting to observe further that as the flow rate was reduced to 0.1 mL/h (ES-F4, Figure 5.4d), the fibres showed some defects with increased size and distribution range. Thus, the quality of electrospun chitosan fibres and their diameter are affected by the flow rate of the electrospinning solution. The diameters of the fibres at varying flow rates are presented in Figure 5.5.

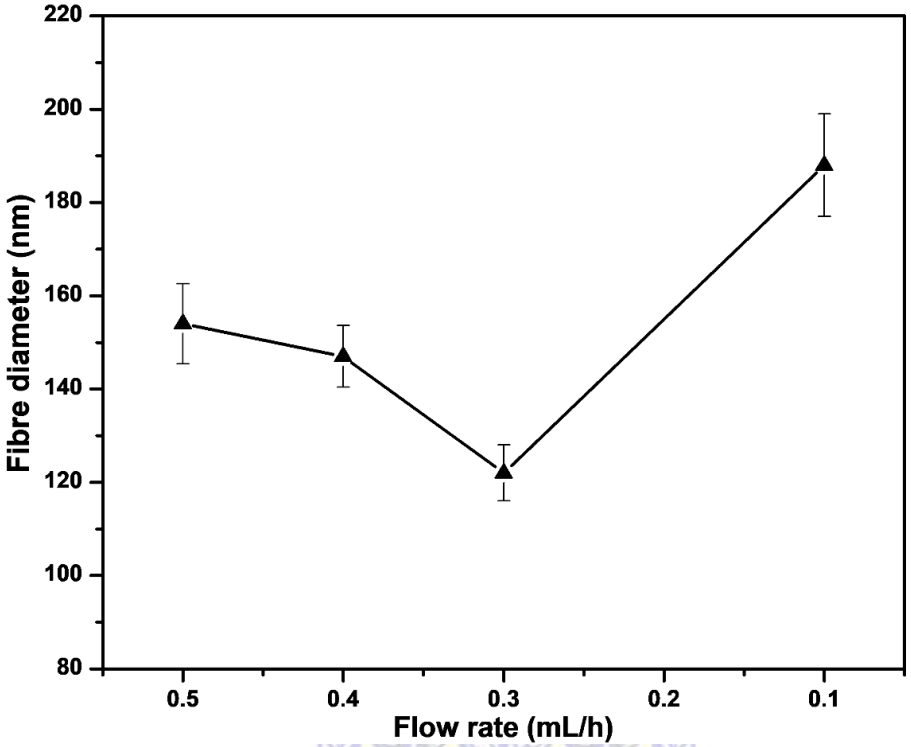

Figure 5. 5: Fibre diameter distribution of CHS at varying flow rates (a) 0.5, (b) 0.4, (c) 0.3 and (d) 0.1 mL/h (polymer concentration in TFA - 5 wt %; voltage - 25 kV and collector distance - 100 mm).

The formation of beads and microspheres on the fibres as the flow rate varied (Figure 5.4) could be because of irregular polymer flow. Polymer flow rate and electric field strength must align to prevent too little or too much polymer jet flowing and interacting with the field force. Increased flow rate leads to the release of a larger amount of the polymer into the field, which caused the viscous force of the Taylor cone to overcome the field force leading the disruption of continuous flow and formation of deposits with incomplete solvent evaporation (Haider *et al*., 2012). This interruption causes a defect in the fibres, and appears as beads and/or microspheres. On the other hand, the reduced flow rate below the threshold could lead to the supply of too little polymer from the syringe and subsequent evaporation of the solvent at the spinneret. This causes the polymer to be drawn into the field by the electric force preventing the formation of the Taylor cone and ultimately producing fibres with beads and microspheres (Charernsriwilaiwat *et al*., 2010). For spinning and polymer deposition to continue, a Taylor cone ought to form. Therefore, the interruption of flow due to the low flow rate allowed the formation of defects. This could explain the defects observed on the micrograph in Figure 5.4d when the flow rate was reduced to 0.1 mL/h under a constant field strength.

These results were in agreement with the findings of Bhardwaj and Kundu (2010) who studied the electrospinning of shrimp chitosan at a high applied voltage (30 kV) and flow rates (0.6 – 1.2 mL/h). Another important parameter in the electrospinning of chitosan, the distance between the spinneret tip to the grounded collector, is discussed in the next section.

5.2.4 *Effect of tip-to-collector distance*

This section presents the results of the optimisation of the needle tip-to-collector distance for the electrospinning of BSF chitosan. The experimental protocol is described in Section 3.3.4. of Chapter 3. The codes for the investigations are ES-D1 for 50 mm, ES-D2 for 80 mm, ES-D3 for 100 mm, and ES-D4 for 120 mm. When varying the collector distances, other factors of concentration (5 wt% in TFA), voltage (25 kV), and flow rate (0.3 mL/h) were kept constant. Figure 5.6 presents the micrographs of the electrospun samples at various tip-to-collector distances.

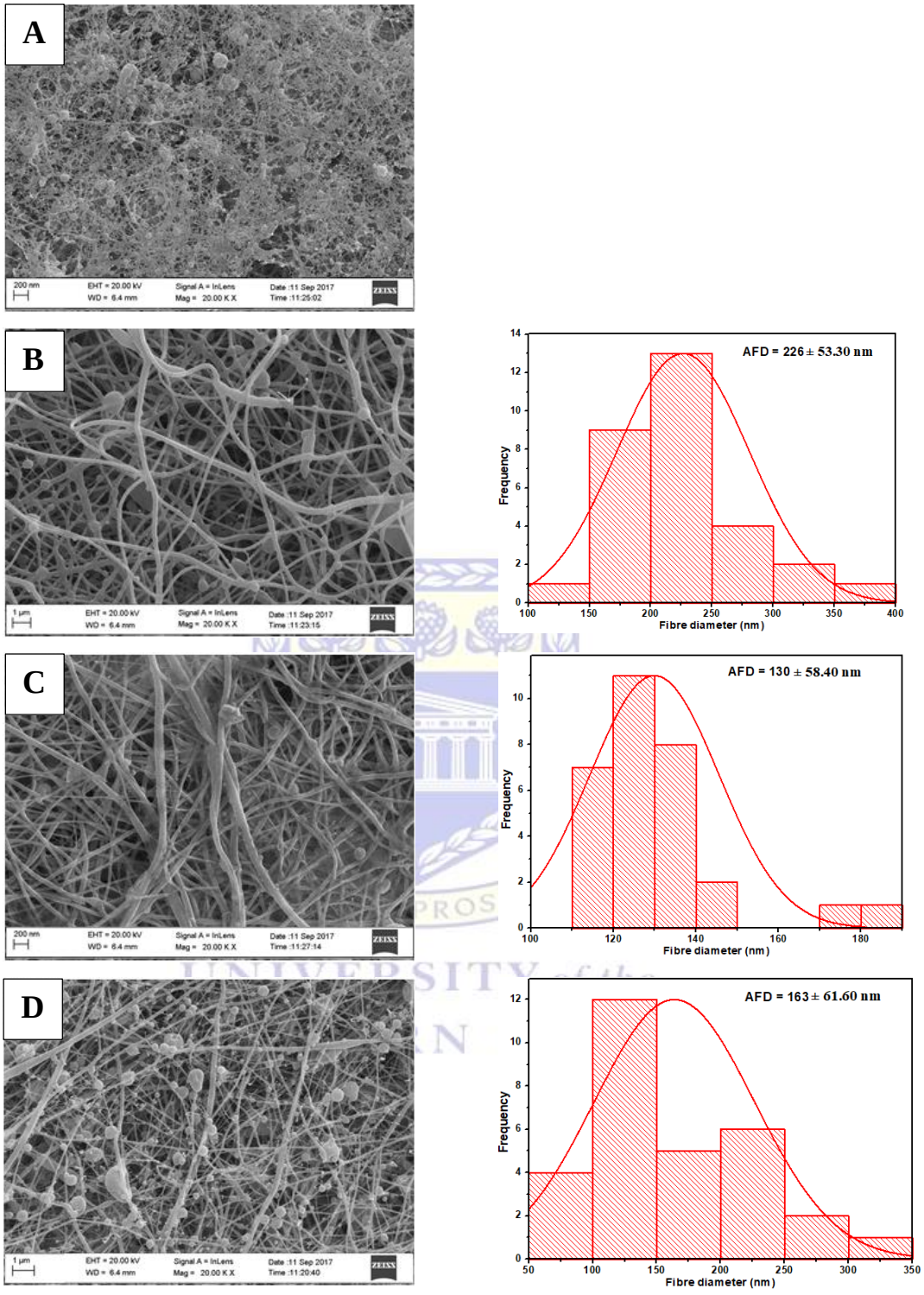

Figure 5. 6: Micrographs of electrospun fibres and their corresponding fibre diameter distributions at various needle tip–to-collector distances of (a) 50 (ES-D1), (b) 80 (ES-D2), (c) 100 (ES-D3) and (d) 120 (ES-D4) mm (flow rate - 0.3 mL/h; voltage - 25 kV and chitosan concentration - 5 wt% in TFA).

In Figure 5.6a, the reduced tip-to-collector distance of 50 mm (ES-D1), was too short to induce full stretching of the emerging jets and thus increasing the instability of the jet. This at the same

time increased the electric field strength causing the jets to accelerate at a faster speed within the field environment. At a short distance, the field strength, a ratio of the voltage to the distance, is too strong and thus causes an increase in the instability of the ensuing jets. This resulted in the deposition of wet fibres with a web-like appearance at the collector due to the limited time for solvent evaporation (Figure 5.6a). At a relatively small tip-to-collector distance, the unevaporated solvents on the fibres may cause the fibres to entangle forming joints along with the fibre cylindrical structure thereby resulting to inter- and intra-layer bonding (Ray *et al.*, 2019). The fibres formed at this low flow rate (Figure 5.6a) were so small and entangled with beads that their diameters could not be determined.

An increase in the tip-to-collector distance from 50 (ES-D1) to 80 mm (ES-D2) led to the deposition of fibres with improved morphology. This may have resulted from the polymer jets being fully stretched and having quality time within the flight regime to evaporate the solvents. Small beads were observed on the micrographs implying that the distance was not yet the ideal condition for beadless fibre fabrication. The fibre diameter of ES-D2 was found to be 226 nm. A further increase in the collector distance to 100 mm (ES-D3) produced fibres with better quality and reduced fibre diameter distributions (Figure 5.6c). Beads and microspheres were nearly non-existent under these conditions. The average diameters of the electrospun fibres were also observed to have decreased significantly from 226 nm at a distance of 80 mm (Figure. 5.6b) to 130 nm at 100 mm (Figure 5.6c). However, the decreasing fibre diameter trend reversed when the collector distance increased to 120 mm (ES-D4, Figure 5.6d). This increment induced the formation of beads and microspheres along with the fibres.

As the tip-to-collector distance increased, the field strength tends to reduce. In Figure 5.6b, the electric field possesses the required electric potential to stretch the emerging jets but having limited time to produce complete bead-less fibres resulting in increased fibre diameters (Ray *et al*., 2019).

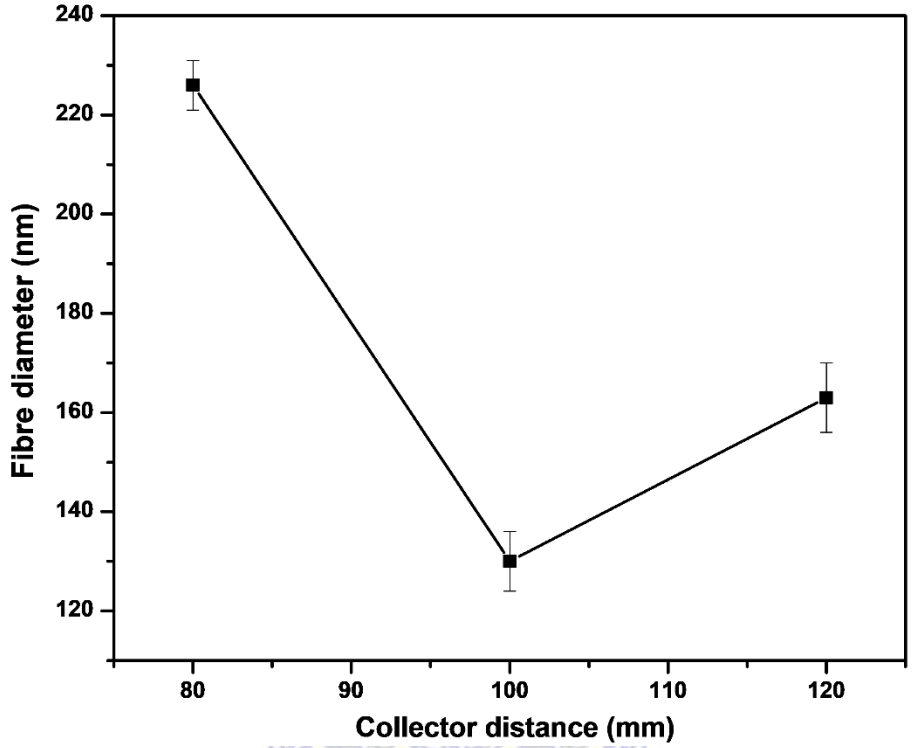

Figure 5. 7: Variation of fibre diameter with respect to needle tip–to-collector distances of 80, 100 and 150 mm (flow rate - 0.3 mL/h; voltage - 25 kV and concentration - 5 wt % in TFA). The 50 mm data were excluded from this plot because of fibre entanglement and small fibre diameter.

The needle tip-to-collector distance plays an essential role in determining the nature and the morphology of electrospun fibres. It affects the electric field strength of the electrospinning process, which in turn affects the jet's velocity, the extent of stretching, the flight time, the rate of solvent evaporation and the degree of instability of the jet (Subbiah *et al*., 2005). Geng *et al*. (2005) in their study of chitosan dissolved in acetic acid solution had posited that complete bead-less fibres were produced when the minimum distance required for sufficient drying and stretching of the polymer jet was attained. Other than this distance, beaded fibres would be obtained with too short or too long tip-to-collector distances. This is because, at reduced distances, the field strength becomes too strong causing an increase in the instability of the emerging jets resulting in the deposition of fibres with beads and microspheres (Bhattarai *et al*., 2019). The decrease in the average diameter of the nanofibres may have resulted from the larger electrostatic force which induced an accelerated jet flight time and stretching hence favouring the formation of fibres with a reduced diameter (Haider *et al*., 2010, Sedghi and Shaabani, 2016). Therefore, changing the tip-to-collector distance of an electrospinning set-up had a profound effect on the solution's time of flight and the strength of the electric field. To

produce microsphere and bead-free nanofibres, the ensuing jet must have ample time for full stretching within the electric field and for the solvents to completely evaporate.

Table 5.1 presents the optimal electrospinning conditions established in this study. The average fibre diameter obtained corroborates with those obtained by Austero *et al*. (2012) and Kiechel *et al*. (2013) who independently reported an average fibre diameter of 133±53 nm using shrimp chitosan in TFA solution. Table 5.1 presents the optimised electrospinning conditions for BSF chitosan nanofibre (ES-D3) fabrication.

Table 5. 1: Optimised electrospinning conditions for PCH21_9 to nanofibre (ES-D3)

Parameters	Conditions
Chitosan concentration (wt %)	5
Voltage (kV)	25
Flow rate (mL/h)	0.3
Distance to the collector (mm)	100
Average fibre diameter (nm)	130
Fibre diameter range (nm)	80 - 180

5.3 Characterisation of the electrospun nanofibres

In this section, further characterisation methods were adopted to elucidate the properties of the electrospun BSF nanofibres (ES-D3). The optimal conditions for the electrospinning were a chitosan concentration of 5 wt% in TFA, applied voltage of 25 kV, spinneret tip to collector distance of 100 mm and a flow rate of 0.3 mL/hr.

5.3.1 *ATR-FTIR analysis of electrospun BSF nanofibre*

The FTIR study was done to investigate the chemical compositions of the sample and the signals of various functional groups on the electrospun nanofibre (ES-D3). It would also show if the structure of the electrospun nanofibres conforms to the extracted BSF chitosan. Figure 5.8 shows the spectra of the extracted BSF chitosan (PCH21_9) and the electrospun nanofibre (ES-D3) obtained using the optimal conditions in this study.

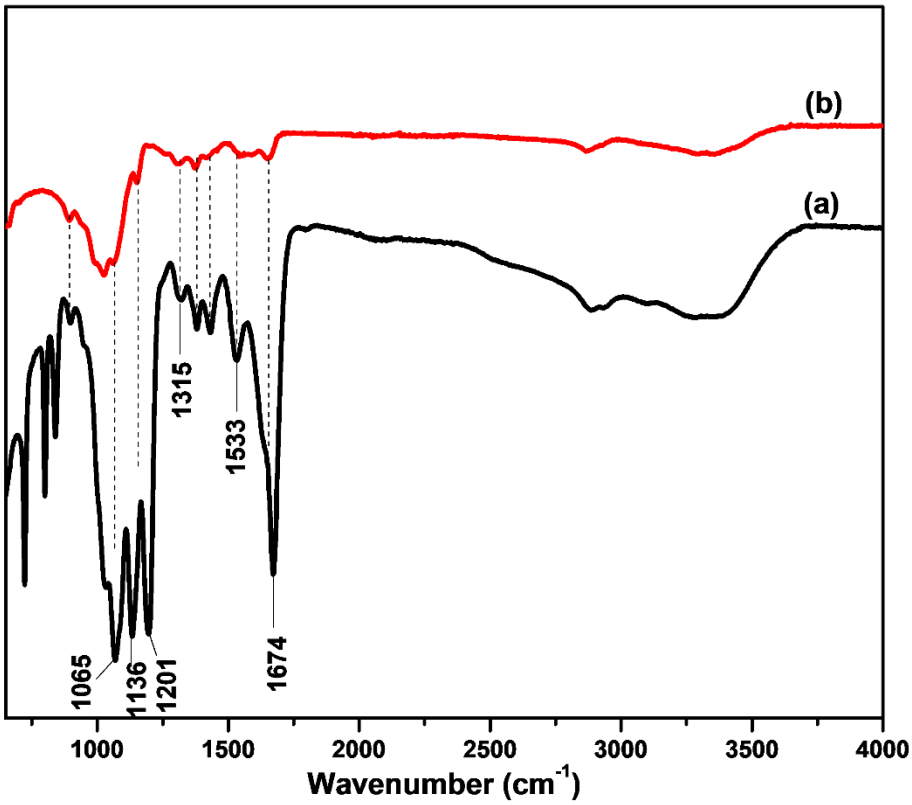

Figure 5. 8: FTIR spectra of PCH21_9 (a), electrospun BSF chitosan (ES-D3) fibres (b). Electrospinning conditions are concentration - 5 wt% in TFA, applied voltage - 25 kV, collector distance - 100 mm and flow rate - 0.3 mL/hr.

From the FTIR spectrum of the chitosan nanofibre (Figure 5.8a), the presence of most absorption signals of the extracted bulk chitosan was observed. The absorption signal at 1674 cm^{-1} corresponds to the carbonyl group (C=O) vibration and stretching of Amide I. The peak at 1533 cm^{-1} corresponded to N-H bending and C-N stretching vibrations of the Amide II, while the peak at 1315 cm^{-1} is associated with CH_2 bend, and CH_3 symmetric distortion (Amide III). The signal at 1136 cm^{-1} is assigned to the asymmetric in-phase ring stretch mode, while the peak at 1065 cm^{-1} resulted from C-O-C symmetric stretch in-phase ring of the glucosamine unit (Alhosseini *et al.*, 2012).

The electrospinning of the chitosan solution induced slight modifications in the FTIR spectrum of the nanofibre (ES-D3). There were clear changes in the carbonyl-amide region (from 1000 to 1700) of the spectrum. The characteristic peak observed at 1674 cm^{-1} in the nanofibre spectra, the Amide 1 peak of the electrospun fibres were shifted to a higher wavenumber (from 1660 in PCH21_9 spectra) with an increase in peak intensity. The shift in the frequency may have resulted from the interaction of the carbonyl group (C=O) of the chitosan and the

trifluoroacetate (CF_3COO^-) ions of the electrospinning solvent (Ali *et al.*, n.d, Cooper *et al*., 2011). This interaction resulted in the increased signal of the absorption bands at 1674, 1200, 1136 1065 and 894 cm^{-1} (Sangsanoh and Supaphol, 2006; Torres-Giner *et al*., 2008). Similarly, the N-H functional group of the Amide 11 was observed at a lower absorption band (1533 cm^{-1}) on the ES-D3 spectra. This observation signifies the conversion of the ionic bonds (NH_4^+) to stable amide bonds on interaction with the solvent (Ali *et al.*, n.d, Cooper *et al*., 2011) with an increase in peak intensity when compared to the PCH21_9 spectra.

Generally, all the absorption bands of the ES-D3 exhibited increased absorption peaks (with the exception of the Amide 11 band). The absence of a peak at 1750 - 1776 cm^{-1}, indicates the absence of the carboxylic acid moiety in the nanofibre spectra (Schiffman and Schauer, 2007). This shows that the solvents were reasonably well evaporated during the electrospinning process. The peak at 894 cm^{-1}, which appeared at the same frequency on both spectra, is associated with the saccharide structure of the chitosan (Ibitoye *et al*., 2018). In effect, the characteristic functional groups of the PCH21_9 were preserved in the spectra of ES-D3. The spectra displayed the characteristic N-H and C=O groups, which mostly confers on chitosan its potency in various applications. Thus, the TFA and the electrospinning processes did not alter the chemical structure of the chitosan, rather it increased the intensity of the peaks of most functional groups. Furthermore, the absence of carboxylic acid signal in ES-D3 spectra shows that the solvent completely evaporated from the fibre mats.

The findings of this study corroborate the results obtained by Torres-Giner *et al*. (2008) who reported the retention of the protonated groups of chitosan and high antimicrobial activity of electrospun fibres fabricated from crab shells using TFA-DCM co-solvents. However, this result is in contrast with Schiffman and Schauer (2007) who reported the presence of a carboxylic acid signal at 1750 cm^{-1} in their study of shrimp chitosan electrospun using TFA, an indication that the electrospinning solvent was partly retained in their nanofibres. The ES-D3 were further characterised to determine its thermal behaviour in the next section.

5.3.2 *Thermal gravimetric analysis of the chitosan nanofibres*

Thermal analysis was conducted to investigate the behaviour of ES-D3 under the influence of temperature. The thermal profiles were obtained using a PerkinElmer Pyriss TGA/DTA Analyzer (TG-4000) over a temperature ranging from 20 to 900 $^{\circ}C$ and at a 10 $^{\circ}C$/min heating rate under an inert nitrogen atmosphere. The experimental procedure is presented in Section

3.9.5 of Chapter 3. Figure 5.9 presents the derivative thermograms of the degradation of ES-D3 compared to the PCH21_9 with an inset showing the effect of improper drying of the fibres.

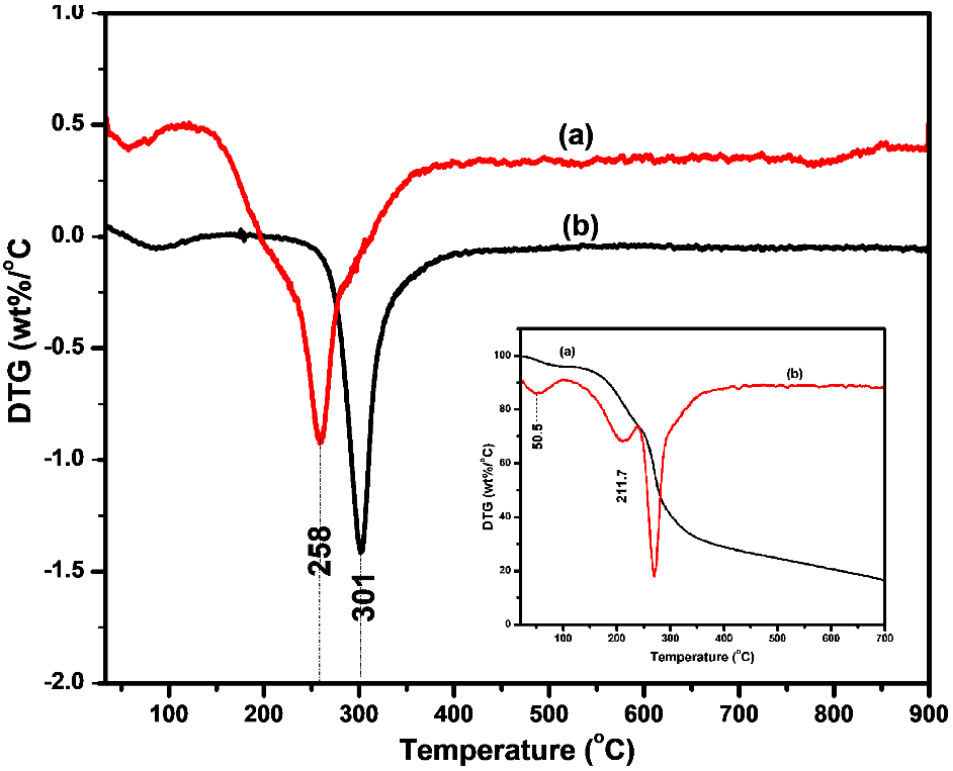

Figure 5. 9: Derivative thermograms of ES-D3 (a) compared to PCH21_9 (b) in nitrogen. Electrospinning conditions: concentration = 5 wt%, voltage = 25 kV, flow rate = 0.3 mL/h and tip-to-collector distance =100 mm. The inset shows TGA and DTG profile of ES-D3 dried for only 2 h.

From Figure 5.9, it could be observed that the DTG profile of ES-D3 has two pronounced decomposition stages. The first stage of decomposition, as described previously (Section 4.4.3), corresponds to the loss of bound or lattice water contained in the nanofibre structure. The temperature at which the maximum water loss occurred was at 57 ˚C (starting from 22 ˚C to 103 ˚C). The weight loss associated with this decomposition (corresponding to water loss) is 6%. In comparison, the PCH21_9 had a maximum water loss at 87 ˚C with a 3% mass reduction. The larger surface area of the ES-D3 and their lower N-acetyl content tends to increase its hygroscopic properties by absorbing moisture from the atmosphere. The second decomposition stage, corresponding to the depolymerisation and decomposition of the structural units and the saccharide backbone of the chitosan (Paulino *et al.*, 2006) was also observed between 134 ˚C and 390 ˚C (Figure 5.9). The maximum amount of the fibres degraded

occurred at 258 ^{o}C. The second stage of degradation was accompanied by a 59% weight loss, indicating pyrolysis.

The TGA in Figure 5.9 shows a third decomposition stage (the inset) with its maximum degradation temperature occurring at 212 $^{\circ}$C. This stage of decomposition involves the evaporation of the remaining trifluoroacetate (CF_3COO^-) component strongly linked to the ES-D3 structure. This is evident by the absence of this degradation stage on the chitosan thermogram (Figure 5.9b) and the profile of ES-D3 (Figure 5.9 inset) dried for a period of 24 h. This stage of degradation (in the inset) was accompanied by a weight loss of 10%.
The inset, therefore, highlights the importance of proper drying and storage of electrospun chitosan nanofibres under dry conditions. Fibres oven-dried at a shorter time had three degradation stages compared to 24 h oven-dried sample, which had two degradation stages synonymous with chitosan. Table 5.2 presents the parameters deduced from the thermal profile of the electrospun BSF chitosan (ES-D3).

Table 5. 2: Parameters deduced from the derivative thermograms of the electrospun BSF chitosan (ES-D3) compared to the extracted bulk BSF chitosan (PCH21-9).

Processes	Parameters	ES-D3	PCH21_9
Evaporation (first stage)	Temperature ($^{\circ}$C)	22 – 103	20 – 128
	T_{me} ($^{\circ}$C)	57	82
	Mass loss (%)	6	3
Degradation (second stage)	Temperature ($^{\circ}$C)	134 – 390	224 – 402
	T_{md} ($^{\circ}$C)	258	301
	Mass loss (%)	59	46
Degradation (third stage) (Inset)	Temperature ($^{\circ}$C)	112 - 239	-
	T_{md} ($^{\circ}$C)	212	-
	Mass loss (%)	10	-

T_{me} = temperature of maximum evaporation; T_{md} = temperature of maximum degradation.

The thermal studies have shown that the electrospinning process influenced the thermal properties of ES-D3. The nanofibre (ES-D3) has reduced thermal stability compared to PCH21_9. This may also have resulted from the interaction of the chitosan molecules with the trifluoroacetate ions, which in turn affected the *N*-acetyl content of the chitosan (Nam *et al*., 2010). The results obtained in this study corroborates the findings of Cooper *et al*. (2011) who fabricated chitosan nanofibres via electrospinning technique using TFA/MC (methylene

chloride) mixed solvents. The structural properties of ES-D3 were further examined in the next section using the X-ray diffraction technique.

5.3.3 *Structural properties of BSF nanofibre*

To investigate the variations in the structure of PCH21_9 as a result of electrospinning, the nanofibres (ES-D3) were characterised using X-ray diffraction technique (XRD). The XRD protocol is described in Section 3.9.5 of Chapter 3. The X-ray profiles of the bulk BSF chitosan and the electrospun nanofibres are shown in Figure 5.10.

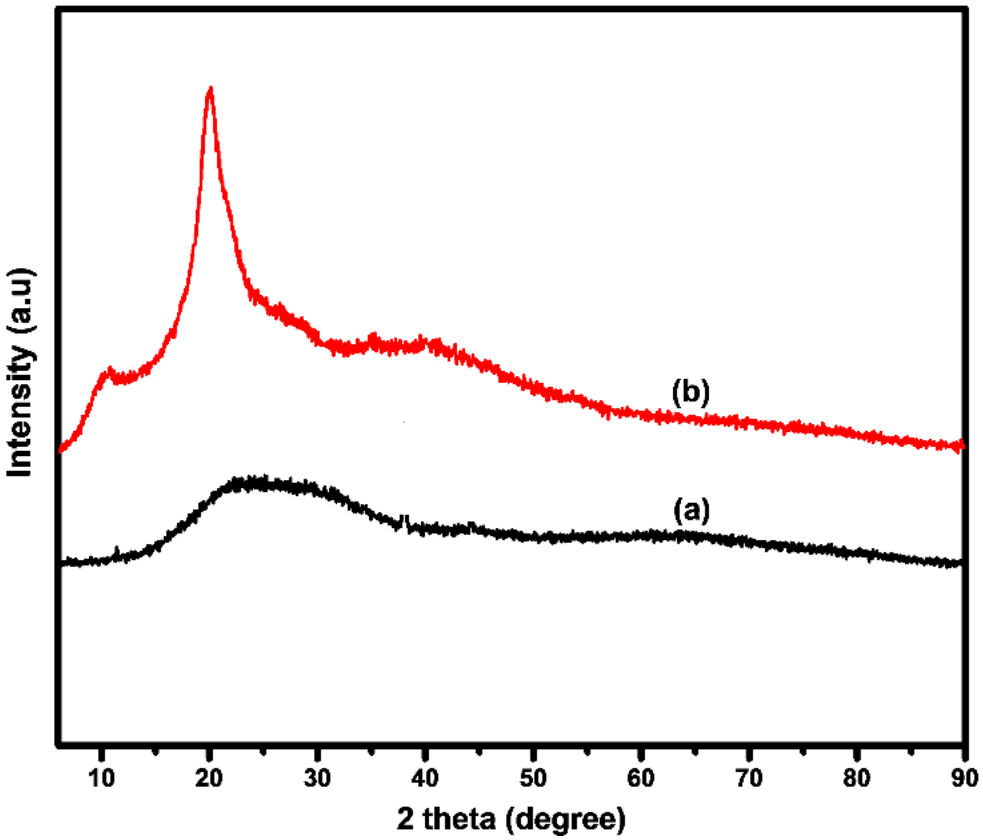

Figure 5. 10: X-ray profiles of the ES-D3 (a) at optimum conditions compared to the extracted PCH21_9 (b). Electrospinning conditions are: concentration = 5 wt%, voltage = 25 kV, flow rate = 0.3 mL/h and tip-to-collector distance =100 mm.

Figure 5.10a shows that ES-D3 displayed a lower ordered structure than PCH21_9. Figure 5.10b displayed well-defined reflections characterising chitosan which depicts a more intense band at 2θ = 10.5° and 20.10° with a broad shoulder at 2θ = 40.50° for PCH21_9. These peaks were not visible on the spectra of ES-D3 (Figure 5.10a). The peak at 2θ = 20.10° and 22.30-32.10° for PCH21_9 and ES-D3, respectively corresponds to the (110) plane of chitosan. The

lack of this peak is an indication of decreasing order and could be due to the random disruption of ordered -OH groups on the chitosan backbone (Cooper *et al*., 2011).

Various studies have reported the structural features of electrospun polymers. Hadjizadeh *et al*. (2011) have stated that most electrospun chitosan mats exhibit both disordered and ordered reflections and they were attributed to the semi-crystalline structure of the polymer. Rathna *et al.* (2013) had reported the structural disorder and lack of repeating long-range order of electrospun polymers results from the limited time of flight, the processes of solvent evaporation and fibre solidification. They further argued that these conditions might affect the regular arrangement of the subunits of the molecules leading to the formation of disordered polymers. Kim *et al*. (2004) have opined that the presence of ordered repeating units in the backbone of a structure produces XRD profiles with increased intensities while disordered polymers show broad bands.

Therefore, the electrospinning process in this study affected the regular, repeating arrangement of the unit cells of PCH21_9. As a result, the order of the ES-D3 was reduced and the intensity of the peaks decreased, favouring the formation of disordered structure in comparison with the PCH21_9. The next section describes in detail the characterisation of the BSF nanoparticles synthesised in this study.

5.4: Synthesis and characterisation of chitosan nanoparticles

This section details the result of the characterisation of the synthesised nanoparticles in this study. The nanoparticles were synthesised by chance during the optimisation process for the electrospinning of PCH21_9. Attempts to optimise the electrospraying parameters resulted to either beaded nanofibres or creamy coloured chitosan films. The nanoparticles were, therefore, synthesised using 6 wt% PCH21_9 dissolved in aqueous TFA in a ratio of 9:1 (TFA: deionised water). The experimental detail is presented in Section 3.3 of Chapter 3. The BSF chitosan nanoparticles is denoted as BSF_NPs. Figure 5.11 shows the BSF_NPs on an aluminium foil collector (A) and patterns left when scrapped off the collector. Section 5.4.1 presents the FTIR characterisation of the BSF_NPs.

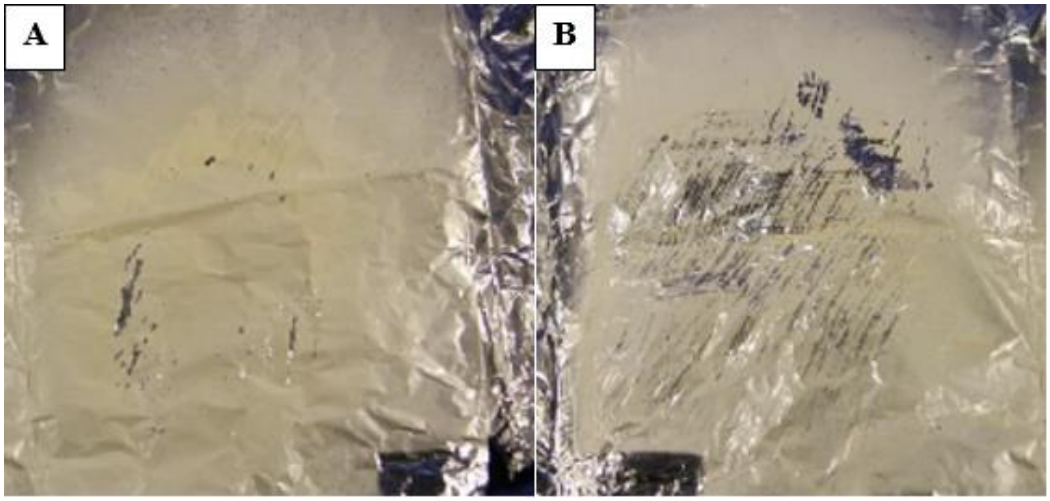

Figure 5. 11: A) nanoparticles deposited on aluminium collector, B) BSF_NPs scrapped of the collector. The PCH21_9 sample was electrosprayed and the particles deposited on the aluminium collector as brownish-powdery substances.

5.4.1 *FTIR analysis*

The FTIR of the obtained BSF_NPs were compared to the extracted chitosan (ES-D3) presented as PCH21_9 in this section and onwards. This was to ascertain if there were observed differences in the spectrum of the nanoparticles. The detailed protocol of the analysis is presented in Section 3.9.3 of Chapter 3.

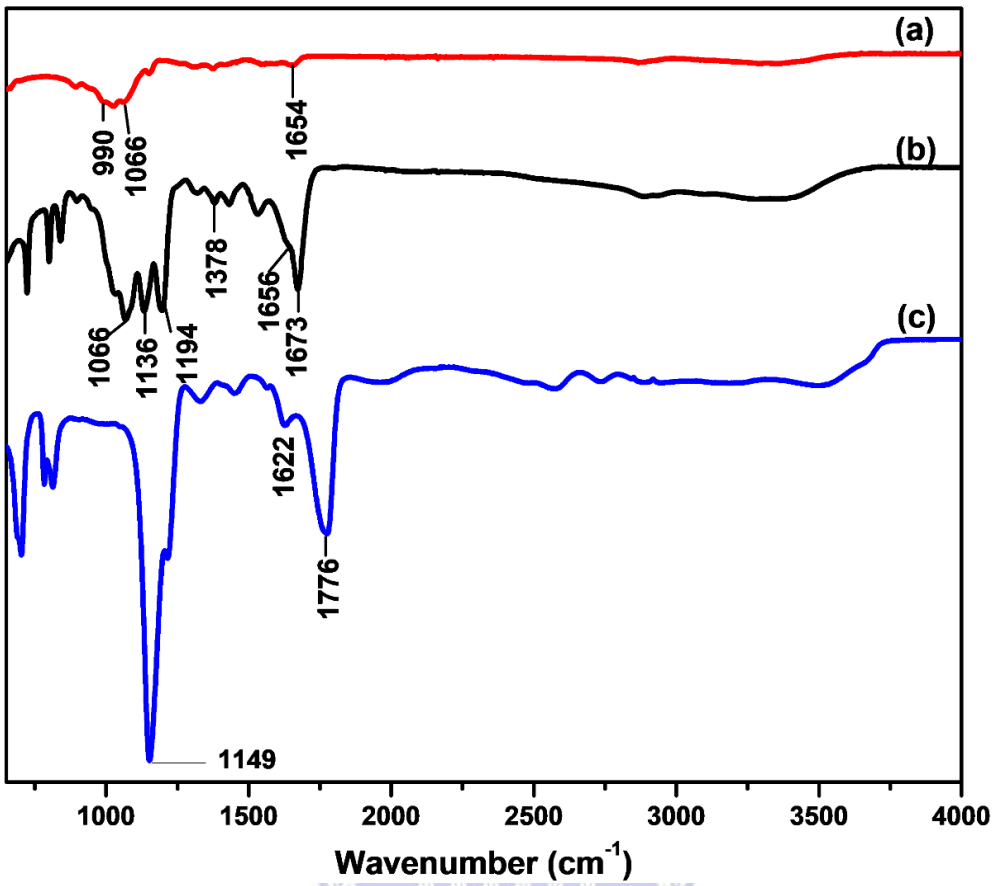

Figure 5. 12: FTIR spectra of PCH21_9 (a), BSF_NPs (b) and the solvent TFA (c) showing the variations in the functional groups of each spectrum. Electrospraying conditions are concentration - 6 wt%, applied voltage - 25 kV, collector distance - 100 mm and flow rate - 0.6 mL/hr.

The spectra of the nanoparticles (Figure 5.12b) displayed similar spectral features as ES-D3 shown in Figure 5.8b of Section 5.3.1. The broad absorption band at 3154 – 3475 cm^{-1} is due to the characteristic OH group signal and indicates an enhanced hydrogen bonding on the BSF_NPs structure. The absorption band at 1673 and 1656 cm^{-1} corresponds to the carbonyl group (C=O) vibration and stretching of Amide 1. The signal at 1526 cm^{-1} was assigned to the N-H bend, C-N stretch (the characteristic band for Amide 11), while the peak at 1378 cm^{-1} is associated with the CH_2 bend, CH_3 symmetric distortion (amide 111). The peak at 1136 cm^{-1} was assigned to asymmetric in-phase ring stretch mode, while the band at 1066 cm^{-1} corresponds to the C-O-C symmetric stretch in-phase ring of the glucosamine unit (Alhosseini *et al*., 2012).

Since the spectra of BSF_NPs and ES-D3 (BSF chitosan nanofibre) were similar, the descriptions of all the functional groups as detailed in Section 5.3.1 will suffice. The surface morphology of the BSF_NPs is discussed next.

5.4.2 *High-resolution scanning electron microscopy analysis*

The HRSEM of the PCH21_9 and the BSF_NPs were studied to ascertain if there were observed differences in the surface morphologies of the two samples. The analysis was conducted according to the description detailed in Section 3.9.6 of Chapter 3. Figure 5.13 (A and B) showed that there was a marked difference in the observed morphologies of both samples as the BSF_NPs had a significant reduction in the particle size to a nano-scale range for polymeric materials.

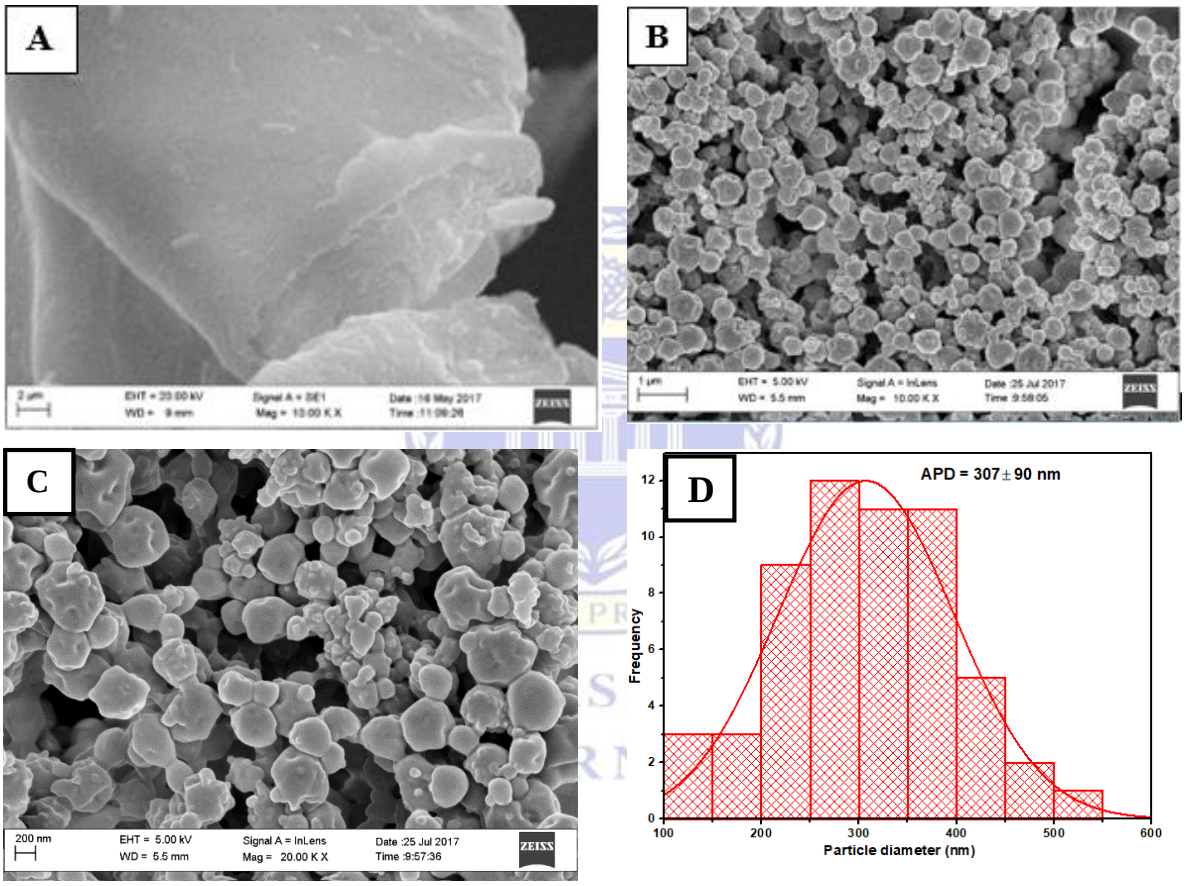

Figure 5. 13: Micrographs of (A) PCH21_9) (B) BSF_NPs (C) higher magnification of the (B) and the particle size distributions of the BSF_NPs (D). Electrospraying conditions are concentration - 6 wt%, applied voltage - 25 kV, collector distance - 100 mm and flow rate - 0.6 mL/hr.

Figure 5.13A showed that the PCH21_9 had a smooth surface with no particle formation. Following the electrospraying of the chitosan, irregularly shaped nanoparticles of fairly uniform distribution with an average particle diameter of 307±90 nm were formed (Figure 5.13B). The process of electrospraying broke the particles of PCH21_9 into smaller sizes of nanometer range. Increase in the magnification revealed that some of the BSF_NPs displayed

crevices on their surfaces as could be seen in Figure 5.13C. The occurrence of crevices is a regular feature on polymeric particles obtained by electrospraying technique (Zhang and Kawakami, 2010). Zhang and Kawakami (2010) had explained that the presence of crevices results from the drying and shrinkage of the samples as the electrospinning solvent evaporates on interaction with the electric field. The HRSEM analysis shows that there were variations in the surface morphologies of the PCH21_9 and the synthesised BSF_NPs. The hydrodynamic properties of PCH21_9 and the BSF_NPs were further investigated and is discussed in the next section.

5.4.3 *Hydrodynamic parameters determination*

a. Particle size

The experiment was carried out to determine the particle size of the samples in solution. The hydrodynamic particle size of both the PCH21_9 and the BSF_NPs were determined using Nano ZS90 Zetasizer equipment (UK). The detailed description of the analysis is in Section 3.9.14 of Chapter 3. Figures 5.17 presents the average hydrodynamic particle size distributions of both samples.

			Size (d.nm):	% Intensity:	St Dev (d.nm):
Z-Average (d.nm):	1436	Peak 1:	4170	70,2	854,4
PdI:	0,704	Peak 2:	494,8	29,8	69,34
Intercept:	0,964	Peak 3:	0,000	0,0	0,000
Result quality :	Refer to quality report				

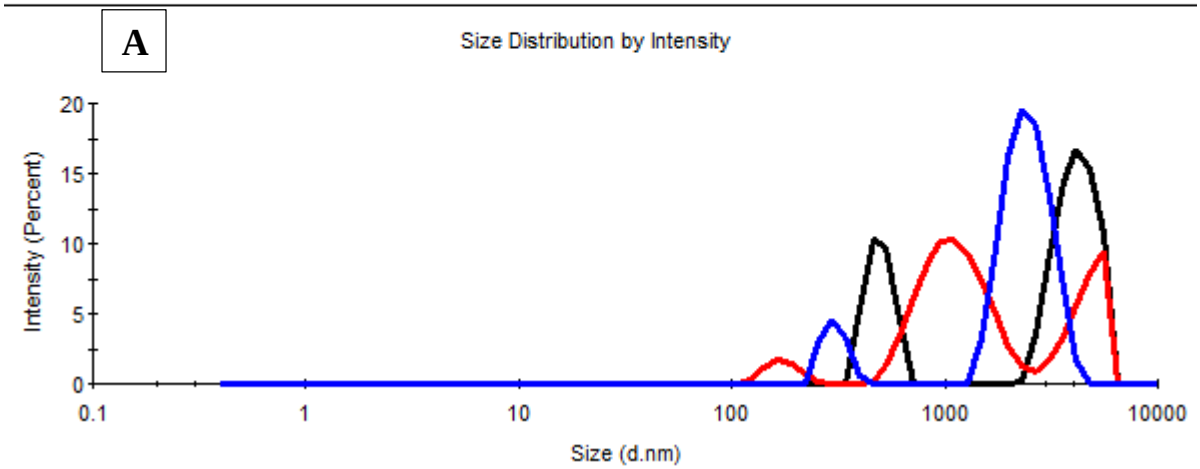

			Size (d.nm):	% Intensity:	St Dev (d.nm):
Z-Average (d.nm):	286,0	Peak 1:	332,2	100,0	97,68
PdI:	0,160	Peak 2:	0,000	0,0	0,000
Intercept:	0,864	Peak 3:	0,000	0,0	0,000
Result quality :	Refer to quality report				

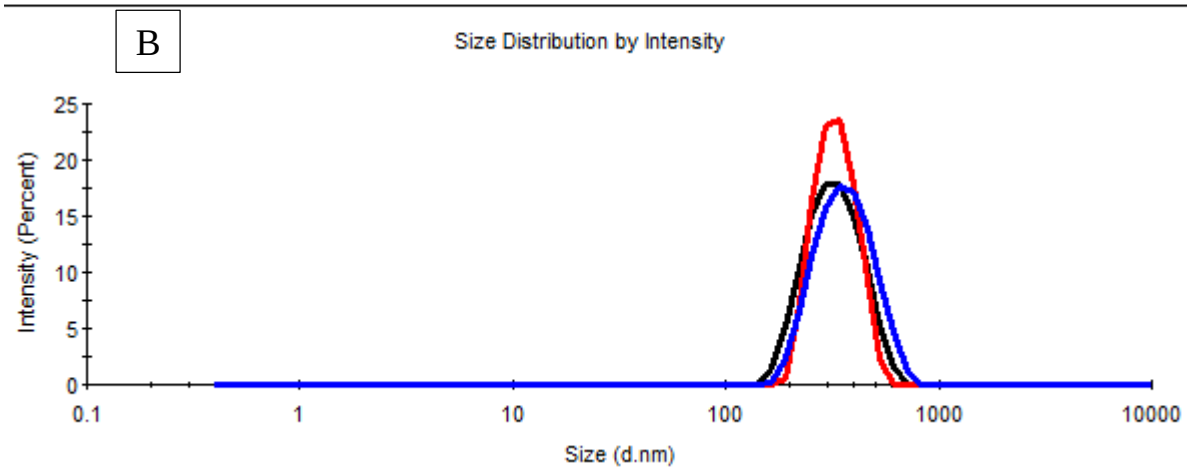

Figure 5. 14: The particle size distribution of (A) PCH21_9 and (B) BSF_NPs measured by laser diffraction spectrometry.

From Figure 5.14A, the particle sizes of the PCH21_9 in solution were not uniform as shown by the series of peaks displayed on the graph. The hydrodynamic particle size ranged from 200 nm to 7000 nm with most of the particles having values of 1000 nm and above. The average

particle size was determined to be 1436±854 nm. However, a fairly uniform particle size distribution was observed for the BSF_NPs. The average size of 286±98 nm was obtained after electrospraying the PCH21_9, and the sample electrophoretically analysed (Figure 5.14B). Electrospraying led to a 402% reduction in the particle size of the PCH21_9 to nanoscale size. The obtained result (286±98 nm) is in agreement with the result obtained from HRSEM analysis (307±90 nm) with only a slight (7%) difference in size.

It is pertinent to note that the definition of nanomaterial is not restricted to materials with a size lower than 100 nm. Polymeric particles have unique properties and Jahangiri and Barghi (2018) have stated that polymer particles within a range of 10 to 1000 nm fall within the purview of polymeric nanoparticles due to their ability to penetrate the cell wall of microorganisms and induce lysis. This drastic hydrodynamic size reduction observed on the BSF_NPs solution could be as a result of the Coulomb force acting on the BSF_NPs solution arising from the high electrical field interaction during synthesis and acts on the chitosan solution droplet causing its breakage into nanoparticles (Bock *et al.*, 2011).

The result of the hydrodynamic particle size of the nanoparticles (BSF_NPs) obtained in this study corroborates the findings of Soppimath *et al.* (2001) who obtained particle sizes ranging from 200 – 1000 nm and Yien *et al.* (2012) whose study on the correlation between the physical properties of chitosan nanoparticles obtained by ionic gelation method and their antifungal activities yielded particles with size ranges of 101 – 348 nm. The BSF_NPs could, therefore, be said to fall within the sizes generally referred to as nanoparticles.

b. Surface charge/zeta potential

The investigation was conducted to determine the electrical charge on the particles of the PCH21_9 and BSF_NPs in solution. It also determines the magnitude of these charges which will, in turn, determine the extent of the attraction or repulsion exhibited by these particles in solution. The zeta potential (ZP) of the samples was measured using a Zetasizer Nano-ZS90 (Malvern Instruments, Malvern, UK). The analysis was performed as described in Section 3.9.14 of Chapter 3. Figure 5.15 shows the obtained ZP values for both extracted PCH21_9 or BSF_NPs.

		Mean (mV)	Area (%)	St Dev (mV)
Zeta Potential (mV): 29,3	Peak 1:	33,6	100,0	6,42
Zeta Deviation (mV): 37,3	Peak 2:	0,00	0,0	0,00
Conductivity (mS/cm): 0,0777	Peak 3:	0,00	0,0	0,00

Result quality : See result quality report

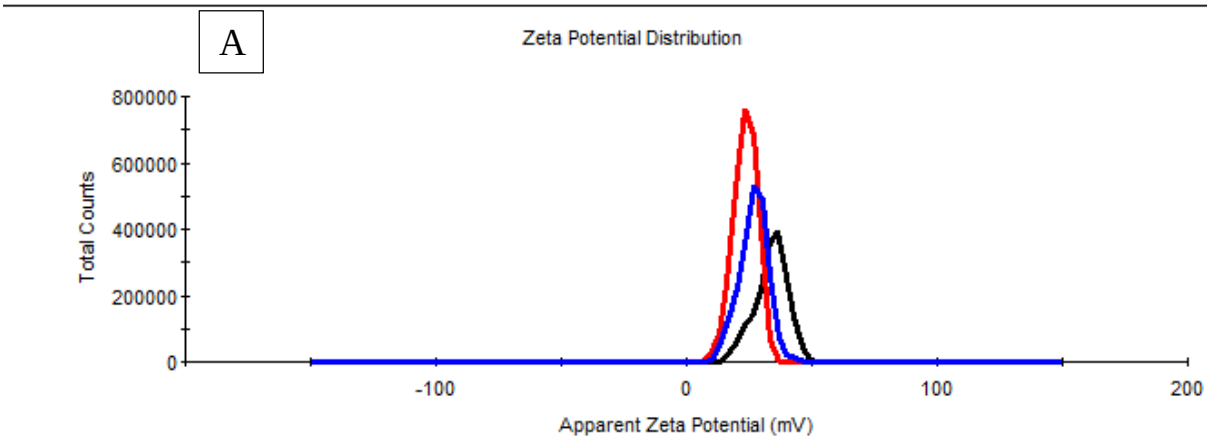

		Mean (mV)	Area (%)	St Dev (mV)
Zeta Potential (mV): 54,7	Peak 1:	54,7	100,0	2,96
Zeta Deviation (mV): 2,96	Peak 2:	0,00	0,0	0,00
Conductivity (mS/cm): 0,760	Peak 3:	0,00	0,0	0,00

Result quality : Good

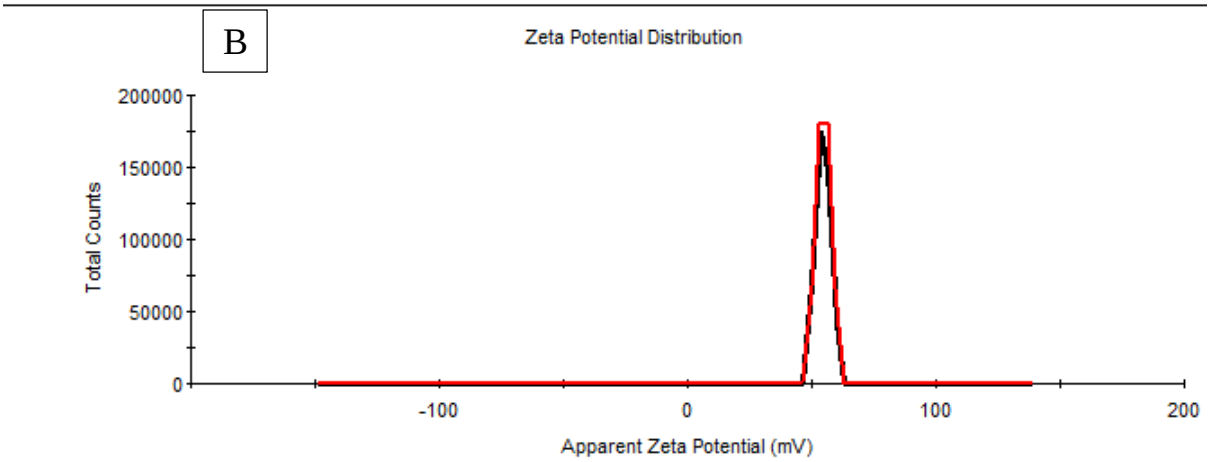

Figure 5. 15: The ZP profiles of (A) PCH21_9 and (B) BSF_NPs showing a noticeable increase in potential values of the nanoparticles.

Figure 5.15 present the ZP of the PCH21_9 and the BSF_NPs. The result showed a net positive surface charge for both samples, an indication of the cationic nature of chitosan in solution. The PCH21_9 had a value of 29.3±6.42 mV. On electrospraying of PCH21_9 to BSF_NPs, the

potential value increased to 54.7±2.96 mV. This signifies an 87% increase in the ZP value. The increase could be due to the capability of BSF_NPs to accommodate some of the current interacting with it on atomisation and flight time during the electrospraying process. The ZP is the potential difference inherent on the layer of a charged particle. It gives information on the surface charge of a particle, the magnitude of the charge, the stability and the overall quality of a suspension (Lu *et al.,* 2018). The ZP is important and contributes significantly to determining the antimicrobial effect of samples and their level of interactions with negatively charged microbial surfaces (Chen *et al.,* 2010). High ZP value is significant in microbial studies as it affects the cell binding ability of the material and also influences the stability of a suspension (Kong *et al*., 2010). Marsalek (2014) had stated that a ZP value less than ±30 mV indicate the tendency of suspended particles to agglomerate while above ±30 mV shows the stability of the particles in suspension due to inhibition of aggregation by the high surface charge. A ZP value of zero, referred to as the isoelectric point, is the most expressive indication that the particles will precipitate/flocculate (Delgado *et al*., 2007; Marsalek, 2014; Shamsa *et al*., 2018). The high zeta potential value of 54.7±2.96 mV for the BSF_NPs shows that the particles were stable in suspension while that of the PCH21_9 (29.3±6.42 mV) might not be stable in suspension.

Previous studies have synthesised chitosan nanoparticles with varying ZP values. Costa *et al.* (2018) reported a ZP of 27.1 mV in their investigation of chitosan as inhibitors of antibiotic-resistant skin microorganisms, while Loutfy *et al.* (2016) synthesised chitosan nanoparticles by ionic gelation method using tripolyphosphate and obtained a surface charge of 40 mV. Madureira *et al.* (2015) reported a ZP of 21.7 mV in their study of chitosan nanoparticles as an antimicrobial agent against food pathogens, while Silva *et al*. (2015) reported a value of 22.9 mV on the investigation of chitosan nanoparticles as drug delivery medium for ocular treatment.

The surface charges reported by Costa *et al.* (2018), Loutfy *et al.* (2016) and Madureira *et al.* (2015) were all lower than the value reported in this study. The underlying difference could have resulted from the method of preparation. The studies of Costa *et al.* (2018), Loutfy *et al.* (2016) and Madureira *et al.* (2015) utilised the ionic gelation method in the nanoparticle preparation while this study adopted the electrospraying technique. Therefore, the electrospraying process and also the source of the chitosan could have contributed to the increased ZP value obtained in this study.

c. The polydispersity index (PdI)

The polydispersity index (PdI) of chitosan nanoparticles show how homogenous or heterogenous the particles of the samples are in suspension. Low values indicate homogenous and uniform particles while values above 0.5 are an indication of a higher heterogeneity of the sample particles. PdI values range from zero to one. PdI measurement of BSF_NPs is very important because it is an indication of possible agglomeration or stability of the particles in solution. Figure 5.14 shows a drastic change in PdI values as the PCH21_9 undergo the electrospraying process. The values reduced from 0.704 in PCH21_9 (Figure 5.14A) to 0.160 in the BSF_NPs (Figure 5.14B). This decrease may have resulted from the reduced MW of the BSF_NPs due to the coulombic forces acting on the sample induced by the electric field. The obtained value of 0.160 for BSF_NPs is, however, slightly higher than the recommended value (0.07) for a homogeneous suspension as described in ISO 224122 (2017) and shows that the BSF_NPs is slightly heterogeneous in size. The heterogeneity is well pronounced in the PCH21_9 samples as shown in Figure 5.14.

5.5 Chapter summary

Electrospinning, a process that utilises electrical force to produce fibres from polymer solutions, is a special technique for the fabrication of nanofibres from both biological and synthetic polymers with unique and controllable features. This process was adopted in this study aimed at synthesising bead-free nanofibres from a pure BSF chitosan (PCH21_9) solution in TFA. The electrospinning of pure chitosan has been challenging to researchers over the years. Thus, the need to blend chitosan with synthetic polymers by various researchers. After many trials and optimisation of electrospinning conditions, this chapter recorded success without the addition of synthetic polymers. The optimised electrospinning conditions determined were a chitosan concentration of 5 wt%; applied voltage of 25 kV; solution flow rate of 0.3 mL/h and a collector distance of 100 mm. The chitosan nanofibres (ES-D3) obtained at the optimum conditions had diameters ranging between 80 - 180 nm with an optimised average fibre diameter of 128 nm.

Investigation using FTIR showed that the chemical structure of the biopolymer did not change during the electrospinning process. It further showed that the fibres maintained the Amide 1,11 and 111 functional groups inherent in bulk BSF chitosan (PCH21_9). However, the Amide 1 signal shifted to a higher wavenumber while Amide 11 was observed at a lower wavelength with all having increased intensity, an indication of the formation of a stable amide bond. The structural studies conducted using XRD revealed that the chitosan nanofibres were disordered

with broad absorption shoulders. The thermal studies showed that the electrospinning process influenced the thermal properties of the electrospun nanofibres, imparting reduced thermal stability compared to the extracted bulk chitosan. The TGA results presented the thermal properties of the electrospun fibres and further revealed the importance of proper drying and storage of nanofibres in a moisture-free environment.

The synthesised nanoparticles (BSF_NPs) displayed the same spectral features as the nanofibres (ES-D3) when studied with FTIR in this study. However, their morphologies differ significantly from both the PCH21_9 and the ES-D3 under HRSEM. The BSF_NPs had particles sizes ranging from 100 – 800 nm while the PCH21_9 ranged from 350 to 8000 nm, an indication of transformation from bulky samples to nano sizes. Further examination of the hydrodynamic parameters of the BSF_NPS yielded the zeta potential, hydrodynamic size and the polydispersity index. The hydrodynamic particle size was determined to be 289±98 nm, 402% less than the size of the PCH21_9. This size falls within the definition of polymeric nanomaterials. The zeta potential of the BSF_NPs in solution was determined to be higher than the PCH21_9 at 54.7±2.96 mV, an indication of its cationic nature and sample stability in solution. However, the particles were slightly heterogenous as shown by the PdI value of 0.16.

Therefore, bead-free homogenous nanofibres with a smaller diameter suitable for varied applications were successfully fabricated via electrospinning of the extracted BSF chitosan. Furthermore, the nanoparticles have improved physicochemical properties after electrospraying and points to its potency in antimicrobial, medical and biomedical applications.

CHAPTER 6

CROSSLINKING OF BSF CHITOSAN NANOFIBRES

6.0 Introduction

In this chapter, the nanofibres obtained in Chapter 5 were crosslinked with tannic acid (TA) for stability in aqueous media. The concentration of the crosslinker solutions was varied in the process to determine the optimal concentration. This chapter also investigated the solubility tests of the crosslinked adsorbents in different media of 1.0 M acetic acid (AA), deionised water or 1.0 M NaOH at ambient conditions. In addition, since the mats will be applied for adsorption studies, the mat from the optimal crosslinker concentration and the solubility studies was subjected to a swelling test to determine the extent of its moisture absorption. Furthermore, the obtained adsorbent was characterised by FTIR and TGA to investigate its chemical and thermal properties.

6.1 Crosslinking of nanofibres using tannic acid

In this section, the stability of the BSF chitosan nanofibrous mats in aqueous solution was improved by the crosslinking process using tannic acid. The investigation followed the two-step crosslinking method where the electrospun nanofibres (optimised in Sections 5.2.1 - 5.2.4 of Chapter 5) were introduced into the three concentrations of TA solutions. The aim was to determine the concentration (wt%) of the crosslinker that would stabilise and maintain the fibrous structures of the electrospun mats after immersion in solutions of AA, water and NaOH over a period of 10 minutes or 72 h. The experimental protocol coded as TA_CHS_1, TA_CHS_2 and TA_CHS_3 for 3, 5 and 7 wt% TA solutions are presented in Section 3.5.5 of Chapter 3. The outcomes of these investigations were captured using HRSEM and the micrographs are presented in Figure 6.1.

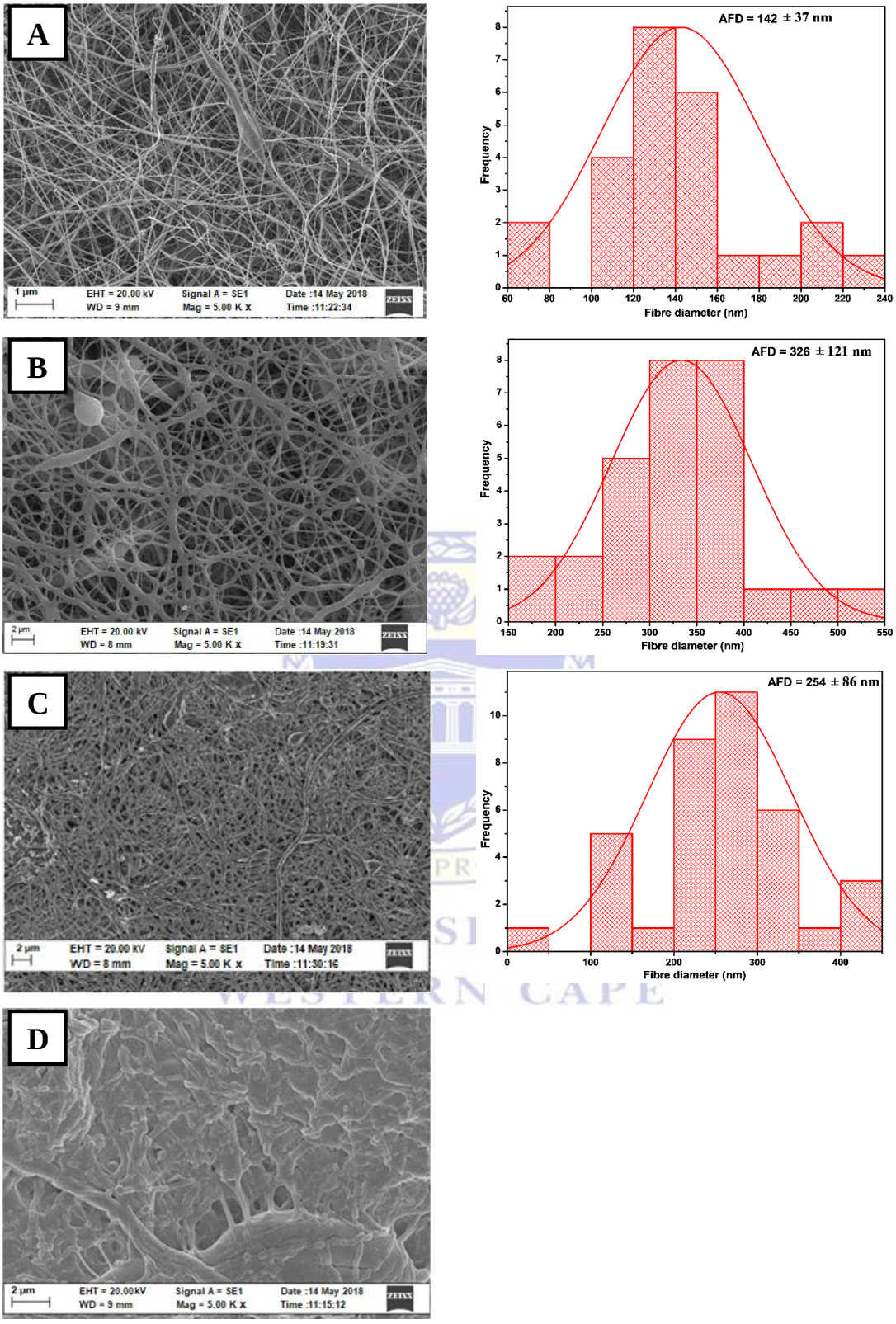

Figure 6. 1: HRSEM images of (A) as-spun chitosan nanofibrous membrane (B) TA_CHS_1, (C) TA_CHS_2, (D) TA_CHS_3 and their corresponding fibre distributions.

Crosslinking of chitosan fibres with a known crosslinking agent plays an important role in ensuring the stability of fibre mats. After crosslinking, the fibres appeared brown in colour while uncrosslinked nanofibres appeared white. Before the crosslinking, the average diameter of the electrospun fibres was 142 ± 65 nm (Figure 6.1A). Crosslinking with 3 wt% TA (TA_CHS_1) altered the appearance of the fibres. The fibres became non-uniformly branched with ribbon-like shapes and occasional joints along its lengths. The crosslinking influenced the fibre distribution with the diameter increasing far above the as-spun uncrosslinked mats and averaging at 326 ± 121 nm (Figure 6.1B), a 131% increase from the uncrosslinked fibres. The increase in fibre diameter in TA_CHS_1 may be that the crosslinks were formed at a slow pace within the polymer chain due to the low concentration of the TA. The reduced concentration which could not induce a complete crosslink of the fibre may have led to the absorption of moisture in the TA_CHS_1 crosslinked fibres which could have influenced the increase in fibre diameter (Sionkowska *et al.,* 2015).

Figure 6.1C shows that as the concentration of the TA increased, the fibre diameter of TA_CHS_2 decreased with mostly unbranched cylindrical fibres contrary to TA_CHS_1 branched fibres. The TA_CHS_2 retained its fibrous structure with an average fibre diameter of 254 ± 86 nm. This average fibre diameter was 79% higher than the as-spun chitosan and 22% less than the TA_CHS_1 fibre. The observed increase in fibre diameter both in TA_CHS_1 or TA_CHS_2 micrographs compared to the as-spun CHS nanofibres may have resulted from initial modification of the CHS backbone by the TA crosslinker. This modification and increased interaction could have led to the formation of a strong polymer chain with the crosslinker bonds and thus prevent the thinning of the fibres (Kaczmarek *et al*., 2019). But as the concentration of TA increased in the crosslinking solution, the chain repulsion and/or the swelling capability of the fibres decreased. The decreased fibre diameter observed on TA_CHS_2 compared to the TA_CHS_1 micrograph may have resulted from low water penetration into the fibre mats due to enhanced crosslinking by the TA. Increase in the concentration of the crosslinking agent (TA) tends to fuse the fibres together hence the observed differences in the individual fibre distances from each other in the micrographs. The TA_CHS_1 fibres were clearly separated from one another and were linked by occasioned branching in some instances. In the TA_CHS_2, the fibres were very close to one another while TA_CHS_3 shrank and were all fused together owing to the increased concentration of the TA crosslinking agent.

The reduction in size, shrinking and fusing together of the fibres as the concentration increased from TA_CHS_1 to TA_CHS_3 could be due to the extensive and immediate crosslinking of the fibres. After full crosslinking of the fibre chains, the excess of the crosslinking agent still acted on the fibres leading to shrinking and eventual fusing together as observed in the micrograph of TA_CHS_3.

Crosslinking enables the functional groups on the TA to interact with the amino and hydroxyl groups of CHS thereby reducing the number of amino groups facilitating the interaction with water molecules. N-acetylation can be formed with some crosslinking agents on the chitosan backbone in the presence of water. Here, the reduction of hydrophilic groups by N-acetylation would decrease the solubility of the crosslinked films (Rubentheren *et al*., 2015). Rubentheren and co-workers reported that this could have resulted from the reaction between the carboxylic group and the amino group to form an amide, causing the elimination of water in the process. Rivero *et al*. (2010), and Kadam and Lele (2018) observed that crosslinking chitosan film with tannic acid reduced the ability of the film to absorb moisture. The next section examined the solubility of the crosslinked materials in aqueous solutions.

6.2 Solubility/stability tests of the crosslinked adsorbents

The morphologies of the crosslinked membranes at various concentrations of the TA have been ascertained in Section 6.1. To further justify the optimal crosslinking condition, the mats were subjected to solubility/stability tests. This subsection investigated the stability of the TA_CHS_1, TA_CHS_2, TA_CHS_3 and the as-spun mats in aqueous, neutral and basic media at varying time intervals. A definite size and mass of the adsorbents was cut and placed in separate beakers containing the test solutions with constant stirring. The solubility of the mats was measured using a spectrometer and visual examination after 10 mins or 72 h of immersion. The experimental protocol is as described in Section 3.3.6 of Chapter 3. Figure 6.2 presents the bar charts of the solubility studies conducted on the crosslinked nanofibrous membranes at various conditions.

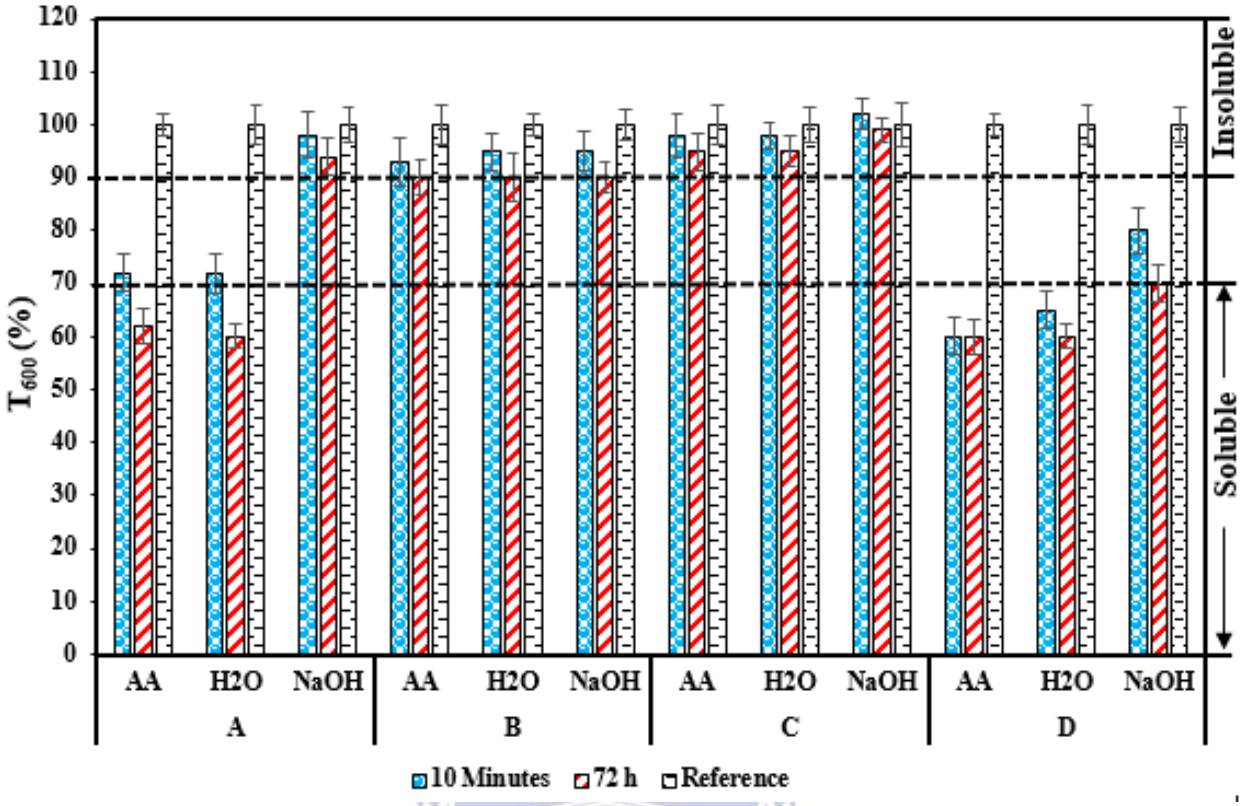

Figure 6. 2: Stability results of crosslinked mats (A = TA_CHS_1, B = TA_CHS_2, C = TA_CHS_3 and D = as-spun chitosan mats which served as control) in 1.0 M AA, deionised water or 1.0 M NaOH after 10 min or 72 h immersion measured as percentage solution transmittance at 600 nm using a spectrophotometer. Reference = test solutions without the mats (crosslinked or as-spun nanofibres).

From Figure 6.2, the stability of the crosslinked nanofibre mats in acidic, neutral and basic media was investigated after 10 minutes or 72 h. It was determined that the higher the solubility of the mats, the lower the transmittance value of the solutions. Depending on the stability of the crosslinked fibre mats in the solutions investigated, the percentage transmittances obtained were in the range of 60 - 102%. Variation of light transmittance was explained in terms of solubility, partial solubility or insolubility of the TA crosslinked fibres mats. Fully soluble mats had lower transmittance values than partially soluble mats and the insoluble mats. The transmittance values (T_{600}) combined with a visual examination (VE) of the fibres after immersion in the solutions were used to arrive at the outcome about the stability of each crosslinked mat in the three media studied. The percentage transmittances of the solutions (1.0 M acetic acid, distilled water or 1.0 M NaOH solutions) after 10 minutes or 72 h of immersion of the fibres with stirring at 200 rpm were in the order of insoluble mats > partially soluble mats > soluble mats (Figure 6.2). The designation of soluble, partially soluble and insoluble in this study is explained thus: when the fibres were visually observable in the solution after

stirring and at the same time the % transmittance of an aliquot of the solution was between 70% and 90%, the fibres were designated as partially soluble in the given solution. Additionally, if the fibres were visually observed in the given solution and the % transmittance value of an aliquot of the solution was above 90%, it is an indication that the fibres were insoluble over the period of study in the given solution(s). Furthermore, if the fibres were not observed in the solution(s) after 10 minutes or 72 h and the % transmittance was less than 70%, it is an indication that the fibres were completely soluble in the solution.

The TA_CHS_1 were partially soluble after 10 minutes when immersed in both 1.0 M AA and distilled water but were insoluble in 1.0 M NaOH solution. However, after 72 h immersion in 1.0 M AA and distilled water with stirring at 200 rpm, both visual examination and transmittance values show that the fibres were completely soluble except in 1.0 M NaOH solution. The TA_CHS_2 were insoluble in the three solutions of 1.0 M AA and distilled water and 1.0 M NaOH after 10 minutes or 72 h as the % transmittances of an aliquot of the three solutions were greater than 90%. Similarly, the TA_CHS_3 were insoluble in all the solutions as the mats were visually observable in the solutions and the transmittance values were ≥ 90%. The as-spun, uncrosslinked CHS, mats were soluble in both 1.0 M AA and deionised water throughout the studied time intervals but partially soluble in 1.0 M NaOH solution. Li *et al*. (2013) have opined that electrospun chitosan nanofibres are not stable as they tend to dissolve instantly when in contact with aqueous solutions. This phenomenon, they stated, resulted from the protonation of the amino groups ($-NH_2$) of the chitosan which causes the insoluble group to be converted to soluble salts ($-NH_3^+$).

The incorporation of TA crosslinker to the fibres improved their stability in aqueous solutions. The improvement in stability resulted from the modification of the $-NH_2$ groups of the CHS by the TA and probably the complexation of CHS with gallic acid dimers formed by the decomposition of TA (Aelenei *et al*., 2009). Table 6.1 present the comprehensive stability results of the adsorbents in various media.

Table 6. 1: The comprehensive stability results of the adsorbents in various media.

	10 minutes			72 h		
CHS mats	Visual examination	T_{600}	Remarks	Visual examination	T_{600}	Remarks
1 M AA (pH 3)						
As-spun CHS	No	60	Soluble	No	60	Soluble
TA_CHS_1	Yes	72	Partially soluble	No	62	Soluble
TA_CHS_2	Yes	93	Insoluble	Yes	90	Insoluble
TA_CHS_3	Yes	98	Insoluble	Yes	95	Insoluble
1.0 M AA (Ref.)	--	100	--	--	100	--
Distilled water (pH 6.5)						
As-spun CHS	No	65	Soluble	No	60	Soluble
TA_CHS_1	Yes	72	Partially soluble	No	60	Soluble
TA_CHS_2	Yes	95	Insoluble	Yes	90	Insoluble
TA_CHS_3	Yes	98	Insoluble	Yes	95	Insoluble
Distilled water (Ref.)	--	100	--	--	100	--
1.0 M NaOH (pH 13)						
As-spun CHS	Yes	80	Partially soluble	Yes	70	Partially soluble
TA_CHS_1	Yes	98	Insoluble	Yes	94	Insoluble
TA_CHS_2	Yes	95	Insoluble	Yes	90	Insoluble
TA_CHS_3	Yes	102	Insoluble	Yes	99	Insoluble
1.0 M NaOH (Ref.)	--	100	--	--	100	--

Ref. = Reference/control sample

Table 6.1 presents the result of the stability studies of the nanofibrous mats in 1.0 M AA, water and 1.0 M NaOH solutions. The percentage transmittance of the solutions in contact with the mats coupled with the visual examination of the fibres in the solutions jointly determined the stability/solubility or otherwise of the fibres. Column 3 of Table 6.1 shows the transmittance results of the mats in the three media studied while Column 2 describes the mats when visually examined to confirm if they were present in the solutions or dissolved. The visual examination complemented the spectroscopic results of this study to arrive at the solubility decision.

From Figures 6.1 and 6.2, likewise Table 6.1, the TA_CHS_2 maintained its fibrous structure after the crosslinking more than TA_CHS_1. TA_CHS_3 shrank, losing its fibre network. Furthermore, the TA_CHS_2 mats were insoluble in the three media and throughout the 72 h

study period, unlike the TA_CHS_1 which were partially soluble after 10 mins but completely dissolved by 72 h of the study. Judging from these observations, the TA_CHS_2 was selected for further investigation and characterisation.

6.3 Swelling behaviour of the crosslinked BSF nanofibre

It is important to investigate the swelling behaviour of the TA_CHS_2 nanofibres to ascertain its durability in aqueous solution since the mats would be applied in adsorption studies. Swelling measurement is an appropriate technique of demonstrating the success of crosslinking of a substance. Approximately 5.0 mg of the nanofibre was weighed and immersed in 10 mL of phosphate-buffered saline (PBS) solution for different times ranging from 0.5 to 24 h with mild stirring. Afterwards, the adsorbents were retrieved, dried and reweighed. The experimental procedure is described in Section 3.3.7 of Chapter 3. Figure 6.3 shows the swelling performance of the TA_CHS_2 adsorbent in PBS solution over a 24 h interval.

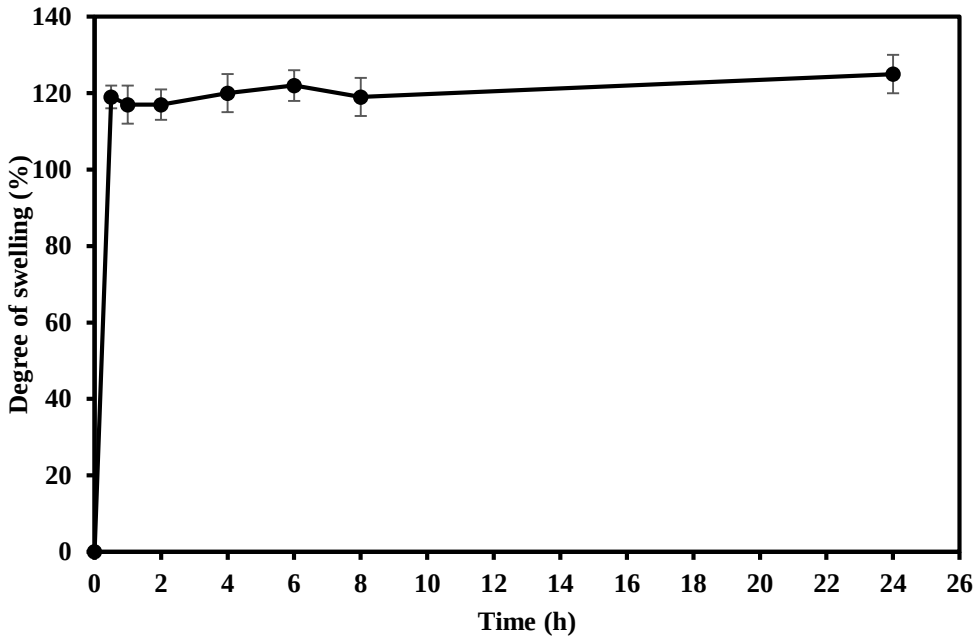

Figure 6. 3: The swelling behaviour of the TA_CHS_2 membranes in PBS.

In the first instance, the as-spun uncrosslinked BSF nanofibres dissolved instantly after immersion in the PBS solution and, therefore, could not be plotted for comparative purpose. Figure 6.3 presents the swelling studies (determined according to Equation 3.3 of Chapter 3) conducted on the TA_CHS_2 adsorbent in PBS solution for a period of 24 h. The result shows that the swelling of the adsorbent increased rapidly within the first few minutes of the

investigation and attained the highest percentage swelling of 120% at 0.5 h (30 minutes) of the investigation. After this time, the swelling started levelling off. There was a negligible reduction (1.5%) in the determined degree of swelling (120% at 0.5 h) after 1 and 2 h of the investigation. Slight fluctuations were further observed from 4 h of the investigation to 24 h. Since the variations were not significant, it is assumed that the equilibrium percentage swelling of the TA_CHS_2 adsorbent is 120%. Knaul *et al*. (1999) and Habiba *et al*. (2016) have suggested that swelling of crosslinked materials could result from the reactions occurring on or close to the surface of the fibres functional groups and that the majority of the core may not be affected. The crosslinking reaction of TA with chitosan nanofibres implies that few amino groups were present on the polymer structure for protonation. Habiba and coworkers further asserted that the swelling results from the ionic interactions of the polymer chains, and the interaction is dependent on the degree of crosslinking attained. Therefore, the remaining amino groups on the crosslinked TA_CHS_2 adsorbent tends to absorb water due to their hydrophilic properties. This could account for the 120% degree of swelling recorded in this study. This implies that an increase in the degree of crosslinking would decrease the degree of swelling of the adsorbent thereby reducing the water absorption capacity of the adsorbent.

The equilibrium swelling percentage of 120±3% computed in this study corroborates the result of Sangsanoh and Supaphol (2006) who obtained a swelling index of 100% with chitosan nanofibres crosslinked with glutaraldehyde but is quite low compared to the value of 600% swelling index reported by Li *et al.* (2011).

6.4 General characterisation of the crosslinked nanofibres

Further characterisations were conducted to investigate the physicochemical properties of the TA_CHS_2 adsorbent. The results of these analyses which includes chemical compositions and thermal properties are presented in this section.

6.4.1 *ATR-FTIR spectra of the TA_CHS_2 adsorbent*

FTIR spectroscopy could provide information pertaining to changes occurring at the molecular level on the structure of the electrospun chitosan nanofibre as a result of its crosslinking with tannic acid. This study was, therefore, conducted to investigate the chemical compositions and signals of various functional groups inherent in the spectrum of the TA_CHS_2 nanofibres as compared to the spectra of the raw tannic acid (TA-Raw) and the as-spun uncrosslinked chitosan nanofibre (ES-D3 obtained in Chapter 5). The FTIR experimental protocol is

described in Section 3.9.3 of Chapter 3. Figure 6.4 shows the spectra of the TA_CHS_2 adsorbent, the TA-Raw and the as-spun BSF nanofibres.

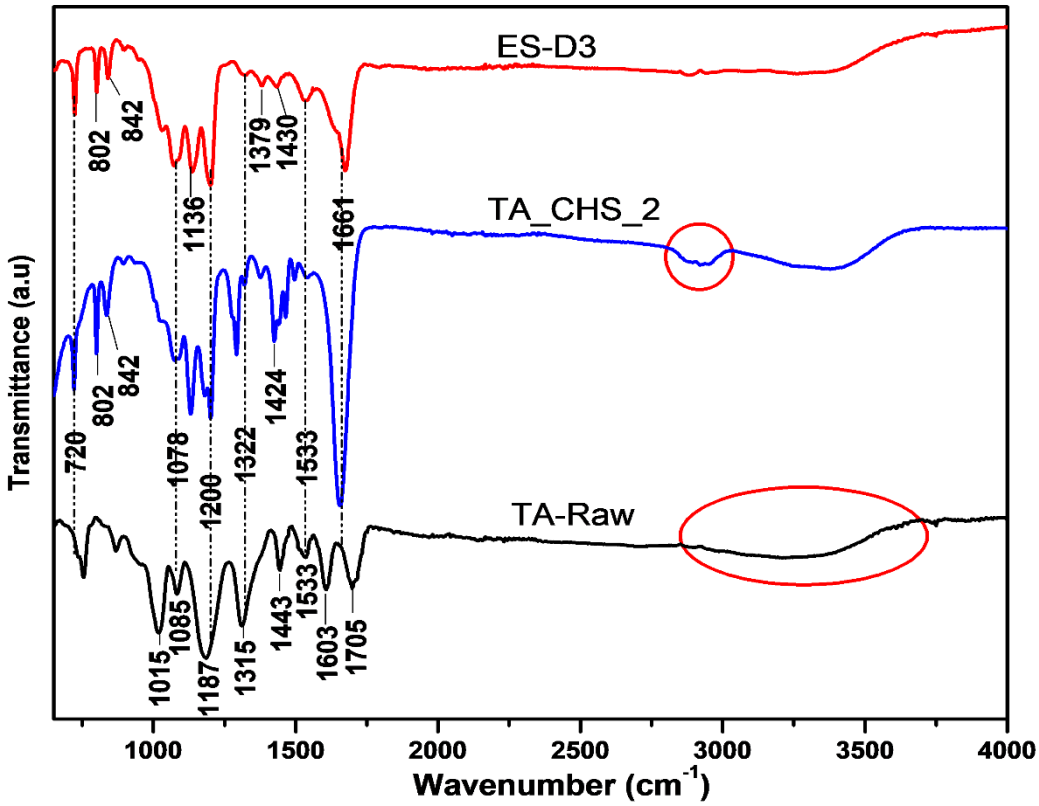

Figure 6. 4: The FTIR spectra of the TA_CHS_2 adsorbent, as-spun BSF nanofibres and the raw tannic acid (TA-Raw) showing the various functional groups.

FTIR spectra of TA-Raw reveals the following characteristic absorption bands: 3500 - 3000 cm^{-1} resulting from the overlap of the O-H and the amine groups stretching vibration which shows the intense interaction of hydrogen bonds of the phenol group of the tannic acid. The peak at 1705 cm^{-1} is attributed to the carbonyl (C=O) bond associated with the ester moiety. The signal at 1603 cm^{-1} results from the stretching of the aromatic C=C ring while the signal occurring at a wavelength of 1533 cm^{-1} resulted from the stretching of the aromatic C–C bond. Additionally, the signals at 1443 and 1315 cm^{-1} correspond to the bending vibration of the C–H bond. The peak at 1187 cm^{-1} corresponds to the stretching of the C–O while the signal at 1015 cm^{-1} emanated from the O-H bending vibration of the tannic acid (Baruah *et al.*, 2016). The series of peaks on the spectrum of the TA-Raw resulted from the existence of multiple hydroxyl, benzene rings and carbonyl functional groups on the tannic acid structure. TA is known to contain about 25 phenolic hydroxyl groups. These groups could function effectively

as reactive sites for the amide groups of chitosan and could be exploited during crosslinking (Fei *et al.*, 2016).

After crosslinking, the spectrum of TA_CHS_2 displayed a weakened but steeper OH region. Two additional signals, corresponding to the "symmetric and asymmetric stretching" of the C-H group from the $–CH_3$ moiety of the carboxylic group were observed in the region of 2878 – 2958 cm^{-1}. These two additional bands, though present with a diminished signal on the spectrum of ES-D3, were non-existent on TA-Raw spectrum. The three amine groups were all observed in the spectrum of the TA_CHS_2 nanofibres. The strong signal at 1661 cm^{-1} which was observed at 1674 cm^{-1} in the spectrum of ES-D3 emanated from the C=O stretching vibrations of the Amide 1. The shift in frequency to a lower wavenumber and appreciable increase in the signal is an indication of crosslinking. This crosslinking resulted from the angular deformation of the asymmetric NH_3^+ group (Fei *et al.*, 2016), and strong chemical interaction due to the hydroxyl groups of the tannic acid and the chitosan nanofibres (Picchio *et al.*, 2018).

The band at a wavelength of 1533 cm^{-1} corresponds to the N-H bending and C-N stretching of the Amide 11. The peak at 1322 cm^{-1} is associated with CH_2 bend and CH_3 symmetric distortion of the Amide III. The peak at 1603 cm^{-1} in the TA-Raw spectrum is assigned to aromatic ring stretching vibration and this peak was not observed on the TA_CHS_2 spectra. The band located at 1187 cm^{-1} is associated with the C-O stretching mode of the ester moiety. This band appeared weakened in the TA_CHS_2 spectra and occurred at a wavelength of 1200 cm^{-1}. The results show that several functional groups of chitosan nanofibres (ES-D3) and the raw tannic acid (TA-Raw) could be modified by crosslinking. The wavelengths of the absorption signals in the spectra of TA_CHS_2 chitosan shifted to lower frequencies after crosslinking. This suggests that the crosslinking process was effective and the tannic acid/chitosan complex obtained displayed spectral features of its various functional groups.

6.4.2 *Thermal gravimetric analysis*

Thermogravimetric analysis was carried out on the TA_CHS_2 adsorbent to investigate the behaviour of the material under varying temperatures. The thermal analysis was performed using a PerkinElmer Pyriss Simultaneous TGA/DTA Analyzer (TG-4000) under an inert nitrogen atmosphere, a heating rate of 10 °C/min and a temperature of 20 - 700 °C. Experimental

detail is described in Section 3.9.5. of Chapter 3. Figure 6.5 presents the derivative thermograms of the degradation of the TA_CHS_2 nanofibres adsorbent.

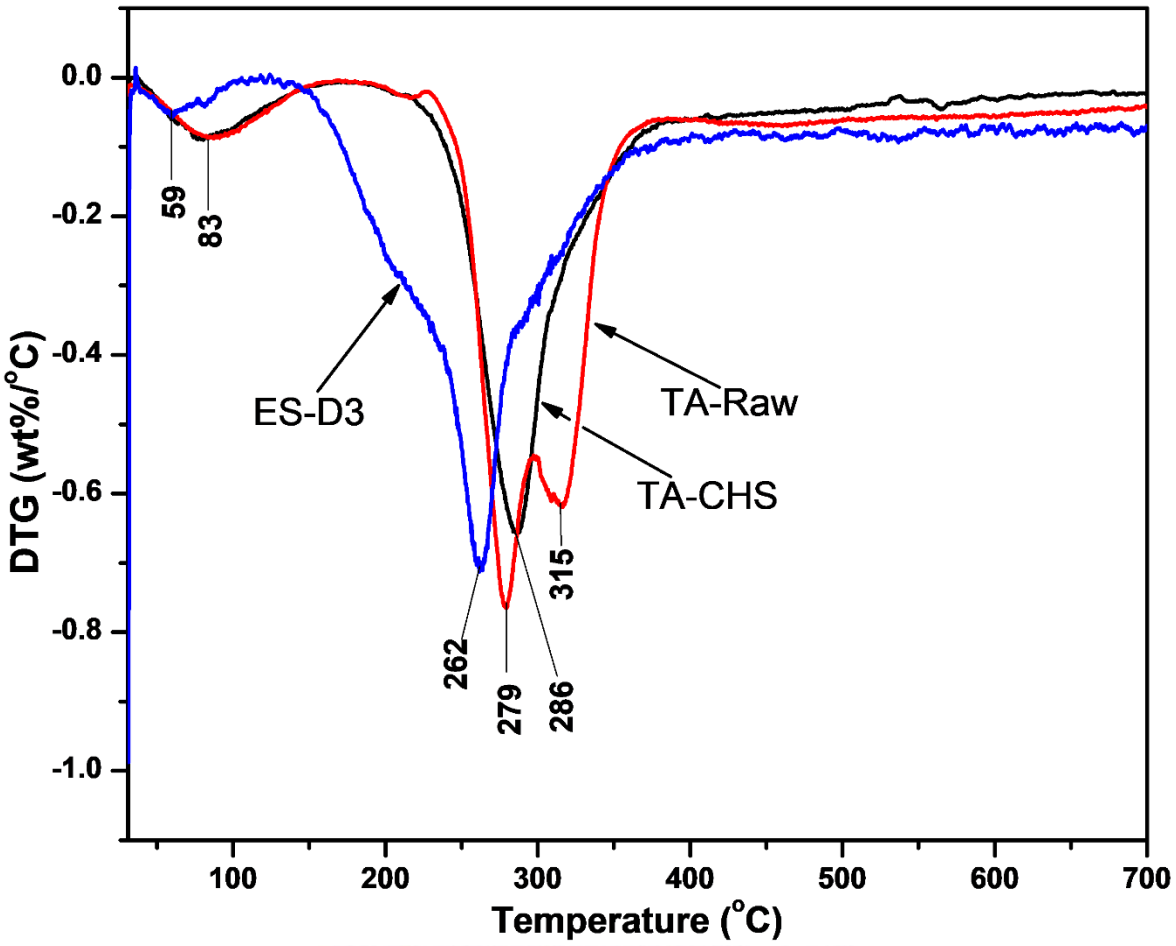

Figure 6. 5: Derivative thermograms of the TA_CHS_2 adsorbent compared to the as-spun BSF nanofibres (ES-D3) and the raw tannic acid (TA-Raw).

From Figure 6.5, it could be observed that the DTG profile of the electrospun nanofibres (ES-D3) has two pronounced decomposition stages. The first stage of decomposition, as described previously (Section 4.4.3 and 5.42), corresponds to the loss of bound or lattice water contained in the nanofibres structure. The temperature at which the maximum water loss occurred was at 59 °C. The weight loss associated with this decomposition (corresponding to water loss) is 4%. The second decomposition stage, corresponding to the depolymerisation and decomposition of the structural units and the saccharide backbone of the chitosan (Paulino *et al.*, 2006) had a maximum degradation temperature of 262 °C. The second stage of degradation was accompanied by a 62% weight loss.

The thermal profile of TA-Raw shows three stages of mass loss. The first, of course, corresponds to the dehydration process with maximum moisture loss occurring at 83 °C. Total mass loss as a result of this dehydration process was determined to be 7%. This mass loss provided information about the water content of the sample before the thermal analysis. The second stage, which occurred between 228 – 296 °C with a maximum degradation temperature, DTG_{max}, of 279 °C is associated with the dehydroxylation of the tannic acid backbone. The third decomposition occurred between 298 – 374 °C with a DTG_{max} of 315 °C and is linked with the oxidation of the carbon backbone of the TA-Raw releasing CO_2, H_2O, CO in the process (Mahmoud *et al*., 2015).

The profile of the TA_CHS_2 adsorbent shows that the mats have only two degradation stages. The first stage represents the dehydration of moisture contained in the structure of the TA_CHS_2 mats. The second degradation stage is associated with the thermal disintegration of the chitosan/tannic acid complex. The structure of tannins is complex, stable and condensed and thus confers it with high thermal degradation values (DTG_{max}). This TA_CHS_2 had a stability value (286 °C) between the average DTG_{max} of TA-Raw (297 °C) and the ES-D3 nanofibres (262 °C) as exemplified by the DTG_{max} value of 286 °C.

The thermal profiles obtained in this study is in agreement with the result of Mahmoud *et al.* (2015) who investigated *Rhus tripartitum* root barks tannin for application in wood adhesive formulation and obtained DTG_{max} value of 277 °C at the second degradation profile. This study shows that the TA_CHS_2 adsorbent is stable in water and thermally, and therefore could be applied in investigations not exceeding 200 °C.

6.5 Chapter summary

This chapter focused on the crosslinking of the BSF chitosan nanofibres to achieve its stability in aqueous solution. The as-spun BSF nanofibres dissolved in aqueous solutions. This is due to the existence of $-NH_3^+$ salt residue on the fibres. This solubility problem necessitated this study. Tannic acid was adopted due to its ability to form ionic, hydrophobic and hydrogen interactions with biopolymers. Moreover, they are natural compounds and are non-toxic, unlike glutaraldehyde. The optimised crosslinker concentration of 5 wt% was chosen in this study. This was because 5 wt% tannic acid solution maintained the fibrous structure of the BSF nanofibres after crosslinking. The crosslinked mat had a 72% increase (254 ± 86 nm) in fibre diameter when compared to the as-spun BSF nanofibres (142 ± 65 nm). Additionally, the

adsorbent was insoluble in 1.0 M acetic acid (pH 3), deionised water (pH 6.5) and 1.0 M NaOH (pH 13) solutions after 10 minutes or 72 h of investigation as the fibres were still visible and the transmittance values measured at 600 nm (T_{600}) were ≥ 90% in each of the solutions. The swelling studies showed that the TA_CHS_2 adsorbent had a 120% swelling, implying the existence of hydrophilic groups of the crosslinked adsorbent. The chemical properties of the adsorbent were further analysed using a spectroscopic technique. The FTIR study suggested that the crosslinking process was effective as the TA_CHS_2 spectra displayed differing spectral features (lower wavenumber, increased signal) at wavelengths of 2878 – 2958 and 1674 cm^{-1} compared to both the TA-Raw or ES-D3 while maintaining the Amide 1, 11 and 111 signals characteristic of chitosan. The thermal analysis shows that the TA_CHS_2 had two degradation profiles compared to the TA-Raw with three degradation profiles while having higher thermal stability than the ES-D3 (electrospun nanofibres).

Therefore, the BSF nanofibres was successfully crosslinked and the crosslinked fibres showed stability in aqueous solution while maintaining the characteristic Amide 1, 11 and 111 functional groups of chitosan.

CHAPTER 7

ADSORPTION STUDIES OF Pb^{2+} or Cd^{2+} ON THE TANNIC ACID CROSSLINKED CHITOSAN NANOFIBRE

7.0 Introduction

This chapter presents the findings from the adsorption experiments performed using the tannic acid crosslinked chitosan (TA_CHS_2) nanofibres described in Section 6.1 – 6.4 of Chapter 6. The toxic metals examined in this study were Pb^{2+} or Cd^{2+} and adsorption tests were conducted in batch processes. The experiment was aimed at investigating the performance of the synthesised crosslinked chitosan nanofibres on the adsorption of Pb^{2+} or Cd^{2+} from aqueous solution and also the reusability of the nanofibres. This chapter has three sections. The first section deals with the optimisation of adsorption parameters including solution pH, metal ion concentration, contact time and reaction temperature and their effect on the adsorption of Pb^{2+} or Cd^{2+} by the synthesised nanofibres. The experiments were conducted by varying a parameter while keeping others constant. The second section of this chapter focuses on the application of various models to analyse the obtained data from the first section. Langmuir and Freundlich's isotherms, likewise pseudo-first-order and pseudo-second-order kinetic models were applied in describing the relationship between the adsorbent and the adsorbates. The last section of this chapter discusses the desorption, regeneration and reusability experiments for the adsorbent.

The concentrations (initial and final) of both metals ions were determined using the ICP-OES technique described in Section 3.9.7 of Chapter 3. The results obtained from the analysis of both metal ions are discussed in the subsequent section.

7.1 Evaluation and optimisation of adsorption parameters of Pb^{2+} or Cd^{2+} onto TA_CHS_2 adsorbents

The adsorption studies were conducted in a batch process as described in Section 3.4 of Chapter 3. The purpose was to determine the optimised adsorption capacities of the TA_CHS_2 nanofibres on Pb^{2+} or Cd^{2+} using Equation 3.3 described in Section 3.4.2 of Chapter 3. Furthermore, the isotherms and the kinetics of the adsorption experiments were studied and determined. The parameters investigated in this study were the effect of pH, adsorbate concentration, contact time and temperature on the removal efficiency of the TA crosslinked CHS nanofibres. The concentrations of the adsorbates were prepared from a 1000 mg/L stock

solution of Pb^{2+} or Cd^{2+} as described in Section 3.4 and stored in a refrigerator. The following sub-sections highlight the results obtained.

7.1.1 *Effect of pH*

The effect of pH on the adsorption process of Pb^{2+} or Cd^{2+} unto TA_CHS_2 was studied. The pH of a solution is an important parameter in the adsorption of metal ions from solutions. pH affects the solubility and mobility of the adsorbates in aqueous solution. The pH was studied to ascertain the adsorption efficiency of the electrospun TA_CHS_2 at various pH values. 20 mL of aqueous solutions containing 50 mg/L of Pb^{2+} or Cd^{2+} were introduced into an Erlenmeyer flask containing 0.005 g of the nanofibres and stirred using a shaker at a speed of 200 rpm for 2 h at room temperature. The solutions were filtered and analysed using ICP-OES. The detailed description of the experimental protocol could be found in Section 3.4.1 of Chapter 3. Figure 7.1 presents the amount of Pb^{2+} or Cd^{2+} adsorbed by the TA_CHS_2 nanofibres at various pH.

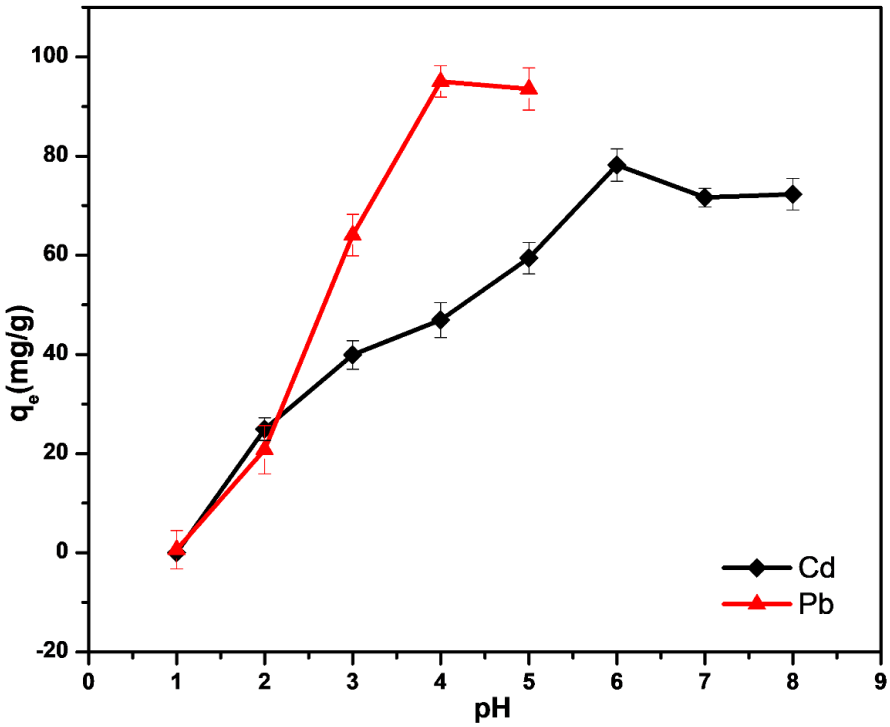

Figure 7. 1: Effect of initial pH on adsorption capacity of Pb^{2+} or Cd^{2+} onto TA_CHS_2 (initial metal concentration - 50 mg/L; the weight of adsorbent - 0.005 g; contact time - 2 h).

Figure 7.1 shows that there was a sustained increase in the adsorption capacity for both metal ions with increase in pH of the solution(s). No adsorption was observed at pH 1.0 while

marginal adsorption occurred at pH 2.0 for both metal ions. Adsorption of Pb^{2+} had a steeper increase, an indication that more Pb^{2+} was being adsorbed than Cd^{2+} as the pH increased. Pb^{2+} adsorption peaked at pH 4 and remained almost constant at pH 5 while Cd^{2+} had maximum adsorption upon the TA_CHS_2 at pH 6.0 and thereafter decreased slightly. From Figure 7.1, the adsorption of the two metal ions onto the TA_CHS_2 nanofibres increased as the pH increased and achieved a maximum value of 94.74 or 77.86 mg/g for Pb^{2+} or Cd^{2+} at pH 4 and 6, respectively.

The variation in the observed adsorption values at various pH could be attributed to the competition between protonation and chelation in the adsorption process. At acidic pH, the amine groups of the TA_CHS_2 adsorbents transformed to ionic state, NH_3^+, (Equation 4.1), causing electrostatic repulsion between the positively charged Pb^{2+} or Cd^{2+} and the NH_3^+ of the nanofibres (Equation 4.2) which impeded their sorption onto the adsorbents (Liao *et al.*, 2016).

$$R—NH_2 + H^+ \rightleftharpoons R—NH_3^+ \qquad 4.1$$

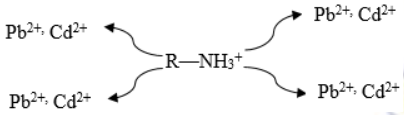

4.2

Also, a higher concentration of H^+ existing in the aqueous solution at low pH created additional competition for the active sites on the adsorbent with the cationic metal ions. The low adsorption capacity of the adsorbent at low pH was, therefore, due to saturation of the active sites of the adsorbent by H^+ (Akpomie and Dawodu, 2014; Zhang *et al.*, 2016). As the pH increased, the positive charge on the adsorbent's surface tends to decrease favouring an increase in the number of negatively charged sites available. This increased availability of charged sites induced a potential difference between the negatively charged adsorbent surface and the positively charged metal ions. This difference causes electrostatic attraction of these metal ions, leading to increased adsorption efficiency with increase in pH as more amino groups chelate the metal ions (Maleki *et al*., 2016). Above these observed maximum pH, the adsorption capacity of TA_CHS_2 decreased for both metal ions. This could be attributed to, for Pb, the formation of lead(II) hydroxide at pH above 5.0 which leads to a decrease in the capability of Pb^{2+} to bind to surfaces. Hong *et al*. (2015) and Musyoka *et al*. (2011) have previously reported this phenomenon as a common trend in the adsorption studies with Pb. To

this effect, pH above 5.0 was not considered in this study to avoid the precipitation of the metal ions, as at pH 6.0 the solution appeared cloudy. Therefore, 4.0 or 6.0 for Pb^{2+} or Cd^{2+}, respectively were chosen as the optimum pH for further adsorption studies using TA_CHS_2 adsorbent. These optimum pH values were applied for the optimisation of other adsorption parameters in the subsequent sub-sections.

7.1.2 *Effect of concentration*

This investigation was conducted to ascertain the optimal Pb^{2+} or Cd^{2+} concentration for the adsorption of TA_CHS_2. The study also determined the adsorption isotherms of the metal ions onto TA_CHS_2 adsorbent. In general, the behaviour of the adsorbent as a function of the concentration of the two metal ion solutions was investigated. 20 mL of 10, 20, 40, 60, 80, 100, 150 and 200 mg/L of Pb^{2+} or Cd^{2+} adjusted to pH 4.0 or 6.0 (optimal pH was previously determined in Section 7.1.1), respectively using NaOH or HCl (0.1 M) were prepared. 0.005 g of TA_CHS_2 was stirred in 20 mL of each solution for 2 h at 25 ˚C and 200 rpm. The resulting solutions were filtered and analysed using ICP-OES. The removal efficiencies (q_e) of the two metal ions by the nanofibres adsorbent were determined. Details of the experimental protocol are described in Section 3.5.4 of Chapter 3. The results of the effect of concentration on the adsorption of Pb^{2+} or Cd^{2+} is presented in Figure 7.2.

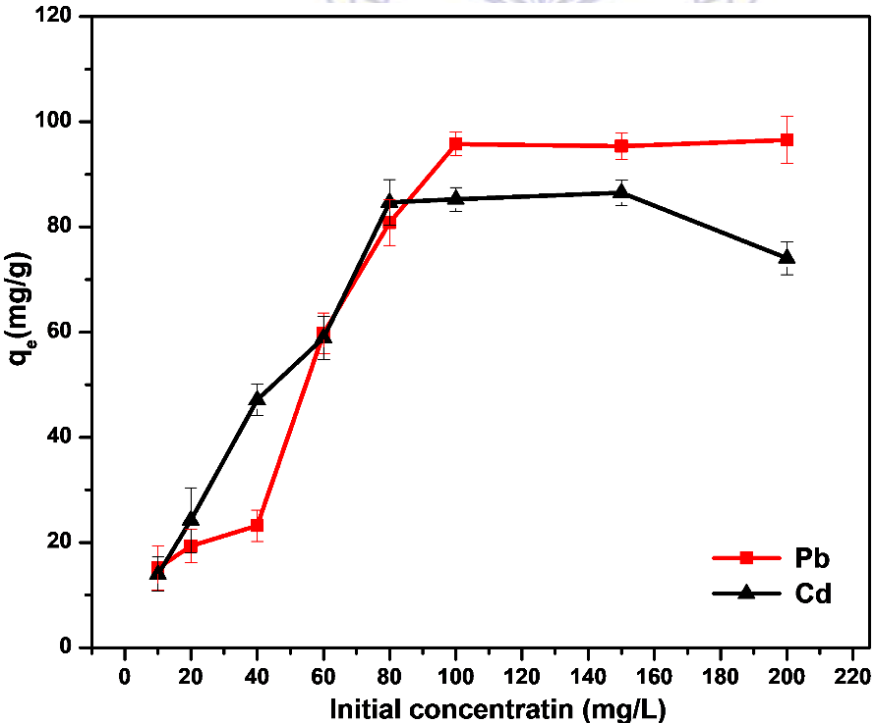

Figure 7. 2: The effect of the initial concentration of Pb^{2+} or Cd^{2+} on their removal efficiency using TA_CHS_2 fibres at pH 4.0 or 6.0 for Pb^{2+} or Cd^{2+} respectively, the weight of the adsorbent - 0.005 g; contact time - 2 h.

From Figure 7.2, it is observed that the adsorption capacity for Cd^{2+} rapidly increased, while Pb^{2+} displayed a slower uptake with an increasing amount of metal ion concentration in solution. At 80 and 100 mg/L for Cd^{2+} or Pb^{2+}, respectively, the equilibrium capacity of the adsorbent (95.767 or 85.325 mg/g, accordingly) was attained and subsequently saturation of the active sites was achieved. The adsorption of Pb^{2+} was no longer increasing rather it remained fairly constant with a further increase in concentration. A similar trend was observed for Cd^{2+} but with minimal adsorption increase at low concentration (between 10 and 40 mg/L). The observed increase in adsorption capacity as the concentration increased for each metal ion could have resulted from the availability of more adsorption sites on the adsorbent at a lower metal ion concentration. At low concentration, the metal ions available in the individual solutions could not fill up all the available adsorption sites on the adsorbent. As the metal concentration increased in solution, the amino groups of the adsorbent tend to adsorb more of the adsorbates until equilibrium was attained. This, therefore, signifies that the adsorption of Pb^{2+} or Cd^{2+} is dependent on the availability of sorption sites on the adsorbent's surface and the ability of these metal ions to attach to these active sites which are pH-dependent as previously noted. The obtained data for either of the metal ions were applied to adsorption isotherm models to study the nature of the adsorption process and is discussed in detail in Section 7.3.

7.1.2.1 Comparison of TA_CHS_2 nanofibre with chitosan and modified chitosan sorbents for sorption of Pb or Cd ions

The adsorption properties of TA_CHS_2 nanofibres for Pb^{2+} or Cd^{2+} were compared to some of the results of studies utilising chitosan or modified chitosan sorbents found in the literature. Table 7.1 and 7.2 present the summaries of adsorption capacities for Pb^{2+} or Cd^{2+} studies, respectively. The comparison is purely based on the extent of removal of the metal ions.

Table 7. 1 Adsorption capacities of some chitosan/chitosan modified sorbents for Pb^{2+} sorption compared to the present study

Sorbent	Metal	pH	Time (h)	Adsorption capacity (mg/g)	Reference
CHS cross-linked with ECH-TPP	Pb^{2+}	5.0		166.94	Laus *et al*., 2010
GLA-crosslinked metal-complexed chitosans	Pb^{2+}	5.0		105.26	Cheng *et al*., 2009
Procion Green H-4G immobilized pHEMA/chitosan	Pb^{2+}	6		68.81	Genc *et al*., 2003

Continuation of adsorption capacities of some chitosan/chitosan modified sorbents for Pb^{2+} sorption compared to the present study

Xanthate-modified magnetic chitosan	Pb^{2+}	5	1.0	87.53	Tianguo *et al*., 2018.
Chitosan–pectin pellets	Pb^{2+}	5	Nd	11.2	Debbaudt *et al*., 2004
Chitosan/magnetite nanocomposite beads	Pb^{2+}	6	2.0	63.3	Tran *et al*., 2010
Xanthate-modified magnetic chitosan	Pb^{2+}	4	2.0	76.9	Zhu *et al*., 2012
Composite nanofibers membranes of poly(vinyl alcohol)/chitosan	Pb^{2+}	6.0	3.20	266.12	Karim *et al*., 2019
Crosslinked and ion-imprinted chitosan nanofiber mats	Pb^{2+}	7	2.5	110.0	Li *et al*., 2015
EGTA-chitosan	Pb(II)	4	24	103.5	Zhao *et al*., 2013
Polyaniline grafted chitosan	Pb^{2+}	6	1	13.23	Kyzas *et al*., 2014
TA_CHS_2 (this study)	Pb^{2+}	4.0	1.0	95.77	This study

Table 7. 2: Adsorption capacities of some chitosan/chitosan modified sorbents for Cd sorption compared to the present study.

Sorbent	Metal	pH	Time (h)	Adsorption capacity (mg/g)	Reference
Modified plantain peels (MPP)	Cd^{2+}	4.36	Nd	70.92	Garba *et al*., 2016
CHS cross-linked with ECH-TPP	Cd^{2+}	7.0		83.75	Laus *et al*., 2010
CHS modified with BPMAMF complexing agent	Cd^{2+}	2.0		38.5	Justi *et al*., 2005
Procion Green H-4G immobilized pHEMA/chitosan	Cd^{2+}	6		43.60	Genc *et al*., 2003
chitosan–pectin pellets	Cd^{2+}	7		1.23	Debbaudt *et al*., 2004
Chitosan nanofibrils	Cd^{2+}	5.0		60.9	Liu *et al*., 2014
Composite nanofibers membranes of poly(vinyl alcohol)/chitosan	Cd^{2+}	8.0	1.0	148.79	Karim *et al*., 2019
EGTA-chitosan	Cd^{2+}	4.0	24	83.18	Zhao *et al*., 2013
Polyaniline grafted chitosan	Cd^{2+}	6.0	1.0	12.87	Kyzas *et al*., 2014
TA_CHS_2 (this study)	Cd^{2+}	6.0	1.0	85.33	This study

The q_e value of the TA_CHS_2 nanofibres performed excellently and compared effectively to, and in some instances, outperformed some of the previously reported chitosan adsorbents for the sorption of both Pb^{2+} or Cd^{2+}. Though some of the adsorbents reported in Table 7.1 and 7.2 show better performance, their performance may have been enhanced by the blending with other materials. Ion-imprinted chitosan nanofibres (Li *et al*., 2015), GLA-crosslinked metal-complexed chitosan (Cheng *et al*., 2009), modified plantain peels (Garba *et al*., 2016) and poly (vinyl alcohol)/chitosan composite (Karim *et al.*, 2019) were the materials having better sorption capacity than the TA_CHS_2 adsorbent for removing both metal ions. Their method of preparation was complex and some of them took longer to achieve equilibrium adsorption capacity. In general, the TA_CHS_2 adsorbents have sorption properties comparable to most sorbents so far reported in the literature. Additionally, its inherent fast kinetics was an added advantage as it was able to achieve equilibrium capacity within 60 minutes for either Pb^{2+} or Cd^{2+} as shown in Section 7.1.3 whereas some of the sorbents reported in the literature took up to 24 h to achieve equilibrium (Table 7.1 and 7.2).

7.1.3 *Effect of time*

Contact time is a significant parameter in understanding the suitability of adsorbents for various applications. To determine the adsorption kinetics, the influence of contact time on the adsorption of Pb^{2+} or Cd^{2+} onto TA_CHS_2 was studied. This was done as described in Section 3.4.3. Seven samples containing 20 mL of 50 mg/L of Pb^{2+} or Cd^{2+} at pH 4.0 and 6.0, respectively were stirred with 0.005 g TA_CHS_2 for 10, 20, 40, 60, 80, 100 and 120 minutes at 200 rpm. The resultant solutions were filtered and analysed using ICP-OES as described in Section 3.9.7 of Chapter 3. The adsorption capacity (q_e) was calculated according to Equation 3.3 of Chapter 3. The adsorption kinetics of the process was investigated by using pseudo-first-order and pseudo-second-order kinetic models according to Equations 3.10 and 3.12, respectively. Figure 7.3 presents the adsorption of Pb^{2+} or Cd^{2+} onto TA_CHS_2 as the contact time is varied.

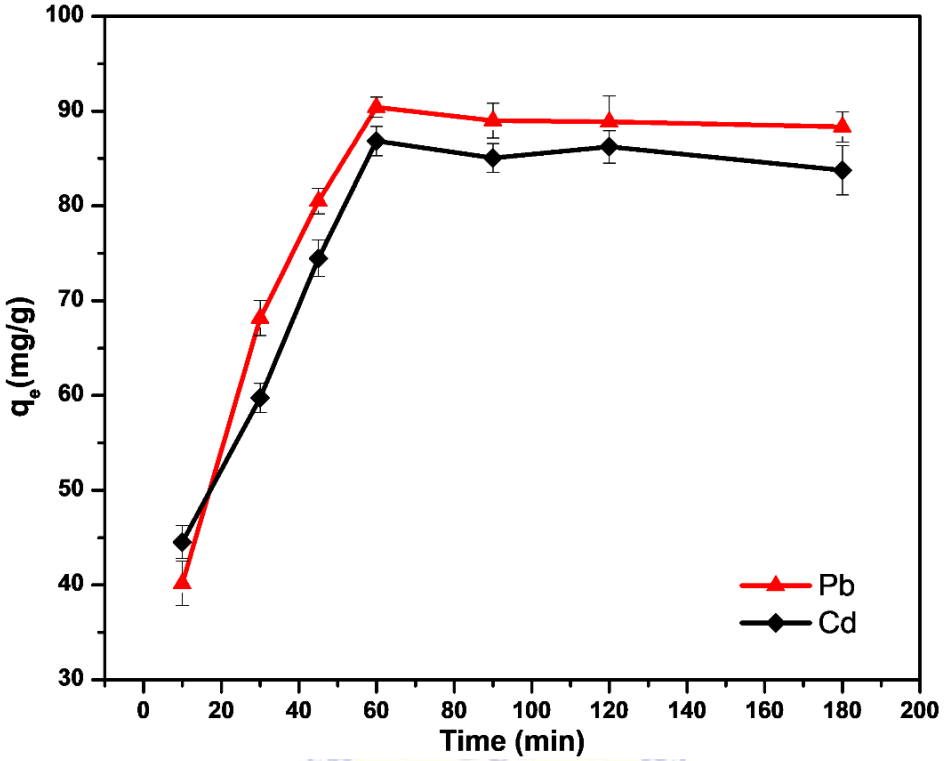

Figure 7. 3: Effect of contact time on the adsorption capacity of Pb^{2+} or Cd^{2+} onto TA_CHS_2 (initial concentration of metal ions - 50 mg/mL; the weight of adsorbent - 0.005 g; initial pH - 4.0 and 6.0 for Pb^{2+} or Cd^{2+} respectively).

Figure 7.3 shows the adsorption capacities of both metal ions onto the TA_CHS_2 nanofibres at varying contact times. It was found that the rate of adsorption of the metal ions by the TA_CHS_2 adsorbent increased constantly from 10 to 60 minutes, after which there was no further increment. This implies that saturation was attained after 60 minutes of contact time. After 60 mins, Cd^{2+} showed slight fluctuation in the adsorption capacity while Pb^{2+} remained relatively constant. The fluctuation may have resulted from the attachment of the metal ions to the active surface while other less accessible sites remained unoccupied but later got filled. The constant increment in the adsorption capacity observed in the first 60 minutes could be as a result of the availability of many adsorption sites on the surface of TA_CHS_2. Therefore, as time increased, the quantity of the metal ions adsorbed onto the active sites gradually reached its maximum. Further increase in contact time led to the attainment of equilibrium. No significant metal ion adsorption occurred thereafter due to the complete occupation of the active sites on the TA_CHS_2 by the metal ions. At the equilibrium time (60 minutes), the adsorption capacity of the adsorbent was found to be 90.41 or 87.56 mg/g for Pb^{2+} or Cd^{2+}, respectively.

7.1.4 *The effect of temperature*

Temperature is an important parameter considered in adsorption studies. This is due to its effect on the solid/liquid interface, the swelling property of adsorbents and the mobility of ions in solution. Furthermore, temperature influences the adsorption parameters by affecting the molecular actions and reactions, and solubility of the adsorbates. Five temperature regimes of 25, 35, 45, 55 and 65 ˚C were studied at a metal concentration of 50 mg/L and pH of 4.0 and 6.0 for Pb^{2+} or Cd^{2+}, respectively. The resultant solutions were filtered and analysed using ICP-OES as described in Section 3.9.7 of Chapter 3. The adsorption capacity (q_e) were calculated according to Equation 3.3 while the thermodynamic parameters of Gibb's free energy (ΔG°), entropy (ΔS°) and enthalpy (ΔH°) changes were also computed using the Van't Hoffs Equation (Equation 3.17) to determine the nature of the adsorption processes. The detailed description of the experimental protocol is found in Section 3.4.4 of Chapter 3. Figure 7.4 shows the plot of the adsorption capacity with variations in temperature for the two metal ions.

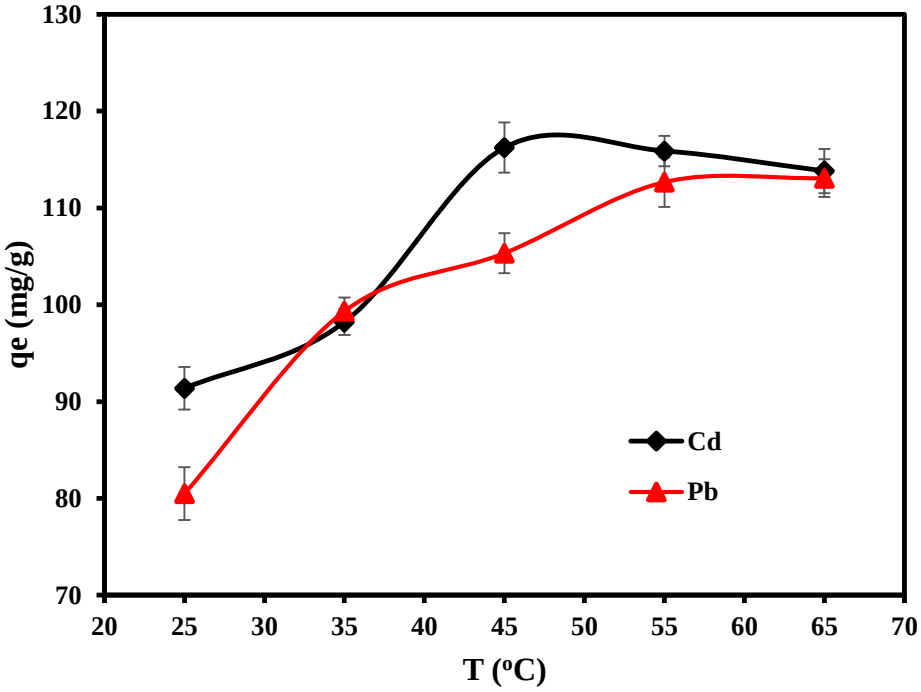

Figure 7. 4: Effect of temperature on the adsorption of Pb^{2+} or Cd^{2+} onto TA_CHS_2 (initial concentration of metal ions - 50 mg/L; the weight of adsorbent - 0.005 g; initial pH - 4.0 or 6.0 for Pb^{2+} or Cd^{2+}, respectively).

Figure 7.4 shows an increasing trend of adsorption of the metal ions as temperature increased from 25 to 65 ˚C. Both metal ions had similar adsorption capacity of 99 mg/g at 35 ˚C but Cd^{2+} adsorption had a more rapid increase and reached its equilibrium capacity after 45 ˚C. On the contrary, Pb^{2+} showed much slower adsorption after 35 ˚C. The TA_CHS_2 adsorbent had

removed 88% of its maximum Pb^{2+} adsorption capacity at 45 ºC with the remaining 12% occurring between 45 and 55 ˚C. Despite removing 88% of the Pb^{2+} by 45 ˚C, the equilibrium capacity of TA_CHS_2 onto Pb^{2+} was observed at a temperature of 55 ˚C. The adsorption capacity of Cd^{2+} showed a decreasing trend after 55 ºC while Pb^{2+} equilibrated at this temperature.

The observed increase in adsorption as temperature initially increased could be that the applied heat caused the swelling of the polymer within the solution. This swelling subsequently impacted on the hydration layer of the Pb^{2+} or Cd^{2+} before their respective adsorptions onto the adsorbent (Bozorgi *et al*., 2018). The energy required for the hydration sheath removal was, thus, higher than the exothermic energy required by the metal ions to relocate from the liquid phase where they existed to the solid phase of the TA_CHS_2 adsorbents. This phenomenon was also observed by Liao *et al.* (2016), Talebi *et al*. (2017) and Bozorgi *et al*. (2018). The observed increase could also be due to the increase of chemical interactions among the TA_CHS_2 functional groups by the heat-induced breakage of some bonds on the adsorbent's edges and surfaces. The temperature-induced breakages could cause an increment in the force of attraction between the metal ions in solution and the active sites on the adsorbent surface leading to increased adsorption capacity (Mohan *et al*., 2017). This points towards the adsorption process for these two metal ions being endothermic. The increment in the temperature after the equilibrium capacity also led to the increased mobility of the ions in solution. Therefore, the observed downward trend of the adsorption capacities of both metal ions after 55 ˚C (Figure 7.4) could be attributed to desorption and dechelation of some of the chelated metal ions from the adsorbent due to increased randomness and mobility of the ions at higher solution temperature (Maleki *et al*., 2016; Zhang *et al*., 2016).

7.2 Adsorption isotherms

To understand and describe the interactions between the adsorbent and the adsorbates in a solution at equilibrium concentration, the isotherms were utilised. From these interactions, the optimum sorption capacity can be determined. Several isotherm models exist for investigating equilibrium parameters of adsorption processes. Of these models, Langmuir and Freundlich models are some of the most common and were applied in this study.

7.2.1 *Langmuir isotherm*

The Langmuir isotherm is dependent on four assumptions including that monolayer adsorption occurs on the adsorbent surface, the adsorbent surface is homogeneous, adsorption occurs at identical sites and that there are no lateral interactions between molecules of the adsorbate (Meroufel *et al.*, 2013). The linear form of the Langmuir model is given as Equation 3.6 of Section 3.4.2. The correlation coefficient values obtained from the linear plot of the model was used to assess the applicability of the model to the adsorption process. Figure 7.5 presents the linear plots of the Langmuir isotherms for the two metal ions investigated in this study.

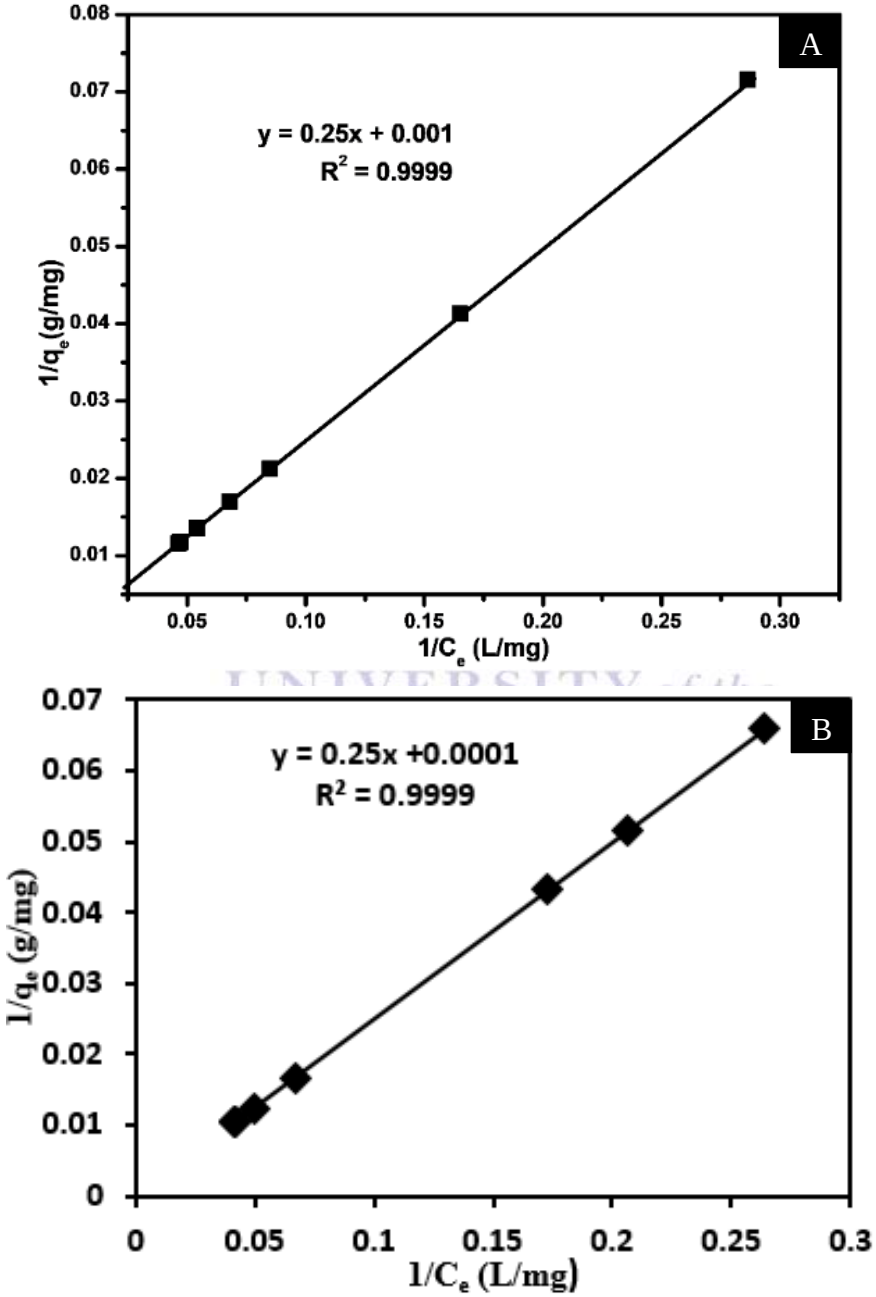

Figure 7. 5: Linear plot of Langmuir isotherm for the adsorption of (A) Pb^{2+} or (B) Cd^{2+}onto TA_CHS_2 nanofibres.

Figure 7.5 shows that the data had a good fit with the model. This is an indication that the adsorption of Pb^{2+} or Cd^{2+} took place on the homogenous surface of the TA_CHS_2. Additionally, the correlation coefficient (R^2) values obtained for this study is 0.9999 for both Pb^{2+} or Cd^{2+} suggesting that the adsorption process was as a result of monolayer formation. In monolayer formation, adsorption takes place specifically on an active site and once the adsorbate is attracted to this site, no additional adsorption will occur at this specific site. This suggest that the adsorption process for Pb^{2+} or Cd^{2+} onto the TA_CHS_2 nanofibres was in agreement with the Langmuir model. The parameters deduced from Figure 7.5 are enumerated in Table 7.3. Of particular importance in the Langmuir isotherm is the dimensionless separation parameter (R_L). This parameter relates to the tendency of the adsorption process occurring. The factor is classified into various groups: $R_L = 0$ (irreversible), $0<R_L< 1$ (favourable), $R_L = 1$ (linear) and $R_L >1$ (unfavourable) (Ayanda *et al*., 2019). The R_L value is computed using Equation 3.7 of Section 3.4.2. Figure 7.6 shows the plot of the R_L value for both metal ions.

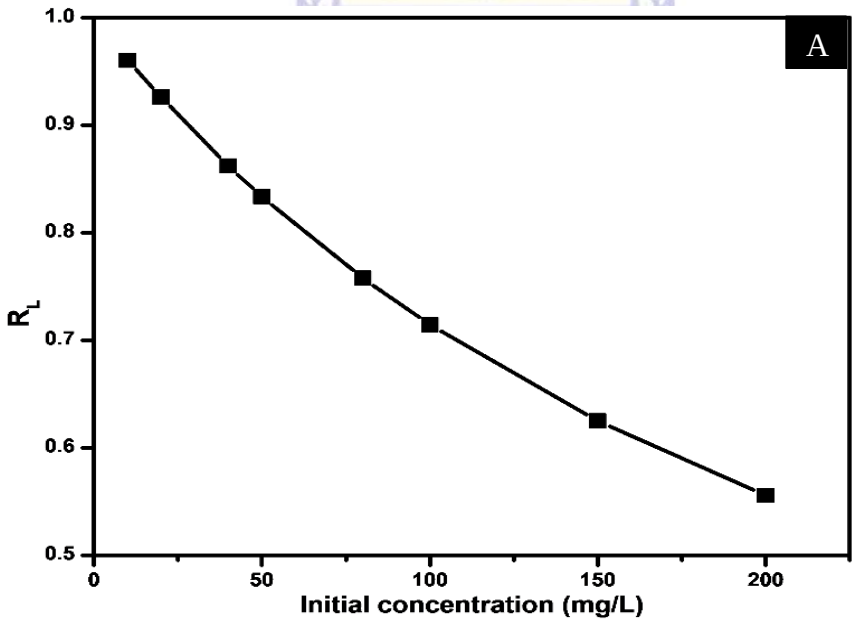

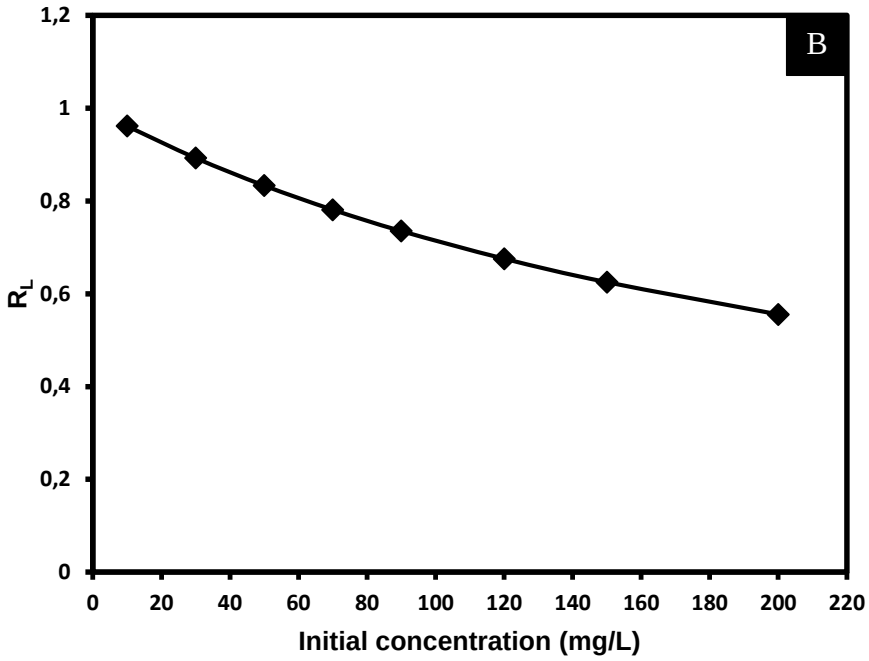

Figure 7. 6: R_L plot for the adsorption of (a) Pb^{2+} (b) Cd^{2+} onto TA_CHS_2 nanofibre.

Figure 7.6 shows that as the concentration of the adsorbate increase, the R_L value decreased towards zero. This shows that at high concentrations of the adsorbate, the rate of adsorption onto the adsorbent decreases, possibly due to the saturation of the active sites of the adsorbates. Therefore, the Langmuir model cannot completely account for the adsorption of Pb^{2+} or Cd^{2+} onto the TA_CHS_2 nanofibres (Farasati *et al.*, 2015). The R_L value computed in this study ranged from 0.55 - 0.99 for Pb^{2+} or 0.55 - 0.96 for Cd^{2+}, confirming that the adsorption process is favourable at the optimum conditions used in this study.

7.2.2 *Freundlich Isotherm*

Freundlich isotherm explains the relationship between the concentration of the adsorbates and the adsorbent's surface in contact with it at equilibrium conditions. This isotherm works on the assumptions that the adsorbate adsorbs onto the heterogeneous surface of the adsorbent and that the energy associated with the adsorbent and the adsorbate at the surface is not rate-limiting (Maleki *et al.*, 2016). This isotherm is used where a heterogeneous surface with irregular localisation of adsorption energies on their surfaces are considered. The Freundlich isotherm is obtained using Equation 3.8 and the linearised form is given as Equation 3.9 in Section 3.4.2 of Chapter 3. Figure 7.7 presents the linear plots of the Freundlich model for the adsorption of Pb^{2+} or Cd^{2+} onto TA_CHS_2 adsorbent.

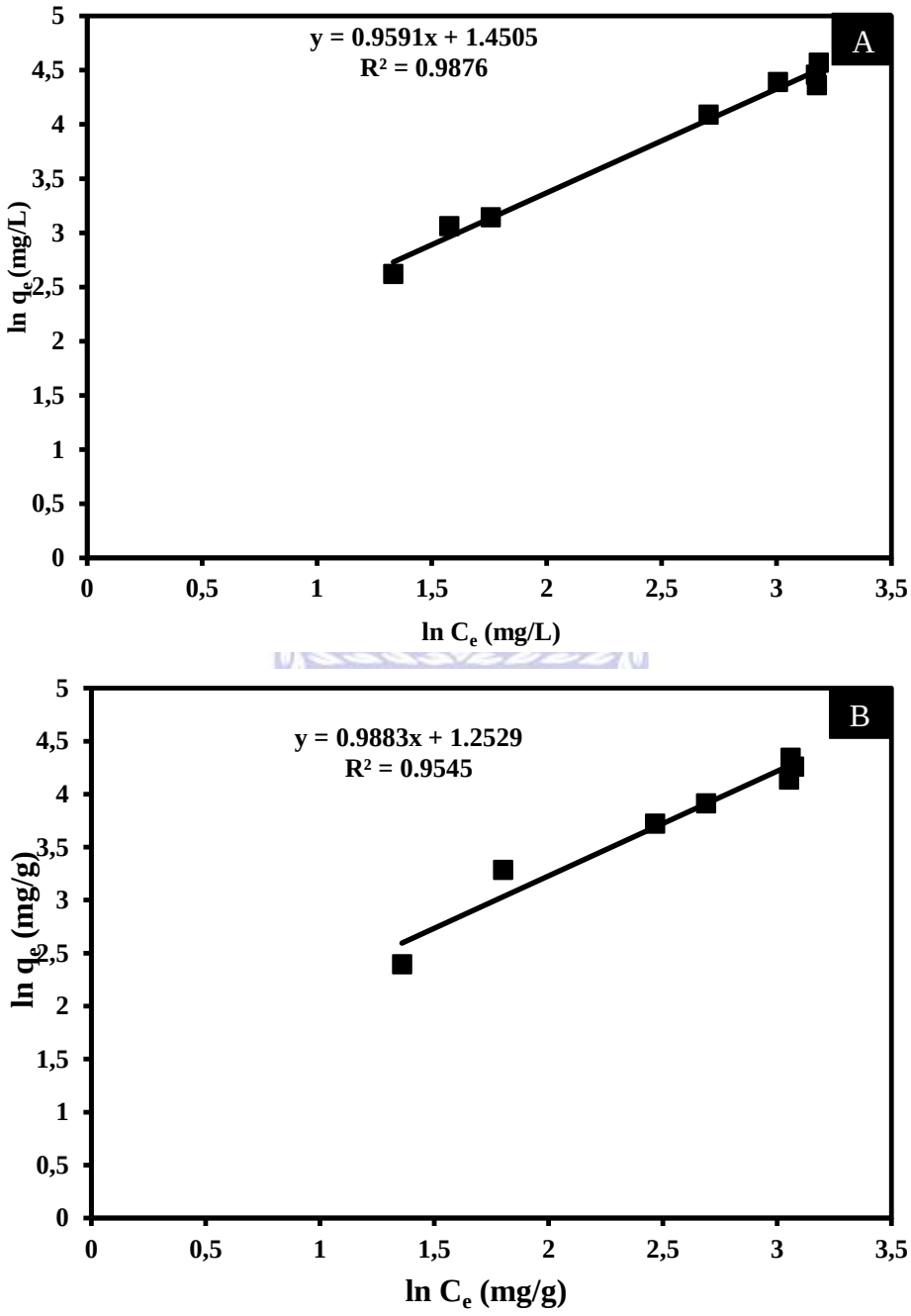

Figure 7. 7: Linearised plot of Freundlich isotherm for the adsorption of (A) Pb^{2+} or (B) Cd^{2+} onto TA_CHS_2.

From Figure 7.7, the R^2 values are relatively high but not as high as that of the Langmuir model. The value of R^2 could be an indication of heterogeneous distribution of the adsorbates on the surface of the adsorbent. The Freundlich model forecasts the increment in the amount of the adsorbate on the adsorbent's surface as the concentration of the adsorbate increases. Table 7.3 presents the parameters deduced from the Langmuir and Freundlich models.

Table 7. 3: Parameters deduced from the plot of Langmuir and Freundlich isotherms for Pb^{2+} and Cd^{2+} adsorption onto TA_CHS_2 nanofibres

	Langmuir isotherm				Freundlich isotherm		
Metal ion	R^2	b (L/mg)	q_{e_exp} (mg/g)	q_{e_cal} (mg/g)	R^2	n	k_f [(mg/g)(mg/L)$^{1/n}$)]
Pb^{2+}	0.9999	0.004	95.767	96.241	0.9876	1.043	3.719
Cd^{2+}	0.9999	0.0004	85.325	87.154	0.9545	1.012	2.255

Table 7.3 shows that the optimal adsorption capacities of Pb^{2+} or Cd^{2+} by the TA_CHS_2 adsorbents are 96.241 or 87.154 mg/g, respectively for the Langmuir model. The values were similar to those obtained experimentally (95.767 and 85.325 mg/g for Pb^{2+} or Cd^{2+}, accordingly). Both the model and the experimental equilibrium adsorption capacities of Pb^{2+} were higher than those of Cd^{2+}. The correlation coefficient (R^2) values obtained shows that the Langmuir model had a better fit (0.999) for both metal ions and is, therefore, more precise in explaining the adsorption process than the Freundlich model (0.9876 or 0.9545 for Pb^{2+} or Cd^{2+}, respectively). Furthermore, the values of the constants K_f (3.719 and 2.255) and n (1.043 and 1.012) for Pb^{2+} or Cd^{2+}, respectively deduced from the Freundlich model, suggest that some of the adsorbates were adsorbed on heterogeneous surfaces of the adsorbent. However, since the Langmuir model had a better fit, it, therefore, suggests that most of the adsorption process was as a result of monolayer formation. The Freundlich constant, n, has values above unity for both Pb^{2+} or Cd^{2+} while the R_L values lie $0< R_L< 1$. This implies that the adsorption of Pb^{2+} or Cd^{2+} by TA_CHS_2 adsorbent was favourable over the concentration range studied (Onwordi *et al.*, 2019).

7.3 Adsorption kinetics

Various kinetic models exist that describe the behaviour of the batch adsorption process. Kinetic models are important as they are applied to study the adsorption mechanisms and the rate-controlling steps of the process which could be mass transport or chemical reaction. Among the models used in fitting the experimental data are the "pseudo-first-order and the pseudo-second-order kinetic models". These two models, depicted by Equations 3.10 and 3.12, respectively were applied to the obtained data in the investigation of the adsorption kinetics. Figure 7.8 and 7.9 presents the plots of the "pseudo-first-order and pseudo second-order" kinetic data for these two metal ions. respectively. The parameters obtained from the adsorption kinetic plots of Pb^{2+} or Cd^{2+} are presented in Table 7.4.

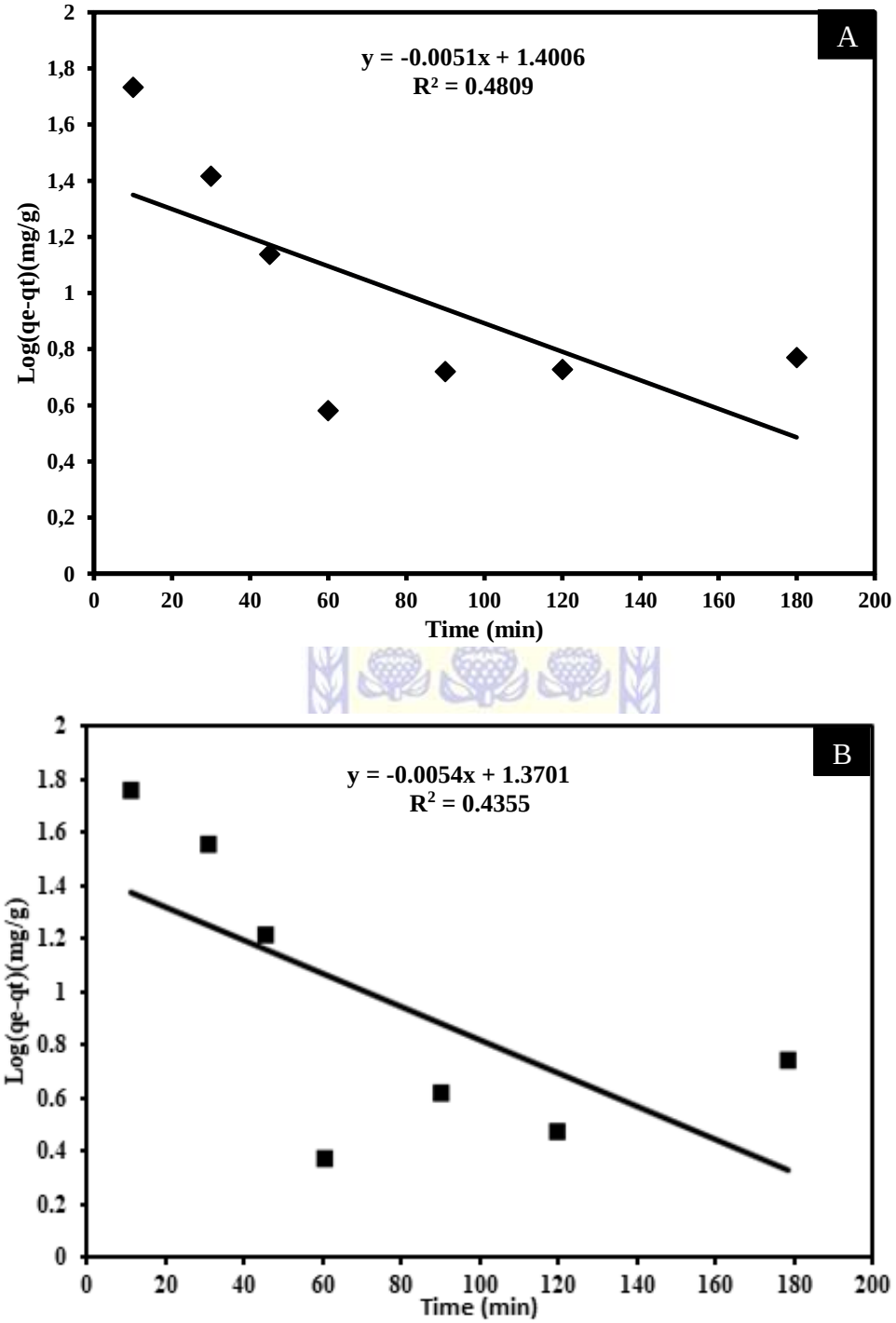

Figure 7. 8: Pseudo first-order rate equation plots for (A) Pb^{2+} or (B) Cd^{2+} adsorption onto TA_CHS_2.

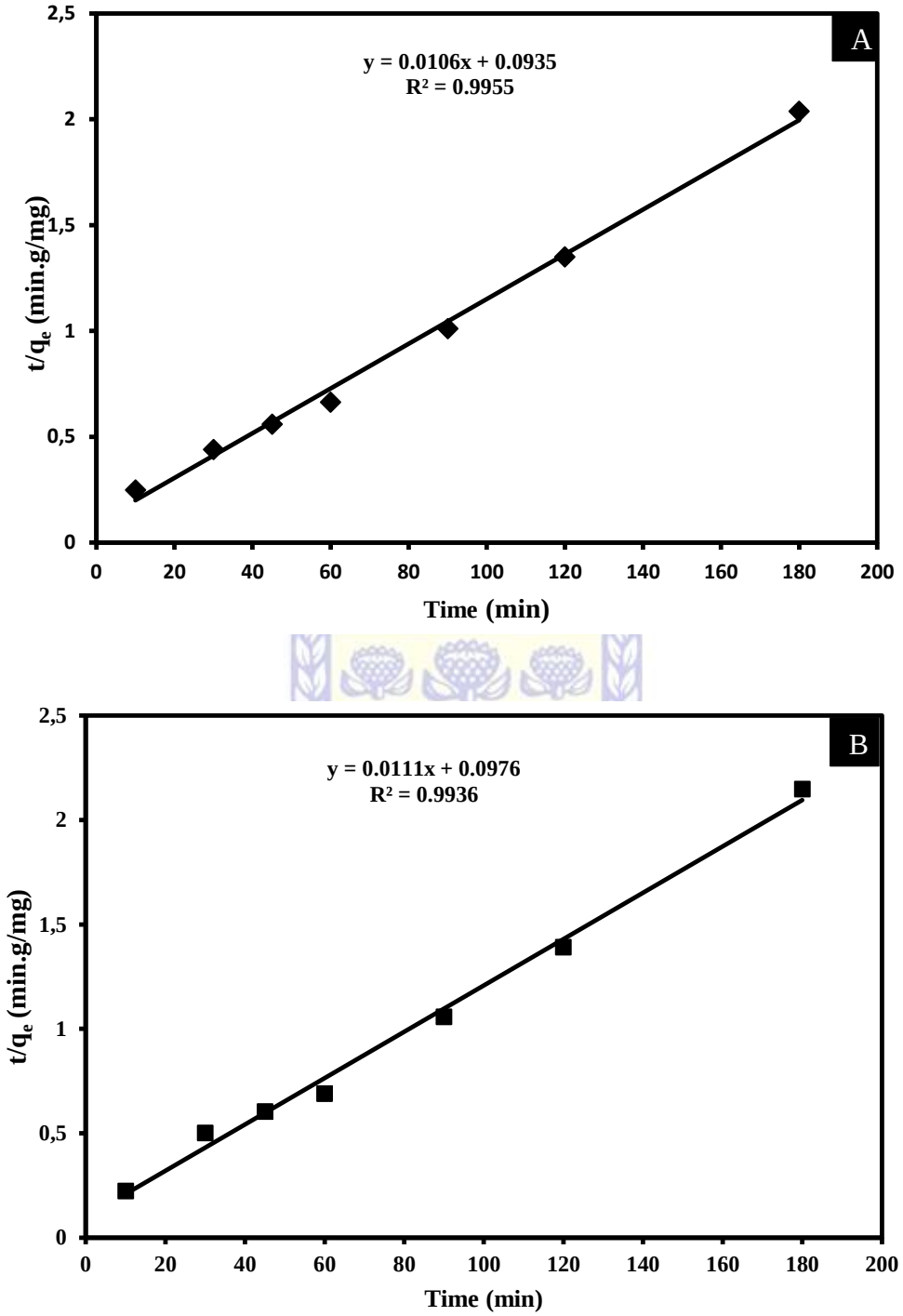

Figure 7. 9: Plots of pseudo-second-order model for (A) Pb^{2+} or (B) Cd^{2+} adsorption onto TA_CHS_2.

Table 7. 4: The kinetic parameters deduced from the adsorption of Pb^{2+} or Cd^{2+} onto TA_CHS_2.

Pseudo-first-order model					Pseudo-second-order model		
Metal ion	R^2	K_1 (min^{-1})	q_{e_cal} (mg/g)	q_{e_exp} (mg/g)	R^2	K_2	q_e ($gmg^{-1}min^{-1}$)
Pb^{2+}	0.4809	0.0051	0.148	90.418	0.9955	0.001	94.34
Cd^{2+}	0.4355	0.0054	0.137	87.561	0.9936	0.001	90.01

Table 7.4 presents the parameters computed from the kinetic plots of the adsorption studies using TA_CHS_2. The pseudo-second-order R^2 values for Pb^{2+} (0.9955) and Cd^{2+} (0.9936) were much higher when compared the pseudo-first-order R^2 values for Pb^{2+} (0.4809) and Cd^{2+} (0.4355). This is an indication that the pseudo-second-order kinetic model is more appropriate in describing the amount of Pb^{2+} or Cd^{2+} sorbed onto the TA_CHS_2 adsorbent. Moreso, the adsorption capacities computed (q_{e_cal}) from the linearised pseudo-second-order model (94.340 mg/g for Pb^{2+} and 90.009 for Cd^{2+}) were closely in agreement with the experimental (q_{e_exp}) values (90.418 mg/g for Pb^{2+} and 87.561 for Cd^{2+}). This suggest that the adsorption process is controlled by chemical reaction. Chemical sorption, otherwise called chemisorption, as a rate-limiting process, is associated with the interchange rather than the mass transfer of electrons between the adsorbate and the adsorbent in the solution (Liao *et al*., 2016; Ayanda *et al*., 2019).

7.4 Thermodynamic studies

The thermodynamic parameters were determined by plotting the natural logarithm of the distribution coefficient against the inverse of the absolute temperatures of the measurements, according to the Van't Hoff Equation (Equation 3.17). The linear graph is presented in Figure 7.10.

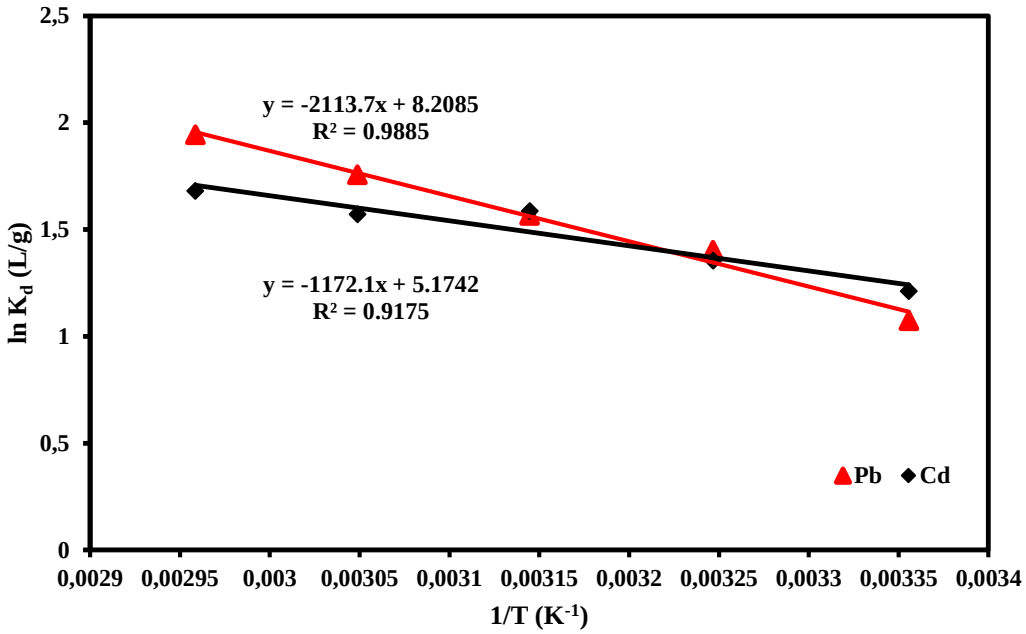

Figure 7. 10: Thermodynamic studies for the sorption of Pb^{2+} or Cd^{2+} onto TA_CHS_2.

Figure 7.10 shows the linearised plot of Van't Hoff's Equation (Equation 3.17). From the plot of lnK_d against 1/T, the enthalpy change (ΔH°, J/mol) and entropy change (ΔS°, J/mol.K) were computed from the slope and intercept of the linear relation, respectively. Table 7.3 shows the thermodynamic parameters, especially Gibb's free energy (ΔG°) values at each studied temperature. The positive value of ΔH° (17.57 and 9.74 kJ/mol for Pb^{2+} or $Cd^{2+,}$ respectively) proved that the sorption of the metallic ions onto TA_CHS_2 nanofibres was an endothermic reaction. The positive value of ΔS° (68.25 and 43.02 J/mol.K for Pb^{2+} or $Cd^{2+,}$ respectively) confirmed the increased randomness and disorderliness of the metal ions at the solid-solution interphase as temperature increased (Lawal *et al.*, 2017). The value of the entropy change could point to whether an adsorption process underwent associative or dissociative mechanisms. Values ≥10 $Jmol^{-1}k^{-1}$ are indication that an adsorption process followed a dissociative mechanism (Abbasizadeh *et al.*, 2014). The value of ΔS° for both Pb^{2+} or Cd^{2+} were greater than 10 J $mol^{-1}k^{-1}$ and, therefore, it could be infered that the adsorption process followed the dissociative mechanism. This result show that the ratio of free Pb^{2+} or Cd^{2+} in solution to the ions interacting with the TA_CHS_2 adsorbent were greater than the metal ions in the adsorbed state.

The ΔG° values at all the temperatures studied for both metal ions were negative. This shows that the adsorption process of Pb^{2+} or Cd^{2+} onto TA_CHS_2 adsorbents were spontaneous. Also

observed from Table 7.5 is the fact that as the temperature increased, there were corresponding increases in ΔG° values. This observed trend is an indication that the adsorption process shows more spontaneity at high temperatures than at low temperatures. Liu *et al*. (2014) observed this trend in their study of recycled chitosan nanofibres for the chelation of metallic ions and concluded that it could be as a result of the dispersion of the nanofibre adsorbents at high temperatures. This assertion is corroborated by the high removal percentage (88% for Pb^{2+} and 96% for Cd^{2+}) observed at higher temperatures in this study than at lower temperatures (Figure 7.4).

Table 7. 5: The determined thermodynamic parameters for Pb^{2+} or Cd^{2+} adsorption onto TA_CHS_2 nanofibre.

Metal ion	ΔS (J/mol.K)	ΔH (KJ/mol)	R^2	ΔG (KJ/mol) T (˚C) 25	35	45	55	65
Pb^{2+}	68.25	17.57	0.9885	-7.25	-10.41	-12.67	-15.79	-19.61
Cd^{2+}	43.02	9.74	0.9175	-8.32	-9.92	-12.92	-13.13	-15.10

7.5 Desorption and reusability studies

The reuse of an adsorbent is crucial in adsorption studies. The desorption and reusability of the adsorbent influences the adsorption efficiency, capacity, economic cost and practical applications of the adsorbent. The reuse of an adsorbent is determined by its regeneration capacity and could have many benefits such as the reduction of process cost, reduction of waste and the recovery of pollutants. The desorption and reusability studies were done as described in Section 3.5 of Chapter 3. The experiments were conducted to regenerate the TA_CHS_2 previously used in the adsorption of Pb^{2+} or Cd^{2+} at the conditions of pH 4 and 6 for Pb^{2+} or $Cd^{2+,}$ respectively, the initial metal concentration of 50 mg/L at a contact time of 1.0 h and room temperature. The resulting solutions were filtered and analysed using ICP-OES (Section 3.9.7 of Chapter 3) and the percentage of the metal ions desorbed was determined using Equation 3.18 and are presented in Figure 7.11. The mats were rinsed using deionised water and dried at 50 ºC for 24 h in an oven. The adsorbents were reused in three different adsorption-desorption cycles following the same procedure and adopting the same variables enumerated. The results of the regeneration performance of the adsorbent are presented in Table 7.6 and Figure 7.12.

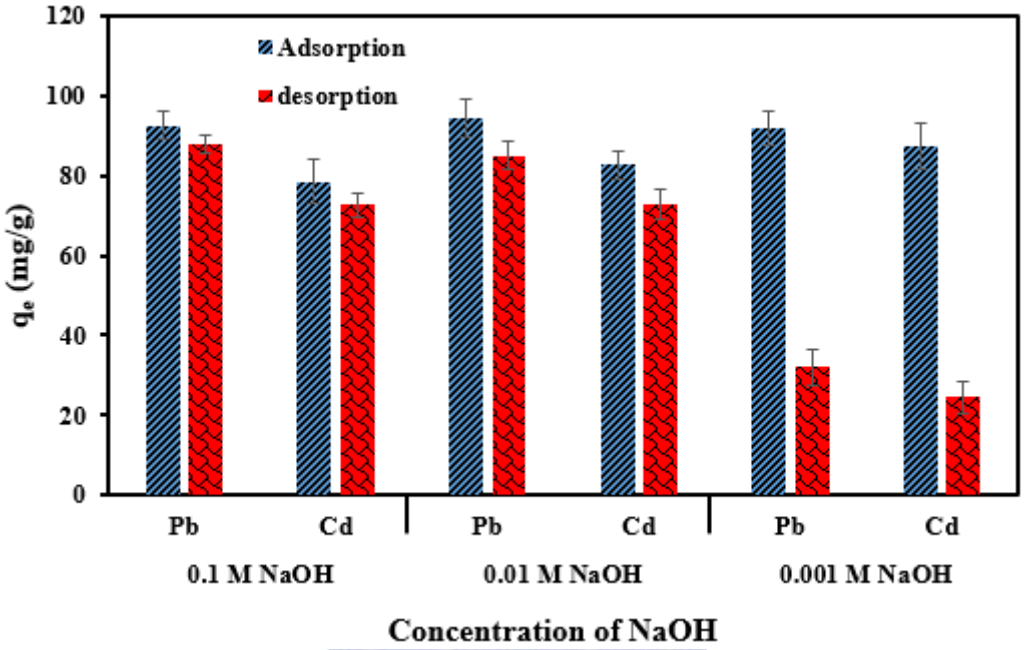

Figure 7. 11: Adsorption-desorption studies of 0.005 g TA_CHS_2 loaded with Pb^{2+} or Cd^{2+} using different concentrations of NaOH.

Figure 7.11 shows the adsorption-desorption experiments of TA_CHS_2 nanofibres using 10 mL of 0.1 M, 0.01 M and 0.001 M NaOH. The aim was to determine the best concentration of NaOH needed for the desorption of the Pb^{2+} or Cd^{2+} from the adsorbent. The results indicate that the desorption experiments were effective using NaOH but depended on the concentration of the solution. The efficient desorption of the Pb^{2+} or Cd^{2+} from the TA_CHS_2 adsorbent observed could be as a result of weakened electrostatic interactions between the adsorbent and the adsorbates in the alkaline environment (Zhang *et al*., 2016). The highest desorption value was observed when 0.1 M NaOH solution was used as the eluent. A value of 95 or 92% (87.81 and 72.56 mg/g out of 92.43 and 78.54 mg/g) of the previously adsorbed metal ions were determined for Pb^{2+} or Cd^{2+}, respectively. The use of 0.01 M NaOH solution desorbed 90 and 88% (84.94 and 72.79 mg/g out of 94.38 and 82.72 mg/g) while 0.001 M NaOH gave the lowest desorption result of 35 and 28% (32.13 and 24.42 mg/g out of 91.81 and 87.20 mg/g) adsorbed by the TA_CHS_2 adsorbents. Though 0.1 M NaOH solution gave the highest percentage desorption for both Pb^{2+} or Cd^{2+} after the first cycle of regeneration, the TA_CHS_2 nanofibres became brittle, breaking off as they were handled and, therefore, could not be re-used in further reusability experiments. In view of this, the experiments were conducted using 0.01 M NaOH to desorb and regenerate the TA_CHS_2 adsorbents.

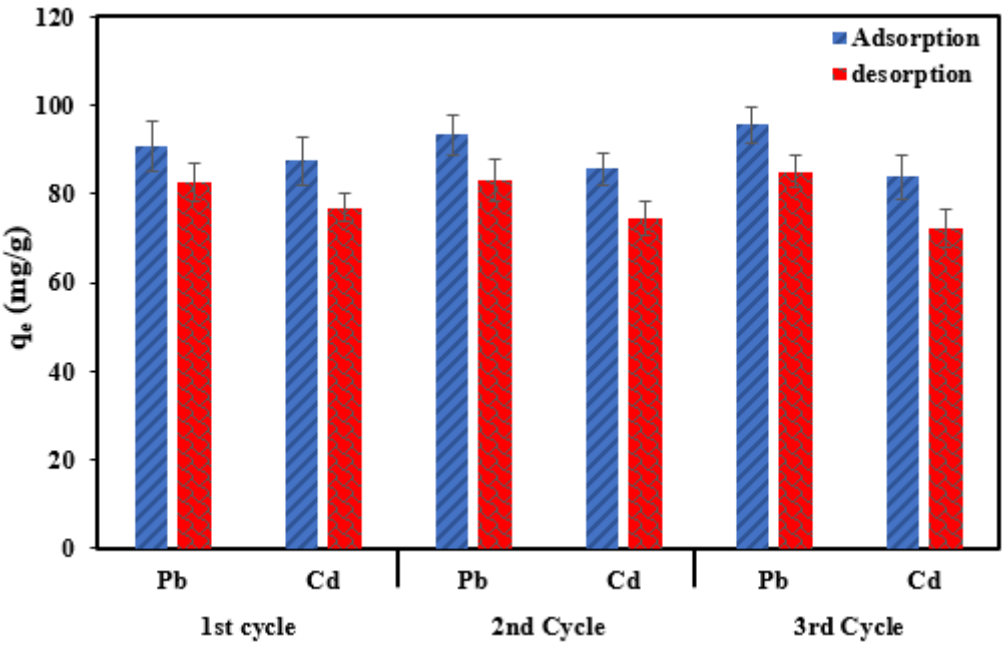

Figure 7. 12: Adsorption-desorption cycles of 0.005 g TA_CHS_2 nanofibre. Desorption of the sorbed Pb^{2+} or Cd^{2+} were done using 0.01 M NaOH solution.

Table 7. 6: Regeneration performance of TA_CHS_2 adsorbent for the sorption of Pb^{2+} or Cd^{2+} after three adsorption-desorption cycles (initial metal ion concentration - 50 mg/L; adsorbent dosage - 0.005 g; eluent – 0.01 M NaOH; desorption time - 60 min).

Regeneration performance (%)					
1st cycle		2nd cycle		3rd cycle	
Pb^{2+}	Cd^{2+}	Pb^{2+}	Cd^{2+}	Pb^{2+}	Cd^{2+}
91.0	88.0	89.0	87.0	89.0	86.0

Figure 7.12 shows the regeneration experiments of the TA_CHS_2 adsorbent. The results show that the TA_CHS_2 could be effectively regenerated by using 0.01 M NaOH and the desorbed sorbent could be reused for three cycles without significant reduction in the affinity of the metal ions to the active sites or reduction in the stability of the material. The first cycle shows that 91% and 88% desorption efficiency were achieved for Pb^{2+} or Cd^{2+}, respectively. Interestingly, in the second and the third cycles, Pb^{2+} had slightly higher adsorption capacity (Figure 7.12) than in the first regeneration cycle although the percentage desorption (Table 7.6) was lower in both cycles than in the first cycle. In the second adsorption-desorption cycle, 89 and 87% desorptions were obtained for Pb^{2+} or Cd^{2+}, accordingly while the third cycle had 89 or 86% desorptions, respectively. The slight increase in the adsorption capacity after the first

regeneration cycle could be as a result of the excellent level of accessibility of the nanofibres adsorbent's active sites (Da'na, 2017). This, therefore, results in increased adsorption capacity.

The results of the reusability efficiency of the TA_CHS_2 indicate that the adsorbent has a high uptake capacity for both the metal ions. The adsorption capacities of both Pb^{2+} or Cd^{2+} were not significantly affected during the adsorption-desorption cycle with the adsorbents still having high regeneration efficiency for Pb^{2+} or Cd^{2+} after the third cycle. Regeneration studies are performed principally to recover pollutants in the adsorbed phase and to reactivate the active sites of the adsorbent for further pollutant removal from solution. The result obtained in this study were better than the outcomes of the study by Chauhan and Sankararamakrishnan (2008) who obtained 26% desorption of Pb^{2+} using NaOH for chitosan functionalised by xanthate.

7.5 Chapter summary

This chapter focused on the application of tannic acid crosslinked chitosan nanofibres for the sorption of metallic ions in aqueous solution. Various batch experiments were performed to determine the optimal conditions for the sorption of Pb^{2+} or Cd^{2+}. The parameters studied were pH, initial concentration, contact time and temperature of the adsorption process. From these experiments, the optimal conditions that gave the highest adsorption capacities were established. The obtained adsorption data were modelled using kinetic and isotherm models and the appropriate model that fits the experimental data were established. Furthermore, desorption and reusability studies of the adsorbents were conducted.

The investigation of the optimal pH of the studies showed that the adsorption capacity for both metal ions increased with an increase in pH before attaining equilibrium. The optimal pH for the sorption of Pb^{2+} or Cd^{2+} in this study were 4.0 or 6.0, respectively. These pH values were subsequently selected for further testing of the TA_CHS_2 adsorbent. The concentration of the metal ions in solution followed a similar pattern as pH, where the adsorption capacity for both Cd^{2+} or Pb^{2+} increased with an increase in concentration. This show that the nanofibres had excellent sorption capacity for the specific metal ions of 95.77 or 85.34 mg/g for Pb^{2+} or Cd^{2+}. The data had a good fit with the Langmuir model with an R^2 value of 0.9999 for both metal ions, an indication that most of the adsorption of Pb^{2+} or Cd^{2+} took place on the homogenous surface of the TA_CHS_2. The Freundlich model had a lower R^2. The computed Langmuir adsorption capacities (96.24 or 87.15 mg/g for Pb^{2+} or Cd^{2+}, respectively) were in close

agreement with the experimental values (95.77 or 85.34 mg/g for Pb^{2+} or Cd^{2+}, respectively). The favourability of the adsorption process was further ascertained with the dimensionless separation factor, $R_{L,}$ having values between 0 and 1 for both metal ions.

The equilibrium sorption time was determined to be 60 minutes for both metal ions. The Pseudo-second order kinetic model was more appropriate in explaining the adsorption processes as the R^2 values (0.9955 for Pb^{2+} and 0.9936 for Cd^{2+}) were higher than those of the pseudo-first-order models (0.4809 for Pb^{2+} and 0.4355 for Cd^{2+}). The further results obtained from the thermodynamic studies indicate that the adsorption process was endothermic, spontaneous with increased randomness at the solid-liquid boundary, as shown by the $\Delta H°$, $\Delta G°$ and $\Delta S°$ values. Furthermore, it was found that the adsorption process followed the dissociative mechanism step as the value of $\Delta S°$ was greater than 10 $Jmol^{-1}k^{-1}$, signifying that the ratio of the metal ions in the solution to the ions interacting with the adsorbent was greater than the metal ions adsorbed already by the adsorbent. Desorption studies were conducted and it was found that Pb^{2+} or Cd^{2+} loaded TA_CHS_2 adsorbent could be easily desorbed using a 0.01 M NaOH solution and the adsorbent could achieve 89 or 86% desorption for Pb^{2+} or Cd^{2+}, respectively after three consecutive regeneration cycles.

The results obtained in this chapter have shown that tannic acid crosslinked chitosan nanofibres could serve as an efficient adsorbent for the removal of Pb^{2+} or Cd^{2+} from aqueous solution.

CHAPTER 8

ANTIMICROBIAL AND CYTOTOXIC EFFECTS OF EXTRACTED AND ELECTROSPRAYED BSF CHITOSAN BIOMATERIALS.

8.0 Introduction

The effects of synthesised BSF chitosan biomaterials on selected microbial species were investigated and compared with that of commercial shrimp chitosan biomaterials. The samples used in this study have the following codes: BSF chitosan (PCH21_9), commercial shrimp chitosan (CM_CHS) and BSF chitosan nanoparticles (BSF_NPs). The microbial species studied were *Enterococcus faecalis, Streptococcus mutans* or *Candida albicans*. This chapter has four sections. The first section comparatively discusses the antimicrobial efficacy of 3% PCH21_9 or CM_CHS on the studied microbial species. The second section also studied the effects of BSF_NPs on the microorganisms while the third section detailed the effect of PCH21_9 or BSF_NPs on the three studied microorganisms. The fourth section of this chapter detailed the risk assessment of the synthesised materials (PCH21_9 or BSF_NPs) by investigating their cytotoxicity in contact with human skin fibroblast cells. Sections one, two and three utilised the Time-kill analysis technique in determining the effects of the PCH21_9, CM_CHS or BSF_NPs on the three studied microorganisms (*E. faecalis, S. mutans* or *C. albicans*). The Time-kill analysis examines the time it took a given chitosan sample to completely eliminate each microbial species independently. The non-parametric Kaplan-Meir survival function test was used to statistically analyse the obtained data. Cell viability studies were adopted in section four. The test measured the survival rate of human skin fibroblast cell lines in contact with the BSF_NPs or PCH21_9. Subsequent sub-sections present the results obtained from the investigations of the chitosan biomaterials.

8.1 The effect of 3% PCH21_9 or CM_CHS on studied microbial species

The effect of both PCH21_9 or CM CHS on exposure to *S. mutans, E. faecalis* or *C. albicans* was investigated using the Time-Kill test technique described in Section 3.6 of Chapter 3. Next sub-section focused on the effect of the PCH21_9 or CM_CHS against *E. faecalis*.

8.1.1 *The effect of PCH21_9 or CM_CHS against E. faecalis*

The investigation was conducted to determine the effect of extracted BSF chitosan and low MW commercial shrimp chitosan on *E. faecalis*. This study was performed according to the

procedure described in Section 3.6 of Chapter 3. The concentration of both chitosan solutions were 3% in acetic acid solution. Figure 8.1 shows the mean Log of the colony-forming units (CFU/mL) of *E. faecalis* exposed to PCH21_9 or CM_CHS over a 24 h period.

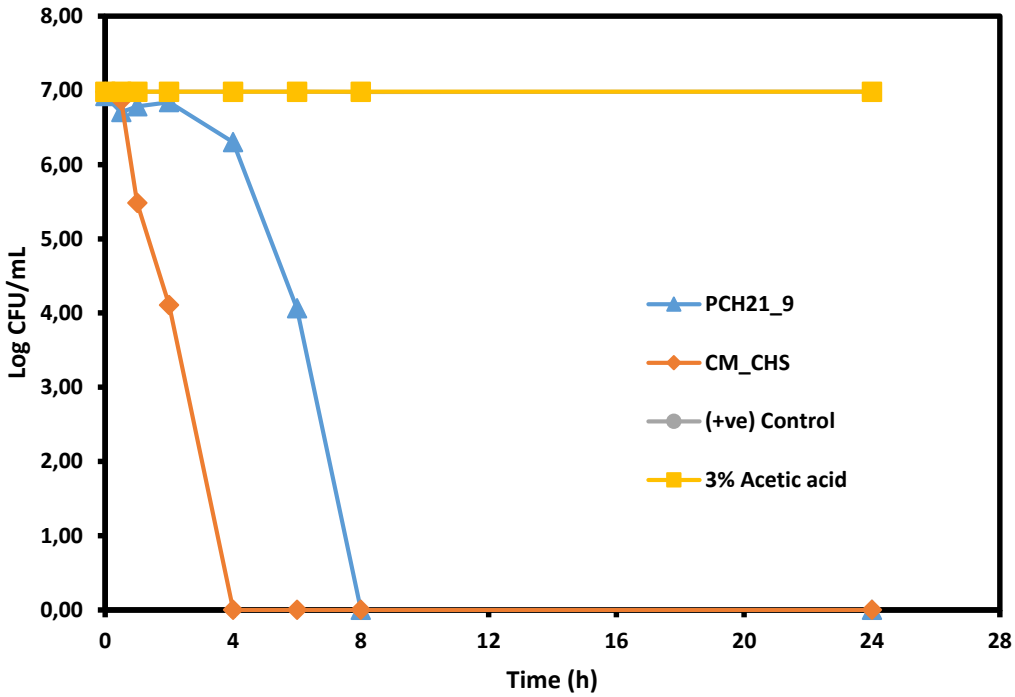

Figure 8. 1: The Log CFU/mL of *E. faecalis* when exposed to PCH21_9 or CM_CHS for 24 h period.

From Figure 8.1, visible differences in the survival time plots of *E. faecalis* in contact with PCH21_9 or CM_CHS were observed. There was a progressive reduction in the mean Log CFU/mL for the PCH21_9 or CM_CHS over time. The CM_CHS showed a steeper decline than the PCH21_9. After 0.5 h (30 minutes) of inoculation, there were a 3% and 2% reduction in the microbial load in contact with PCH21_9 or CM_CHS, respectively. These values dropped significantly to 41% (4.11) after 2 h with CM_CHS but slightly increased (6.84) in samples treated with PCH21_9. Total eradication of the organisms was achieved after 4 h of contact with the CM_CHS whereas it took the PCH21_9 8 h contact time to achieve total elimination of the microorganism, *E. faecalis*, in the test media.

To further study the data obtained on the exposure of *E. faecalis* to 3% PCH21_9 or CM_CHS, the non-parametric Kaplan-Meir survival function curve was plotted. The test measures the fraction of the living microorganisms observed/that survived over a period after exposure to

the samples (Goel *et al.*, 2010). Figure 8.2 shows the Kaplan-Meir survival function plot of *E. faecalis* on exposure to PCH21_9 or CM_CHS.

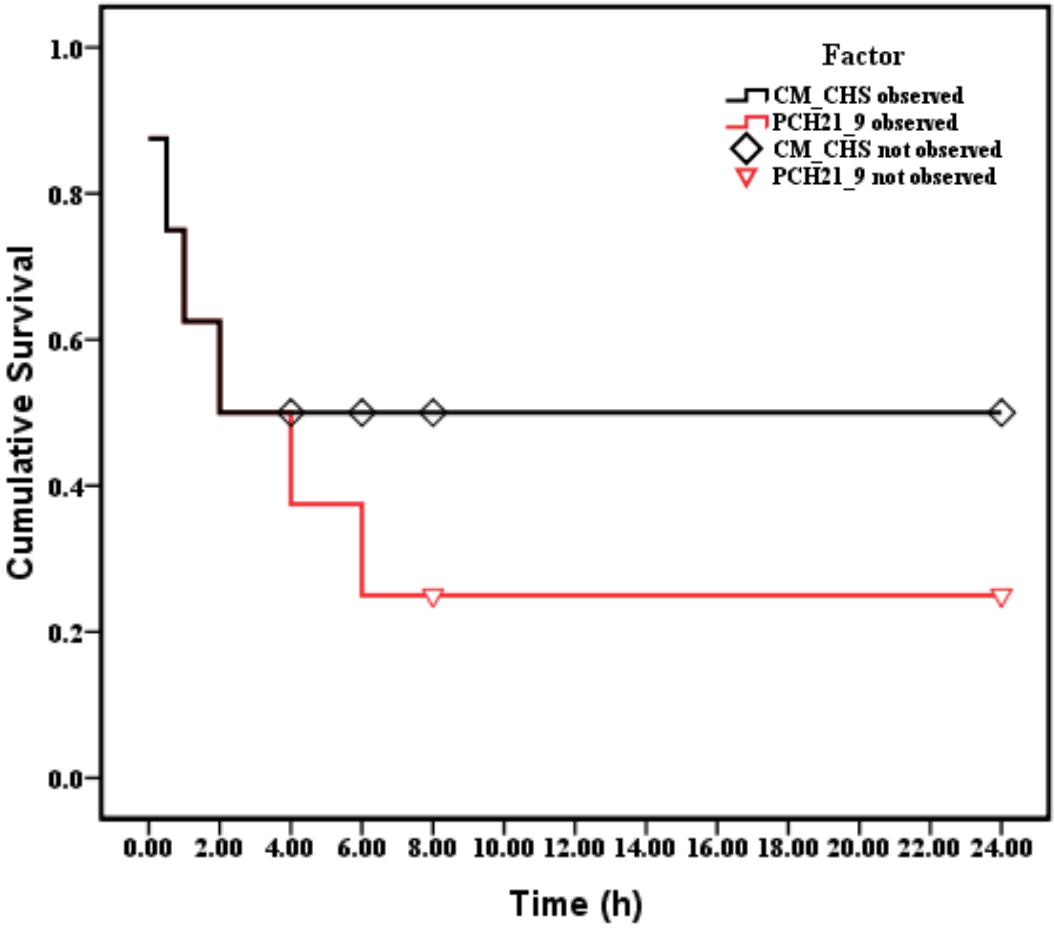

Figure 8. 2: The Survival function curve of *E. faecalis* showing the survival time of the organism on exposure to PCH21_9 or CM_CHS over a 24 h period.

Figure 8.2 shows that the microorganisms were observed on both test media at zero hours, 0.5 h, 1 h and 2 h. The organisms exposed to CM_CHS were not observed from 4 h onward. This implies that 2 h is the survival time for the *E. faecalis* in CM_CHS while in contact with PCH21_9, their survival time was 8 h.

Cummins and Harris (1956) reported that *E. faecalis* is Gram-positive bacteria with the presence of a single cell wall. This cell wall is characterised by insolubility in various solvents and its rigidity. To this end, they reported that *E. faecalis* behave in different ways in contact with an external agent. The behaviour ensures that their defence mechanisms are modified to suit the situation. This study showed that CM_CHS has a lower MW compared to the PCH21_9 (Section 4.2.10 of Chapter 4). The MW variation could, therefore, explain the different

behaviour of *E. faecalis* in the presence of PCH21_9 or CM_CHS under the same conditions. The interaction of these two chitosan samples points to the occurrence of reactions leading to the hydrolysis of the peptidoglycans present in the cell walls of the *E. faecalis*. This interaction could cause the leakage of intracellular electrolytes within the cell wall, causing lysis of the cell membranes which eventually could lead to the death of the microorganism (Zheng and Zhu, 2003; Goy *et al.*, 2016). Younes *et al.* (2014) have studied the antibacterial effect of high and low MW chitosan against Gram-positive and Gram-negative bacteria. Their study revealed that increasing the MW of chitosan increased their antibacterial effect on *E. faecalis*, a Gram-positive bacterium. Although, the MW of the chitosan they used was not stated.

The work of Younes *et al*. (2014) is in agreement with the result of this study since both studies found that chitosan exhibited bactericidal effect against *E. faecalis*. The pictorial images of the colony-forming units of *E. faecalis* in the experimental cells are shown in Figure 8.3.

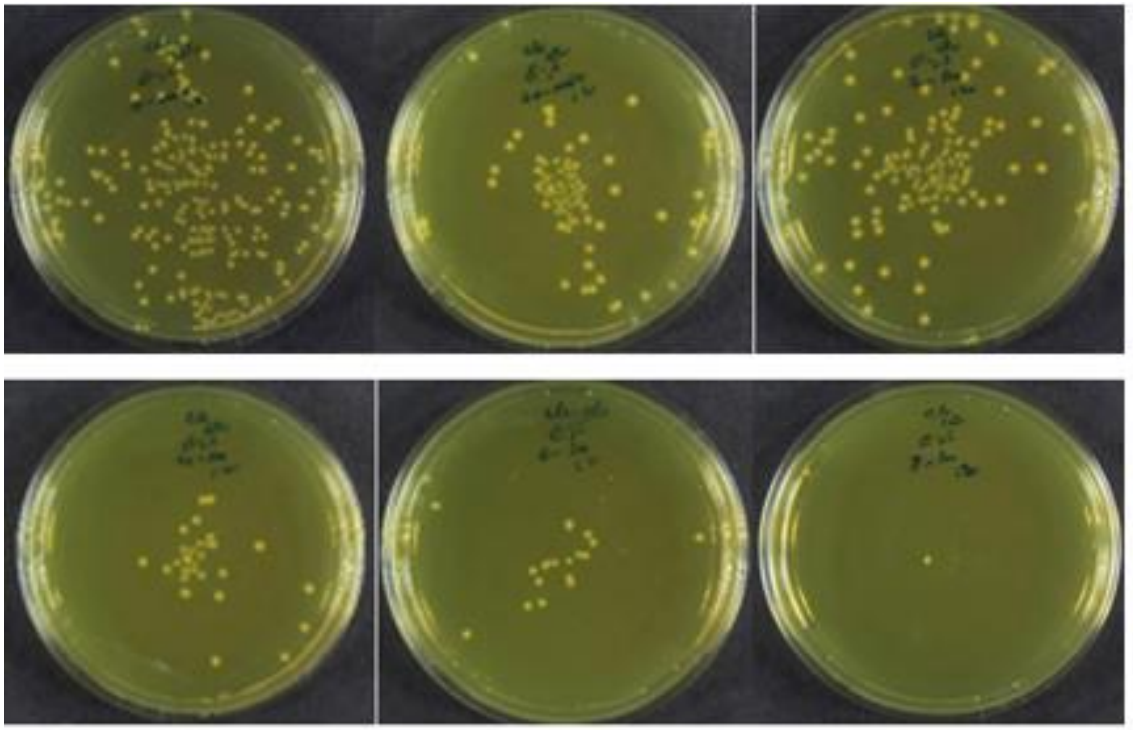

A

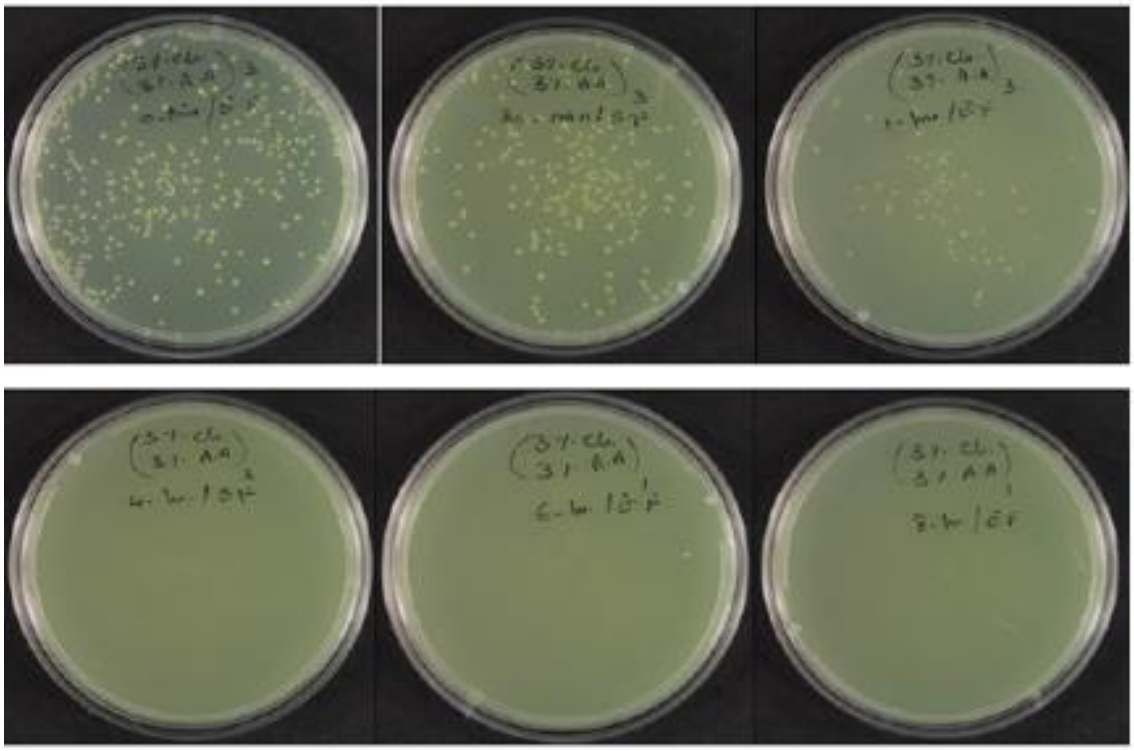

B

Figure 8. 3: The colony-forming units of *E. faecalis* when exposed to 3% (A) PCH21_9 and (B) CM_CHS at different time intervals.

8.1.2 *The effect of PCH21_9 or CM_CHS against S. mutans*

The investigation was conducted to determine the effect of PCH21_9 or CM_CHS on *S. mutans* over a period of 24 h. This study was performed according to the procedure described in Section 3.6 of Chapter 3. Figure 8.4 shows the mean Log of the colony-forming units (CFU/mL) of *S. mutans* exposed to PCH21_9 or CM_CHS over a 24 h period.

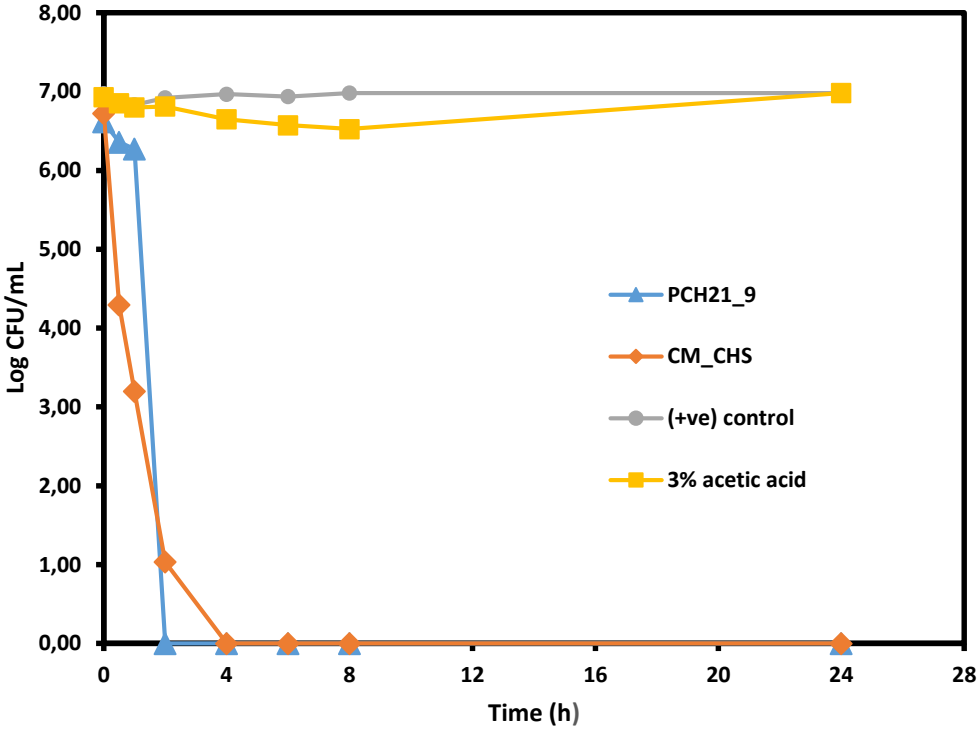

Figure 8. 4: The Log CFU/mL of *S. mutans* when exposed to PCH21_9 or CM_CHS for 24 h period.

The values of the Log CFU/mL for PCH21_9 or CM_CHS at zero hours was 6.62. The PCH21_9 had no noticeable effect (only 5% decrease) on the organisms (*S. mutans*) within the first hour of contact. On the contrary, the CM_CHS had an immediate impact on the organisms as the Log of the colony count declined significantly to 4.30 amounting to a 36% reduction within 0.5 h of inoculation. Continued contact with the CM_CHS led to a 52% and 85% reduction in microbial (*S. mutans*) load after 1 and 2 h of contact, respectively. Total elimination of *S. mutans* by CM_CHS occurred after 4 h of contact. Contrary to what was observed with *E. faecalis*, PCH21_9 completely eradicated *S. mutans* within 2 h of contact. This implies that PCH21_9 is more potent than the CM_CHS in treating *S. mutans*.

To further ascertain the survivability or otherwise of the *S. mutans*, the non-parametric Kaplan-Meir survival analysis was conducted on the data generated after exposure of the microbes to

PCH21_9 or CM_CHS. Figure 8.5 presents the cumulative survival curve of *S. mutans* on exposure to PCH21_9 or CM_CHS.

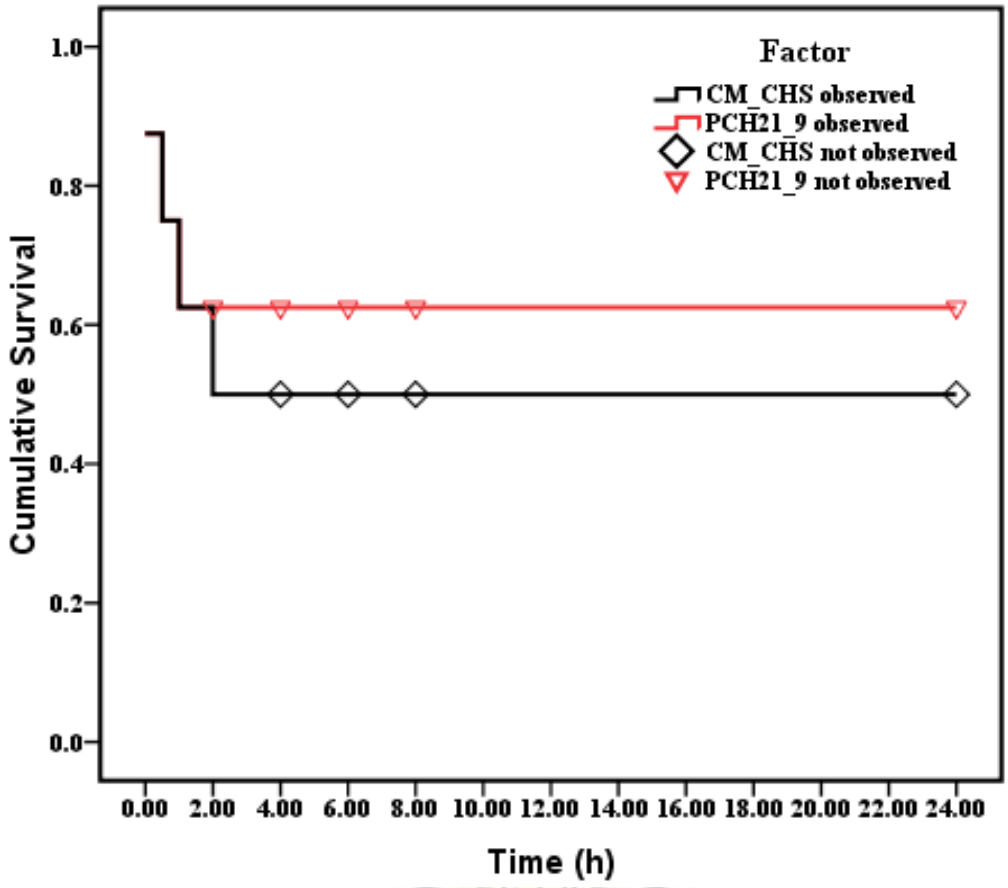

Figure 8. 5: The Survival function curve of S. *mutans* showing survival time of the organisms on exposure to PCH21_9 or CM_CHS over a 24 h period.

The survival function curve (Figure 8.5) indicates that *S. mutans* were observed from zero hours up to 2 h of contact with CM_CHS. By 4 h of contact, all the microorganisms had been totally eradicated. On the contrary, by 2 h of contact with the PCH21_9, all the *S. mutans* in the test media had been completely eliminated. This is a further indication that PCH21_9 is more potent than the CM_CHS in treating *S. mutans*. Figure 8.6 shows the pictorial view of the CFU/mL of *S. mutans* on exposure to PCH21_9 or CM_CHS over a 24 h period.

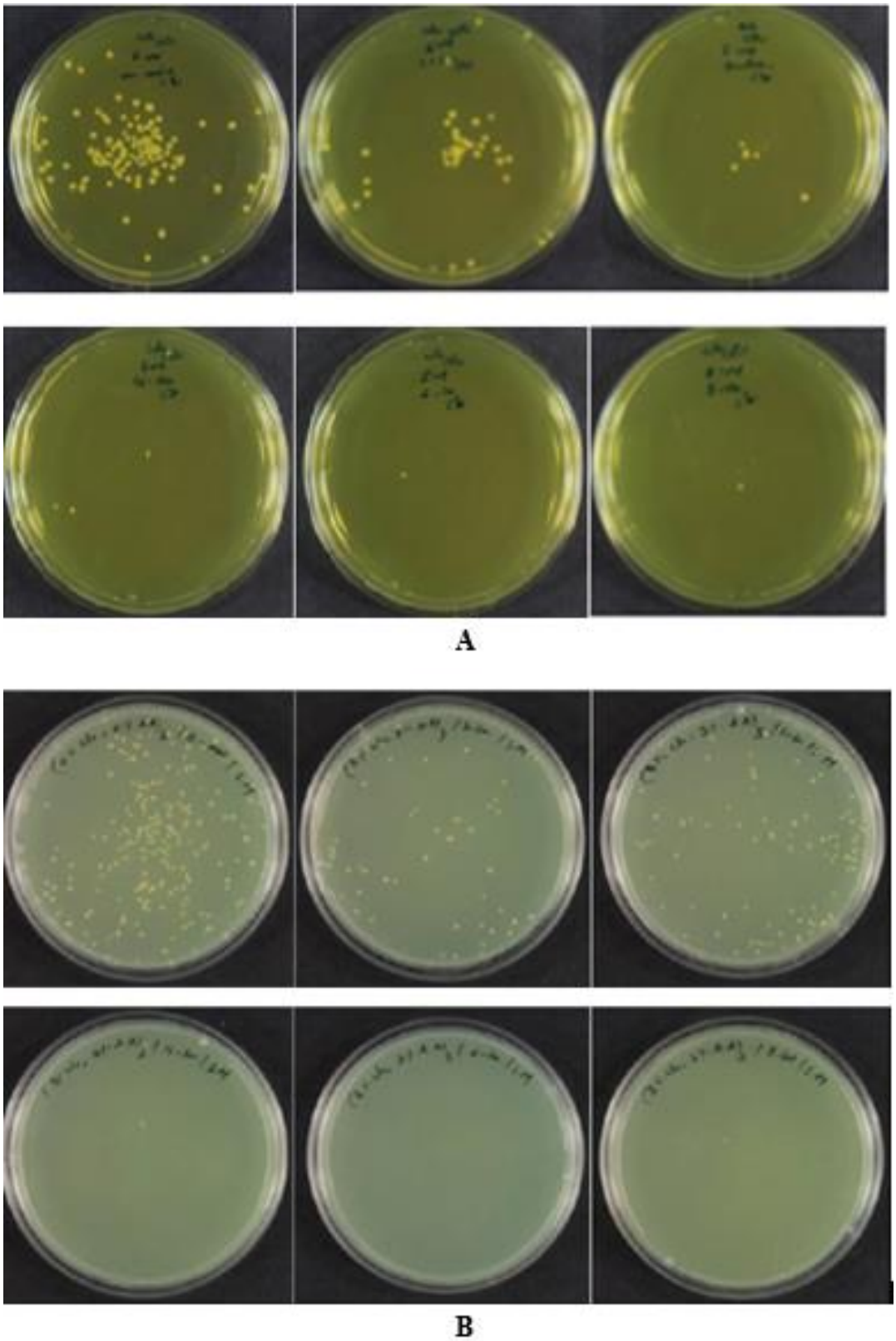

Figure 8. 6: The pictorial view of the colony-forming units of *S. mutans* when exposed to 3% (A) PCH21_9, (B) CM_CHS over a 24 h period.

8.1.3 *The effect of PCH21_9 or CM_CHS against C. albicans*

The investigation was conducted to determine the effect of PCH21_9 or CM_CHS on *C. albicans*. This study was performed according to the procedure described in Section 3.6 of Chapter 3. Figure 8.7 shows the mean plot of the Log of the colony-forming units (CFU/mL) of *C. albicans* exposed to 3% PCH21_9 or CM_CHS over a 24 h period.

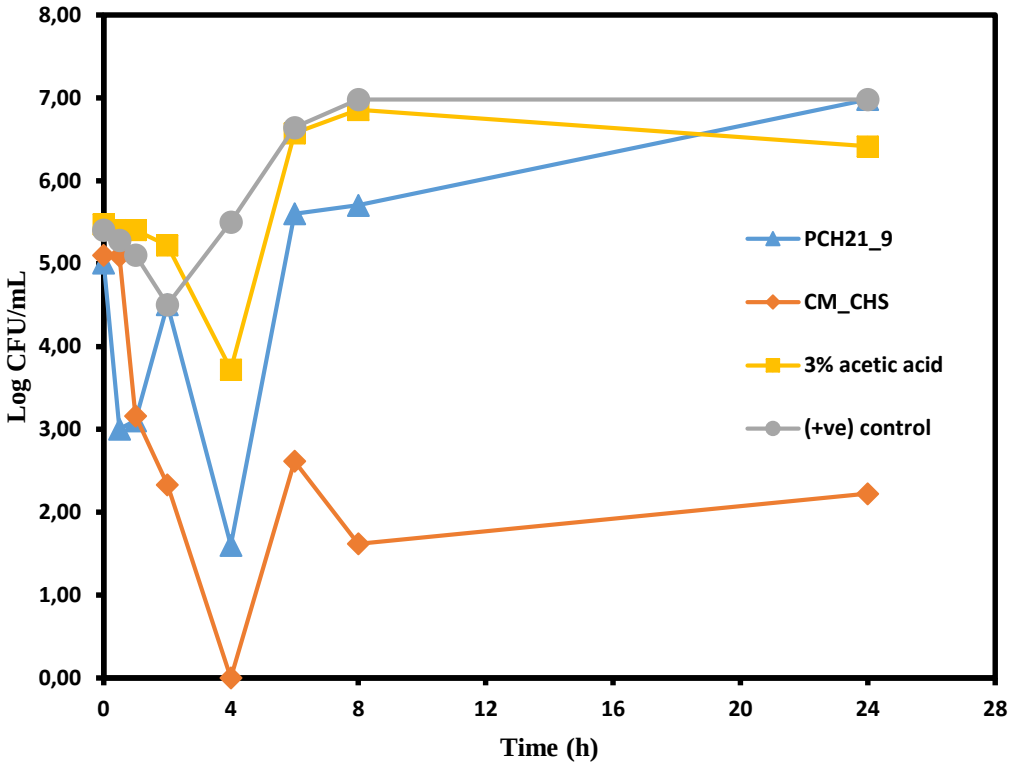

Figure 8. 7: The Log CFU/mL of *C. albicans* when exposed to PCH21_9 or CM_CHS for 24 h period.

Figure 8.7 presents the Log of the CFU/mL for PCH21_9 or CM_CHS over a 24 h period. At zero hour, the CFU/mL value was approximately 5.00. The PCH21_9 initially showed a better inhibitory effect after 0.5 h by the reduction of the CFU/mL count by 40%. After 1 h of exposure, the inhibitory effect of both samples was observed to be approximately equal at 3.10 CFU/mL. The highest reduction of the microbial load by the PCH21_9 was observed after 4 h with a value of 1.6 CFU/mL, representing a 68% reduction in microbial load. Similarly, the CM_CHS had a Zero CFU/mL momentarily after 4 h of incubation. Interestingly, the microorganisms increased in number on both media after 6 h of contact. The organisms increased by 250% and 262% from 4 h to 6 h of contact with PCH21_9 or CM_CHS, respectively. A further increase was subsequently observed with the PCH21_9 treated *C. albicans* while the CM_CHS treated samples fluctuated. Figure 8.7, therefore, indicates that

neither the 3% concentration of PCH21_9 nor CM_CHS was effective against *C. albicans* over the 24 h study period. Rather both chitosan samples did exhibit fungistatic effect after 4 h of contact, after which it did promote the proliferation of the microorganisms from 6 h to the 24 h of the investigation. This observation may be related to the potentiality of the *C. albicans* to adjust and finally adapt to the negative environment in which it found itself. Bogosian and Bourneuf (2001) had reported that injured microorganisms could regrow under a favourable environment. This could, therefore, explain the consequent proliferation of *C. albicans* in the test media for PCH21_9 or CM_CHS.

The inability of PCH21_9 or CM_CHS to achieve a durable fungicidal action may have also resulted from the microbes utilising the chitosan and incorporating it in their cell wall. Russell (2003) had reported that the cell wall of microorganisms consists of different materials. According to the authors, the cell wall of bacteria is composed of peptidoglycan whereas fungal cell walls consist of chitin, chitosan, glucan and mannan (Russell, 2003). Judging from the report of Russell, it could be stated that *C. albicans* cell walls contain chitosan. Therefore, the presence of chitosan could have been responsible for the fluctuations in the observed effect (fungistatic) of PCH21_9 or CM_CHS in this study as the organisms try to adjust in the test media. These adjustments/fluctuations were observed as the reduction of the mean of Log CFU/mL of the organisms. Kanafani and Perfect (2008) reported the susceptibility of *C. albicans* to different antifungal agents, including chitosan, and concluded that their susceptibility was different with different strains of *C. albicans.* This may also have influenced the growth fluctuations in the Log of CFU/mL of *C. albicans* observed in the study.

The data obtained from the exposure of *C. albicans* to PCH21_9 or CM_CHS were further analysed using the non-parametric Kaplan-Meir survival function test. This statistical test shows the time the organisms were able to survive or die on exposure to the chitosan solution. Figure 8.8 presents the cumulative survival curve of *C. albicans* on exposure to PCH21_9 or CM_CHS.

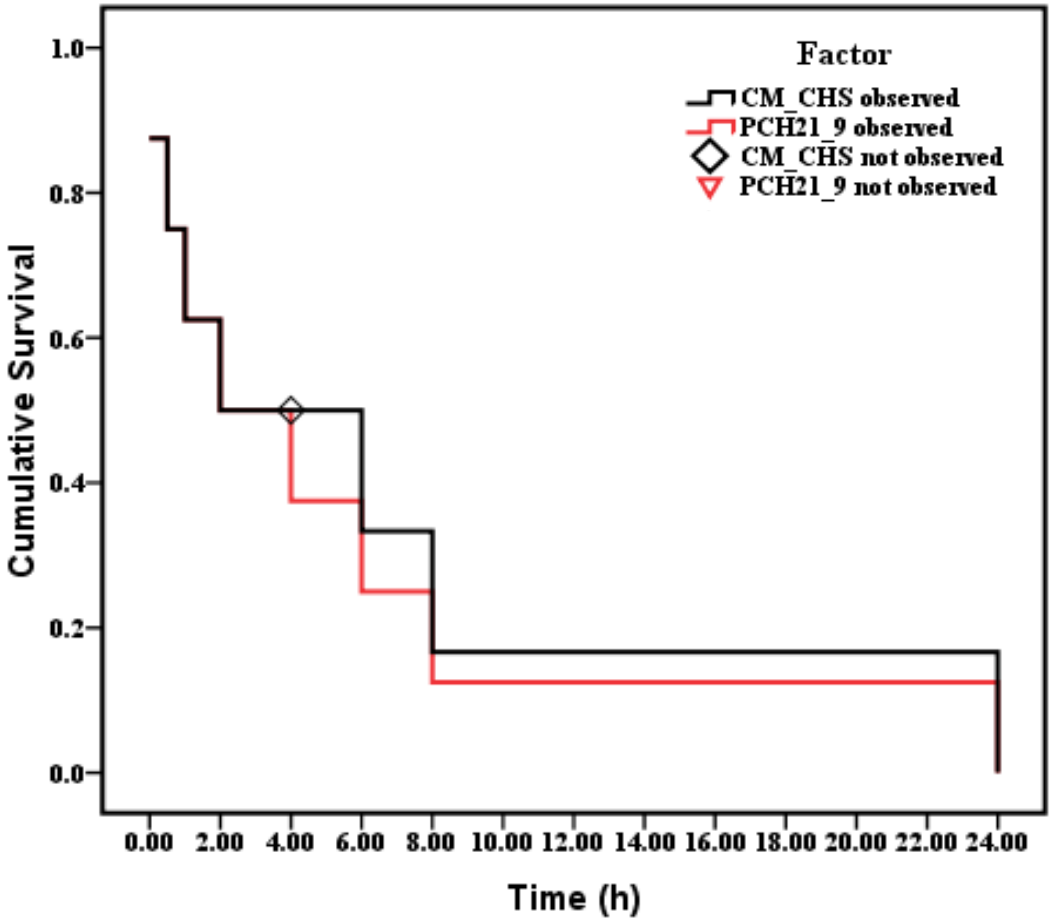

Figure 8. 8: The Survival function curve of C. *albicans* showing the survival time of the organisms on exposure to PCH21_9 or CM_CHS over a 24 h period.

Figure 8.8 shows that *C. albicans* was observed at all times over the 24 h study period. This simply implies that the PCH21_9 were not effective in eliminating the microbial species in this study. A similar observation was made on the CM_CHS treated *C. albicans*. However, at 4 h of contact, no organisms were observed on the media. As the investigation continued, ironically, the microorganisms were observed once again at 6 h until the 24 h the investigation lasted. Figure 8.9 presents the pictorial view of the colony-forming units of *C. albicans* when exposed to PCH21_9 or CM_CHS.

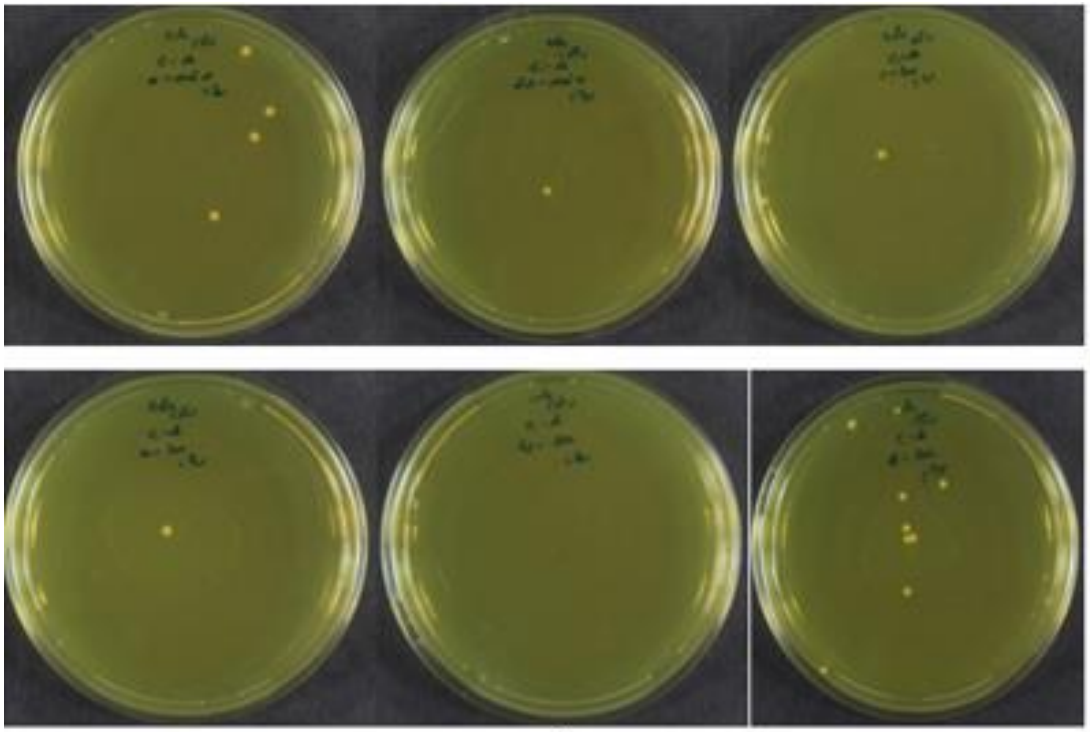

A

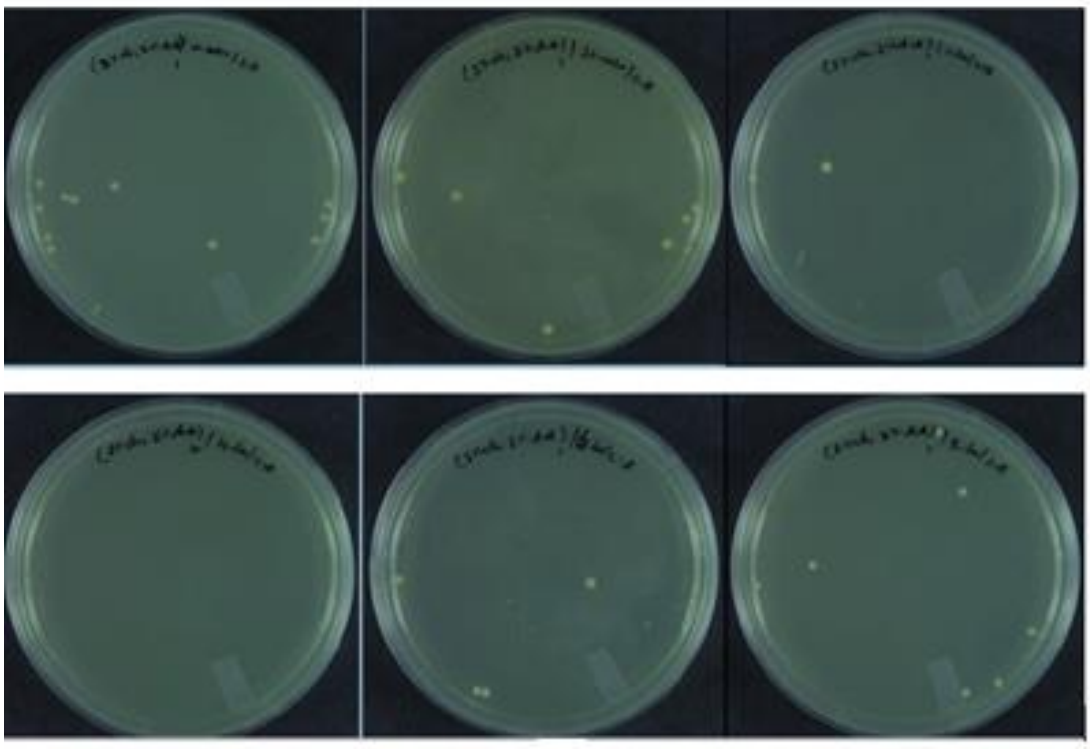

B

Figure 8. 9: The pictorial view of the colony-forming units of *C. albicans* when exposed to (A) PCH21_9 or (B) CM_CHS.

8.1.4 *Test of Equality of survival distributions for the different microbial species*

The Generalised Wilcoxon test was adopted in comparing the effect of PCH21_9 or CM_CHS on all the studied microbial species. Table 8.1 presents the pairwise comparison of the antimicrobial effect of PCH21_9 or CM_CHS.

Table 8.1: Pairwise comparison of the antimicrobial effect of PCH21_9 or CM_CHS against *E. faecalis, S. mutans* or *C. albicans*.

Pairwise comparison						
	Test organisms	Chitosan samples	PCH21_9		CM_CHS	
			Chi-Square	Sig.	Chi-Square	Sig.
Breslow (Generalized Wilcoxon)	*E. faecalis*	PCH21_9			0.142	0.706
		CM_CHS	0.142	0.706		
	S. mutans	PCH21_9			0.083	0.777
		CM_CHS	0.083	0.777		
	C. albicans	PCH21_9			0.45	0.832
		CM_CHS	0.45	0.832		

Table 8.1 shows that PCH21_9 or CM_CHS presented differing probability and Chi-square values in this study. The results of the tests, therefore, signifies that no statistical difference exists between the use of PCH21_9 or CM_CHS as an antimicrobial agent against the three microbial species of *E. faecalis, S. mutans* or *C. albicans.* The reason for the absence of statistical difference is that the probability value (depicted as Sig. column in Table 8.1) is > 0.05. The next section discusses the outcome of this investigation conducted to eliminate the impact of the positive control (acetic acid) and the normal growth media (negative control) on the observed bactericidal or fungistatic effects of the PCH21_9 or CM_CHS samples.

8.2 Effect of the control samples against the studied microorganisms

This investigation was undertaken to determine if the control samples (+ve and –ve controls) contributed to the observed bactericidal or fungistatic effects of the chitosan samples on the microbial species studied. The solvent applied in the dissolution of the solid chitosan samples was acidic and tends to protonate in solution. Furthermore, the cell wall of microorganisms is negatively charged. There is the tendency for the positively charged solvent to attract the negatively charged cell walls of the microorganisms. Therefore, to exclude the effect of 3% acetic acid on the survival rate of *S. mutans, E. faecalis* or *C. albicans*, the 3% acetic acid was

used as the negative control in this study. The mean number of the Log CFU/mL of the microbial species was compared to that of the positive control group in all the three microbial species studied. The next subsection discusses the effect of 3% acetic acid on *E. faecalis*.

8.2.1 *Effect of 3% acetic acid on E. faecalis*

The effect of acetic acid on *E. faecalis* was studied. The experimental protocol was set out in Section 3.6 of Chapter 3. The plot of the Log CFU/mL values of *E. faecalis* in both the positive and negative control groups are presented in Figure 8.10. There was overlapping of the positive control group by the negative control group (3% acetic acid).

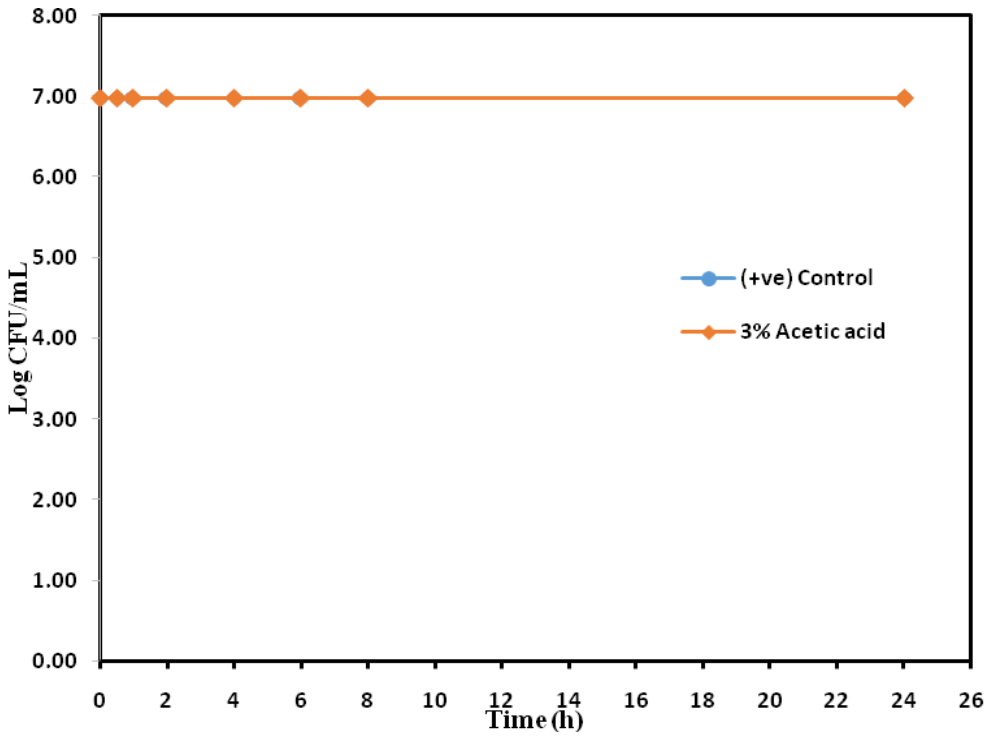

Figure 8. 10: The mean Log CFU/mL of *E. faecalis* following exposure to the normal growth rate (+ve control) and 3% acetic acid (-ve control) over a 24 h period.

From Figure 8.10, the use of 3% acetic acid in the dispersion of PCH21_9 or CM_CHS did not contribute to the observed bactericidal effect on *E. faecalis*. The values of the Log CFU/mL remained constant over the 24 h period of investigation. Similar values were observed for the positive control group. This necessitated the overlapping of both graphs as observed in Figure 8.10. The results showed that the use of acetic acid as a solvent for the chitosan samples did not contribute to the observed bactericidal effect over the 24 h study period. This, therefore, indicates that the observed antimicrobial effect in this study resulted from the PCH21_9 or CM_CHS rather than any other control sample. Pictorial view of the test plates showing the

colony-forming units of *E. faecalis* on exposure to the positive and the negative control groups over a 24 h period is presented in Figure 8.11.

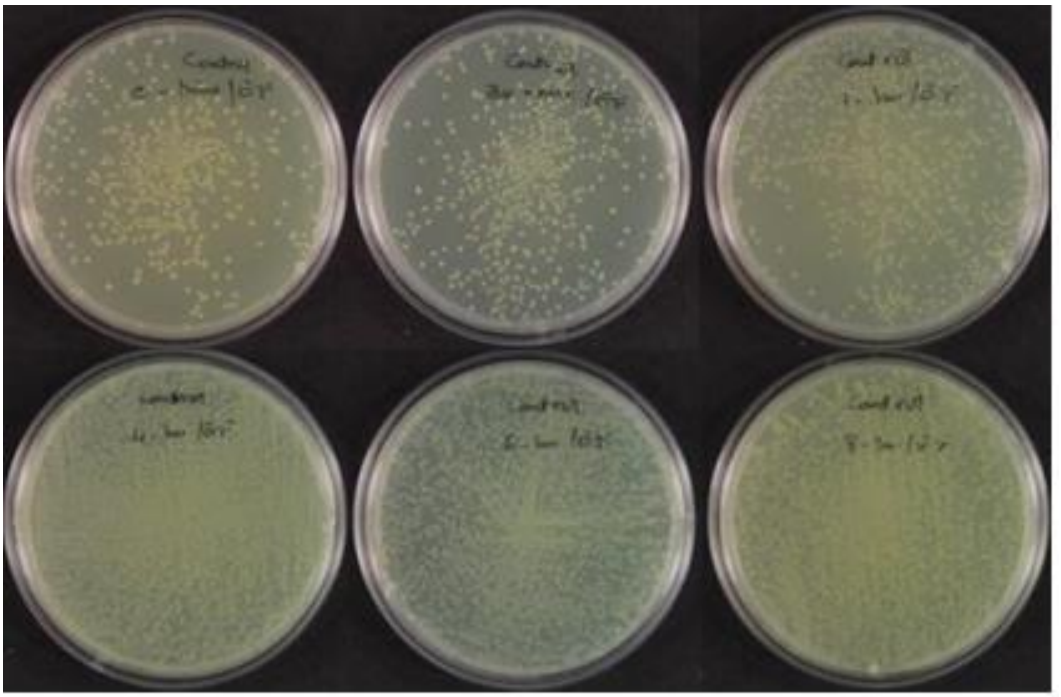

A

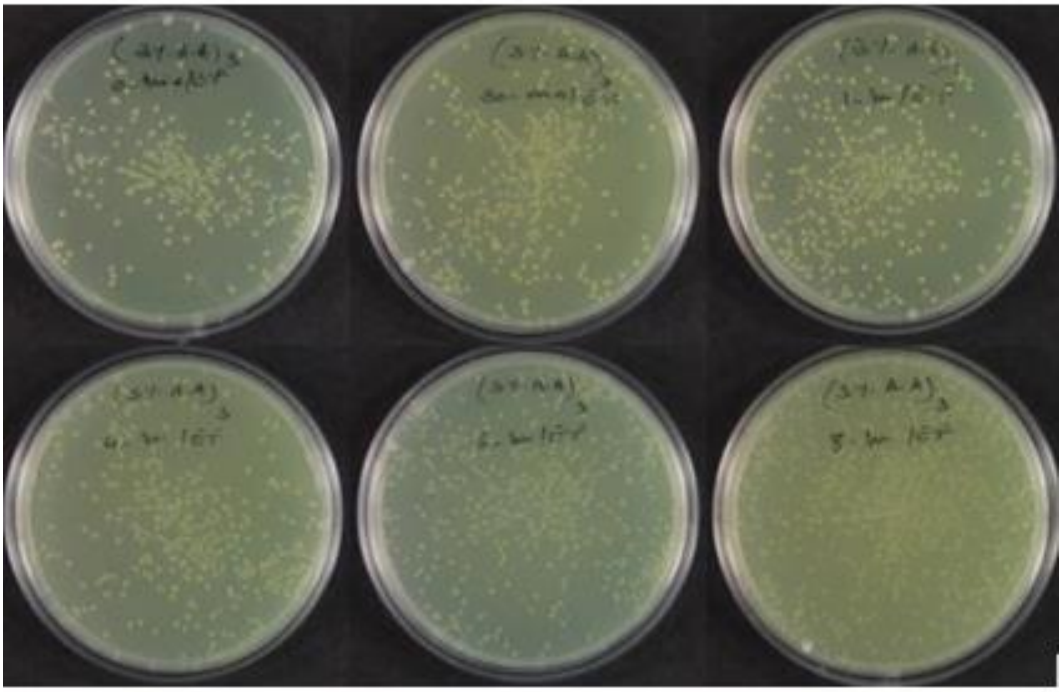

B

Figure 8. 11: Pictorial view of the colony-forming units of *E. faecalis* on exposure to (A) the positive control group, (B) the negative control group over a 24 h period.

Figure 8.11 (A and B) shows that the microorganisms were too numerous to count (TNTC) in the test plates thereby corroborating the observation from Figure 8.1 and 8.3 of Section 8.2.1 that the control groups did not contribute to the observed effects of the PCH21_9 or CM_CHS on *E. faecalis*. The next subsection discusses the effect of 3% acetic acid on *S. mutans*.

8.2.2 *Effect of 3% acetic acid on S. mutans*

The effect of acetic acid on *S. mutans* was also studied. The experimental protocol, as stated earlier, are detailed in Section 3.6 of Chapter 3. The plot of the Log CFU/mL values of *S. mutans* for both the positive and negative control groups are presented in Figure 8.12.

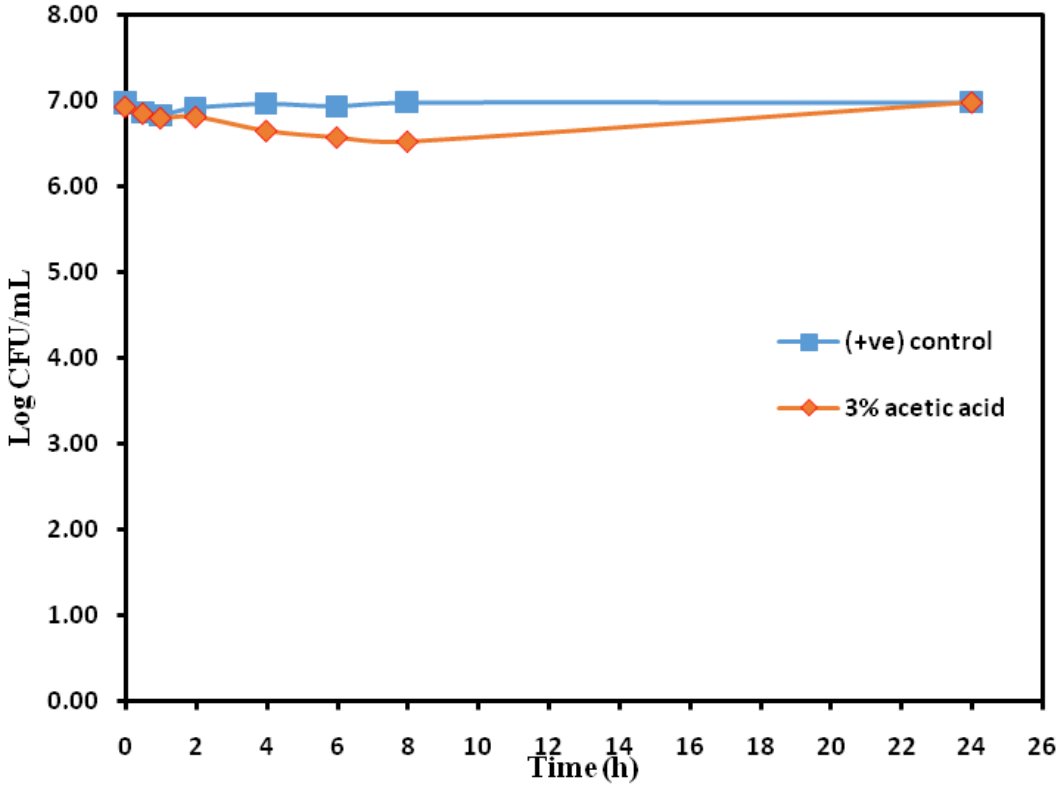

Figure 8. 12: The mean Log CFU/mL of *S. mutans* following exposure to the normal growth rate (+ve control) and 3% acetic acid (-ve control) over a 24 h period.

The mean values of the Log CFU/mL were constant in the positive control group except at 0.5 and 1 h when the values decreased to 6.86 and 6.83 CFU/mL, respectively. In the 3% acetic acid (-ve control), the CFU/mL values decreased progressively from 6.93 at 0 h to 6.52 at 8 h of contact; a 6% reduction, before increasing further. The mean values of the Log CFU/mL of both the negative control group and the positive control group attained the same value (6.98) at 24 h contact time (Figure 8.12). The images of the colony-forming units of *S. mutans* in test plates for both the positive and negative control groups are presented in Figure 8.13.

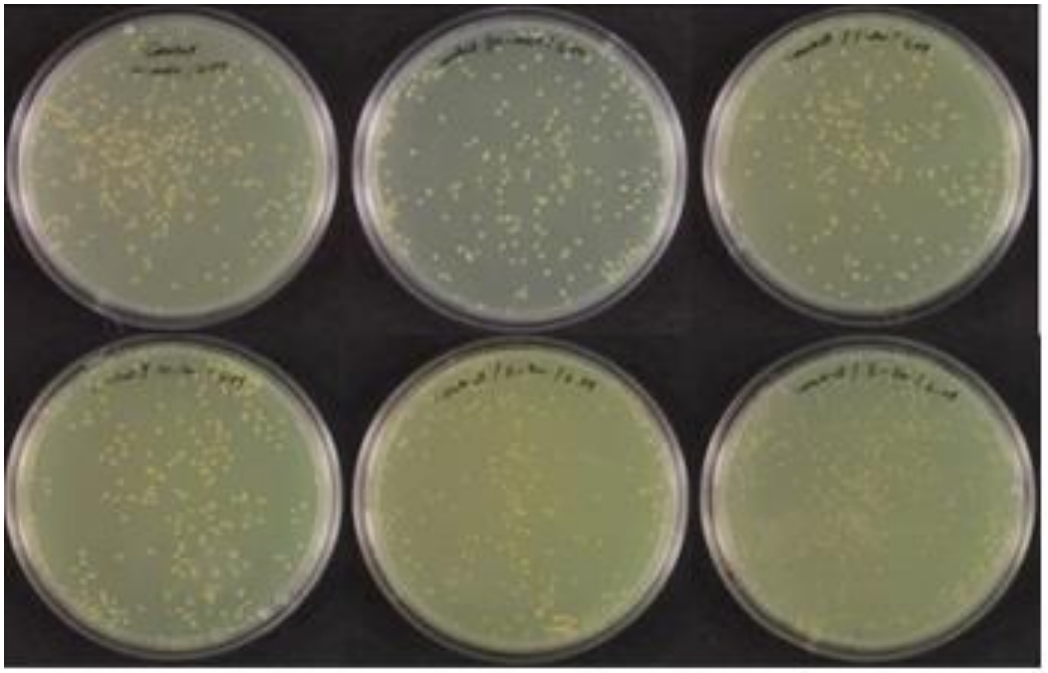

A

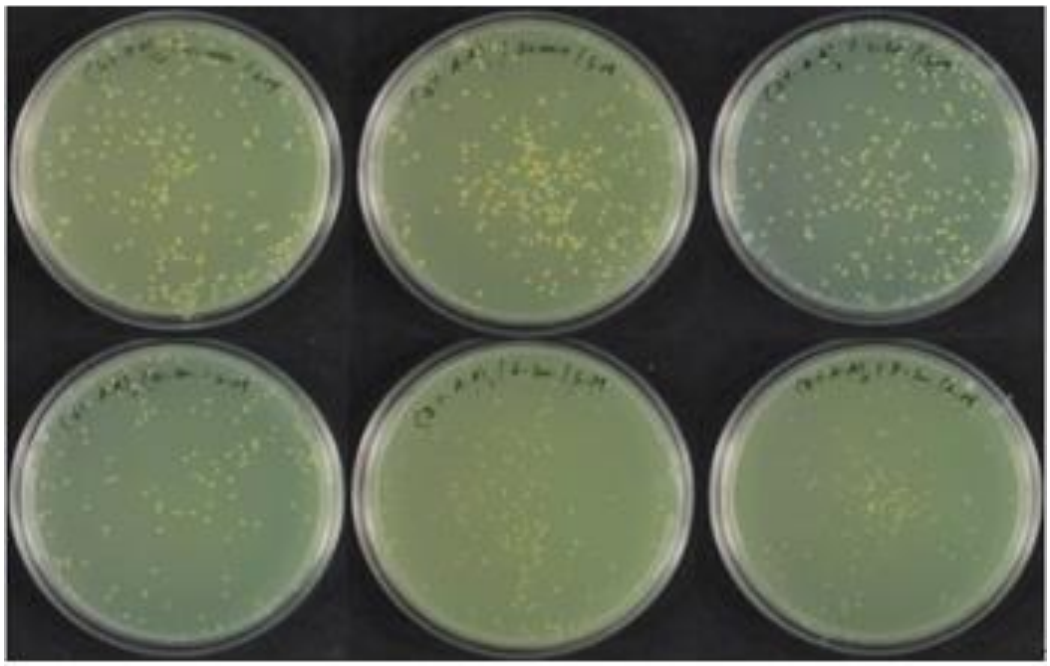

B

Figure 8. 13: Pictorial view of the colony-forming units of *S. mutans* on exposure to (A) the positive control group, (B) the negative control group over a 24 h period.

Figure 8.13 (A and B) shows that the microorganisms were also too numerous to count (TNTC) in the test plates thereby corroborating the observation from Figure 8.4 of Section 8.2.2 that the control groups did not contribute in any manner to the observed bactericidal effects of the

PCH21_9 or CM_CHS on the *S. mutans*. Next subsection discusses the effect of 3% acetic acid on *C. albicans.*

8.2.3 *Effect of 3% acetic acid on C. albicans*

The effect of acetic acid on *C. albicans* was also investigated in this study. The experimental procedure is found in Section 3.6 of Chapter 3. The plot of the Log CFU/mL values of *C. albicans* for both the positive and negative control groups are presented in Figure 8.14.

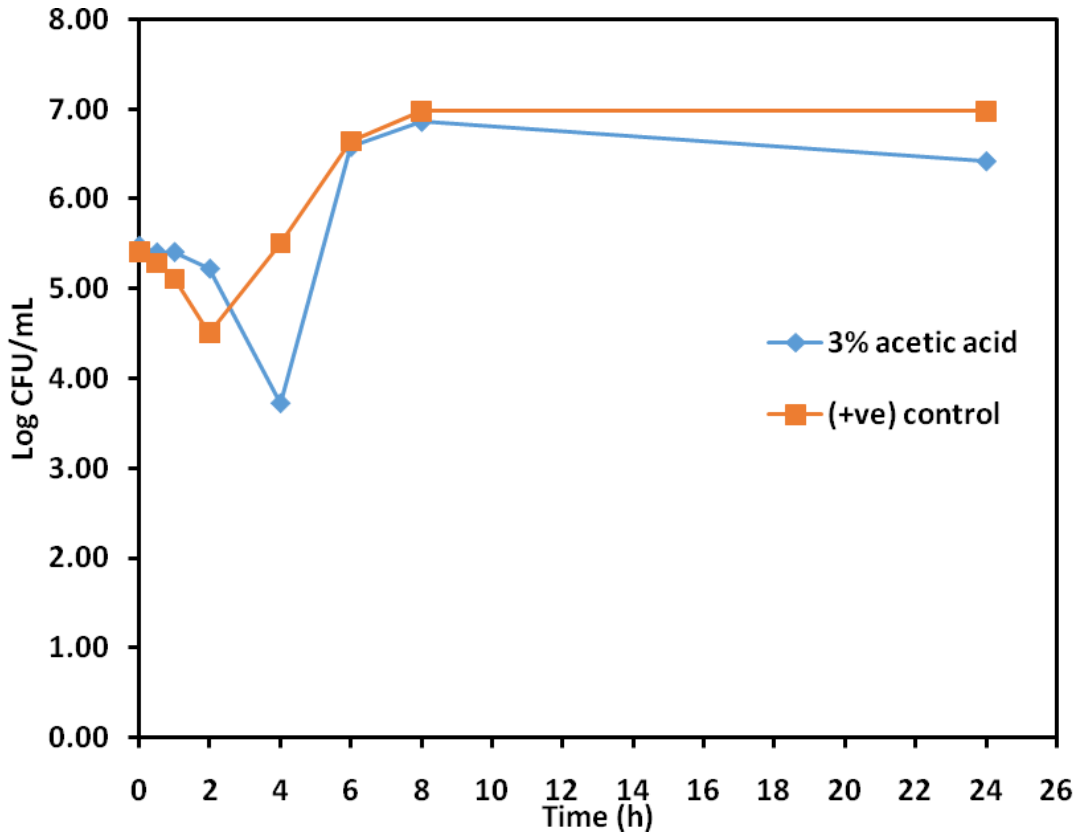

Figure 8. 14: The mean Log CFU/mL of C. *albicans* following exposure to the normal growth rate (+ve control) and 3% acetic acid (-ve control) over a 24 h period.

From Figure 8.14, *C. albicans* showed a deviation from the observed effect on *S. mutans* or *E. faecalis* by the 3% acetic acid. In the presence of nutrient medium (the positive control group), the Log CFU/mL value was 5.41 at the inception (zero hours). This value progressively decreased to 4.51, representing a 17% reduction in the microbial load after 2 h of contact. However, this observed trend reversed and subsequently increased from 4.51 to 6.98, 35% (two-fold) increase by 8 h of contact time. Similarly, on exposure to 3% acetic acid (negative control group), the Log CFU/mL values at zero hours were recorded as 5.47. This value

gradually decreased, as was also observed in the positive control group, to 3.72 by 4 h of contact. The number increased two-folds at 8 h of contact and thereafter reduced slightly to 6.42 at 24 h contact (Figure 8.14).

It is a known fact that Candida spp is susceptible to acetic acid (Hickey *et al*., 2012) as it is used to treat patients suffering from a Candida infection. However, the 3% acetic acid used in this study could not absolutely inhibit the *C. albicans*. This could be due to the acetic acid dissociating to acetate in the cells which could not cross the plasma membrane barrier of the Candida by passive transport resulting from their negative polarity (Cottier *et al*., 2017). The acetate ions then tend to accumulate within the cell membrane and attain higher concentrations leading to increase in turgor pressure, oxidative stress, reduction of ribosomal RNA which could be injurious to the microorganisms (Mira *et al*., 2010). These activities could have accounted for the reduction in the CFU/mL of the *C. albicans* between 2 and 4 h contact in this study. At inhibitory concentrations of acetic acid in the cells, the transporter gene, CgTpo3 is triggered which aids in reducing the concentration of acetic acid in the cells as reported by Bernardo *et al.* (2016). Furthermore, Costa *et al*. (2013) found that the gene, CgAqr1, which acts as a drug efflux pump provides protection to *C. glabrata*, a specie of Candida, against acetic acid. Therefore, the combination of activities of CgTpo3 and CgAqr1 genes could have contributed to the proliferation of the *C. albicans* after the noticeable decrease in the microbial load between 2 and 4 h contact. The images of the CFU/mL of *C. albicans* in test plates for both the positive and the negative control groups are presented in Figure 8.15.

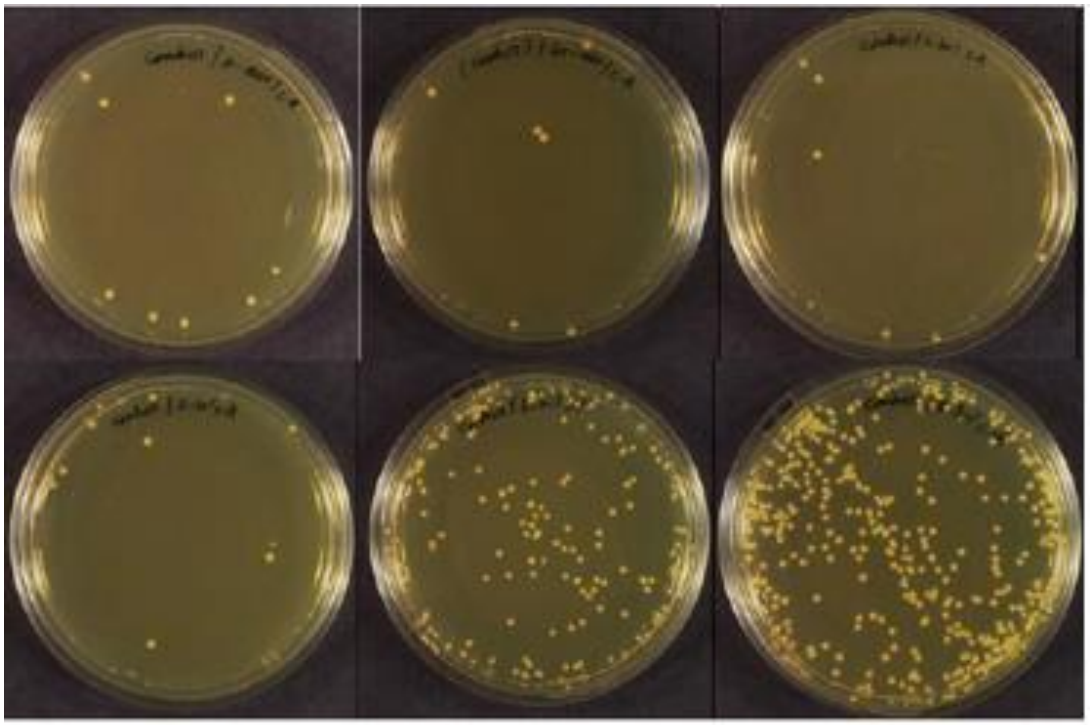

A

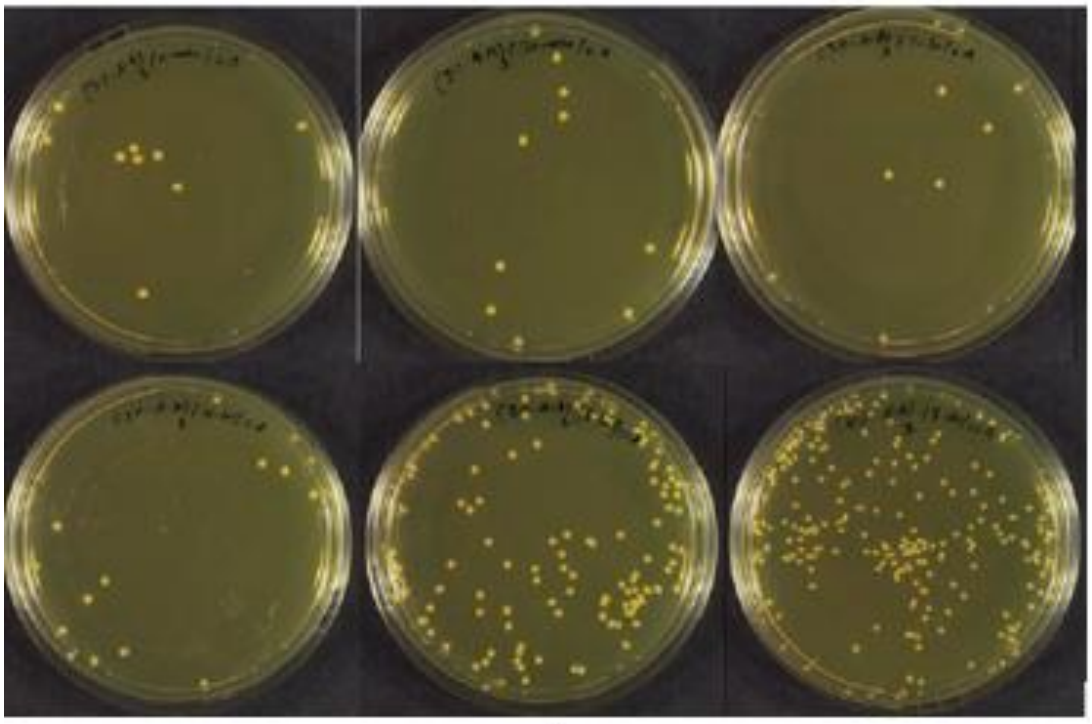

B

Figure 8. 15: Pictorial view of the CFU/mL of *C. albicans* on exposure to (A) the positive control group and (B) the negative control group over a 24 h period.

8.3 *Antimicrobial effects of BSF_NPs on microbial species*

The extracted BSF chitosan nanoparticles were investigated for efficacy against selected microbial species. The microbial species studied were *Enterococcus faecalis, Streptococcus mutans* and *Candida albicans*. The Time-kill test method was adopted in this study. This technique examines the time it took the synthesised BSF_NPs to completely eliminate each microbial species independently. The experimental protocol is detailed in Section 3.7 of Chapter 3. The effect of the studied BSF_NPs on the organisms, *E. faecalis* is discussed in details in the next subsection.

8.3.1 *Effect of BSF_NPs on E. faecalis*

The investigation was conducted to determine the effect of extracted BSF chitosan nanoparticles (BSF_NPs) on *E. faecalis*. The observed effects were compared to the mean Log of CFU/mL of the organism's normal growth rate. Figure 8.16 shows the mean Log of the colony-forming units (CFU/mL) of *E. faecalis* exposed to 3% BSF_NPs (overlapped) compared to the normal growth rate over a 24 h period.

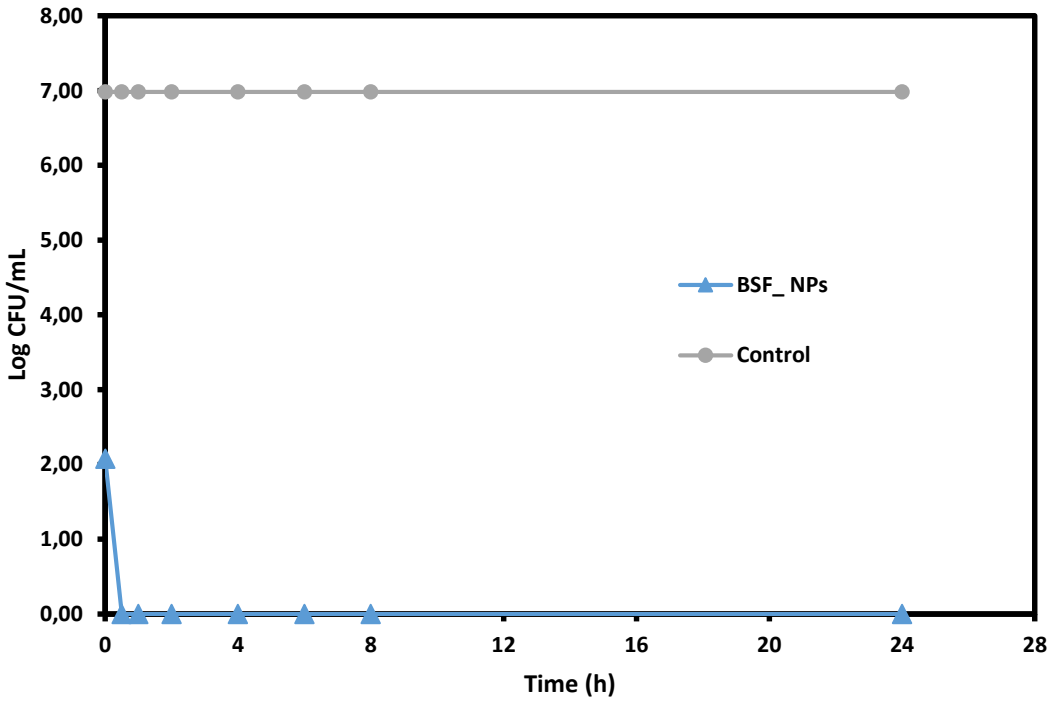

Figure 8. 16: The Log CFU/mL of *E. faecalis* when exposed to BSF_NPs for 24 h period.

From Figure 8.16, visible differences in the survival time plots of *E. faecalis* in contact with BSF_NPs and the normal growth rate were observed. At inception, zero hours, *E. faecalis* had a mean Log CFU/mL of 2.08. This number was completely eliminated after 0.5 h (30 minutes)

of contact with BSF_NPs without further growth observed up to 24 h of the investigation. The normal growth rate of the *E. faecalis*, as observed in Figure 8.16 was constant (6.98) throughout the 24 h investigation period. This implies that the observed bactericidal effect on *E. faecalis* was due to the BSF_NPs and that the test media did not contribute, whatsoever, to the observed eradication of the microbes.

To further study the data obtained on the exposure of *E. faecalis* to 3% BSF_NPs, the non-parametric Kaplan-Meir survival function analysis was conducted. The test measures the fraction of the living microorganisms observed or that survived over a period after exposure to the BSF_NPs (Goel *et al.*, 2010). Figure 8.17 shows the Kaplan-Meir survival function plot of *E. faecalis* on exposure to BSF_NPs.

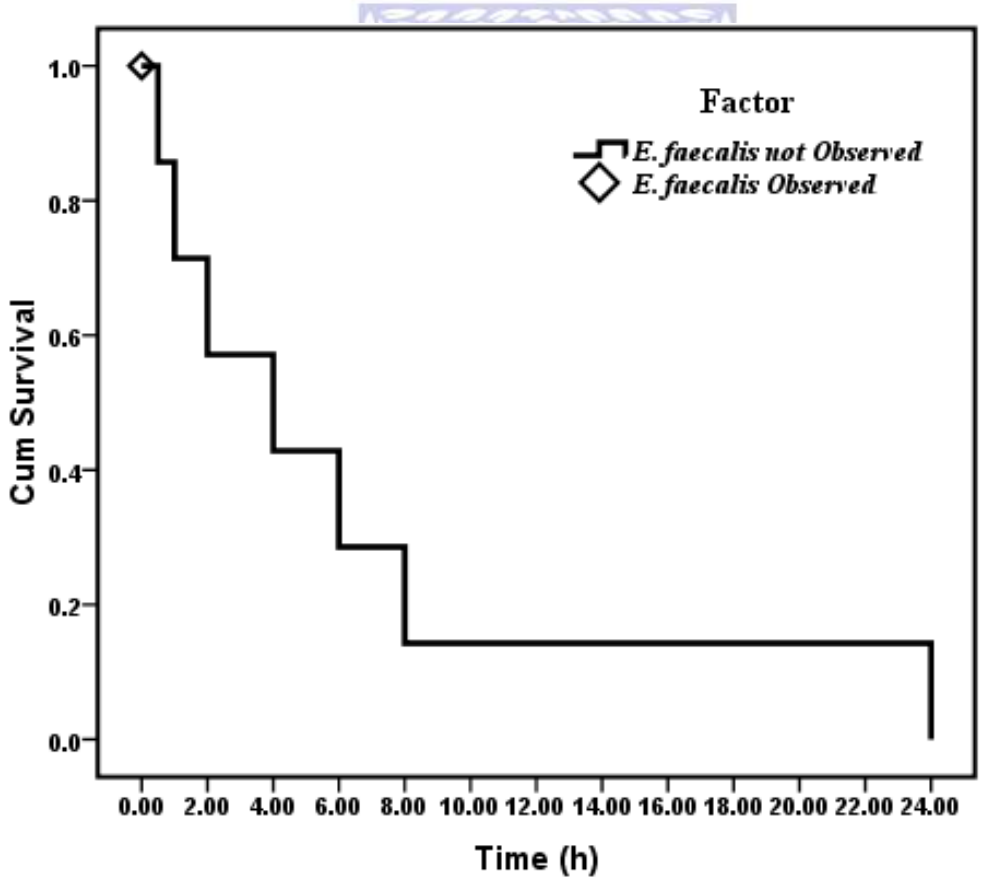

Figure 8. 17: The Survival function curve of *E. faecalis* showing the survival time of the organism on exposure to BSF_NPs over a 24 h period.

Figure 8.17 shows that the microorganisms (*E. faecalis*) were observed on the media treated with BSF_NPs at zero hours only. No microbe was observed in the test media from 30 minutes to the 24 h period of the investigation. This result implies that the BSF_NPs were effective in

the eradication of *E. faecalis*. The BSF_NPs eliminated the microbes almost immediately as they were exposed to the microbes. They penetrated the cell walls of the microbes due to their reduced hydrodynamic size and positively charged amine groups. While inside the cell, they bind to the negatively charged cell membrane components forming an impermeable layer around the cell. This formed layer affects cell permeability and inherently blocks material transport in and out of the cell which causes death by influencing the leakage of the intracellular electrolytes within the cells (Goy *et al*., 2016). Therefore, the survival time of the *E. faecalis* in contact with BSF_NPs was less than 0.5 h. The pictorial images of the test plates used in the study showing the colony-forming units of *E. faecalis* in the experimental cells are shown in Figure 8.18.

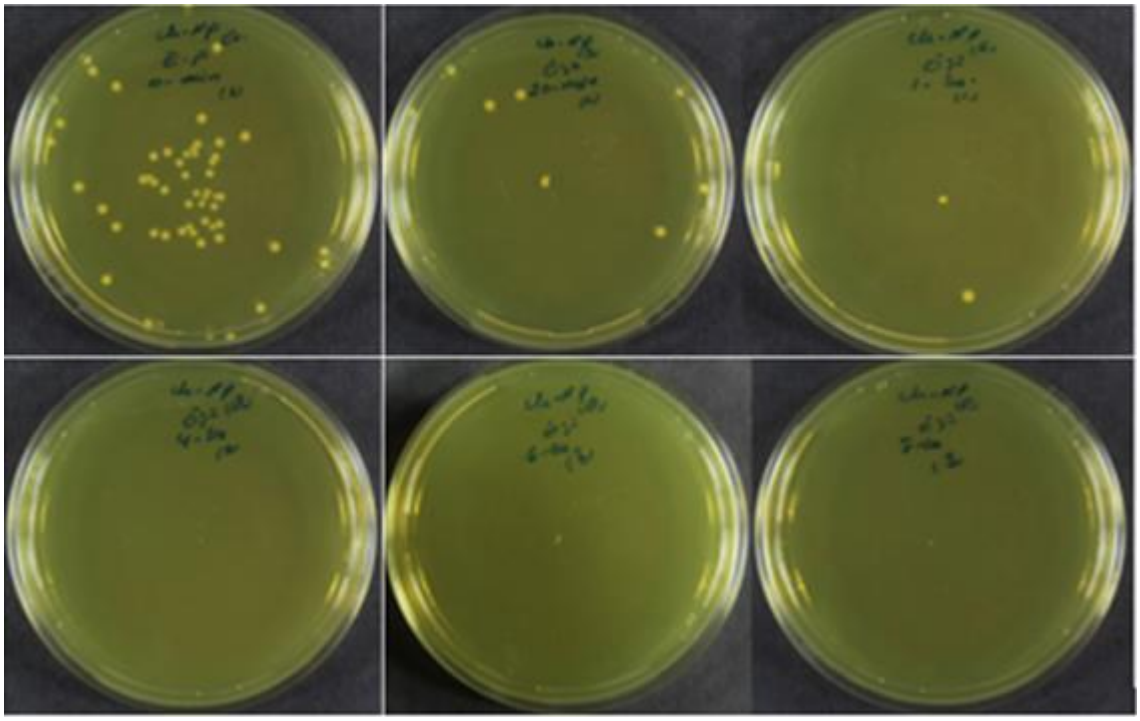

Figure 8. 18: The colony-forming units of *E. faecalis* when exposed to 3% BSF_NPs.

8.3.2 *Effect of BSF_NPs on S. mutans*

The investigation was conducted to determine the effect of BSF_NPs on *S. mutans*. This study was performed according to the procedure described in Section 3.7 of Chapter 3. Figure 8.19 shows the mean Log of the colony-forming units (CFU/mL) of *S. mutans* exposed to BSF_NPs (overlapped) over a 24 h study period.

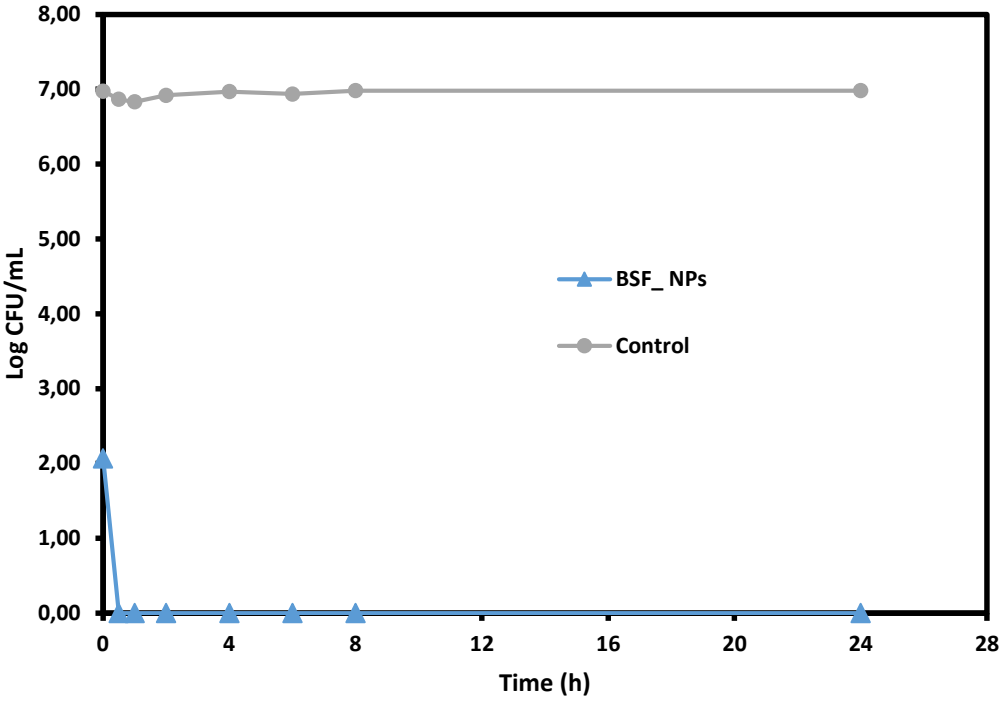

Figure 8. 19: The Log CFU/mL of *S. mutans* when exposed to BSF_NPs for 24 h period.

The values of the Log CFU/mL for BSF_NPs at zero hours was 2.07. By 0.5 h (30 minutes) of contact, no microorganism was observed in the test media. This implies a complete elimination of the *S. mutans* within 0.5 h. The control fluctuated slightly at the inception of the experiment (0.5 and 1.0 h) but later stabilised and remained constant up to the 24 h period of investigation and, therefore, did not contribute to the observed eradication of the *S. mutans* in this study.

To further ascertain the survivability or otherwise of the *S. mutans*, the non-parametric Kaplan-Meir survival function test was conducted on the data generated after exposure of the microbes to BSF_NPs. Figure 8.20 presents the cumulative survival curve of *S. mutans* on exposure to BSF_NPs.

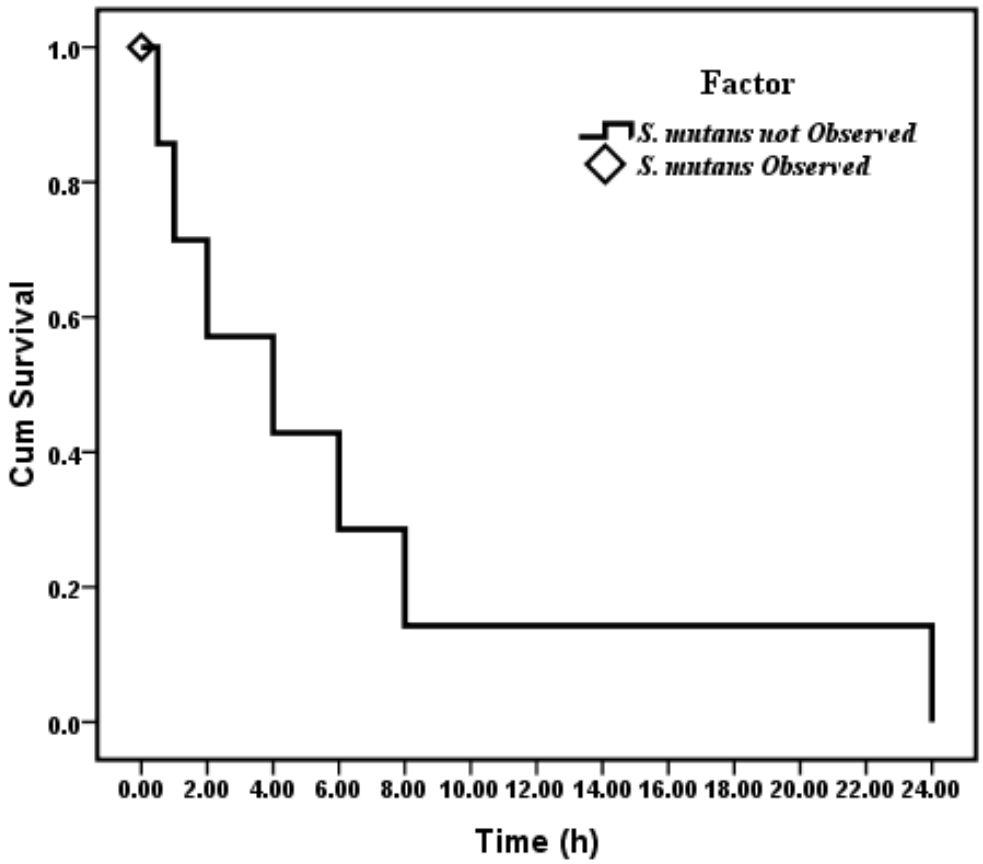

Figure 8. 20: The Survival function curve of S. *mutans* showing survival time of the organisms on exposure to 3% BSF_NPs over a 24 h period.

The survival function curve (Figure 8.20) indicate that *S. mutans* were only observed at zero hours on the test media treated with 3% BSF_NPs. No further microbes were observed from 0.5 h up to the 24 h period of contact. This implies that BSF_NPs eradicated the organism, *S. mutans* at a fast rate of less than 0.5 h. Figure 8.21 presents the pictorial images of the test plates used in the study showing the CFU/mL of *S. mutans* on exposure to 3% BSF_NPs over a 24 h period.

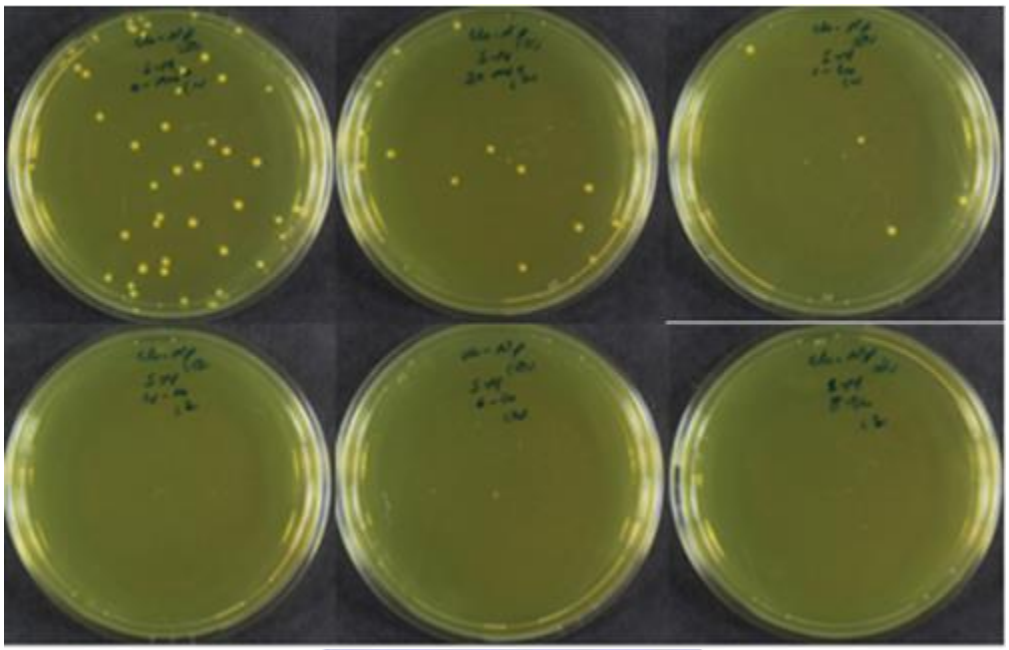

Figure 8. 21: The pictorial view of the colony-forming units of *S. mutans* when exposed to 3% BSF_NPs over a 24 h period.

8.3.3 *Effect of BSF_NPs against C. albicans*

The investigation was conducted to determine the effect of BSF_NPs on *C. albicans*. This study was performed according to the procedure described in Section 3.7 of Chapter 3. Figure 8.22 shows the mean plot of the Log of the colony-forming units (CFU/mL) of *C. albicans* exposed to 3% BSF_NPs over a 24 h period.

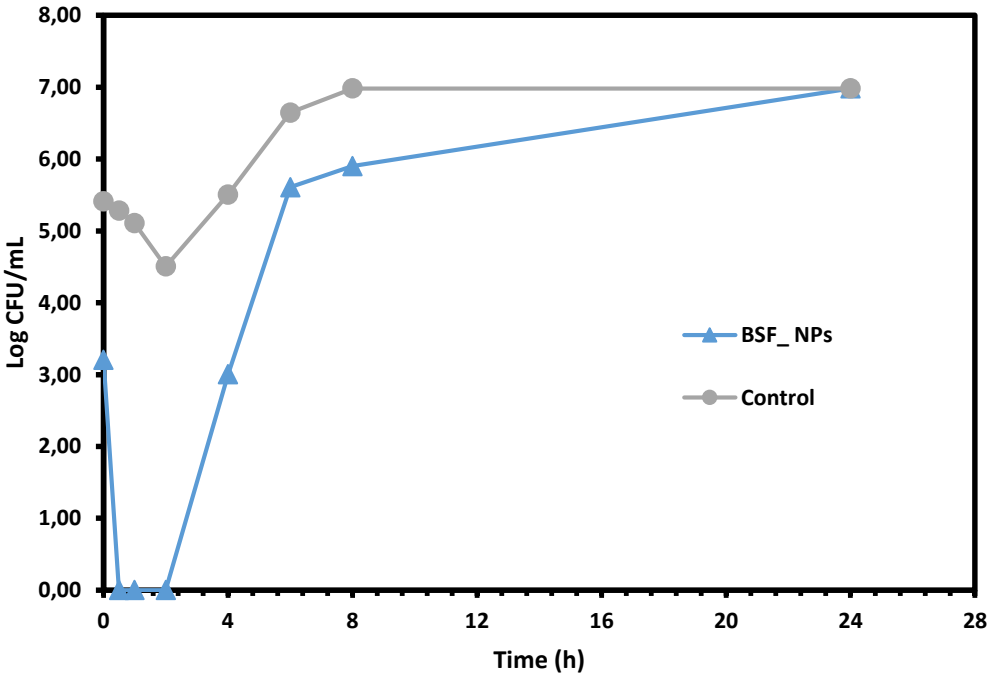

Figure 8. 22: The Log CFU/mL of *C. albicans* when exposed BSF_NPs for 24 h period.

Figure 8.22 presents the Log of the CFU/mL for BSF_NPs over a 24 h period. The mean Log CFU/mL for BSF_NPs inoculated *C. albicans* was 3.20 at zero hours. This value decreased to zero CFU/mL at 0.5 h, 1.0 h and 2.0 h. By the fourth hour (4 h) of contact, the *C. albicans* had developed resistance to the nanoparticles, with about 93% of the organisms re-emerging within the test media. The mean CFU/mL of the *C. albicans* continued to increase in the media (above its initial value of 3.20 CFU/mL at zero hours) from 6 h (5.61) to 8 h (5.90) reaching a mean maximum value of 6.98, an 118% increase at 24 h the investigation lasted. Figure 8.22, therefore, indicates that the 3% BSF_NPs was not effective against C. *albicans* over the 24-hour study period. Rather the BSF_NPs did exhibit fungistatic effect.

The data obtained from the exposure of *C. albicans* to BSF_NPs were further analysed using the non-parametric Kaplan-Meir survival function test. This statistical test shows the time the organisms were able to survive or die on exposure to the BSF_NPs. Figure 8.23 presents the cumulative survival curve of *C. albicans* on exposure to BSF_NPs.

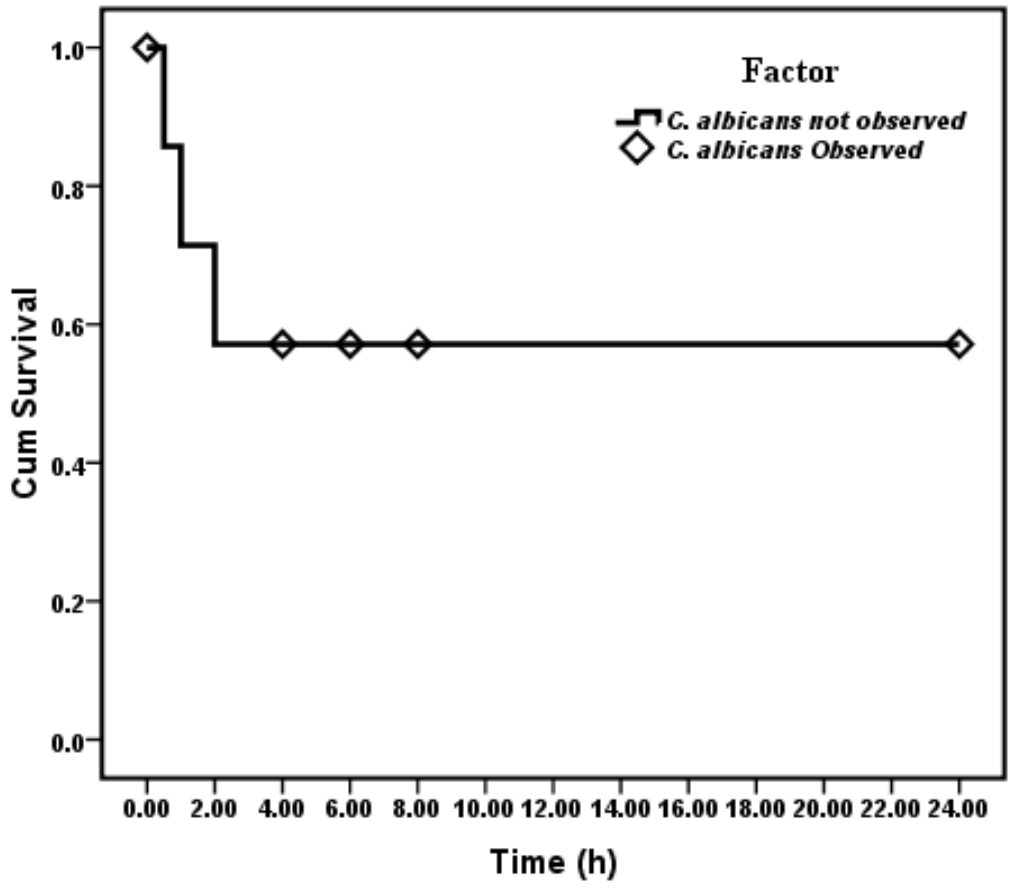

Figure 8. 23: The Survival function curve of C. *albicans* showing survival time of the organisms on exposure to BSF_NPs over a 24 h period.

Figure 8.23 shows that *C. albicans* was observed at zero hours. No such microbes were observed from 0.5 h up to 2 h of contact time. Further observation of the microbes in the test plates was made from 4 h of contact time up to 24 h. By implication, the *C. albicans* after temporarily denatured from 0.5 h to 2 h, acquired resistance and start increasing in number till the 24 h of the investigation. Figure 8.24 presents the pictorial view of the colony-forming units of *C. albicans* when exposed to BSF_NPs.

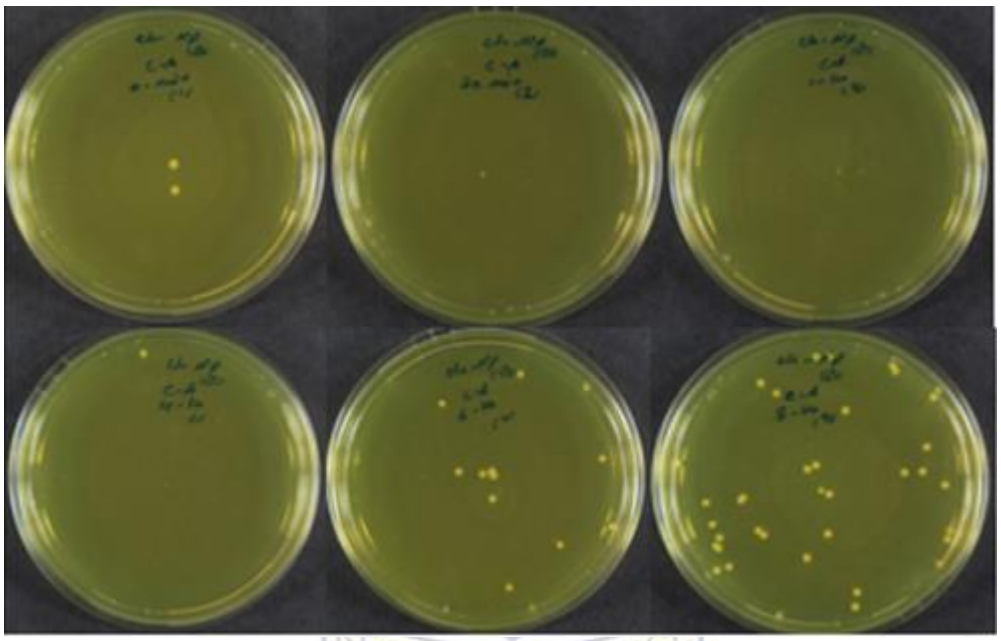

Figure 8. 24: The pictorial view of the colony-forming units of *C. albicans* when exposed to BSF_NPs.

8.4 Comparison of the antimicrobial effect of BSF_NPs to PCH21_9

The effect of 3% BSF_NPs and 3% PCH21_9 against the investigated microorganism, *S. mutans*, *E. faecalis* or *C. albicans* was compared further to determine which of the biopolymers were more effective. The obtained data were analysed using the time-kill test and the Kaplan-Meir survival function test. The mean, median and standard error of the survival rate of each microbial species on exposure to 3% BSF_NPs or 3% PCH21_9 were also determined. Subsequent subsections are dedicated to a detailed comparative study of the effects of the extracted PCH21_9 or the BSF_NPs on the studied microorganisms.

8.4.1 *The antimicrobial effect of BSF_NPs or PCH21_9 against E. faecalis*

This comparative study was done to determine the level of effectiveness of each sample on *E. faecalis.* The mean Log CFU/mL of *E. faecalis* on inoculation with 3% BSF_NPs or 3%

PCH21_9 were compared and plotted with the mean Log CFU/mL of the microorganism under normal growth rate conditions. Figure 8.25 presents the time-kill plots of BSF_NPs or PCH21_9 against *E. faecalis.*

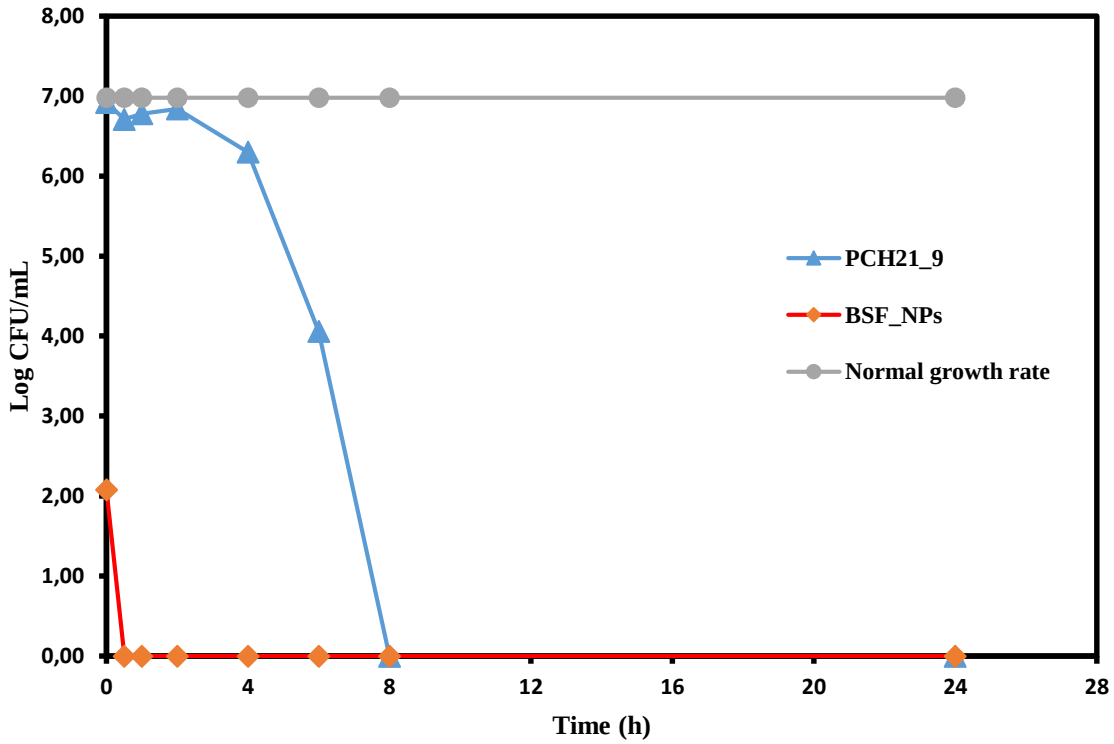

Figure 8. 25: The Log CFU/mL of *E. faecalis* on exposure to BSF_NPs or PCH21_9 compared to the control group.

From Figure 8.25, the mean Log CFU/mL of *E. faecalis* at zero hours on exposure to 3% BSF_NPs was 2.08. By 0.5 h of contact with the microbes, this mean value had reduced to zero CFU/mL, implying total eradication of the *E. faecalis* by the nanoparticles. The study was continued up to 24 h without the re-emergence of the microorganisms. On the contrary, the mean Log CFU/mL of *E. faecalis* on exposure to the 3% solution of PCH21_9 was determined to be 6.92 at zero hours. This value, though reduced, fluctuated between 6.71 and 6.84 within the first 2 h of contact with the 3% PCH21_9. At 4 h of contact, the mean Log CFU/mL of *E. faecalis* was 6.30 which declined further to 4.06 at 6 h. Total elimination of the microbes was observed at 8 h of contact with the PCH21_9 without further growth in the test media at 24 h the experiment lasted. It is, therefore, determined that the BSF_NPs was more potent than the PCH21_9 in eradicating the microorganisms, *E. faecalis* in this study. This was because of the complete eradication of *E. faecalis* observed after 0.5 h contact with BSF_NPs whereas it took PCH21_9 8 h to achieve total elimination of the same microorganisms under exact conditions.

The non-parametric Kaplan-Meir survival function test was further utilised to analyse the behaviour of *E. faecalis* in contact with 3% BSF_NPs or 3% PCH21_9. This was achieved by using an SPSS® statistics software version 24 (by IBM). Figure 8.26 presents the Kaplan-Meir function curve for *E. faecalis* on exposure to 3% BSF_NPs or 3% PCH21_9.

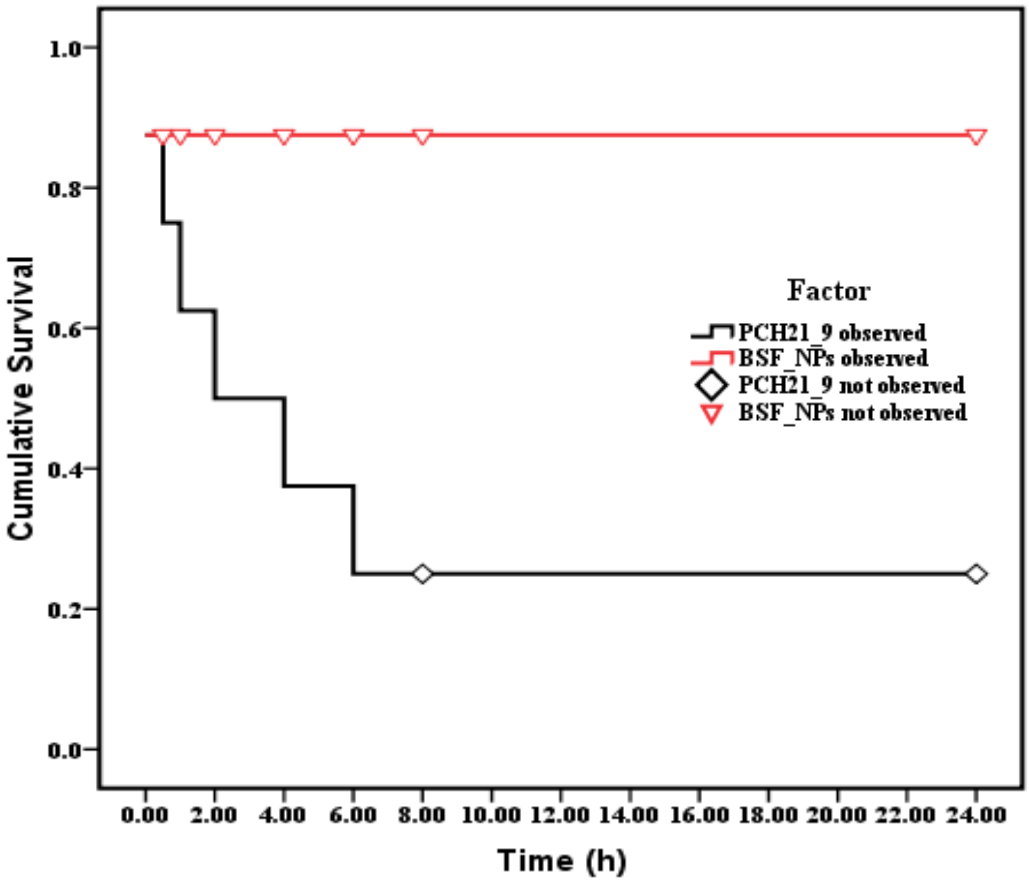

Figure 8. 26: The Survival function curve of *E. faecalis* showing survival time of the organisms on exposure to BSF_NPs or PCH21_9 over a 24 h period.

Figure 8.26 presents the Kaplan-Meir survival function analysis. The curve shows that the *E. faecalis* was not observed when treated with PCH21_9 at 8 h and beyond while the BSF_NPs treated *E. faecalis* took just 0.5 h to eradicate the microbes.

8.4.2 *The antimicrobial effect of BSF_NPs or PCH21_9 against S. mutans*

This comparative study was done to determine the level of effectiveness of BSF_NPs or PCH21_9 on *S. mutans.* The mean Log CFU/mL of *S. mutans* in contact with 3% BSF_NPs or 3% PCH21_9 were compared and plotted with the mean Log CFU/mL of the microorganism under normal growth rate conditions. Figure 8.27 presents the Time-kill plots of BSF_NPs or PCH21_9 against *S. mutans.*

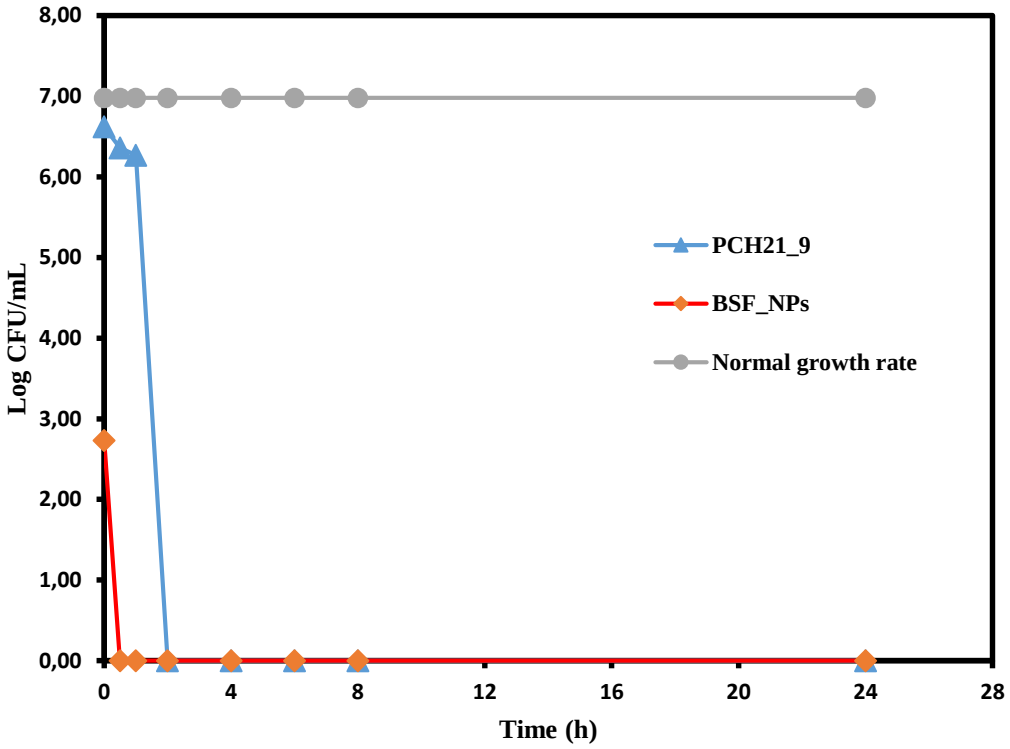

Figure 8. 27: The Log CFU/mL of *S. mutans* on exposure to BSF_NPs or PCH21_9 and the control group.

At the inception of the experiment, zero-hours (0 h), the mean Log CFU/mL of *S. mutans* on exposure to 3% BSF_NPs was determined to be 2.73. By 0.5 h (30 minutes) of contact with these nanoparticles, the mean Log CFU/mL had reduced to 0.00, achieving a comprehensive elimination of the *S. mutans* from the test media. Meanwhile, at zero hours, the mean Log of CFU/mL of the *S. mutans* on exposure to PCH21_9 was 6.62. This value had a slight (4%) reduction at 0.5 h of contact with 3% PCH21_9 to 6.36 CFU/mL. At 1.0 h contact time, the mean value had marginally declined to 6.27 CFU/mL. Total elimination of the *S. mutans* in the test plates was observed at 2 h of contact with the PCH21_9. As the investigation progressed to 4 h; 6 h; 8 h and 24 h, no microorganisms were further observed, an indication that the 3% PCH21_9 completely eradicated the *E. faecalis* in the test media. Therefore, the total elimination of *S. mutans* by the BSF_NPs occurred at 0.5 h (30 minutes) of exposure whereas it took 2 h on the exposure of the organisms to 3% PCH21_9 to completely eradicate the *S. mutans* in this study. This implies that the BSF_NPs were more potent and effective for treating the microbial species, *S. mutans* under similar condition. This could be due to the smaller size of the nanoparticles which allows for fast mobility and penetration into the cell membrane of the *E. faecalis*. The penetration ensures ion interaction and binding to cell membranes causing

the leakage of electrolytes within the cells leading to lysis (Goy *et al*., 2016). The mean Log CFU/mL was further analysed using the Kaplan-Meir survival function test. Figure 8.28 presents the survival function curve of *S. mutans* exposed to 3% BSF_NPs or PCH21_9 over a 24 h period.

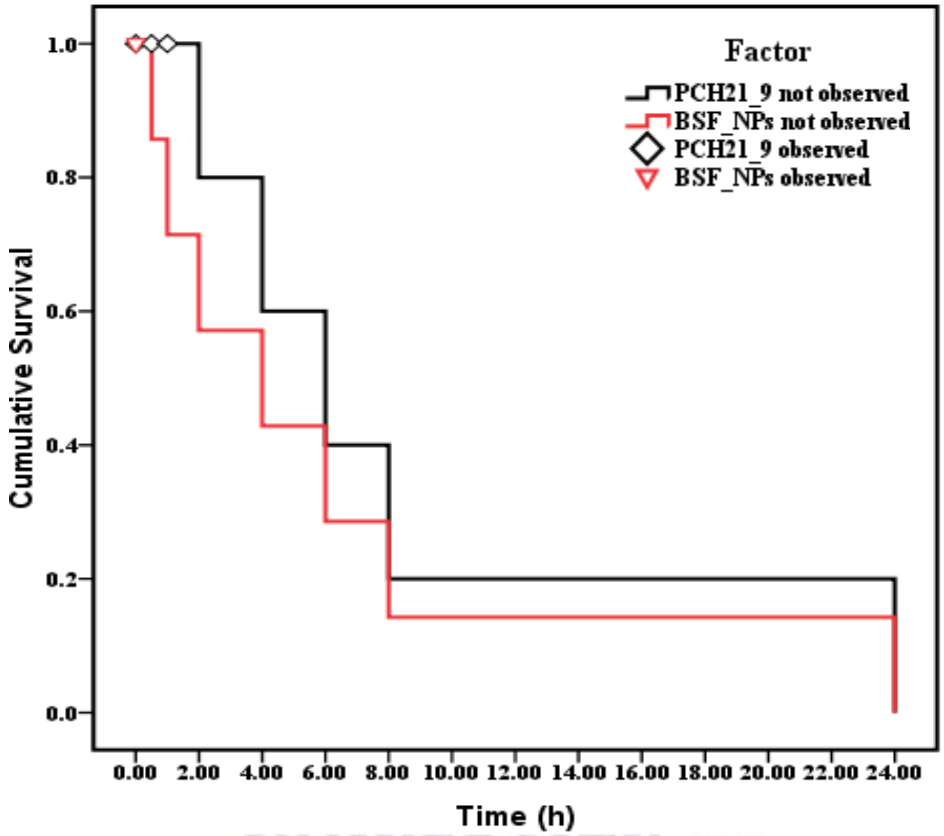

Figure 8. 28: The Survival function curve of *S. mutans* showing survival time of the organisms on exposure to BSF_NPs or PCH21_9 over a 24 h period.

8.4.3 *The antimicrobial effect of BSF_NPs or PCH21_9 against C. albicans*

The effects of the BSF_NPs or the PCH21_9 on the *C. albicans* microbial cells were compared in this study. This comparative study was done to determine the level of effectiveness of BSF_NPs or PCH21_9 on *C. albicans.* The mean Log CFU/mL of *C. albicans* in contact with 3% BSF_NPs or 3% PCH21_9 were compared and plotted with the mean Log CFU/mL of the microorganism under normal growth rate conditions. This was to eliminate the impact of the growth media on any effect of 3% BSF_NPs or 3% PCH21_9 on the test organisms. Figure 8.29 presents the Time-kill plots of BSF_NPs or PCH21_9 against *C. albicans.*

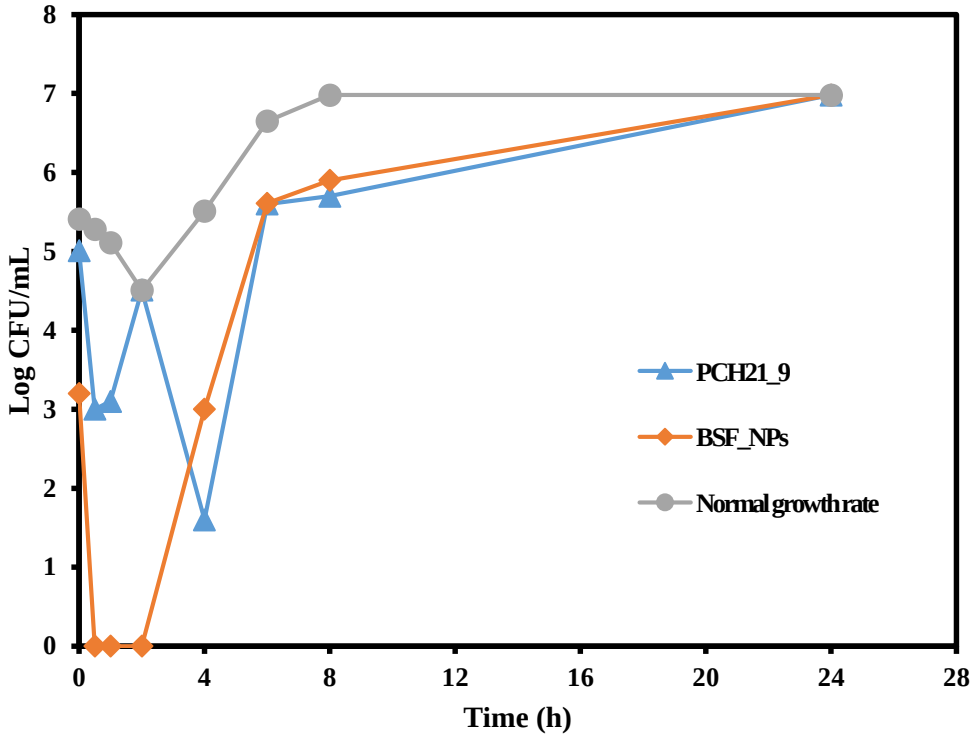

Figure 8. 29: The Log CFU/mL of *C. albicans* on exposure to BSF_NPs or PCH21_9 and the control group.

Following the exposure of the *C. albicans* to the BSF_NPs, the mean Log CFU/mL at zero hours was 3.20. This value reduced to 0.00 at 0.5 h (30 minutes), 1 h up to 2 h of exposure with the nanoparticles. However, at 4 h of contact, the *C. albicans* re-emerged and proliferated. This increase was sustained as the mean CFU/mL value rose to 5.61 at 6 h, 5.7 at 8 h and attaining the highest value of 6.98 at 24 h. A similar trend was observed with the PCH21_9 exposed *C. albicans*. The initial CFU/mL value was 5.01. This number fluctuated around 3.00 CFU/mL at 0.5 h and 1 h contact times. A 45% increment in the microbial load was observed at 2 h of contact in comparison with the value at 1 h. Ironically, the observed mean value at 2 h dropped by a significant 65% to 1.61 CFU/mL at 4 h. However, the mean microbial load in the test media increased at 6 h contact to a value of 5.60 CFU/mL before attaining its highest value of 6.98 CFU/mL at 24 h. Comparatively, BSF_NPs showed more potency than PCH21_9 as it reduced the microbial load in the test media to zero CFU/mL for a 2 h period before the *C. albicans* re-grew. PCH21_9 was able to achieve a reduction up to 1.6 CFU/mL before the microbes readjusted and proliferated. It could, therefore, be said that BSF_NPs or PCH21_9 both showed a fungistatic effect towards the *C. albicans* since they were not able to totally eradicate (fungicidal effect) the microbes over the 24 h study period.

To further analyse the obtained data, the Kaplan-Meir survival function test was utilised for the analysis. The analysis measures the fraction of the living *C. albicans* that survived on exposure to BSF_NPs or PCH21_9 over a period of 24 h. Figure 8.30 presents the Kaplan-Meir function curve for *E. faecalis* on exposure to 3% BSF_NPs or 3% PCH21_9.

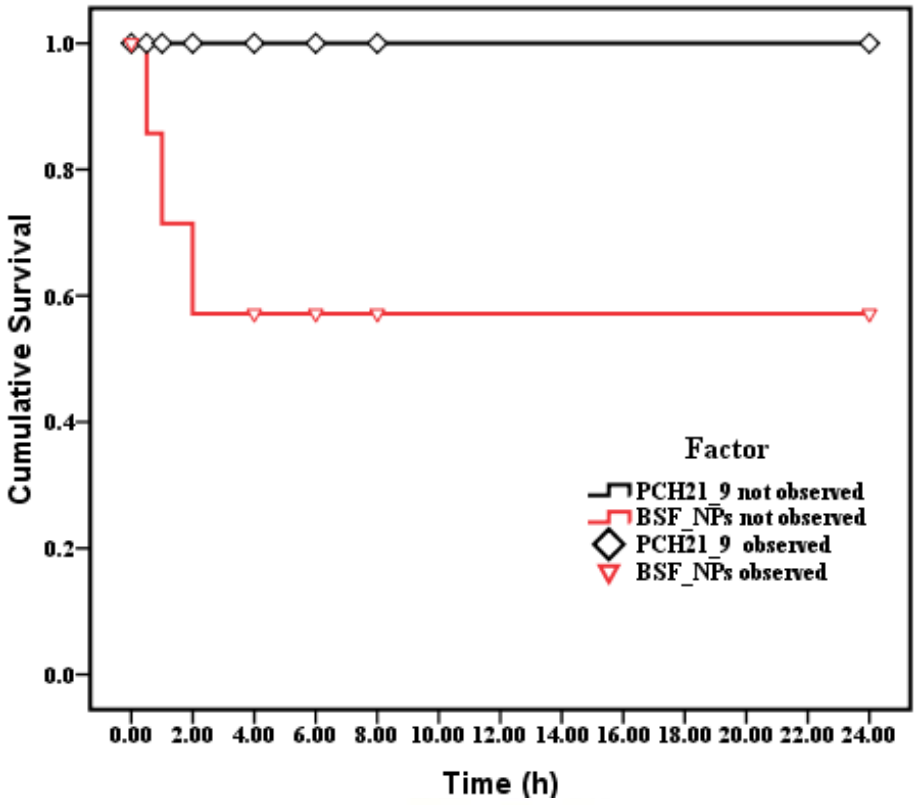

Figure 8. 30: The Survival function curve of *C. albicans* showing survival time of the organisms on exposure to BSF_NPs or PCH21_9 over a 24 h period.

Figure 8.30 showed that *C. albicans* were observed in the test media at zero hours. As contact with the BSF_NPs prolonged, they were not observed from 0.5 h up to 2 h of study. However, they re-emerged at 4 h and continued to proliferate up to the 24 h of investigation. On the contrary, the *C. albicans* were observed throughout the experiment in contact with PCH21_9 in the test media. The statistical significance of the investigation using the test of equality of the survival distributions is discussed in the next sub-section.

8.4.4 *Test of Equality of survival distributions for the different microbial species*

The Generalised Wilcoxon test was adopted in comparing the effect of BSF_NPs or PCH21_9 on all the studied microbial species. Table 8.2 presents the pairwise comparison of the antimicrobial effect of BSF_NPs or PCH21_9 on the three studied microbial species.

Table 8.2: Pairwise comparison of the antimicrobial effect of BSF_NPs or PCH21_9 against *E. faecalis, S. mutans* or *C. albicans*.

Pairwise comparison						
	Test organisms	Chitosan samples	BSF_NPs		PCH21_9	
			Chi-Square	Sig.	Chi-Square	Sig.
Breslow (Generalized Wilcoxon)	*E. faecalis*	BSF_NPs			2.456	1.117
		PCH21_9	2.456	0.035		
	S. mutans	BSF_NPs			2.062	0.151
		PCH21_9	2.062	0.151		
	C. albicans	BSF_NPs			2.945	0.086
		PCH21_9	2.945	0.086		

Table 8.2 presents the comparative analysis of the effect of BSF_NPs or PCH21_9 against the investigated microbial species using the Breslow (Generalized Wilcoxon) test. The results of the tests signify that no statistical difference existed between the use of BSF_NPs or PCH21_9 as an antimicrobial agent against *S. mutans* or *C. albicans* ($p > 0.05$). Contrary to the above observation, there exists a statistical difference between the use of BSF_NPs or PCH21_9 as an antimicrobial agent against *E. faecalis* ($p < 0.05$), as shown in Table 8.2.

The comparative study of the efficacy of the BSF_NPs or the PCH21_9 was investigated in this section and there were observed differences in the time of kill of the three studied microorganisms by both chitosan samples. The observed differences in the BSF_NPs or the PCH21_9 against all the three investigated species of *E. faecalis, S. mutans* or *C. albicans* could be attributed to the variation in the size of the sample particles, as discussed in Sections 5.5.1.2 and 5.5.1.3 of Chapter 5. The BSF_NPs were smaller than the particles of PCH21_9 due to effect of electrospraying. The nanoscale size of BSF_NPs (286±98 nm) could have enhanced the deep penetration into the extracellular matrix of the cell walls of the microorganisms than the particles of PCH21_9 (1436±854 nm) causing damage to the cells. The BSF_NPs eradicated the *S. mutans* or the *E. faecalis* completely with 0.5 h in this study.

Another factor that could have contributed to this increased bactericidal effect of BSF_NPs compared to the PCH21_9 is the high value of its (BSF_NPs) zeta potential (ZP). The high ZP values ensured that the nanoparticles remained stable in the solution and prevent the possible flocculation/coagulation since repulsive forces exceeded attractive forces of the particles

(Hanaor *et al.*, 2012). The high positive charge (±54.7 mV) on the surface of the BSF_NPs (see Section 5.5.1.3 of Chapter 5) could have contributed significantly in binding to the negatively charged bacterial cell walls (Qi *et al.*, 2004; Kong *et al*., 2010) causing the rapid disruptions in the normal functions of the cells.

The ZP values have been previously reported in the literature. Costa *et al.* (2018) reported a ZP of 27.1 mV in their investigation of chitosan as inhibitors of antibiotic-resistant skin microorganisms. Madureira *et al.* (2015) reported a ZP of 21.7 mV while investigating chitosan nanoparticles as antimicrobial agents against food pathogens and Silva *et al*. (2015) reported a value of 22.9 mV while using chitosan nanoparticles as drug delivery medium for ocular treatment. The ZP value reported in this study is higher than those mentioned above. The superior ZP value of the BSF_NPs could have resulted from the method of nanoparticle synthesis. The above-mentioned studies adopted the ionic gelation method in the preparation of the nanoparticles while this study utilised the electrospraying technique. Therefore, this study reported superior ZP values for chitosan nanoparticles compared to the studies of Costa *et al.* (2018), Madureira *et al.* (2015) and Silva *et al.* (2015) reported in the literature.

Furthermore, the BSF_NPs were homogeneous in solution. This is depicted by a low polydispersity index (PdI) of 0.16 as against a higher PdI value of 0.74 for PCH21_9. The low PdI value may have ensured that more of the nanoparticles penetrated the cell membrane of the *both E. faecalis* or *S. mutans* and were effectively distributed within the cells to inflict cell damage and eventual lysis within 0.5 h of investigation. This finding corroborates the results of Kong *et al*. (2010), González-Campos *et al*. (2013) and Sarwar *et al*. (2014).

The *C. albicans* reacted differently to the presence of BSF_NPs and PCH21_9 in this study. The difference in the behaviour of the *C. albicans* could be attributed to the particle size of the samples and the genetic makeup of the *C. albicans*. At the inception of the experiment, the BSF_NPs were effective against the *C. albicans* (0 CFU/mL) up to 2 h of the investigation while the PCH21_9 were not as potent as the BSF_NPs. As time progressed (after 2 h), the *C. albicans* started to proliferate, hence adapting to the new environment. This adaptation could have been enabled by the production of genetically altered strains that are resistant to the nanoparticles or the triggering of the transporter or the efflux genes, CgTpo3 or CgAqr1 which protected it from the nanoparticles (Costa *et al.*, 2013; Bernardo *et al*., 2017). This phenomenon was reported by Kim *et al*. (2015) who stated that *C. albicans* possesses a rare capability to

adjust in any environment by producing species with modified genetic makeup for better adaptation in its new environment. G´omez-Rivas *et al*. (2004) noted that fungi exhibited a certain degree of adaptation in the presence of chitosan. They suggested that it could be due to the increase in chitinase production by the organisms (fungi) and that the produced enzymes tend to degrade the chitosan which the organism used as a source of energy. These adduced reasons could explain the absence of *C. albicans* in the BSF_NPs treated media from 0.5 h to 2 h, and their subsequent proliferation and therefore the observed difference between the BSF_NPs or the PCH21_9 samples in this study. Furthermore, researchers have observed that chitosan was ineffective against some fungal agents. Arancibia *et al*. (2015) observed that chitosan was ineffective and had no antifungal activity against *Aspergillus niger* and *Fusarium solani* in their study of the impact of extracting conditions on the antimicrobial and rheological properties of chitosan. The insensitivity of chitosan against fungi was reported by Allan and Hadwiger (1979) to have resulted from the presence of chitosan in the cell wall of fungi. Russell (2003) corroborated the study of Allan and Hadwinger that the cell walls of fungi consist of, among other components, chitosan. Hence the presence of chitosan as a cell wall component of any fungi could reduce or totally eliminate the antifungal activity of chitosan against such organism.

The combination of the three factors of smaller nanosized particles, higher zeta potential value and lower polydispersity index could have played a significant role in the observed rapid bactericidal actions of the BSF_NPs on *E. faecalis* or *S. mutans* and an improved fungistatic activity on *C. albicans* compared to the PCH21_9 in this study. The next section examines the cytotoxic implication of the use of PCH21_9 or BSF_NPs on human skin cells.

8.5 Risk assessment studies

The synthesised biomaterials were constantly handled (though with protective equipment) during the investigation. Since nanoparticles were involved, there could arise the risk of penetration or absorption into human tissues through the dermal (skin) route. To study the risk associated with this constant handling and possible contact with the skin and for any future medical applications, the cytotoxic effect of PCH21_9 or BSF_NPs were investigated using the KMST-6 human skin fibroblast cells. The experimental protocol is described in Section 3.8 of Chapter 3. Subsequent subsections discuss these effects in detail.

8.5.1 *Cytotoxicity investigation of PCH21_9 to KMST-6 skin fibroblast cell lines*

This investigation was performed to determine the cytotoxic effects of the PCH21_9 on human skin fibroblast cell lines. The test measured the survival rate of human skin fibroblast cell lines in contact with the PCH21_9. Table 8.3 presents the descriptive statistics of the mean of the optical density of the cell lines exposed to PCH21_9 or the control sample.

Table 8.3: The mean, standard deviation and standard error of the mean of the optical density of skin fibroblast cells exposed to PCH21_9 or the control sample

Group	Mean	Standard deviation	Standard error of the mean
PCH21_9	0.44	0.03	0.01
Control	0.41	0.03	0.01

Table 8.3 shows that the exposure of the human skin fibroblast cells to PCH21_9 solution led to an increase in the mean optical density of the cells. The mean value increased from 0.41 in the control group to 0.44 in the PCH21_9 treated group, an indication of cell proliferation in the test plates. The increase in the number of cells in the test media implies that the PCH21_9 samples showed no toxic effect on the skin cells used in this study. The statistical difference between the PCH21_9 or the control groups were evaluated using the student's t-test and are presented in Table 8.4.

Table 8.4: An independent sample t-test showing the statistical relationship between the growth rates of the KMST-6 skin fibroblast cells in contact with PCH21_9 or the control groups

Levene's Test for Equality of Variances		t-test for Equality of Means						
F	Sig.	t	df	Sig. (2-tailed	Mean Difference	Std. Error Difference	95% Confidence Interval of the Difference	
3.32	0.57	3.46	30	0.002	0.03	0.01	0.01	0.05

The independent sample t-test was used to compare the mean growth rates of the KMST-6 skin fibroblast cells in contact with PCH21_9 or the control group. This was done to determine the statistical relationship between the two samples. There was indeed a statistical difference ($p < 0.05$) between the growth rates of the KMST-6 skin fibroblast cells in normal conditions (control) likewise when exposed to PCH21_9 (Figure 8.32B). The implication of this is that the PCH21_9 did not induce mortalities in the skin cells rather the cells proliferated to a statistically significant level.

8.5.2 *Cytotoxicity investigation of BSF_NPs to KMST-6 skin fibroblast cell lines*

This investigation was performed to determine the cytotoxic effects of the BSF_NPs on skin fibroblast cell lines by determining the cell viability in the nanoparticle solution. The test measured the survival rate of human skin fibroblast cell lines in contact with the BSF_NPs. Table 8.5 presents the descriptive statistics of the mean of the optical density of the human skin fibroblast cells exposed to BSF_NPs or the control samples.

Table 8.5: The mean, standard deviation and standard error of the mean of the optical density of skin fibroblast cells exposed to BSF_NPs or the control samples.

Group	Mean	Standard deviation	Standard error of the mean
BSF_NPs	0.43	0.05	0.01
Control	0.41	0.03	0.01

Table 8.5 shows that the exposure of the human skin fibroblast cells to BSF_NPs solution induced the increase in the mean of the optical density of the cell lines. The mean value increased to 0.43, an additional 5% increase from the control groups mean value (0.41).

Table 8.6: An independent sample t-test showing the statistical relationship between the growth rates of the KMST-6 skin fibroblast cells in contact with the BSF_NPs or the control groups

Levene's Test for Equality of Variances		t-test for Equality of Means						
F	Sig.	t	df	Sig. (2-tailed	Mean Difference	Std. Error Difference	95% Confidence Interval of the Difference	
3.32	0.08	1.48	30	0.15	0.02	0.01	-	0.05

The independent sample t-test was used to compare the mean growth rates of the KMST-6 skin fibroblast cells in contact with BSF_NPs or the control group. This was done to determine the statistical relationship between the two samples. There was no statistical difference ($p > 0.05$) between the growth rates of the KMST-6 skin fibroblast cells in normal conditions (control) likewise when exposed to BSF_NPs. Figure 8.31 presents the micrographs of the cell viability studies of the KMST-6 skin fibroblasts in contact with BSF_NPs or PCH21_9.

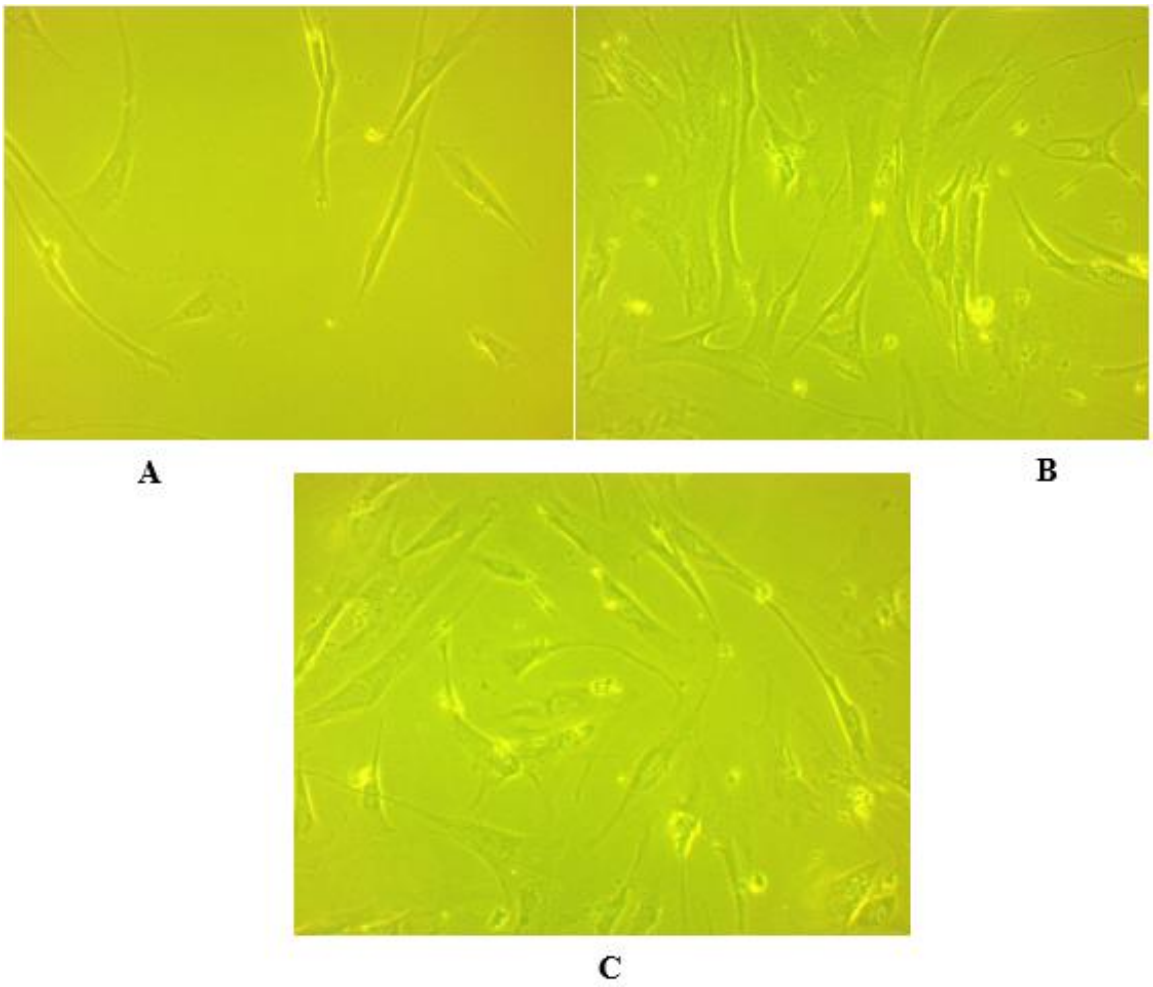

Figure 8. 31: KMST-6 skin fibroblast cells showing growth rate in contact with the studied samples as captured using an optical microscope; (A) Under normal conditions (control experiment), (B) when exposed to PCH21_9 and (C) when exposed to BSF_ NPs.

Figure 8.31 (B and C) shows that there was an increase in the number of the KMST-6 cell lines, an indication that the PCH21_9 or BSF_NPs did not hinder the growth of the cells; rather the samples enhanced the cells' growth and proliferation. The overall survival of the cells induced with PCH21_9 or BSF_NPs is discussed in the next subsection.

8.5.3 *Survival rate of KMST-6 skin fibroblast cell lines*

The cells exposed to PCH21_9 or BSF_NPs showed positive growth in the test medium (Figure 8.31). The KMST-6 skin cells showed 100% growth rate in the control group, which increased to 105% and 109% in contact with the BSF_NPs and PCH21_9, respectively. Figure 8.32 shows the plot of the survivability and proliferation of the fibroblast cells in the test media.

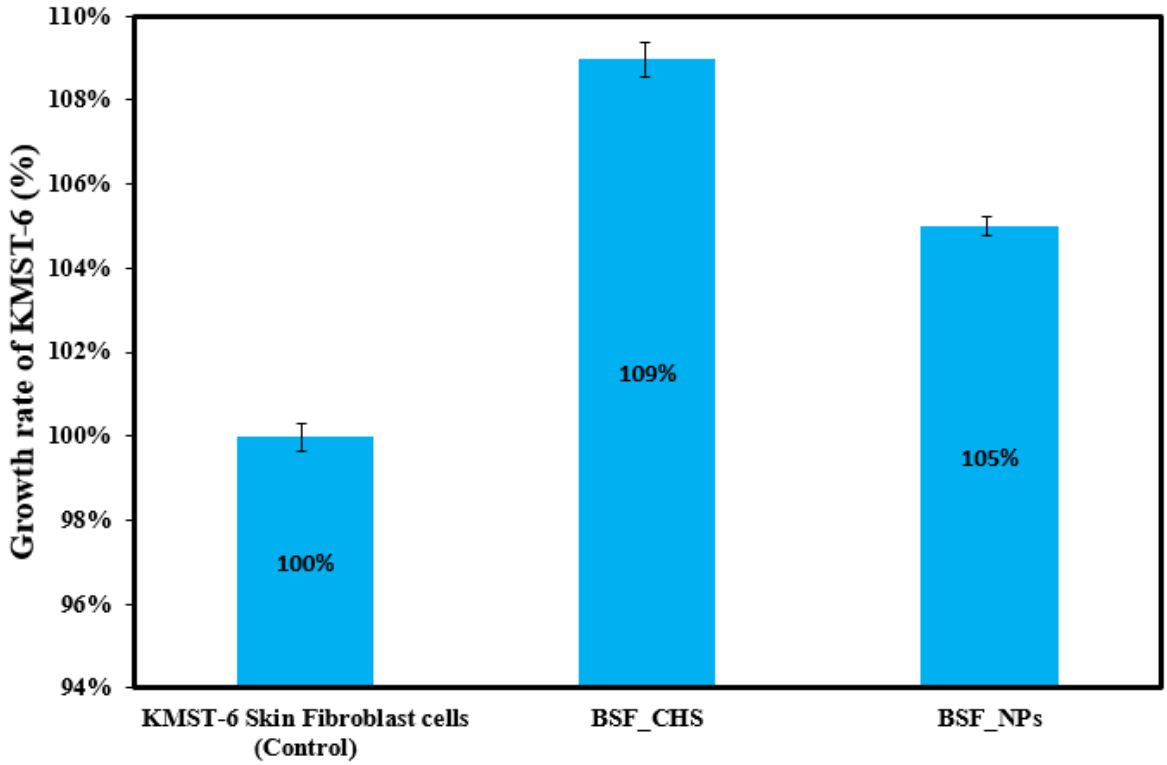

Figure 8. 32: Bar chart showing the growth rate of skin fibroblast cells when exposed to PCH21_9, BSF_NPs or the control.

The synthesised PCH21_9 or BSF_NPs from BSF waste was toxic against microbial species studied, showing complete elimination of *E. faecalis* or *S. mutans* within a short time interval (Section 8.2 and 8.3) while showing a fungistatic effect against *C. albicans*. Contrary to these observations, PCH21_9 or BSF_NPs did not exhibit similar toxic effects on KMST-6 human fibroblast cell lines as the cells rather grew in contact with the samples. This study was designed to investigate the cytotoxicity of these synthesised biomaterials on human skin cells when in contact with it. The cytotoxicity of a sample to a cell line could be determined using three different methods: by measuring the damage induced by the sample unto the cells; by measuring cell growth in contact with the sample or by investigating a specific area of the cell's metabolism (Kirkpatrick *et al.*, 1998). In this study, the skin cell lines' growth and viability were measured by adopting the MTT assay. Before the test, the appearance of the cells was examined before and after exposure to the PCH21_9 or BSF_NPs (Figure 8.31) using an optical microscope (Olympus CK2 inverted microscope, Japan). No significant difference was observed on the physical structures of the cell lines in the test media, rather there was a considerable increase in the number of cells in the test media inoculated with PCH21_9 or BSF_NPs compared to the control group. The result shows that there was a higher percentage increase in the PCH21_9 treated samples (109%) than in the BSF_NPs groups (105%). The

observed difference in cell proliferation could be due to the reduced particle size and MW of the samples of the BSF_NPs (discussed in Section 5.4 of Chapter 5). The electrospraying of the PCH21_9 to BSF_NPs (nanoparticles) resulted in decreased size and invariably reduced the MW of the BSF_NPs and hence the decreased cell proliferation observed when compared with the PCH21_9 samples. Grobler and Perchyonok (2018) have reported that an increase in MW of shrimp chitosan promoted the 3T3 cell lines in their study of the effect of different MW on mouse fibroblast cells. Similarly, the study of Lahiji *et al.* (2000) and Gao *et al.* (2012) independently revealed the biocompatibility nature of chitosan to promote the growth and sustained activities of human osteoblasts and chondrocytes.

Therefore, the PCH21_9 or BSF_NPs used in this study promoted the growth of the KMST-6 skin fibroblast cells and points to the ability of the samples to stimulate the healing of incapacitated parts of human skin cells exposed to PCH21_9 or BSF_NPs samples. To the best of our knowledge, nanoparticles have not been synthesised from chitosan obtained from BSF previously. This study, therefore, would open up numerous medical applications of the BSF chitosan and their synthesised nanoparticles in the area of wound dressing, gene delivery, drug delivery and targeted nano-systems for cancer treatments. This is important as insect chitosan (BSF) is non-allergenic to humans unlike seafood (crustaceans) by-product sources of chitosan.

8.6 Chapter summary

This chapter discussed the effectiveness of the extracted BSF chitosan (PCH21_9) and the chitosan nanoparticles (BSF_NPs) as an antimicrobial agent and the cytotoxic effects of the biomaterials on human skin cells. The microbial species investigated were *Enterococcus faecalis*, *Streptococcus mutans* and *Candida albicans*. The Time-kill analysis was adopted in determining the potency or otherwise of the synthesised biomaterials. The PCH21_9 totally eradicated the microorganism, *E. faecalis* by 8 h of contact time while it took just 2 h for the PCH21_9 to totally kill the *S. mutans* in the test media, which were monitored for 24 h without any growth observed. Contrary to the observation *on E. faecalis* or *S. mutans* treated with PCH21_9, the 3% PCH21_9 concentrations were not effective against *C. albicans* over the 24 h study period. The *C. albicans* in this study were denatured with the lowest CFU/mL value observed at 4 h of contact time after which the organisms exponentially grew in the test media until the 24 h study period. This implies that the PCH21_9 were not effective against *C. albicans* in this study except as a fungistatic agent. The positive and the negative controls were investigated to determine if they contributed to the observed bactericidal or fungistatic effects

of the 3% PCH21_9 samples on the microbial species studied. The results show that the control groups did not contribute to the observed bactericidal or fungistatic effects of PCH21_9 against the microbial species over the 24 h study period. The plots of *E. faecalis* or *S. mutans* were parallel to the horizontal (time) axis while the plot of *C. albicans* fluctuated slightly.

The BSF_NPs were also investigated for its potency against the three studied microorganisms. The total eradication of the *E. faecalis* or *S. mutans* by the BSF_NPs was witnessed after 0.5 h of contact without further growth of the microbes in the test media throughout the 24 h study period. The *C. albicans* showed a contrary result. The nanoparticles (BSF_NPs) were not effective against the *C. albicans* over the 24 h period of investigation. Rather, a fungistatic action was observed, as the microbial load (CFU/mL) decreased progressively to zero after 2 h of contact. At 4 h of contact, the *C. albicans* were, once again, observed and they increased in number in the test media up to the 24 h of investigation.

The effect of the PCH21_9 or BSF_NPs in contact with human skin cell lines were further investigated. The result showed that the biomaterials promoted the growth of the KMST-6 skin cell lines over a 24 h study period.

This study, to the best of our knowledge, is the first to successfully synthesise chitosan nanoparticles from BSF through electrospraying technique. The nanoparticles synthesised had superior zeta potential values compared to chitosan nanoparticles reported in the literature. This study is also the first to successfully apply synthesised chitosan nanoparticles from Black Soldier fly (BSF_NPs) as an antimicrobial agent against selected pathogenic microorganisms of *E. faecalis*, *S. mutans* or *C. albicans.*

CHAPTER 9

CONCLUSION, NOVELTY AND RECOMMENDATIONS

9.0 Introduction

In this chapter is presented the findings and the conclusions derived from this study *vis-à-vis* the answers to the research questions proposed in Chapter 1 which were important in achieving the aim of this study. This chapter also highlights the novelty of this work and the suggestions proposed for future research in this area. Chitin and chitosan extraction from both pupal and adult BSF were carried out by varying the process parameters of concentration, time and temperature to achieve the optimum extraction conditions. The resulting chitosan biomaterials after characterising using ATR-FTIR, HRSEM, XRD and TGA were electrospin into nanofibres (ES-D3) and nanoparticles (BSF_NPs). The nanofibres were crosslinked using tannic acid to improve its stability in aqueous solutions. Afterwards, the tannic acid crosslinked BSF nanofibres (TA_CHS_2) were employed in the adsorption of inorganic metals ions (Pb^{2+} or Cd^{2+}) in a batch process. The pH of the solution, the concentration of the metals ions, the time and the temperature of the reactions were investigated to ascertain the equilibrium adsorption capacities of the adsorbent. The adsorbent was desorbed and regenerated using 0.01 M NaOH solution. In addition, the application of the PCH21_9 or the BSF_NPs as antimicrobial agents were carried out in this study. The time-kill technique was adopted in investigating the antimicrobial efficacy of the chitosan biomaterials. The obtained data from the antimicrobial studies were analysed using the non-parametric Kaplan-Meier survival function test and the Generalised Wilcoxon test to compare the effect of PCH21_9 or BSF_NPs on all the studied microbial species. The microbial species studied were *E. faecalis, S. mutans* or *C. albicans* due to their prevalence within the human environment. Finally, the cytotoxic effect of both PCH21_9 or BSF_NPs on skin cell lines were ascertained using the MTT assay. The investigation was conducted using KMST-6 human skin fibroblast cell lines.

9.1 Conclusion

This study, therefore, provided answers to these proposed research questions as contained in Chapter 1 of this study.

a. **What are the optimal extraction conditions for chitin and chitosan from both pupal exuviae or adult BSF**?

The extraction of chitin involved three processes of demineralisation, deproteination and deacetylation. These processes were optimised and a total of forty-six (46) trials were conducted on both the pupae and adult BSF wastes. The parameters involved in these processes were concentration, temperature and time. The optimal demineralisation conditions for both samples were 1.0 M NaOH, 100 mins, 50 °C; deproteination were 1.0 M NaOH, 14 h, 95 °C for pupae samples and 1.0 M NaOH, 12 h, 95 °C for adult samples. Deacetylation was 70% NaOH, 100 °C, 5 h for both samples. The optimised conditions at each extraction process were utilised for the overall synthesis of the chitin and chitosan.

b. **Between adult and pupae BSF samples which will have better chitin and chitosan yield?**

The percentage yield of the chitin and chitosan from both the pupal and the adult BSF samples were determined. The dry weight chitin contents of the adult BSF and pupae casings were computed to be 5.3 and 14.1%, respectively. The chitosan yield obtained from the optimised conditions of the deacetylation process for both pupal (PCH21_9) and adult (ACH20_9) chitosan samples were 11.3 and 2.5%, accordigly. The pupal BSF samples had three times more chitin yield and more than 4 times (352%) chitosan yield than the adult samples. The pupal BSF samples thus had a better chitin and chitosan yield than the adult samples.

c. **Can the extracted chitosan from BSF be electrospun to nanofibres and nanoparticles without blending with synthetic polymers**?

This study specifically investigated the parameters affecting electrospinning, which include the process parameters and solution properties to determine the optimum conditions for the electrospinning of extracted PCH21_9. After many trials (16 in total) and optimisation of electrospinning conditions, the pupal BSF chitosan (PCH21_9) was successfully electrospun into nanofibres without the addition of synthetic polymers/blending.

d. **What are the optimum conditions for the electrospinning of BSF chitosan biopolymer into nanofibres?**

The electrospinning process was undertaken to synthesise bead-free nanofibres from pure BSF chitosan solution in TFA. The optimised electrospinning conditions determined were a chitosan concentration of 5 wt%; voltage of 25 kV; solution flow rate of 0.3 mL/h and a needle tip-to-collector distance of 100 mm. The chitosan nanofibres obtained at the optimum conditions have a mean fibre diameter of 128 nm. The characterisation of the electrospun nanofibres (ES-D3) using the FTIR showed that the chemical structure of the biopolymer did not change during the electrospinning process. It further showed that the fibres maintained the characteristic Amide 1,11 and 111 functional groups inherent in PCH21_9. However, the Amide 1 signal shifted to a higher wavenumber while Amide 11 was observed at a lower wavelength with all having increased intensity, an indication of the formation of a stable amide bond.

e. **Can tannic acid effectively crosslink chitosan nanofibres?**

Tannic acid was able to crosslink the chitosan mats. The crosslinked mats had an increased fibre diameter of 72% more than the as-spun chitosan nanofibres. The fibres mats were not soluble in 1.0 M acetic acid, deionised water or 1.0 M NaOH solutions after 72 h. Therefore, the ES-D3 was successfully crosslinked and the crosslinked fibres showed excellent stability in aqueous solution needed for adsorption studies while maintaining the characteristic Amide 1, 11 and 111 functional groups of chitosan.

f. **What is the effect of pH, concentration, time and temperature variations on the adsorption capacity of Pb^{2+} or Cd^{2+} by the TA crosslinked chitosan nanofibres?**

The investigation shows that the adsorption capacity for both Pb^{2+} or Cd^{2+} increased with an increase in pH of the solution(s). The equilibrium adsorption capacities of 94.74 or 77.86 mg/g were achieved at pH 4 or 6 for Pb^{2+} or Cd^{2+}, respectively. The effect of concentration on the adsorption capacity of the TA_CHS_2 adsorbent was investigated at the optimised pH of 4 or 6 for Pb^{2+} or Cd^{2+}, respectively. The investigation revealed that as the concentration increased, the adsorption capacities of both metal ions increased. The optimal adsorption capacities were 95.767 or 85.325 mg/g for Cd^{2+} or Pb^{2+}, respectively. The study further revealed that the Langmuir model had a better fit for the adsorption data and, therefore, could precisely explain the adsorption process. In addition, the adsorption process was favourable at the concentration range studied and occurred as a result of monolayer formation. The effect of contact time on the adsorption of Pb^{2+} or Cd^{2+} metal ions onto TA_CHS_2 adsorbent showed that adsorption

capacities increased as the time of reaction increased and attained equilibrium after 1 h (60 minutes) of contact time. The equilibrium adsorption capacities were determined to be 90.41 or 87.56 mg/g for Pb^{2+} or Cd^{2+}, respectively. The adsorption kinetics revealed that the pseudo-second-order model was more appropriate in describing the amount of Pb^{2+} or Cd^{2+} sorbed onto the TA_CHS_2 adsorbent. Similarly, the adsorption capacity of the adsorbent increased with increase in temperature with Pb^{2+} attaining quasi-equilibrium at 35 $^{\circ}$C, thereafter increasing and attaining equilibrium capacity of 112.6 mg/g at 55 $^{\circ}$C. The Cd^{2+} attained equilibrium capacity of 116 mg/g at 45 $^{\circ}$C. The thermodynamic studies indicate that the adsorption process for both Pb^{2+} or Cd^{2+} were endothermic, spontaneous and with increased randomness at the solid-liquid boundary as revealed by the ΔH°, ΔG° and ΔS° values. Furthermore, it was found that the adsorption process followed the dissociative mechanism step.

g. **Can the crosslinked BSF nanofibre adsorbents be regenerated after adsorption of Pb^{2+} or Cd^{2+}?**

The experiments were conducted to regenerate the TA_CHS_2 previously used in the adsorption of Pb^{2+} or Cd^{2+} using three different concentrations of NaOH (0.1, 0.01 and 0.001 M). The obtained result showed that Pb^{2+} or Cd^{2+} loaded TA_CHS_2 adsorbent could be easily desorbed using 0.01 M NaOH solution. The study further revealed that the adsorbent could achieve 89 or 86% desorption for Pb^{2+} or Cd^{2+}, respectively after three consecutive regeneration cycles. The desorbed sorbent could be reused for three cycles without significant reduction in the affinity of the metals ions to the active sites or reduction in the stability of the material.

h. **How effective are the chitosan nanoparticles in eradicating microbial cells of *E. faecalis, S. mutans* or *C. albicans*?**

The effectiveness of BSF_NPs in eradicating microorganisms was investigated using *E. faecalis, S. mutans* or *C. albicans* cells. The Time-kill analysis was adopted in this investigation. The results show that both the BSF_NPs or the PCH21_9 were effective in the complete eradication of the *E. faecalis* or the *S. mutans* in this study. The BSF_NPs showed more potency as it eliminated all the microorganisms within 0.5 h of investigation, unlike PCH21_9 which took 2 or 8 h to totally kill the *S. mutans* or the *E. faecalis*, respectively. However, both the BSF_NPs or the PCH21_9 were not effective against *C. albicans*. The BSF_NPs produced a fungistatic effect as the *C. albican* cells decreased progressively to zero

CFU/mL up to 2 h in contact with the BSF_NPs after which the organisms re-emerged and subsequently proliferated in the test media up to the 24 h of the investigation.

i. **Are the nanoparticles and the chitosan toxic to human skin cells?**

The cytotoxicity of the PCH21_9 or the BSF_NPs on KMST-6 human skin fibroblast cell lines were investigated. The results show that the samples did not exhibit any toxic effect on the human fibroblast cell lines as the cells rather grew when in contact with the biomaterials. The PCH21_9 treated samples had a 9% increase in population after a 24 h period while the BSF_NPs treated samples showed a 5% proliferation. This, therefore, suggest that both PCH21_9 and BSF_NPs promoted the growth of the KMST-6 skin fibroblast cells in this study.

9.2 Novelty

This study succeeded in optimising the process conditions for the extraction of chitosan from commercially reared Black soldier fly waste materials and accurately determined the chitin content of both samples. The information is vital in upscaling and commercial production of chitin and chitosan and have already been applied for this purpose. Furthermore, this study is reporting the optimisation of the process parameters and, thus, the electrospinning of BSF chitosan for nanofibres fabrication for the first time. Additionally, the synthesis of nanoparticles from BSF chitosan by electrohydrodynamic spraying is reported for the first time in this study. This study is also the first to successfully apply chitosan nanoparticles synthesised from Black soldier fly as an antimicrobial agent against selected pathogenic microorganisms of *E. faecalis*, *S. mutans* or *C. albicans*. Finally, the use of tannic acid crosslinked chitosan (TA_CHS_2) for adsorption purpose is reported for the first time in this study and the adsorbent exhibited excellent adsorption capacity.

9.3 Recommendation/suggestions for future studies

Most of the critical questions formulated in this study have been addressed. However, there are certain aspects which were not fully investigated due to resource or time constraints. This study, therefore, recommends further studies be conducted to investigate the adsorption potentials and kinetics of the TA_CHS_2 adsorbent from 1.0 - 10 minutes of contact time. Equally important is the pH point of zero charge (pHpzc) of the adsorbent to develop and explain the mechanism(s) for the adsorption of Pb^{2+} or Cd^{2+} in solution. Additionally, experiments showing the adsorption potential of the TA_CHS_2 adsorbent for Pb^{2+} and Cd^{2+} in a multicomponent cation system should be investigated. Moreso, the regeneration of the

adsorbent should be conducted at increased number of cycles. The conduct of Brunauer-Emmett-Teller (BET) analysis on the TA_CHS_2 nanofibres adsorbent is highly recommended. Besides, future investigations should centre on the impact of the degree of TA crosslinking on the adsorption efficiency of the BSF chitosan nanofibres This study finally recommends that more effort should be geared towards the use of acetic acid, a more environmentally friendly solvent than TFA, in the electrospinning of BSF chitosan.

REFERENCES

Abbasizadeh, S., Keshtkar, A.R. and Mousavian, M.A. (2014). Sorption of heavy metal ions from aqueous solution by a novel cast PVA/TiO_2 nanohybrid adsorbent functionalized with amine groups. *Journal of Industrial and Engineering Chemistry*, **20**: 1656–1664.

Abdelmalek, B.E., Sila, A., Haddar, A., Bougatef, A. and Ali, M. (2017). β-chitin and chitosan from squid gladius: biological activities of chitosan and its application as clarifying agent for apple juice. *International Journal of Biological Macromolecules*, **104**: 953–962. doi: 10.1016/j. ijbiomac.2017.06.107.

Abdel-Rahman, R.M., Hrdina, R; Abdel-Mohsen, A.M., Fouda, M.M.G., Soliman, A.Y Mohamed, F.K., Mohsin, K. and Pinto, T.D. (2015). Chitin and chitosan from Brazilian atlantic coast: Isolation, characterization and antibacterial activity. *International Journal of Biological Macromolecules*, **80**: 107–120.

Abdolmaleki, Y.A., Zilouei, H., Khorasani, N.S. and Abdolmaleki, A. (2017). Optimization and characterization of electrospun chitosan/poly (vinyl alcohol) nanofibers as a phenol adsorbent via response surface methodology. *Polymers for Advanced Technologies,* **28**(12): 1872–1878. doi: 10.1002/pat.4075.

Abdou, E.S., Nagy, K.S.A. and Elsabee, M.Z. (2008). Extraction and characterization of chitin and chitosan from local sources. *Bioresource Technology*, **99**: 1359–1367. doi: 10.1016/j.biortech.2007.01.051.

Abdulwadud, A., Muhammed, T.I., Surajudeen, A., Abubakar, J.M. and Alewo, O.A. (2013). Extraction and characterisation of chitin and chitosan from mussel shell. *Civil and Environmental Research*, **3**: 109–14.

Abraham, A., Soloman, P.A. and Rejin, V.O. (2016). Preparation of Chitosan-Polyvinyl Alcohol Blends and Studies on Thermal and Mechanical Properties. *Carbohydrate Polymers*, **24:** 741-748. doi: 10.1016/j.protcy.2016.05.206.

Adato, R. and Altug, H. (2013). In-situ ultra-sensitive infrared absorption spectroscopy of biomolecule interactions in real time with plasmonic nanoantennas. *Nature communications*, **4**(1): 1-10.

Adeosun, S.O., Gbenebor, O.P., Akpan, E.I. and Olaleye, S.A. (2017). Characterization of chitin synthesized from snail shell. *Proceedings of 146th Annual Meeting of* the Minerals, Metals & Materials Society, The Minerals, Metals & Materials Series, doi: 10.1007/978-3-319-51493-2_25.

Aelenei, N., Popa, M. I., Novac, O., Lisa, G. and Balaita, L. (2009). Tannic acid incorporation in chitosan-based microparticles and in vitro controlled release. *Journal of Materials Science: Materials in Medicine*, **20**(5), 1095–1102. doi:10.1007/s10856-008-3675-z.

Afshari, M. (2017). *Electrospun Nanofibers.* Woodhead Publishing, Cambridge.

Ahing, F. A. and Wid, N. (2016). Extraction and characterization of chitosan from Shrimp shell waste in Sabah. *Transactions on Science and Technology*, **3**(12): 227–237.

Ahyat, N. M. and Azmi, A. A. (2016). 'A review on chitin derivatives and its uses in silver nanoparticles synthesis. *Middle-East Journal of Scientific Research*, **24**(6): 2159–2165. doi: 10.5829/idosi.mejsr.2016.24.06.23656.

Aimé, C. and Coradin, T. (2017). Inorganic nanoparticles. In *Bionanocomposites: Integrating biological processes for bioinspired nanotechnologies*, Aimé, C. and Coradin, T. (eds.) John Wiley & Sons, Inc, NJ, USA. pp 131.

Akhtar, K., Khan, S.A., Khan, S.B. and Asiri, A.M. (2018). Scanning electron microscopy: principle and applications in nanomaterials characterisation. In: Sharma, S. (ed) Handbook of materials characterisation. Springer, Cham, Switzerland. doi: 10.1007/978-3-319-92955-2_4.

Akpomie, K.G. and Dawodu, F.A. (2014). Efficient abstraction of nickel(II) and manganese(II) ions from solution onto an alkaline-modified montmorillonite. *Journal of Taibah University for Science*, **8**: 343–356.

Akpomie, K.G. and Dawodu, F.A. (2016). Acid-modified montmorillonite for sorption of heavy metals from automobile effluent. *Beni-Suef University Journal of Basic and Applied Sciences*, **5**: 1–12. doi: 10.1016/j.bjbas.2016.01.003.

Al Sagheer, F.A., Al-Sughayer, M.A., Muslim, S. and Elsabee, M.Z. (2009). Extraction and characterization of chitin and chitosan from marine sources in Arabian Gulf. *Carbohydrate Polymers,* **77**(2): 410-419. doi: 10.1016/j.carbpol.2009.01.032Y.

Albadarin, A. B., Collins, M. N., Naushad, M., Shirazian, S., Walker, G. and Mangwandi, C. (2017). Activated lignin-chitosan extruded blends for efficient adsorption of methylene blue. *Chemical Engineering Journal*, **307**: 264–272. doi: 10.1016/j.cej.2016.08.089.

Al-Enizi, A., Zagho, M., and Elzatahry, A. (2018). Polymer-based electrospun nanofibers for biomedical applications. *Nanomaterials,* **8**(4): 259. doi: 10.3390/nano8040259.

Alhosseini, S.N., Moztarzadeh, F., Mozafari, M., Asgari, S., Dodel, M., Samadikuchaksaraei, A., Kargozar, S. and Jalali, N. (2012). Synthesis and characterization of electrospun polyvinyl alcohol nanofibrous scaffolds modified by

blending with chitosan for neural tissue engineering. *International Journal of Nanomedicine*, **7:** 25.

Ali, F. A. A., Haider, S., Al-masry, W. A. and Al-zeghaye, Y. (no date) Fabrication of chitosan nanofibers membrane and its treatment, pp. 1–4.

Aliabadi, M., Irani, M., Ismaeili, J., Piri, H. and Parnian, M.J. (2013). Electrospun nanofiber membrane of PEO/Chitosan for the adsorption of nickel, cadmium, lead and copper ions from aqueous solution. *Chemical Engineering Journal*, **220**: 237–243.

Aliasghari, A., Khorasgani, M. R., Vaezifar, S., Rahimi, F., Younesi, H. and Khoroushi, M. (2016). Evaluation of antibacterial efficiency of chitosan and chitosan nanoparticles on cariogenic streptococci: an *in vitro* study. *Iranian Journal of Microbiology*, **8**(2): 93-100.

Allais, M., Mailley, D., Hébraud, P., Ihiawakrim, D., Ball, V., Meyer, F., Hébraud, A. and Schlatter, G. (2018). Polymer-free electrospinning of tannic acid and cross-linking in water for hybrid supramolecular nanofibres. *Nanoscale*, **10**(19): 9164–9173. doi: 10.1039/c8nr01067f.

Allan, C.R. and Hadwiger, L.A. (1979). The fungicidal effect of chitosan on fungi of varying cell wall composition. *Experimental Mycology*, **3**: 285-287.

Amariei, N., Manea, L.R., Bertea, A.P., Bertea, A. and Popa, A. (2017). The Influence of polymer solution on the properties of electrospun 3D nanostructures. *IOP Conference Series: Material Science and Engineering*, **209:** 012092.

Angammana, C.J. and Jayaram, S.H. (2015). Fundamentals of electrospinning and processing technologies. *Particulate Science and Technology*, **34:** 72–82.

Anush, S. M., Vishalakshi, B., Kalluraya, B.and Manju, N. (2018). Synthesis of pyrazole-based Schiff bases of Chitosan: Evaluation of antimicrobial activity. *International Journal of Biological Macromolecules*, **119**: 446-452.

AOAC. (2000). Official methods of analysis, method 942.05 (17th ed.). Gaithersberg, MD: *Association of Official Analytical Chemists*.

Aranaz, I., Mengíbar, M., Harris, R., Paños, I., Miralles, B., Acosta, N. and Heras, Á. (2009). Functional characterization of chitin and chitosan. *Current Chemical Biology*, **3**: 203–230. doi: 10.2174/187231309788166415.

Arancibia, M. Y., Alemán, A., Calvo, M. M., López-Caballero, M. E., Montero, P. and Gómez-Guillén, M. C. (2014). Antimicrobial and antioxidant chitosan solutions enriched with active shrimp (*Litopenaeus vannamei)* waste materials. *Food Hydrocolloids*, **35**: 710–717. doi: 10.1016/j.foodhyd.2013.08.026.

Arancibia, M. Y., López-Caballero, M. E., Gómez-Guillén, M. C., Fernández-García, M., Fernández-Martín, F. and Montero, P. (2015). Antimicrobial and rheological properties of chitosan as affected by extracting conditions and humidity exposure. *LWT - Food Science and Technology*, **60**(2): 802–810. doi: 10.1016/j.lwt.2014.10.019.

Arbia, W., Arbia, L., Adour, L. and Amrane, A. (2013). Chitin extraction from crustacean shells using biological methods – A review. *Food Technology and Biotechnology,* **51** (1): 12–25.

Ardila, N., Ajji, Z., Heuzey, M.-C. and Ajji, A. (2018). Chitosan electrospraying: mapping of process stability and micro and nanoparticle formation. *Journal of Aerosol Science,* **126**: 85 – 98. doi: 10.1016/j.jaerosci.2018.08.010.

Arinstein, A. (2018). *Electrospun polymer nanofibers.* Pan Stanford Publishing Pte, Singapore. ISBN: 978-1-315-36462-9.

Arnold, N.D., Brück, W.M., Garbe, D. and Brück, T.B. (2020). Enzymatic modification of native chitin and conversion to specialty chemical products, a review. *Marine Drugs,* **18**: 93. doi: 10.3390/md18020093.

Austero, M.S., Donius, A.E., Wegst, U.G.K. and Schauer, C.L. (2012). New crosslinkers for electrospun chitosan fibre mats. I. Chemical analysis. *Journal of The Royal Society Interface*, **9**(75): 2551–2562. doi: 10.1098/rsif.2012.0241.

Ayanda, O.S., Amodu, O.S., Adubiaro, H., Olutona, G.O., Ebenezer, O, T., Nelana, S.M. and Naidoo, E.B. (2019). Effectiveness of termite hill as an economic adsorbent for the adsorption of alizarin red dye. *Journal of Water Reuse and Desalination*, **9**(1): 83-93. doi: 10.2166/wrd.2018.026.

Bae, H.-S., Haider, A., Selim, K.M.K., Kang, D.-Y., Kim, E.-J. and Kang, I.-K. (2013). Fabrication of highly porous PMMA electrospun fibers and their application in the removal of phenol and iodine. *Journal of Polymer Research,* **20**(7): 1–7.

Bajaj, M., Winter, J. and Gallert, C. (2011). Effect of deproteinisation and deacetylation conditions on viscosity of chitin and chitosan extracted from *Crangon crangon* shrimp waste. *Biochemical Engineering Journal,* **56:** 51–62.

Baran, T. and Menteş, A. (2015). Cu(II) and Pd(II) complexes of water soluble O-carboxymethyl chitosan Schiff bases: synthesis, characterization. *International Journal of Biological Macromolecules,* **79**: 542–554. doi: 10.1016/j.ijbiomac.2015.05.021.

Barry, J. E., Finkelstein, M. and Ross, S. D. (1984). Hydrogen-bonded complexes. 5. Phenol amine complexes. *Journal of Organic Chemistry,* **49**(9): 1669–1671.

Baruah, P., Duarah, R. and Karak, N. (2016). Tannic acid-based tough hyperbranched epoxy thermoset as an advanced environmentally sustainable high-performing material. *Iranian Polymer Journal*, **25**(10): 849–861. doi:10.1007/s13726-016-0471-3.

Benecke, M. (2001). A brief history of forensic entomology. *Forensic Science International*, **120**: 2-14.

Benhabiles, M.S., Abdi, N., Drouiche, N., Lounici, H., Pauss, A., Goosen, M.F.A. and Mameri, N. (2013). Protein recovery by ultrafiltration during isolation of chitin from shrimp shells Parapenaeus longirostris. *Food Hydrocolloids*, **32**: 28–34. doi: 10.1016/j.foodhyd.2012.11.035.

Bernardi, S., Corso, M. P., Baraldi, I. J., Colla, E. and Canan, C. (2018). Obtaining concentrated rice bran protein by alkaline extraction and stirring–optimization of conditions. *International Food Research Journal*, **25**(3): 1133-1139.

Bernardo, R. T., Cunha, D. V., Wang, C., Pereira, L., Silva, S., Salazar, S. B., Schröder, M.S., Okamoto, M., Takahashi-Nakaguchi, A., Chibana, H., Aoyama, T., Sá-Correia, I., Azeredo, J., Butler, G., and Mira, N.P. (2016). The CgHaa1-regulon mediates response and tolerance to acetic acid stress in the human pathogen *Candida glabrata*. *G3: Genes, Genomes, Genetics*, **7**(1): 1-18.

Bhardwaj, N. and Kundu, S. C. (2010) Electrospinning: a fascinating fiber fabrication technique. *Biotechnology Advances*, **28**(3): 325–347. doi: 10.1016/j.biotechadv.2010.01.004.

Bhatia, S. (2016). Nanoparticles types, classification, characterization, fabrication methods and drug delivery applications. *Natural Polymer Drug Delivery Systems*. Springer, Cham, pp. 33-93.

Bhattarai, R., Bachu, R., Boddu, S. and Bhaduri, S. (2019). Biomedical applications of electrospun nanofibers: drug and nanoparticle delivery. *Pharmaceutics*, **11**(1): 5.

Blackwell, J., Parker, K.D. and Rudall, K.M. (1965). Chitin in pogonophore tubes. *Journal of the Marine Biological Association, UK*, **45**: 659–661.

Bock, N., Dargaville, T. and Woodruff, M. (2012). Electrospraying of polymers with therapeutic molecules: state of the art. *Progress in Polymer Science*, **37**(11): 1510–1551.

Bock, N., Woodruff, M. A., Hutmacher, D. W. and Dargaville, T. R. (2011). Electrospraying, a reproducible method for production of polymeric microspheres for biomedical applications. *Polymers*, **3**(1): 131-149.

Bogdanova, O.I., Polyakov, D.K., Streltsov, D.R., Bakirov, A.V., Blackwell, J. and Chvalun, S.N. (2016). Structure of β-chitin from *Berryteuthis magister* and its transformation during whisker preparation and polymerization filling. *Carbohydrate Polymers*, **137**: 678–684.

Bogosian, G. and Bourneuf, E. V. (2001). A matter of bacterial life and death. *EMBO Reports*, **2**(9): 770-774.

Bowman, K. and Leong, K. W. (2006). Chitosan nanoparticles for oral drug and gene delivery. *International Journal of Nanomedicine*, **1**(2): 117-128. doi:10.2147/nano.2006.1.2.117.

Bozorgi, M., Abbasizadeh, S., Samani, F., and Mousavi, S. E. (2018). Performance of synthesized cast and electrospun PVA/chitosan/ZnO-NH_2 nano-adsorbents in single and simultaneous adsorption of cadmium and nickel ions from wastewater. *Environmental Science and Pollution Research*, **25**(18): 17457–17472. doi:10.1007/s11356-018-1936-z.

Calvo, P., Remunan-Lopez, C., Vila-Jato, J. L. and Alonso, M. (1997). Novel hydrophilic chitosan-polyethylene oxide nanoparticles as protein carriers. *Journal of Applied Polymer Science*, **63**(1): 125-132.

Campana-Fillho, S. P., De Britto, D., Curti, E., Abreu, F. R., Cardoso, M. B., Battisti, M. V., Sim, P. C. and Lvall, R. L. (2007). Extraction, structures, and properties of alpha and beta-chitin. *Quimica Nova*, **30:** 644−650. doi: 10.1590/S0100-40422007000300026.

Cárdenas, G., Cabrera, G., Taboada, E. and Miranda, S. P. (2004). Chitin characterization by SEM, FTIR, XRD, and13C cross polarization/mass angle spinning NMR. *Journal of Applied Polymer Science*, **93**(4): 1876–1885. doi: 10.1002/app.20647.

Casadidio, C., Peregrina, D. V., Gigliobianco, M. R., Deng, S., Censi, R. and Di Martino, P. (2019). Chitin and chitosans: characteristics, eco-friendly processes, and applications in cosmetic science. *Marine Drugs*, **17**(6): 369. doi: 10.3390/md17060369.

Cauchie, H.-M. (2002). Chitin production by arthropods in the hydrosphere. *Hydrobiologia*, **470**: 63–95.

Charernsriwilaiwat, N., Opanasopit, P., Rojanarataa, T., Ngawhirunpat, T. and Supaphol, P. (2010). Preparation and characterization of chitosan-hydroxybenzotriazole/polyvinyl alcohol blend nanofibers by the electrospinning technique. *Carbohydrate Polymers*, **81**: 675–680.

Chattopadhyay, D.P. and Inamdar, M.S. (2010). Aqueous behaviour of chitosan. *International Journal of Polymer Science*, **939536**: 7. doi: 10.1155/2010/939536.

Chauhan, D. and Sankararamakrishnan, N. (2008). Highly enhanced adsorption for decontamination of lead ions from battery wastewaters using chitosan functionalized with xanthate. *Bioresources Technology*, **99**: 9021–9024.

Chaúque, E. F. C., Dlamini, L. N., Adelodun, A. A., Greyling, C. J. and Catherine Ngila, J. (2016). Modification of electrospun polyacrylonitrile nanofibers with EDTA for the removal of Cd and Cr ions from water effluents. *Applied Surface Science*, **369**: 19–28. doi: 10.1016/j.apsusc.2016.02.018.

Chávez de Paz, L. E., Resin, A., Howard, K. A., Sutherland, D. S. and Wejse, P. L. (2011). Antimicrobial effect of chitosan nanoparticles on Streptococcus mutans biofilms. *Applied and Environmental Microbiology*, **77**(11): 3892-3895.

Cheng, A.H., Yang, C.Y., Chen, C.Y., Chen, C.Y. and Chen, C.W. (2009). The chemically crosslinked metal-complexed chitosans for comparative adsorptions of Cu(II), Zn(II), Ni(II) and Pb(II) ions in aqueous medium. *Journal of Hazardous Materials*, **163:** 1068–1075.

Chen, C., Tang, Y., Vlahovic, B., Yan, F. (2017). Electrospun polymer nanofibers decorated with noble metal nanoparticles for chemical sensing. *Nanoscale Research Letters,* **12:** 451.

Chen, L.C., Kung, S.K., Chen, H.H., and Lin, S.B. (2010). Evaluation of zeta potential difference as an indicator for antibacterial strength of low molecular weight chitosan. *Carbohydrate Polymers*, **82**(3): 913–919. doi: 10.1016/j.carbpol.2010.06.017.

Chong, E.J., Phan, T.T., Lim, I.J., Zhang, Y.Z., Bay, B.H., Ramakrishna, S. and Lim, C.T. (2007). Evaluation of electrospun PCL/gelatin nanofibrous scaffold for wound healing and layered dermal reconstitution. *Acta Materialia*, **3**: 321–30.

Chung, Y.-C., Su, Y.-P., Chen, C.-C., Jia, G., Wang, H. L., Wu, J. G. and Lin, J. G. (2004). Relationship between antibacterial activity of chitosan and surface characteristics of cell wall. *Acta Pharmacologica Sinica*, **25**(7): 932-936.

Cooper, A., Oldinski, R., Ma, H., Bryers, J. D. and Zhang, M. (2011). Chitosan-based nanofibrous membranes for antibacterial filter applications. *Carbohydrate Polymers*, **92**(1): 254–259. doi: 10.1016/j.carbpol.2012.08.114.

Cortizo, M.S., Berghoff, C.F. and Alessandrini, J.L. (2008). Characterization of chitin from Illex argentinus squid pen. *Carbohydrate Polymers*, **74**: 10–15.

Costa, C., A. Henriques, C. Pires, J. Nunes, M. Ohno et al., (2013) The dual role of Candida glabrata drug:H+ antiporter CgAqr1 (ORF CAGL0J09944g) in antifungal drug and acetic acid resistance. *Frontiers in Microbiology*, **4**: 170.

Costa, C.N., Teixeira, V.G., Delpech, M.C., Souza, J.V.S. and Costa, M.A.S. (2015). Viscometric study of chitosan solutions in acetic acid/sodium acetate and acetic acid/sodium chloride. *Carbohydrate Polymers*, **133**: 245–250.

Costa, E. M., Silva, S., Veiga, M., Tavaria, F. K. and Pintado, M. M. (2018). Exploring chitosan nanoparticles as effective inhibitors of antibiotic resistant skin microorganisms – From in vitro to *ex vitro* testing. *Carbohydrate Polymers*, **201:** 340–346. doi: 10.1016/j.carbpol.2018.08.083.

Cottier, F., Tan, A. S. M., Yurieva, M., Liao, W., Lum, J., Poidinger, M. and Pavelka, N. (2017). The transcriptional response of Candida albicans to weak organic acids, carbon source, and MIG1 inactivation unveils a role for HGT16 in mediating the fungistatic effect of acetic acid. *G3: Genes, Genomes, Genetics*, **7**(11): 3597-3604.

Cremar, L., Gutierrez, J., Martinez, J., Materon, L., Gilkerson, R., Lozano, K. and Xu, F. (2018). Development of antimicrobial chitosan based nanofiber dressings for wound healing applications. *Nanomedicine Journal*, **5**(1): 6-14. doi: 10.22038/nmj.2018.05.002.

Croisier, F. and Jerome, C. (2013). Chitosan-based biomaterials for tissue engineering. *European Polymer Journal*, **49**(4): 780–792. doi: 10.1016/j.eurpolymj.2012.12.009.

Cummins, C. and Harris, H. (1956). The chemical composition of the cell walls in some gram-positive bacteria and its possible value as a taxonomic character. *Microbiology*, **14**(3): 583-600.

Cuong, H. N., Minh, N. C., Van Hoa, N. and Trung, T. S. (2016). Preparation and characterization of high purity β-chitin from squid pens (Loligo chenisis). *International Journal of Biological Macromolecules*, **93**: 442–447. doi: 10.1016/j.ijbiomac.2016.08.085.

Da'na, E. (2017). Adsorption of heavy metals on functionalized-mesoporous silica: a review. *Microporous and Mesoporous Materials*, **247**: 145-157.

Daraghmeh, N. H., Chowdhry, B. Z., Leharne, S. A., Al Omari, M. M. and Badwan, A. A. (2011). *Chitin. Profiles of drug substances, excipients and related methodology* (1st ed., Vol. 36). pp. 35-102. Academic Press. doi: 10.1016/B978-0-12-387667-6.00002-6.

de Queiroz Antonino, R., Lia Fook, B., de Oliveira Lima, V., de Farias Rached, R., Lima, E., da Silva Lima, R. and Lia Fook, M. (2017). Preparation and characterization of chitosan obtained from shells of shrimp (Litopenaeus vannamei Boone). *Marine Drugs*, **15**(5): 141.

Debbaudt, A.L., Ferreira, M.L. and Gschaider, M.E. (2004). Theoretical and experimental study of M^{2+} adsorption on biopolymers. III. Comparative kinetic pattern of Pb, Hg and Cd. *Carbohydrate Polymers*, **56:** 321–332.

Deitzel, J.M., Kleinmeyer, J., Harris, D. and Tan, N.C.B. (2001). The effect of processing variables on the morphology of electrospun nanofibers and textiles. *Polymer*, **42**: 261-272.

Deitzel, J.M., Kosik, W., McKnight, S.H., Ten, N.C.B., Desimone, J.M. and Crette, S. (2002). Electrospinning of polymer nanofibers with specific surface chemistry. *Polymer*, **43**:1025–1029.

Delgado, A. V., González-Caballero, F., Hunter, R. J., Koopal, L. K. and Lyklema, J. (2007). Measurement and interpretation of electrokinetic phenomena. *Journal of Colloid and Interface Science*, **309**(2): 194–224. doi: 10.1016/j.jcis.2006.12.075.

Demir, M.M., Yilgor, I., Yilgor, E. and Erman, B. (2002). Electrospinning of polyurethane fibers. *Polymer*, **43**: 3303–3309.

Di Mario, F., Rapanà, P., Tomati, U. and Galli, E. (2008). Chitin and chitosan from Basidiomycetes. *International Journal of Biological Macromolecules*, **43**(1): 8–12. doi: 10.1016/j.ijbiomac.2007.10.005.

Diener, S., Zurbrügg, C., Gutiérrez, F.R., Nguyen, D.H., Morel, A., Koottatep, T. and Tockner, K. (2011). Black soldier fly larvae for organic waste treatment - prospects and constraints. *Proceedings of the WasteSafe 2nd International Conference on Solid Waste Management in the Developing Countries Khulna, Bangladesh*, **52:** 1-8.

Divya, K. and Jisha, M. S. (2017). Chitosan nanoparticles preparation and applications. *Environmental Chemistry Letters*, **16**(1), 101–112. doi: 10.1007/s10311-017-0670-y.

Dizaj, S. M., Lotfipour, F., Barzegar-Jalali, M., Zarrintan, M. H. and Adibkia, K. (2014). Antimicrobial activity of the metals and metal oxide nanoparticles. *Materials Science and Engineering: C*, **44**: 278-284.

Dongre, R.S. (2019). Chitosan formulations: chemistry, characteristics and contextual adsorption in unambiguous modernization of science and technology. In Longbiao, L. (Ed.), *Hysteresis of composites.* IntechOpen publications. doi: 10.5772/intechopen.83391.

Dumitriu, S. (2004). *Polysaccharides:* structural diversity and functional versatility, 2nd ed. CRC Press, New York, USA. Pg 1224. ISBN 9780824754808.

Dun, Y., Li, Y., Xu, J., Hu, Y., Zhang, C. and Liang, Y. (2019). Simultaneous fermentation and hydrolysis to extract chitin from crayfish shell waste. *International Journal of Biological Macromololecules*, **123**: 420–426. doi: 10.1016/j.ijbiomac.2018.11.088.

El-Dib, F. I., Mohamed, D. E., El-Shamy, O. A. A. and Mishrif, M. R. (2019). Study the adsorption properties of magnetite nanoparticles in the presence of different synthesized surfactants for heavy metal ions removal. *Egyptian Journal of Petroleum.* Article in press. doi: 10.1016/j.ejpe.2019.08.004.

El-hefian, E.A., Nasef, M.M. and Yahaya, A.H. (2011). Chitosan Physical Forms: A Short Review. *Australian Journal of Basic and Applied Sciences*, **5**(5): 670-677.

Erdogan, S. and Kaya, M. (2016) High similarity in physicochemical properties of chitin and chitosan from nymphs and adults of a grasshopper. *International Journal of Biological Macromolecules* **89**: 118–126. doi: 10.1016/j.ijbiomac.2016.04.059.

Erdogan, S., Kaya, M. and Akata, I. (2017). Chitin extraction and chitosan production from cell wall of two mushroom species (*Lactarius vellereus* and *Phyllophora ribis*). *Proceedings of American Institute of Physics Conference* **1809:** 020012. doi:10.1063/1.4975427.

Erickson, M.C., Islam, M., Sheppard, C., Liao, J. and Doyle, M.P. (2004). Reduction of *Escherichia coli* O157:H7 and *Salmonella enterica* serovar Enteritidis in chicken manure by larvae of the black soldier fly. *Journal of Food Protection*, **67**:685–90.

Esteves, V.P.P., Esteves, E.M.M., Bungenstab, D.J., Feijo, G.L.D., Araújo, O.D.Q.F. and Morgado, C.D.R.V. (2017). Assessment of greenhouse gases (GHG) emissions from the tallow biodiesel production chain including land use change (LUC). *Journal of Cleaner Production*, **151:** 578-591.

Fan, W., Yan, W., Xu, Z. and Ni, H. (2012). Formation mechanism of monodisperse, low molecular weight chitosan nanoparticles by ionic gelation technique. *Colloids and Surfaces B: Biointerfaces*, **90**: 21-27.

Farasati, M., Haghighi, S., and Boroun, S. (2015). Cd removal from aqueous solution using agricultural wastes. *Desalination and Water Treatment*, **57**(24): 11162–11172. doi: 10.1080/19443994.2015.1043588.

Fawole, F. J., Adeoye, A. A., Tiamiyu, L. O., Ajala, K. I., Obadara, S. O. and Oluwaseun, G. I. (2020). Substituting fishmeal with Hermetia illucens in the diets of African catfish (Clarias gariepinus): Effects on growth, nutrient utilization, haemato-physiological response, and oxidative stress biomarker. *Aquaculture*, **580**: 734849. doi: 10.1016/j.aquaculture.2019.734849.

Fei, X., Zhao, F., Wei, W., Luo, J., Chen, M. and Liu, X. (2016). Tannic acid as a bio-based modifier of epoxy/anhydride thermosets. *Polymers*, **8**(9): 314. doi: 10.3390/polym8090314.

Fiamingo, A., Delezuk, J. A. de M., Trombotto, S., David, L. and Campana-Fillho, S. P. (2016). Extensively deacetylated high molecular weight chitosan from the multistep ultrasound-assisted deacetylation of beta-chitin. *Ultrasonics Sonochemistry*, **32:** 79–85. doi: 10.1016/j.ultsonch.2016.02.021.

Filho, B. P., Lemos, F. J., Secundino, N. F., Pascoa, V., Pereira, S. T. and Pimenta, P. F. (2002). Presence of chitinase and beta-*N*-acetylglucosaminidase in the *Aedes aegypti*. A chitinolytic system involving peritrophic matrix formation and degradation. *Insect Biochemistry and Molecular Biology*, **32:** 1723–1729.

Focher, B; Beltrame, P.L. Naggi, A. and Torri, G. (1990). Alkaline N-deacetylation of chitin enhanced by flash treatments; reaction kinetics and structure modifications. *Carbohydrate polymers*, **12**: 405-418.

Franca, E. F., Freitas, L. C. and Lins, R. D. (2011). Chitosan molecular structure as a function of *N*-acetylation. *Biopolymers*, **95(**7): 448-460.

Fu, X., Shen, Y., Jiang, X., Huang, D. and Yan, Y. (2011). Chitosan derivatives with dual-antibacterial functional groups for antimicrobial finishing of cotton fabrics. *Carbohydrate Polymers*, **85**(1): 221–227. doi: 10.1016/j.carbpol.2011.02.019.

Furuzono, T., Ishihara, K., Nakabayashi, N. and Tamada, Y. (2000). Chemical modification of silk fibroin with 2-methacryloyloxyethyl phosphorylcholine. II. Graft-polymerization onto fabric through 2-methacryloyloxyethyl isocyanate and interaction between fabric and platelets. *Biomaterials*, **21:** 327–333.

G´omez-Rivas, L., Escudero-Abarca, B.I., Aguilar-Uscanga, M.G., Hayward-Jones, P.M., Mendoza, P. and Ram´ırez, M. (2004). Selective antimicrobial action of chitosan against spoilage yeasts in mixed culture fermentations. *Journal of Industrial Microbiology and Biotechnology*, **31**(1): 16–22. doi:10.1007/s10295-004-0112-2.

Gámiz-González, M. A., Correia, D. M., Lanceros-Mendez, S., Sencadas, V., Ribelles, J. G. and Vidaurre, A. (2017). Kinetic study of thermal degradation of chitosan as a function of deacetylation degree. *Carbohydrate polymers*, **167**: 52-58.

Gan, Q., Wang, T., Cochrane, C. and McCarron, P. (2005). Modulation of surface charge, particle size and morphological properties of chitosan–TPP nanoparticles intended for gene delivery. *Colloids and Surfaces B: Biointerfaces*, **44**(2): 65-73.

Gao, W., Lai, J. C. K. and Leung, S. W. (2012). Functional enhancement of chitosan and nanoparticles in cell culture, tissue engineering, and pharmaceutical applications. *Frontiers in Physiology*, **3**: 321. doi: 10.3389/fphys.2012.00321.

Garba, Z. N., Ugbaga, N.I. and Abdullahi, A.K. (2016). Evaluation of optimum adsorption conditions for Ni (II) and Cd (II) removal from aqueous solution by modified plantain peels (MPP). *Beni-Suef University Journal of Basic and Applied Sciences* **5**: 170–179.

Gardner, K. H. and Blackwell, J. (1975). Refinement of structure of β-chitin. *Biopolymers*, **14,** 1581-1595.

Garrido-Maestu, A., Ma, Z., Paik, S.-Y.-R., Chen, N., Ko, S., Tong, Z. and Jeong, K. C. (2018). Engineering of chitosan-derived nanoparticles to enhance antimicrobial activity against foodborne pathogen Escherichia coli O157:H7. *Carbohydrate Polymers*, **197**: 623–630. doi: 10.1016/j.carbpol.2018.06.046.

Gbenebor, O.P., Adeosun, S.O., Lawal, G.I., Jun, S. and Olaleye, S.A. (2017). Acetylation, crystalline and morphological properties of structural polysaccharide from shrimp exoskeleton. *Engineering Science and Technology, an International Journal*, **20**(3): 1155–1165.

Genc, O., Soysal, L., Bayramo˘glu, G., Arica, M.Y. Bektas, S. (2003). Procion Green H-4G immobilized poly(hydroxyethylmethacrylate/chitosan) composite membranes for heavy metal removal. *Journal of Hazardous Materials B*, **97:** 111–125.

Geng, X., Kwon, O.H. and Jang, J. (2005). Electrospinning of chitosan dissolved in concentrated acetic acid solution. *Biomaterials*, **26**(27): 5427–5432. doi: 10.1016/J.biomaterials.2005.01.06.

Ghorbel-Bellaaj, O., Younes, I., Maâlej, H., Hajji, S. and Nasri, M. (2012). Chitin extraction from shrimp shell waste using Bacillus bacteria. *International Journal of Biological Macromolecules*, **51**(5): 1196–1201. doi: 10.1016/j.ijbiomac.2012.08.034.

Ghormade, V., Deshpande, M.V. and Paknikar, K.M. (2011). Perspectives for nano-biotechnology enabled protection and nutrition of plants. *Biotechnology Advances*, **29**(6): 792–803.

Goel, M. K., Khanna, P., and Kishore, J. (2010). Understanding survival analysis: Kaplan-Meier estimate. *International Journal of Ayurveda Research*, **1**(4): 274 - 278.

Gonil, P., and Sajomsang, W. (2012). Applications of magnetic resonance spectroscopy to chitin from insect cuticles. *International Journal of Biological Macromolecules*, **51**(4): 514–522.

González-Campos, J. B., Mota-Morales, J. D., Kumar, S., Zárate-Triviño, D., Hernández-Iturriaga, M., Prokhorov, Y. and Luna-Bárcenas, G. (2013). New insights into the bactericidal activity of Chitosan-Ag bionanocomposite: The role of the electrical conductivity. *Colloids and Surfaces B, Biointerfaces*, **111**: 741–746.

Goy, R.C., Morais, T.B. and Assis, B.G. (2016). Evaluation of the antimicrobial activity of chitosan and its quaternized derivative on *E. coli* and *S. aureus* growth. *Revista Brasileira de Farmacognosia*, **26**(1): 122 – 127. doi: 10.1016/j.bjp.2015.09.010.

Greiner, A. and J. H. Wendorff (2007). "Electrospinning: A fascinating method for the preparation of ultrathin fibres." *Angewandte Chemie-International Edition,* **46**(30): 5670-5703.

Grobler, S. R. and Perchyonok, V. (2018). Cytotoxicity of low, medium and high molecular weight chitosan's on Balb/c 3T3 mouse fibroblast cells at a 75-85% de-acetylation degree. *Material Science and Engineering with Advanced Research*, **2**(2): 27-30.

Guarino, V., Altobelli, R., Cirillo, V., Cummaro, A. and Ambrosio, L. (2015). Additive electrospraying: a route to process electrospun scaffolds for controlled molecular release. *Polymers for Advanced Technologies*, **26**(12): 1359-1369.

Guo, X. and Wang, J. (2019). A general kinetic model for adsorption: theoretical analysis and modeling. *Journal of Molecular Liquids*, **288:** 111100.

Habiba, U., Islam, M. S., Siddique, T. A., Afifi, A. M. and Ang, B. C. (2016). Adsorption and photocatalytic degradation of anionic dyes on chitosan/PVA/Na–titanate/TiO2 composites synthesized by solution casting method. *Carbohydrate Polymers*, **149**: 317–331. doi: 10.1016/j.carbpol.2016.04.127.

Hadjizadeh, A., Ajji, A., and Bureau, M.N. (2011). Nano/micro electro-spun polyethylene terephthalate fibrous mat preparation and characterization. *Journal of the Mechanical Behavior of Biomedical Materials* **4**(3): 340-351.

Haghi, A. K. and Akbari, M. (2007). Trends in electrospinning of natural nanofibers. *Physica Status Solidi (A),* **204**(6): 1830–1834. doi: 10.1002/pssa.200675301.

Haider, A., Haider, S., and Kang, I.K. (2018). A comprehensive review summarizing the effect of electrospinning parameters and potential applications of nanofibers in biomedical and biotechnology. *Arabian Journal of Chemistry,* **11**: 1165-1188. doi: 10.1016/j.arabjc.2015.11.015.

Haider, S. and Park, S.-Y. (2009). Preparation of the electrospun chitosan nanofibers and their applications to the adsorption of Cu(II) and Pb(II) ions from an aqueous solution. *Journal of Membrane Science,* **328**(1-2): 90–96. doi: 10.1016/j.memsci.2008.11.046.

Haider, S., Al-Masry, W.A., Bukhari, N. and Javid, M. (2010). Preparation of the chitosan containing nanofibers by electrospinning chitosan–gelatin complexes. *Polymer Engineering & Science*, **50**(9): 1887-1893.

Haider, S., Al-Zeghayer, Y., Al-Masry, W. A. and Fekri A.A.A. (2012). Fabrication of chitosan nanofibers membrane with improved stability and britility. *Advanced Science Letters*, **17**: 217–223.

Haider, A., Haider, S. and Kang, I.-K. (2015). A comprehensive review summarizing the effect of electrospinning parameters and potential applications of nanofibers in biomedical and biotechnology. *Arabian Journal of Chemistry.* doi: 10.1016/j.arabjc.2015.11.015.

Haider, S., Al-Zeghayer, Y., Fekri, A.A.A., Haider, A., Mahmood, A., Al- Masry, W.A., Imran, M. and Aijaz, M.O. (2013). Highly aligned narrow diameter chitosan electrospun nanofibers. *Journal of Polymer Research*, **20**: 105. doi 10.1007/s10965-013-0105-9.

Hajji, S., Younes, I., Ghorbel-Bellaaj, O., Hajji, R., Rinaudo, M., Nasri, M. and Jellouli, K. (2014). Structural differences between chitin and chitosan extracted from three different marine sources, *International Journal of Biological Macromolecules*, **65**: 298-306. doi.org/10.1016/j.ijbiomac.2014.01.045.

Hamer, S. N., Cord-Landwehr, S., Biarnés, X., Planas, A., Waegeman, H., Moerschbacher, B. M. and Kolkenbrock, S. (2015). Enzymatic production of defined chitosan oligomers with a specific pattern of acetylation using a combination of chitin oligosaccharide deacetylases. *Scientific Report*, **5:** 8716. doi: 10.1038/srep08716.

Hardick, O., Stevens, B. and Bracewell, D.G. (2011). Nanofibre fabrication in a temperature and humidity controlled environment for improved fibre consistency. *Journal of Material Science*, **46**: 3890–3898.

Harmsen, R.A.G., Tuveng, T.R., Antonsen, S.G., Eijsink, V.G.H. and Sørlie, M. (2019). Can we make chitosan by enzymatic deacetylation of chitin? Brief report. *Molecules*, **24**: 3862. doi: 10.3390/molecules24213862.

Hartman, R., Brunner, D., Camelot, D., Marijnissen, J. and Scarlett, B. (2000). Jet break-up in electrohydrodynamic atomization in the cone-jet mode. *Journal of Aerosol Science*, **31**(1): 65–95. doi: 10.1016/S0021-8502(99)00034-8.

Hatton, R.A., Miller, A.J. and Silva, S.R.P. (2008). Carbon nanotubes: a multifunctional material for organic optoelectronics. *Journal of Materials Chemistry*, **18**: 1183–1192.

Hegedus, D., Toprak, U. and Erlandson, M. (2016). Lepidopteran peritrophic matrix composition, function, and formation Raman (Ed.), *Short Views on Insect Genomics and Proteomics*, Springer International, Switzerland, pp. 63-87.

Helander, I., Nurmiaho-Lassila, E.-L., Ahvenainen, R., Rhoades, J. and Roller, S. (2001). Chitosan disrupts the barrier properties of the outer membrane of Gram-negative bacteria. *International Journal of Food Microbiology*, **71**(2): 235-244.

Hembach, L., Cord-Landwehr, S. and Moerschbacher, B.M. (2017). Enzymatic production of all fourteen partially acetylated chitosan tetramers using different chitin deacetylases acting in forward or reverse mode. *Scientific Reports*, **7**: 17692.

Hickey, R. J., Zhou, X., Pierson, J. D., Ravel, J. and Forney, L. J. (2012). Understanding vaginal microbiome complexity from an ecological perspective. *Translational Research*, **160**(4): 267-282.

Hohman, M.M., Shin, M., Rutledge, G. and Brenner, M.P. (2001). Electrospinning and electrically forced jets. I. Stability theory. *Physics of Fluids*, **13**:2201–2220.

Homayoni, H., Ravandi, S. A. H. and Valizadeh, M. (2009). Electrospinning of chitosan nanofibers: Processing optimization. *Carbohydrate Polymers*, **77**(3): 656–661. doi: 10.1016/j.carbpol.2009.02.008.

Hong, G., Li, X., Shen, L., Wang, M., Wang, C., Yu, X. and Wang X. (2015). High recovery of lead ions from aminated polyacrylonitrile nanofibrous affinity membranes with micro/nano structure. *Journal of Hazardous Materials*, **295:** 161-169.

Hongkulsup, C., Khutoryanskiy, V. and Niranjan, K. (2016). Enzyme assisted extraction of c hitin from shrimp shells (Litopenaeus vannamei). *Journal of Chemical Technology an d Biotechnology*, **91** (5): 1250-1256. doi: doi.org/10.1002/jctb.4714.

Hossain, M.S. and Iqbal, A. (2014) Production and characterisation of chitosan from shrimp waste. *Journal of the Bangladesh Agricultural University*, **12**(1): 153-160. Retrieved from http://ageconsearch.umn.edu/bitstream/209911/2/21405-76710-1-PB.pdf.

Hou, X., Amais, R.S., Jones, B.T. and Donati, G.L. (2000). Inductively coupled plasma optical emission spectrometry. In *Encyclopaedia of analytical chemistry*. John Wiley & Sons, p. 1–25. doi: 10.1002/9780470027318.a5110.pub3.

Hu, J., Wang, X., Ding, B., Lin, J., Yu, J. and Sun, G. (2011). One-step electrospinning/netting technique for controllably preparing polyurethane nanofiber/net. *Macromolecular Rapid Communications*, **32:** 1729–1734.

Hu, Z., Lei, L., Li, Y. and Ni, Y. (2003). Chromium adsorption on high-performance activated carbons from aqueous solution. *Separation and Purification Technology*, **31:** 13–18.

Huan, S., Liu, G., Han, G., Cheng, W., Fu, Z., Wu, Q. and Wang, Q. (2015). Effect of experimental parameters on morphological, mechanical and hydrophobic properties of electrospun polystyrene fibers. *Materials*, **8**(5): 2718–2734. doi: 10.3390/ma8052718.

Huang, Z.M., Zhang, Y.Z., Kotaki, M. and Ramakrishna, S. (2003). A review on polymer nanofibers by electrospinning and their applications in nanocomposites. *Composites Science and Technology*, **63**: 2223–2253.

Hwang, J.K. and Shin, H.H. (2000). Rheological properties of chitosan solutions. *Korea-Australia Rheology Journal*, **12**(3/4): 175-179.

Ianiro, A., Giosia, M., Fermani, S., Samorì, C., Barbalinardo, M., Valle, F., Pellegrini, G., Biscarini, F., Zerbetto, F., Calvaresi, M. and Falini, G. (2014). Customizing properties of β-chitin in Squid pen (Gladius) by chemical treatments. *Marine Drugs,* **12**(12): 5979–5992. doi: 10.3390/md12125979.

Ibitoye, E. B., Lokman, I. H., Hezmee, M. N. M., Goh, Y. M., Zuki, A. B. Z., and Jimoh, A. A. (2018). Extraction and physicochemical characterization of chitin and chitosan isolated from house cricket. *Biomedical Materials*, **13**(2): 025009. doi: 10.1088/1748-605x/aa9dde.

Ikono, R., Vibriani, A., Wibowo, I., Saputro, K.E., Muliawan, W., Bachtiar, B.M., Mardliyati, E., Bachtiar, E.W., Rochman, N.T., Kagami, H., Xianqi, L., Nagamura-Inoue, T. and Tojo, A. (2019). Nanochitosan antimicrobial activity against Streptococcus mutans and Candida albicans dual-species biofilms. *BMC Research Notes,* **12**(1). doi: 10.1186/s13104-019-4422-x.

Inglezakis, V.J., Loizidou, M.D. and Grogoropoulou, H.P. (2003). Ion exchange of Pb^{2+}, Cu^{2+}, Fe^{3+} and Cr^{3+} on natural clinoptilolite: selectivity determination and influence of acidity on metal uptake. *Journal of Colloid and Interface Science,* **261:** 49–54.

Islam, M. M., Masum, S. M., Molla, M. A. I., Rahman, M. M., Shaikh, A. A. and Roy, S. K. (2011). Preparation of chitosan from shrimp shell and investigation of its properties. *Intenational Journal of Basic and Applied Sciences,* **11**(1)**:** 116-130.

ISO 22412 (2017). International Standards Organization. Particle size analysis - Dynamic light scattering.

Ivashchenko, G.L., Shakhtshneider, T.P., Boldyrev, V.V., Bazarnova, N.G., Ivanov, A.V. and Gartman, O.R. (2002). Mechanical activation as a method to obtain water-soluble forms of chitin and chitosan in the solid phase. *Chemistry for Sustainable Development*, **1**(2): 39–46.

Jahangiri, A. and Barghi, L. (2018). Polymeric nanoparticles: review of synthesis methods and applications in drug delivery. *Journal of Advanced Chemical and Pharmaceutical Materials*, **1**(2): 38-47.

Jang, M.K., Kong, B.G., Jeong, Y.I., Lee, C.H. and Nah, J.W. (2004). Physicochemical characterization of α-chitin, β-chitin, and γ-chitin separated from natural resources. *Journal of Polymer Science Part A*: *Polymer Chemistry*, **42**(14): 3423–3432. doi:10.1002/pola.20176.

Jardine, A. and Sayed, S. (2016). Challenges in the valorisation of chitinous biomass within the biorefinery concept. *Current Opinion in Green and Sustainable Chemistry,* **2:** 34–39. doi: 10.1016/j.cogsc.2016.09.007.

Jaworek, A. (2007). Micro- and nanoparticle production by electrospraying. *Powder Technology*, **176**(1): 18-35.

Jaworska, M. M. (2012). Kinetics of enzymatic deacetylation of chitosan. *Cellulose,* **19:** 363–369. doi: 10.1007/s10570-012-9650-3.

Jayakumar, R., Prabaharan, M., Nair, S.V. and Tamura, H. (2010). Novel chitin and chitosan nanofibers in biomedical applications. *Biotechnology Advances,* **28**: 142-150.

Jeon, Y.J., Park, P.J., and Kim, S.K. (2001). Antimicrobial effect of chitooligosaccharides produced by bioreactor. *Carbohydrate Polymers,* **44:** 71–76.

Jolanta, K; Małgorzata, C; Zbigniew, K; Anna, B; Krzysztof, B; Jorg, T. and Piotr, S. (2010). Application of spectroscopic methods for structural analysis of chitin and chitosan. *Marine Drugs,* **8**: 1567–636.

Jonassen, H., Kjoniksen, A.L. and Hiorth, M. (2012). Stability of chitosan nanoparticles cross-linked with tripolyphosphate. *Biomacromolecules,* 1**3**(11): 3747–3756.

Jung, J. and Zhao, Y. (2013). Impact of the structural differences between α- and β-chitosan on their depolymerizing reaction and antibacterial activity. *Journal of Agricultural and Food Chemistry,* **61**(37): 8783–8789. doi: 10.1021/jf4018965.

Jurak, M., Wiącek, A. E., Mroczka, R. and Łopucki, R. (2017). Chitosan/phospholipid coated polyethylene terephthalate (PET) polymer surfaces activated by air plasma. *Colloids and Surfaces A: Physicochemical and Engineering Aspects,* **532**: 155–164. doi: 10.1016/j.colsurfa.2017.05.061.

Justi, K.C., Favere, V.T., Laranjeira, M.C.M., Neves, A. and Peralta, R.A. (2005). Kinetics and equilibrium adsorption of Cu(II), Cd(II), and Ni(II) ions by chitosan functionalized with 2[-bis-(pyridylmethyl)aminomethyl]-4-methyl-6-formylphenol, *Journal of Colloids and Interface Science,* **291:** 369–374.

Kaczmarek, M.B., Struszczyk-swita, K., Li, X., Szczesna-antczak, M. and Daroch, M. (2019). Enzymatic modifications of chitin, chitosan and chitooligosaccharides. *Frontiers in Bioengineering and Biotechnology,* **7**: 243. doi: 10.3389/fbioe.2019.00243.

Kadam, D. and Lele, S. S. (2018). Cross-linking effect of polyphenolic extracts of Lepidium sativum seedcake on physicochemical properties of chitosan films. *International Journal of Biological Macromolecules,* **114:** 1240–1247. doi: 10.1016/j.ijbiomac.2018.04.018.

Kanafani, Z. A., and Perfect, J. R. (2008). Resistance to antifungal agents: mechanisms and clinical impact. *Clinical Infectious Diseases*, **46**(1): 120-128.

Kang, B., Vales, T., Cho, B.-K., Kim, J.-K. and Kim, H.-J. (2017). Development of gallic acid-modified hydrogels using interpenetrating chitosan network and evaluation of their antioxidant activity. *Molecules*, **22**(11): 1976. doi: 10.3390/molecules22111976.

Kapadnis, G., Dey, A., Dandekar, P. and Jain, R. (2019). Effect of degree of deacetylation on solubility of low molecular weight chitosan produced via enzymatic breakdown of chitosan. *Polymer International,* **68:** 1054–1063. doi:10.1002/pi.5795.

Karim, M. R., Aijaz, M. O., Alharth, N. H., Alharbi, H. F., Al-Mubaddel, F. S. and Awual, M. R. (2019). Composite nanofibers membranes of poly(vinyl alcohol)/chitosan for selective lead(II) and cadmium(II) ions removal from wastewater. *Ecotoxicology and Environmental Safety*, **169**: 479–486. doi: 10.1016/j.ecoenv.2018.11.049.

Kasaai, M. (2008). A review of several reported procedures to determine the degree of N-acetylation for chitin and chitosan using infrared spectroscopy. *Carbohydrate Polymers*, **71**(4): 497–508. doi: 10.1016/j.carbpol.2007.07.009.

Kasaai, M. R. (2010). Determination of the degree of N-acetylation for chitin and chitosan by various NMR spectroscopy techniques: A review. *Carbohydrate Polymers*, **79**(4): 801–810. doi: 10.1016/j.carbpol.2009.10.051.

Katya, K., Borsra, M. Z. S., Ganesan, D., Kuppusamy, G., Herriman, M., Salter, A. and Ali, S. A. (2017). Efficacy of insect larval meal to replace fish meal in juvenile barramundi, Lates calcarifer reared in freshwater. *International Aquatic Research*, **9**(4): 303–312. doi:10.1007/s40071-017-0178-x.

Kawasaki, K., Hashimoto, Y., Hori, A., Kawasaki, T., Hirayasu, H., Iwase, S., Hashizume, A., Ido, A., Miura, C., Miura, T., Nakamura, S., Seyama, T., Matsumoto, Y., Kasai, K. and Fujitani, Y. (2019). Evaluation of Black Soldier Fly (Hermetia illucens) larvae and pre-pupae raised on household organic waste, as potential ingredients for poultry feed. *Animals*, **9**(3): 98. doi: 10.3390/ani9030098.

Kaya, M., Akyuz, B., Bulut, E., Sargin, I., Eroglu, F. and Tan, G. (2016b). Chitosan nanofiber production from Drosophila by electrospinning. *International Journal of Biological Macromolecules*, **92**: 49–55. doi: 10.1016/j.ijbiomac.2016.07.021.

Kaya, M., Baran, T., Asan-Ozusaglam, M., Cakmak, Y. S., Tozak, K. O., Mol, A., Mentes, A. and Sezen, G. (2015). Extraction and characterization of chitin and chitosan with antimicrobial and antioxidant activities from cosmopolitan Orthoptera species (Insecta). *Biotechnology and Bioprocess Engineering*, **20**(1): 168–179. doi: 10.1007/s12257-014-0391-z.

Kaya, M., Baran, T., Erdoğan, S., Menteş, A., Özüsağlam, M.A. and Çakmak, Y. S. (2014a). Physicochemical comparison of chitin and chitosan obtained from larvae and adult Colorado potato beetle (Leptinotarsa decemlineata). *Materials Science and Engineering: C*, **45:** 72–81. doi: 10.1016/j.msec.2014.09.004.

Kaya, M., Seyyar, O., Baran, T. and Turkes, T. (2014b). Bat guano as new and attractive chitin and chitosan source. *Frontiers in Zoology*, **11**: 59.

Kaya, M., Sofi, K., Sargin, I. and Mujtaba, M. (2016a). Changes in physicochemical properties of chitin at developmental stages (larvae, pupa and adult) of Vespa crabro (wasp). *Carbohydrate Polymers*, **145:** 64–70. doi: 10.1016/j.carbpol.2016.03.010.

Kaya, M., Tozak, K.Ö., Baran, T., Sezen, G. and Sargın, İ. (2013). Natural porous and nano fiber chitin structure from *Gammarus argaeus* (gammaridae crustacea). *Excli Journal*, **12:** 503-510.

Khor, E. (2014). Overview of chitin and chitosan research. In: Chitin, fulfilling a biomaterials promise, (2nd Ed) Elsivier Publication pp 1 – 19.

Kiechel, M. A. and Schauer, C. L. (2013). Non-covalent crosslinkers for electrospun chitosan fibers. *Carbohydrate Polymers*, **95**(1): 123–133. doi: 10.1016/j.carbpol.2013.02.034.

Kim, M.-W., Han, Y. S., Jo, Y. H., Choi, M. H., Kang, S. H., Kim, S.-A. and Jung, W.-J. (2016). Extraction of chitin and chitosan from housefly, *Musca domestica*, pupa shells. *Entomological Research*, **46**(5): 324–328. doi: 10.1111/1748-5967.12175.

Kim, S. H., Clark, S. T., Surendra, A., Copeland, J. K., Wang, P. W., Ammar, R., Collins, C., Tullis, D. E., Nislow, C. and Hwang, D. M. (2015). Global analysis of the fungal microbiome in cystic fibrosis patients reveals loss of function of the transcriptional repressor Nrg1 as a mechanism of pathogen adaptation. *PLoS Pathogens*, **11**(11): 1-26.

Kim, S. K. and Rajapakse, N. (2005). Enzymatic production and biological activities of chitosan oligosaccharides (COS): A review. *Carbohydrate Polymers*, **62:** 357–368. doi: 10.1016/j.carbpol.2005.08.012.

Kim, D.S., Park, H.B., Rhim, J.W. and Lee, Y.M. (2004). Preparation and characterization of crosslinked PVA/SiO2 hybrid membranes containing sulfonic acid groups for direct methanol fuel cell applications. *Journal of Membrane Science*, **240**(1): 37-48.

Kirkpatrick, C., Bittinger, F., Wagner, M., Köhler, H., Van Kooten, T., Klein, C., and Otto, M. (1998). Current trends in biocompatibility testing. *Proceedings of the Institution of Mechanical Engineers, Part H: Journal of Engineering in Medicine,* **212**(2): 75-84.

Knaul, J.Z., Hudson, S.M. and Creber, K.A.M. (1999). Crosslinking of chitosan fibers with dialdehydes: proposal of a new reaction mechanism. *Journal of Polymer Science: Part B: Polymer Physics,* **37:** 1079–1094.

Knidri, H.E., Belaabed, R., Addaou, A., Laajeb, A. and Lahsini, A. (2018). Extraction, chemical modification and characterization of chitin and chitosan: A review. *International Journal of Biological Macromolecules.* doi: 10.1016/j.ijbiomac.2018.08.139.

Knidri, H, E., Khalfaouy, R.E., Laajeb, A. Addaou, A. and Lahsini, A. (2016). Eco-friendly extraction and characterization of chitin and chitosan from the shrimp shell waste via microwave irradiation. *Process Safety and Environmental Protection*, **104:** 395–405.

Kong, M., Chen, X. G., Xing, K. and Park, H. J. (2010). Antimicrobial properties of chitosan and mode of action: a state of the art review. *International Journal of Food Microbiology*, **144**(1): 51-63.

Kravanja, G., Primožič, M., Knez, Z. and Leitgeb, M. (2019). Chitosan-based (nano)materials for novel biomedical applications. *Molecules,* **24**(10): 1960. doi: 10.3390/molecules24101960.

Krishnani, K.K., Meng, X., Christodoulatos, C. and Boddu, V.M. (2008). Biosorption mechanism of nine different heavy metals onto biomatrix from rice husk. *Journal of Hazardous Materials*, **153**(3): 1222-1234.

Kumar, A.B.V., Varadaraj, M.C., Gowda, L.R., and Tharanathan, R.N. (2005). Characterization of chitooligosaccharides prepared by chitosanolysis with the aid of papain and pronase, and their bactericidal action against *Bacillus cereus* and *Escherichia coli*. *Biochemical Journal,* **391:** 167–175.

Kumari, S., Kumar, A. S. H., Abanti, S. and Kumar, R. P. (2017). Physicochemical properties and characterization of chitosan synthesized from fish scales, crab and shrimp shells. *International Journal of Biological Macromolecules,* **104**: 1697–1705. doi: 10.1016/j.ijbiomac.2017.04.119.

Kumari, S., Rath, P., Kumar, A.S.H. and Tiwari, T.N. (2015). Extraction and characterization of chitin and chitosan from fishery waste by chemical method. *Environmental technology and innovation,* **3:** 77-85.

Kumirska, J., Czerwicka, M., Kaczyński, Z., Bychowska, A., Brzozowski, K., Thöming, J. and Stepnowski, P. (2010). Application of spectroscopic methods for structural analysis of chitin and chitosan. *Marine Drugs*, **8**(5): 1567–1636. doi: 10.3390/md8051567.

Kurita, K. (2001) Controlled functionalisation of polysaccharide chitin. *Progress in polymer science*, **26:** 1921- 1971.

Kyzas, G.Z., Siafaka, P.I., Lambropoulou, D.A., Lazaridis, N.K. and Bikiaris, D.N. (2014). Poly (itaconic acid)-grafted chitosan adsorbents with different cross-linking for Pb(II) and Cd(II) uptake. *Langmuir*, **30**(1): 120–131. doi: 10.1021/la402778x.

Kyzas, G. and Bikiaris, D. (2015). Recent Modifications of Chitosan for Adsorption Applications: A Critical and Systematic Review. *Marine Drugs,* **13**(1): 312–337. doi: 10.3390/md13010312.

Lagergren, S. (1898). About the theory of so-called adsorption of soluble substances. *Kungliga Svenska Vetenskapsakademiens Handlingar* **24**(4): 1-39.

Lahiji, A., Sohrabi, A., Hungerford, D.S. and Frondoza, C.G. (2000). Chitosan supports the expression of extracellular matrix proteins in human osteoblasts and chondrocytes. *Journal of Biomedical Materials Research*, **51**(4): 586-595.

Laka, M. and Chernyavskaya, S. (2006). Preparation of chitosan powder and investigation of its properties. *Proceedings of the Estonian Academy of Science, Chemistry*, **55(**2): 78–84.

Laus, R., Costa, T.G., Szpoganicz, B. and Favere, V.T. (2010). Adsorption and desorption of Cu(II), Cd(II) and Pb(II) ions using chitosan crosslinked with epichlorohydrin-triphosphate as the adsorbent. *Journal of Hazardous Materials*, **183**: 233–241.

Law, Y. and Wein, L. (2018). Reversing the nutrient drain through urban insect farming—opportunities and challenges, a review. *AIMS Bioengineering,* **5**(4): 226–237. doi: 10.3934/bioeng.2018.4.226.

Lawal, O. S., Ayanda, O. S., Rabiu, O. O. and Adebowale, K. O. (2017). Application of black walnut (Juglans nigra) husk for the removal of lead (II) ion from aqueous solution. *Water Science and Technology*, **75**(10): 2454–2464. doi: 10.2166/wst.2017.125.

Lemma, S. M., Bossard, F. and Rinaudo, M. (2016). Preparation of pure and stable chitosan nanofibers by electrospinning in the presence of poly (ethylene oxide). *International Journal of Molecular Sciences*, **17**(11).

Lertsutthiwong, P., How, N.C. and Chandrkrachang, S. (2002). Effects of chemical treatment on the characteristics of shrimp chitosan. *Journal of Metal and Minerals*, **12**(1): 11-18. doi: 10.1007/s10924-011-0331-3.

Li, C., Lou, T., Yan, X., Long, Y., Cui, G. and Wang, X. (2018). Fabrication of pure chitosan nanofibrous membranes as effective absorbent for dye removal. *International Journal of Biological Macromolecules*, **106**: 768–774. doi: 10.1016/j.ijbiomac.2017.08.072.

Li, J., Wu, Y. and Zhao, L. (2016). Antibacterial activity and mechanism of chitosan with ultra high molecular weight. *Carbohydrate Polymers,* **148**, 200–205. doi: 10.1016/j.carbpol.2016.04.025.

Li, M., Han, B. and Liu, W. (2011). Preparation and properties of a drug release membrane of mitomycin C with N-succinyl-hydroxyethyl chitosan, *Journal of Materials Science: Materials in Medicine*, **22**: 2745-2755.

Li, Q., Zheng, L., Cai, H., Garza, E., Yu, Z. and Zhou, S. (2011). From organic waste to biodiesel: Black soldier fly, *Hermetia illucens*, makes it feasible. *Fuel*, **90**(4): 1545–1548.

Li, Y., Qiu, T. and Xu, X. (2013). Preparation of lead-ion imprinted crosslinked electro-spun chitosan nanofiber mats and application in lead ions removal from aqueous solutions. *European Polymer Journal*, **49**(6): 1487–1494. doi: 10.1016/j.eurpolymj.2013.04.002.

Li, Y., Zhang, J., Xu, C. and Zhou, Y. (2015). Crosslinked chitosan nanofiber mats fabricated by one-step electrospinning and ion-imprinting methods for metal ions adsorption. *Science China Chemistry*, **59**(1): 95–105. doi: 10.1007/s11426-015-5526-3.

Li, Y., Zhang, J., Xu, C. and Zhou, Y.F. (2016). Crosslinked chitosan nanofiber mats fabricated by one-step electrospinning and ion-imprinting methods for metal ions adsorption. *Science China Chemistry*, **59**: 95–105. doi: 10.1007/s11426-015-5526-3.

Liao, B., Sun, W., Guo, N., Ding, S. and Su, S. (2016). Comparison of Co^{2+} adsorption by chitosan and its triethylene-tetramine derivative: Performance and mechanism. *Carbohydrate Polymers*, **151**: 20–28.

Lin, K., Chua, K., Christopherson, G.T., Lim, S. and Mao, H. (2007). Reducing electrospun nanofiber diameter and variability using cationic amphiphiles. *Polymer*, **48**(21): 6384-94.

Liu, D., Lia, Z., Zhu, Y., Li, Z. and Kumar, R. (2014). Recycled chitosan nanofibril as an effective Cu(II), Pb(II) and Cd(II)ionic chelating agent: Adsorption and desorption performance. *Carbohydrate Polymers,* **111:** 469–476.

Liu, S., Sun, J., Yu, L., Zhang, C., Bi, J., Zhu, F., Qu, M., Jiang, C. and Yang, Q. (2012). Extraction and characterization of chitin from the beetle Holotrichia parallela motschulsky. *Molecules*, **17**: 4604–4611. doi: 10.3390/molecules17044604.

Loutfy, S.A., El-Din, H.A.M., Elberry, M. H., Allam, N.G., Hasanin, M.T.M. and Abdellah, A.M. (2016). Synthesis, characterization and cytotoxic evaluation of chitosan nanoparticles: *in vitro* liver cancer model. *Advances in Natural Sciences: Nanoscience and Nanotechnology*, **7**: 035008. doi:10.1088/2043-6262/7/3/035008.

Lu, P.J., Fu, W.E., Huang, S.C., Lin, C.Y., Ho, M.L., Chen, Y.P. and Cheng, H.F. (2018). Methodology for sample preparation and size measurement of commercial ZnO nanoparticles. *Journal of Food and Drug Analysis*, **26**(2): 628–636. doi: 10.1016/j.jfda.2017.07.004.

Ma, Y.; Xin, L.; Tan, H.; Fan, M.; Li, J.; Jia, Y.; Ling, Z.; Chen, Y. and Hu, X. (2017). Chitosan membrane dressings toughened by glycerol to load antibacterial drugs for wound healing. *Material Science and Engineering Part C*, **81**: 522–531.

Madureira, A. R., Pereira, A., Castro, P. M. and Pintado, M. (2015). Production of antimicrobial chitosan nanoparticles against food pathogens. *Journal of Food Engineering*, **167**(Part B): 210–216.

Maeda, H. (2001). SMANCS and polymer-conjugated macromolecular drugs: advantages in cancer chemotherapy. *Advanced Drug Delivery Reviews*, **46:** 169–185.

Mahmoud, S.B., Saad, H., Charrier, B., Pizzi, A., Rode, K., Ayed, N. and Charrier-El Bouhtoury, F. (2015). Characterization of sumac (Rhus tripartitum) root barks tannin for a potential use in wood adhesives formulation**.** *Wood Science and Technology*, **49**: 205–221. doi: 10.1007/s00226-014-0686-4.

Makkar, H. P. S., Tran, G., Heuzé, V. and Ankers, P. (2014). State-of-the-art on use of insects as animal feed. *Animal Feed Science and Technology*, **197**: 1–33. doi: 10.1016/j.anifeedsci.2014.07.008.

Maleki, A., Hayati, B., Najafi, F., Gharibi, F. and Joo, S.W. (2016). Heavy metal adsorption from industrial wastewater by PAMAM/TiO2 nanohybrid: preparation, characterization and adsorption studies, *Journal of Molecular Liquids* **224:** 95–104.

Malmiri, H.J., Jahanian, M.A.G. and Berenjian, A. (2012). Potential applications of chitosan nanoparticles as novel support in enzyme immobilization. *American Journal of Biochemistry and Biotechnology*, **8**(4): 203–219.

Malvern Zetasizer (2017). Zetasizer nano series user manual, Worcestershire, United Kingdom.

Manikandan, V., Velmurugan, P., Park, J.-H., Chang, W.-S., Park, Y.-J., Jayanthi, P., Cho, M. and Oh, B.-T. (2017). Green synthesis of silver oxide nanoparticles and its antibacterial

activity against dental pathogens. *3 Biotech*, **7**(1): 72–80. doi: 10.1007/s13205-017-0670-4.

Mardhiah, H.H., Ong, H.C., Masjuki, H., Lim, S. and Lee, H. (2017). A review on latest developments and future prospects of heterogeneous catalyst in biodiesel production from non-edible oils. *Renewable and Sustainable Energy Review*, **67**: 1225-1236.

Marei, N. H., El-Samie, E. A., Salah, T., Saad, G. R., and Elwahy, A. H. M. (2016). Isolation and characterization of chitosan from different local insects in Egypt. *International Journal of Biological Macromolecules*, **82**: 871–877. doi: 10.1016/j.ijbiomac.2015.10.024.

Marquis-Duval, F.O. (2008). Isolation et valorisation des constituants de la carapace de la crevette nordique. Ph.D. Dissertation, Laval University, Quebec, Canada.

Marsalek, R. (2014). ParticlesSize and zeta potential of ZnO. *APCBEE Procedia*, **9:** 13–17. doi: 10.1016/j.apcbee.2014.01.003.

Martín, D.M., Ahmed, M.M., Rodríguez, M., García, M. and Faccini, M. (2017). Aminated polyethylene terephthalate (PET) nanofibers for the selective removal of Pb(II) from polluted water. *Materials*, **10**(12): 1352. doi: 10.3390/ma10121352.

Martinou, A., Bouriotis, V., Stokke, B. T. and Vårum, K. M. (1998). Mode of action of chitin deacetylase from Mucor rouxii on partially N-acetylated chitosans. *Carbohydrate Research*, **311**(1-2): 71–78. doi: 10.1016/S0008-6215(98)00183-9.

Matabola, K.P. and Moutloali, R.M. (2013). The influence of electrospinning parameters on the morphology and diameter of poly(vinyledene fluoride) nanofibers-effect of sodium chloride. *Journal of Materials Science*, **48** (16): 5475.

Mazoochi, T. and Jabbari, V. (2011). Chitosan nanofibrous scaffold fabricated via electrospinning: the effect of processing parameters on the nanofiber morphology. *International Journal of Polymer Analysis and Characterization*, **16**(5): 277–289. doi: 10.1080/1023666X.2011.587943.

Megelski, S., Stephens, J.S., Bruce Chase, D. and Rabolt, J.F. (2002). Micro- and nanostructured surface morphology on electrospun polymer fibers. *Macromolecules*, **35** (22): 8456–8466.

Mekhail, M., Jahan, K. and Tabrizian, M. (2014). Genipin-crosslinked chitosan gels promote fibroblast adhesion and proliferation. *Carbohydrate Polymers*, **108:** 91–98.

Meroufel, B., Benali, O., Benyahia, M., Benmoussa, Y. and Zenasni, M.A. (2013). Adsorptive removal of anionic dye from aqueous solutions by Algerian kaolin: characteristics, isotherm, kinetic and thermodynamic studies. *Journal of Material and Environmental*

Science, **4** (3): 482-491.

Merzendorfer, H., Kelkenberg, M. and Muthukrishnan, S. (2016). Peritrophic matrices. In Cohen, E. and Moussian, B. (Eds.), *Extracellular composite matrices in arthopods*. Springer International, Switzerland, pp: 255-324. doi: 10.1007/978-3-319-40740-1_8.

Min, B-M., Lee, S.W., Lim, J.N., You, Y., Lee, T.S., Kang, H.P. and Park, W.H. (2004). Chitin and chitosan nanofibers: electrospinning of chitin and deacetylation of chitin nanofibers. *Polymer*, **45**(21): 7137-7142.

Min, L.-L., Yuan, Z.-H., Zhong, L.-B., Liu, Q., Wu, R.-X. and Zheng, Y.-M. (2015). Preparation of chitosan based electrospun nanofiber membrane and its adsorptive removal of arsenate from aqueous solution. *Chemical Engineering Journal*, **267**, 132–141. doi: 10.1016/j.cej.2014.12.024.

Minke, R. and Blackwell, J. (1978). The Structure of α-chitin. *Journal of Molecular Biology*, **120**: 167-181.

Mira, N. P., Teixeira, M. C. and Sá-Correia, I. (2010). Adaptive response and tolerance to weak acids in *Saccharomyces cerevisiae:* a genome-wide view. *Omics: A Journal of Integrative Biology*, **14**(5): 525-540.

Mishra, M. (Ed.) (2016). Handbook of encapsulation and controlled release. CRC Press, New York. ISBN: 13: 978-1-4822-3234-9.

Mitra, A. and Dey, B. (2011). Chitosan microspheres in novel drug delivery systems. *Indian Journal of Pharmaceutical Sciences*, **73**(4): 355.

Mit-uppatham, C., Nithitanakul, M. and Supaphol, P. (2004). Ultrafine electrospun polyamide-6 fibers: effect of solution conditions on morphology and average fiber diameter. *Macromolecular Chemistry and Physics*, **205**(17): 2327–2338.

Mohammed, M.H., Williams, P.A. and Tverezovskaya, O. (2013). Extraction of chitin from prawn shells and conversion to low molecular mass chitosan. *Food Hydrocolloids*, **31**: 166-171.

Mohan, S., Kumar, V., Singh, D.K. and Hasan, S.H. (2017). Effective removal of lead ions using graphene oxide-MgO nanohybrid from aqueous solution: isotherm, kinetic and thermodynamic modeling of adsorption. *Journal of Environmental Chemical Engineering*, **5**: 2259–2273.

Mohanasrinivasan, V., Mishra, M., Paliwal, J., Singh, S., Selvarajan, E., Suganthi, V. and Subathra, C. D. (2014). Studies on heavy metal removal efficiency and antibacterial activity of chitosan prepared from shrimp shell waste. *Biotechnology*, **4**(2): 167- 175.

Mohanty, A. K., Misra, M. and Drzal, L. T. (Eds.) (2005). *Natural fibers, biopolymers and biocomposites*. Boca Raton: CRC Press. doi: 10.1201/9780203508206.

Moraru, C., Mincea, M. M., Frandes, M., Timar, B. and Ostafe, V. (2018). A Meta-analysis on randomised controlled clinical trials evaluating the effect of the dietary supplement chitosan on weight loss, lipid parameters and blood pressure. *Medicina*, **54**(6): 109.

Mori, T., Rezai-Zadeh, K., Koyama, N., Arendash, G. W., Yamaguchi, H., Kakuda, N., Horikoshi-Sakuraba, Y., Tan, J. and Town, T. (2012). Tannic acid is a natural β-secretase inhibitor that prevents cognitive impairment and mitigates Alzheimer-like pathology in transgenic mice. *Journal of Biological Chemistry*, **287**(9): 6912–6927. doi: 10.1074/jbc.m111.294025.

Mosmann, T. (1983). Rapid colorimetric assay for cellular growth and survival: application to proliferation and cytotoxicity assays. *Journal of Immunological Methods*, **65**(1-2): 55-63.

Mudzielwana, R., Gitari, W. M. and Ndungu, P. (2019). Removal of As(III) from synthetic groundwater using Fe-Mn bimetal modified kaolin clay: adsorption kinetics, isotherm and thermodynamics studies. *Environmental Processes*, **6**: 1005 - 1018. doi: 10.1007/s40710-019-00397-4.

Müller, A., Wolf, D. and Gutzeit, H. O. (2017). The Black soldier fly, *Hermetia illucens* – a promising source for sustainable production of proteins, lipids and bioactive substances. *Zeitschrift Für Naturforschung C*, **72**(9-10): 351–363. doi: 10.1515/znc-2017-0030.

Musyoka, S., Ngila, C., Moodley, B., Kindness, A., Petrik, L. and Greyling, C. (2011). Oxolane-2,5-dione modified electrospun cellulose nanofibers for heavy metals Adsorption. *Journal of Hazardous Materials*, **192:** 922– 927.

Muthukrishnan, S., Merzendorfer, H., Arakane, Y. and Kramer, K. J. (2012). Chitin metabolism in insects. *In Insect molecular biology and biochemistry,* Gilbert, L.I. (Ed). Academic Press, MA, USA. pp 193–235. doi: 10.1016/b978-0-12-384747-8.10007-8.

Muxika, A., Etxabide, A., Uranga, J., Guerrero, P. and De La Caba, K. (2017). Chitosan as a bioactive polymer: processing, properties and applications. *International Journal of Biological Macromolecules*, **105**: 1358-1368.

Muyonga, J. H., Cole, G.B. and Duodu, K.G. (2004). Characterisation of acid soluble collagen from skins of young and adult Nile perch (*lates niloticus*). *Food chemistry*, **85**: 81 – 89.

Nam, Y.S., Park, W.H., Ihm, D., and Hudson, S.M. (2010). Effect of the degree of deacetylation on the thermal decomposition of chitin and chitosan nanofibers. *Carbohydrate Polymers*, **80(**1): 291–295.

Namazi, H. (2017). Polymers in our daily life. *Bioimpacts*, **7**(2): 73-74. doi:10.15171/bi.2017.09.

Ndayambaje, G., Laatikainen, K., Laatikainen, M., Beukes, E., Fatoba, O., van der Walt, N., Petrik, L. and Sainio, T. (2016). Adsorption of nickel (II) on polyacrylonitrile nanofiber modified with 2-(2′-pyridyl) imidazole. *Chemical Engineering Journal*, **284**: 1106-1116.

Nessa, F., Masum, S. M., Asaduzzaman, M., Roy, S., Hossain, M. and Jahan, M. (2011). A process for the preparation of chitin and chitosan from prawn shell waste. *Bangladesh Journal of Scientific and Industrial Research*, **45**(4). doi: 10.3329/bjsir.v45i4.7330.

Newton, L., Sheppard, C., Watson, D. W. and Burtle, G. (2005). Using the Black Soldier fly, *Hermetia illucens*, as a value-added tool for the management of swine manure executive summary. Avialable at www.organicvaluerecovery.com/studies/studies_htm_files/bsf_value_added.pdf.

Nezarati, R. M., Eifert, M. B. and Cosgriff-Hernandez, E. (2013). Effects of humidity and solution viscosity on electrospun fiber morphology. *Tissue Engineering Part C: Methods*, **19**(10): 810–819. doi: 10.1089/ten.tec.2012.0671.

Ngah, W. S., Teong, L. C. and Hanafiah, M. A. K. M. (2011). Adsorption of dyes and heavy metal ions by chitosan composites: A review. *Carbohydrate Polymers*, **83**(4): 1446–1456. doi: 10.1016/j.carbpol.2010.11.004.

Ngo, A.N., Ezouline, M.J.M., Murowchick, J.B., Gounev, A.D., and Youan, B.B.C (2016). Sodium acetate coated tenofovir-loaded chitosan nanoparticles for improved physicochemical properties. *Pharmaceutical Research*, **33**: 367-383.

Nguyen, H. C., Nguyen, M. L., Liang, S.-H., Su, C.-H. and Wang, F.-M. (2019). Switchable solvent-catalyzed direct transesterification of insect biomass for biodiesel production. *BioEnergy Research*, 1-8. doi: 10.1007/s12155-019-10085-8.

Nguyen, D. N., Clasen, C. and Van den Mooter, G. (2016). Pharmaceutical Applications of Electrospraying. *Journal of Pharmaceutical Sciences*, **105**(9): 2601–2620. doi: 10.1016/j.xphs.2016.04.024.

No, H. K. and Meyers, S. P. (1995). Preparation and characterization of chitin and chitosan-A review. *Journal of Aquatic Food Product Technology*, **4**(2): 27-52.

Noishiki, Y., Takami, H., Nishiyama, Y., Wada, M., Okada, S. and Kuga, S. (2003). Alkali-induced conversion of β-chitin to α-chitin. *Biomacromolecules,* **4**(4): 896–899. doi: 10.1021/bm0257513.

Norowski, P.A., Fujiwara, T., Clem, W.C., Adatrow, P.C., Eckstein, E.C., Haggard, W.O. and Bumgardner, J.D. (2015). Novel naturally crosslinked electrospun nanofibrous chitosan mats for guided bone regeneration membranes: material characterization and cytocompatibility. *Journal of Tissue Engineering and Regenerative Medicine*, **9:** 577–583.

Nthunya, L. N., Masheane, M. L., Malinga, S. P., Nxumalo, E. N. and Mhlanga, S. D. (2018). Electrospun chitosan-based nanobres for removal of phenols from drinking water. *Water SA,* **44**(3): 377. doi: 10.4314/wsa.v44i3.05.

Oberlerchner, J.T., Rosenau, T. and Potthast, A. (2015). Overview of methods for the direct molar mass determination of cellulose. *Molecules,* **20:** 10313-10341.

Ogawa, Y., Kimura, S., Wada, M. and Kuga, S. (2010). Crystal analysis and high-resolution imaging of microfibrillar α-chitin from Phaeocystis. *Journal of Structural Biology,* **171**(1), 111–116. doi: 10.1016/j.jsb.2010.03.010.

Ohkawa, K., Kim, H., Lee, K. and Yamamoto, H. (2004). Electrospun non-woven fabrics of poly(ecaprolactone) and their biodegradation by pure cultures of soil filamentous fungi. *Macromolecular Symposia*; **216**: 301–306.

Ohya, Y., Shiratani, M., Kobayashi, H. and Ouchi, T. (1994). Release behavior of 5-fluorouracil from chitosan-gel nanospheres immobilizing 5-fluorouracil coated with polysaccharides and their cell-specific cytotoxicity. *Journal of Macromolecular Science. Part A-Pure and Applied Chemistry,* **31:** 629–642.

Omotunde, I., Okonkwo, A. and Oluwashina, O. (2018). Derived and thiourea- functionalised silica for cadmium removal: isotherm, kinetic and thermodynamic studies. *Applied Water Science*, **8**(21). doi: 10.1007/s13201-018-0652-7.

Onwordi, C.T., Uche, C.C., Ameh, A. E and Petrik, L.F. (2019). Comparative study of the adsorption capacity of lead (II) ions onto bean husk and fish scale from aqueous solution. *Journal of water reuse and desalination*, **9**(3): 249-262. doi: 10.2166/wrd.2019.061.

Oonincx, D.G., van Itterbeeck, J., Heetkamp, M.J., van den Brand, H., van Loon, J.J. and van Huis, A. (2010). An exploration on greenhouse gas and ammonia production by insect species suitable for animal or human consumption. *PLoS One*, **5:** e14445.

Pal, K., Paulson, A. T. and Rousseau, D. (2013). Biopolymers in controlled-release delivery systems. In *handbook of biopolymers and biodegradable plastics*. Elsevier Inc. 329–363. doi: 10.1016/b978-1-4557-2834-3.00014-8.

Palmeira-de-Oliveira, A., Ribeiro, M., Palmeira-de-Oliveira, R., Gaspar, C., Costa-de-Oliveira, S., Correia, I., Pina Vaz, C., Martinez-de-Oliveira, J., Queiroz, J. and Rodrigues, A. (2010). Anti-Candida activity of a chitosan hydrogel: mechanism of action and cytotoxicity profile. *Gynecologic and Obstetric Investigation*, **70**(4): 322-327.

Pancholi, K., Ahras, N., Stride, E. and Edirisinghe, M. (2009). Novel electrohydrodynamic preparation of porous chitosan particles for drug delivery. *Journal of Materials Science: Materials in Medicine*, **20**(4): 917-923.

Panthi, G., Park, M., Kim, H-Y. and Park, S-J. (2015). Electrospun polymeric nanofibers encapsulated with nanostructured materials and their applications: A review. *Journal of Industrial and Engineering Chemistry*, **24**: 1–13. doi: 10.1016/j.jiec.2014.09.011.

Park, J.-Y. and Lee, I.-H. (2010). Relative humidity effect on the preparation of porous electrospun polystyrene fibres. *Journal of Nanoscience and Nanotechnology*, **10**(5): 3473–3477.

Paulino, A. T., Simionato, J. I., Garcia, J. C. and Nozaki, J. (2006). Characterization of chitosan and chitin produced from silkworm crysalides. *Carbohydrate Polymers*, **64**(1): 98–103.

Pelgrift, R. Y. and Friedman, A. J. (2013). Nanotechnology as a therapeutic tool to combat microbial resistance. *Advanced Drug Delivery Reviews*, **65**(13): 1803 - 1815.

Pelipenko, J., Kristl, J., Jankovic´, B., Baumgartner, S. and Kocbek, P. (2013). The impact of relative humidity during electrospinning on the morphology and mechanical properties of nanofibers. *International Journal of Pharmaceutics*, **456** (1): 125–134.

Pereao, O. K., Bode-Aluko, C., Ndayambaje, G., Fatoba, O. and Petrik, L. F. (2016). Electrospinning: polymer nanofibre adsorbent applications for metal ion removal. *Journal of Polymers and the Environment*. doi: 10.1007/s10924-016-0896-y.

Pereira, P., Carvalho, V., Ramos, R. and Gama, M. (2011). Chitosan nanoparticles for biomedical applications. In Davis, S.P. (Ed.), chitosan: manufacture, properties, and usage. Nova Science Publishers, Inc. New York, USA, pp 321 – 364. ISBN 978-1-61728-831-9.

Peschel, A., Jack, R.W., Otto, M., Collins, L.V., Staubitz, P., Nicholson, G., Kalbacher, H., Nieuwenhuizen, W.F., Jung, G., Tarkowski, A., van Kessel, K.P. van Strijp, J.A. (2001). Staphylococcus aureus resistance to human defensins and evasion of neutrophil killing via the novel virulence factor MprF is based on modification of membrane lipids

with l-lysine. *Journal of Experimental Medicine*, **193**(9): 1067-76. doi: 10.1084/jem.193.9.1067.

Petit, T. and Puskar, L. (2018). FTIR spectroscopy of nanodiamonds: methods and interpretation. *Diamond and Related Materials*, **89**: 52-66.

Pettenazzo, E., Thiene, G., Gatti, A.M., Pasquino, E., Talenti, E., Noera, G., Bottio, T. and Valente, M. (2001). Is the tricuspid position suitable for testing replacement bioprosthetic valves in the sheep model? *The Journal of Heart Valve Disease*, **10**(4): 513-519.

Philibert, T., Lee, B. H. and Fabien, N. (2016). Current status and new perspectives on chitin and chitosan as functional biopolymers. *Applied Biochemistry and Biotechnology*, **181**(4): 1314 – 1337. doi: 10.1007/s12010-016-2286-2.

Picchio, M.L, Linck, Y.G., Monti, G.A., Gugliotta, L.M., Minari, R.J. and Igarzabal, C.I.A. (2018). Casein films crosslinked by tannic acid for food packaging applications. *Food Hydrocolloids*, **84**: 424 - 434. doi: 10.1016/j.foodhyd.2018.06.028.

Popa, R. and Green, T.R. (2012). Using black soldier fly larvae for processing organic leachates. *Journal of Economic Entomology*, **105**: 374–378.

Prashanth, H.K.V. and Thanathan, R. N. (2007). Chitin/chitosan: modifications and their unlimited application potential - an overview. *Trends in Food Science and Technology*, **18:** 117-131.

Prashanth, K.V.H., Kittur, F.S. and Tharanathan, R.N. (2002). Solid state structure of chitosan prepared under different N-deacetylating conditions. *Carbohydrate Polymers*, **50:** 27-33.

Pujol-Luz, J. R., Francez, P. A. da C., Ururahy-Rodrigues, A. and Constantino, R. (2008). The Black Soldier-fly, Hermetia illucens (Diptera, Stratiomyidae), used to estimate the postmortem interval in a case in Amapá State, Brazil. *Journal of Forensic Sciences*, **53**(2), 476–478. doi: 10.1111/j.1556-4029.2008.00659.x.

Qasim, S., Zafar, M., Najeeb, S., Khurshid, Z., Shah, A., Husain, S. and Rehman, I. (2018). Electrospinning of chitosan-based solutions for tissue engineering and regenerative medicine. *International Journal of Molecular Sciences*, **19**(2): 407. doi: 10.3390/ijms19020407.

Qi, L., Xu, Z., Jiang, X., Hu, C. and Zou, X. (2004). Preparation and antibacterial activity of chitosan nanoparticles. *Carbohydrate Research*, **339**(16): 2693-2700.

Raafat, D. and Sahl, H.G. (2009). Chitosan and its antimicrobial potential - a critical literature survey. *Microbial Biotechnology*, **2**(2): 186–201. doi: 10.1111/j.1751-7915.2008.00080.x.

Raafat, D., von Bargen, K., Haas, A. and Sahl, H.G. (2008). Insights into the mode of action of chitosan as an antibacterial compound. *Applied and Environmental Microbiology*, **74**(12): 3764–3773.

Rajak, A., Hapidin, D. A., Iskandar, F., Munir, M. M., and Khairurrijal, K. (2019). Controlled morphology of electrospun nanofibers from waste expanded polystyrene for aerosol filtration. *Nanotechnology*, **30**(42): 425602.

Rao, M.S., Muñoz, J. and Stevens, W.F. (2000). Critical factors in chitin production by fermentation of shrimp biowaste. *Applied Microbiology and Biotechnology*, **54**: 808–813.

Rashmi, B. N., Harlapur, S. F., Avinash, B., Ravikumar, C. R., Nagaswarupa, H. P., Kumar, M. R. A., Gurushantha, K. and Santosh, M. S. (2019). Facile green synthesis of silver oxide nanoparticles and their electrochemical, photocatalytic and biological studies. *Inorganic Chemistry Communications*, **107580**. doi: 10.1016/j.inoche.2019.107580.

Rass-Hansen, J., Falsig, H., Jørgensen, B., and Christensen, C. H. (2007). Perspective bioethanol: fuel or feedstock. *Journal of Chemical Technology and Biotechnology*, **82**: 329–333. doi:10.1002/jctb.

Rathna, G., Birajdar, M.S., Bhagwani, M. and Paul, V. (2013). Studies on fabrication, characterization, and metal extraction using metal chelating nonwoven nanofiber mats of poly (vinyl alcohol) and sodium alginate blends. *Polymer Engineering & Science* **53**(2): 321-33

Ray, S. S., Chen, S. S., Nguyen, N. C. and Nguyen, H. T. (2019). Electrospinning: a versatile fabrication technique for nanofibrous membranes for use in desalination. In *Nanoscale Materials in Water Purification.* Elsevier, pp. 247-273.

Reneker, D. H. and Yarin, A. L. (2008). Electrospinning jets and polymer nanofibers. *Polymer*, **49**(10): 2387–2425. doi: 10.1016/j.polymer.2008.02.002.

Rinaudo, M., Pavlov, G. and Desbrie`res, J. (1999). Influence of acetic acid concentration on the solubilization of chitosan. *Polymer*, **40**: 7029–7032.

Rinaudo, M. (2006). Chitin and chitosan: properties and applications. *Progress in Polymer Science*, **31**(7): 603–632. doi: 10.1016/j.progpolymsci.2006.06.001.

Rivero, S., García, M. A. and Pinotti, A. (2010). Crosslinking capacity of tannic acid in plasticized chitosan films. *Carbohydrate Polymers*, **82**(2): 270–276. doi: 10.1016/j.carbpol.2010.04.048.

Rizeq, B. R., Younes, N. N., Rasool, K. and Nasrallah, G. K. (2019). Synthesis, bioapplications, and toxicity evaluation of chitosan-based nanoparticles. *International Journal of Molecular Sciences*, **20**(22): 5776. doi:10.3390/ijms20225776.

Robert, G. A. F. (1992). *Chitin Chemistry (1st ed)*, Macmillan, London.

Roberts, G.A.F. (2007). The Road is long... *Advanced Chitin Science*, **10**: 3–10.

Rout, S.K. (2001). Physicochemical, functional, and spectroscopic analysis of crawfish chitin and chitosan as affected by process modification. LSU historical dissertations and theses. 432. https://digitalcommons.lsu.edu/gradschool_disstheses/432.

Rubentheren, V., Ward, T. A., Chee, C. Y. and Tang, C. K. (2015). Processing and analysis of chitosan nanocomposites reinforced with chitin whiskers and tannic acid as a crosslinker. *Carbohydrate Polymers*, **115:** 379–387. doi: 10.1016/j.carbpol.2014.09.007.

Rumpold, B. A. and Schlüter, O. K. (2013). Potential and challenges of insects as an innovative source for food and feed production. *Innovative Food Science & Emerging Technologies*, **17:** 1–11. doi: 10.1016/j.ifset.2012.11.005.

Russell, A. (2003). Similarities and differences in the responses of microorganisms to biocides. *Journal of Antimicrobial Chemotherapy*, **52**(5): 750-763.

Sajomsang, W. and Gonil, P. (2010). Preparation and characterization of α-chitin from cicada sloughs. *Materials Science and Engineering: C*, **30**(3): 357–363. doi: 10.1016/j.msec.2009.11.014.

Sangsanoh, P. and Supaphol, P. (2006). Stability improvement of electrospun chitosan nanofibrous membranes in neutral or weak basic aqueous solutions. *Biomacromolecules*, **7**(10): 2710–2714. doi: 10.1021/bm060286l.

Santos, M. C., Oliveira, A. N. and Nunes, M. L. (2011). Determination of degree of deacetylation of chitosan obtained from "shrimp saburica" (*Macrobrachium jelskii*). *Scientia Plena*, **1877:** 7-9.

Sarwar, A., Katas, H. and Zin, N. M. (2014). Antibacterial effects of chitosan–tripolyphosphate nanoparticles: impact of particle size molecular weight. *Journal of Nanoparticle Research*, **16**(7): 2517-2531.

Sayari, N., Sila, A., Abdelmalek, B. E., Abdallah, R. B., Ellouz-Chaabouni, S., Bougatef, A. and Balti, R. (2016). Chitin and chitosan from the Norway lobster by-products:

Antimicrobial and anti-proliferative activities. *International Journal of Biological Macromolecules*, **87**: 163–171. doi: 10.1016/j.ijbiomac.2016.02.057.

Schaefer, J., Kramer, K.J., Garbow, J.R., Jacob, G.S., Stejskal, E.O., Hopkins, T.L. and Speirs, R.D. (1987). Aromatic cross-links in insect cuticle: detection by solid-state ^{13}C and ^{15}N NMR. *Science*, **235**(4793): 1200-1204.

Schiavone, A., De Marco, M., Martínez, S., Dabbou, S., Renna, M., Madrid, J., Hernandez, F., Rotolo, L., Costa, P. and Gai, F. (2017). Nutritional value of a partially defatted and a highly defatted black soldier fly larvae (Hermetia illucens L.) meal for broiler chickens: Apparent nutrient digestibility, apparent metabolizable energy and apparent ileal amino acid digestibility. *Journal of Animal Science and Biotechnology*, **8**: 51.

Schiffman, J. D. and Schauer, C. L. (2007). Crosslinking chitosan nanofibers. *Biomacromolecules*, **8**(2): 594–601. doi: 10.1021/bm060804s.

Sedaghat, F., Yousefzadi, M., Toiserkani, H. and Najafipour, S. (2017). Bioconversion of shrimp waste *Penaeus merguiensis* using lactic acid fermentation: an alternative procedure for chemical extraction of chitin and chitosan. *International Journal of Biological Macromolecules*, **104**: 883–888. doi: 10.1016/j.ijbiomac.2017.06.099.

Sedghi, R. and Shaabani, A. (2016). Electrospun biocompatible core/shell polymer-free core structure nanofibers with superior antimicrobial potency against multidrug resistance organisms. *Polymer*, **101**: 151-157.

Shahidi, F., Kamil, J., Arachchi, V. and Jeon, Y-J. (1999). Food applications of chitin and chitosans, a review. *Trends in Food Science and Technology*, **10**: 37-51.

Shamim, Z., Saeed, B., Amir, T., Abo Saied, R. and Rogheih, D. (2012). The effect of flow rate on morphology and deposition area of electrospun nylon 6 nanofiber. *Journal of Engineered Fibers and Fabrics*, **7**(4): 42.

Shamsa, E.S., Mahjub, R., Mansoorpour, M., Rafiee-Tehrani, M. and Dorkoosh, F.A. (2018). Nanoparticles prepared from N,N-dimethyl-N-octyl chitosan as the novel approach for oral delivery of insulin: preparation, statistical optimization and *in-vitro* characterization. *Iranian Journal of Pharmaceutical Research*, **17**(2): 442-459.

Sharma, S. (2013). Ferroelectric nanofibers: Principle, processing and applications. *Advanced Materials Letters*, **4**: 522-533.

Sheppard, D. C., Tomberlin, J. K., Joyce, J. A., Kiser, B. C. and Sumner, S. M. (2002). Rearing methods for the Black soldier fly (Diptera: Stratiomyidae). *Journal of Medical Entomology*, **39**(4): 695–698. doi: 10.1603/0022-2585-39.4.695.

Sheppard, D.C., Newton, G.L., Thompson, S.A and Savage, S. (1994). A value added manure management system using the Black soldier fly. *Bioresource Technology*, **50**: 275-279.

Shillito, B., Lechaire, J.P., Goffinet, G. and Gaill, F. (1995). Composition and morphogenesis of the tubes of vestimentiferan worms, in *hydrothermal Vents and Processes,* Parson, L. M., Walker, C. L. and Dixon, D. R. (eds), *Geological Society Special Publication*, **87**: 295-302.

Shirvan, A.R., Shakeri, M. and Bashari, A. (2019). Recent advances in application of chitosan and its derivatives in functional finishing of textiles, In *The impact and prospects of green chemistry for textile technology,* Shahid-ul-Islam and Butola, B.S. (Eds). Elsevier publications. Pg 107-133.

Shushizadeh, M.R., Pour, E.M., Zare, A. and Lashkari, Z. (2015). Persian Gulf β-chitin extraction from S*epia pharaonis* sp. cuttlebone and preparation of its derivatives. *Bioactive Carbohydrates and Dietary Fibre,* **6:**133–142.

Si, Y., Tang, X., Yu, J. and Ding, B. (2014). Electrospun nanofibers: solving global issues. In Ding, B. and Yu, J. (Eds.), Electrospun nanofibers for energy and environmental applications. Springer, New York. ISBN 978-3-642-54160-5.

Silva, N. C., Silva, S., Sarmento, B. and Pintado, M. (2015). Chitosan nanoparticles for daptomycin delivery in ocular treatment of bacterial endophthalmitis. *Drug Delivery*, **22**(7): 885–893.

Sionkowska, A., Kaczmarek, B., Gnatowska, M. and Kowalonek, J. (2015). The influence of UV irradiation on chitosan modified by the tannic acid addition. *Journal of. Photochemical. Photobiology B*, **148**: 333–339.

Skołucka-Szary, K., Ramięga, A., Piaskowska, W., Janicki, B., Grala, M., Rieske, P., Bartczakc, Z. and Piaskowski, S. (2016). Synthesis and physicochemical characterization of chitin dihexanoate; A new biocompatible chitin derivative in comparison to chitin dibutyrate. *Materials Science and Engineering*, **60:** 489–502.

Song, C., Yu, H., Zhang, M., Yang, Y. and Zhang, G. (2013). Physicochemical properties and antioxidant activity of chitosan from the blowfly *Chrysomya megacephala* larvae. *International Journal of Biological Macromolecules* **60**: 347– 354.

Song, J.H., Kim, Y.T., Cho, S., Song, W.J., Moon, S., Park, C.G., Park, S., Myoung, J.M. and Jeong, U. (2017). Surface-embedded stretchable electrodes by direct printing and their uses to fabricate ultrathin vibration sensors and circuits for 3D structures. *Advanced Materials,* **29:** 1702625.

Soon, C. Y., Tee, Y. B., Tan, C. H., Rosnita, A. T. and Khalina, A. (2018). Extraction and physicochemical characterization of chitin and chitosan from Zophobas morio larvae in varying sodium hydroxide concentration. *International Journal of Biological Macromolecules*, **108**: 135-142. doi: 10.1016/j.ijbiomac.2017.11.138.

Soppimath, K. S., Aminabhavi, T. M., Kulkarni, A. R., and Rudzinski, W. E. (2001). Biodegradable polymeric nanoparticles as drug delivery devices. *Journal of Controlled Release*, **70**(1): 1-20.

Sreekumar, S., Goycoolea, F.M., Moerschbacher, B.M. and Rivera-Rodriguez, G.R. (2018). Parameters influencing the size of chitosan-TPP nano- and microparticles. *Scientific Report*, **8**: 4695.

Sripontan, Y., Juntavimon, T., Songin, S. and Chiu, C.-I. (2017). Egg-trapping of black soldier fly, Hermetia illucens (L.) (Diptera : Stratiomyidae) with various wastes and the effects of environmental factors. *Khon Kaen Agriculture Journal*, **45**(1): 179–184.

Stawski, D., Rabiej, S., Herczyńska, L. and Draczyński, Z. (2008). Thermogravimetric analysis of chitins of different origin. *Journal of Thermal Analysis and Calorimetry***, 93**(2): 489–494. doi: 10.1007/s10973-007-8691-6.

Steiner, G. and Koch, E. (2009). Trends in Fourier transform infrared spectroscopic imaging. *Analytical and Bioanalytical Chemistry*, **394**: 671–678.

Su, C.-H., Nguyen, H. C., Bui, T. L. and Huang, D.-L. (2019). Enzyme-assisted extraction of insect fat for biodiesel production. *Journal of Cleaner Production,* **223**: 436-444. doi: 10.1016/j.jclepro.2019.03.150.

Su, F., Xu, H., Yang, N., Wei Liu, W. and Liu, J. (2018). Hydrolytic efficiency and isomerization during de-esterification of natural astaxanthin esters by saponification and enzymolysis. *Electronic Journal of Biotechnology*, **34**: 37–42.

Su, P., Wang, C., Yang, X., Chen, X., Gao, C., Feng, X.-X., Chen, J-Y., Ye, J. and Gou, Z. (2011). Electrospinning of chitosan nanofibers: The favorable effect of metal ions. *Carbohydrate Polymers*, **84**(1): 239–246. doi: 10.1016/j.carbpol.2010.11.031.

Subbiah, T., Bhat, G.S., Tock, R.W., Parameswaran, S. and Ramkumar, S.S. (2005). Electrospinning of nanofibers. *Journal of Applied Polymer Science*, **96**(2): 557–569. doi:10.1002/app.21481.

Suneeta, K., Rath, P. and Sri, H. K. A. (2016). Chitosan from shrimp shell (Crangon crangon) and fish scales (Labeorohita): Extraction and characterization. *African Journal of Biotechnology*, **15**(24): 1258–1268. doi: 10.5897/AJB2015.15138.

Sung, H.W., Liang, I.L., Chen, C.N., Huang, R.N. and Liang, H.F. (2001). Stability of a biological tissue fixed with a naturally occurring crosslinking agent (genipin). *Journal of Biomedical Materials Research*, **55**(4): 538–546.

Synowiecki, J. and Al-Khateeb, N.A. (2003). Production, properties, and some new applications of chitin and its derivatives. *Critical Reviews in Food Science and Nutrition*, **43**(2): 145–171.

Szymańska, E. and Winnicka, K. (2015). Stability of chitosan - a challenge for pharmaceutical and biomedical applications. *Marine Drugs*, **13**: 1819–1846.

Tajik, H., Moradi, M., Rohani, S., Erfani, A. and Jalali, F. (2008). Preparation of chitosan from brine shrimp (Artemia urmiana) cyst shells and effects of different chemical processing sequences on the physicochemical and functional properties of the product. *Molecules*, **13**(6): 1263–1274.

Talebi, M., Abbasizadeh, S. and Keshtkar, A.R. (2017). Evaluation of single and simultaneous thorium and uranium sorption from water systems by an electrospun PVA/SA/PEO/HZSM5 nanofiber. *Process Safety and Environmental Protection*, **109**: 340–356.

Tanner, S.F., Chanzy, H., Vincendon, M., Roux, J.C. and Gaill, F. (1990). High-resolution solid-state carbon-13 nuclear magnetic resonance study of chitin. *Macromolecules*, **23**(15): 3576-3583.

Tayel, A. A., Moussa, S., Wael, F., Knittel, D., Opwis, K. and Schollmeyer, E. (2010). Anticandidal action of fungal chitosan against *Candida albicans*. *International Journal of Biological Macromolecules*, **47**(4): 454-457.

Taylor, G.I. (1969). Electrically driven jets. *Proceedings of the Royal Society A: Mathematical, Physical and Engineering Sciences*, (1934–1990), **313:** 453-475.

Tchobanian, A., Van Oosterwyck, H. and Fardim, P. (2019). Polysaccharides for tissue engineering: current landscape and future prospects. *Carbohydrate Polymers*, **205**: 601-625.

Teli, M. D. and Sheikh, J. (2012). Extraction of chitosan from shrimp shells waste and application in antibacterial finishing of bamboo rayon. *International Journal of Biological Macromolecules*, **50**(5), 1195–1200. doi: 10.1016/j.ijbiomac.2012.04.003.

Teng, D. (2012): From chitin to chitosan. In: *Chitosan-based hydrogels*; functions and applications, CRC Press, New York Pg 1-38.

Theron, S., Zussman, E. and Yarin, A. (2004). Experimental investigation of the governing parameters in the electrospinning of polymer solutions. *Polymer*, **45**(6): 2017-2030.

Tianguo, L., Niu, T., Huang, S., Du, G., Li, B., Zhan, F., Jiang, M. and He, Y. (2018). Effects of xanthate modified chitosan on the adsorption of lead ions. *IOP Conference. Series: Earth and Environmental Science,* **199**: 42-47. doi: 10.1088/1755-1315/199/4/042047.

Tiwari, A., Terada, D., Yoshikawa, C. and Kobayashi, H. (2010). An enzyme-free highly glucose-specific assay using self-assembled aminobenzene boronic acid upon polyelectrolytes electrospun nanofibers-mat. *Talanta*, **82:** 1725–1732.

Tiwari, S. K. and Venkatraman, S. S. (2012). Importance of viscosity parameters in electrospinning: Of monolithic and core–shell fibers. *Materials Science and Engineering: C,* **32**(5): 1037–1042. doi: 10.1016/j.msec.2012.02.019.

Tomberlin, J. K., Adler, P. H., and Myers, H. M. (2009). Development of the Black soldier fly (Diptera: Stratiomyidae) in relation to temperature. *Environmental Entomology*, **38**(3): 930 - 934.

Tomberlin, J. K., Sheppard, D. C. and Joyce, J. A. (2005). Black soldier fly (Diptera: Stratiomyidae) colonization of pig carrion in south Georgia. *Journal of Forensic Sciences,* **50**(1): 152–153.

Torres-Giner, S., Ocio, M.J. and Lagaron, J.M. (2008). Development of active antimicrobial fiber based chitosan polysaccharide nanostructures using electrospinning. *Engineering In Life Sciences*, **8**(3): 303–314.

Tran, H. V., Tran, L. D., and Nguyen, T. N. (2010). Preparation of chitosan/magnetite composite beads and their application for removal of Pb(II) and Ni(II) from aqueous solution. *Materials Science and Engineering C,* **30**: 304–310.

Trutnau, M., Bley, T. and Ondruschka, J. (2011). Chitosan from fungi. In: *Chitosan: manufacture, properties and usage.* Davies, S.P. (Ed.), Nova Science Publishers Inc, New York, pg 1 – 70.

Unal, B., Kirbay, F. O., Yezer, I., Demirkol, D. O. and Timur, S. (2019). Electrospun nanofibers: functional and attractive materials for the sensing and separation approaches in analytical chemistry. *Recent Advances in Analytical Techniques*, **3**(3): 134-178.

Uzoije, A.P., Uche, C.C. and Ashiegbu, D. (2014). Analysis of thermodynamics, kinetics and equilibrium isotherm on Fe^{3+}/Fe^{2+} adsorption onto palm kernel shell activated carbon (PKSAC): a low-cost adsorbent, *American Chemical Science Journal,* **4**(3): 298-325.

van Huis, A., Van Itterbeeck., J., Klunder, H., Mertens, E., Halloran, A., Muir, G. and Vantomme, P. (2013). Potential of insects as food and feed in assuring food security.

Annual Review of Entomology, **58**(1): 563–583. doi: 10.1146/annurev-ento-120811-153704.

Venugopal, J. and Ramakrishna, S. (2005). Applications of polymer nanofibers in biomedicine and biotechnology. *Applied Biochemistry and Biotechnology*, **125:** 147–157.

Vihola, H., Laukkanen, A., Tenhu, H. and Hirvonen, J. (2008). Drug release characteristics of physically crosslinked thermosensitive poly(N-vinylcaprolactam) hydrogel particles. *Journal of Pharmaceutical Sciences,* **97(**11): 4783–4793. doi: 10.1002/jps.21348.

Vilar Junior, J. C., Ribeaux, D. R., Alves da Silva, C. A. and De Campos-Takaki, G. M. (2016). Physicochemical and antibacterial properties of chitosan extracted from waste shrimp shells. *International Journal of Microbiology,* **5127515,** 1–7. doi: 10.1155/2016/5127515.

Wang, C., Wang, J., Zeng, L., Qiao, Z., Liu, X., Liu, H., Zhang, J. and Ding, J. (2019). Fabrication of electrospun polymer nanofibers with diverse morphologies. *Molecules,* **24**(5): 834. doi: 10.3390/molecules24050834.

Wang, C., Lee, M. and Wu, Y. (2012). Solution-electrospun poly (ethylene terephthalate) fibers: processing and characterization. *Macromolecules,* **45**(19): 7939-7947.

Wang, X. and Hsiao, B. S. (2016). Electrospun nanofiber membranes. *Current Opinion in Chemical Engineering*, **12**: 62–81. doi: 10.1016/j.coche.2016.03.001.

Wang, Y., Chang, Y., Yu, L., Zhang, C., Xu, X., Xue, Y., Li, Z. and Xue, C. (2013). Crystalline structure and thermal property characterization of chitin from Antarctic krill (*Euphausia superba*). *Carbohydrate Polymers*, **92**: 90–97. doi: 10.1016/j.carbpol.2012.09.084.

Wang, Y.S. and Shelomi, M. (2017). Review of Black soldier fly (Hermetia illucens) as animal feed and human food. *Foods*, **6**(10): 91. doi: 10.3390/foods6100091.

Waśko, A., Bulak, P., Polak-Berecka, M., Nowak, K., Polakowski, C. and Bieganowski, P. (2016). The first report of the physicochemical structure of chitin isolated from Hermetia illucens. *International Journal of Biological Macromolecules*, **92**: 316-320.

Wu, R.-X., Zheng, G.-F., Li, W.-W., Zhong, L.-B. and Zheng, Y.-M. (2018). Electrospun chitosan nanofiber membrane for adsorption of Cu(II) from aqueous solution: fabrication, characterization and performance. *Journal of Nanoscience and Nanotechnology,* **18**(8): 5624–5635. doi: 10.1166/jnn.2018.15433.

Wysokowski, M., Bazhenov, V.V., Tsurkan, M.V., Galli, R., Stelling, A.L., Stöcker, H., Kaiser, S., Niederschlag, E., Gärtner, G., Behm, T., Ilan, M., Petrenko, A.Y., Jesionowski, T., and Ehrlich, H. (2013). Isolation and identification of chitin in three-

dimensional skeleton of *Aplysina fistularis* marine sponge. *International Journal of Biological Macromolecules*, **62:** 94–100.

Xue, J., Wu, T., Dai, Y. and Xia, Y. (2019). Electrospinning and electrospun nanofibers: methods, materials, and applications. *Chemical Reviews*, **119**(8): 5298–5415. doi: 10.1021/acs.chemrev.8b00593.

Yang, J., Bai, J., Liu, M., Chen, Y., Wang, S. and Yang, Q. (2018). Determination of phosphorus in soil by ICP-OES using an improved standard addition method. *Journal of Analytical Methods in Chemistry*, **1324751:** 1–8. doi: 10.1155/2018/1324751.

Yao, P., Li, P., Jiang, J. and Li, Hy. (2018). Anastomotic stoma coated with chitosan film as a betamethasone dipropionate carrier for peripheral nerve regeneration. *Neural Regeneration Research*, **13**(2)**:** 309-316. doi: 10.4103/1673-5374.226401.

Yen, M. T. and Mau, J. L. (2007). Physicochemical characterization of fungal chitosan from shiitake stipes. *Lwt-Food Science and Technology*, **40**(3): 472-479.

Yen, M. T., Yang, J. H. and Mau, J. L. (2009). Physicochemical characterization of chitin and chitosan from crab shells. *Carbohydrate Polymers*, **75(**1): 15–21.

Yeul, V. S. and Rayalu, S. S. (2013). Unprecedented chitin and chitosan : A chemical overview, pp. 606–614. doi: 10.1007/s10924-012-0458-x.

Yien, L., Zin, N. M., Sarwar, A., and Katas, H. (2012). Antifungal activity of chitosan nanoparticles and correlation with their physical properties. *International Journal of Biomaterials*, 2012: 1-9.

Younes, I. and Rinaudo, M. (2015). Chitin and chitosan preparation from marine sources; structure, properties and applications. *Marine Drugs*, **13**(3): 1133–1174. doi: 10.3390/md13031133.

Younes, I., Sellimi, S., Rinaudo, M., Jellouli, K. and Nasri, M. (2014). Influence of acetylation degree and molecular weight of homogeneous chitosans on antibacterial and antifungal activities. *International Journal of Food Microbiology*, **185**: 57-63.

Younes, I., Hajji, S., Rinaudo, M., Chaabouni, M., Jellouli, K. and Nasri, M. (2016). Optimization of proteins and minerals removal from shrimp shells to produce highly acetylated chitin. *International Journal of Biological Macromolecules*, **84**: 246–253. doi: 10.1016/j.ijbiomac.2015.08.034.

Yuan, X., Zhang, Y., Dong, C. and Sheng, J. (2004). Morphology of ultrafine polysulfone fibers prepared by electrospinning. *Polymer International*, **53**(11): 1704–1710. doi: 10.1002/pi.1538.

Zamani, A., Edebo, L., Sjöström, B. and Taherzadeh, M.J. (2007). Extraction and precipitation of chitosan from cell wall of Zygomycetes fungi by dilute sulphuric acid. *Biomacromolecules*, **8**: 3786-3790.

Zamani, A. and Taberzadeh, M.J. (2010). Production of low molecular weight chitosan by hot dilute sulphuric acid. *Bioresources*, **5**(3): 1554-1564.

Zhang, L., Zeng, Y. and Cheng, Z. (2016). Removal of heavy metal ions using chitosan and modified chitosan: A review. *Journal of Molecular Liquids*, **214**: 175–191. doi: 10.1016/j.molliq.2015.12.013.

Zhang, S. and Kawakami, K. (2010). One-step preparation of chitosan solid nanoparticles by electrospray deposition. *International Journal of Pharmaceutics*, **397**(1-2): 211–217. doi: 10.1016/j.ijpharm.2010.07.007.

Zhang, S., Sun, X. and Liu, D. (2015). Preparation of (3R, 3′R)-astaxanthin monoester and (3R, 3′R)- astaxanthin from Antarctic krill (*Euphausia superba Dana*). *European Food Research and Technology*, **240**(2): 295–299.

Zhang, X., Shi, X., Ma, L., Pang, X. and Li, L. (2019). Preparation of chitosan stacking membranes for adsorption of copper ions. *Polymers*, **11:** 1463. doi: 10.3390/polym11091463.

Zhao, F., Repo, E., Yin, D. and Sillanpaa, M.E. (2013). Adsorption of Cd(II) and Pb(II) by a novel EGTA-modified chitosan material: kinetics and isotherms. *Journal of Colloids and Interface Science*, **409**:174–182. doi: 10.1016/j.jcis.2013.07.062.

Zhao, Y. and Sun, Z. (2017). Effects of gelatin-polyphenol and gelatin–genipin cross-linking on the structure of gelatin hydrogels. *International Journal of Food Properties*, **20**: 2822-2832. doi: 10.1080/10942912.2017.1381111.

Zheng, L.Y., and Zhu, J.F. (2003). Study on antimicrobial activity of chitosan with different molecular weights. *Carbohydrate Polymers*, **54**(4): 527-530.

Zhu, K. Y., Merzendorfer, H., Zhang, W., Zhang, J. and Muthukrishnan, S. (2016). Biosynthesis, turnover, and functions of chitin in insects. *Annual Review of Entomology*, **61**(1): 177–196. doi: 10.1146/annurev-ento-010715-023933.

Zhu, Y., Hu, J. and Wang, J. (2012). Competitive adsorption of Pb(II), Cu(II) and Zn(II) onto xanthate-modified magnetic chitosan. *Journal of Hazardous Materials*, **221-222**: 155–161.

Zhu, Z., Rehman, K., Yu, Y., Liu, X., Wang, H., Tomberlin, J.K., Sze, S., Cai, M., Zhang, J., Yu, Z., Zheng, J. and Zheng, L. (2019). De novo transcriptome sequencing and analysis revealed the molecular basis of rapid fat accumulation by Black soldier fly (*Hermetia*

illucens, L.) for development of insectival biodiesel. *Biotechnology for Biofuels*, **12:**194. doi: 10.1186/s13068-019-1531-7.

Zong, X., Kim, K., Fang, D., Ran, S., Hsiao, B.S. and Chu, B. (2002). Structure and process relationship of electrospun bioadsorbable nanofiber membrane. *Polymer*, **439**: 4403–4412.

Zuber, M., Zia, K.M. and Barikani, N. (2013). Chitin and chitosan based blends, composites and nanocomposites. In Thomas, S., Visakh, P. and Mathew, A. (Eds.) Advances in Natural Polymers. Advanced Structured Materials, Vol 18. Springer, Berlin, Heidelberg. pp 55-119.